EDITED and PUBLISHED *quarterly at the* offices of The American Society of Mechanical Engineers, United Engineering Center, 345 E. 47th St., New York, N. Y. 10017. Cable address, "Mechaneer," New York. Second-class postage paid at New York, N. Y., and at additional mailing offices.
CHANGES OF ADDRESS must be received at Society headquarters seven weeks before they are to be effective. Please send old label and new address.
PRICES: To members, $25.00, annually; to nonmembers, $50.00. Single copies, $15.00 each. Add $1.50 for postage to countries outside the United States and Canada.

INDEXED by the Engineering Index, Inc.

transactions of the ASME

Published Quarterly by
The American Society of
Mechanical Engineers
Volume 100 • Number 4
NOVEMBER 1978

journal of heat transfer

(Contents continued on page 571)

TECHNICAL NOTES

ERRATUM

ANNOUNCEMENTS

B. E. Launder
University of California, Davis
Davis, CA

T. H. Massey
CERL,
Leatherhead, England

The Numerical Prediction of Viscous Flow and Heat Transfer in Tube Banks

A scheme for handling the numerical analysis of viscous flow and heat transfer in tube banks is presented. It involves the use of a cylindrical network of nodes in the vicinity of the tubes with a Cartesian mesh covering the remainder of the flow domain. The approach has been incorporated into the numerical solving algorithm for the Navier Stokes equations of Gosman, et al. [8]. A number of demonstration calculations is presented including a numerical simulation of the staggered square bank for which Bergelin and co-workers [4, 9] have reported experimental results for pressure drop and heat transfer rate. Agreement between predicted and measured characteristics is satisfactory when account is taken of end and entry effects that are present in the experiments but necessarily omitted from the calculations. Indeed the close agreement of the laminar predictions with measurements extends to Reynolds numbers in excess of 1000, a level at which it has hitherto been supposed that turbulent motion in the fluid made a substantial contribution to friction and heat transfer.

1 Introduction

The study of flow normal to a bank of tubes continues to attract interest because of the importance of this flow configuration in the design of heat exchangers. The traditional way of obtaining the desired flow and heat-transfer information is to build a scale model of the tube bank under consideration. Hot gases are blown over the tubes and cooling fluid is circulated within them so that measurements can be made and there from correlations built up of the variations of the dimensionless heat transfer coefficients and pressure losses with Reynolds number and geometry. A comprehensive account of such studies and an excellent compendium of experimental data up to 1970 is provided by Zhukauskas [1].

This approach is expensive, however, since for each new geometry considered a new model must be constructed. An alternative approach to securing data on the performance of tube banks is that of direct numerical solution of the time-averaged, partial-differential equations of momentum, mass and energy. In a typical two-dimensional recirculating flow of reasonably *simple* geometry such predictions may be obtained in about two minute central processor time per run for a CDC 6600 computer; the cost of such an exploration is usually a small fraction of the cost of obtaining only the *mean* coefficients by experiment. An obstacle to the use of numerical methods in tube-bank problems, however, has been the complex geometry. Pioneering work by Thom and Apelt [2] employed conformal mapping so that the boundaries of the tubes coincided with equi-value surfaces of one of the independent variables. As is clear from Fig. 1(*a*), however, this transformation produces a low density of grid lines precisely where accurate numerical solution demands a fine grid, i.e., in the region of the front and rear stagnation points of the cylinder. Later work by Le Clair and Hamielec [3] assumed that each tube within the bank could be treated as an isolated cylinder surrounded by an outer boundary (at a distance related to the pitching of the bank) on which were imposed free-stream boundary conditions. This approach, however, required such a simplistic treatment of the flow geometry that it is hard to envisage it producing useful results. Indeed, differences with the laminar flow data of Bergelin, et al. [4] of up to 40 percent were reported.

The present contribution reports the writers' work in developing a general and flexible numerical procedure for predicting the behavior of flow over tube banks. In the present paper attention is limited to laminar flows in the fully developed regime (a companion paper on the treatment of turbulent flow is in preparation). Here the main points of novelty concern the development of a satisfactory and economical grid on which to perform the numerical solutions; this is discussed in Section 2. The same section presents the conservation equation governing the problem together with the appropriate boundary conditions while Section 3 presents and discusses the numerical results.

2 The Finite-Difference Calculation Method

a. The Choice of Grid and Coordinates. The main deterrent to a numerical study of the tube-bank problem is the complex shape of the flow domain—especially for staggered matrices of tubes.

Contributed by the Heat Transfer Division for publication in the JOURNAL OF HEAT TRANSFER. Manuscript received by the Heat Transfer Division February 10, 1978.

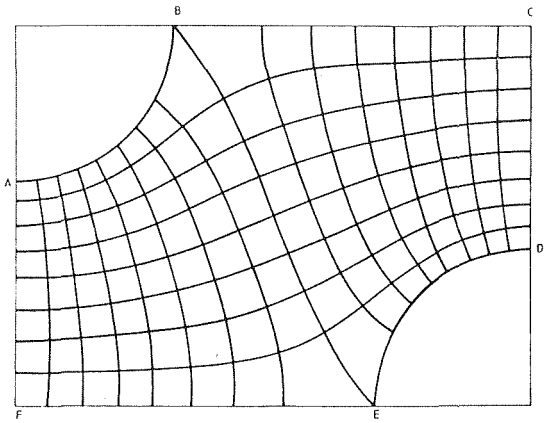

Fig. 1(*a*) Thom and Apelt [2]

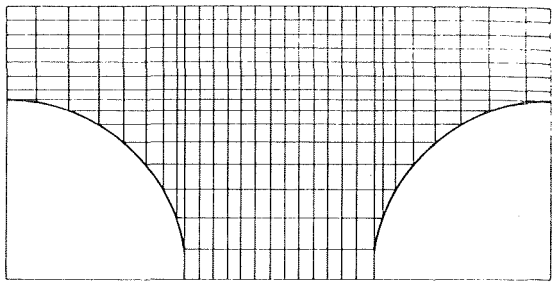

Fig. 1(*b*) Le Feuvre

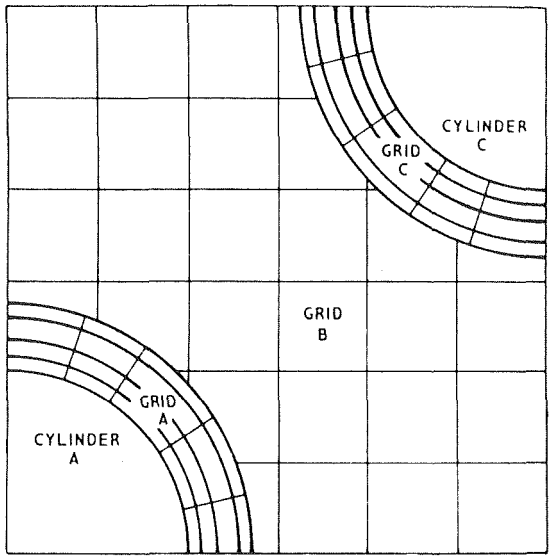

Fig. 1(*c*) Present study

Fig. 1 Possible choices of grid for finite-difference study of tube banks

Strictly there is no *necessity* for any of the grid nodes to lie on the surface of the tube. A uniform Cartesian grid could in principle be adopted and, indeed, is often adopted in heat-conduction problems. In convection studies, however, particularly for turbulent flow, there are compelling advantages to making all rigid surfaces coincide with a surface on which one of the coordinates is uniform. In Thom and Apelt's [2] pioneering work on the tube-bank problem the grid was generated by solving the Laplace equation for the flow domain with uniform but different potentials maintained on the two quarter cylinders. The resultant grid, shown in Fig. 1(*a*) had two main disadvantages. First, the density of grid nodes was least in the vicinity of the forward and rear stagnation points—precisely in regions where a *high* node density is necessary to secure grid-independent results. Secondly, the governing differential equations, expressed in terms of the new coordinates, are more complex than in Cartesian coordinates. In the only other numerical work we know of on flow in tube banks Le Feuvre [5] adopted a Cartesian grid in which the spacing between nodes was adjusted so that all the near-wall nodes fell on the cylindrical surfaces an indicated in Fig. 1(*b*). This grid, which had been earlier adopted by Thoman and Szewczyk [6] to study flow about a single cylinder, thus retained the simple form of the convective flow equations. It is clear from Fig. 1(*b*), however, that the grid is far from ideal since it produces high densities of nodes in regions far from the wall where they are not needed. Le Feuvre also found that it was particularly susceptible to false diffusion due to the streamlines near the cylinder cutting diagonally across the grid.

Close to each cylinder the steepest gradients of flow properties are in the radial direction. This suggested to us the desirability of adopting a cylindrical polar grid in the neighborhood of the cylinders. The region between these two grids was filled with a Cartesian mesh as indicated in Fig. 1(*c*). The final structure adopted allowed the cylindrical and Cartesian grids to be entirely independent of one another. A false row of nodes was introduced to both the Cartesian and the polar grids in the region of overlap as indicated in Fig. 2 to provide

Nomenclature

D = diameter of cylinder
f = friction factor $\Delta p/2\rho V_m N^2$
$\underline{G}$ = mass velocity vector
N = number of rows in tube bank
Nu = local Nusselt number
p = static pressure
P = nondimensional pressure coefficient $(p_0 - p_w)/2\rho V_m{}^2$
p_L = x-direction distance between one row and next
P_T = y-direction distance between one row and next
r = radial coordinate
Re = Reynolds number, $\rho V_m D/\mu$
St = mean Stanton number
T = fluid temperature
V_m = mean velocity through section of minimum area in bank
V_r = radial velocity component
V_x = x-direction velocity component
V_y = y-direction velocity component
V_θ = circumferential velocity component
x = Cartesian coordinate in mean flow direction
y = Cartesian coordinate
$\overline{\alpha}$ = mean heat transfer coefficient
ΔP = drop in static pressure in passing through bank
θ = circumferential (angle) coordinate
μ = dynamic fluid viscosity
ρ = density
σ = Prandtl number
ϕ = a representative dependent variable
ψ = stream function defined by equation (3) or (4)
ω = vorticity component parallel to tube axis

Subscripts

B = bulk fluid value
NE, NW, SE, SW = compass point location of nodes with respect to node p
nw = node adjacent to wall
p = particular grid node under study
w = wall value

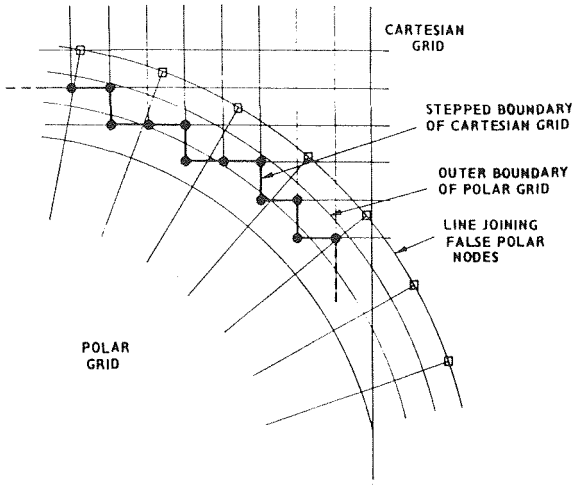

Fig. 2 Use of false nodes for interpolating between polar and Cartesian grids

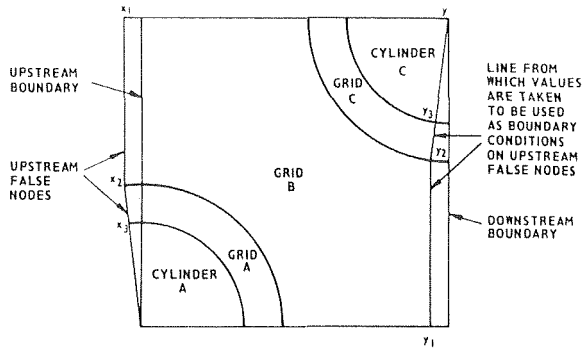

Fig. 3 Periodic boundary conditions for a staggered tube bank

a connection between the cylindrical and polar regions.[1] The values of the dependent variables are transferred between the polar and Cartesian grid regions as described in the following section.

b. The Describing Equations. The mean flow field in the tube bank may be described in terms of the two-dimensional vorticity equation:

$$\text{div}\,(\underline{G}\,\omega) = \text{div}\,(\text{grad}(\mu\,\omega)) \tag{1}$$

and one of the following stream function equations

$$\frac{\partial}{\partial r}\left(\frac{r}{\rho}\frac{\partial \psi}{\partial r}\right) + \frac{\partial}{\partial \theta}\left(\frac{1}{\rho r}\frac{\partial \psi}{\partial \theta}\right) = -r\omega \tag{2a}$$

$$\frac{1}{\rho}\frac{\partial^2 \psi}{\partial x^2} + \frac{1}{\rho}\frac{\partial^2 \psi}{\partial y^2} = -\omega \tag{2b}$$

according to whether the flow region is being analyzed in cylindrical polar or Cartesian coordinates. The stream function and vorticity are related to the velocity components in the plane normal to the tube axis by

$$\omega = \frac{1}{r}\left(\frac{\partial}{\partial r}(rV_\theta) - \frac{\partial V_r}{\partial \theta}\right)$$

$$V_r = \frac{1}{\rho r}\frac{\partial \psi}{\partial \theta};\; V_\theta = -\frac{1}{\rho}\frac{\partial \psi}{\partial r} \tag{3}$$

or, in Cartesian coordinates:

$$\omega = \frac{\partial V_y}{\partial x} - \frac{\partial V_x}{\partial y}$$

$$V_x = \frac{1}{\rho}\frac{\partial \psi}{\partial y};\; V_y = -\frac{1}{\rho}\frac{\partial \psi}{\partial x} \tag{4}$$

Attention is limited to cases where the contribution of mean kinetic energy and shear work to the energy balance is negligible and where the thermophysical properties are uniform. In these circumstances the temperature level in the tube bank is governed by the following enthalpy transport equation:

$$\text{div}\,(\underline{G}\,T) = \text{div}\left(\frac{\mu}{\sigma}\,\text{grad}\,T\right) \tag{5}$$

[1] Several other schemes for connection between the cylindrical and Cartesian and polar regions were explored before this method was evolved. All the schemes, which are reviewed in Massey's thesis [7], required at least twice as much computer time as the one finally adopted due to the uneconomic distribution of grid nodes that they produced.

Equations (1, 2), and (5) have been solved numerically using the general finite-difference procedure of Gosman, et al. [8]. This method is so widely known that only its main features will be mentioned. Discretized forms of equations (1, 2), and (5) are obtained by integrating the conservation equations over contiguous control volumes surrounding each node. The method was developed by its originators for arbitrary orthogonal coordinates, a feature which makes it particularly attractive in the present case where different coordinate systems are used in different regions. One merely needs to assign the metric coefficients according to the coordinate system appropriate to the region. The finite-difference procedure adopts an 'upwind' treatment of the convective terms and the difference equations are solved iteratively by a point-by-point Gauss-Siedel procedure.

c. Boundary Conditions. The describing equations are elliptic requiring boundary conditions to be prescribed around all boundaries. Four types of boundary are present which are handled as follows.

Symmetry Planes. On the lower and upper symmetry of the solution domain the stream function is respectively set equal to zero and to a uniform value (which corresponds to the mean flow rate per unit length of tube). The vorticity and the gradient of the temperature normal to the symmetry planes are both set to zero.

Inlet and Outlet Plane. The present study has limited attention to *fully-developed* flow in a tube bank, i.e., the situation where the flow pattern is exactly repeated from one row to the next. In practice this repetitive pattern is found to develop after about seven rows of tubes so, in a bank consisting of 50 rows, the fully-developed model is clearly a reasonable one from which to deduce the performance of real tube banks. Fig. 3 illustrates the salient features of the periodic boundary-condition treatment. The method relies on a column of false nodes on the upstream side of the flow; one in the Cartesian grid and one in the leading polar grid. For fully-developed flow the values of the dependent variables will be the same on the line of false nodes $x_1x_2x_3$ as on the line $y_1y_2y_3$ located at the same distance upstream of the downstream boundary as $x_1x_2x_3$ is of the upstream boundary. At the end of each cycle the values on $y_1y_2y_3$ are transferred to $x_1x_2x_3$. Likewise values of the dependent variables are taken from the upstream boundary and placed on the downstream boundary to serve as boundary conditions during the next cycle of iteration.

In the case of the temperature, the scheme described above is modified to account for the fact that due to heat transfer from the cylinder the inlet and exit temperatures are not exactly the same. A uniform heat flux is applied at the tube surfaces and thus to each temperature one either adds or subtracts the mean temperature rise across the solution domain according to whether one is transferring information forward or backward.

Intersections between Polar and Cartesian Grids. The values of the dependent variables on the false polar nodes are obtained by interpolation from the four surrounding nodes as indicated in Fig. 4(*a*). Referring to the notation on this figure, the value of any dependent variable ϕ is obtained as

$$\phi_p = [(\phi_{NE}x_1 + \phi_{NW}x_2)y_1 + (\phi_{SE}x_1 + \phi_{SW}x_2)y_2]/[(x_1 + x_2)\,(y_1 + y_2)] \tag{6}$$

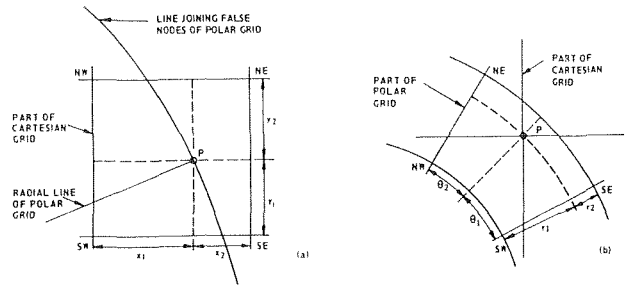

Fig. 4 Notation for linear-interpolation scheme for false nodes (a) polar nodes, (b) Cartesian nodes

Correspondingly, values at the Cartesian false nodes are obtained from Fig. 4(*b*) as

$$\phi_p = [(\phi_{NE} r_1 + \phi_{NW} r_2)\theta_1 + (\phi_{SE} r_1 + \phi_{SW} r_2)\theta_2]/[(\theta_1 + \theta_2)(r_1 + r_2)] \quad (7)$$

It will be noted that equations (6) and (7) weight the importance of the four surrounding nodes inversely with distance from the false node.

Cylinder Surfaces. The value of the stream function is uniform around the cylinders, corresponding with an impermeable wall. Its value is the same as long the adjacent symmetry planes.

The vorticity is not quite so easily handled since its magnitude depends on the mean velocity gradients at the wall, which are unknown until the end of the calculation. In effect a formula for wall vorticity is obtained by solving simultaneously equations (1) and (2) neglecting convective transport and circumferential diffusion, approximations which are permissible in the immediate vicinity of the surface. Straightforward algebra leads to:

$$\omega_w = \left[\frac{\omega_{nw} r_w \alpha}{r_{nw} - r_w} - \frac{\psi_{nw} - \psi_w}{\rho}\right] \Big/ \left(\frac{\alpha r_w}{(r_{nw} - r_w)} - B\right) \quad (8)$$

where

$$\alpha \equiv \frac{1}{4}((r_{nw}^2 + r_w^2) \ln r_{nw}/r_w - (r_{nw}^2 - r_w^2))$$

$$\beta \equiv \frac{1}{4}((r_{nw}^2 - r_w^2) - 2r_w^2 \ln r_{nw}/r_w)$$

Finally, as mentioned above, the thermal boundary condition applied in the present tests is that of a uniform heat flux around the perimeter of the cylinder.

d. Miscellaneous Matters. The first series of tests of the numerical procedure was aimed at determining the best relative size of the polar and Cartesian grids and the node density in each region. Our criterion for best was the arrangement allowing sensibly grid-independent predictions with the smallest number of active nodes. Of course the optimum arrangement may well differ according to the pitch: diameter ratios of the tube bank and Reynolds number. It was impractical to explore such dependences however; all grid-exploration studies were made for downstream and cross-stream pitches of 1.5:1 and 3.0:1 respectively at a Reynolds number of 75. It emerged that the polar grids should be confined to the region close to the cylinders extending only about $0.35r_w$ from the surface. It was found that a higher node density was needed in these polar regions because of the increasingly steep variation of the independent variables as the cylinders were approached. Moreover, a finer grid was needed for polar grid A (covering the downstream half of a cylinder) than for grid C (covering the upstream half); the reason appeared to be connected with resolving accurately the separation point on the downstream side. Flow indicators except the length of the trailing vortex became sensibly grid independent for grid $A = 11 \times 16$ (radial and circumferential), grid $B = 26 \times 26$ and grid $C = 11 \times 11$. As the grid was further refined the separation vortex increased in length until it too became grid independent for grid $A = 11 \times 31$, grid $B = 41 \times 41$ and grid $C = 11 \times 11$ (1717 active nodes). The streamline patterns predicted with the two grids are shown in Fig. 5.

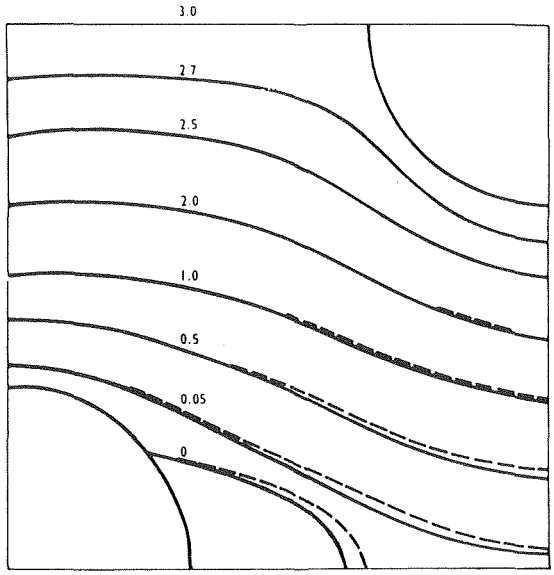

Fig. 5 Stream function contours in square staggered bank P_L:P_T = 1.5:3; Re = 75 showing effects of grid refinement: ——828 active nodes, - - - 1727 active nodes

A disadvantage of solving the flow field through the stream-function and vorticity equations is that the pressure distribution, if needed, must be recovered from the converged stream-function and vorticity fields. For a tube bank the pressure drop per row ΔP is one of the most important quantities to be predicted. Although the *general* equations to recover the pressure field are rather complicated ΔP can be easily obtained as follows. Along the symmetry planes of the flow

$$\rho \frac{\partial p}{\partial x} = -\frac{1}{2}\frac{\partial}{\partial x}\left[\left(\frac{\partial \psi}{\partial y}\right)^2\right] - \rho\mu \frac{\partial \omega}{\partial y} \quad (9a)$$

$$\rho \frac{\partial p}{\partial r} = -\frac{1}{2}\frac{\partial}{\partial r}\left[\left(\frac{1}{r^2}\left(\frac{\partial \psi}{\partial \theta}\right)^2\right] - \frac{\rho\mu}{r}\frac{\partial \omega}{\partial \theta} \quad (9b)$$

while around the surface of the cylinders

$$\frac{\partial p}{\partial \theta} = \mu r \frac{\partial \omega}{\partial r} \quad (10)$$

Integration of (9) or (10) as appropriate begins at point A in Fig. 6 and proceeds along BCD. A transfer is then made to E (which in this connection can be regarded as the same point as D) and the integration completed by following route EFGH, i.e.,

$$p_H - p_A = \int_A^B \frac{\partial p}{\partial x} dx + \int_B^C \frac{\partial p}{\partial r} \cdot dr + \int_C^D \frac{\partial p}{\partial \theta} d\theta + \int_E^F \frac{\partial p}{\partial \theta} \cdot d\theta + \int_F^G \frac{\partial p}{\partial r} dr + \int_G^H \frac{\partial p}{\partial x} \cdot dx \quad (11)$$

The integration CD-EF also provides the detailed pressure distribution on the cylinder surface. Examples of the pressure distribution around the cylinder at two Reynolds numbers are provided in Fig. 7. At a Reynolds number of 50 a typical inertia-dominated variation is displayed with the minimum pressure occurring at approximately 90 deg followed by a slow recovery. It is interesting to note that the "blip" in surface pressure which, at higher Reynolds numbers gives a good indication of the separation point, is not evident here (separation occurred at 135 deg in this test). The pressure profile for Re = 3 is, not unexpectedly, entirely different. Due to the dominance of viscous stresses the pressure falls smoothly from the front to the rear of the cylinder with no separation.

Finally we would note that though, in the present paper, computations are presented only for staggered tube banks, the complete methodology developed in Section 2 carries over intact for handling

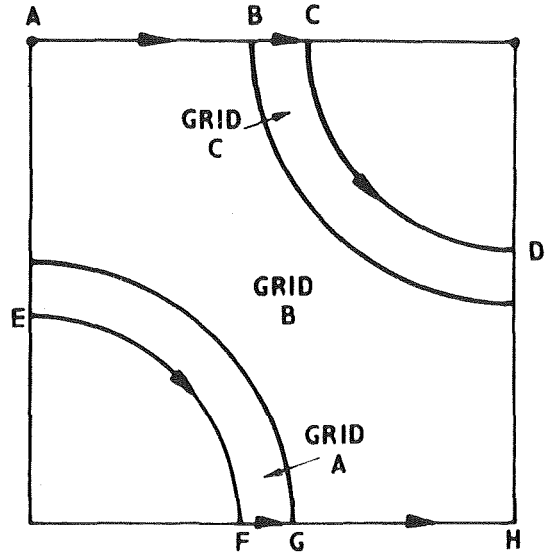

Fig. 6 Integration path for obtaining pressure drop

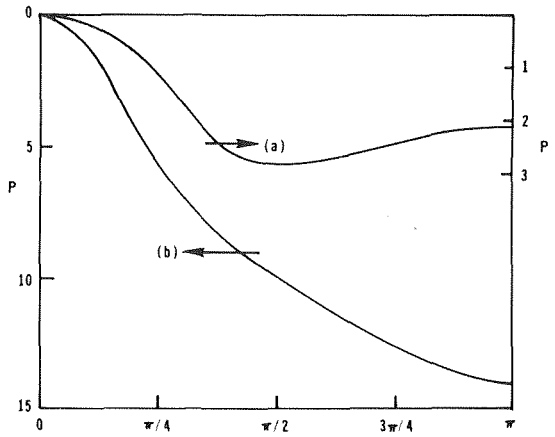

Fig. 7 Variation of surface pressure around cylinder in staggered square bank $P_L:P_T$ = 1.5:3.0, (a) Re = 50, (b) Re = 3

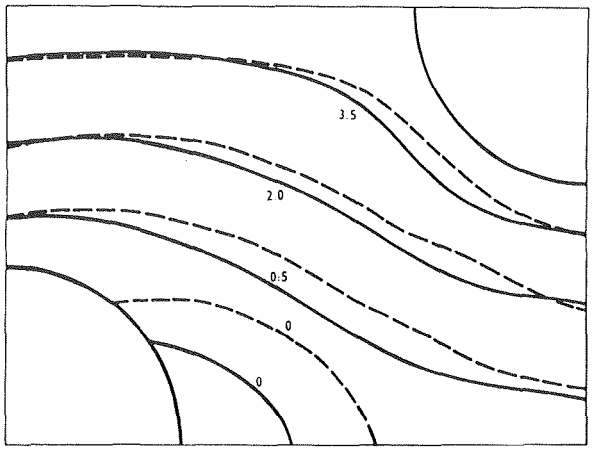

Fig. 8(*a*) Stream function contours

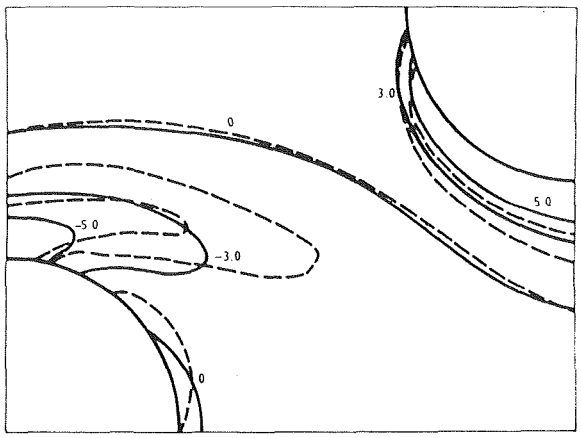

Fig. 8(*b*) Vorticity contours

Fig. 8 Flow field predictions for Thom and Apelt's geometry, $P_L:P_T$ = 1.67:2.44 at Re = 75. - - - Thom and Apelt [2], ——Present study

in-line arrangements. Indeed, for the case of turbulent flow Massey [7] presents results for both staggered and in-line banks.

3 Some Demonstration Calculations

Comparison is made first with the early predictions of Thom and Apelt [2] for the staggered bank shown in Fig. 8 at a Reynolds number of 50. The vorticity and stream function contours obtained in the present study show significant differences from the Thom and Apelt results particularly on the downstream side of the cylinder. The discrepancies may be due to the differences in node density between the two studies: the present explorations have employed approximately seven times as many grid points as Thom and Apelt's computations. Moreover, the curvilinear coordinate transformation used by the latter workers produces particularly poor coverage near the stagnation points in the flow. It thus appears probable that numerical diffusion in the original study represent the cause of the observed differences in the predicted behavior.

Comparison is made in Figs. 9 and 10 with actual tube-bank experiments, the data being those obtained in the staggered 0.89 × 1.77 lattice of Bergelin, et al. [8, 4] (Model 3). Fig. 9 provides comparison with the overall friction factor obtained, as described above, by integrating around the domain boundaries to find the pressure loss per row. Again we found it necessary to employ more than twice as many nodes to resolve the pressure distribution accurately as for other interesting flow characteristics such as the heat transfer rate. The predicted behavior is seen to follow very much the same pattern as measurements not just for Reynolds numbers below 100, over which range f varies nearly inversely with Reynolds number, but up to values of Re as high as 1500. This result may seem initially surprising in view of the fact that the "transitional regime" for tube banks (in which turbulent flow is present within the bank although the boundary layer on the cylinders upstream of separation is laminar) is frequently held to begin at Reynolds numbers below 100. It must be said, however, that the departure of the friction factor curve from an Re^{-1} behavior is usually used as *the basis for identifying the onset of significant turbulence within the bank.* For example Bergelin, et al. [9] write that "the curves . . . (of pressure drop versus velocity) . . . have a slope of unity at low velocities, indicating viscous flow, but above a velocity of approximately 1 ft/s, the slopes begin to increase showing an increasing amount of turbulence in the bank." This association of laminar flow only with the linear drag-velocity region has perhaps arisen because such a linear relation does pertain for the case of fully-developed laminar flow in a pipe. However, the drag for laminar flow on a flat plate does not vary linearly with the free stream velocity so there is no reason to suppose that in the vastly more complex flow found in a tube bank a linear law should apply. The present numerical results for laminar flow give essentially as close agreement with experimental data at a Reynolds number of 1000 as at 10. While this does not strictly prove that, at the higher Reynolds number, the real flow *is* in steady, laminar flow, it does at any rate suggest that the effects of turbulence (or of some more ordered unsteadiness), if present, is not important.

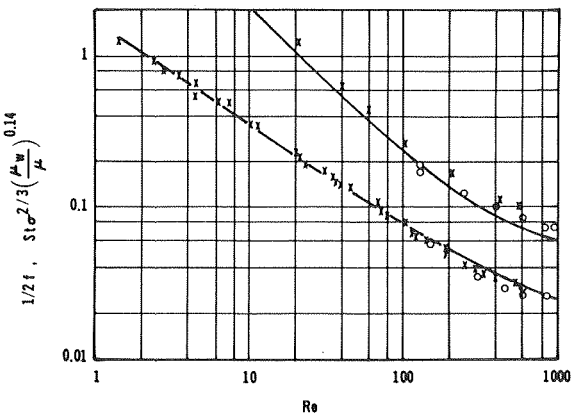

Fig. 9 Friction factor and Stanton number in a staggered square bank, P_L:P_T = 0.89:1.77. *x* Bergelin, et al. [8]; *o* Bergelin, et al. [4], ——present predictions

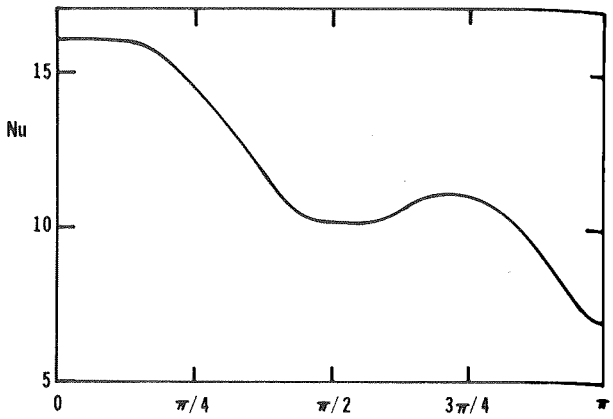

Fig. 10 Variation of local Nusselt number around tube surface, Re = 20

The absolute level of the predicted friction factor is lower than the experimental values by about 15 percent. The main reason for the difference is that while the predictions were made for truly fully-developed conditions the experimental data (obtained in a 14-row lattice) inevitably included the flow-development region too since the pressure drop was recorded with static pressure taps upstream and downstream of the bank. Some indication of the magnitude of the entrance effects can be inferred from Pierson's [10] measurements of the pressure drop per row for a series of staggered banks containing from one to ten rows. These suggest that, in the Bergelin tests, entrance effects were responsible for raising the average friction factor by about 10 percent. The figure is admittedly not precise because Pierson's tests were made at a Reynolds number of 8,000; however, the insensitivity of the difference between measured and calculated friction factors to changes in Reynolds numbers from 10 to 1500 encourages the view that the magnitude of the effects found by Pierson may well apply to the Bergelin data too.

End effects also contribute to raising the measured friction factors. A rough estimate of the drag associated with the end plates (in the absence of tubes) would suggest an augmentation of less than 0.5 percent from this source. In practice, however, the end walls will cause horseshoe vortices to form around the tubes adjacent to the walls producing a larger (though unquantifiable) effect on the friction factor. Thus, in view of the inherent differences between the actual experiments and our idealized two-dimensional, fully-developed model, the level of agreement may be regarded as fully satisfactory.

The corresponding data for the mean Stanton number are also shown in Fig. 9, the mean heat transfer coefficient $\bar{\alpha}$ being obtained by integration of the local value around the perimeter

$$\text{i.e.,}\quad \bar{\alpha} = \frac{1}{2\pi}\int_0^{2\pi} (\dot{q}_w''/(T_w - T_B))d\theta$$

The predictions have been obtained assuming a uniform viscosity and a Prandtl number of 20. These conditions correspond closely with the measurements in [4] using a light oil as working fluid. Earlier studies in the same geometry [9] had employed a heavier oil with highly temperature dependent viscosity; variations in viscosity between the tube walls and the bulk fluid ranged from 2:1 and 5:1 according to operating conditions with Prandtl numbers varying between approximately 250–1000. Despite these steep property variations however Bergelin, et al. [9] found that, within the precision of their data, multiplication of the Stanton number by $\sigma^{2/3}$ $(\mu_w/\mu_B)^{0.14}$ accounted for the effects of Prandtl number and viscosity ratio on their results.[2] It is this modified form of Stanton number with which comparison is made in Fig. 9. In fact the predicted curve is scarcely distinguishable from the measurements. While pleasing, such complete agreement is somewhat fortuitous for end and entrance effects (of necessity omitted from the computations) will have been present in the measurements. It appears, however, that these two effects may be of opposite sign. Conduction in the end plates and the presence of horseshoe vortices mentioned above will tend to raise heat transfer rates between the fluid and the tubes. The entrance region, however, characterized especially by low vorticity levels in the outer stream and a larger reverse flow region behind the tubes than in fully developed flow, could foreseeably give rise to *lower* mean heat transfer coefficients. Certainly Pierson's [10] results applied to the Bergelin data would suggest that entrance effects should cause the average Nusselt number for the experiments to be about ten percent less than the true fully-developed value. As with the hydrodynamic data, Pierson's findings cannot be applied conclusively to the Bergelin experiments because of the difference in Reynolds numbers between the two studies.

One of the reasons for seeking to replace experimental testing of tube banks with computational approaches such as the present one is that the latter provide far more detail about the flow than is usually convenient to acquire in an experimental study. An example of this is provided in Fig. 10 which shows the variation of local heat transfer coefficient around the cylinder for the Bergelin configuration at a Reynolds number of 20; the mean heat-transfer coefficient in this case is 11.8. As expected, the higher levels of heat transfer coefficient are found over the leading half of the cylinder with a saddle occurring in the region of 90 deg. The heat transfer coefficient is essentially flat at its stagnation point value over the leading 35 deg from the forward stagnation point—a pattern which is in general accord with heat transfer measurements on a single cylinder.

Summarizing Remarks

The paper has presented a scheme for using overlapping cylindrical and Cartesian grids that facilitates the numerical study of the flow and heat transfer characteristics of tube banks. Sample predictions for laminar flow in staggered-row assemblies have indicated that:

1 The early flow predictions of Thom and Apelt appear to be significantly in error due to an insufficient node density, particularly in the region of the separation point.

2 In the close-packed, staggered geometries studied by Bergelin, et al. turbulence and/or flow unsteadiness, if present, does not contribute significantly to the overall friction factor at Reynolds numbers up to 1000. This result runs counter to folklore which has hitherto associated the onset of turbulence with departures from a linear relation between drag and velocity.

3 The mean level of Stanton number for Reynolds numbers up to 600 is nearly proportional to $\sigma^{-2/3}$, as suggested by the experiments of Bergelin, et al.

The adaptation of the method reported here to turbulent flows will be presented in a forthcoming publication.

[2] The present study provides additional support for the use of $\sigma^{2/3}$ in the ordinate of Fig. 9. The first sets of computations, which were inadvertently made at a Prandtl number of unity, led to values of $St\sigma^{2/3}$ differing by no more than 5 percent from those reported here.

Acknowledgments

The research reported was principally carried out at the Central Electricity Research Laboratories, Leatherhead and is published with the permission of the Central Electricity Generating Board. We are pleased to acknowledge the support of and interest in every stage of the work by Mr. J. A. Hitchcock of CERL. Authors' names appear alphabetically.

References

1 Zhukauskas, A., "Heat Transfer from Tubes in Cross Flow," *Advances in Heat Transfer*, Vol. 8, 1972, pp. 93–160.

2 Thom, A., Apelt, C. J., *Field Computations in Engineering and Physics*, Van Nostrand, London, 1961.

3 Le Clair, B. P., Hamielec, A. E., "Viscous Flow through Particle Assemblages at Intermediate Reynolds Number," *Ind. Eng. Chem. Fund.*, Vol. 9, 1970, pp. 608–613.

4 Bergelin, O. P., Brown, G. A., Doberstein, S. C., "Heat Transfer and Fluid Friction During Flow across Banks of Tubes—IV," Trans. ASME, 74, 1952, pp. 953–960.

5 Le Feuvre, R. F., "Laminar and Turbulent Forced Convection Processes through In-Line Tube Banks," Imperial College London, Mech. Engr. Dept., HTS/74/5, 1973.

6 Thoman, D. C., Szewcyzk, A. A., "Time-Dependent Viscous Flow over a Circular Cylinder," *Physcis of Fluids*, Supplement II, 1969, pp. II-76 to II-86.

7 Massey, T. H., "The Prediction of Flow and Heat Transfer in Banks of Tubes in Cross-Flow," Ph.D. thesis, Central Electricity Research Laboratories, Leatherhead, Surrey, Feb. 1976.

8 Gosman, A. D., Pun, W. M., Runchal, A. K., Spalding, D. B., Wolfshtein, M. W., *Heat and Mass Transfer in Recirculating Flows*, Academic Press, London, 1969.

9 Bergelin, O. P., Davis, E. S., Hull, H. L., "A Study of Three Tube Arrangements in Unbaffled Tubular Heat Exchangers," Trans. ASME, 71, 1949, pp. 369–374.

10 Pierson, D. L., "Experimental Investigation of the Influence of Tube Arrangement on Convection Heat Transfer and Flow Resistance in Cross Flow of Gases over Tube Banks," Trans. ASME, 59, 1937, pp. 563–572.

E. M. Sparrow
B. R. Baliga
S. V. Patankar

Department of Mechanical Engineering,
University of Minnesota,
Minneapolis, Minn. 55455

Forced Convection Heat Transfer from a Shrouded Fin Array with and without Tip Clearance

An analysis is made of the laminar heat transfer characteristics of an array of longitudinal fins with an adiabatic shroud situated adjacent to the fin tips. The analysis involves the solution of the velocity field in the inter-fin space and in the shroud clearance gap beyond the tips, after which the governing energy equations for the fluid and the fins are solved simultaneously. Solutions are obtained for representative values of dimensionless parameters which describe the system geometry and the fin conductance. For the fin, the results show that the heat loss is a minimum adjacent to the base and increases along the fin in the direction of the tip. The maximum fin heat loss occurs either at the tip or intermediate between the base and the tip, depending on whether or not there is clearance between the fin tips and the shroud. The calculated heat transfer coefficients vary along the fin and, in some cases, take on negative values. Heat loss variations are also encountered along the base surface, the extent of which depends on the fin conductance, the inter-fin spacing, and the extent of the clearance gap. With regard to the overall heat loss, the fin is, on a unit area basis, a more efficient transfer surface than is the base. The results demonstrate that the conventional uniform heat transfer coefficient model is inapplicable to shrouded fin arrays.

Introduction

The fins that are employed in the totality of present-day heat exchange equipment encompass a remarkable variety of geometrical shapes and of orientations with respect to the flows with which they are in contact. In general, the flow passages which are encountered in finned devices are highly complex, giving rise to nonelementary velocity distributions which can have a profound effect on the heat transfer characteristics. This paper is concerned with such a situation.

Attention is focused here on longitudinal fins the height of which does not span the entire cross section of the duct in which they are situated. The physical situation to be considered is depicted in a schematic cross-sectional view at the left of Fig. 1. Fluid flows in the direction perpendicular to the plane of the page. The flow cross section is made up of the spaces between the fins and the open area which extends upward from the tips of the fins to the upper wall of the passage. The flowing fluid, in seeking the path of least resistance, will favor the open area in preference to the relatively constrained inter-fin spaces. The flow imbalance will become more severe when the fins are closely packed and when the open space is large.

Since such an imbalance gives rise to low velocities near the fin base and high velocities near the fin tip, it appears possible that the fin could dissipate more heat near its tip than near its base. Such a finding, if actually encountered, would stand in contrast to the traditional fin analyses which, owing to severe oversimplifications, show the base region to be the most active heat transfer zone. This matter and others will be explored in the present paper.

The present analysis is aimed at obtaining both local results (i.e., distributions along the fin and the base surface) which will provide insights into the transfer mechanisms and average results for design applications. To fulfill these objectives, the convection in the fluid and the conduction in the fins are solved as a conjugate problem. The analysis is based on first principles, that is, the differential equations for momentum and energy in the fluid and the differential equation for heat conduction in the fins. This approach obviates the need for

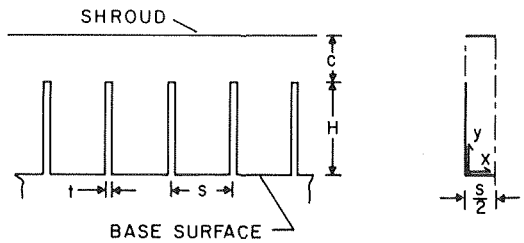

Fig. 1 Schematic cross-sectional view of the shrouded fin array

Contributed by the Heat Transfer Division for publication in the JOURNAL OF HEAT TRANSFER. Manuscript received by the Heat Transfer Division January 5, 1978.

arbitrary assumptions about the heat transfer coefficient on the fin and on the base surface. Rather, the surface distribution of the heat transfer coefficient will be one of the results of the analysis.

The analysis is performed for laminar flow and for thermally and hydrodynamically developed conditions. The base surface and the fins are thermally active, while the upper surface is adiabatic. Two types of thermal boundary conditions are studied within the framework of the thermally developed regime. In one, the temperature of the base surface is uniform both in the streamwise direction and in the cross section. In the other, there is a uniform rate of heat transfer per unit axial length, and the base temperature is uniform in any given cross section (but varies axially). For both of these cases, the temperature and heat flux distributions along the fin are allowed to vary as they will in accordance with the conservation laws, with no arbitrary constraints imposed.

The configuration investigated here may occur either by directed design or by more or less casual shrouding of a longitudinal fin array to prevent escape of the flowing fluid. It also bears a kinship to internally longitudinally finned circular tubes inasmuch as for that case, as well as for the present case, the fins do not span the entire cross section.

No prior analytical work on the present configuration was found in the published literature, but two analyses for internally finned tubes were encountered [1, 2]. In both of these studies, a specific thermal boundary condition (either uniform heat flux or uniform temperature) was assigned along the height of the fin, which eliminated the mutual interaction between the fin conduction and the fluid convection. Although a substantial body of results was presented, local distributions along the fin and the base surface were not given.

Analysis

The velocity distributions serve as input to the analysis of the thermal problem and they will, therefore, be analyzed first. Then, the temperature solutions for prescribed temperature and prescribed streamwise heat input will be dealt with.

The geometrical symmetries that are apparent in the left-hand diagram of Fig. 1 enable the analysis to be performed for a typical module that is illustrated in the diagram at the right. The boundaries of the module consist of both solid walls and symmetry lines. As drawn, the right-hand diagram reflects the thin fin assumption, $t \ll H$ and $t \ll s$, which has been invoked to keep the number of parameters within reason. In the analysis, the following dimensionless coordinates and geometrical groupings will be employed

$$X = x/H,\ Y = y/H,\ Z = (z/H)/(\overline{w}H/\alpha),\ C = c/H,\ S = s/H \quad (1)$$

Velocity. For hydrodynamically developed flow, the momentum equation reduces to a balance between the viscous and pressure forces. In dimensionless terms, the reduced momentum equation can be written as

$$\partial^2 W/\partial X^2 + \partial^2 W/\partial Y^2 + 1 = 0 \quad (2)$$

where W is a dimensionless velocity

$$W = \frac{w}{(H^2/\mu)(-dp/dz)} \quad (3)$$

Equation (2) is to be solved subject to $W = 0$ on the solid walls and to $\partial W/\partial X = 0$ on the symmetry boundaries. The solutions depend on the prescribed values of the two parameters S and C which define the geometry of the flow cross section. The spacing parameter S was assigned values 0.1 and 0.5 and, for each of these, the clearance parameter C was given values of 0, 0.25, 0.5, and 1.0.

Each solution yielded the distribution of W throughout the flow cross section and, in addition, the mean value $\overline{W}$ of the distribution was obtained. The normalized velocity field $W/\overline{W}$ was thus available as input for the solution of the energy equation. Furthermore, as will be indicated later, $\overline{W}$ is inversely proportional to the friction factor—Reynolds number product.

Equation (2) is a standard Poisson equation. Since a number of numerical schemes can be successfully employed for its solution, there is no need to describe the present finite-difference method in any detail. A grid consisting of 21 by 50 nodal points, respectively in the x and y directions, was deployed in the solution domain. A higher density of points was employed adjacent to the solid boundaries, with special care being taken in the neighborhood of the fin tip where the boundary condition changes from $W = 0$ to $\partial W/\partial X = 0$ at $Y = 1$ ($y = H$).

Heat Transfer (Prescribed Wall Temperature). The first heat transfer problem to be considered is that in which the temperature T_w of the base surface ($y = 0$) is uniform both axially and in the cross section. The fin temperature distribution is not preassigned, but varies along the height (i.e., as a function of y) in accordance with the conservation laws. At the upper bounding wall (i.e., the shroud wall), there is no heat transfer. Both the fin and shroud temperature distributions vary axially, decaying exponentially toward T_w, as is characteristic of the thermally developed state for problems of this type.

The thermally developed regime is characterized by a dimensionless

Nomenclature

C = clearance parameter, c/H
c = clearance
D_e = equivalent diameter, equation (24a)
f = friction factor, equation (24)
H = fin height
h_B = local base-surface heat transfer coefficient, $q_B/(T_w - T_b)$
h_f = local fin heat transfer coefficient, $q_f/(T_f - T_b)$
$\overline{h}$ = average heat transfer coefficient for fin and base surface, equation (23)
k = thermal conductivity of fluid
k_f = thermal conductivity of fin
$\dot{m}$ = total mass flow rate
$\dot{m}_f$ = mass flow rate in inter-fin space
Nu_B = local base-surface Nusselt number, $h_B H/k$
$\overline{\mathrm{Nu}}_B$ = average base-surface Nusselt number
Nu_f = local fin Nusselt number, $h_f H/k$
$\overline{\mathrm{Nu}}$ = average Nusselt number for fin and base surface, $\overline{h}H/k$
p = pressure
Q = overall heat transfer rate
Q_B = base-surface heat transfer rate
Q_f = fin heat transfer rate
Q' = prescribed uniform heat transfer rate per unit length
q_B = local base-surface heat flux
$\overline{q}_B$ = average base-surface heat flux
q_f = local fin heat flux
$\overline{q}_f$ = average fin heat flux
Re = Reynolds number, $\overline{w}D_e/\nu$
S = inter-fin spacing parameter, s/H
s = inter-fin spacing
T = temperature
T_b = bulk temperature
T_f = local fin temperature
T_w = base-surface temperature
t = fin thickness
W = dimensionless velocity, equation (3)
w = axial velocity
$\overline{w}$ = mean axial velocity
X, Y = dimensionless coordinates, x/H, y/H
x, y = cross-sectional coordinates
Z = dimensionless axial coordinate, equation (1)
z = axial coordinate
α = thermal diffusivity
θ = dimensionless temperature, equation (4)
λ = bulk temperature gradient, equation (5)
μ = viscosity
ν = kinematic viscosity
τ = dimensionless temperature, equation (15)
ϕ = scaled temperature variable, θ/λ
Ω = fin conductance parameter, equation (11)

temperature distribution that remains invariant with the streamwise coordinate, that is,

$$(T - T_w)/(T_b - T_w) = \theta(X, Y) \tag{4}$$

where the invariance is reflected in the fact that θ is not a function of z. Furthermore, as the flow proceeds in the streamwise direction, the difference between the bulk temperature T_b and the uniform temperature T_w of the base surface decays exponentially to zero, so that

$$(dT_b/dZ)/(T_b - T_w) = \text{constant} = \lambda \tag{5}$$

In terms of the new variables of equations (1, 3, 4, 5), the conservation of energy equation takes the form

$$(W/\overline{W})\theta\lambda = \partial^2\theta/\partial X^2 + \partial^2\theta/\partial Y^2 \tag{6}$$

Then, when expressed in terms of θ, the thermal boundary conditions at the base surface, along the symmetry lines, and on the adiabatic shroud are, respectively,

$$\theta = 0, \quad \partial\theta/\partial X = 0, \quad \partial\theta/\partial Y = 0 \tag{7}$$

At any location y along the fin, there is a balance between the net conduction along the fin and the heat which passes into the fluid. For a one-dimensional model of the fin, such a balance is expressed as

$$k_f(t/2)(d^2T_f/dy^2) = -k(\partial T/\partial x)_{x=0} \tag{8}$$

where the subscript f refers to the fin and $(\partial T/\partial x)_{x=0}$ is the temperature gradient in the fluid at $x = 0$ (i.e., at the surface of the fin). In dimensionless terms, equation (8) becomes

$$(k_f(t/2)/kH)(d^2\theta_f/dY^2) = -(\partial\theta/\partial X)_{x=0} \tag{9}$$

For the solution of the temperature distribution in the fin, the boundary conditions,

$$\theta_f = 0 \quad \text{and} \quad d\theta_f/dY = 0 \tag{10}$$

respectively at the fin base and tip, are employed, where the latter reflects the aforementioned thin-fin assumption. The inclusion of heat exchange at the fin tip would have resulted in an additional dimensionless parameter. When considering the results to be presented later, it should be noted that the neglect of tip heat exchange is actually conservative with regard to the general importance of the tip region in the overall fin heat transfer.

The conjugate heat transfer problem encompassing the flowing fluid and the fin is defined by equations (6, 7, 9, 10). The solution of this problem is subject to three prescribable parameters: S and C, the geometrical parameters, and

$$\Omega = k_f(t/2)/kH \tag{11}$$

which will henceforth be termed the fin conductance parameter. In addition, there is another parameter λ, whose value is initially unknown and has to be found so that the solution is compatible with the definition of the bulk temperature which, in dimensionless form, is

$$\int\int \theta(W/\overline{W})dXdY/(1 + C)(S/2) = 1 \tag{12}$$

where the integration extends over the typical module shown at the right of Fig. 1.

To determine λ, it is convenient to introduce a scaled temperature variable ϕ as follows

$$\phi = \theta/\lambda, \quad \phi_f = \theta_f/\lambda \tag{13}$$

With this, equations (6, 7, 9, 10) remain unchanged, but with θ and θ_f replaced by ϕ and ϕ_f, and the bulk temperature relation (12) becomes

$$\lambda = (1 + C)(S/2)/\int\int \phi(W/\overline{W})dXdY \tag{14}$$

The procedure for solving the conjugate heat transfer problem and for determining λ will now be described. In the discussion that follows, whenever equations (6, 7, 9, or 10) are mentioned, it will be understood that θ and θ_f have been replaced by ϕ and ϕ_f.

First, a distribution of ϕ is selected, either as a guess or taken from the converged output of a prior case. This distribution is used as input to equation (14) to determine λ and is, in addition, used to evaluate ϕ on the left-hand side of equation (6). Thus, the left-hand side of (6) can be regarded as known at all grid points in the flow cross section.

Furthermore, the selected ϕ distribution enables the evaluation of the derivatives $(\partial\phi/\partial X)_{x=0}$ at points along the fin surface. With these derivatives as input, equation (9) can be solved numerically, subject to the boundary conditions (10), for the fin temperature distribution $\phi_f(Y)$. Then, $\phi_f(Y)$ is used as a boundary condition on ϕ at the fin-fluid interface, supplementing those already stated in equation (7) for the other bounding surfaces of the flow cross section.

The differential equation (6), with known left-hand side and with the aforementioned boundary conditions, is then solved numerically to obtain a new distribution for ϕ. This new distribution replaces that which was originally selected, and the entire procedure is repeated iteratively until convergence is attained to six significant figures.

Once convergence is achieved, the θ distribution is obtained via the relation $\theta = \lambda\phi$. All heat transfer results then follow directly.

Heat Transfer (Prescribed Heating). The other heat transfer problem to be investigated is characterized by a uniform rate of heat transfer per unit length. The base surface temperature T_w is assumed to be uniform in each cross section while the fin temperature is nonuniform and varies in accordance with the conservation laws. In the thermally developed regime, to which the present study is directed, all temperatures vary linearly in the axial direction.

As before, there is a dimensionless temperature distribution that is invariant from cross section to cross section. A convenient temperature variable expressing this property is

$$\frac{T - T_w}{Q'/k} = \tau(X, Y) \tag{15}$$

where Q' is the rate of heat input per unit length for the module shown at the right of Fig. 1. The temperature gradient in the axial direction is readily derived via an overall energy balance which, in dimensionless terms, yields

$$\frac{d}{dZ}\left(\frac{T_w}{Q'/k}\right) = \frac{d}{dZ}\left(\frac{T_b}{Q'/k}\right) = \frac{1}{(S/2)(1 + C)} \tag{16}$$

Then, the dimensionless energy equation for the fluid can be written as

$$\frac{(W/\overline{W})}{(S/2)(1 + C)} = \frac{\partial^2\tau}{\partial X^2} + \frac{\partial^2\tau}{\partial Y^2} \tag{17}$$

The boundary conditions for τ on the base, the symmetry lines, and the shroud are, respectively

$$\tau = 0, \quad \partial\tau/\partial X = 0, \quad \partial\tau/\partial Y = 0 \tag{18}$$

For the fin, the derivation of the prior section continues to apply, so that the governing equation for τ_f is

$$\Omega(d^2\tau_f/dY^2) = -(\partial\tau/\partial X)_{x=0} \tag{19}$$

with Ω given by equation (11) and with boundary conditions

$$\tau_f = 0 \quad \text{and} \quad \partial\tau_f/\partial Y = 0 \tag{20}$$

at the base and tip, respectively.

The governing equations (17–20) were solved numerically using a solution procedure which differs slightly from that of the prior section. As before, an initial distribution for τ is selected. This distribution enables $(\partial\tau/\partial X)_{x=0}$ to be evaluated and, with these derivatives, $\tau_f(Y)$ is obtained by solving equation (19) subject to the boundary conditions (20). The thus-obtained $\tau_f(Y)$ is used as a boundary condition on τ at the fin-fluid interface, thereby supplementing the other boundary conditions (18).

For this set of boundary conditions, equation (17) is solved to yield a new τ distribution, which is used to replace that initially selected, and the entire process is repeated iteratively to convergence to six significant figures. The solutions for τ yield all of the heat transfer

results of interest, as will be reported in the next section of the paper.

Results and Discussion

The presentation that follows will include both local and average results. Local distributions of temperature, heat flux, and Nusselt number along the fin are presented in graphical form, as are the heat flux and Nusselt number distributions along the base surface. The overall heat loss results for the fin and the base surface are tabulated together with the average Nusselt number for the entire heat transfer surface. Also given in tabular form are the results for the friction factor and the flow distribution.

The aforementioned results were obtained for the following operating conditions: (a) fin spacing parameter $S = s/H = 0.1$ and 0.5, (b) clearance parameter $C = c/H = 0$, 0.25, 0.5, and 1, (c) fin conductance parameter $\Omega = \infty$, 25, 10, 5, and 1, where $\Omega = \infty$ represents an isothermal fin. Results corresponding to these parameter ranges will be presented both for prescribed uniform base surface temperature T_w and for prescribed uniform heat transfer Q' per unit axial length. For concreteness, the results will be discussed from the viewpoint that the base surface is hotter than the fluid, i.e., the heat flow is from the wall into the fluid.

Local Fin Temperature, Heat Flux, and Nusselt Number. The distributions of temperature, heat flux, and Nusselt number along the fin are presented in Figs. 2(*a, b, c*) and in Figs. 3(*a, b, c*), respectively for fin spacings $S = 0.5$ and 0.1. The (*a, b, c*) parts correspond to clearances C of 0, 0.25, and 1. Because of space limitations, only partial results for the $C = 0.5$ case are presented, and these are included in the insets of Figs. 2(*c*) and 3(*c*).

Each figure is made up of a vertical array of graphs. The lower-most and next-to-lowest graphs respectively display temperature and heat flux distributions, while the two upper graphs show the Nusselt number distributions. For the temperature distributions, the local fin-to-base temperature drop $(T_w - T_f)$ is plotted relative to the base-to-bulk temperature difference $(T_w - T_b)$. The heat flux distributions are also plotted in dimensionless form as $q_f/\bar{q}_f$, where $\bar{q}_f$ is the average fin heat flux. Local Nusselt numbers were evaluated from the definitions

$$h_f = q_f/(T_f - T_b), \quad \mathrm{Nu}_f = h_f H/k \tag{21}$$

where both q_f and T_f vary along the fin.

The solid curves in these figures correspond to the case of prescribed T_w, and the dashed curves are for prescribed Q'. The curves are parameterized by the fin conductance parameter Ω which ranges from ∞ to 1. In certain of the graphs, some of the Ω curves have been omitted because of overlapping and crowding.

Attention will first be turned to Figs. 2(*a, b, c*), i.e., to the more widely spaced fins. Among the results presented in these figures, those for the fin heat loss distributions merit first consideration because of their novelty. As was noted in the Introduction, the conventional treatment of fins includes the more or less arbitrary assumption of a uniform heat transfer coefficient. This gives rise to a fin heat loss which is a maximum adjacent to the base and decreases monotonically along the fin. As will now be discussed, the $q_f/\bar{q}_f$ distributions pre-

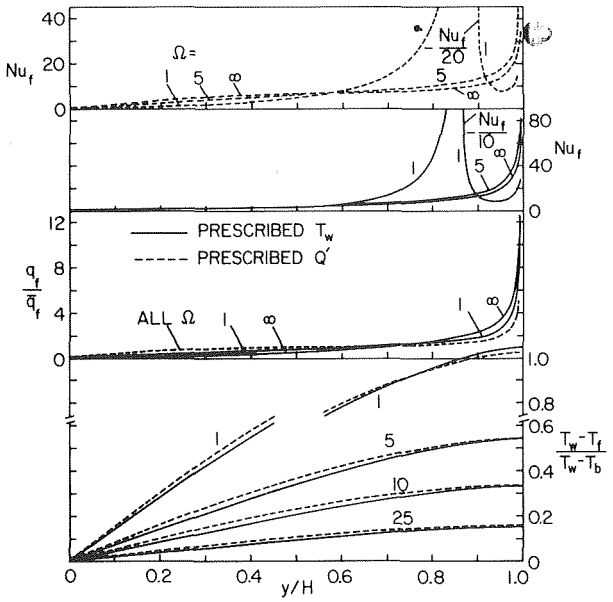

Fig. 2(*b*) Fin temperature, heat flux, and Nusselt number distributions for fin spacing $S = 0.5$ and clearance $C = 0.25$

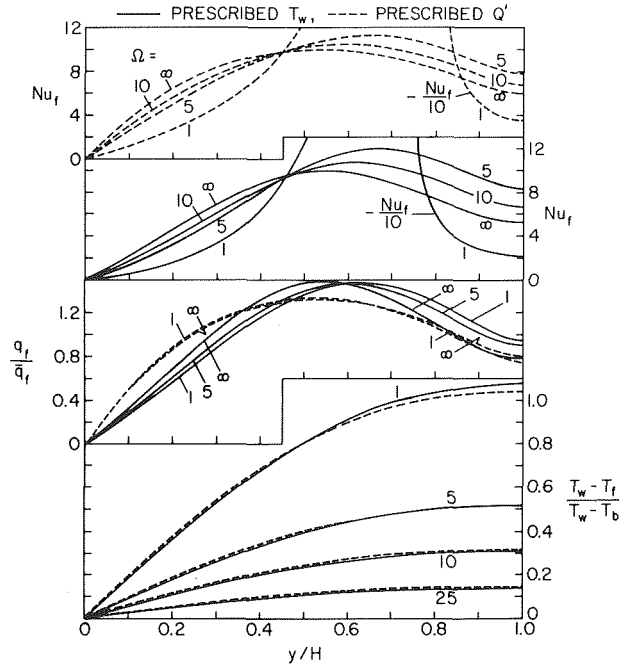

Fig. 2(*a*) Fin temperature, heat flux, and Nusselt number distributions for fin spacing $S = 0.5$ and clearance $C = 0$

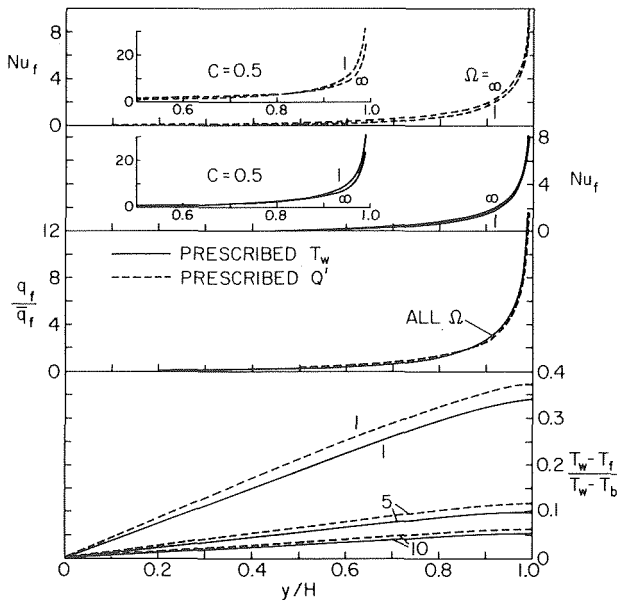

Fig. 2(*c*) Fin temperature, heat flux, and Nusselt number distributions for fin spacing $S = 0.5$ and clearance $C = 1$

sented in Figs. 2(*a, b, c*) display trends that are markedly different from that of the conventional model.

The $q_f/\overline{q}_f$ curves of Fig. 2(*a*) reflect the absence of clearance between the tips of the fins and the shroud. As seen in the figure, $q_f/\overline{q}_f$ rises from a near-zero value at the base, attains a maximum in the range $q_f/\overline{q}_f \cong 1.25 - 1.35$, and then diminishes to a value $q_f/\overline{q}_f \cong 0.8 - 1$ at the tip. These trends are in evidence for all values of the fin conductance parameter Ω and for both the prescribed T_w and prescribed Q' boundary conditions.

The nature of the $q_f/\overline{q}_f$ distribution is physically plausible. The parts of the fin adjacent to the base and adjacent to the tip are both washed by relatively low velocity fluid, while the central region of the fin is washed by relatively high velocity fluid. As a result, the highest heat loss takes place in the central region. Furthermore, the fluid adjacent to the base surface has a higher temperature than that of the fluid adjacent to the adiabatic shroud. As a result, the heat loss in the region of the fin base is substantially lower than that in the region of the fin tip.

When there is clearance between the fin tips and the shroud, the fin heat loss increases monotonically from the base to the tip, taking on a maximum value at the tip that is (in Figs. 2(*b*) and (*c*)) on the order of ten times $\overline{q}_f$. This trend is diametrically opposite to that of the heat flux distribution of the conventional fin model, and this contradiction underscores the errors that may result from an arbitrary assumption about the fin heat transfer coefficient.

The presence of a clearance space above the fins provides an alternative fluid flow path to that between the fins. As the clearance increases, the flow resistance of the alternative path diminishes relative to that of the inter-fin spaces, so that the highest velocities occur in the clearance gap. Under these conditions, a significant portion of the fin may be washed by low velocity fluid, with the part near the tip being washed by relatively higher velocities. This explains why the highest heat loss occurs in the tip region. At larger clearances, the low velocity zone blankets more and more of the fin, thereby further accentuating the primacy of the tip region. This trend with increasing clearance can be seen by comparing Figs. 2(*b*) and 2(*c*). The distributions of $q_f/\overline{q}_f$ are seen to be relatively insensitive to both the fin conductance parameter Ω and to the T_w or Q' boundary condition.

Attention may next be turned to the dimensionless fin temperature distributions that are plotted on the lowermost graphs of Figs. 2(*a, b, c*). Aside from the $\Omega = \infty$ curve, which coincides with the abscissa axis, all the distribution curves reflect a decrease of temperature along the height of the fin, that is, increasing values of $(T_w - T_f)/(T_w - T_b)$ as y/H increases. As expected, the extent of the temperature drop is accentuated at smaller values of the fin conductance parameter Ω. It is especially noteworthy that in some cases, in particular, for zero or small clearances and for small values of the conductance parameter, the local fin temperature in the region near the tip is lower than the fluid bulk temperature, that is, $|T_w - T_f| > |T_w - T_b|$. The effect of this behavior on the heat transfer coefficient will be examined shortly.

By making comparisions among the successive figures, it is seen that the dimensionless temperature drop along the fin is smaller at larger clearances, e.g., Fig. 2(*c*). This is because the wall-to-bulk temperature difference (denominator of the dimensionless temperature) becomes relatively large when the clearance gap is large, reflecting the increase of the overall thermal resistance to heat flow from the active surfaces (i.e., fin and base) to the fluid. A comparison of the solid and dashed lines in the various figures shows that the dimensionless temperature distributions are relatively insensitive to whether T_w or Q' is prescribed.

The Nusselt number graphs in the upper portions of Figs. 2(*a, b, c*) will now be discussed, where Nu_f is defined by equation (21). For the zero-clearance case (Fig. 2(*a*)), the Nusselt number distributions for the large and intermediate values of the fin conductance parameter tend to reproduce the general shape of the $q_f/\overline{q}_f$ distributions. The numerical values of Nu_f for these cases vary along the fin from approximately zero to ten. Such variations are decidedly different from the conventional Nu_f = constant assumption.

The $\Omega = 1$ Nusselt number curves in Fig. 2(*a*) portray a behavior different from the other Nusselt number distributions. Since $(T_f - T_b)$ actually goes negative along the upper portion of the fin while q_f remains positive, the resulting Nusselt numbers are negative, as is indicated in the graphs. Thus, not only do the enormous variations experienced by the low-Ω results negate the Nu_f = constant assumption, but the sign change suggests a more fundamental flaw—that is, that the local fin heat loss is not properly described by $q_f = h_f(T_f - T_b)$. The non-applicability of this form of the venerable Newton's law of cooling stems from the fact that T_b is too remote to serve as a proper participant in the ΔT which drives the local heat flow.

The Nusselt number results for $C = 0.25$ (moderate clearance), as presented in Fig. 2(*b*), follow the same pattern as those discussed in connection with Fig 2(*a*). That is, the Nu_f curves for large and intermediate Ω reproduce the shapes of the $q_f/\overline{q}_f$ curves, while the curves for $\Omega = 1$ experience a sign change so that Nu_f is negative along the upper portion of the fin. For those cases where there is no sign change, the maximum Nusselt number occurs at the fin tip, where very large values are in evidence.

The Nusselt number results for larger clearances, $C = 0.5$ and 1, are presented in Fig. 2(*c*), with the former appearing in the insets. For these clearances $(T_f - T_b) > 0$ for all of the cases studied, so that $\mathrm{Nu}_f > 0$. The Nusselt number distributions increase monotonically along the fin and attain a steep maximum at the tip.

Viewed broadly, the Nusselt number results indicate that the h_f = constant assumption used in the conventional fin model is not applicable to situations such as that treated here. Because of this, the oft-used fin efficiencies, which are universally based on h_f = constant, are also inapplicable.

The focus of the discussion will now be directed to the results for the narrower fin spacing, i.e., $S = 0.1$. These results are presented in Figs. 3(*a, b, c*) using a format that is the same as that used in Figs. 2(*a, b, c*). Because of the narrowness of the inter-fin space, the flow is highly responsive to the presence or absence of a clearance gap above the fin. In the absence of a gap, the flow is fully confined to the inter-fin space and serves as an effective heat transfer medium. However, when there is a gap of even modest size, the fluid prefers the less restrictive flow path provided by the gap. As a consequence, the major part of the inter-fin space is filled with slow moving, relatively hot fluid whose heat transfer capabilities are low. Therefore, there is little heat loss from those parts of the fin that are washed by this convectively ineffective fluid. Only in the region of the fin tip does the relatively cool, high velocity fluid passing through the clearance gap assert itself, with the result that the heat loss in that region is large.

A comparison of Figs. 3(*a, b, c*) with their counterparts Figs. 2(*a, b, c*) indicates that the qualitative trends that were identified for the latter continue in force, but with differences in detail. The heat loss distributions for the zero-clearance case continue to display maxima at locations intermediate to the ends, and there are substantial variations of the Nusselt number. When there is clearance, the heat loss is virtually zero along most of the fin, as is the Nusselt number; in the region of the tip, both the heat loss and the Nusselt number are large.

Local Base Heat Flux and Nusselt Number. Distributions of the local heat flux and Nusselt number along the base surface are presented in Figs. 4(*a, b*) and Figs. 5(*a, b*) for the respective fin spacings $S = 0.5$ and 0.1. To keep the presentation to a reasonable length, only the results for the zero-clearance ($C = 0$) and largest clearance ($C = 1$) cases are shown, respectively in the (*a*) and (*b*) parts of the figures. Each figure consists of two graphs, the lower of which is for prescribed T_w (solid lines) and the upper of which is for prescribed Q' (dashed lines). The curves are parameterized by the fin conductance Ω ranging from ∞ to 1.

The ordinate variable is the ratio of the local heat flux q_B to the average base surface heat flux $\overline{q}_B$ (note that B is used to denote the base surface in contradistinction to b for bulk). In addition, the ordinate also represents the ratio of the local and average base surface Nusselt numbers, where

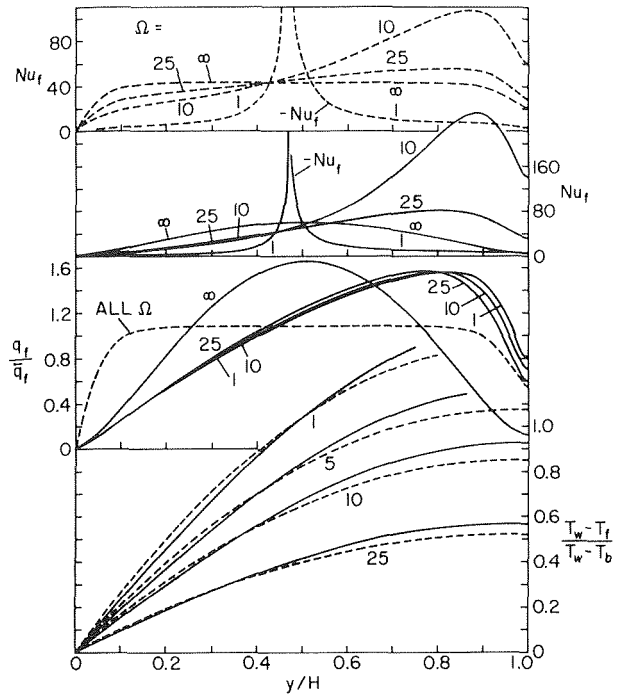

Fig. 3(*a*) Fin temperature, heat flux, and Nusselt number distributions for fin spacing $S = 0.1$ and clearance $C = 0$

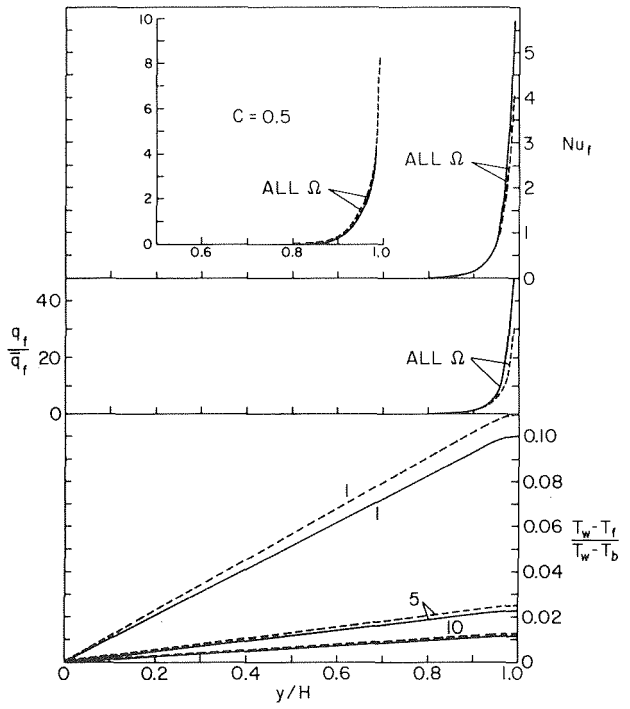

Fig. 3(*c*) Fin temperature, heat flux, and Nusselt number distributions for fin spacing $S = 0.1$ and clearance $C = 1$

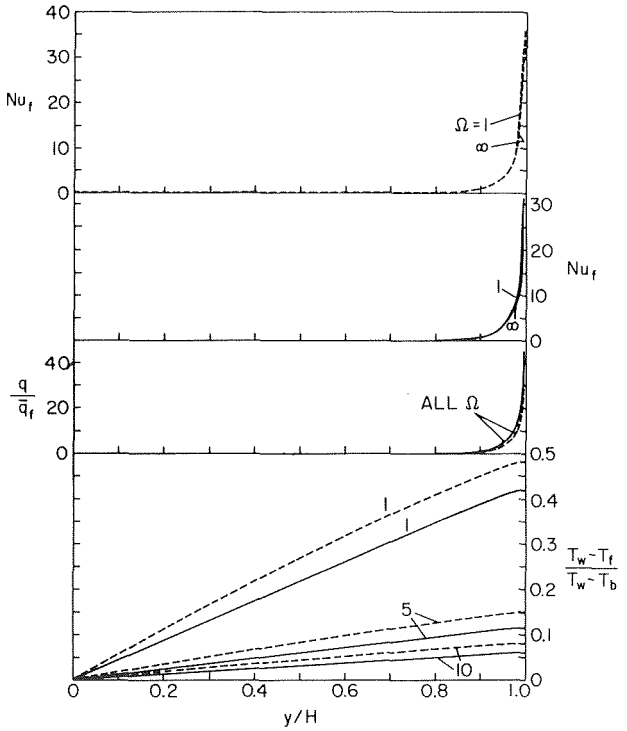

Fig. 3(*b*) Fin temperature, heat flux, and Nusselt number distributions for fin spacing $S = 0.1$ and clearance $C = 0.25$

$$h_B = \frac{q_B}{T_w - T_b}, \qquad \mathrm{Nu}_B = \frac{h_B H}{k},$$

$$\bar{h}_B = \frac{\bar{q}_B}{T_w - T_b}, \qquad \mathrm{Nu}_B = \frac{\bar{h}_B H}{k} \tag{22}$$

from which it follows that $\mathrm{Nu}_B/\overline{\mathrm{Nu}}_B = q_B/\bar{q}_B$. Numerical values of $\overline{\mathrm{Nu}}_B$ are indicated on the respective curves. The abscissa variable is the dimensionless base surface coordinate, where $x/H = 0$ corresponds to the corner at the intersection of the fin and base, and $x/H = 0.25$ (Figs. 4(*a*, *b*)) and 0.05 (Figs. 5(*a*, *b*)) is the midpoint between fins.

If attention is first turned to Fig. 4, it is seen that the heat flux (and Nusselt number) varies along the base surface, taking on its smallest value in the corner and increasing in the direction of the midpoint. It is especially noteworthy that the extent of the base-surface heat flux variation is markedly affected by the conductance characteristics of the fin. In the presence of highly conducting fins (i.e., large Ω), large variations of q_B are in evidence. On the other hand, when the fin conductance parameter is small (~1), q_B is nearly uniform.

These effects of the fin on the distribution of q_B are entirely plausible in that higher fin heat transfer brings about a blanketing of adjacent portions of the base with hotter, less-heat-receptive fluid. The lower velocities in the corner region also contribute to the nonuniformity of q_B.

As is seen by examining Figs. 4(*a*) and (*b*), there are some interesting differences in detail in the base-surface heat flux distributions depending on the absence or presence of fin tip clearance. In general, the distributions tend to be more uniform when there is clearance. This is due, at least in part, to the diminished importance of convection as a direct factor in the base surface heat loss. Owing to the very low velocities that prevail in the inter-fin space, conduction is the primary mechanism for transporting heat from the base surface to convectively active fluid in the clearance gap.

The average base-surface Nusselt numbers reflect the marked increase of thermal resistance which corresponds to the aforementioned diminished role of convection. A comparison of Figs. 4(*a*) and (*b*) shows that in the presence of clearance, the $\overline{\mathrm{Nu}}_B$ values can be one or two orders of magnitude lower than those for the zero-clearance case, depending on the specific operating conditions. Another clear characteristic of the $\overline{\mathrm{Nu}}_B$ results is the generally higher values in evidence for uniform heating compared with those for uniform wall temperature. This relationship between uniform heating and uniform wall temperature is consistent with that of duct flows in general.

If attention is next directed to the results for the narrow spacing ($S = 0.1$) in Figs. 5(*a*) and (*b*), it is seen that all of the trends that were identified and discussed in connection with Figs. 4(*a*) and (*b*) continue to prevail. The major distinction between Figs. 4 and 5 is that the more closely spaced fins are much more sensitive to the presence of clear-

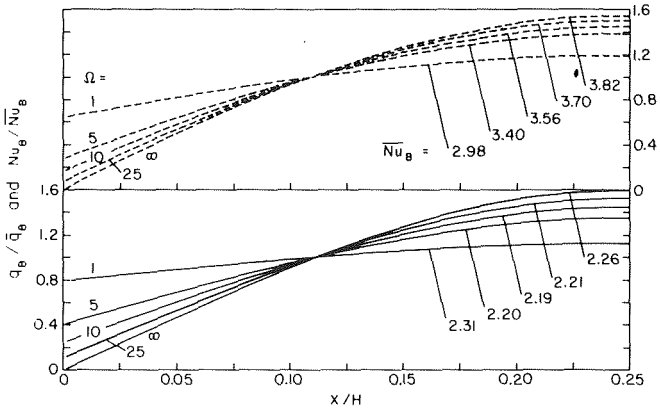

Fig. 4(*a*) Base-surface heat flux and Nusselt number distributions for fin spacing $S = 0.5$ and clearance $C = 0$

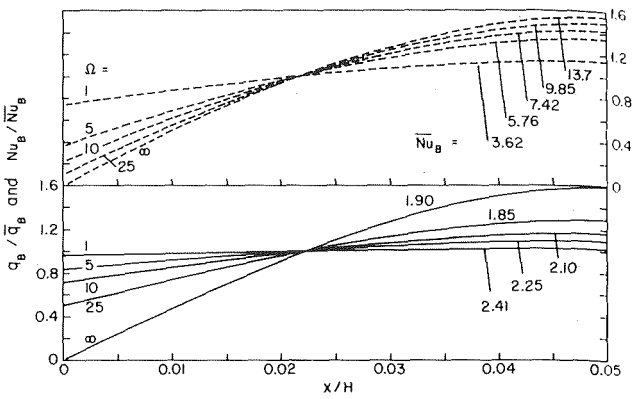

Fig. 5(*a*) Base-surface heat flux and Nusselt number distributions for fin spacing $S = 0.1$ and clearance $C = 0$

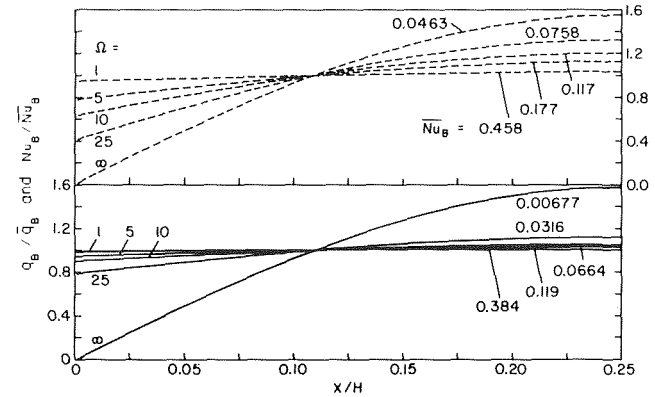

Fig. 4(*b*) Base-surface heat flux and Nusselt number distributions for fin spacing $S = 0.5$ and clearance $C = 1$

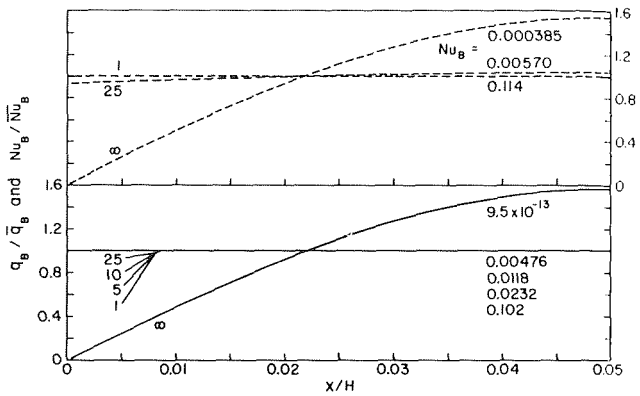

Fig. 5(*b*) Base-surface heat flux and Nusselt number distributions for fin spacing $S = 0.1$ and clearance $C = 1$

ance. Thus, in Fig. 5(*b*), the q_B distributions are quite uniform, except for that corresponding to $\Omega = \infty$.

Aside from the numerical results themselves, the main message of Figs. 4 and 5 is the strong dependence of the base-surface heat transfer on the fin conductance parameter and on the geometrical parameters which specify the fin spacing and the tip clearance.

Overall Heat Transfer Results. The overall heat transfer characteristics of the system will be presented via two dimensionless groups: the ratio Q_f/Q and the average Nusselt number $\overline{\mathrm{Nu}}$. In the first of these, Q_f is the surface-integrated fin heat loss, and Q is the sum of the heat loss from the fin and the base surface; in addition, $Q_B/Q = 1 - (Q_f/Q)$. The base-surface heat loss Q_B corresponds to the range $0 \le x \le s/2$, which is half of the span between adjacent fins. Such a half span, taken together with one face of a given fin, make up a typical module as pictured at the right of Fig. 1. The average Nusselt number was evaluated as

$$\bar{h} = \frac{Q}{(H + s/2)(T_w - T_b)}, \quad \overline{\mathrm{Nu}} = \frac{\bar{h}H}{k} \tag{23}$$

Numerical values of Q_f/Q and $\overline{\mathrm{Nu}}$ are listed in Table 1, in which the results for prescribed T_w and prescribed Q' respectively appear in the upper and lower portions of the table.

The table shows that for the closely spaced fin array, the fins contribute about ninety-nine percent of the overall heat loss for all Ω except $\Omega = 1$, for which the fin contribution is about ninety-five percent. For the more widely spaced fins, Q_f/Q is, for the most part, in excess of 0.9, with lower values (0.72 − 0.80) for $\Omega = 1$. For the two fin spacings considered, the ratio of the fin surface area to the total heat transfer area is 0.95 and 0.80, respectively. Since Q_f/Q exceeds these area ratios except for $\Omega = 1$, it follows that the fin is a more efficient transfer surface than the base, except when the fin conductance is very low. This finding refutes a commonly held notion that a fin is a less efficient transfer surface than its base.

The average Nusselt numbers vary widely, depending on the operating conditions. The largest Nusselt numbers correspond to zero-clearance, high fin conductance, and close spacing. In general, the Nusselt number decreases as the clearance increases, but to a lesser degree at large fin spacings than at small fin spacings. Decreases also generally occur as the conductance parameter decreases, but to a different extent depending on the spacing and clearance. For all cases, the Nusselt numbers for prescribed Q' are higher than are those for prescribed T_w.

Friction Factor and Mass Flow Ratios. To complete the presentation of results, numerical values of the friction factor and of a flow distribution parameter will now be given. The friction factor was evaluated from its standard definition

$$f = (-dp/dz)D_e/\tfrac{1}{2}\rho\overline{w}^2 \tag{24}$$

in which the equivalent diameter D_e for the typical module is

$$D_e = 4(H + c)(s/2)/(H + s) \tag{24a}$$

where the denominator is the wetted perimeter. In terms of the variables of the analysis, equation (24) becomes

$$f\mathrm{Re} = (8/\overline{W})((1 + C)S/(1 + S))^2 \tag{25}$$

with

$$\mathrm{Re} = \overline{w}D_e/\nu \tag{26}$$

Table 1 Overall heat transfer results. Prescribed T_w (upper table) prescribed Q' (lower table)

		$C = 0$		$C = 0.25$		$C = 0.5$		$C = 1$	
S	Ω	Q_f/Q	$\overline{Nu}$	Q_f/Q	$\overline{Nu}$	Q_f/Q	$\overline{Nu}$	Q_f/Q	$\overline{Nu}$
0.1	∞	0.997	34.02	1.000	0.616	1.000	0.236	1.000	0.114
	25	0.996	22.38	0.998	0.607	0.998	0.234	0.998	0.114
	10	0.993	14.45	0.995	0.593	0.995	0.231	0.995	0.113
	5	0.982	9.045	0.990	0.572	0.990	0.227	0.990	0.112
	1	0.951	2.327	0.952	0.441	0.952	0.197	0.952	0.104
0.5	∞	0.922	5.806	0.987	4.448	0.997	1.424	0.997	0.513
	25	0.917	5.337	0.974	4.105	0.986	1.379	0.987	0.505
	10	0.908	4.750	0.956	3.661	0.971	1.316	0.973	0.493
	5	0.891	4.012	0.930	3.089	0.947	1.223	0.950	0.475
	1	0.759	1.923	0.780	1.460	0.794	0.806	0.798	0.381
0.1	∞	0.983	38.73	0.995	0.987	0.999	0.279	1.000	0.128
	25	0.981	24.94	0.993	0.959	0.997	0.276	0.998	0.127
	10	0.978	16.28	0.990	0.919	0.994	0.272	0.995	0.126
	5	0.974	10.34	0.985	0.861	0.989	0.265	0.990	0.124
	1	0.937	2.727	0.946	0.580	0.951	0.223	0.952	0.114
0.5	∞	0.888	6.805	0.923	6.183	0.957	2.322	0.986	0.651
	25	0.880	6.149	0.915	5.466	0.948	2.178	0.976	0.635
	10	0.868	5.388	0.902	4.672	0.934	1.997	0.962	0.615
	5	0.849	4.494	0.882	3.788	0.913	1.761	0.939	0.584
	1	0.722	2.142	0.747	1.683	0.770	0.989	0.791	0.438

Table 2 Fluid flow results

	$S = 0.1$				$S = 0.5$			
$C =$	0	0.25	0.5	1	0	0.25	0.5	1
fRe	84.46	48.73	16.78	5.759	62.06	80.63	75.49	50.03
$\dot{m}_f/\dot{m}$	1.000	0.333	0.073	0.0125	1.000	0.814	0.500	0.171

The fRe results obtained from the numerical solutions are listed in Table 2. For the zero-clearance case, the tabulated values for both $S = 0.1$ and $S = 0.5$ are in excellent agreement with literature information. The trend of the fRe with increasing clearance reflects two effects. One of these is a decrease of the pressure gradient (for a given mean velocity $\overline{w}$), while the second is an increase in the equivalent diameter. These conflicting factors are responsible for the nonmonotonic behavior of fRe results for $S = 0.5$.

To characterize the flow distribution, the ratio $\dot{m}_f/\dot{m}$ was evaluated, where $\dot{m}_f$ is the mass flow rate in the inter-fin space and $\dot{m}$ is the total mass flow rate in the module. The numerical values of this ratio are given in Table 2. For the zero-clearance case, all of the mass passes through the inter-fin space and $\dot{m}_f/\dot{m} = 1$. As the clearance increases, more and more mass passes through the clearance gap, and $\dot{m}_f/\dot{m}$ decreases. The decrease is very sharp for the narrow fin spacing. Thus, for example, when $S = 0.1$ and $C = 1$, only about one percent of the flow passes between the fins. Therefore the $\dot{m}_f/\dot{m}$ results of Table 2 confirm the earlier remarks about the weakness of convection in the inter-fin space at large clearances.

Concluding Remarks

In the present analysis, the heat transfer characteristics of a shrouded fin array have been determined by simultaneous solution of the governing energy equations for the fin and the flowing fluid. This approach has obviated the need for arbitrary assumptions about the heat transfer coefficients on the fin and on the base surface. It has been customary in the past to assume that these coefficients are uniform and are known in advance.

When there is no clearance between the fin tips and the shroud, the solutions show that the fin heat loss distribution attains a maximum between the base and the tip. In the presence of clearance, the heat loss increases monotonically along the fin from the base to the tip. At large clearances, and especially at smaller fin spacings, the heat loss is virtually zero along most of the fin, but increases markedly near the tip. These distributions are in sharp contrast to that predicted by the uniform heat transfer coefficient model, according to which the heat loss is largest near the base and decreases along the fin to a minimum at the tip.

The calculated distributions of the local fin heat transfer coefficient are markedly nonuniform. In addition, for certain operating conditions (i.e., small values of the fin conductance parameter), the heat transfer coefficient takes on negative values along the upper part of the fin. This finding calls into question the validity of the bulk temperature as a participant in the thermal driving force in complex situations such as that studied here.

The heat loss is also nonuniform along the base surface, with the smallest values at the corner where the fin and the base intersect. The extent of this base-surface nonuniformity depends on the fin conductance parameter and on the fin spacing and the tip clearance.

With regard to the overall heat transfer, it was found that per unit area, the fin is a more efficient transfer area than the base surface.

On the basis of the results presented here, it may be concluded that the conventional uniform heat transfer coefficient model is inapplicable to shrouded fin arrays.

Acknowledgment

This research was performed under the auspices of NSF Grant ENG-7518141.

References

1 Hu, M. H. and Chang, Y. P., "Optimization of Finned Tubes for Heat Transfer in Laminar Tube Flow," ASME JOURNAL OF HEAT TRANSFER, Vol. 95, 1975, pp. 332–338.

2 Masliyah, J. H. and Nandakumar, K., "Heat Transfer in Internally Finned Tubes," ASME JOURNAL OF HEAT TRANSFER, Vol. 98, 1976, pp. 257–261.

J. P. Chiou
Professor.
Department of Mechanical Engineering,
University of Detroit
Detroit, Mich. 48221
Mem. ASME

Thermal Performance Deterioration in Crossflow Heat Exchanger due to the Flow Nonuniformity

A mathematical method to determine the effectiveness of the crossflow heat exchanger accounting for the effect of two-dimensional nonuniform fluid flow distribution is presented. By using a successive substitution technique, the exchanger effectiveness and its deterioration due to the fluid flow nonuniformity effect have been calculated for four typical fluid flow maldistributions. A Flow Nonuniformity Factor has been developed as the principal parameter for predicting the degree of deterioration of the exchanger effectiveness.

Introduction

The fluid flow distribution over the heat exchanger core is usually not uniform under actual operating conditions. The flow nonuniformity through the heat exchanger is generally associated with improper exchanger entrance configuration and imperfect flow passage caused by various problems in design, manufacturing or fouling.

The flow nonuniformity through the exchanger core is known to be detrimental to its thermal performance [1–11]. Most of these investigations consider only one-dimensional flow nonuniformity. In actual operating conditions, the flow nonuniformity over the heat exchanger core is generally two-dimensional, especially for the cases where the core frontal area is larger than the inlet duct or when the exchanger is placed close to the exit or inlet of the fluid moving device. Information of this nature is limited [12, 13] and is the subject matter presented in this paper.

The heat exchanger considered here is a direct transfer type, single pass, crossflow unit. The fluid flow distribution on either hot or cold side may be nonuniform. The thermal performance deterioration of the heat exchanger due to the effects of four typical models of flow nonuniformity are presented for various exchanger design and operating conditions. A Flow Nonuniformity Factor is developed as the principal parameter for determination of the degree of performance deterioration.

Analysis

A direct transfer type, single pass, crossflow heat exchanger may be visualized as having a wall separating the two fluid streams flowing at right angles, as shown by Figs. 1 and 2. Consider that the fluid (either cold or hot) flowing in y' direction is not uniformly distributed over the exchanger core on the $x'z'$ plane. Consider also that the fluid (either hot or cold) flowing in x' direction is uniformly distributed over the exchanger core on the $y'z'$ plane. Other idealizations for this analysis are:

1 Steady-state condition.

2 Axial heat conduction in either fluid is neglected. Their temperatures remain constant and uniform over their respective inlet sections.

3 Both fluids pass in crossflow patterns on both sides of the exchanger wall. Each fluid stream is assumed to have been broken up into a large number of separate flow tubes for passage through the exchanger with no cross or transverse mixing [16]. In other words, change of flow distribution inside the exchanger is neglected.

4 Thermo-physical properties of both fluids and the exchanger wall are independent with respect to the temperatures.

5 The convection heat transfer coefficient between fluids and their respective heat transfer surfaces is directly proportional to the mass velocity of the fluid flow, or $h \sim G^{\beta}$.

6 The heat transfer surface configurations and the heat transfer areas on both sides per unit base area are constant and uniform throughout the exchanger.

7 Thermal resistance through the exchanger wall in the directions normal and parallel to the fluid flows are neglected.

8 No heat generates within the exchanger. No phase changes in the fluid streams flowing through the exchanger. Heat transfer between the exchanger and the surroundings is negligible.

Based on these idealizations, the governing differential equations of heat transfer activities of the subject system are:

$$\frac{-C_x}{y_0 z_0}\frac{\partial T'}{\partial x'} = (\eta h a')_x\,(T' - \theta') \tag{1}$$

$$\frac{C_y \alpha}{x_0 z_0}\frac{\partial t'}{\partial y'} = (\eta' h' a')_y\,(\theta' - t') \tag{2}$$

Contributed by the Heat Transfer Division for publication in The Journal of Heat Transfer. Manuscript received by The Heat Transfer Division December 9, 1977.

$$(\eta h a')_x\,(T' - \theta') = (\eta' h' a')_y\,(\theta' - t') \tag{3}$$

The boundary conditions are:

$$T'\,(0, y', k) = T'_{\text{in}} \tag{4}$$

$$t'\,(x', 0, k) = t'_{\text{in}} \tag{5}$$

Obviously these equations and their solutions presented above are applicable to cases where any one fluid may be in either x' or y' direction. In other words, the results presented in this paper hold when the flow nonuniformity is either on the hot or cold fluid side.

The above equations can be normalized to

$$\frac{\partial T}{\partial x} + \text{NTU}_x\,(T - \theta) = 0 \tag{6}$$

$$\frac{\partial t}{\partial y} + \text{NTU}_y\,\alpha^{\beta-1}\,(t - \theta) = 0 \tag{7}$$

$$V.\text{NTU}_x\,(T - \theta) + \text{NTU}_y\,\alpha^{\beta}\,(t - \theta) = 0 \tag{8}$$

Therefore,

$$\frac{\partial T}{\partial x} + \text{NTU}_1\,(T - \theta) = 0 \tag{9}$$

$$\frac{\partial t}{\partial y} + \text{NTU}_2\,(t - \theta) = 0 \tag{10}$$

$$V.\text{NTU}_1\,(T - \theta) + \alpha\,\text{NTU}_2\,(t - \theta) = 0 \tag{11}$$

with the boundary conditions which are the inlet fluid temperatures on both sides.

$$\begin{cases} T\,(0, y, k) = 1.0 \\ t\,(x, 0, k) = 0.0 \end{cases} \quad \text{or} \quad \begin{cases} T\,(0, y, k) = 0.0 \\ t\,(x, 0, k) = 1.0 \end{cases} \tag{12, 13}$$

Numerical Solutions

The crossflow heat exchanger is divided into $M \times N \times L$ subdivisions as shown in Fig. 2. For each $x'y'$ plane, the arrangement of the subdivision is shown in Fig. 3. If the size of the subdivision is small enough, the temperature of the wall structure of each subdivision can be considered to be at its nodal point and is designated as $\theta_{i,j,k}$. For the same reason, the fluid temperatures can be considered uniform across the respective flow cross sections and vary only in the direction of its flow length. The inlet and exit temperatures of the x' direction fluid flowing through the subdivision (i, j, k) are designated as $T_{i,j,k}$ and $T_{i,j+1,k}$. The inlet and exit temperatures of the y' direction fluid flowing through the subdivision (i, j, k) are designated as $t_{i,j,k}$ and $t_{i+1,j,k}$. Here $1 \le i \le M$; $1 \le j \le N$ and $1 \le k \le L$. The inlet temperatures of the x' and y' direction fluids to the exchanger are therefore $T_{i,1,k}$ and $t_{1,j,k}$ respectively.

As shown in [12, 14, 15], equation (9) can be expressed as

$$\theta_{i,j,k} + BT_{i,j,k} - DT_{i,j+1,k} = 0 \tag{14}$$

or

$$\theta_{i,j-1,k} + BT_{i,j-1,k} - DT_{i,j,k} = 0 \tag{15}$$

thus,

$$T_{i,j,k} = \frac{1}{D}\,\theta_{i,j-1,k} + \frac{B}{D}\,T_{i,j-1,k} \tag{16}$$

Nomenclature

a' = heat transfer area (on either flow side) per unit core volume, m^2/m^3

$a = a'\,x_0 y_0 z_0$ = total heat transfer area (on either flow side), m^2

C = total fluid heat capacity rate on either flow side, J/s K

G = mass flow velocity (on either flow side), kg/m^2 s

h, h' = convection heat transfer coefficient (on either flow side) based on average and local mass flow rates, respectively, W/m^2 K

L, M, N = number of subdivisions in z', y', or x' direction respectively

r = an integer

T', t' = fluid temperature of the uniform flow (x' direction flow) or of the nonuniform flow (y' direction flow), °C

x' = coordinate in x' direction, m

x_0 = overall dimension of exchanger core in x' direction, m

y' = coordinate in y' direction, m

y_0 = overall dimension of exchanger core in y' direction, m

z' = coordinate in z' direction (non-flow direction), m

z_0 = overall dimension of exchanger core in z' direction, m

$A = -\text{NTU}_1 - \alpha\,\text{NTU}_2/V$

$B' = \text{NTU}_1\Delta x$; $B = (1 - 0.5\,B')/B'$; $D = (1 + 0.5\,B')/B'$

$\text{E}' = \text{NTU}_2\Delta y$; $\text{E} = (1 - 0.5\,\text{E}')/\text{E}'$; $F = (1 + 0.5\,\text{E}')/\text{E}'$

$H = 0.5\,\text{NTU}_2\alpha/V$

NTU_x = number of heat transfer units on the x' direction flow (uniform fluid flow) side based on the average mass velocity
$= (\eta h a)_x/C_x$

NTU_y = number of heat transfer units on the y' direction flow (nonuniform fluid flow) side based on the average mass velocity
$= (\eta h a)_y/C_y$

$\text{NTU}_1 = \text{NTU}_x$; $\text{NTU}_2 = \text{NTU}_y \cdot \alpha^{\beta-1}$

NTU = number of heat transfer units for the entire heat exchanger (the average mass velocity on the nonuniform flow side is used)

$$= \frac{1}{C_{\min}\left[\left(\frac{1}{\eta h a}\right)_x + \left(\frac{1}{h a}\right)_y\right]}$$

$$P_1 = \frac{\text{R}}{D}\left[1 + \frac{B}{D}\right];\; P_2 = \frac{H}{F}\left[1 + \frac{\text{E}}{F}\right]$$

$$P_3 = P_1\left(\frac{B}{D}\right);\; P_4 = P_2\left(\frac{\text{E}}{F}\right)$$

$\text{R} = 0.5\,\text{NTU}_1$; $S = (\eta h a)_x/(\eta h a)_y$

$T = (T' - t'_{\text{in}})/(T'_{\text{in}} - t'_{\text{in}})$; $t = (t' - t'_{\text{in}})/(T'_{\text{in}} - t'_{\text{in}})$

$$V = C_x/C_y;\; W = A + \frac{\text{R}}{D} + \frac{H}{F}$$

$x = x'/x_0$; $y = y'/y_0$; $z = z'/z_0$

θ' = exchanger wall temperature, °C

α = local flow nonuniformity parameter which is defined as the ratio of the actual local mass flow rate to the average mass flow rate if the fluid flow is uniformly distributed

β = a constant such as $h \sim G^{\beta}$

ϵ = exchanger heat transfer effectiveness

$$= \frac{C_x\,(T'_{\text{in}} - T'_{\text{exit}})}{C_{\min}(T'_{\text{in}} - t'_{\text{in}})} \text{ or}$$

$$= \frac{C_y\,(t'_{\text{exit}} - t'_{\text{in}})}{C_{\min}\,(T'_{\text{in}} - t'_{\text{in}})}$$

$\Delta\epsilon$ = deterioration of exchanger effectiveness due to the two-dimensional flow nonuniformity

η, η' = overall surface efficiency based on average or local mass velocity

θ = three-subscripted dimensionless temperature of exchanger wall = $(\theta' - t'_{\text{in}})/(T'_{\text{in}} - t'_{\text{in}})$

θ^* = two-subscripted dimensionless temperature of exchanger wall (defined as θ)

$\tau = \dfrac{\Delta\epsilon}{\epsilon}$ = exchanger thermal performance deterioration factor as defined by equation (28)

ψ = flow nonuniformity factor as defined by equation (34)

Subscripts

exit = exit

I = subscript of the two-dimensional variable as defined in equation (22)

i, j, and k = subscripts of three-dimensional variable indicating ith row, jth column on the kth x' y' plane

in = inlet

max = maximum magnitude

min = minimum magnitude

x = direction of uniform fluid flow or indicates that the variable is for the uniform fluid flow side

y = direction of nonuniform fluid flow or indicates that the variable is for the nonuniform flow side

(All variables are dimensionless unless specified otherwise)

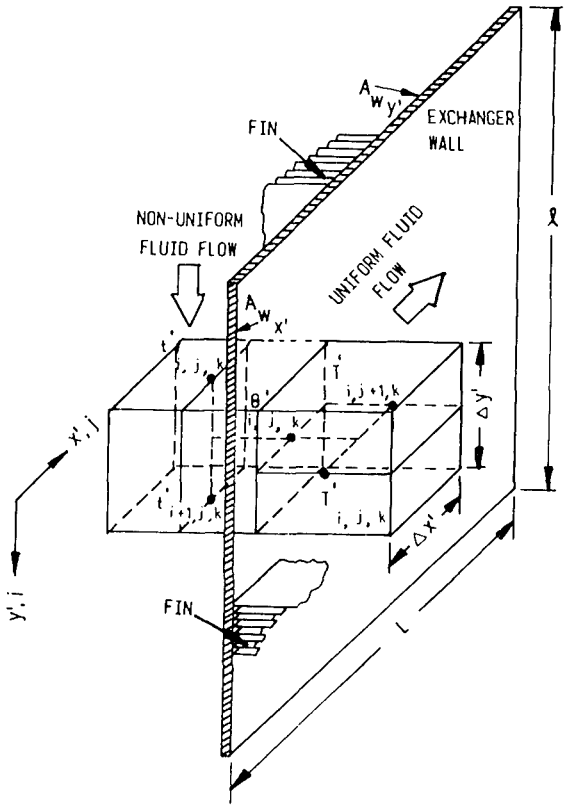

Fig. 1 Single pass crossflow heat exchanger

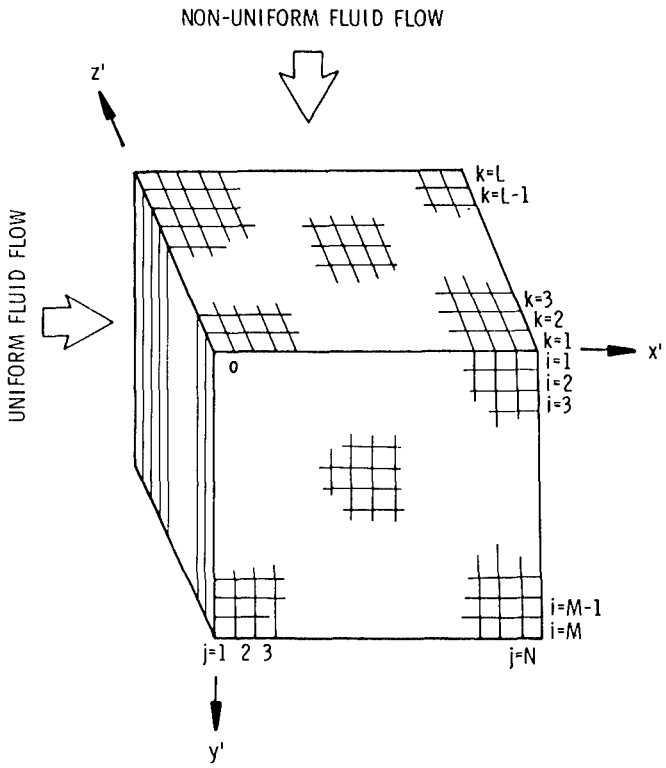

Fig. 2 Single pass crossflow heat exchanger—arrangement of subdivisions

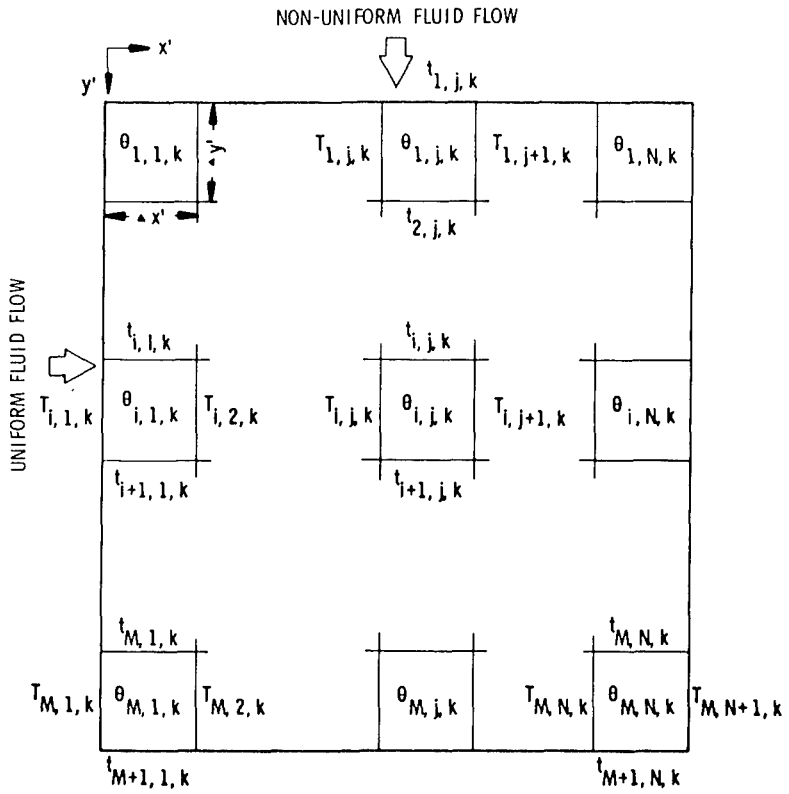

Fig. 3 Subdivisions on *k*th *x'y'* plane

substituting equation (16) into equation (14) then

$$T_{i,j+1,k} = \frac{\theta_{i,j,k}}{D} + \frac{B}{D^2}\theta_{i,j-1,k} + \frac{B^2}{D^2}T_{i,j-1,k} \tag{17}$$

By this technique of successive substitution [12, 14, 15], it can be shown that

$$T_{i,j+1,k} = \frac{1}{D}\left\{\theta_{i,j,k} + \left[\frac{B}{D}\right]\theta_{i,j-1,k} + \left[\frac{B}{D}\right]^2\theta_{i,j-2,k} + \left[\frac{B}{D}\right]^3\theta_{i,j-3,k} + \left[\frac{B}{D}\right]^4\theta_{i,j-4,k} + \cdots + \left[\frac{B}{D}\right]^{j-1}\theta_{i,1,k}\right\} + \left[\frac{B}{D}\right]^j T_{i,1,k} \tag{18}$$

therefore,

$$T_{i,j,k} = \frac{1}{D}\left\{\theta_{i,j-1,k} + \left[\frac{B}{D}\right]\theta_{i,j-2,k} + \left[\frac{B}{D}\right]^2\theta_{i,j-3,k} + \left[\frac{B}{D}\right]^3\theta_{i,j-4,k} + \cdots + \left[\frac{B}{D}\right]^r\theta_{i,j-r-1,k} + \cdots + \left[\frac{B}{D}\right]^{j-2}\theta_{i,1,k}\right\} + \left[\frac{B}{D}\right]^{j-1}T_{i,1,k} \tag{19}$$

Similarly from equation (10), the following relations can be established:

$$t_{i,j,k} = \frac{1}{F}\left\{\theta_{i-1,j,k} + \left[\frac{E}{F}\right]\theta_{i-2,j,k} + \left[\frac{E}{F}\right]^2\theta_{i-3,j,k} + \left[\frac{E}{F}\right]^3\theta_{i-4,j,k} + \cdots + \left[\frac{E}{F}\right]^r\theta_{i-r-1,j,k} + \cdots + \left[\frac{E}{F}\right]^{i-2}\theta_{1,j,k}\right\} + \left[\frac{E}{F}\right]^{i-1}t_{1,j,k} \tag{20}$$

Equations (19) and (20) indicate that the fluid temperatures $T_{i,j,k}$ and $t_{i,j,k}$ can be related to the wall temperatures of all their upstream subdivisions in their respective flow channels and the inlet temperatures of the fluids at those flow channels, $T_{i,1,k}$ and $t_{1,j,k}$ which are known.

Similarly equation (11) can be expressed as

$$W\,\theta_{i,j,k} + P_1\,\theta_{i,j-1,k} + P_2\,\theta_{i-1,j,k} + P_3\left\{\theta_{i,j-2,k} + \left[\frac{B}{D}\right]\theta_{i,j-3,k} + \left[\frac{B}{D}\right]^2\theta_{i,j-4,k} + \cdots + \left[\frac{B}{D}\right]^{j-3}\theta_{i,1,k}\right\} + P_4\left\{\theta_{i-2j,k} + \left[\frac{E}{F}\right]\theta_{i-3j,k} + \left[\frac{E}{F}\right]^2\theta_{i-4j-k} + \cdots + \left[\frac{E}{F}\right]^{i-3}\theta_{1j,k}\right\}$$

$$= -\,\mathrm{R}\left[1 + \frac{B}{D}\right]\left[\frac{B}{D}\right]^{j-1}T_{i,1,k} - H\left[1 + \frac{E}{F}\right]\left[\frac{E}{F}\right]^{i-1}t_{1,j,k} \tag{21}$$

In equation (21), the wall temperature $\theta_{i,j,k}$ is expressed in a two-dimensional array on any kth plane. Because the wall temperature of all the related subdivisions are present, identification of each element and its coefficient in the matrix is confusing. In order to simplify this problem, the two-dimensional array $\theta_{i,j,k}$ on any kth plane is transformed into a one-dimensional array $\theta^*_{I,k}$ on that kth plane, here

$$I = (i-1)\,N + j \tag{22}$$

The general arrangement of the one-dimensional array, $\theta^*_{I,k}$ on any kth plane is shown in Fig. 4. After this transformation, equation (21) may be written as

$$W\,\theta^*_{I,k} + P_1\,\theta^*_{I-1,k} + P_2\,\theta^*_{I-N,k} + P_3\left\{\theta^*_{I-2,k} + \left[\frac{B}{D}\right]\theta^*_{I-3,k} + \left[\frac{B}{D}\right]^2\theta^*_{I-4,k} + \cdots + \left[\frac{B}{D}\right]^{j-3}\theta^*_{I-j+1,k}\right\} + P_4\left\{\theta^*_{I-2N,k} + \left[\frac{E}{F}\right]\theta^*_{I-3N,k} + \left[\frac{E}{F}\right]^2\theta^*_{I-4N,k} + \cdots + \left[\frac{E}{F}\right]^{i-3}\theta^*_{j,k}\right\}$$

$$= -\,\mathrm{R}\left[1 + \frac{B}{D}\right]\left[\frac{B}{D}\right]^{j-1}T_{i,1,k} - H\left[1 + \frac{E}{F}\right]\left[\frac{E}{F}\right]^{i-1}t_{1,j,k} \tag{23}$$

Equation (23) represents the wall temperature of node $\theta^*_{I,k}$ which is the wall temperature of the subdivision (i, j, k) on the kth $x'y'$ plane. The node I and its related nodes in equation (23) are also shown in Fig. 4.

Equation (23) is the principal finite-difference equation used in this investigation. This equation must be formulated for every subdivision of the system. Therefore, there are $M \times N$ equations to form a set of simultaneous equations in any $x'y'$ plane. The unknown variables in these equations are θ^*'s of the related subdivisions. After the θ^*'s are determined, they are transformed back to the two-dimensional array, $\theta_{i,j,k}$ on the kth plane concerned. The temperature distributions of the two fluid streams on this kth $x'y'$ plane are then calculated by

$$T_{i,j+1,k} = (\theta_{i,j,k} + B\,T_{i,j,k})/D \tag{24}$$

$$t_{i+1,j,k} = (\theta_{i,j,k} + \mathrm{E}\,t_{i,j,k})/\mathrm{E} \tag{25}$$

The average dimensionless exit temperatures of the two fluid streams from the heat exchanger are:

$$T_{\text{exit}} = \left(\sum_{k=1}^{L}\sum_{i=1}^{M} T_{i,N+1,k}\right)\Big/(M \cdot L) \tag{26}$$

$$t_{\text{exit}} = \left(\sum_{k=1}^{L}\sum_{j=1}^{N} \alpha\, t_{M+1,j,k}\right)\Big/\sum \alpha \tag{27}$$

Next T and t are transformed back to T' and t' respectively. The heat transfer effectiveness ϵ can then be determined.

The Exchanger Thermal Performance Deterioration Factor τ is introduced to illustrate the influence of the two-dimensional flow nonuniformity on the deterioration of exchanger thermal performance. It is defined as

$$\tau = \frac{\Delta\epsilon}{\epsilon} = \frac{\epsilon_{\text{uniform flow}} - \epsilon_{\text{nonuniform flow}}}{\epsilon_{\text{uniform flow}}} \tag{28}$$

The deterioration factors were calculated for four typical flow maldistribution models and for various exchanger design and operating parameters. These parameters are V, S and the exchanger NTU. All these parameters are based on the uniform flow distribution conditions.

NTU_x and NTU_y used in the various equations developed before are determined from V, S and NTU as shown below.

For the case when C_x is $C_{\min}$,

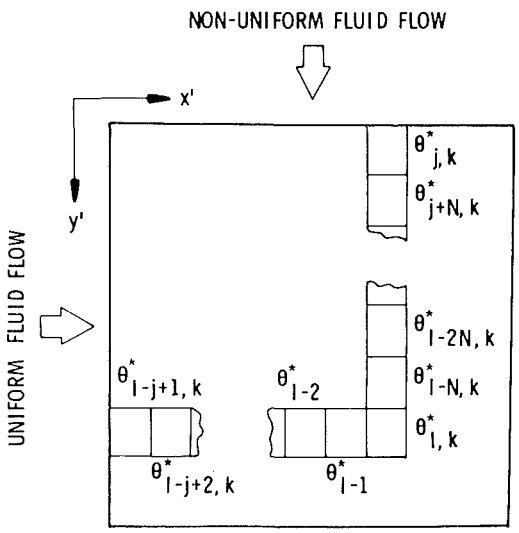

Fig. 4 Related nodes on any kth $x'y'$ plane

$$NTU_x = NTU\ (1 + S);\ NTU_y = NTU\left(1 + \frac{1}{S}\right) V \qquad (29)$$

For the case when C_y is C_{min},

$$NTU_x = NTU\ (1 + S)/V;\ NTU_y = NTU\left(1 + \frac{1}{S}\right) \qquad (30)$$

The accuracy of the solution obtained by finite-difference method depends on the number of the subdivisions used. Use of a greater number of subdivisions not only can produce results of higher accuracy but can also enhance the convergence. Practically, the number of subdivisions used must be determined by a compromise between the accuracy desired and the time required on the computer. It was demonstrated [14, 15] that if a system of 10 × 10 matrix on any one $x'y'$ plane was used, the results obtained by using the same technique for similar problems were accurated to the third digit for most cases. Thus, 10 × 10 matrix arrangement on any $x'y'$ plane was used throughout this investigation.

Results and Discussions

Four typical models of fluid flow maldistributions across the exchanger core were used in this investigation. The Local Flow Nonuniformity parameter, α, of these four flow distribution models is presented in Tables 1–4. In each flow model, there are 10 × 10 α's, which correspond to the 10 × 10 subdivisions on the $x'z'$ plane perpendicular to the direction of the nonuniform fluid flow. Because of the flow distribution, which is symmetric with respect to the center axes of the plane perpendicular to the fluid flow, only one-fourth of α's are presented. Models 1 to 3 are data obtained from wind tunnel experiments. These are typical maldistributions of air flow through the exchanger core when the fan is placed close to the exchanger, such as in the cases of automobile radiators. In these models, the maximum air mass velocities are located at centers of the two half-sections of the exchanger cores. Model 4 is the typical flow maldistribution when the flow inlet manifold is at the center of the core [3]. The inlet manifold is smaller than the exchanger core frontal area and no adequate transition duct is provided. Fig. 5 shows the schematic views of the relative mass velocity distribution of the models.

Typical relationships between the Exchanger Thermal Performance Deterioration Factor τ and the design/operating parameters of the exchangers are presented in Figs. 6–11. Information presented in these figures is restricted to the cases when the flow patterns in the exchangers are predominantly fully developed, turbulent mode only. Thus the convection heat transfer coefficient h is considered to be proportional to $G^{0.8}$ in preparation of these figures. However, the analysis and equations presented in previous sections can be applied to any flow pattern if appropriate β's are used. The range of the design and operating parameters of the exchanger used in this investigation are V (0.125 to 8.0), S (0.5, 1.0 and 2.0) and NTU (0.1 to 100.0).

Fig. 6 shows the τ – NTU relationships for cases of S = 1.0 and $V \leq 1.0$ and for fluid model No. 1. Under this condition,

$$C_x = C_{min},\ NTU_1 = 2\ NTU, \text{ and } NTU_2 = 2\ NTU \cdot V\ \alpha^{\beta-1} \qquad (31)$$

From the analysis presented previously, it can be shown that if $NTU_1 > NTU_2$, the deterioration of the exchanger thermal performance will be supressed; whereas if $NTU_2 > NTU_1$, this performance deterioration will be augmented. It is noted from equation (31), when NTU increases, NTU_2 increases much slower than NTU_1 does. Thus the exchanger performance deterioration is surpressed and τ decreases when NTU increases as shown in Fig. 6. The smaller the V, the stronger is this supression and the lower is τ as shown also in this figure. When NTU decreases and approaches zero, the influence of $\alpha^{\beta-1}$ on τ gradually becomes significant, especially for cases of small V. In other words, τ depends predominantly on $\alpha^{\beta-1}$ and not on NTU or V. Thus τ appears to approach a common constant value under this situation. When V = 1.0 and S = 1.0, then

$$C_x = C_y,\ NTU_1 = 2\ NTU, \text{ and } NTU_2 = 2\ NTU \cdot \alpha^{\beta-1} \qquad (32)$$

Because $\Sigma\alpha^{\beta-1}$ is larger than 1.0 for all the fluid models under this investigation, when NTU increases, the influence of NTU_2 on the deterioration of exchanger performance exceeds that contributed by NTU_1. Thus τ increases with NTU as shown in Fig. 6. For cases when $V > 0.5$, the τ – NTU relationships gradually change from the form of low V to that of V = 1.0 as is also shown in this figure.

Fig. 7 shows the τ – NTU relationships for cases of $V \geq 1.0$ and S = 1.0, and for fluid model No. 1. Now,

Table 1 Local flow nonuniformity parameters, α, for flow distribution model No. 1

(Flow Nonuniformity Factor, ψ, = 0.1915)

i or j =	1; 10	2; 9	3; 8	4; 7	5; 6
k = 1; 10	0.175	0.450	0.925	0.450	0.275
2; 9	0.450	0.825	1.275	1.150	0.200
3; 8	0.825	0.925	1.375	1.650	0.450
4; 7	0.925	1.100	1.475	1.700	0.925
5; 6	1.325	1.475	1.750	1.725	1.200

Table 2 Local flow nonuniformity parameters, α, for flow distribution model No. 2

(Flow Nonuniformity Factor, ψ, = 0.2572)

i or j =	1; 10	2; 9	3; 8	4; 7	5; 6
k = 1; 10	0.080	0.200	0.400	0.200	0.100
2; 9	0.314	0.575	0.889	0.802	0.139
3; 8	0.825	0.925	1.375	1.650	0.450
4; 7	1.018	1.210	1.623	1.870	1.018
5; 6	1.656	1.844	2.188	2.156	1.500

Table 3 Local flow nonuniformity parameters, α, for flow distribution model No. 3

(Flow Nonuniformity Factor, ψ, = 0.4033)

i or j =	1; 10	2; 9	3; 8	4; 7	5; 6
k = 1; 10	0.080	0.100	0.100	0.080	0.080
2; 9	0.100	0.200	0.300	0.200	0.100
3; 8	0.400	0.500	1.000	1.000	0.600
4; 7	0.960	1.000	2.500	2.000	1.100
5; 6	1.000	3.000	4.000	3.000	1.600

Table 4 Local Flow nonuniformity parameters, α, for flow distribution model No. 4

(Flow Nonuniformity Factor, ψ, = 0.1221)

i or j =	1; 10	2; 9	3; 8	4; 7	5; 6
k = 1; 10	0.720	0.720	0.720	0.720	0.720
2; 9	0.720	1.000	1.000	1.000	1.000
3; 8	0.720	1.000	1.000	1.000	1.000
4; 7	0.720	1.000	1.000	1.500	1.500
5; 6	0.720	1.000	1.000	1.500	2.180

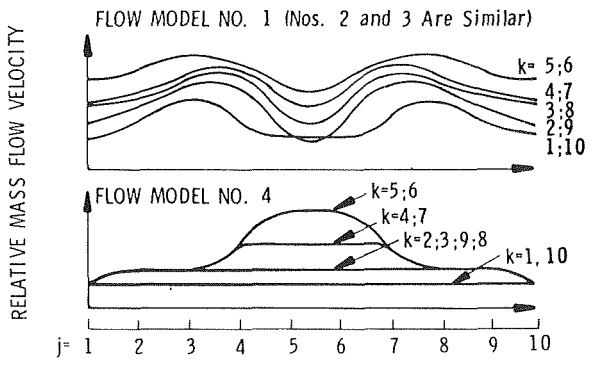

Fig. 5 Flow distribution models

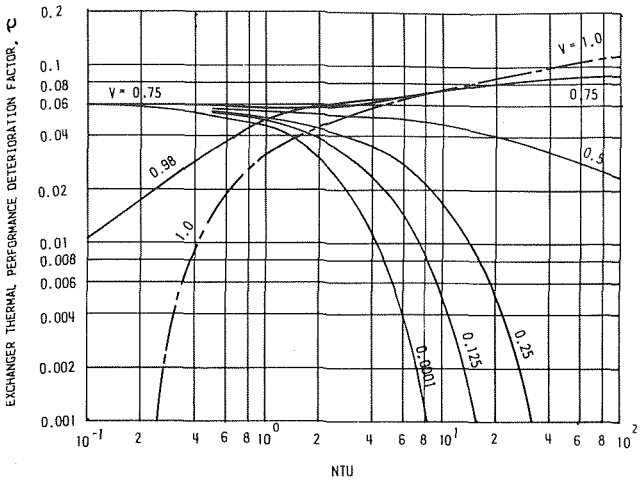

Fig. 6 Relations between exchanger thermal performance deterioration factor τ and various parameters for flow distribution model 1 and $S = 1.0$

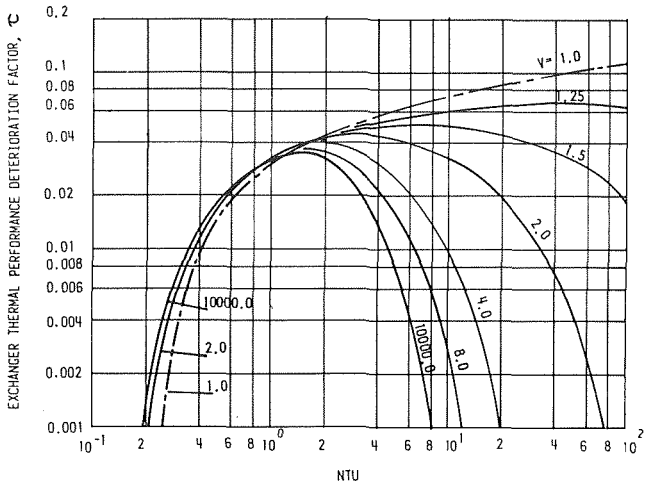

Fig. 7 Relations between exchanger thermal performance deterioration factor τ and various parameters for flow distribution model 1 and $S = 1.0$

$$C_y = C_{\min},\ \mathrm{NTU}_1 = 2\ \mathrm{NTU}/V,\ \text{and}\ \mathrm{NTU}_2 = 2\ \mathrm{NTU} \cdot \alpha^{\beta-1} \quad (33)$$

From equation (33) it is noted that when NTU increases, NTU_2 increases more rapidly than NTU_1 does. Thus τ increases with NTU as shown in Fig. 7. It is also noted that $\mathrm{NTU} = (\eta ha)_{x \text{ or } y}/2\, C_y$. As NTU increases to a larger number, then C_y in turn decreases to a relatively smaller value in comparison with $(\eta ha)_{x \text{ or } y}$. Under this condition, the influence of the flow nonuniformity, of course, diminishes. Thus τ decreases when NTU increases to a large number. In short, τ first increases, then decreases when NTU increases as shown in this figure. The larger the value of V, the less the influence of the flow nonuniformity on the exchanger performance is observed. Thus τ appears to be smaller for larger V at the same NTU as also shown in this figure.

Fig. 8 shows the τ-NTU relationships for various V's and using S as parameter. Based on equations (29) and (30) and the discussion presented above, these relationships shown in Fig. 8 can be recognized. Figs. 9–11 present the τ-NTU relationships for fluid model Nos. 2 to 4. These relationships are similar to those of fluid model No. 1 as shown in Figs. 6 and 7.

The deterioration of thermal performance of single pass crossflow heat exchanger due to flow nonuniformity presented above is generally similar to those reported in previous investigations [1, 4, 5, 9]. However, the type of the exchanger and the fluid maldistribution model considered in this investigation are basically different from those reported previously; direct comparison is thus not possible nor practical.

The relations present in these figures may be used when either the hot or cold fluid flow is not distributed uniformly provided all other parameters are unchanged.

It is noted that the deterioration of the exchanger performance due to flow nonuniformity depends on many parameters, such as V, S, NTU, NTU_x, NTU_y, α, β etc. Development of a useful correlation between τ and these parameters is needed. Hopefully this can be accomplished soon. At this time, a somewhat limited correlation involving only τ, α and NTU for the case of $V = 1.0$ and $S = 1.0$ is presented below.

It seems likely [17, 18] that the local exchanger effectiveness is related to the following parameters:

$$\alpha;\ e^{-(x/x_0)} \quad \text{and} \quad e^{-(y/y_0)}$$

Based on the concept of standard deviation or variance [19, 20, 21], a Flow Nonuniformity Factor, ψ, on the deterioration of exchanger thermal performance is devloped. It is:

$$\psi = \sqrt{\frac{\sum_{i=1}^{M}\sum_{j=1}^{N}\left[(1-\alpha)\, e^{-i/M}\, e^{-j/N}\right]^2}{M \cdot N}} \quad (34)$$

This factor is found to be relevant to the determination of the exchanger's overall effectiveness and its deterioration due to the two-dimensional flow nonuniformity as shown in Fig. 12.

Fig. 12 presents the relationships of Exchanger Thermal Performance Deterioration Factor, τ, and the Flow Nonuniformity Factor, ψ, for the four different fluid flow distributions studied in this investigation. It is noted that a generalized correlation can be established. This demonstrates the relevance of using this Flow Nonuniformity Factor, ψ, or its modifications as the principal parameter for predicting the exchanger performance deterioration due to the effect of the two-dimensional flow nonuniformity. Future research work of expanding this factor to include all other parameters, such as V, S, NTU_x, NTU_y and β is highly recommended.

Conclusions

A successive substitution technique and a numerical method were developed to determine the exchanger heat transfer effectiveness and its deterioration due to the two-dimensional flow nonuniformity on either hot or cold fluid sides. The ranges of the design and operating parameters covered are in the range of general interest. The methods developed, however, are not limited to within these ranges, and also can be applied to treat various other heat exchanger and solar collector problems as well.

A Flow Nonuniformity Factor, ψ, has been developed for predicting the deterioration of exchanger thermal performance due to the two-dimensional flow nonuniformity. A generalized relation has been observed between the deterioration of the exchanger performance and this Flow Nonuniformity Factor for all the four flow distribution models considered in this investigation. It is noted that this Factor should be expanded to include all relevant parameters if possible. Future work in this area is needed and recommended.

The information obtained in this study clearly indicates that the deterioration of thermal performance of single pass crossflow heat exchanger due to the two-dimensional flow nonuniformity may become significant in some typical applications. This deterioration in thermal performance should not be ignored in the analysis and design of the subject heat exchanger, as has been the case so far in industry.

References

1 McDonald, J. S. and Eng, K. Y., "Tube Side Flow Distribution Effects on Heat Exchanger Performance," *AIChE, Chem. Eng. Prog. Sym.*, Ser. No. 41, Vol. 59, 1963, pp. 11–17

2 Cichelli, M. T. and Boucher, D. F., "Design of Heat Exchanger Heads for Low Holdup," *AIChE, Chem. Eng. Prog.*, Vol. 52, No. 5, 1956, pp. 213–218.

3 Wilson, D. G., "A Method of Design for Heat Exchanger Inlet Headers," ASME Paper No. 66-WA/HT-41, 1966.

4 Dobryakov, B. A., Gagarina, M. V., Efremov, A. S., Mokin, V. N., Mor-

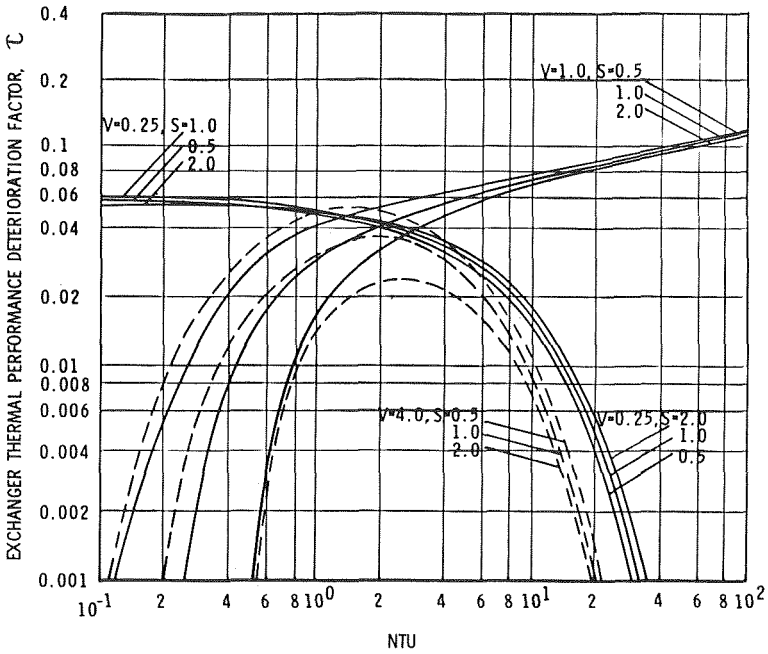

Fig. 8 Relations between exchanger thermal performance deterioration factor τ and various parameters for flow distribution model 1

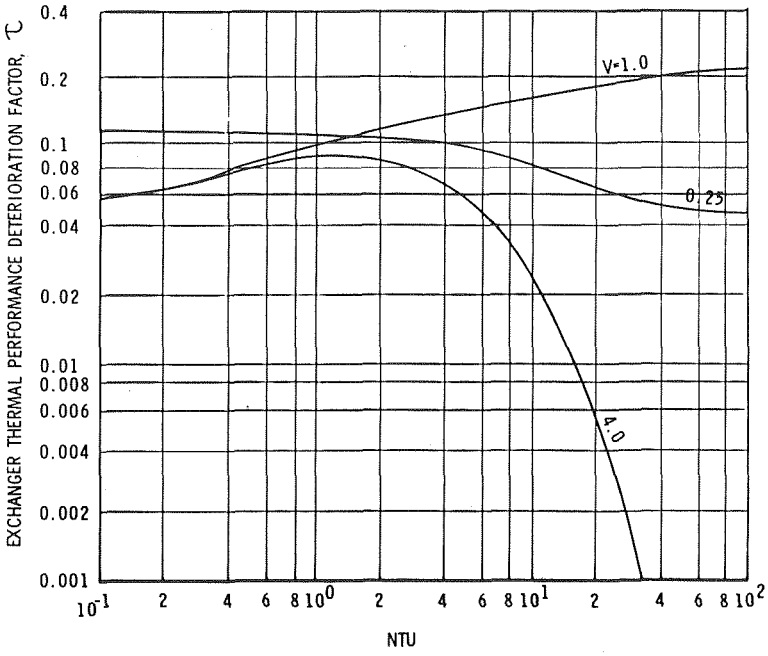

Fig. 9 Relations between exchanger thermal performance deterioration factor τ and various parameters for flow distribution model 2 and $S = 1.0$

gulis-Yakushev, V. Y. and Rostovtsev, V. I., "The Calculation of Heat Exchanger Equipment with Crossflow of the Heat Transfer Agents," *International Chem. Eng.*, Vol. 13, No. 1, 1973, pp. 81–84.

5 Kutchey, J. A. and Julien, H. L., "The Measured Influence of Flow Distribution on Regenerator Performance," *SAE TRANS*, Vol. 83, Paper No. 740164, 1974.

6 London, A. L., "Laminar Flow Gas Turbine Regenerators—The Influence of Manufacturing Tolerances," *ASME Journal of Engineering for Power*, Vol. 92, 1970, pp. 46–56.

7 Shah, R. K. and London, A. L., "Influence of Brazing on Very Compact Heat Exchanger Surfaces," ASME Paper No. 71-HT-29. 1971.

8 Mondt, J. R., "Effects of Nonuniform Passages on Deepfold Heat Exchanger Performance," ASME Paper No. 76-WA/HT-32, 1976.

9 Mueller, A. C., "An Inquiry of Selected Topics on Heat Exchanger Design," Donald Q. Kern Award Lecture, 16th National Heat Transfer Conference, August 1976.

10 Taborek, J., "Fouling—The Major Unresolved Problem in Heat Transfer, Part I," *AIChE, Chem. Eng. Prog.*, Vol. 68, No. 2, 1972, pp. 59–67.

11 Taborek, J., "Predictive Methods for Fouling Behavior," *AIChE, Chem. Eng. Prog.*, Vol. 68, No. 7, 1972, pp. 69–78.

12 Chiou, J. P., "The Effect of Nonuniform Fluid Flow Distribution on Thermal Performance of Crossflow Heat Exchanger," ASME Paper No. 77-WA/HT-3, 1977.

13 Chiou, J. P., "Thermal Performance Deterioration in Crossflow Heat

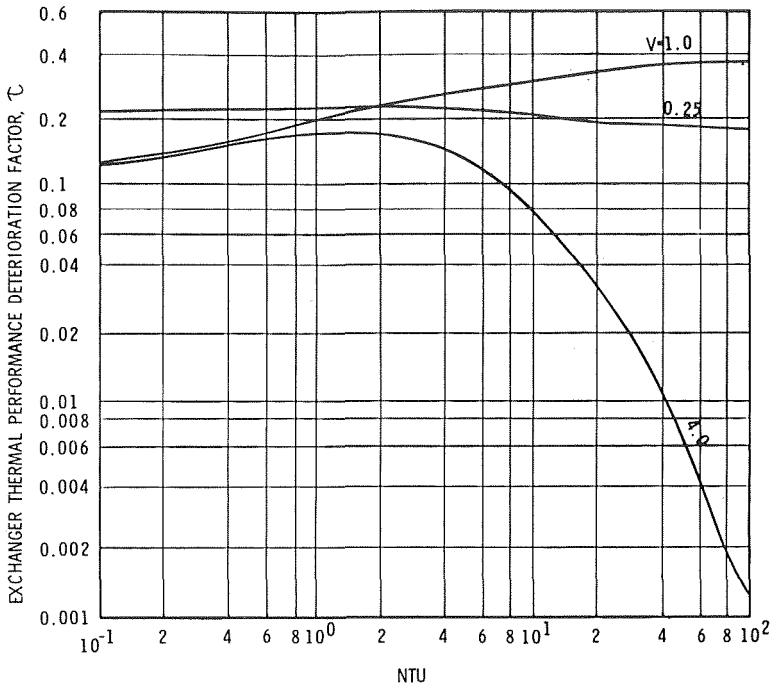

Fig. 10 Relations between exchanger thermal performance deterioration factor τ and various parameters for flow distribution model 3 and $S = 1.0$

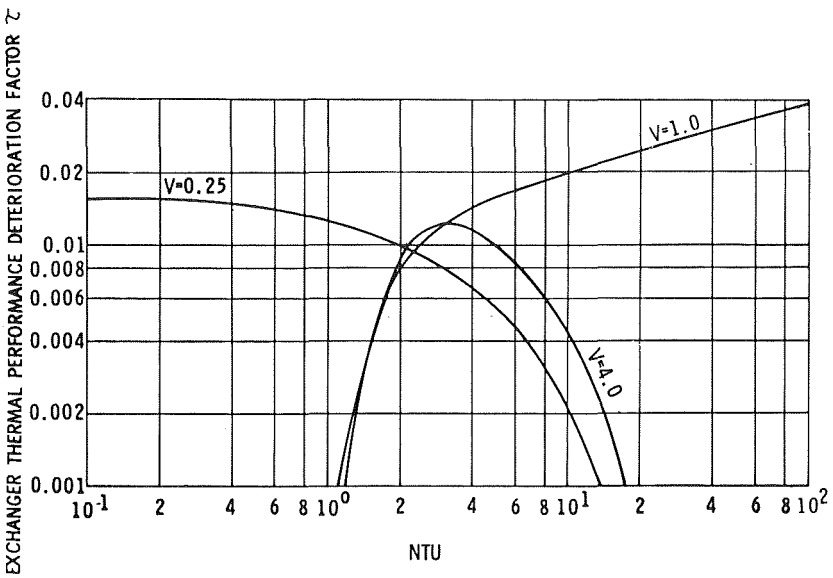

Fig. 11 Relations between exchanger thermal performance deterioration factor τ and various parameters for flow distribution model 4 and $S = 1.0$

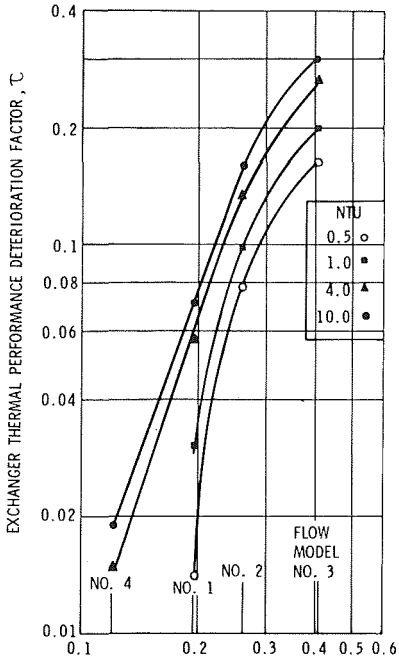

Fig. 12 Relations between exchanger thermal performance deterioration factor τ and the flow nonuniformity factor ψ

Exchanger due to Flow Nonuniformity on Both Hot and Cold Sides," Paper No. HX-16 presented at the Sixth International Heat Transfer Conference, Toronto, Canada, August 1978. Also in the Conference Proceedings, Vol. 4, pp. 279–284.

14 Chiou, J. P., "Thermal Performance Deterioration in Crossflow Heat Exchanger due to Longitudinal Heat Conduction in the Wall," ASME Paper No. 76-WA/HT-8, 1976.

15 Chiou, J. P., "The Effect of Longitudinal Heat Conduction on Crossflow Heat Exchanger," ASME JOURNAL OF HEAT TRANSFER, Vol. 100, 1978, pp. 346–351.

16 Kays, W. and London, A. L., *Compact Heat Exchangers*, 2nd ed., McGraw-Hill, New York, 1964.

17 Peters, D. L., "Heat Exchanger Design with Transfer Coefficient Varying with Temperature or Length of Flow Path," *Wärme und Stoffübertragung*, Vol. 3, No. 4, 1970, pp. 210–226.

18 Chiou, J. P., "Correction Factor to Unit Core Heat Transfer Capability of Heat Exchanger Core due to Variation of Tube Length," *SAE TRANS*, Vol. 84, Paper No. 750884, 1975.

19 Young, H. D., *Statistical Treatment of Experimental Data*, McGraw-Hill, New York, 1962.

20 Blum, J. R., and Rosenblatt, J. I., *Probability and Statistics*, W. B. Saunders Co., Philadelphia, 1972.

21 Breman, S. M., *Mathematical Statics*, Intext, Scranton, 1971.

K. K. Koram
E. M. Sparrow

Department of Mechanical Engineering,
University of Minnesota,
Minneapolis, Minn.

Turbulent Heat Transfer Downstream of an Unsymmetric Blockage in a Tube

Pipe flow experiments were performed to study the heat transfer in the separation, reattachment, and redevelopment regions downstream of a wall-attached blockage in the form of a segmental orifice plate. Water was the working fluid, and the Reynolds number encompassed the range from about 10,000–60,000. The extent of the flow blockage was varied from one-fourth to three-fourths of the tube cross section. Heat transfer coefficients were determined both around the circumference of the uniformly heated tube and along its length. The axial distributions of the circumferential average Nusselt numbers show an initial increase, then attain a maximum, and subsequently decrease toward the fully developed regime. These Nusselt numbers are much higher than those for a conventional thermal entrance region. The unsymmetric blockage induces variations of the Nusselt number around the circumference of the tube. Axial distributions of the Nusselt number at various fixed angular positions reveal the presence of two types of maxima. One of these is associated with the reattachment of the flow and the other occurs due to the impingement of flow deflected by the blockage onto the tube wall. The circumferential variations decay with increasing downstream distance, but the rate of decay for the case of the smallest blockage is remarkably slow. Although most of the tests were performed for Pr = 4, supplementary experiments for Pr = 8 showed that the results are valid for a range of Prandtl numbers.

Introduction

Heat transfer in tubes and ducts in the presence of flow separation and recirculation (i.e., backflow) is widely encountered in practice. These complex flows may, for example, be caused by abrupt changes in duct cross section, valves, wall-attached baffles, orifices, and other partial blockages of the flow passage. In general, the resulting flow fields are three-dimensional. On the other hand, in the research literature on separation related heat transfer in ducts, attention appears to have been focused on geometrically symmetric configurations intended to provide two-dimensional flow conditions. The present research was undertaken in order to study the heat transfer characteristics associated with three-dimensional separation and its associated flow phenomena.

The experiments to be described here are concerned with turbulent heat transfer downstream of a segmental orifice plate that is situated at the entrance cross section of a uniformly heated circular tube. As illustrated schematically in Fig. 1, a segmental orifice plate is a wall-attached blockage in the shape of a circular segment. The presence of the orifice plate causes a nonaxisymmetric constriction of the flow followed by strongly three-dimensional expansion in the downstream region. Behind the plate itself, there is a separation zone filled with recirculating fluid. The flow reattaches to the wall downstream of the separation zone and then redevelops, ultimately attaining an axisymmetric fully developed velocity distribution.

It is expected that the heat transfer characteristics will be markedly affected by the separation, reattachment, and redevelopment of the flow. Furthermore, circumferential nonuniformities should be induced by the nonaxisymmetric deflection of the flow by the orifice plate. For large blockages, impingement of the deflected flow on the tube wall opposite the blockage appears likely. It is against the background of these expectations that the research was initiated.

The experiments were performed using water as the working fluid. The test section tube was heavily instrumented with thermocouples

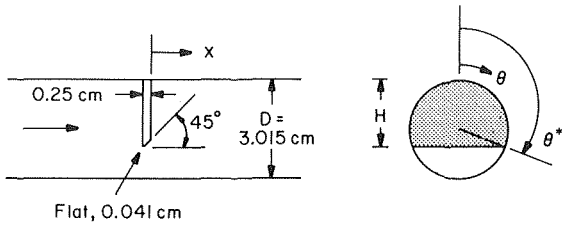

Fig. 1 Diagram of segmental blockage element

Contributed by the Heat Transfer Division for publication in the JOURNAL OF HEAT TRANSFER. Manuscript received by the Heat Transfer Division January 10, 1978.

in order to detect both circumferential and axial distributions. Heating was accomplished by ohmic dissipation in the tube wall. Three degrees of flow blockage were investigated, respectively 1/4, 1/2, and 3/4 of the tube cross-sectional area. The Reynolds number range extended from 10,000–60,000. For most of the experiments, the Prandtl number was maintained at a value of 4. To examine the trends of the results with Prandtl number, supplementary experiments were carried out at Pr = 8.

The results of the experiments encompass both circumferential and axial distributions of the heat transfer coefficient. These detailed local distributions provide insights into the transport processes and also serve to identify the locations of possible hot (or cold) spots. In addition, at each cross section, circumferential average heat transfer coefficients have been evaluated.

As was noted earlier, experiments of the type performed here do not appear to have been reported in the literature. Related heat transfer problems which have been studied experimentally include the flow downstream of an axisymmetric orifice [1] or a sudden enlargement [2] in a tube, and of a sudden enlargement in a rectangular duct [3]. These papers will be revisited in connection with the discussion of the present results.

The Experiments

The experimental apparatus was a closed-loop, pressurized-water facility. Along the path of flow, it included a turbine-type water pump, the unheated hydrodynamic development length, the test section and exit section, an orifice-type flow meter, and a heat exchanger. The starting length, test section, and exit section were all cut from a single piece of type 304 stainless steel tubing. The bore of each tube was honed to a smooth finish, with a resulting inside diameter of 3.015 cm (1.187 in.). To determine the wall thickness, short axial lengths were cut from the ends of the respective tubes and each length was slit longitudinally into two halves, thereby exposing its inner surface. Thicknesses at numerous locations were measured via a specially fitted micrometer, yielding a mean value of 0.084 ± 0.0025 cm (0.033 ± 0.001 in.). The lengths of the hydrodynamic development section, the test section, and exit section were 60, 33, and 10 diameters, respectively. These components were arranged horizontally along a common centerline.

The test section was designed to be free of supporting fixtures in order to avoid extraneous heat losses. Coupling between the test section and the entrance and exit sections was via delrin (plastic) bushings sandwiched between the flanged ends of the respective members. To minimize circumferential heat conduction which might influence the temperature distribution in the adjacent portion of the test section, the flanges were made of stainless steel, the thermal conductivity of which is the lowest among other candidate metals. As a further precaution, numerous holes were drilled in the flange at the upstream end of the test section in order to break up possible conduction paths.

Table 1 Characteristics of orifice plate (Fig. 1)

Blockage ratio			
Nominal	Actual	H, cm	θ^*, deg
1/4	0.264	0.940	68
1/2	0.486	1.49	89
3/4	0.730	2.07	112

The segmental orifice plate was housed in the bushing at the upstream end of the test section. The plates were made of delrin and were machined to a thickness of 0.254 cm (0.1 in.) in accordance with ASME orifice standards. Also, as specified by the standards, a short flat section, 0.041 cm (0.016 in.) in length, and a 45 deg bevel were machined on the exposed lip of the plate. The choice of delrin, a plastic, as the orifice plate material, in lieu of a metal, was made to minimize fin-like heat conduction.

The orifice plate dimensions were selected so as to give rise to nominal blockages of 1/4, 1/2, and 3/4 of the cross-sectional area of the tube. The actual blockage area ratios which resulted from the machining are listed in Table 1. Also given in the table are the blockage height H and lip angle θ^* which are defined in Fig. 1. As shown in the figure, the plate was positioned in the upper part of the cross section, with geometric symmetry about the vertical diameter.

Fittings were attached to the respective ends of the test section tube to carry a-c electric current for the ohmic heating of the tube wall. In the design of these fittings, account was taken of the high currents to be carried (up to about 600 amp) and of the need to minimize heat conduction which might affect the temperature of the wall. In particular, had a copper or aluminum ring been affixed to each end of the tube to convey the current, conduction in the ring would have diminished otherwise existing circumferential temperature variations in the adjacent tube wall. In view of this, discontinuous copper rings, each consisting of twelve separate segments, were used instead of continuous rings.

Current was carried to (or from) each segment via a 0.635 cm (1/4 in.) dia copper rod. The assemblage of the twelve rods at each end of the tube resembled the spokes of a wheel, especially since their outer ends terminated in a large circular copper rim to which the electrical cables were attached. Heat conduction along the rods was suppressed by guard heating/cooling applied to the rim via water-carrying tubes. The water temperature was adjusted so as to equalize the readings of thermocouples situated at the inner and outer ends of the respective rods.

The test section was insulated with silica aerogel powder, whose thermal conductivity is less than that of air. Those parts of the electrical system which protruded from the powder were insulated with fiberglass.

The circumferential and axial temperature distribution on the

Nomenclature

A = cross-sectional area of tube, $\pi D^2/4$
A_{open} = open area at blockage cross section
D = inside diameter of tube
H = blockage height, Fig. 1
$\bar{h}_x$ = circumferential average heat transfer coefficient at x, equation (2)
$h_x(\theta)$ = local coefficient at θ and x, equation (1)
k_w = thermal conductivity of tube wall
k = thermal conductivity
$\dot{m}$ = mass rate of flow
$\overline{\mathrm{Nu}_x}$ = circumferential average Nusselt number at x, $\bar{h}_x D/k$
$\mathrm{Nu}_x(\theta)$ = local Nusselt number at θ and x, $h_x(\theta)D/k$
Nu_{fd} = fully developed Nusselt number
Pr = Prandtl number
q = local heat flux
$\bar{q}$ = average heat flux
Re = Reynolds number, $4\dot{m}/\mu\pi D$
r = radial coordinate
r_i = inside radius of tube
r_o = outside radius of tube
S = volume rate of ohmic heating
T = temperature
T_b = bulk temperature
$T_{wx}(\theta)$ = inside wall temperature at x, θ
$\overline{T}_{wx}$ = average inside wall temperature at x
x = axial coordinate, Fig. 1
θ = angular coordinate, Fig. 1
θ^* = lip angle, Fig. 1
μ = viscosity

Subscripts

x = at axial station x

outside surface of the test section tube was measured with a total of 88 calibrated 30-gage iron-constantan thermocouples. At each of ten axial stations between $x/D = 1$ and 15, eight thermocouples were deployed uniformly at 45 deg intervals around the circumference, starting at $\theta = 0$ (see Fig. 1). At $x/D = 18, 21, 27$, and 32, there were two thermocouples per station, respectively at $\theta = 0$ and 180. The junction of each thermocouple was affixed to the tube surface with copper oxide cement, which is both a good heat conductor and an excellent electrical insulator.

Measurements were also made of the inlet and outlet bulk fluid temperatures. For this purpose, multi-baffle mixing boxes were positioned at the inlet of the hydrodynamic development section and at the downstream end of the exit section. Each mixing box was equipped with three thermocouples. The temperature measurements in the upstream mixing box were corroborated to within 2 μV or better by four thermocouples deployed along the length of the hydrodynamic development section. Both mixing boxes were well insulated.

The system was equipped with a number of vent valves positioned so as to enable air to be bled, and bleeding operations were painstakingly performed prior to each data run. Flow control was achieved by throttling and by-pass valves. All piping in the system was insulated with fiberglass except for the most critical components, for which the silica aerogel powder was employed. After each data run, the system was drained. The test section was cleaned periodically, but significant deposits were never encountered.

Further information about the apparatus and the experimental procedure are available in the thesis [4] from which this paper is drawn.

Data Reduction

The evaluation of the heat transfer coefficients from the measured outside tube wall temperatures and the power input will now be described. Two types of heat transfer coefficients will be considered. The first is the circumferential local coefficient, which is specific to an angular position θ as well as to an axial station x. It will be denoted by $h_x(\theta)$ and evaluated from the definition

$$h_x(\theta) = \frac{q_x(\theta)}{T_{wx}(\theta) - T_{bx}} \tag{1}$$

in which $q_x(\theta)$ and $T_{wx}(\theta)$ are, respectively, the local convective heat flux and local inside wall temperature at an angular position θ, and T_{bx} is the bulk temperature. All of the aforementioned quantities are specific to an axial station x.

The other heat transfer quantity of interest is the circumferential average transfer coefficient $\overline{h}_x$ at an axial station x, which is defined here as

$$\overline{h}_x = \frac{\overline{q}_x}{\overline{T}_{wx} - T_{bx}} \tag{2}$$

where the barred quantities represent circumferential averages at the inside surface of the tube.

For the evaluation of both $h_x(\theta)$ and $\overline{h}_x$, it is evident that the inside wall temperature and heat flux must first be determined. For this purpose, the heat conduction equation for the tube wall can be employed. The problem is simplified because both the net axial conduction and the heat loss from the outer surface of the tube are negligible, having respectively been estimated to be less than 0.1 and 0.15 percent of the local heat input. The temperature dependence of the tube-wall thermal conductivity can also be neglected.

With regard to the wall thickness, it was noted earlier that variations of ±3 percent were measured in samples of tubing that were cut from the ends of the test section tubes. These variations did not follow a regular pattern and, therefore, are not able to be taken into account in the analysis. Consequently, the heat fluxes calculated on the basis of a uniform wall thickness (equal to the mean) are uncertain to the same degree as the thickness variation.

The energy equation appropriate to the analysis is the Poisson equation in r,θ coordinates

$$\frac{1}{r}\frac{\partial}{\partial r}\left(r\frac{\partial T}{\partial r}\right) + \frac{1}{r^2}\frac{\partial^2 T}{\partial \theta^2} + \frac{S}{k_w} = 0 \tag{3}$$

In this equation, S is the volume rate of heat generation which, in view of the suppression of heat losses, was evaluated as the power input divided by the volume of the tube wall. The quantity k_w is the thermal conductivity of the stainless steel wall. Equation (3) is to be solved subject to the boundary conditions that (1) the outer surface of the tube is adiabatic and (2) the temperature is known (via measurement) at discrete angular positions on the outer surface $r = r_0$. In mathematical terms, these conditions are

$$\partial T/\partial r = 0 \text{ at } r = r_0 \tag{4a}$$

$$T(r_0, \theta_j) = \text{known at } \theta_j = (j-1)\pi/4,\ j = 1, \ldots, 8 \tag{4b}$$

Two types of solutions were obtained for equations (3) and (4). One of these is a separation of variables—Fourier series solution which, aside from the features now to be discussed, follows standard textbook lines. The first step in the analysis is to reduce equation (3) to Laplace's equation by introducing a new temperature variable $\phi = T + S(r^2 - r_0^2)/4k_w$. A conventional r,θ separation of variables solution is written for ϕ, and the boundary condition (4a) is employed to determine certain of the integration constants. The other integration constants are obtained by applying equation (4b) and expanding the discrete outside surface temperature data in an eight-term trigonometric series which resembles a truncated Fourier series [5, p. 298]. As indicated in [5], the Fourier coefficients for discrete data are evaluated as weighted averages of the data. With all of the integration constants thus determined, the solution can be applied at the inner surface of the tube ($r = r_i$) to yield both the circumferential distribution of the temperature and the heat flux.

The other solution of equation (3) is based on the assumption that the net circumferential conduction, which is proportional to $\partial^2 T/\partial\theta^2$, is negligible. This assumption has a high degree of plausibility since the tube wall is thin, its thermal conductivity is moderate (among the lowest among all metals), and the convective heat transfer coefficient is high. Neglect of circumferential conduction reduces equation (3) to a one-dimensional problem. From its solution, the temperature drop across the wall is given by

$$\Delta T_w = (Sr_0^2/4k_w)(r_i^2/r_0^2 - 1 - 2\ln(r_i/r_0)) \tag{5}$$

independent of θ. According to the one-dimensional model, the desired inside wall temperatures are obtained by subtracting equation (5) from the measured outside wall temperatures. Furthermore, when circumferential conduction is negligible, the heat flux at the inner surface of the tube is uniform and can be evaluated as

$$q_x(\theta) = \text{constant} = P/\pi DL \tag{6}$$

where P is the power input, D is the inside diameter, and L is the tube length. In view of equation (6), $\overline{q} = q_x(\theta)$ for the one-dimensional model.

The results of the one and two-dimensional analyses will now be compared. All circumferential average quantities (i.e., $\overline{q}_x$, $\overline{T}_{wx}$, and $\overline{h}_x$) from the two analyses are identical, provided that the averaging is performed in the same manner. The local heat flux $q_x(\theta)$ given by the two-dimensional model is circumferentially uniform to one two percent or better, even at the lowest Reynolds number and at the measurement stations closest to the blockage. Furthermore, for these most stringent conditions of comparison, the local Nusselt numbers from the two analyses agreed in the one to two percent range. There were one or two isolated exceptions to these findings which are, in all likelihood, due to data scatter.

In view of the foregoing and taking note of the unaccounted ±3 percent variations in wall thickness, it may be concluded that two-dimensional wall conduction effects are negligible. Therefore, the one-dimensional model was employed in the final reduction of the data, and Simpson's rule was used for the circumferential averaging.

Once $h_x(\theta)$ and $\overline{h}_x$ were evaluated from equations (1) and (2), the

corresponding Nusselt numbers followed from

$$\mathrm{Nu}_x(\theta) = h_x(\theta)D/k,\ \overline{Nu_x} = \bar{h}_x D/k \tag{7}$$

The results were paramaterized by the Reynolds and Prandtl numbers

$$\mathrm{Re} = 4\dot{m}/\mu\pi D,\ \mathrm{Pr} = c_p\mu/k \tag{8}$$

All thermophysical properties were evaluated at the mean bulk temperature. In this connection, it may be noted that the bulk temperature rise from inlet to outlet was typically only about 1°C (2°F).

Results and Discussion

As a logical prelude to the separated flow experiments, auxiliary tests were performed without flow blockage. These studies encompassed five Reynolds numbers between 11,000 and 60,000 for Pr = 4 and three Reynolds numbers between 11,000 and 40,000 for Pr = 8. The local heat transfer coefficients for the thermal entrance region will be reported shortly as part of the corresponding presentation of results for the blockage experiments. The measured fully developed heat transfer coefficients were compared with the most recent and discriminating of the available empirical correlations, namely, those of Petukhov [6] and of Sleicher [7].

The average deviations of the present fully developed Nusselt numbers from the Petukhov and Sleicher correlations are two percent and three percent, respectively. This excellent level of agreement provides confidence in the instrumentation and experimental technique of the present study. The comparison also confirms the absence of significant variable properties effects in that the variable property correction factor $(\mu/\mu_w)^{0.11}$ recommended by Petukhov is very close to one for the operating conditions of the experiments. In general, the heating rate was adjusted so that the wall-to-bulk temperature difference in the fully developed regime was in the 5°C (10°F) range.

For the nonblockage runs, the measured wall temperatures displayed a high degree of circumferential uniformity. Typically, the deviations from uniformity, referred to the wall-to-bulk temperature difference at the respective axial station, were within two percent.

Attention will now be turned to the results of the blockage experiments. In the presentation that follows, the circumferential average heat transfer coefficients and their axial distribution will be dealt with first because of their more immediate relevance to design. Then, the local coefficients specific to various circumferential positions will be presented both in terms of angular distributions and axial distributions.

Circumferential Average Heat Transfer Coefficients. Axial distributions of the circumferential average heat transfer coefficient are presented in Fig. 2 for Pr = 4 and for all three area blockage ratios. The figure is subdivided into three graphs, each of which contains results for a specific blockage ratio. In each graph, the ratio of the circumferential average Nusselt number $\overline{\mathrm{Nu}_x}$ to the corresponding fully developed value Nu_{fd} is plotted as a function of x/D for five Reynolds numbers between 11,000 and 60,000. Curves have been faired through the data to provide continuity. To provide perspective on the effect of the blockage, results are also shown for the case in which the blockage is absent (i.e., for the conventional thermal entrance region). The no-blockage Nusselt numbers are given for Re = 11,000, 25,000, and 60,000, one in each graph.

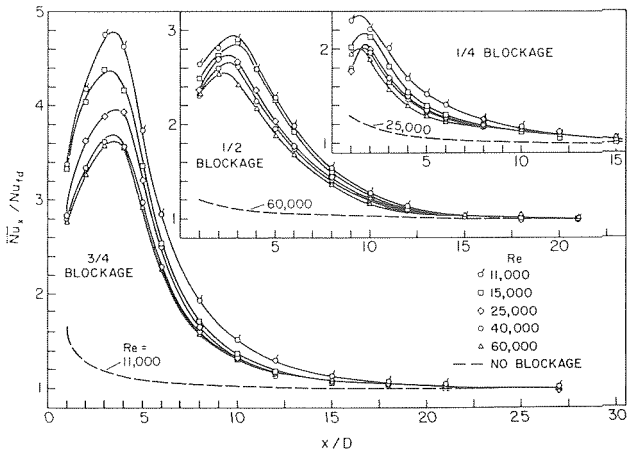

Fig. 2 Axial distributions of the circumferential average Nusselt number

Inspection of Fig. 2 reveals a pattern with x/D whereby the Nusselt number increases at first, attains a maximum, and then decreases monotonically toward its fully developed value. This pattern is fundamentally different from the monotonic decrease that is characteristic of the conventional thermal entrance region. Furthermore, the blockage-related Nusselt numbers are very much greater than those for the conventional entrance region.

The figure shows that sensitivity of the heat transfer results to the presence of the blockage is enhanced as the Reynolds number decreases. Thus, the lower the Reynolds number, the greater is the blockage-induced augmentation. The extent of the augmentation is markedly affected by the degree of blockage, with greater blockages bringing forth higher heat transfer coefficients. These trends may be illustrated numerically by noting that the peak value of $\overline{\mathrm{Nu}_x}/\mathrm{Nu}_{fd}$ varies from 3.6–4.8 as Re decreases from 60,000–11,000 for the ¾ blockage, whereas the corresponding peak values for the ¼ blockage are 2.0 and 2.4.

It may also be seen from the figure that the peak of the distribution curve is positioned farther downstream at higher blockage ratios, but is nearly independent of the Reynolds number at a given blockage. In general, the curves tend to peak more sharply at higher blockages.

The shapes of the distribution curves of Fig. 2 are not unlike those in the literature for nominally two-dimensional flows downstream of axisymmetric orifices and of abrupt expansions [1–3]. In the literature, the high heat transfer coefficients at small x/D are attributed to the high velocities that exist in this region and to the eddying and mixing of the recirculating flow contained within the separation zone. The peak in the distribution curve is associated with the position where the flow reattaches and the subsequent decrease with the redevelopment of the flow. These attributions continue to be generally valid in the present situation, but not fully. First of all, owing to the three-dimensional nature of the flow, the reattachment need not necessarily take place at the same x/D at all angular positions. Second, the impingement of the deflected flow on the wall bordering the unblocked part of the cross section may contribute to the augmented heat transfer coefficients and to the peak. These occurrences will be more fully aired when the local circumferential results are reported.

The peak Nusselt numbers $\overline{\mathrm{Nu}}_{\max}$ are indicative of the general level of augmentation, and it has been customary to seek a correlation for these results. It was found possible to correlate the dependence of the $\overline{\mathrm{Nu}}_{\max}$ on both the Reynolds number and the blockage by the relation

$$\overline{\mathrm{Nu}}_{\max} = 0.158\mathrm{Re}^{0.73}/(A_{\mathrm{open}}/A)^{0.64} \tag{9}$$

where A_{open} is the open area at the blockage cross section and A is the total cross-sectional area. The correlating equation (which is based on least squares) and the data are shown in Fig. 3.

A detailed comparison of the present $\overline{\mathrm{Nu}}_{\max}$ results with those of [1] and [2], respectively for flow downstream of an axisymmetric orifice and an abrupt expansion, is available in [4]. Only a few of the main features will be summarized here. First, the Reynolds number dependence of $\mathrm{Nu}_{\max}$ in the cited references was found to be $\mathrm{Re}^{2/3}$ instead of $\mathrm{Re}^{0.73}$. If this small departure is indeed real, it can be rationalized by the differences in the flow processes which occur (e.g., the aforementioned jet-like impingement on the wall bordering the open area). Second, when the correlations of [1] and [2] are written in terms of the pipe Reynolds number Re, a factor $(A_{\mathrm{open}}/A)^{-1/3}$ emerges rather than $(A_{\mathrm{open}}/A)^{-0.64}$. Another outcome of the com-

parison is that the x/D values at the peak are greater for the present flow configuration than for those of [1, 2].

The sensitivity of the $\overline{Nu}_x/Nu_{fd}$ distributions to Prandtl number was examined via supplementary experiments performed for Pr = 8 and for the intermediate blockage ratio of ½. These results are compared with those for Pr = 4 in Fig. 4, where the data symbols have been omitted to preserve clarity. Inspection of the figure indicates that there are only slight differences in the distribution curves for the two Prandtl numbers. This suggests that the results of Fig. 2 are valid for a range of Prandtl numbers bracketing Pr = 4.

Circumferential Local Results. From the measurements, local Nusselt numbers are available at eight circumferential positions for a succession of axial stations. The characteristics of these local Nusselt numbers will first be examined by fixing the angular coordinate and plotting the axial distribution of the Nusselt number at that coordinate. Figs. 5 and 6 have been prepared on this basis, respectively for the ¾ blockage and for the ½ and ¼ blockages. The left and right-hand portions of the figures respectively convey results for Re = 11,000 and 60,000. In each graph, the ratio $Nu_x(\theta)/Nu_{fd}$ is plotted as a function of the dimensionless axial coordinate x/D. Curves are shown for angular positions θ = 0, 45, 90, 135, and 180 deg. To preserve clarity, the data symbols are not shown. Also, for this same reason, separate curves are not included for $\theta = \pm 45$, ± 90, and ± 135 deg because of geometric symmetry (see Fig. 1). To take account of any slight thermal asymmetries, the plotted curves at these positions are the averages of those at the plus and minus angles.

Attention will first be focused on Fig. 5, which is for the ¾ blockage. For this blockage, Table 1 shows that the lip angle θ^* is 112 deg. Consequently, the line θ = constant = 0 deg which lies along the wall passes through the separated region before encountering reattachment and redevelopment, and similarly for the lines θ = 45 and 90 deg. On the other hand, the lines θ = 135 and 180 deg lie outside the separated region. Therefore, the distribution curves for θ = 0, 45, and 90 deg should reflect the successive separation, reattachment, and redevelopment processes, whereas the curves for 135 and 180 deg should reflect other processes which will be identified shortly.

Inspection of either of the graphs in Fig. 5 shows that the curves for θ = 0, 45, and 90 deg increase at first, attain a maximum, and then decrease, as is characteristic of the separation, reattachment, and redevelopment sequence. It is noteworthy, and somewhat surprising, that the x/D at reattachment (taken to coincide with the peak of the curve) decreases only slightly with θ in the range between 0 and 90 deg.

The distribution curve for θ = 180 deg is of particular interest. In the left-hand graph of Fig. 5, this curve displays a maximum value. This maximum may be attributed to the jet-like impingement of the flow deflected by the blockage onto the wall which borders the open area. As the Reynolds number increases, the impingement is expected to occur at smaller values of x/D, so that for Re = 60,000 it is upstream of the first measurement station and is not shown in the figure. Thus, for the segmental blockage studied here, there are two types of Nusselt number peaks, one associated with reattachment and one associated with impingement. This is in contrast to separated flow configurations studied heretofore [1–3], where only the reattachment type peak occurred.

The distribution curve for θ = 135 deg is believed to be influenced both by the flanks of the separation zone and by the aforementioned impingement process. Its shape, therefore, tends to be irregular.

Consideration may next be given to the results for the ½ blockage in Fig. 6. For this case, the lip angle θ^* is 90 deg (Table 1), so that the curves for θ = 0, 45, and 90 deg continue to reflect the separation, reattachment, and redevelopment sequence. The distribution curves

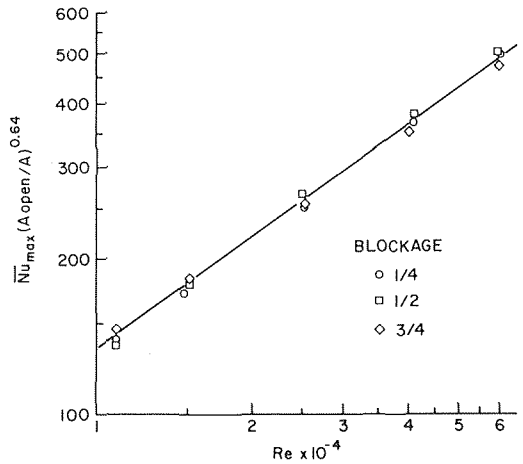

Fig. 3 Correlation of the peak values of the circumferential average Nusselt number

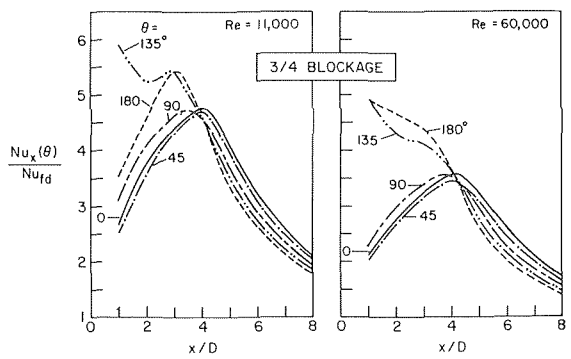

Fig. 5 Axial distributions of the circumferential local Nusselt number, blockage ratio = 3/4

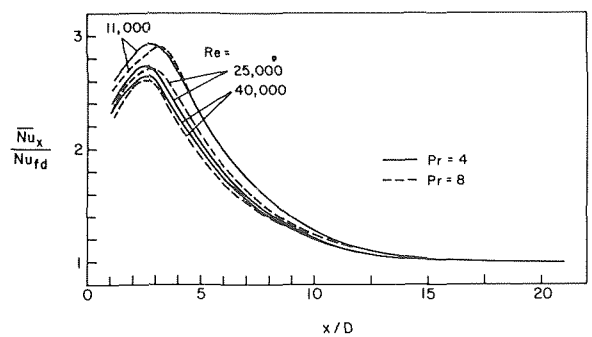

Fig. 4 Effect of Prandtl number on the circumferential average Nusselt number, blockage ratio = 1/2

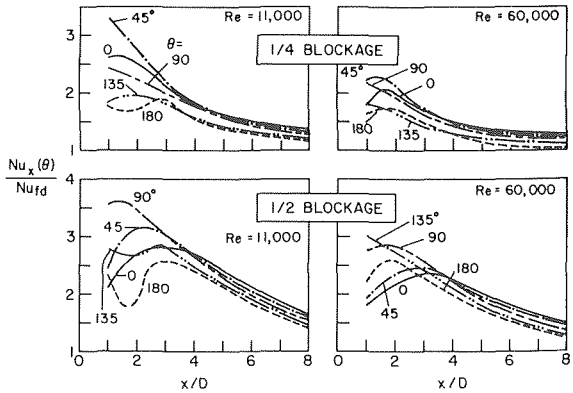

Fig. 6 Axial distributions of the circumferential local Nusselt number, blockage ratios = 1/2 and 1/4

for $\theta = 180$ deg are indicative of the jet impingement phenomenon, but there is a wave in the curve for Re = 11,000 that suggests still another flow process whose identity remains uncertain.

The 1/4 blockage (top of Fig. 6) is characterized by a lip angle θ^* of 68 deg. Consequently, only the curves for $\theta = 0$ and 45 deg pass through the separated region. Since the x/D values at reattachment and impingement are both relatively small for this blockage, the fluid flow events reflected by the distribution curves are more difficult to detect than for the other blockages.

A different perspective on the circumferential local Nusselt numbers can be obtained from an examination of angular distributions. To this end, the ratio $\mathrm{Nu}_x(\theta)/\overline{\mathrm{Nu}}_x$ has been evaluated as a function of θ at each axial station x/D, where $\overline{\mathrm{Nu}}_x$ is the circumferential average at that x/D. A complete presentation of such angular distributions is available in [4], but only representative results can be given here because of space limitations. For the interpretation of these results, it is well to recall that the blockage is in the upper part of the tube (Fig. 1).

In Figs. 7 and 8, angular distributions of $\mathrm{Nu}_x(\theta)/\overline{\mathrm{Nu}}_x$ are respectively presented for the 3/4 and 1/4 blockages. Each figure is subdivided into upper and lower portions, which correspond respectively to Re = 11,000 and 60,000. In each portion, there are a succession of graphs in which are plotted the angular distributions for all of the axial stations which had been instrumented with eight thermocouples. The ordinate values (i.e., the values of $\mathrm{Nu}_x(\theta)/\overline{\mathrm{Nu}}_x$) in each graph are arranged in a centrally placed vertical column. Each ordinate value is positioned by a short hash mark (not to be confused with a minus sign).

From these figures, it is seen that there are marked differences between the angular distributions at small x/D and those at intermediate and large x/D. The former are characterized by large variations and are of relatively complex form, whereas the latter display lesser variations and are simple in shape. There are various interesting features in these results depending on the extent of the blockage, and these will now be discussed.

For the 3/4 blockage (Fig. 7), the overall variation at the first station is about 125 percent, with the lowest values of $\mathrm{Nu}_x(\theta)$ in the separated region at the upper part of the tube. The distributions at the successive axial stations $x/D = 2$, 3, and 4 evolve in such a way that the differences between the $\mathrm{Nu}_x(\theta)$ values in the upper and lower parts of the tube diminish. Then, a reversal occurs such that the largest $\mathrm{Nu}_x(\theta)$ are in the upper part of the tube. Subsequently, the variations decay so that circumferential uniformity is in evidence at $x/D = 12 - 15$.

The circumferential distributions at the initial x/D stations are the result of separation, reattachment, and impingement. On the other hand, those at subsequent stations are influenced by differences in the redevelopment pattern in upper and lower parts of the tube. In the upper part, redevelopment of the flow begins just downstream of reattachment, whereas in the lower part the flow development begins farther upstream. The higher coefficients in the upper part are, therefore, due to its lesser degree of development.

For the 1/4 blockage (Fig. 8), the largest variations in the $\mathrm{Nu}_x(\theta)/\overline{\mathrm{Nu}}_x$ are, again, at the first station. However, the largest Nusselt numbers are now generally in the upper part of the tube, although there is a low point at $\theta = 0$ deg (the circumferential mid-point of the separated region). This low point fills in at axial stations beyond the separation zone, giving rise to a distribution at $x/D = 5$ not unlike those of Fig. 7. The subsequent behavior constitutes the most surprising finding of this study, namely, the remarkably slow decay of the circumferential variations with increasing downstream distance. As is seen from Fig. 8, substantial nonuniformities persist at $x/D = 15$, which is the last of the heavily instrumented axial stations. Data at $x/D = 27$, where there are two thermocouples, showed a ± 5 percent variation for Re = 60,000.

The remarkably long-lived effect of the 1/4 blockage was in evidence for all five of the Reynolds numbers investigated [4], so that it cannot be regarded as a chance occurrence. The reasons for this phenomenon remain to be clarified.

The effect of Prandtl number on the circumferential distributions is illustrated in Fig. 9, which is a comparison of results for Pr = 4 (open symbols) and Pr = 8 (black symbols). The figure is for the intermediate case of Re = 25,000 and blockage ratio of 1/2. Inspection of the figure shows that the distribution curves for the two Prandtl numbers are very nearly identical, aside from small differences at $x/D = 1$. This finding affirms the applicability of the Pr = 4 results for a range of neighboring Prandtl numbers.

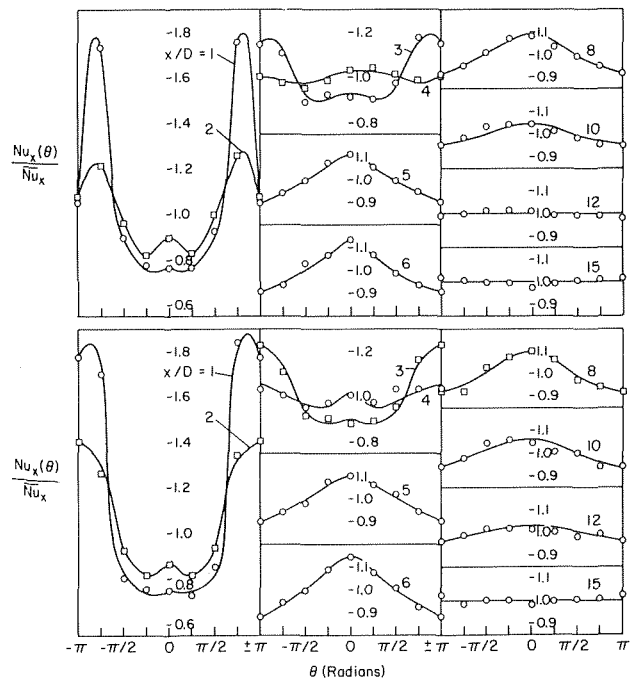

Fig. 7 Angular distributions of the local Nusselt number, blockage ratio = 3/4. Lower graph, Re = 60,000; upper graph, Re = 11,000

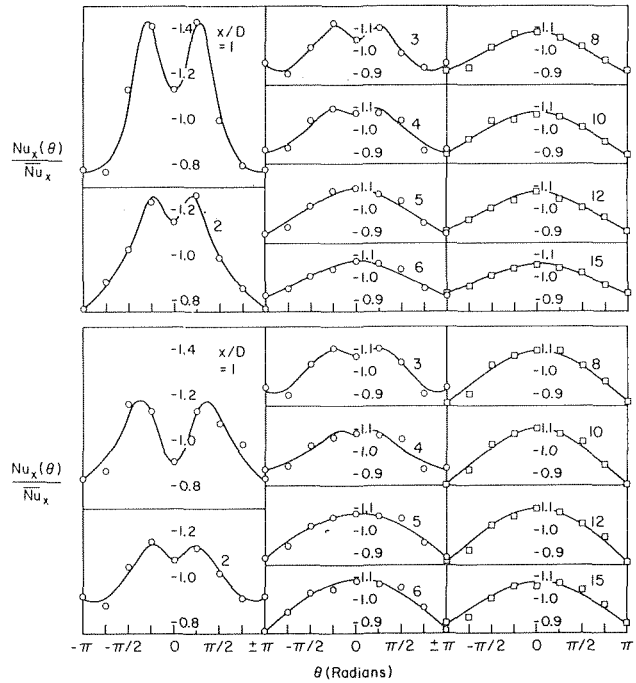

Fig. 8 Angular distributions of the local Nusselt number, blockage ratio = 1/4. Lower graph, Re = 60,000; upper graph, Re = 11,000

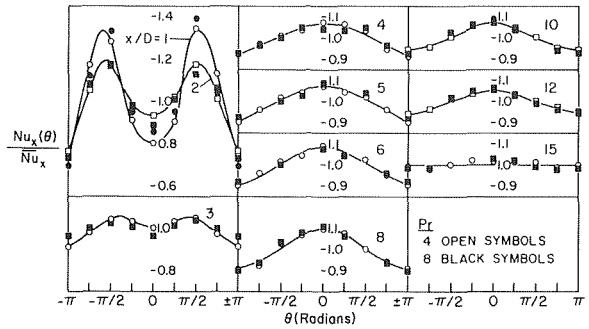

Fig. 9 Effect of Prandtl number on the angular distributions of the local Nusselt number, Reynolds number = 25,000, blockage ratio = 1/2.

Concluding Remarks

The present heat transfer results for flow downstream of an unsymmetric blockage share some common features with those for symmetric blockages, but also display a number of unique characteristics. The axial distributions of the circumferential average Nusselt number are similar in shape to the Nusselt number distributions for the symmetric case. Both distributions show an initial increase, then attain a maximum, and subsequently decrease monotonically toward the fully developed regime. The Nusselt numbers for both cases are substantially higher than those for a conventional thermal entrance region and this augmentation is more marked at lower Reynolds numbers and for greater blockages. In contradistinction to the symmetric case, the results for the unsymmetric case are more sensitive to the degree of blockage, and the position of the peak Nusselt number is farther downstream.

The unsymmetric blockage induces variations of the Nusselt number around the circumference of the tube. Axial distributions of the Nusselt number at various fixed angular positions reveal the presence of two types of maxima. One of the peaks is associated with the reattachment of the separated flow behind the blockage. The other can be attributed to the impingement of the flow deflected by the blockage onto the wall which borders the unblocked part of the cross section. The latter process is not encountered for the symmetric blockage.

The circumferential variations are large (up to 100 percent) just downstream of the blockage and tend to decay with increasing downstream distance. The decay is, however, remarkably slow in the case of the smallest blockage, so that ±5 percent variations are still in evidence at $x/D = 27$.

Subsequent to the completion of this work, a separate but complementary investigation of the pressure and flow characteristics was undertaken. The scope of that study and its results are too extensive to be reported here, but a complete description is available in [8].

References

1 Krall, K. M. and Sparrow, E. M., "Turbulent Heat Transfer in the Separated, Reattached, and Redevelopment Regions of a Circular Tube," ASME JOURNAL OF HEAT TRANSFER, Vol. 88, 1966, pp. 131–136.

2 Zemanick, P. P. and Dougall, R. S., "Local Heat Transfer Downstream of Abrupt Circular Channel Expansion," ASME JOURNAL OF HEAT TRANSFER, Vol. 92, 1970, pp. 53–60.

3 Filetti, E. G. and Kays, W. M., "Heat Transfer in Separated, Reattached, and Redevelopment Regions Behind a Double Step at Entrance to a Flat Duct," ASME JOURNAL OF HEAT TRANSFER, Vol. 89, 1967, pp. 163–168.

4 Koram, K. K., "Heat Transfer Downstream of an Asymmetric Flow Separation in a Circular Tube," Ph.D. Thesis, Department of Mechanical Engineering, University of Minnesota, Minneapolis, Minn., 1977.

5 Scheid, F., *Theory and Problems of Numerical Analysis, Shaum's Outline Series*, McGraw-Hill, New York, 1967.

6 Petukhov, B. S., "Heat Transfer and Friction in Turbulent Pipe Flow with Variable Physical Properties," *Advances in Heat Transfer*, Vol. 6, 1970, pp. 503–560.

7 Sleicher, C. A. and Rouse, N. W., "A Convenient Correlation for Heat Transfer to Constant and Variable Property Fluids in Turbulent Pipe Flow," *International Journal of Heat and Mass Transfer*, Vol. 18, 1975, pp. 677–683.

8 Lau, S. C., "Flow Field Phenomena Downstream of a Segmental Blockage in a Turbulent Pipe Flow," M.S. Thesis, Department of Mechanical Engineering, University of Minnesota, Minneapolis, Minn., 1978.

G. B. Wallis
H. J. Richter
Thayer School of Engineering,
Dartmouth College,
Hanover, N. H. 03755

An Isentropic Streamtube Model for Flashing Two-Phase Vapor-Liquid Flow

Introduction

"Flashing" can occur when liquid flows into a region where the local pressure is below the saturation pressure corresponding to the liquid temperature. As a result of the depressurization, vapor is formed. If the drop in pressure is large a two-phase flow with considerable vapor content is created. In some applications, such as a postulated break in the coolant circuit of a pressurized water reactor or in a boiler feedwater system, the downstream pressure can be only a small fraction of the upstream saturation pressure and the discharge rate is limited by choked flow at or near the smallest cross section of the passage.

Flashing occurs in several stages. If the incoming liquid is subcooled, the initial stage is the nucleation of the first vapor, usually in the form of bubbles. These bubbles grow rapidly and tend to agglomerate, forming continuous regions of vapor that are accelerated more rapidly than the denser liquid. If the void fraction becomes large enough, a vapor core, probably containing some liquid droplets, is likely to develop, while the liquid may be displaced to the wall. The development of these successive flow patterns depends on many phenomena including the initial "nucleation centers" present in the fluid, three dimensional inertial effects that may cause phase separation, trace impurities that inhibit agglomeration, fluid properties that determine rates of interphase heat, mass and momentum transfer and so on. Since analysis of these effects is difficult, it is convenient to have available a few self-consistent analyses of certain "limiting cases" that may approximately describe the overall characteristics and may form the basis for more elaborate studies.

This paper presents a new model for the flashing flow of a two-phase liquid-vapor mixture under the influence of steep pressure gradients. A method for predicting choked or "critical" flow is developed. The theory describes an idealized situation in which there are no irreversible processes. The description is thermodynamically and mechanically consistent and requires no additional assumptions beyond straightforward ones of reversible equilibrium flow without mixing, heat transfer or friction across streamlines.

It is not claimed that this model gives a realistic picture of the details of the flow. However, it provides a useful "ideal case" for comparison with practical situations in which several irreversible processes occur. It also appears to predict critical flow rates at least as well as previous theories and avoids some of the earlier conceptual difficulties.

Previous Work

Three approaches, each of them treating the flow as one-dimensional, have previously been taken to this critical flow problem:

1 *Homogeneous Equilibrium Flow.* The two-phase flow is treated by the familiar methods used to analyze single phase flow. The phases are assumed to be intimately mixed and to have equal velocities and temperatures.

2 *Slip Flow.* The vapor and liquid are allowed to have different velocities. The ratio between these velocities is specified in various ways, often without taking account of the physics of the flow.

3 *Separated Flow.* Separate one-dimensional conservation laws are written for each phase. These equations contain "interaction terms" describing heat, mass and momentum transfer between the phases. The more sophisticated theories may contain descriptions of bubble nucleation and growth. Average phase temperatures and velocities are unequal.

The first two approaches have been followed about as far as is feasible by numerous previous workers [1–4]. The homogeneous equilibrium model is self-consistent and compatible with an assumption of reversibility; its disadvantage is inaccuracy since it fails to account for differences in behavior between the phases. The slip flow model requires some additional assumption, since the constraint of equal velocity is relaxed. Usually this appears as a formula for calculating the velocity ratio (v_g/v_f); for example, Fauske [1] equated it to $(\rho_f/\rho_g)^{1/2}$ while Zivi [4] or Moody [2] chose $(\rho_f/\rho_g)^{1/3}$. Any assumption about relative motion tends to conflict with the notion of reversibility (which is often assumed at the same time) since, when phase change occurs, the transferred mass is required to be suddenly accelerated from the liquid velocity to the vapor velocity, presumably by irreverisble friction or mixing. The one-dimensional approach is forced to compromise somewhere and it is apparently impossible to conserve energy, momentum and entropy without introducing concepts such as "effective interface velocity" or apparent interfacial forces that may appear artificial [5].

The separated flow model is the subject of much current research and may eventually provide more accurate and realistic predictions. However, at present, proven methods of formulating the "interaction terms," including both reversible and irreversible components, do not exist.

Contributed by the Heat Transfer Division for publication in the JOURNAL OF HEAT TRANSFER. Manuscript received by the Heat Transfer Division January 26, 1978.

The Present Theory

The model which we will describe gets around the difficulties with the usual slip flow theory by allowing velocity and thermodynamic state to vary normal to the main flow direction.

The vapor flow is assumed to develop into different streamtubes that are independent of each other. These streamtubes form at the liquid-vapor interface (Fig. 1). There is no friction, mixing nor heat transfer across streamlines, nor is there any impulsive velocity change upon evaporation (or condensation). Flow in each vapor streamtube is isentropic, yet each streamtube is different because it originates from a different point on the liquid-vapor interface (and hence at a different saturation temperature when pressure changes are present in the flow field). The liquid is assumed to have a uniform velocity and temperature across a single streamtube and to be in equilibrium with the vapor which contacts it. The pressure is assumed to be uniform across the cross section normal to the main flow direction. It is also assumed that the flow is sufficiently one-dimensional for the neglect of velocity components perpendicular to the main flow direction.

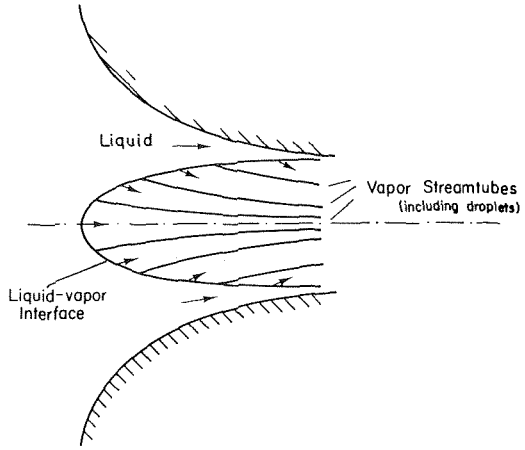

Fig. 1 Development of streamtubes in a nozzle

Saturated Inlet Stagnation Conditions. Assuming saturated liquid at the entrance into a nozzle, the pressure drop by a certain small amount Δp will cause the first flashing, creating a vapor-liquid mixture. The assumption is now that the first vapor formed due to the pressure drop Δp will flow in a streamtube (which we have arbitrarily located at the centerline of the nozzle). A further decrease by another Δp will flash more liquid and form a second streamtube in which initially saturated steam flows, decreasing the amount of liquid assumed to flow along the wall (or indeed anywhere in the nozzle as long as it forms a continuous stream; for example the liquid could flow as a jet down the center of the nozzle, surrounded by the vapor).

The vapor in the center streamtube created in the preceding pressure drop step will expand isentropically as a result of this further pressure drop by Δp. The initially saturated steam will condense partially but the liquid fraction is very small. Therefore this small amount of liquid, probably droplets, will be assumed to have the same velocity as the steam in this streamtube.

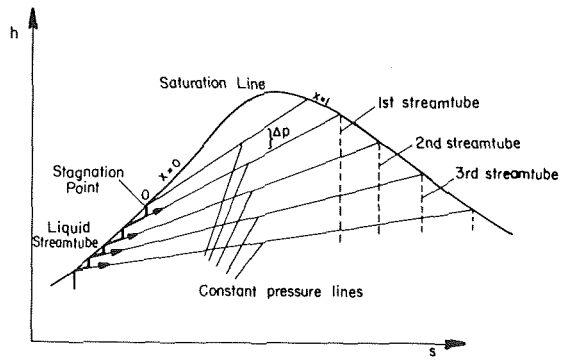

Fig. 2 Enthalpy-entropy diagram with paths for different streamtubes

Each discrete drop in pressure will create one new streamtube in which initially saturated steam flows. At the same time the homogeneous mixtures in each existing streamtube expand isentropically as indicated in the enthalpy-entropy diagram (Fig. 2). If the step Δp is taken very small a continuous expansion and flow field is created. For computation purposes a finite step size is chosen, sufficiently small for it to have negligible effect on the overall result. (With decreasing step size certain calculation instabilities were observed depending upon the accuracy of the steam tables used in this computer program. This led to some oscillations in the results. However, the predictions of the choked flow condition and the corresponding velocity profile were insensitive to these variations for Δp smaller than 1 bar, as shown in Fig. 7).

Let us normalize on the basis of unit mass flow rate. Denote the fraction of the total mass flow rate in the ith vapor streamtube, created in the ith Δp step, by y_i and the corresponding normalized liquid flow rate after the ith flash by Y_i. Then the ith flashing "stage" consists of isentropic conversion of a liquid flow rate Y_{i-1}, with velocity v_{i-1}, enthalpy h_{i-1}', and entropy s_{i-1}', to a liquid rate Y_i, with properties v_i, h_i', and s_i', and a vapor flow rate y_i, with properties v_i, h_i'', and s_i'' (see Fig. 3).

Mass is conserved if:

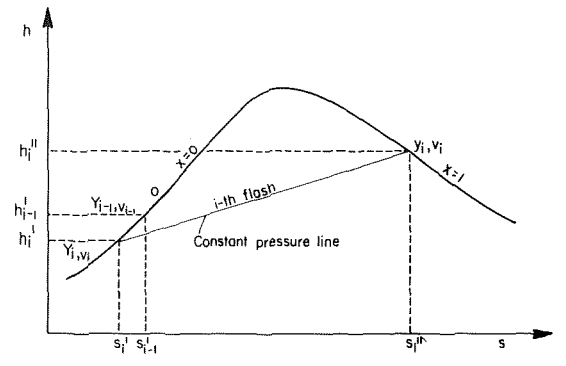

Fig. 3 Details of the ith flash on an enthalpy-entropy diagram

Nomenclature

G = mass flux
G_c = critical mass flux
h' = enthalpy of saturated water
h'' = enthalpy of saturated steam
p = pressure
p_{sat} = saturation pressure
s' = entropy of saturated water
s'' = entropy of saturated steam
T = temperature
v = velocity
x = quality
x_0 = initial quality
Y = normalized liquid mass flow rate (dimensionless)
y_i = fraction of total mass flow rate in ith streamtube (vapor + droplets)
y_0 = initial moisture content $y_0 = 1 - x_0$
W = mass flow rate
ρ' = density of saturated water
ρ'' = density of saturated steam
ϵ = slip ratio

Subscripts

0 = stagnation value
i, n = numbers of steps

$$Y_{i-1} = Y_i + y_i \tag{1}$$

Entropy is conserved if:

$$Y_{i-1}s_{i-1}' = Y_i s_i' + y_i s_i'' \tag{2}$$

and energy is conserved if:

$$Y_{i-1}\left(h_{i-1}' + \frac{v_{i-1}^2}{2}\right) = Y_i\left(h_i' + \frac{v_i^2}{2}\right) + y_i\left(h_i'' + \frac{v_i^2}{2}\right) \tag{3}$$

Combining (1) and (2) we may solve for y_i:

$$y_i = Y_{i-1}\frac{s_{i-1}' - s_i'}{s_i'' - s_i'} \tag{4}$$

while combination of (1) and (3) gives v_i:

$$v_i^2 = v_{i-1}^2 + 2\left[h_{i-1}' - h_i' - \frac{y_i}{Y_{i-1}}(h_i'' - h_i')\right] \tag{5}$$

Since the thermodynamic properties are known from the pressure steps, (4) and (5) can be used to calculate y_i and v_i in successive stages of flashing. Y_i follows from (1).

An interesting interpretation of (5) is possible if we use the thermodynamic identity,

$$h_i'' - h_i' = T_i(s_i'' - s_i') \tag{6}$$

Substituting (4) in (5) and using (6) yields

$$\frac{v_i^2 - v_{i-1}^2}{2} = h_{i-1}' - h_i' - T_i(s_{i-1}' - s_i') \tag{7}$$

If Δp is small this is equivalent to

$$v\Delta v = \Delta h' - T\Delta s' = \frac{\Delta p}{\rho'} \tag{8}$$

which is just what would be expected if Bernoulli's equation had been applied to the liquid (a reasonable approach since there is no force besides the pressure that acts on the liquid stream and no reaction from the flashing vapor since it suffers no finite change in velocity).

Once the vapor is created it expands isentropically with s_i, the specific entropy of the ith streamtube, equal to s_i'', the vapor specific entropy at the originating pressure (Fig. 4). The initial conditions, the pressure at which the streamtube is created and the flow rate y_i are known, therefore the quality, enthalpy, velocity, density and flow area of the streamtube can be calculated as a function of downstream pressure.

For the ith streamtube, created in the ith Δp step, the quality at the nth Δp step downstream is

$$x_{i,n} = \frac{s_i - s_n'}{s_n'' - s_n'} \tag{9}$$

The enthalpy is then

$$h_{i,n} = (1 - x_{i,n})h_n' + x_{i,n}h_n'' \tag{10}$$

and the velocity

$$v_{i,n} = [2(h_i - h_{i,n}) + v_i^2]^{1/2} \tag{11}$$

Since the homogeneous density in the ith streamtube is

$$\rho_{i,n} = \frac{1}{\dfrac{(1 - x_{i,n})}{\rho_n'} + \dfrac{x_{i,n}}{\rho_n''}} \tag{12}$$

The total mass flow per unit overall cross-section area is obtained as the reciprocal of the sum of the areas of all streamtubes, per unit normalized flow as

$$G = \left[\sum_{i=1}^{n}\frac{y_i}{\rho_{i,n}v_{i,n}} + \frac{Y_n}{\rho_n' v_n}\right]^{-1} \tag{13}$$

The criterion for critical flow is

$$\frac{dG}{dp} = 0 \tag{14}$$

i.e., the mass flow per unit area is a maximum.

Since the fluid in each streamtube has a different velocity, with the vapor that is first created being the fastest, a velocity profile is developed in the nozzle.

Subcooled Inlet Conditions. This method can be extended to predict flows in which subcooled liquid enters the nozzle. The liquid is accelerated in the nozzle isentropically and Benouilli's equation can be used until the saturation pressure is reached. At that point the same calculation procedure as indicated earlier for saturated liquid can be applied starting with a finite velocity equal to $\{2(p_0 - p_{sat})/\rho_f\}^{1/2}$ at the onset of flashing.

Two-Phase Inlet Conditions. A similar approach can be adopted when a steam-water mixture enters the nozzle. The only boundary condition necessary in this case is some assumption about the vapor and liquid velocities at the entrance.

In the absence of better information we have assumed equal phase velocities at the nozzle inlet.

The calculation procedure is illustrated on an enthalpy-entropy diagram in Fig. 5. For the first pressure drop by a certain small amount Δp it is assumed that the phases have equal velocities. Thereafter two streamtubes form and the previous calculation procedure is followed.

An Example

This calculation procedure will be illustrated by means of an example. The initial state is chosen as saturated water with zero velocity and an entrance pressure of $p_0 = 3.98$ MPa, corresponding to $T_0 = 250°C$. The pressure drop step size Δp is 0.1 MPa. Fig. 6 shows the predicted mass flux versus the pressure drop. It can be seen that a maximum is reached at about a pressure drop of 1.05 MPa. Fig. 7 shows the corresponding velocity profile at this "critical flow" condition for a cylindrical duct and a total flow rate of $W = 1$ kg/s; two different predictions are shown for $\Delta p = 0.1$ MPa and $\Delta p = 0.05$ MPa.

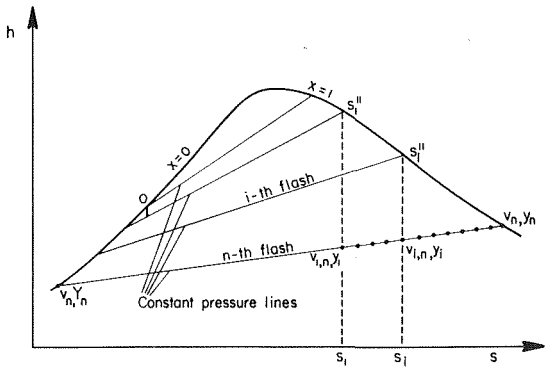

Fig. 4 States of streamtubes after the nth flash

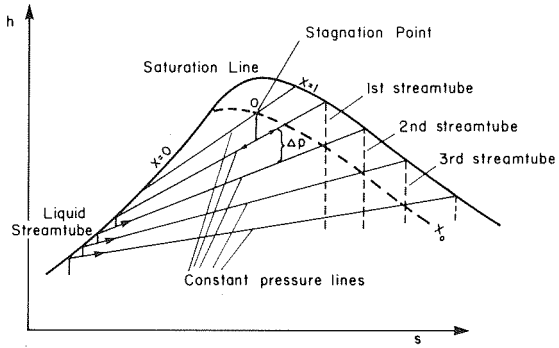

Fig. 5 Enthalpy-entropy diagram with paths for different streamtubes. A vapor-liquid mixture with a quality of x_0 enters the nozzle

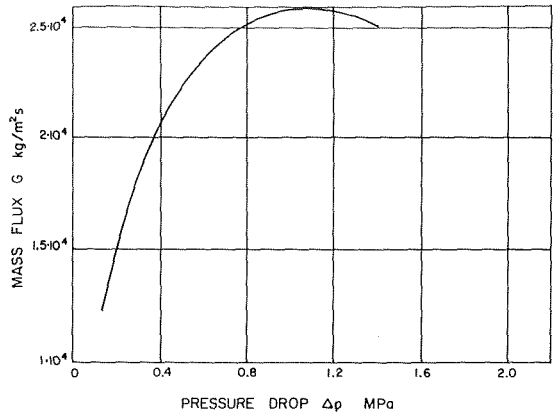

Fig. 6 Mass flux versus pressure drop for water flashing from a stagnation temperature of $T_0 = 250°$ C. ($P_o = 3.98$ MPa)

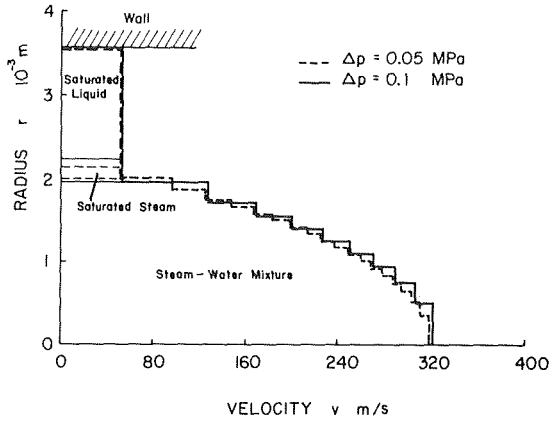

Fig. 7 Predicted velocity profiles in the throat of a nozzle for two different pressure drop steps, Δp ($W = 1$ kg/s, $P_o = 3.98$ MPa, $T_0 = 250$ °C - - - - - $\Delta p = 0.05$ MPa —— $\Delta p = 0.1$ MPa)

We also calculated average phase velocities at each step, using the definitions

$$\bar{v}_{g,n} = \frac{\sum_1^n y_i v_{i,n} x_{i,n}}{\sum_1^n y_i x_{i,n}} \tag{15}$$

$$\bar{v}_{f,n} = \frac{\sum_1^n y_i v_{i,n}(1 - x_{i,n}) + Y_n v_n}{\sum_1^n y_i (1 - x_{i,n}) + Y_n} \tag{16}$$

and deduced an effective slip ratio,

$$\epsilon_n = \frac{\bar{v}_{g,n}}{\bar{v}_{f,n}} \tag{17}$$

The result is compared with two previous theories in Fig. 8.

Prediction of Critical Mass Flux

Calculations were pursued for saturated water expanding from various stagnation pressures. In Fig. 9 the critical mass flux G_c is plotted versus the stagnation pressure p_0 at the entrance to the nozzle. The present theory is compared with the homogeneous theory and two classical slip flow theories. The results obtained from this theory are between the extremes of homogenous flow and the maximum flux for a slip ratio of the cube root of the density ratio.

Comparison with Data

Fig. 10 shows comparison with experiments using saturated water

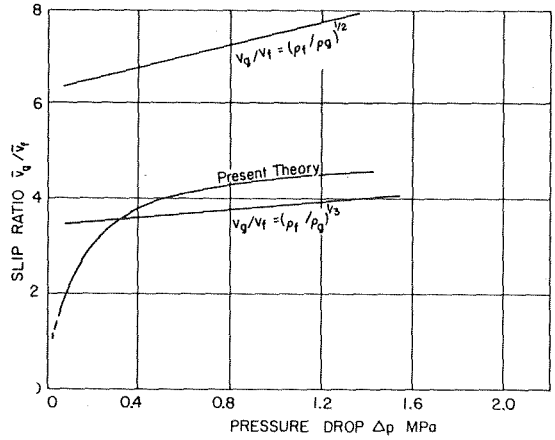

Fig. 8 Slip ratio versus pressure drop for water expanding from $T_0 = 250°$C, $p_0 = 3.98$ MPa

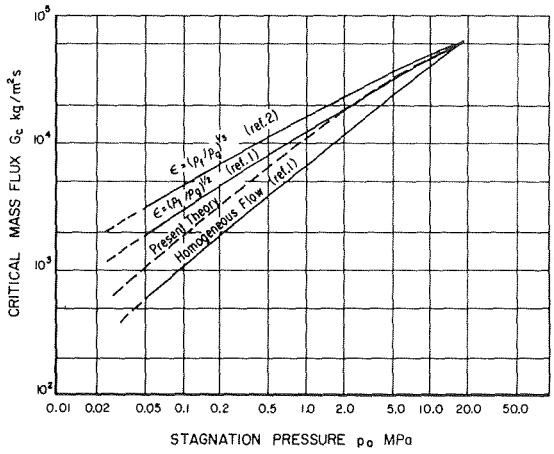

Fig. 9 Critical mass flux versus stagnation pressure for saturated water at inlet

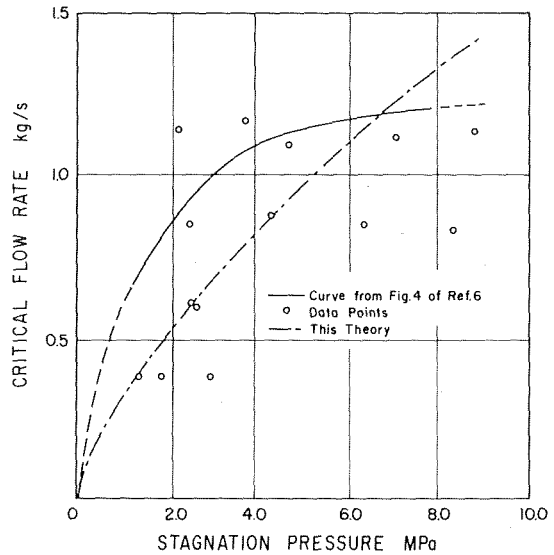

Fig. 10 Comparison between this theory and experiments by Schrock, et al. [6] for saturated water at inlet into the nozzle

entering a nozzle (Schrock, Starkman, et al. [6]).[1] The predictions of the streamtube model seem to give better agreement with the widely scattered data than the curve plotted in reference [6].

Comparison of the streamtube model with other experimental results from the same authors [6, 7] for a different shaped nozzle for saturated as well as subcooled water entering the nozzle shows good agreement (Fig. 11).

Earlier data of Starkman, Schrock, et al. [8] for steam-water mixtures of different qualities at the nozzle entrance are compared with the streamtube model in Fig. 12. The agreement is very good for low pressures.

In the paper by Deich, et al. [9] experiments in nozzles were described for different moisture contents, $y_0 = 1 - x_0$, at the inlet (Fig. 13). The agreement with the present theory is good for low qualities and the data appear to lie between our predictions and the calculations based on the homogeneous equilibrium model.

Even comparisons with tube data as described by Moody show rather good agreement (Fig. 14). Since inertia effects tend to dominate near critical flow the details of the upstream flow in the pipe can probably be neglected as long as the pipe is not too long. The same figure also shows Moody's theory which uses a slip ratio equal to $(\rho_f/\rho_g)^{1/3}$. In order to obtain these predictions, which are based on quality at the point of critical flow, we varied the "effective inlet stagnation quality" at each pressure until choking was predicted at the desired exit quality.

[1] These data were taken from [6], an ASME preprint, but do not appear in the JOURNAL OF HEAT TRANSFER version of the paper [7]. We have checked with the senior author that these data are valid.

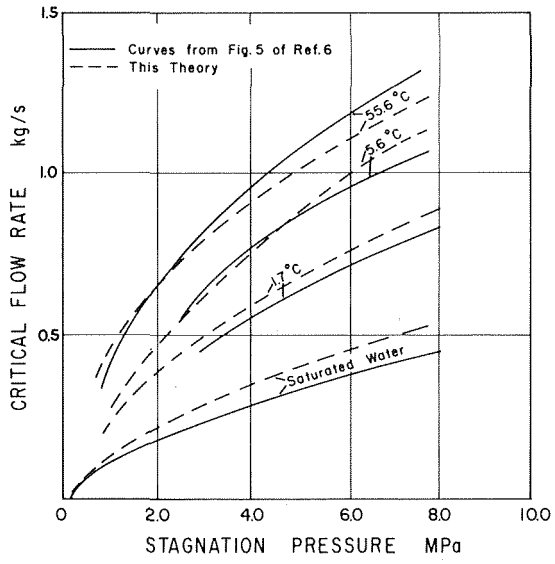

Fig. 11 Comparison between this theory and experiments by Schrock, et al. [6] for saturated and subcooled water at inlet into the nozzle

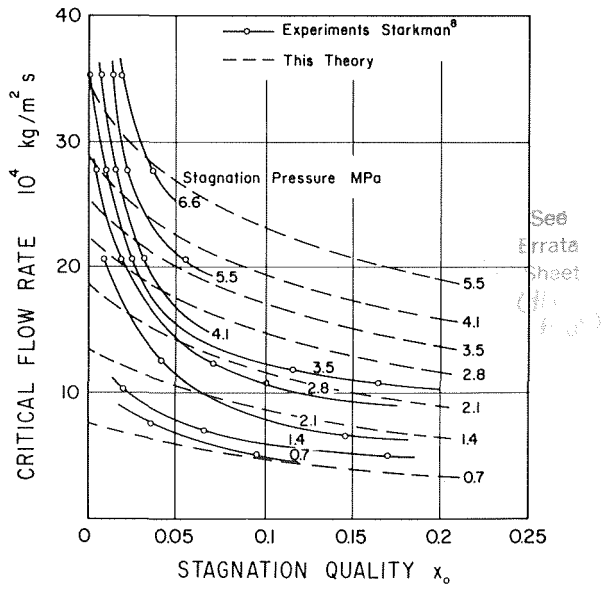

Fig. 12 Comparison between this theory and experiments by Starkman, et al. [8] for saturated water and steam-water mixtures entering the nozzle

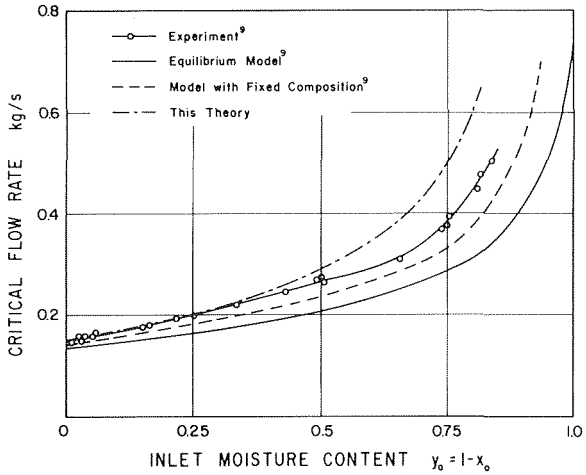

Fig. 13 Comparison between this theory, experiments by Deich, et al. [9] for different steam-water mixtures at inlet of the nozzle and two theories by Deich, et al.

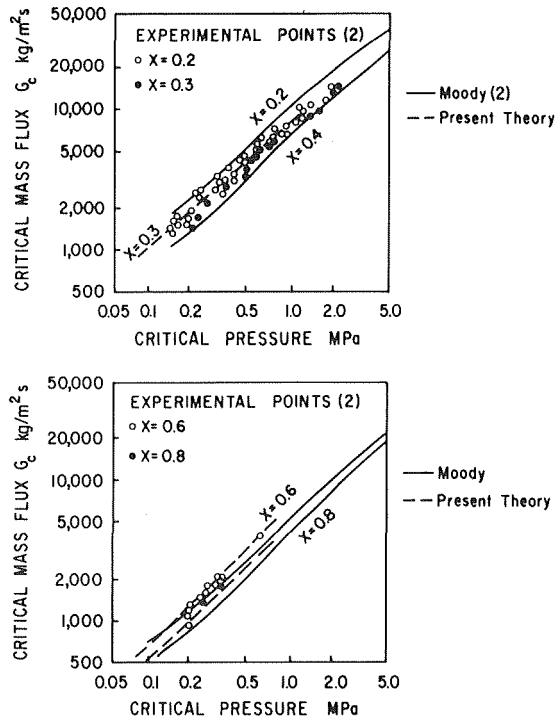

Fig. 14 Comparison between calculated mass flux from Moody [2], this theory and experimental data in tubes for two ranges of steam quality at the choking point

Conclusions

This present model for prediction of choked or critical flow is more consistent in its assumptions than many other models and predicts observed critical flow rates competitively. It does not represent the details of choking realistically but it can be considered as a certain ideal limit, comparable to the isentropic predictions of the characteristics of compression or expansion machines, which do not give the complete picture either but are very helpful for providing standards for comparison with actual performance and as starting points for the development of more elaborate theories.

Acknowledgment

The authors gratefully acknowledge the support for this work from the Electric Power Research Institute (EPRI), Contract (RP-443-2).

References

1 Fauske, H. K., "Critical Two-Phase, Steam-Water Flow," ANL-6633, 1963, pp. 79–89.

2 Moody, F. J., "Maximum Flow Rate of a Single Component, Two-Phase Mixture," ASME JOURNAL OF HEAT TRANSFER, 1965, pp. 134–142.

3 Levy, S., "Prediction of Two-Phase Critical Flow Rate," ASME JOURNAL OF HEAT TRANSFER, 1965, pp. 53–58.

4 Zivi, S. M., "Estimation of Steady State Steam Void Fraction by Means of the Principle of Minimum Entropy Production," ASME JOURNAL OF HEAT TRANSFER, 1964, pp. 247–252.

5 Wallis, G. B., *One Dimensional Two-Phase Flow*, McGraw-Hill, New York, 1969, pp. 73–80.

6 Schrock, V. E., E. S. Starkman and R. A. Brown, "Flashing Flow of Initially Subcooled Water in Convergent-Divergent Nozzles," ASME paper 76-HT-12.

7 Schrock, V. E., E. S. Starkman and R. A. Brown, "Flashing Flow of Initially Subcooled Water in Convergent-Divergent Nozzles," ASME JOURNAL OF HEAT TRANSFER, Vol. 99, May, 1977, pp. 263–268.

8 Starkman, E. S., V. E. Schrock, K. F. Neusen, and D. J. Maneely, "Expansion of a Very Low Quality Two-Phase Fluid Through a Convergent-Divergent Nozzle," *Journal of Basic Engineering*, June, 1964, pp. 247–256

9 Deich, M. E., V. S. Danilin, G. V. Tsiklauri, and V. K. Shanin, "Investigation of the Flow of Wet Steam in Axi-Symmetric Laval Nozzles over a Wide Range of Moisture Content," *High Temperature* 7, Vol. 2, 1969, pp. 294–299.

A. A. Sonin
P. W. Huber

Department of Mechanical Engineering,
Massachusetts Institute of Technology,
Cambridge, Mass. 02139

On the Scaling Laws for Air Clearing in Water-Type Pressure Suppression Systems[1]

A set of scaling laws is derived for the small-scale simulation of the air clearing phase of a loss-of-coolant accident in a nuclear powerplant with a water-type pressure suppression system. The laws are a refinement of those suggested by F. J. Moody. This paper discusses the assumptions underlying their derivation and deals with the problem of scaling the vent flow.

1 Introduction

During the past three years, considerable work has been done to establish a proper design basis for the hydrodynamic loads in the water-type pressure suppression containment systems of boiling water nuclear reactors (BWRs). Three generations of such systems have been developed in the U.S. In early 1975, during the testing of the latest generation of these systems, it became apparent that certain loads that might occur during a loss-of-coolant accident (LOCA) had not been adequately considered in the two earlier designs. At that time, there were 25 BWR reactors with first-generation containments in the United States, 19 of them operational, and a number of reactors with second-generation containments in advanced construction stages. A strong research and testing program was immediately mounted by the nuclear industry and the U.S. Nuclear Regulatory Commission to re-evaluate the design loads as quickly as possible [1, 2].

Of major concern were the forces which would be exerted on the containment during the initial stages of a LOCA, when the air in the drywell and vent system is displaced by the steam from the (postulated) pipe rupture and ejected into the wetwell of the containment system. This causes at first a sharp downward force on the wetwell floor as the vents clear of water, and then an upward load on the wetwell as the air trapped over the water is compressed by the rapid upheaval of the condensation pool ("pool swell"). The pool swell also causes impact loads on the internal structures of the wetwell.

The pool swell process is a complex one, for geometrical and other reasons, and the most promising method for predicting the loads appeared to be small-scale experimental modeling, using scaling laws to determine full-scale conditions from the small-scale results. This is the approach that the nuclear industry took in 1975, when it began simulating the air expulsion stage of LOCAs in a 1/12 scale model of a typical first-generation BWR containment. The model used actually represented a two-downcomer, 7.5 deg segment of the full 360 deg first-generation containment torus. The following year, the nuclear industry sponsored further tests in a similar 1/4 scale model, and the Nuclear Regulatory Commission funded the Lawrence Livermore Laboratory to carry out tests in a more elaborate 1/5 scale model of a 90 deg segment of the first-generation containment torus. Small-scale tests of both the first and second-generation containments were also undertaken at the Stanford Research Institute under the guidance of the Electric Power Research Institute. The bulk of the industrial tests are completed and analyzed, but much of the data remain in proprietary form. The Livermore and some of the SRI/EPRI tests are finished and the data are available [3, 4].

The method of small-scale modeling rests on a knowledge of the modeling laws which ensure that dynamic similarity exists between the model and the full-scale system and which provide the scaling laws for predicting full-scale conditions from the data derived from the model. Because of the complexity of the pool swell process, it turns out to be impossible or impractical to achieve exact dynamic similarity between a small-scale system and a full-scale one. However, by invoking a simplified model of the actual pool swell process, F. J. Moody of the General Electric Company [5] was able to suggest a set of modeling laws which were sufficiently simple to allow convenient small-scale modeling. These laws became the basis for the industry's small-scale tests.

In this paper we discuss the modeling laws for the pool swell process. The approach, if not the derivation itself, follows Moody's, but is more rigorous in its consideration of the vent system's hydraulic resistance. A companion paper [6] describes a series of direct experimental tests of the modeling laws in laboratory-scale systems.

2 The Modeling Laws

Consider a set of geometrically similar rigid systems, like the one in Fig. 1, consisting of a closed "wetwell," partly filled with liquid, connected to a "drywell" by one or several vent or "downcomer" pipes. The initial liquid level is considered part of the geometry. At $t \leq 0$,

[1] Work supported by the U.S. Nuclear Regulatory Commission, Office of Nuclear Regulatory Research, Division of Reactor Safety Research, under Contract No. NRC-04-77-011.

Contributed by the Heat Transfer Division for publication in the JOURNAL OF HEAT TRANSFER. *Manuscript received by the Heat Transfer Division* February 27, 1978.

the pressure in the wetwell and downcomer gas spaces is P_w, and the liquid is stationary. At $t > 0$, the enthalpy h_D and the pressure P_D in the drywell increase rapidly with time. In an actual LOCA the drywell will be pressurized by the injection of high-enthalpy steam. However, we are interested in the early period of the blowdown in the condensation pool, when the gas being ejected from the drywell is mainly displaced air. We therefore assume for simplicity that the gas is a perfect one, and condensation is negligible.

We are interested in the scaling laws for the pressure distribution in the wetwell and the velocity distribution of the wetwell liquid. To understand what these quantities depend on, we consider the following simplified model of the actual pool swell process. First, we assume that the pressure drop which occurs in the downcomer during flow is largely localized; that is, it occurs primarily at one given location in the downcomer, at the "orifice." (This assumption can be relaxed, as we discuss later.) Next, we note that the process involves three separate fluid regions: the region I of gas which is bounded by the orifice on the upstream side and by the liquid on the other, the region II of liquid, and the region III of trapped gas in the wetwell. We assume that in regions I and II the gases are perfect and noncondensable and the pressures uniform (inertial effects occur primarily in the liquid, not in the gas, and acoustic times are short compared with the characteristic blowdown times). As for the liquid, we assume that its motion is incompressible and inviscid (acoustic times in the liquid are also very short, and the Reynolds number very large). After the bubble is formed, we assume that it will drive the pool motion. Heat transfer is neglected between the liquid and the gas, and between the gas and the wetwell structure. Interfacial surface tension effects are also neglected. The key assumption here is that the Rayleigh-Taylor instabilities which may form at the air-water interfaces do not play a significant role in the pool swell process.

Based on this simplified model of the process, we can deduce that the pressure at a given point in the system must have the dependence

$$P = P(P_w, \rho, g, D, \gamma, RT_D\dot{m}, t), \tag{1}$$

where $RT_D\dot{m}$ is in essence the (time-dependent) enthalpy flow rate from the drywell into region I, $\dot{m}$ being the instantaneous mass flow rate, T_D the instantaneous drywell temperature, and R the specific gas constant of the blowdown gas. The other symbols are defined in the Nomenclature. Equation (1) is to be interpreted to mean that P depends on the whole history of the enthalpy flow rate $RT_D\dot{m}$ up to time t. Note that if γ is different in regions I and III, both values of γ must appear in equation (1).

The velocity $\vec{v}$ of the pool at any given point has a dependence entirely similar to equation (1).

It is obvious that P and $\vec{v}$ must depend on ρ, g, D, and t because the latter influence the dynamics of the liquid pool. P_w and γ enter through the isentropic pressure-volume relation for the trapped gas, which controls the boundary condition for the region III side of the pool. The history of $RT_D\dot{m}$ enters because it controls the pool driving pressure P_I in region I. P_I is determined from the region I energy equation,

$$\frac{d}{dt}(\rho_I e_I V_I) = h_D\dot{m} - P_I\frac{dV_I}{dt}, \tag{2}$$

which in our perfect-gas approximation can be written as

$$V_I\frac{dP_I}{dt} + \gamma P_I\frac{dV_I}{dt} = \gamma RT_D\dot{m}. \tag{3}$$

It is clear from equation (3) that if the pool equation of motion and the pool boundary conditions on the region III side are specified by the quantities P_w, γ, ρ, g, D, and t, then the specification of $RT_D\dot{m}$ completes the specification of the pool swell process.

Note that h_D and $\dot{m}$ do not appear separately in equation (1), but only as a product. This is so because the region I mass conservation law, which involves $\dot{m}$ separately, does not affect the pressure-volume relation for the region and hence does not affect the pool dynamics. The pressure-volume relation is controlled by the energy equation alone. The mass conservation law controls the gas density and temperature in region I, but neither the gas density nor the temperature play any role here because inertial effects in the gas phases are neglected and heat transfer is absent. It is precisely because h_D and $\dot{m}$ appear only as a product, but not individually, that it is possible to derive a sufficiently simple set of modeling laws.

Applying straightforward dimensional analysis, we deduce from equation (1) that a *dimensionless* pressure like $(P - P_w)/P_w$ must have the dependence

$$\frac{P - P_w}{P_w} = f\left(\frac{P_w}{\rho g D},\ \gamma,\ \frac{h_D\dot{m}}{\rho g^{3/2}D^{7/2}},\ t\sqrt{g/D}\right). \tag{4}$$

A dimensionless velocity like $\vec{v}/\sqrt{gD}$ has a similar dependence. The implicit assumption, of course, is that we are referring to the pressure or velocity at a particular point in the system; otherwise, a dependence on position must be included.

Equation (4) implies that if $P_w/\rho gD$ and γ are the same in two geometrically similar systems—a full-scale prototype and a small-scale model, say—and if $h_D\dot{m}/\rho g^{3/2}D^{7/2}$ is the same in both at all corresponding values of the dimensionless time $t\sqrt{g/D}$, then the dimensionless pressure and velocity will be the same in both at corresponding values of $t\sqrt{g/D}$.

This recipe for modeling is simple. However, there is still a practical difficulty; one must know how to ensure that $h_D\dot{m}/\rho g^{3/2}D^{7/2}$ is the same in the model as in the prototype at corresponding dimensionless times.

We address this last problem by considering the scaling laws for the flow through a standard orifice or any flow restriction in a pipe system, set between an upstream point where the pressure P_D is specified (in Fig. 1, the drywell) and a downstream point where the pressure is P (in Fig. 1, the region I). We consider the set of geometrically similar restrictions in a pipe of diameter d (the downcomer), and we assume that the region where the pressure drop occurs is sufficiently localized that the flow there can be considered quasi-steady. We can then show from dimensional considerations that a

Nomenclature

c_m = mass flow coefficient through orifice, equation(s) (dimensionless)
D = wetwell diameter, m
e = specific internal energy, J·kg^{-1}
g = acceleration due to gravity, 9.8 m·s^{-2}
h_D = specific stagnation enthalpy of drywell gas, J·kg^{-1}
$\dot{m}$ = mass flow rate, kg·s^{-1}, from drywell into region I in Fig. 1
P = pressure at a given point, Pa
P_I = pressure of gas in region I, Pa
P_D = drywell pressure, Pa
P_w = initial wetwell pressure, Pa
R = specific gas constant (universal gas constant divided by molar mass of gas), J/K·kg
Re = a Reynolds number for gas flow through the orifice, equation (7) (dimensionless)
t = time measured from the initiation of blowdown, s
t^* = dimensionless time = $t\sqrt{g/D}$
T_D = drywell gas absolute temperature, K
$\vec{v}$ = velocity at a given point, m·s^{-1}
V_I = volume of region I in Fig. 1, m^3
γ = ratio of the specific heats of drywell gas (dimensionless)
μ_D = viscosity of drywell gas, kg·m$^{-1}t^{-1}$
π_1 to π_4 = dimensionless scaling parameters (equations (9–13))
ρ = density of wetwell liquid, kg·m^{-3}
ρ_I = density of gas in region I in Fig. 1, kg·m^{-3}

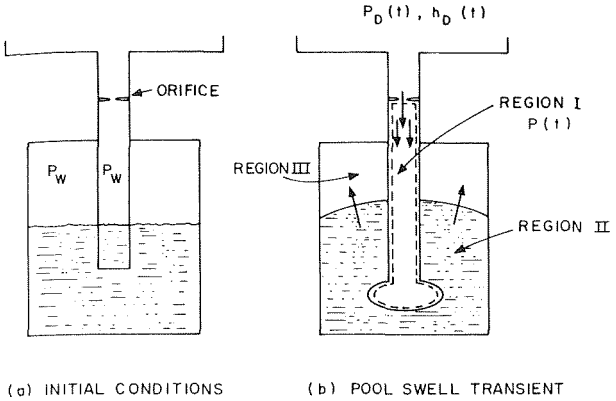

Fig. 1 Modeling of pool swell for scaling laws.

dimensionless mass flux density, which we shall call the mass flow coefficient c_m, in analogy to the discharge coefficient c_d for volume flow in nozzles,[2]

$$c_m \equiv \frac{\dot{m}}{\rho_D \left[\frac{2(P_D - P)}{\rho_D}\right]^{1/2} \frac{\pi d^2}{4}} \tag{5}$$

must have the functional form

$$c_m = c_m\left(\frac{d_i}{d}, \frac{P_D - P}{P_D}, \gamma, \text{Re}\right). \tag{6}$$

Here, ρ_D is the gas density at the upstream station, d_i is the diameter of the standard orifice, and

$$\text{Re} \equiv \frac{\sqrt{\rho_D P_D} d}{\mu_D} = \frac{P_D d}{\mu_D \sqrt{RT_D}} \tag{7}$$

is a characteristic Reynolds number for the flow (see the Nomenclature for the symbols). The dependence of d_i/d in equation (6) is written for the particular case where the resistance is a standard orifice. More generally, the form of equation (6) would simply depend on the geometry of the restriction.

In terms of the mass flow coefficient introduced in equation (5), we can write

$$\frac{h_D \dot{m}}{\rho g^{3/2} D^{7/2}} = \frac{\pi}{2\sqrt{2}} \frac{\gamma}{\gamma - 1} \times \left(\frac{d}{D}\right)^2 \frac{P_D}{P_w} \frac{P_w}{\rho g D} \left[1 - \frac{P_w}{P_D} - \frac{P_w}{P_D}\left(\frac{P - P_w}{P_w}\right)\right]^{1/2} \times c_m \left(\frac{RT_D}{gD}\right)^{1/2}. \tag{8}$$

Now, we have seen that if γ and $P_w/\rho g D$ are the same in the model and the prototype systems, similarity will be achieved—that is, $(P - P_w)/P_w$ will be the same in both systems at corresponding values of dimensionless time $t\sqrt{g/D}$—if $h_D\dot{m}/\rho g^{3/2} D^{7/2}$ is also the same at corresponding $t\sqrt{g/D}$. From equation (8) we see that this condition is satisfied if P_D/P_w and $c_m(RT_D/gD)^{1/2}$ are the same in both systems at corresponding values of dimensionless time $t\sqrt{g/D}$ (d/D is the same in both systems because geometric similarity is presumed). According to equation (6), on the other hand, c_m depends on dimensionless time only via the dimensionless pressure ratio $(P_D - P)/P_D$. Hence, $c_m(RT_D/gD)^{1/2}$ will be the same in both systems at corresponding dimensionless times if it is the same at corresponding values of $(P_D - P)/P_D$.

Our conclusion, then, is that the proper modeling laws for pool swell are that

$$\pi_1 \equiv \gamma \tag{9}$$

and

$$\pi_2 \equiv \frac{P_w}{\rho g D} \tag{10}$$

be the same in the model and the prototype system, that

$$\pi_3 \equiv \frac{P_D}{P_w} \tag{11}$$

be the same in the model and prototype system at corresponding values of

$$t^* \equiv t\sqrt{g/D}, \tag{12}$$

and that

$$\pi_4 \equiv c_m \left(\frac{RT_D}{gD}\right)^{1/2} \tag{13}$$

be the same in the model as in the prototype system at *all* values of the dimensionless pressure drop $(P_D - P)/P_D$ encountered in the process. It then follows that a dimensionless pressure like $(P - P_w)/P_w$, or dimensionless velocity like $\bar{v}/\sqrt{gD}$, at any given point will be the same in the model as in the prototype. In general, the dimensionless quantities will have the form

$$\frac{P - P_w}{P_w} \quad \text{or} \quad \frac{\bar{v}}{\sqrt{gD}} = f(\pi_1, \pi_2, \pi_3, \pi_4, t^*). \tag{14}$$

The modeling procedure is thus the following:

(*a*) Make the model geometrically similar to the prototype, including the location of the flow resistance in the downcomer.

(*b*) Adjust π_4 in the model to that of the prototype system by increasing the magnitude of the resistance (for example, by using an orifice in the line) so as to balance the effect of the smaller D [see equation (13)]. This can be done after several orifices with different d_i's have been calibrated at their design Re's [see equation (6)] over the range of $(P_D - P)/P_D$ expected in the blowdown process. One should try to ensure, by trial and error, that π_4 is approximately the same in both systems over the whole range of $(P_D - P)/P_D$ encountered. An example of how this can be accomplished is given in our companion paper [6].

(*c*) Use the same values of π_1 and π_2 in the model as in the prototype, and the same applied pressure history $\pi_3(t^*)$.

(*d*) Measure $P^* = (P - P_w)/P_w$ and $\bar{v}^* = \bar{v}/\sqrt{gD}$ versus t^* in the model, and calculate P and $\bar{v}$ for the prototype from the knowledge that P^* and $\bar{v}^*$ are the same in both systems at geometrically corresponding locations and t^*.

3 Discussion

The development given above has assumed that the flow resistance in the downcomer is localized, that is, it occurs primarily at a known station. This situation is in fact approximated fairly well in the tests described in our companion paper [6]. Actual containment systems, however, are more complex, and the question arises whether this introduces complications into the modeling. Is only the total flow resistance important, or must one also be concerned with the actual distribution of the resistance in the line?

It should be emphasized that in steady or quasi-steady adiabatic flow it makes no difference to the downstream pressure or the enthalpy flux whether the flow resistance is localized, or distributed in various parts of the piping system. In unsteady flow, however, there may be some difference since the distribution of the resistance in the line affects the time it takes the pipe system to fill up in response to an increased driving pressure. As to how this might affect the modeling, we make the following remarks.

[2] Note that by this definition the pressure drop $P_D - P$ is equal to c_m^{-2} times the dynamic pressure, $\rho_D v^2/2$ based on the drywell gas density and the velocity in the downcomer. Thus, c_m^{-2} is a sort of total head loss coefficient for the downcomer, including both the viscous loss as well as the inviscid Bernoulli pressure drop.

1 In a real containment system, the flow resistance occurs (to a good approximation) in a series of "discrete" locations in the vent system: at the entrance, at bends, area reductions, tees. By applying the energy equation to each uniform-pressure region between successive restrictions, one can easily show that completely accurate modeling should be achieved if in the model the vent system geometry is identical to that of the prototype, but *each* discrete flow resistance is scaled so as to make the local π_4 the same in both systems.

2 If the vent system geometry is accurately modeled, but the main flow restriction in the model is further downstream than in the prototype—as would occur, for example, if a single orifice in the downcomer were used in the model to bring the model's π_4 to the prototype value—then one would expect that the model would tend to show a more violent vent clearing and pool swell than the prototype. This is so because the vent system would tend to follow the rising drywell pressure faster than the properly-scaled value so that at a given dimensionless time, the dimensionless driving pressure would tend to be higher in the model than in the prototype system. The modeling would thus tend to be conservative.

3 If the vent in the model system is not geometrically scaled, but has a smaller volume than the scaled one, and if the total flow resistance is properly scaled so that π_4 is the same in the model as in the prototype, but the model's flow resistance is localized at a point near to the vent exit, then the model should again, if anything, tend to have a more violent vent clearing and pool swell than the prototype. The reason is the same as that given above.

One might stress, in conclusion, that if h_D and $\dot{m}$ had appeared individually in equation (1) rather than as a product, we would have found that instead of π_4 there would be two modeling parameters, $\pi_4' = c_m$ and $\pi_5 = (RT_D/gD)^{1/2}$. If one had to make π_5 the same in a small-scale system as in a large one, modeling would be very difficult because the gas enthalpy would have to be scaled with system size. This difficulty is removed only if one recognized, as Moody did [5], that it is only the product $h_D\dot{m}$ that appears in equation (1). As a result, only the product $c_m(RT_D/gD)^{1/2}$ must be scaled, and this can be done relatively easily by adjusting the line discharge coefficient c_m. It is also interesting that the modeling laws expressed by equations (9–13) ensure that the temperatures in regions I and III of Fig. 1 are the same ratios to T_D in the model as in the full-scale system.

References

1 Cudlin, R. and Kudrick, J. A., "Recent Considerations of Hydrodynamic Forces in Pressure-Suppression Containments (U.S.A.)," paper presented at the International Atomic Energy Agency Meeting on Thermal Hydraulic Consequences of LOCA's Inside and Outside Containments, Cologne, FRG, Dec. 7–8 1976.

2 Telford, J. T., "Current Problems in Reactor Safety," in *Nuclear Power Safety* (J. H. Rust and L. E. Weaver, eds.), Pergamon Press, New York, 1976, pp. 351–358.

3 Kiang, R. L. and Grossi, B. J., "Dynamic Modeling of a Mark II Pressure Suppression System," Electric Power Research Institute Report EPRI-NP-441, April 1977.

4 Collins, E. K., Lai, W., McCauley, E. W., and Pitts, J. H., "Final Air Test Results for the 1/5-Scale Mark I BWR Pressure Suppression Experiment," Lawrence Livermore Laboratory Report UCRL 52371, October 1977.

5 Moody, F. J., "A Systematic Procedure for Scale-Modeling Problems in Unsteady Fluid Mechanics," General Electric Co. unpublished report.

6 Anderson, W. G., Huber, P. W., and Sonin, A. A., "Experimental Tests of the Scaling Laws for Air Clearing in Water-Type Pressure Suppression Systems," ASME JOURNAL OF HEAT TRANSFER, Vol. 100, No. 4, 1978, pp. 605–612.

W. G. Anderson
P. W. Huber
A. A. Sonin

Department of Mechanical Engineering,
Massachusetts Institute of Technology,
Cambridge, Mass. 02139

Experimental Tests of the Scaling Laws for Air Clearing in Water-Type Pressure Suppression Systems[1]

Experiments were conducted to test the validity of the scaling laws which have been put forward for the small-scale modeling of the air clearing phase of flow into the condensation pool of a pressure suppression system. Three geometrically similar wetwells (differing in linear dimension by a factor of 4) were used, along with two liquids (differing in density by a factor of 3) and three gases (differing in enthalpy by a factor of 10). When using different pressures, liquids, and gases, the dimensionless pressures were in excellent agreement as long as the four scaling parameters were held constant. The enthalpy flux must be scaled by the use of an orifice to ensure that the pressures will scale. Our tests uncovered two areas where the scaling laws will not hold if the proper precautions are not taken. First, the vapor pressure of the pool liquid must be sufficiently low. Secondly, peak downloads will scale only if the containment walls are rigid and precautions are taken to eliminate small air bubbles in the liquid.

1 Introduction

In the previous paper [1] we derived a set of scaling laws for the air clearing phase of blowdown into a water-type pressure suppression system of a nuclear powerplant. This set of scaling laws is based on some simplifying assumptions about the underlying physical process involved. Although the assumptions are reasonable, experimental checks of the laws are required. The present paper describes a complete series of such experimental tests. Some initial results of these tests were reported earlier [2].

2 Experiments

The scaling laws were verified experimentally in the somewhat simplified "containment system" geometry system shown in Fig. 1. The wetwell was a simple cylindrical vessel of internal diameter D. A single downcomer with internal diameter $d = 0.182$ D and length $2.73\ D$ entered the wetwell from the top center. The top of the downcomer opened directly into a "drywell" which in our tests was simply a reservoir with a volume large compared with that of the airspace in the wetwell, so that the drywell pressure remained essentially constant during the entire blowdown process. Although our system was not intended to be geometrically identical to any particular existing containment system, its gross geometrical parameters did roughly simulate a first-generation BWR plant (see Table 1).

Wetwells of three different sizes were tested, having diameters D = 14 cm, 28 cm, and 55 cm. These will be referred to as our small, medium-sized, and large wetwells, respectively. The height of the small and medium-sized systems was $2.18\ D$. In both, the wetwell was precisely half-full of water, and the downcomer submergence was $0.364\ D$. The total height of the large system was $2.09\ D$, that is, it was slightly mis-scaled compared with the others. However, the scaled downcomer submergence and the height of the airspace were exactly the same in the large system as in the small and medium-sized systems, although the depth of the water was $1.00\ D$ instead of $1.09\ D$. We believe that this difference is insignificant, because high-speed films have shown that, beneath the bubble which forms during blowdown, the water is essentially stagnant. The floor pressure is then transmitted across stagnant water, and should not be affected by small

Table 1 Geometric parameters of wetwell test systems

$\frac{\text{downcomer area}}{\text{pool area}} = 0.033$	$\frac{\text{liquid depth}}{\text{downcomer diameter}} = 6$
$\frac{\text{submergence}}{\text{downcomer diameter}} = 2$	$\frac{\text{wetwell gas volume}}{\text{liquid volume}} = 1$

[1] Work supported by the U.S. Nuclear Regulatory Commission, Office of Nuclear Regulatory Research, Division of Reactor Safety Research, under Contract No. NRC-04-77-011.

Contributed by the Heat Transfer Division for publication in the JOURNAL OF HEAT TRANSFER. Manuscript received by the Heat Transfer Division February 27, 1978.

changes in the depth of the water. It is, however, important to properly scale the downcomer submergence and the height of the airspace, as was done.

The small and medium-sized wetwells were made of plexiglas, with side wall thicknesses of 0.6 cm and 1.3 cm, respectively. In both systems the roof and floor consisted of plexiglas plates about 2 cm thick. A second small wetwell, with precisely the same internal dimensions as the plexiglas one, was made out of 3 cm thick steel: this was our small system with absolutely rigid walls. The large system was PVC with a side wall thickness of 0.6 cm (heavily reinforced and braced) and roof and wall thicknesses of about 3 cm.

Blowdown was initiated in our system by a pneumatically operated valve consisting of a rubber-lined flat disk that pressed against the top of the downcomer when the valve was closed and which was rapidly withdrawn to open the valve. The opening time was short and did not affect the ensuing flow processes.

The test sections were instrumented to measure pressures (via Kistler Model 206 low-pressure piezotron transducers) at four locations (transducer numbers 1–4) as shown in Fig. 1. The response of the transducers was recorded on a storage oscilloscope and the traces were then photographed for subsequent analysis. High-speed films (1000 frames per second) were also taken of the pool swell in our small and medium-sized test systems.

The discharge coefficient associated with the gas flow rate through the downcomer could be independently controlled by placing interchangeable orifice plates in the downcomer, 11.5 downcomer diameters upstream of the downcomer exit (Fig. 1). The orifices were calibrated with each of the three gases that were used in our experiments. This calibration for c_m as a function of the pressure difference between the drywell and downcomer exit was performed by setting the drywell pressure at P_D and the wetwell (containing no liquid) at a pressure P, and measuring the initial rate of pressure rise in the wetwell when the valve was opened. Starting with the orifice flow equation and the first law of thermodynamics, one can derive the wetwell pressurization rate for adiabatic charging of an ideal gas, and show that the orifice coefficient obeys the equation

$$c_m = \frac{V}{\frac{\pi d^2}{4}\gamma\sqrt{2RT_D}}\left(\frac{P_D - P}{P_D}\right)^{1/2}\frac{1}{\tau} \tag{1}$$

where V is the total volume downstream of the orifice (wetwell plus downcomer), τ is the time it would take the wetwell pressure to reach P_D if it kept rising at its initial rate, and $P_D - P$ is the initial pressure difference between the drywell and the downcomer exit. Fig. 2 shows some typical results of orifice calibrations for different gases as a function of pressure difference between the drywell and wetwell. The data are presented in the dimensionless forms defined by the scaling laws [1]. The dependence of c_m on $(P_D - P)/P_D$ appears to be quite insensitive to the other parameters d_i/d, γ, and Re in equation (6) of [1], since the curves in Fig. 2 for different gases and different orifices have quite similar shapes. Thus modeling requirement (b) in [1] was fully satisfied. We have chosen the value of c_m at $(P_D - P)/P_D = 1/3$

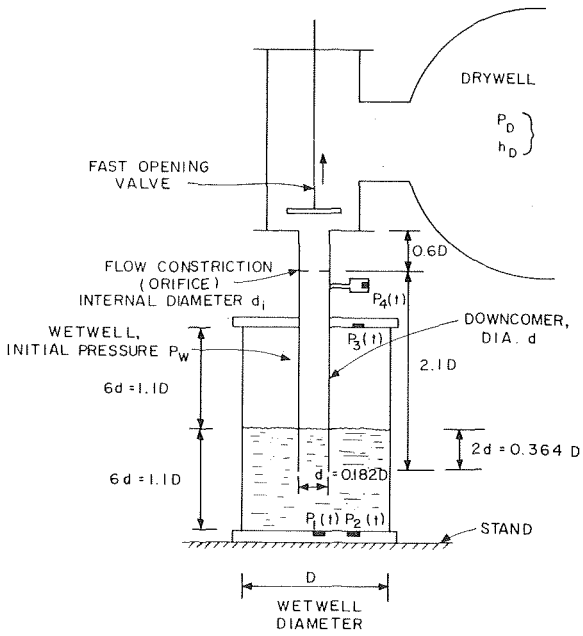

Fig. 1 Experimental system

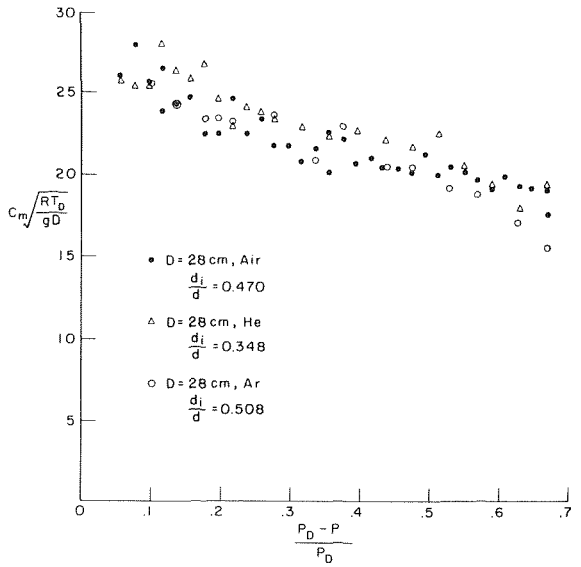

Fig. 2 Typical orifice calibrations

Nomenclature

c_m = mass flow coefficient through orifice, equation (5), [1] (dimensionless)
d = downcomer diameter, m
d_i = orifice internal diameter, m
D = wetwell diameter, m
g = acceleration due to gravity, 9.8 m·s^{-2}
h_D = specific stagnation enthalpy of drywell gas, J/kg
P = pressure at a given point, Pa
$P(0)$ = initial pressure prior to blowdown at a given point, Pa
P_1 to P_4 = pressures from transducers 1–4 (Fig. 1), Pa
P_D = drywell pressure, Pa
P_w = *initial* wetwell pressure, Pa
P^* = dimensionless pressure at a point, equation (2)
R = specific gas constant (universal gas constant divided by molar mass of gas), J/K·kg
Re = a Reynolds number for gas flow through the orifice, equation (7), [1] (dimensionless)
t = time measured from the initiation of blowdown's
t^* = dimensionless time = $t\sqrt{g/D}$
T_D = drywell gas absolute temperature, K
V = total volume of wetwell system downstream of orifice, m^3
γ = ratio of specific heats of drywell gas (dimensionless)
π_1 to π_4 = dimensionless scaling parameters, equations (9–14), [1]
ρ = density of wetwell liquid, kg·m^{-3}
τ = rise time for pressure in empty wetwell (used for orifice calibration), s

as a reference value for each gas-orifice combination, and it is that value which is used in comparing the experimental results discussed in the next section.

Our goal in these experiments was to test the scaling laws outlined in [1] by varying the quantities P_D, P_w, ρ, D, R, and c_m, which are the easily altered scaling parameters, and determining whether the dimensionless dependent variables, such as the dimensionless pressure, were functions of *only* the dimensionless groups, equations (9–13) in [1].

In our test program, the linear system size was varied by about a factor of 4: D = 14–55 cm.

Three gases were used: air (with γ = 1.4) and helium and argon (with γ = 1.67). The latter two were chosen because their gas constant R differs by a factor of 10, and hence allows the parameter π_4 (equation (13) of [1]) to be changed by a factor of 3.2 by changing gas alone, without changing pressures, flow orifice, or system size.

Two liquids were used: water and Meriam manometer fluid (1,1,2,2-tetrabromoethane, specific gravity 2.95). Flow constriction diameters relative to the downcomer diameter, d_i/d, were varied by a factor of 2. Absolute pressures were varied by a factor of about 6 in the wetwell and 9 in the drywell.

Table 2 shows the corresponding ranges over which the dimensionless scaling parameters were varied in our tests. Also shown for reference are the values of the same parameters for a design basis LOCA in a typical first-generation BWR plant.

3 Results and Discussion

3.1 Typical Pressure Histories. Fig. 3 shows some pressure traces measured in the medium-sized system (D = 28 cm). Trace 3(a) is the pressure on the wetwell floor, center (transducer No. 1, Fig. 1), trace 3(b) is the pressure on the wetwell ceiling (transducer No. 3), and trace 3(c) is the pressure in the downcomer just downstream of the orifice (transducer No. 4). The function of transducer No. 4 was to signal the initiation of blowdown, and we measured all times from the start of the increase in pressure at this transducer. Since that transducer was in communication with the downcomer via a narrow hole ($^1/_{16}$ in. diameter and several inches long), its response may have been partially attenuated by the intervening line. The floor pressure measured off-center (transducer No. 2, Fig. 1) was virtually identical to the center floor pressure in our tests. The main features of the trace shown are typical of those obtained in all three systems, with all the gases tested. Fig. 3(a) is a trace of the wetwell floor pressure which has a first peak with no superposed oscillations. Such oscillation-free floor pressure traces were obtained only when special precautions were taken to suppress small suspended gas bubbles in the pool, as will be discussed in more detail later. All the traces in Fig. 3 show the departure in pressure at a given point from the initial pressure at that point before the initiation of blowdown: $P_1 - P_1(0)$, for example.

3.2 Verification of the Scaling Laws. To check for scaling we set out to verify whether the dimensionless forms of the pressures we measured were indeed functions only of the four modeling parameters π_1 to π_4 and the dimensionless time $t^* = t\sqrt{g/D}$. Since our drywell pressure was constant, we found it convenient to define the dimensionless pressure as

$$P^* \equiv \frac{P - P(0)}{P_D}, \tag{2}$$

where P is the pressure at a given point and time, and $P(0)$ is the initial, pre-blowdown pressure at the same point. Our purpose is to show that

$$P^* = P^*(\pi_1, \pi_2, \pi_3, \pi_4, t^*), \tag{3}$$

but that P^* is not affected independently by any of the separate quantities that make up π_1 to π_4 and t^*. Rather than comparing the entire pressure histories for different cases, it is convenient to select some easily recognizable characteristics of the pressure histories and restrict the comparison to those. The following were selected:

(1) The first maximum in the floor pressure, which occurs just after vent clearing (Fig. 3(a)).

(2) The time corresponding to the first maximum in the floor pressure (Fig. 3(a)).

(3) The minimum floor pressure after vent clearing (Fig. 3(a)).

(4) The time corresponding to the minimum floor pressure after vent clearing (Fig. 3(a)).

(5) The first maximum in the ceiling pressure (Fig. 3(b)).

(6) The time corresponding to the first maximum in the ceiling pressure (Fig. 3(b)).

All of the six quantities listed above should be a function *only* of π_1 to π_4.

We note first that our tests uncovered two effects which may cause deviations from the currently accepted scaling laws if the model scale is made too small. The first is caused by excessive water vapor in the wetwell airspace, and tends to give reduced peak uploads. For proper scaling, the absolute pressures must be reduced in proportion to system size, and consequently the proportion of water vapor in the wetwell airspace increases as the model size decreases. This tends to reduce the pressure rise due to the airspace compression, and hence the uploads. The effect can be significant at scales less than about 1/10 at room temperature, but we found that in our experiments the problem could be minimized by cooling the water to near freezing and thereby reducing its vapor pressure (see discussion in Section 3.3 below). All the ceiling pressure data shown from the small and me-

Table 2 Values of dynamic scaling parameters

Parameter	BWR Plant	Our System (Design Conditions)
$\pi_1 = \gamma$	1.4	1.4, 1.67
$\pi_2 = P_w/\rho g D$	2–3†	4.15, 8.29
$\pi_3 = P_D/P_w$	1–3	2.0, 3.0
$\pi_4 = c_m(RT_D/gD)^{1/2}$	*ca:* 25†	8.5–60

† For the BWR plant, we take $D^2 \equiv 4/\pi \times$ (pool area per downcomer).

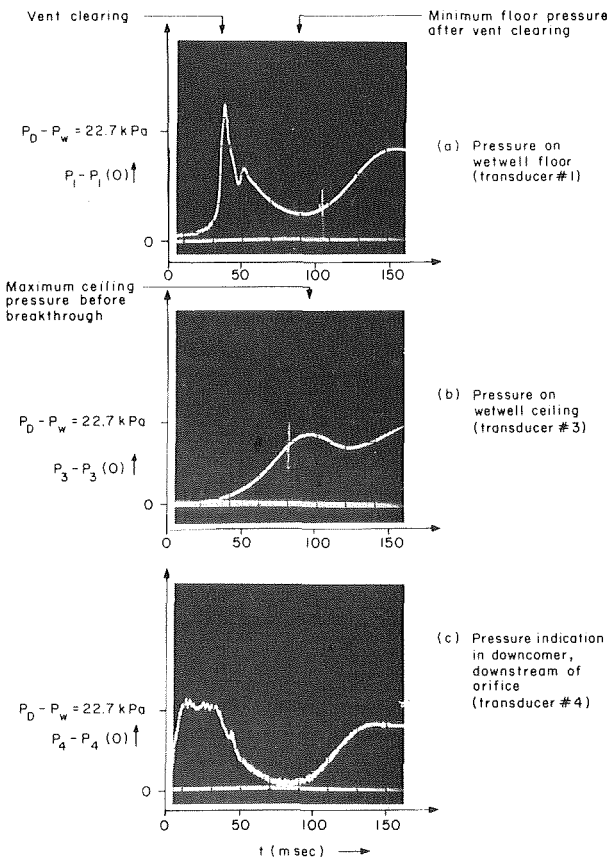

Fig. 3 Pressure histories (air/water, D = 28 cm, π_1 = 1.4, π_2 = 4.15, π_3 = 3, π_4 = 21.4)

dium-sized sytems with water as the liquid are for pool temperatures not too far from freezing. This precaution was not taken with the large system, however, where the absolute gas pressures were relatively high. Nor was it necessary to cool the smaller system when Meriam fluid was used as the wetwell liquid; that fluid has a very low vapor pressure even at room temperature.

The second effect is due to the presence of very small air bubbles suspended in the water or attached to the wetwell walls. These can give a "springiness" to the pool and can cause an effect similar to the fluid-structure interactions which might occur if the containment walls themselves were flexible, namely, an oscillatory component on the pressures measured in the wetwell pool. High-amplitude oscillations can be generated after the almost impulsive loading of the floor that occurs immediately after downcomer clearing [3]. In the presence of the superposed oscillation, floor pressures are no longer properly scaled and the apparent peak downloads can be considerably higher than one would get in the absence of bubbles. The air bubble problem can be eliminated, however, by the addition of a surfactant (such as Kodak "Photo-Flo") to the wetwell water, or by using a different wetwell liquid such as Meriam manometer fluid (see discussion in Section 3.4 below) [4]. Under these conditions, measured downloads scale according to the Moody laws. All the data we show on the scaling of the first peak in the floor pressure (which occurs in response to the almost impulsive loading following vent clearing), with water as the wetwell liquid, are taken with Photo-Flo added. In the experiments in the small system with Meriam fluid as the wetwell liquid, there appeared to be no problems with bubbles.

Figs. 4–8 summarize our results on scaling from all the air tests with both water and Meriam fluid as the wetwell liquids. Note that not all of the graphs include data from all three systems. Figs. 4–6 plot dimensionless pressures against π_4 with π_1, π_2, and π_3 held constant; Figs. 7 and 8 plot dimensionless times against π_4, again with π_1 to π_3 held constant. Results at two values of π_3 ($\pi_3 = 2$ and $\pi_3 = 3$) are shown. Qualitatively similar results were also obtained at a second value of π_2 ($\pi_2 = 8.29$) and are reported elsewhere [4].

The results constitute clear support for the scaling laws. Allowing for some scatter in the data, the dimensionless dependent variables appear to be functions of *only* the proposed scaling parameters. At the same values of π_1 to π_4 the tests in systems of different size (differing in linear dimension by up to a factor of 4) have the same dimensionless pressures or times. It should be emphasized that the *dimensional* dependent variables—for example, the raw pressure data that appear in dimensionless form in Fig. 6—differ in magnitude by

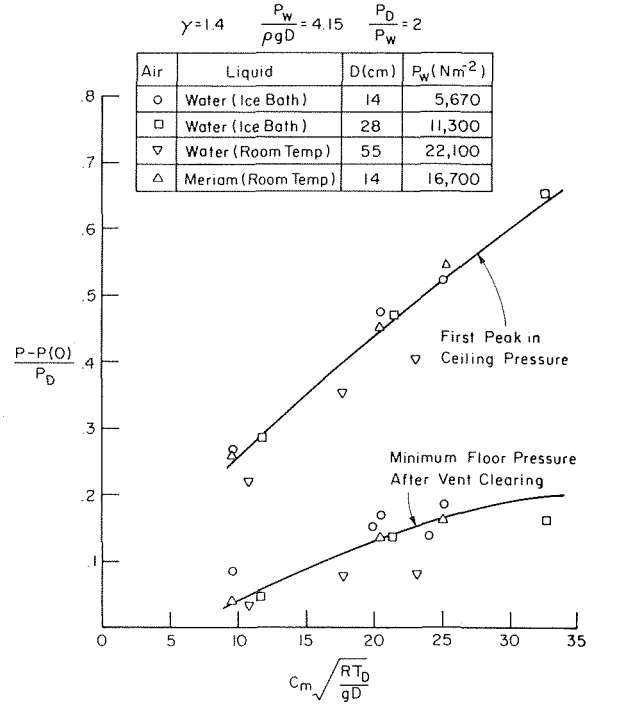

Fig. 5 First peak in wetwell ceiling pressure and minimum floor pressure as functions of π_4 (air tests).

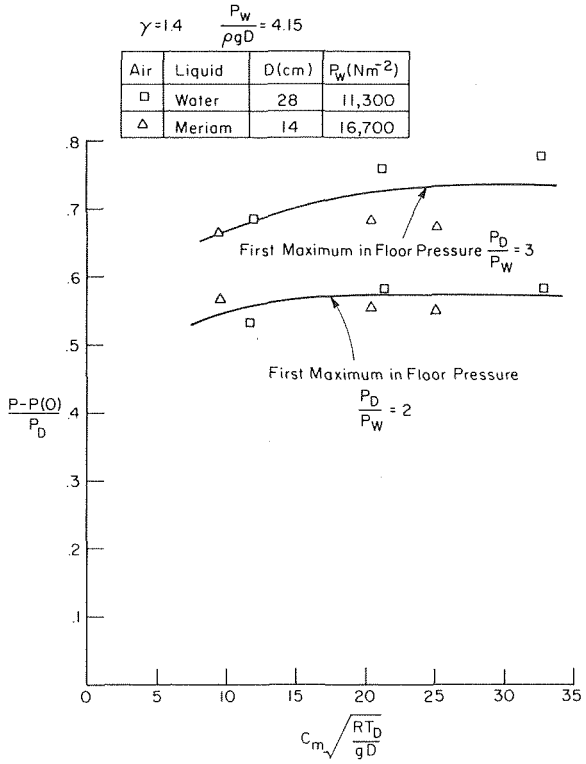

Fig. 4 First peak in floor pressure versus π_4 (air tests)

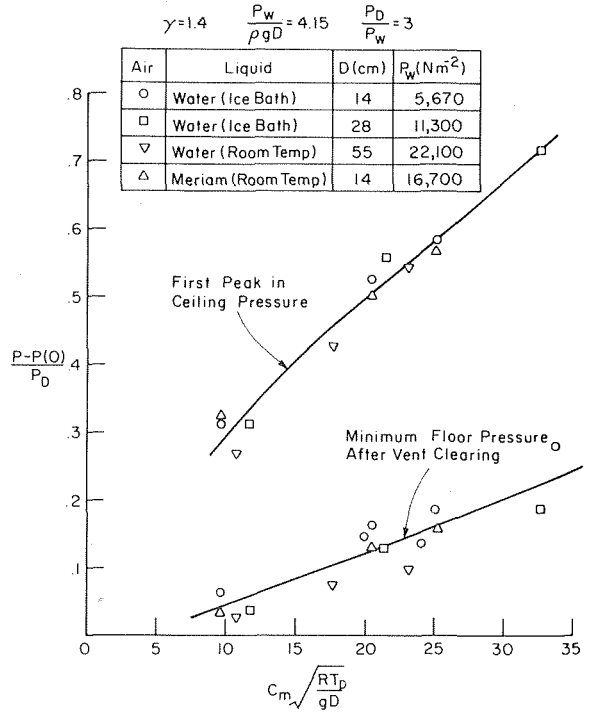

Fig. 6 First peak in wetwell ceiling pressure and minimum floor pressure as functions of π_4 (air tests)

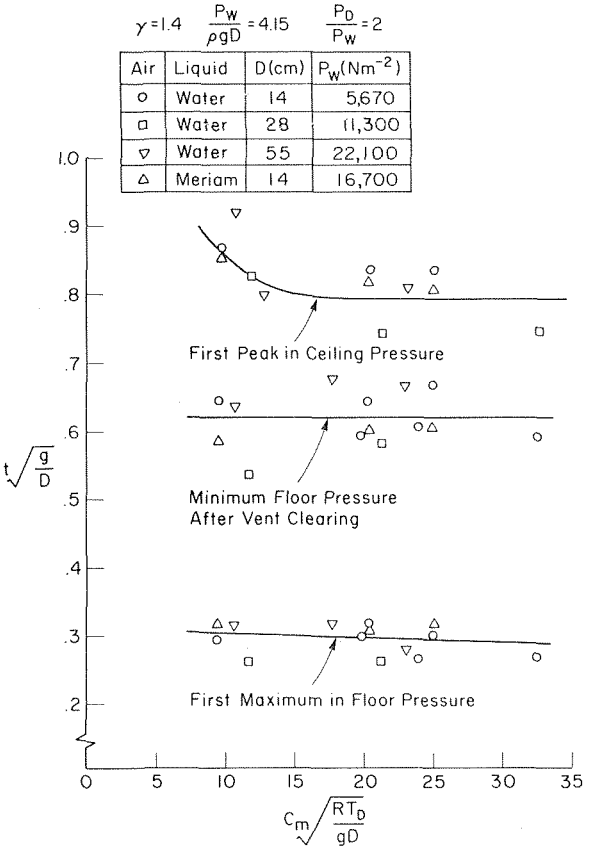

Fig. 7 Dimensionless time versus π_4 (air tests)

up to 400 percent. Only when reduced to dimensionless form do the data for each variable fall on a single smooth curve as shown.

Figs. 9 to 13 are results from the helium and argon tests in the three wetwells. Again, dimensionless pressures and times have been plotted against π_4. Similar results were obtained with $\pi_2 = 8.29$ [4]. In view of the wide range of three of the experimental parameters varied in these tests—a factor of 10 in gas enthalpy, 3 in liquid density, and 4 in system size—the agreement in the dimensionless dependent variables is very good. The importance of the gas enthalpy, which appears in π_4, is clearly confirmed; dynamically similar tests with helium and argon in the same wetwell system required different downcomer orifices, such that the π_4's were matched, to give satisfactory agreement in the recorded pressures and times.

The central role of the enthalpy flux parameter π_4 in modeling the pool swell can be further emphasized by comparing data from systems that have the same values of π_1 to π_3, but have geometrically similar orifices (i.e., are completely geometrically similar) instead of having the same values of π_4. Fig. 14 shows the data from Fig. 6 for the air/water tests in the three systems, but the ordinate is now d_i/d (a dimensionless orifice diameter) which is an indication of downcomer geometry, rather than of π_4, the measured enthalpy flux. It is clear that with π_1 to π_3 exactly matched in the three systems, and at the same value of d_i/d (i.e., exact geometric similarity), but with different π_4, the dimensionless pressures measured in the three systems are quite different. The point is made even more strongly by replotting the data from the helium and argon tests in the same way (Fig. 15). The conclusion is that proper orificing of the downcomer line is an important ingredient of the scaling procedure.

3.3 Effect of Excessive Vapor Pressure in Small-Scale Tests. Our initial test series showed that in experiments with water at room temperature in the wetwell, the dimensionless ceiling pressures in the small system (D = 14 cm) fell below the corresponding values in the medium-sized system (D = 28 cm), and these in turn fell somewhat below the values in the large system (D = 55 cm). However, in tests conducted at low wetwell pool temperatures (close to freezing), dimensionless histories in all three systems with water were the same and agreed with the results from tests in the small system with Mer-

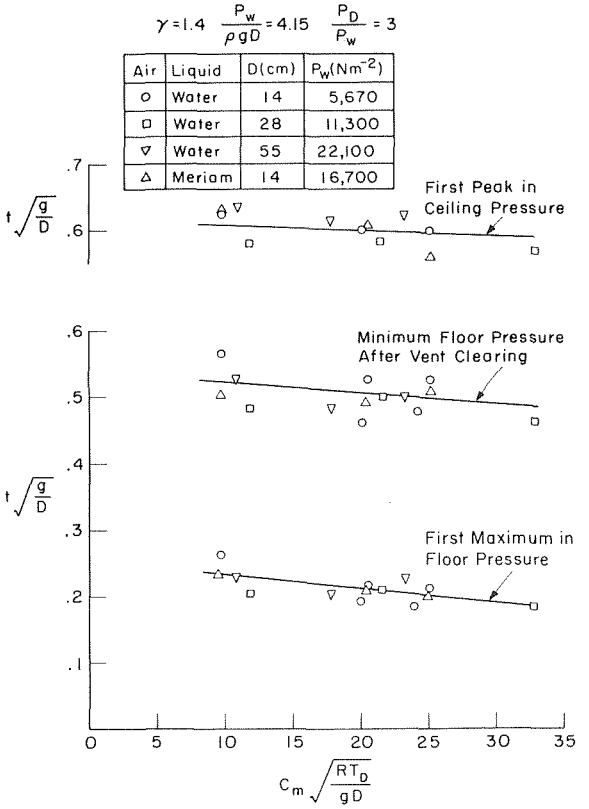

Fig. 8 Dimensionless time versus π_4 (air tests)

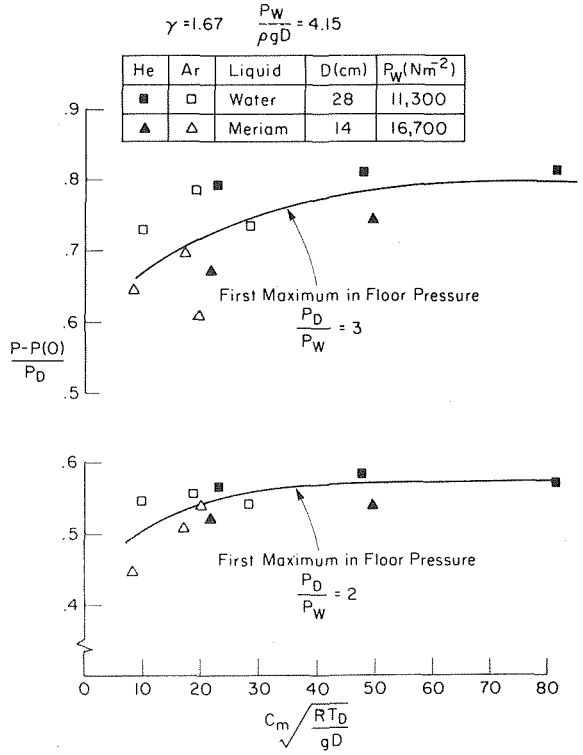

Fig. 9 First peak in floor pressure versus π_4 (helium and argon tests)

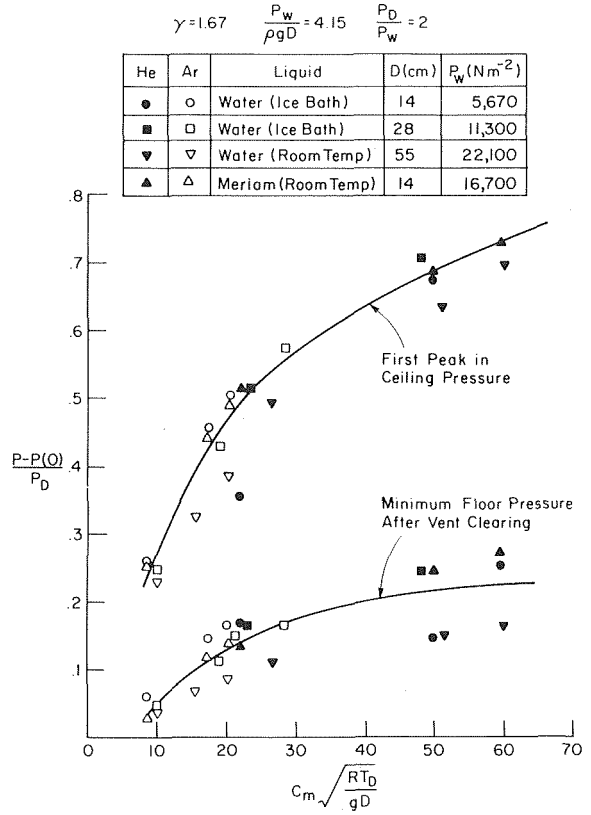

Fig. 10 First peak in wetwell ceiling pressure and minimum floor pressure as functions of π_4 (helium and argon tests)

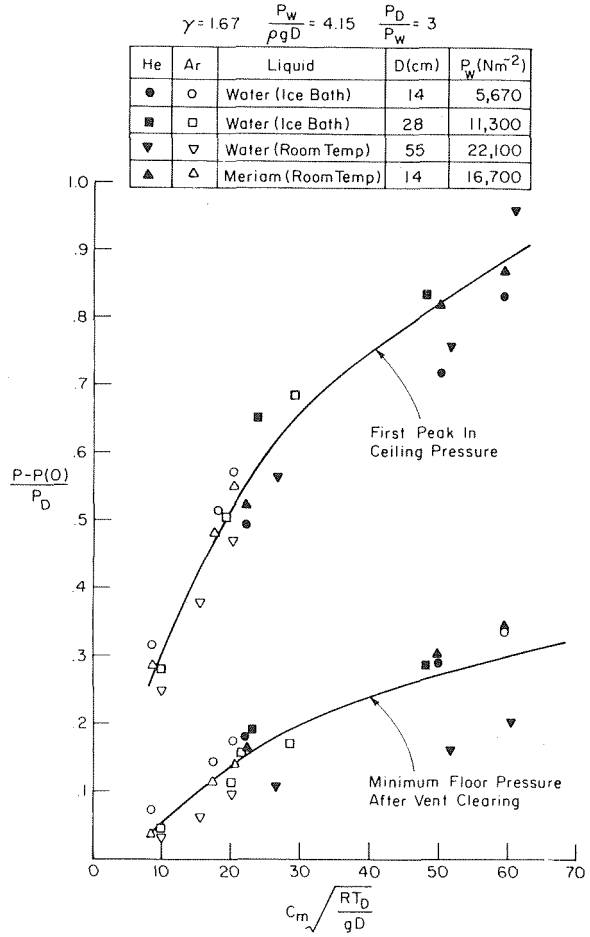

Fig. 11 First peak in wetwell ceiling pressure and minimum floor pressure as functions of π_4 (helium and argon tests)

iam fluid. We attribute this behavior to the presence of water vapor in the wetwell airspace prior to blowdown in the higher temperature tests. Significant amounts of water vapor will not only change the value of γ for the gas in this region, but may also provide a mechanism for condensation and rapid heat transfer during pool swell. These effects are not, of course, accounted for in the scaling analysis. At room temperature the vapor pressure of water is about 3 kPa—a significant fraction of the initial wetwell pressure, 5.67 kPa, required in many of the small system tests. By cooling the wetwell pool in an ice-water bath the water vapor pressure is reduced to about 0.5 kPa, a value which is apparently low enough not to affect the compression of the wetwell airspace significantly. The preliminary data illustrating this effect are reported elsewhere [3]. Generally, in tests with helium, the water vapor problem appeared to be most acute [4]. We attribute this to the fact that helium equilibrates more quickly with water than does either argon or air.

Tests of the floor pressure in our medium-sized system have shown that the water vapor pressure has no important effect on the *pool* pressure histories. All our floor pressure data, with or without surfactant, were taken at room temperature.

It is not suprising that the first indication of conditions in which there is a departure from the scaling laws came from the tests in our smallest system. Apart from the rigidity of the walls and the incompressibility of the liquid, the key assumptions underlying the development of the modeling laws in [1] are perfect and noncondensable gases in the drywell and wetwell, negligible heat transfer from gas to liquid, inviscid motion in the wetwell pool, and negligible surface tension effects. All of these assumptions are more likely to be satisfied as system size is increased. Our results show that except for the first assumption (noncondensable gas in the wetwell pool), the assumptions do hold in systems as small as our smallest wetwell (D = 14 cm), and that provided the pool is cold, even the first assumption is satisfied. This conclusion is very encouraging. The scaling laws clearly do hold in the small-scale systems that we have tested, going down to about 1/24 of full-scale Mark 1 conditions, and there is every reason to believe that they will be equally applicable in any larger-scale tests.

3.4 On the Precautions that Must be Taken to Avoid Pool Oscillations due to Gas in the Liquid. As we noted above, most of our original tests with water as the wetwell liquid showed a strong oscillatory component superposed on the floor pressure near the time of vent clearing. This appears to have been caused by pool oscillations which resulted from the presence of air in the liquid, presumably in the form of very small bubbles either in the liquid or at the liquid/solid boundaries. That the bubbles were the cause, and not actual wall flexure and oscillations (true fluid-structure interactions), was deduced from three observations. First, tests in the absolutely rigid-wall small system, which had 3 cm thick steel walls, showed floor pressure oscillations similar to those in the small system with plexiglas walls. Secondly, the addition of a surfactant (Kodak Photo-Flo, in an amount recommended by the manufacturer) removed the oscillatory component. Finally, when Meriam fluid was used as the wetwell liquid (in the small system only), there appeared to be no problem with trapped gas and the concomitant pressure oscillation.

The hypothesis that the pressure oscillations are due to pool vibrations which result from bubbles was further supported by a series of runs made with a light oil as the wetwell liquid [3]. In successive runs made every minute, the peak floor pressure increased considerably. We believe this is explained by the progressive accumulation of bubbles suspended in the relatively viscous oil of the pool. Our hypothesis that the oscillations are due to bubbles is given further support by the fact that a trace taken after the bubbles had had time to clear (e.g., by allowing the system to stand undisturbed, overnight) usually had a shape free of superposed oscillations.

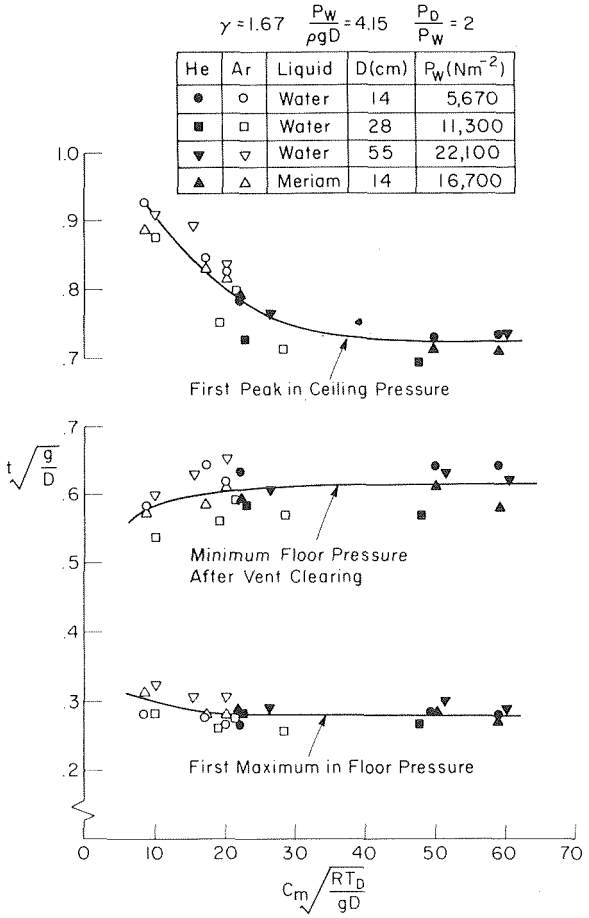

Fig. 12 Dimensionless time versus π_4 (helium and argon tests)

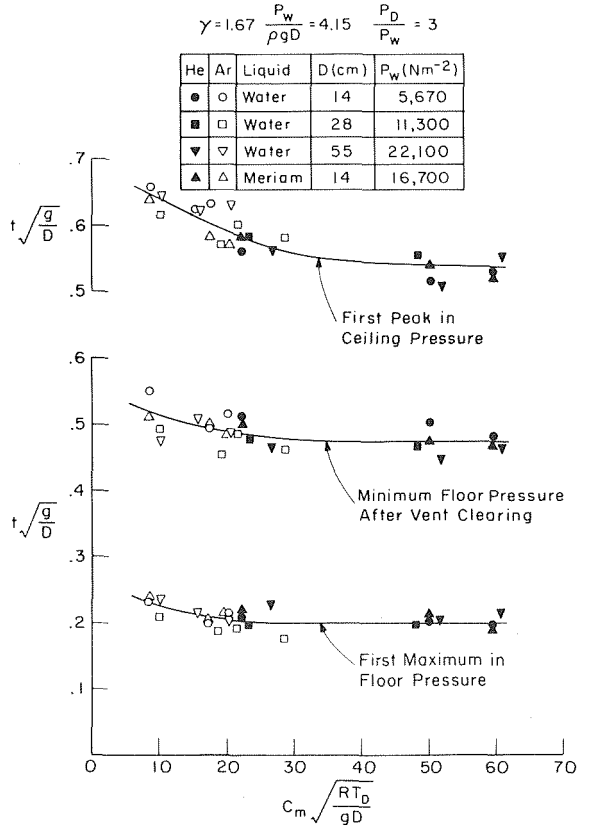

Fig. 13 Dimensionless time versus π_4 (helium and argon tests)

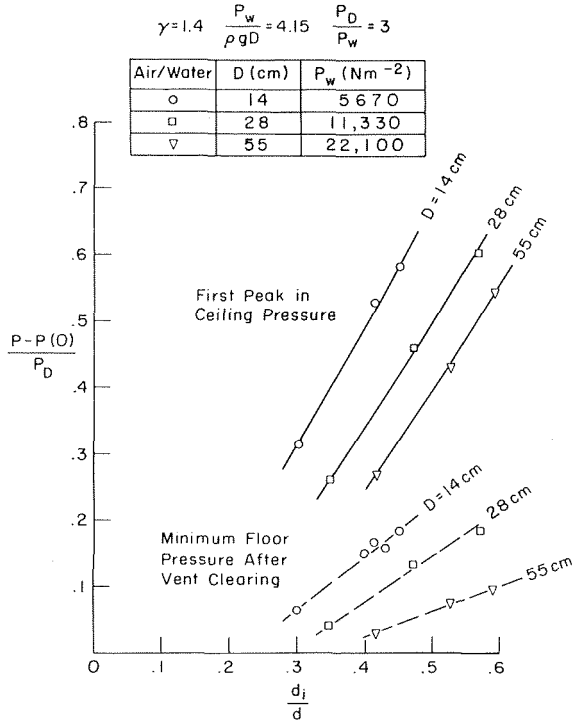

Fig. 14 First peak in ceiling pressure and minimum floor pressure as functions of d_i/d (air tests)

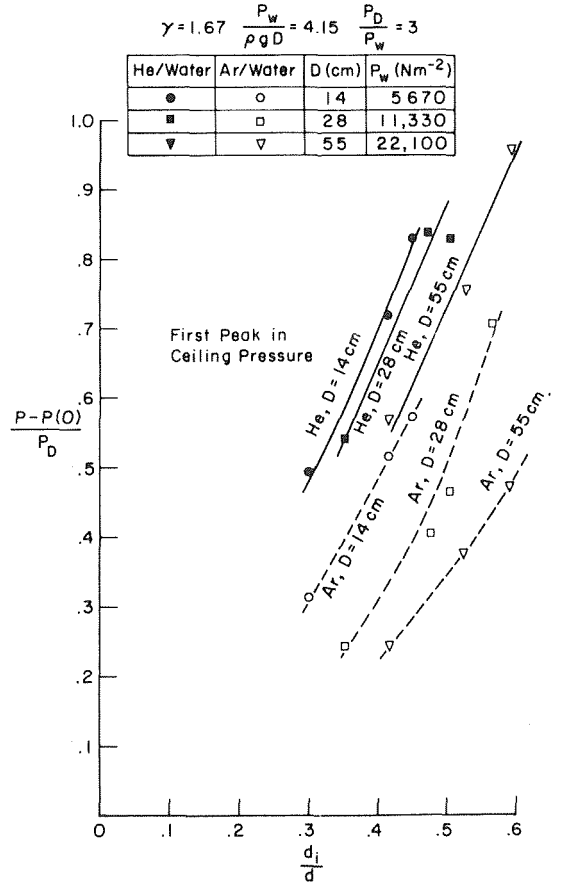

Fig. 15 First peak in ceiling pressure as a function of d_i/d (helium and argon tests)

4 Conclusions

(1) Our experiments confirm the modeling laws outlined in equations (9–14) of [1] for the air clearing phase of the flow into a water-type pressure suppression system. These are a refinement of the laws that were originally put forward by Moody [5], and they require that the enthalpy flux from the downcomer be scaled down in a small model by the use of an orifice, so that the scaling parameter π_4 is properly simulated. If this is not done (for example, as when an appropriate orifice is not used in the small-scale model, although the dynamic conditions are otherwise properly scaled), the wetwell pressures can be significantly mis-scaled. One notes, however, that the first peak in the floor pressure, as well as all the characteristic times, were insensitive to π_4 in our tests, except near the very lowest values of π_4 that we tested. With the derived scaling laws, accurate small-scale testing of the pool swell process is possible.

(2) In order to insure proper scaling in small-scale tests, it is necessary to take precautions against excessive vapor content in the wetwell airspace. In tests with room temperature water at sufficiently small scales (smaller than about 1:10 if the full-scale wetwell is at about standard atmospheric pressure) the presence of excessive water vapor in the wetwell tends to give reduced peak ceiling pressures. This effect of vapor pressure can, however, be minimized by cooling the water to a temperature near freezing, or by replacing the water with another liquid, such as Meriam manometer fluid, which has a very low vapor pressure.

(3) Peak downloads on the wetwell floor can be expected to scale with the proposed scaling laws only if the containment walls are rigid and if precautions are taken to eliminate the presence of small air bubbles in the pool liquid. Both fluid-structure interactions caused by the flexure of the pool bounding walls and the presence of air in the liquid tend to give a springiness to the wetwell pool, and can cause high-amplitude oscillations in the floor pressure after the almost impulsive loading of the floor immediately after downcomer clearing. Such oscillations are not accounted for in the present scaling laws. One may expect that generally, the problem with air bubbles tends to get worse as scale is reduced. We note, however, that the amplitudes of the oscillatory pool motion are very small when compared with system size, and the bulk pool displacements, pool swell velocities, and pressures in the airspaces are not affected by such pool oscillations. The problem with air bubbles can be eliminated by the addition of a surfactant (such as Kodak Photo-Flo) to the wetwell water, or by using a particular wetwell liquid (such as Meriam manometer fluid) where the problem with bubbles appears not to arise. When these precautions are taken, and when the pool boundaries are rigid (that is, the period of their natural oscillation is much shorter than the shortest transient time in the imposed hydrodynamic loading), floor loads scale according to the proposed laws.

References

1 Sonin, A. A. and Huber, P. W., "On the Scaling Laws for Air Clearing in Water-Type Pressure Suppression Systems," ASME JOURNAL OF HEAT TRANSFER, Vol. 100, No. 4, 1978, pp. 601–604.

2 Anderson, W. G., Huber, P. W., and Sonin, A. A., "Small-Scale Modeling of Hydrodynamic Forces in Pressure Suppression Systems: Tests of the Scaling Laws," paper presented at the American Nuclear Society Meeting on Thermal Reactor Safety, July 31–August 4, 1977, Sun Valley, Idaho.

3 Anderson, W. G., Huber, P. W., and Sonin, A. A. "Small-Scale Modeling of Hydrodynamic Forces in Pressure Suppression Systems," U.S. Nuclear Regulatory Commission Report NUREG/CR-0003, March 1978.

4 Anderson, W. G., "Small-Scale Modeling of Hydrodynamic Forces in Pressure Suppression Systems," M.S. Thesis, Department of Mechanical Engineering, Massachusetts Institute of Technology, Nov. 1977.

5 F. J. Moody, "A Systematic Procedure for Scale-Modeling Problems in Unsteady Fluid Mechanics," General Electric Company unpublished report, 1976.

Y. H. Mori
Research Associate.

E. Inui[1]
Graduate Student.

K. Komotori
Professor.

Department of Mechanical Engineering,
Keio University,
3-14-1 Hiyoshi, Kohoku-Ku, Yokohama 223
Japan

Pool Boiling Heat Transfer to Emulsions

The characteristics of steady pool boiling heat transfer from a horizontal wire to various emulsions were obtained experimentally. Sample emulsions were prepared by an ultrasonic method with water, oils whose boiling points are higher than that of water, and emulsifying agents. The kind of emulsifying agent affected remarkably the characteristics of heat transfer to oil-in-water emulsions. The kind of oil affected little the heat transfer to oil-in-water emulsions but strongly that to water-in-oil emulsions.

Introduction

Boiling heat transfer to emulsions has been studied so far by a few researchers in relation to the quenching of metals. Tachibana and Enya [1] and Satoh and Shoji [2] carried out experimental studies expecting to control the quenching rate by mixing oil and water at various fractions. Spindle oil was used exclusively in both studies, while ethyl alcohol and sodium oleate were used as emulsifiers (emulsifying agents) by Tachibana and Enya [1] and Satoh and Shoji [2] respectively. In both studies a heated test piece of copper was dipped into a pool of emulsion. Thermocouples attached to the test piece yielded the cooling curve, from which the boiling curve was obtained. The boiling curves obtained in those studies indicate that there are characteristic regimes which correspond respectively to the nucleate, transition and film-boiling regimes defined in the boiling of usual liquids. It should be noticed, however, that we cannot identify boiling modes in those regimes in the case of boiling of emulsions as nucleate, transition and film boiling for the present, since no observation of boiling behavior has been done so far because of the opacity of emulsions.

It is presumed that the mechanism and characteristics of boiling heat transfer depend not only on the fraction of two liquids composing the emulsion but also on which liquid is continuous (or dispersed) and on the size distribution of globules. Such factors are not specified in the previous studies.

The present study deals with the pool boiling heat transfer from a horizontal wire in the regime corresponding to the nucleate-boiling regime; i.e., the regime available in the course of rise of heat flux between boiling inception and burn-out. Some kinds of oils with a boiling point higher than that of water were used to prepare *O/W* (oil-in-water) and *W/O* (water-in-oil) emulsions. The type (i.e., *O/W* or *W/O*) and globule size were specified for each emulsion sample used in the boiling experiments to prescribe the condition on which the obtained heat transfer characteristics are based.

Experimental

Apparatus. Fig. 1 shows a schematic diagram of the experimental apparatus. Since the volume of emulsion prepared at one time as described later was limited, a relatively small glass beaker was used as the test vessel which was to hold the heating wire and a test liquid (emulsion or water). The heating wire was nickel, 0.2 mm dia and 70 mm long. It was suspended horizontally, being screwed down to the ends of the vertical copper poles, and was heated electrically by use of a stabilized d-c power supply. The heat flux from the wire surface was determined from the resistance of the wire measured by use of a Wheatstone bridge and the voltage-drop across the wire measured

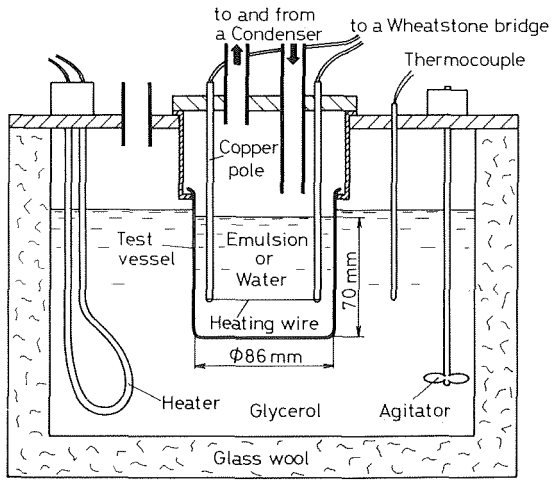

Fig. 1 Schematic of experimental apparatus

[1] Present address: Nippon Kokan Corporation, Yokohama.

Contributed by the Heat Transfer Division for publication in the JOURNAL OF HEAT TRANSFER. Manuscript received by the Heat Transfer Division November 14, 1977.

Table 1 Oils used in preparing emulsions

	Saturation temperature at 101.3 kPa °C	Vapor pressure at 100 °C kPa
KF 96	above 400	negligible
KF 54	above 400	negligible
n-Dodecane	216	2.0
n-Undecane	196	4.2

Table 2 Summary of kinds of emulsions

Dispersed phase/ Continuous phase	Emulsifier (x_e, %)	Arithmetic mean diameter of globules, μm
KF 96/Water	Sodium oleate (0.5)	2–6
KF 96/Water	Tween 80 (1.0)	3–5
KF 54/Water	Sodium oleate (0.5)	4–5
KF 54/Water	Tween 80 (1.0)	3–5
Dodecane/Water	Sodium oleate (0.5)	<1
Undecane/Water	Sodium oleate (0.5)	<1
Water/KF 54	Span 80 (1.0)	4–5
Water/Undecane	Span 80 (1.0)	4–5

by use of a digital voltmeter. The temperature of the wire surface was known from the resistance of the wire. Three glass-sheathed thermocouples were installed in the test vessel to yield the bulk temperature. The condenser connected with the test vessel was not used when *W/O* emulsions were used as the test liquid to prevent "continuous water" from pouring into the vessel.

Preparation of Emulsions. Four kinds of oils used in preparing emulsions are presented in Table 1. KF 96 and KF 54 fluids are dimethyl silicone oil and methylphenyl silicone oil, respectively, prepared by Shin-Etsu Kagaku Co., Tokyo. Dodecane and undecane were reagent grade. Water was distilled after being deionized. The surfactants used as emulsifiers were sodium oleate, Tween 80 (polyoxyethylene sorbitan monooleate) and Span 80 (sorbitan monooleate). Sodium oleate is an anionic surfactant, while the latter two are nonionic surfactants. Either sodium oleate or Tween 80 was dissolved in the water phase in preparing *O/W* emulsions. Span 80 was dissolved in the oil phase in preparing *W/O* emulsions. Water phase and oil phase, either of them including an emulsifier, were superposed in the test vessel taken out of the glycerol bath shown in Fig. 1. The tip of a horn attached to the oscillator of a 300 W ultrasonic magnetostriction generator was immersed near the water-oil interface. The frequency was regulated to a resonant frequency near 20 kHz. The resulting cavitation converted stratified phases in the test vessel into a uniform emulsion. The kinds of emulsions used in this study are summarized in Table 2. The mass fraction of emulsifier, x_e, is based on the total quantity of emulsion. The mass fraction of oil, x_o, for each combination of oil and emulsifier was varied in the range in which stable emulsions could be formed.

The types of prepared emulsions were determined by the dilution method [3]. The globule-size distributions were obtained by photomicrography. Details of the procedure and of calculation process are described in [4]. Sampling of an emulsion for the photomicrography was made just after preparation of the emulsion, and just before and after the boiling experiment as described later.

Procedure. The heating wire attached to the copper poles was cleaned with ethyl alcohol and then installed in the test vessel immersed in the glycerol bath. The emulsion (or water) in the test vessel was heated to 100 °C, i.e., the saturation temperature of water at the atmospheric pressure, and then maintained at that level. Before starting the electrical heating of the wire, the second sampling was made. The arithmetic mean diameter of globules obtained from this sample is given in Table 2 for each kind of emulsion. The heat flux was raised step by step with a small increment, the surface temperature being measured at each step, from the free-convection regime to the boiling regime. In most runs, the heat flux was then decreased step by step to the free-convection regime as described in the succeeding section. After each run the third sampling was made.

Since the bulk temperature was maintained at 100 ± 0.4 °C throughout the present experiments, the difference between surface and bulk temperatures, ΔT, was approximately the same as the superheating of the surface on the basis of saturation temperature of water which was either continuous phase or dispersed phase. Boiling curves are illustrated exclusively on $q - \Delta T$ plane in this paper.

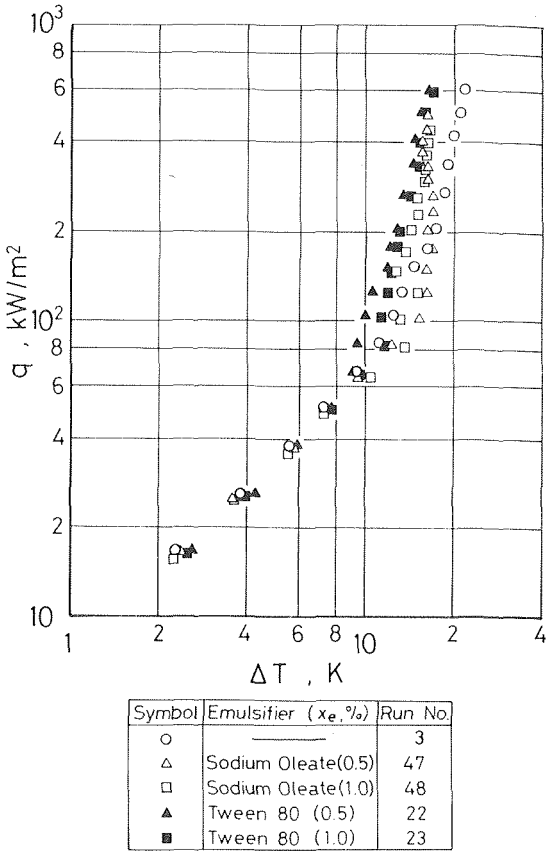

Fig. 2 Boiling curves for water

Results and Discussion

Boiling Curves for Water. As described before, either of two kinds of surfactants was dissolved in water phase as an emulsifier in preparing *O/W* emulsions. Therefore, the boiling curves for water containing either of those surfactants as well as for pure water are shown beforehand in Fig. 2 for the convenience of evaluating the boiling heat transfer to emulsions shown later. Fig. 2 indicates that the addition of such surfactants to water resulted in a little shift of boiling curves in the boiling regime toward lower ΔT. Further dis-

Nomenclature

q = heat flux, kW/m²

ΔT = difference between surface and bulk temperatures, K

x_e = mass fraction of emulsifier

x_o = mass fraction of oil

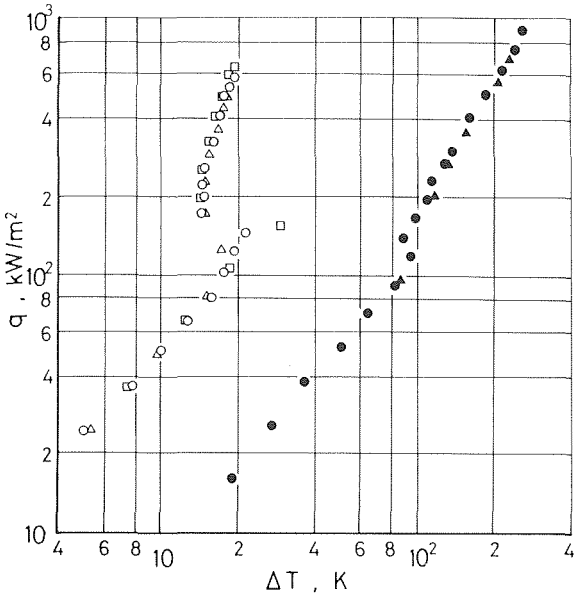

Symbol		Oil (x_o, %)	Emulsifier (x_e, %)	Type	Run No.
○	First ascent of q	KF 96 (10)	Tween 80 (1.0)	O/W	34
△	Succeeding descent of q				
□	Second ascent of q				
●	First ascent of q	KF 54 (85)	Span 80 (1.0)	W/O	28
▲	Succeeding descent of q				

Fig. 3 Stability of boiling curves

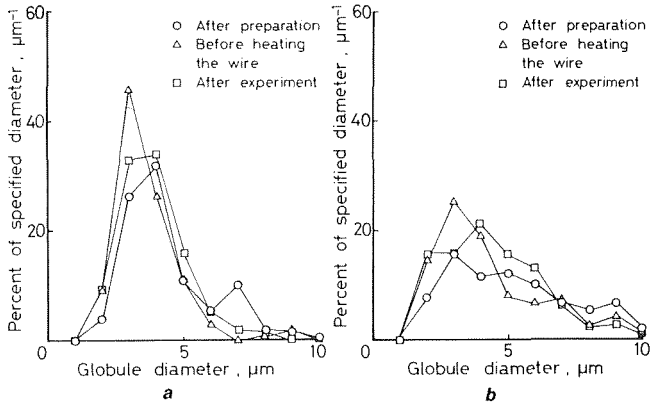

Fig. 4 Globule-size distributions
(*a*) KF 96/water emulsion with Tween 80 (x_o = 10 percent, x_e = 1.0 percent)
(*b*) Water/KF 54 emulsion with Span 80 (x_o = 85 percent, x_e = 1.0 percent)

cussions on this result are not given here, since we are not interested, in this paper, in the effect of surfactants on boiling heat transfer.

Stability of Emulsions. In general, the stability of emulsions decreases with an increase of temperature [5, 6]. It is very likely that the boiling is further unfavorable for the stability of emulsions. It should be noted, particularly for *W/O* emulsions, that steady pool boiling cannot be available in principle, because water globules disappear with time in the course of boiling. Therefore, data were obtained at first with heat flux q progressively increasing from the free-convection regime to a higher value in the boiling regime, and then with q decreasing to free-convection regime in most runs to verify the stability of heat-transfer characteristics. In some runs the heat flux was again raised successively to the boiling regime. In a few runs, however, data were obtained only during the first ascent of q because of the burn-out of the wire (only in case of *O/W* emulsions) or of the blowing-up of emulsion due to a sudden foaming in the bulk. Fig. 3 exemplifies the data obtained in such duplicated or triplicated measurements for *O/W* and *W/O* emulsions. Globule-size distributions measured before and after each run of the two presented in Fig. 3 are illustrated in Fig. 4. It is apparent that the heat transfer characteristics remained constant during each run for both types of emulsions as suggested by the globule-size distributions which did not change remarkably during each run. This fact indicates that the boiling heat transfer characteristics obtained in this study can be considered practically to be those of "steady pool boiling."

Based on the aforementioned result, only the boiling curves obtained during the first ascent of q are presented in Figs. 5 to 7.

Boiling Inception. The inception of boiling could be detected by bubbles which appeared on the free surface, as the heat flux q increased from the free-convection regime. After the inception of boiling of an *O/W* emulsion, ΔT decreased rapidly with an increase of q as shown in Fig. 3, yielding a marked neck of boiling curve. Such a large overshooting of ΔT at the boiling inception seems to be ascribed to the partial wetting of the surface of the heating wire with the oil during the increase of q in the free-convection regime. A film of oil spreading over the wire surface, if it were present, would prevent the bubble formation resulting in the overshooting of ΔT, but would be taken off from the major part of the wire surface once boiling proceeds, whereupon ΔT would decrease rapidly. The overshooting of ΔT occurred also when boiling ceased in the course of decrease of q as shown in Fig. 3, though it was not so remarkable as that at the boiling inception. This fact may be explained by the inversed mechanism; i.e., the rewetting of the limited area of the wire surface with the oil due to a decrease of bubble-formation frequency.

Dependence of Boiling Curve on Fraction of Oil in *O/W* Emulsions. Fig. 5 shows the variation of boiling curve with mass fraction of oil, x_o, in KF 96/water emulsions. It is remarkable as shown in Fig. 5(a) that the boiling curves for emulsions stabilized with sodium oleate lie at lower ΔT than those for water containing sodium oleate and for pure water in a certain range of x_o. Boiling curves shift rightward with an increase of x_o at least in the range $x_o \geq 10$ percent. Quite similar results were obtained for dodecane/water and undecane/water emulsions stabilized also with sodium oleate. When Tween 80 is used as emulsifier instead of sodium oleate, however, boiling curves for KF 96/water emulsions lie always at higher ΔT than that for water containing the emulsifier as shown in Fig. 5(b). It is the same with KF 54/water emulsions stabilized with Tween 80.

It seems curious that some *O/W* emulsions stabilized with sodium oleate give better heat transfer characteristics than water. At present we cannot offer any satisfactory interpretation on this matter.

Effects of Kinds of Oils and Emulsifiers in *O/W* Emulsions. Boiling curves for *O/W* emulsions with 10 percent fraction of oil are given in Fig. 6. It is apparent that the boiling curve is little affected by the kind of oil except KF 54 but affected remarkably by the kind of emulsifier. The deviation in the boiling curve for KF 54/water emulsion stabilized with sodium oleate from the boiling curves for other emulsions with the same emulsifier is due to nothing but a large overshooting of ΔT at the boiling inception. It should be kept in mind that the size of globules sampled from the bulk of emulsion depends on the kind of oil, not the kind of emulsifier, as shown in Table 2. Thus the difference in boiling curves due to the kind of emulsifier should be ascribed to another factor (or factors); e.g., the difference in the manner of interaction between oil globules and the surface of nickel wire. In general, the ability of nonionic surfactant as emulsifier decreases with an increase of temperature, which leads to a decrease of its solubility in water. This characteristic suggests that the oil globules coalesce easily to each other near the wire and may partly cover the wire surface, resulting in an increase of ΔT when Tween 80 is used.

***W/O* Emulsions.** Fig. 7 presents the boiling curves for *W/O* emulsions stabilized with Span 80. The surface temperatures required for boiling inception are quite high and the dependence of q on ΔT is quite weak compared with those for *O/W* emulsions. The difference

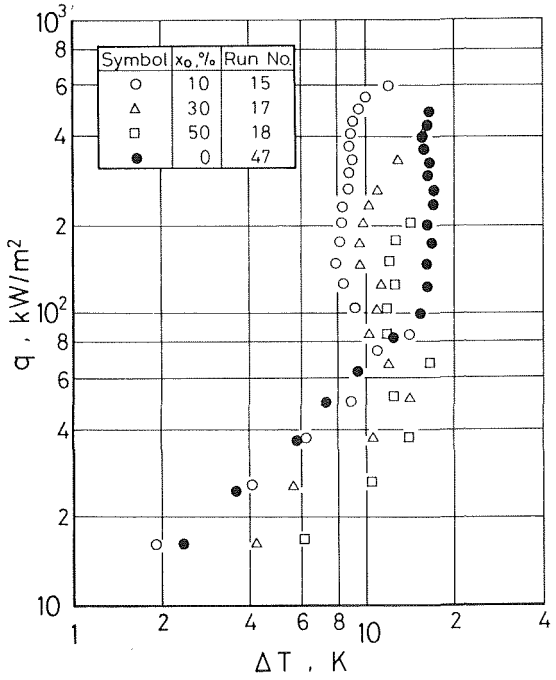

Fig. 5(a) KF 96/water emulsions with sodium oleate (x_e = 0.5 percent)

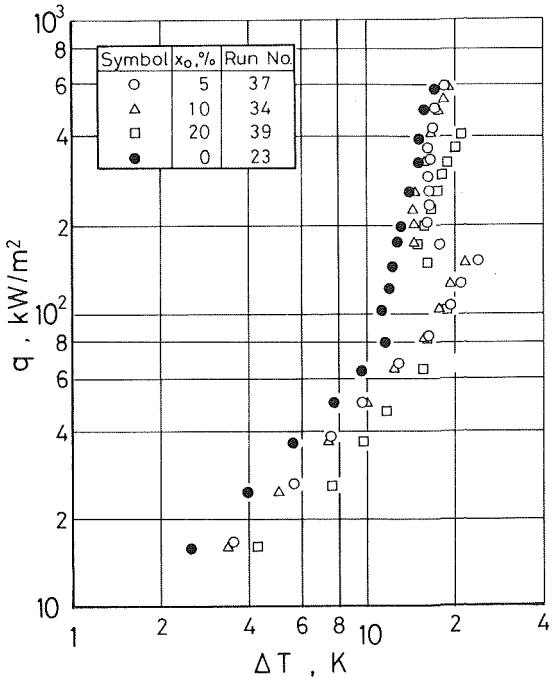

Fig. 5(b) KF 96/water emulsions with Tween 80 (x_e = 1.0 percent)

Fig. 5 Variation of boiling curves with mass fraction of oil in O/W emulsions

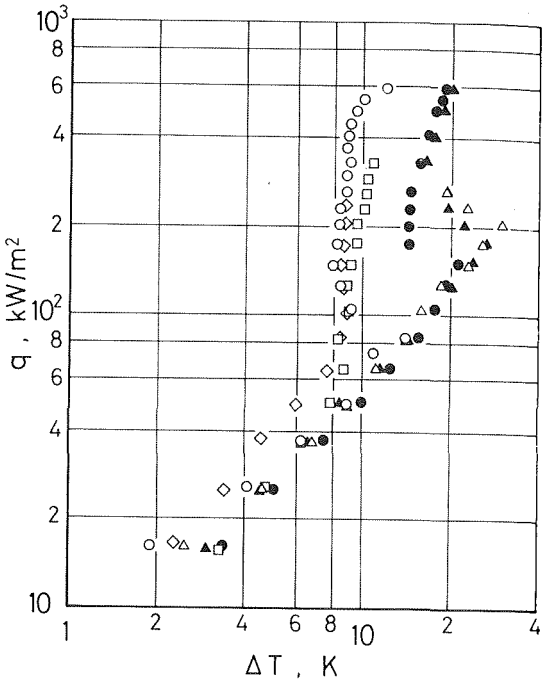

Symbol	Oil	Emulsifier (x_e , %)	Run No.
○	KF 96	Sodium Oleate (0.5)	15
△	KF 54	Sodium Oleate (0.5)	26
□	Dodecane	Sodium Oleate (0.5)	50
◇	Undecane	Sodium Oleate (0.5)	56
●	KF 96	Tween 80 (1.0)	34
▲	KF 54	Tween 80 (1.0)	30

Fig. 6 Effects of kinds of oils and emulsifiers in *O/W* emulsions (x_o = 10 percent)

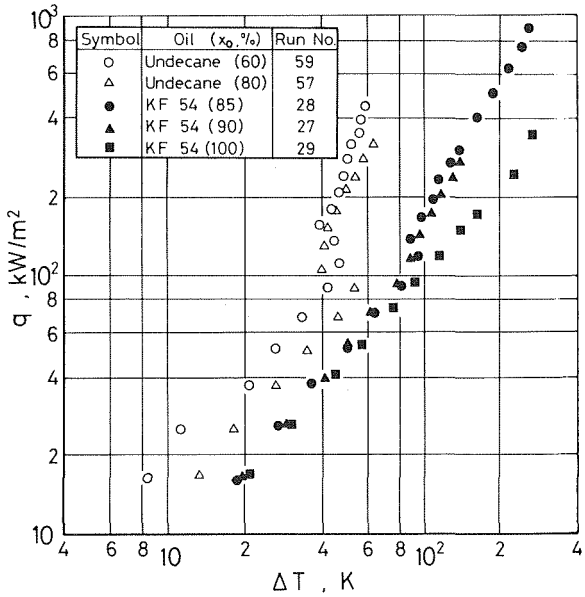

Fig. 7 Boiling curves for *W/O* emulsions

in boiling curves due to the kind of oil is remarkable in contrast with that in *O/W* emulsions. It should be noted that the basic mechanism of nucleation and bubble growth in *W/O* emulsions on the wire surface are utterly unknown for the present, while those in *O/W* emulsions are presumed not to differ essentially from those in single-component liquids.

Jump of Wall Temperature. In the course of increase of heat flux q to *O/W* emulsions, the surface temperature sometimes jumped over 200 to 300 K suddenly as shown in Fig. 8. The decrease of q succeeding the above jump yielded a boiling curve different from that exhibited during the preceding increase of q producing a loop on the $q - \Delta T$ plane. It should be noticed that the surface temperature after the jump exceeded the superheat limit of water [7] though the wire did not burn out. As a matter of fact, the surface temperature (or ΔT)

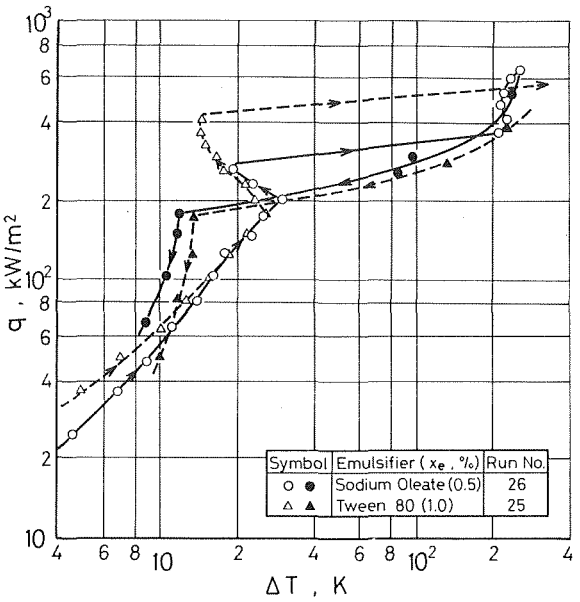

Fig. 8 Jump of surface temperature in KF 54/water emulsions (x_o = 10 percent)

after the jump is close to that for W/O emulsions with the same heat flux (see Fig. 7). This fact indicates that the phase inversion from O/W type to W/O type [8] or the oil separation [6] occurred near the heated wire surface, and thus oil spread over the wire surface resulting in a sudden increase of the surface temperature by suppressing the boiling.

Conclusions

The characteristics of steady pool boiling heat transfer to emulsions have been obtained as follows:

(1) Remarkable overshooting of surface temperature often occurs at the inception and cessation of boiling of O/W emulsions.

(2) Boiling curves shift generally toward higher surface temperature as the fraction of oil increases.

(3) Some kinds of O/W emulsions with relatively small fractions of oil stabilized with a certain kind of emulsifier exhibit higher heat transfer rates than those for pure water and for water containing the same emulsifier.

(4) The kind of oil affects little the heat transfer to O/W emulsions, but affects considerably the heat transfer to W/O emulsions.

(5) The kind of emulsifier affects strongly the heat transfer to O/W emulsions.

(6) In the course of rise of heat flux to O/W emulsions, the surface temperature sometimes exhibits a jump of as much as 200 to 300 K without inducing a burn-out.

Acknowledgment

The authors are much indebted to Messrs. E. Une and K. Matsumoto for their help in the experiments. This work was subsidized by the Grant in Aid for Scientific Research of the Ministry of Education of Japan under Grant No. 175122.

References

1 Tachibana, F., and Enya, S., "Study of Heat Transfer during Quenching," (in Japanese), *Transactions of the Japan Society of Mechanical Engineers,* Vol. 38, No. 309, 1972, pp. 1056–1064.

2 Satoh, K., and Shoji, K., "An Experiment of Boiling Heat Transfer to Oil-Water Mixtures," (in Japanese), *Preprint of the Japan Society of Mechanical Engineers,* No. 731-2, 1973, pp. 133–136.

3 Sherman, P., ed., *Emulsion Science,* Academic Press, London and New York, 1968, pp. 207–208.

4 Inui, E., "Pool Boiling Heat Transfer to Emulsions," (in Japanese), M. Sc thesis, Keio University, Yokohama, March 1977.

5 Jain, K. D., and Sharma, M. K., "Physico-Chemical Studies of Emulsions: Part IV. Effect of Temperature on the Properties of Emulsions," *Journal of the Indian Chemical Society,* Vol. 48, No. 11, 1971, pp. 1027–1031.

6 Vold, R. D., and Mittal, K. L., "The Effect of Temperature on the Stability of Nujol-Water Emulsions," *Journal of Colloid and Interface Science,* Vol. 42, No. 2, 1973, pp. 436–440.

7 Eberhart, J. G., "The Thermodynamic and the Kinetic Limits of Superheat of a Liquid," *Journal of Colloid and Interface Science,* Vol. 56, No. 2, 1976, pp. 262–269.

8 Arai, H., and Shinoda, K., "The Effect of Mixing of Oils and of Nonionic Surfactants on the Phase Inversion Temperature of Emulsions," *Journal of Colloid and Interface Science,* Vol. 25, 1967, pp. 396–400.

M. Shoukri
Research Engineer
Ontario Hydro Research Division,
Toronto, Ontario, Canada

R. L. Judd
Associate Professor
McMaster University
Hamilton, Ontario, Canada

On the Influence of Surface Conditions in Nucleate Boiling—the Concept of Bubble Flux Density

A study of the influence of surface conditions in nucleate pool boiling is presented. The surface conditions are represented by the number and distribution of the active nucleation sites as well as the size and size distribution of the cavities that constitute the nucleation sites. The heat transfer rate during nucleate boiling is shown to be influenced by the surface condition through its effect on the number and distribution of the active nucleation sites as well as the frequency of bubble departure from each of these different size cavities. The concept of bubble flux density, which is a function of both the active site density and the frequency of bubble departure, is introduced. A method of evaluating the bubble flux density is proposed and a uniform correlation between the boiling heat flux and the bubble flux density is found to exist for a particular solid-liquid combination irrespective of the surface finish within the region of isolated bubbles.

1 Introduction

The ultimate objective of any fundamental approach to the problem of nucleate boiling is to be able to predict the rate of heat transfer for given boiling conditions through the knowledge and understanding of the processes involved. It has been observed that the relationship between the boiling heat flux and the surface superheat is considerably influenced by the surface conditions, i,e., microscopic roughness and surface preparation technique in [1, 2, 3, 4] and [5].

Several attempts were made to correlate the nucleate boiling data in a generalized form including the surface effects. The correlation presented in [6] is a special form of the general equation,

$$q/A = C_1(T_w - T_{\text{sat}})^m \tag{1}$$

where the constants C_1 and m are functions of the solid-liquid combination as well as the surface roughness.

Realizing the significance of the active nucleation site density as an important parameter influenced by the surface condition affecting the rate of boiling heat flux, many investigators correlated the boiling data by the general form or special forms of the relationship,

$$q/A = C_2(T_w - T_{\text{sat}})^a(N/A)^b \tag{2}$$

where the constants C_2 a and b are determined experimentally as in [5, 7 and 8]. This method of correlating the boiling data showed a very limited success.

Later Mikic and Rohsenow [9] proposed a boiling model that incorporated surface effects. In this model, the transient conduction mechanism was assumed to prevail over other mechanisms associated with the nucleate boiling phenomenon. The surface effects were introduced by describing the active nucleation site density as a function of the nucleation cavity radii in accordance with Brown [10] while the frequency of bubble departure was assumed independent of the cavity size. These assumptions lead to the correlation

$$N_R = \frac{(q/A)\sqrt{\dfrac{\sigma g_c}{g(\rho_\ell - \rho_v)}}}{h_{fg}\mu_\ell} = B(\psi\Delta T)^{m+1} \tag{3}$$

where B and ψ depend on the boiling surface condition and the fluid properties. Mikic and Rohsenow showed qualitative agreement with their model by being able to use this correlation to draw the boiling data of a number of researchers for different fluids boiling at various levels of pressure into a single curve of N_R versus $\psi\ \Delta T$. Although further qualitative agreement was observed by Judd and Shoukri [11] who were able to draw their data for five different organic fluids boiling on a glass surface into a single curve in a similar fashion, the assumption of the independence of the bubble frequency from the active cavity size is questionable. It is a well established observation that the frequency of bubble departure varies significantly on the boiling surface from one site to another as shown in [5, 12, 13] and [14].

In the present work, a study of the influence of surface conditions in nucleate boiling is presented. Surface conditions are represented by the number and distribution of the active nucleation sites as well as the size and size distribution of the cavities that constitute the active nucleation sites. The boiling heat flux at specified surface superheat and liquid subcooling is shown to be influenced by the surface conditions through its effect on the number and size of the active nucleation cavities which significantly influence the frequency of bubble departure from each of these nucleation sites.

Contributed by the Heat Transfer Division for publication in the JOURNAL OF HEAT TRANSFER. Manuscript received by the Heat Transfer Division March 24, 1978.

2 Bubble Flux Density

It is shown in the literature that an increase in boiling heat flux is always accompanied by an increase in both the number of bubble sources, i.e., active nucleation sites and the ability of these sources to produce more bubbles, i.e., the frequency of bubble emission. These two parameters are combined in what will be called the bubble flux density. The bubble flux density is defined as the rate of bubble emission per unit area of the boiling surface which can be evaluated by summing up the product of the active site density by the frequency of bubble departure all over the boiling surface. The bubble flux density is expected to encompass the surface effects since it is a function of the two parameters most influenced by the surface conditions, namely the active site density and the bubble departure frequency. In order to evaluate the bubble flux density for specified boiling conditions, reliable models must be used to predict the active site density and the frequency of bubble departure.

2.1 Frequency of Bubble Departure. A new theoretical model has been developed by Shoukri and Judd [13] to predict the frequency of bubble departure in nucleate pool boiling as a function of the nucleation cavity radius as well as the surface superheat, liquid subcooling and fluid properties, in which the surface temperature variations throughout the bubble cycle have been incorporated. Determination of the frequency of bubble departure was divided into two parts: determination of the waiting period t_w, which is the time from last bubble departure to the beginning of the next bubble growth, and determination of the growth period t_g, which is the time from the beginning of bubble growth until it departs from the boiling surface.

By incorporating the variations in the surface temperature throughout the bubble cycle, an expression describing the relationship between the waiting period and the nucleation cavity radius was developed in the form,

$$r_c = (\sqrt{\pi\alpha_\ell}/2K)\left(\frac{\sin\beta}{1+\cos\beta}\right) \times\left[\gamma_w \pm \sqrt{{\gamma_w}^2 - 4\left(\frac{A/(\theta_w-\theta_{sat})}{\sqrt{\pi\alpha_\ell}}\right)(1+\cos\beta)K}\right] \quad (4)$$

where

$$K = \left[\sqrt{\frac{1}{t_w+t_g}} + \frac{\theta_{sat}}{\theta_w-\theta_{sat}}\sqrt{\frac{1}{t_w}}\right]$$

$$\gamma_w = 1 - \frac{2}{\pi}\sum_{m=0}^{\infty}\frac{C_m}{m!(2m+1)2^{2m}}\left(\sqrt{\frac{t_g}{t_w+t_g}}\right)^{2m+1}$$

$$C_m = 2(m-1)C_{m-1} \text{ and } C_0 = 1$$

The waiting period is defined implicitly by equation (4) as a function of the nucleation cavity radius, surface superheat, liquid subcooling and the growth period. In the range of active cavity radii usually observed experimentally, this model predicts that the larger the cavity size, the greater the waiting period. Also, according to equation (4), an increase in the surface superheat, or a decrease in the liquid subcooling or the growth period will result in a shorter waiting period.

Three different models have been examined in [13] to evaluate the growth period. The model derived through the use of the bubble growth equation based upon the plane interface approximation together with the correlation for bubble departure size proposed by Staniszewski [15] was generally recommended. From this model, the growth period can be determined by,

$$\sqrt{t_g} = \frac{1}{2}\left[\left(\frac{X}{Y}\right) \pm \sqrt{\left(\frac{X}{Y}\right)^2 + 35.4\,X}\right] \quad (5)$$

where

$$Y = \frac{2}{\sqrt{\pi}}Ja\sqrt{\alpha_\ell} \text{ and } X = 0.4215\,\beta\sqrt{\frac{2\sigma g_c}{g(\rho_\ell-\rho_v)}}$$

According to equation (5), the growth period is a strong function of the surface superheat but independent of the nucleation cavity radius.

The frequency of bubble departure was then determined by,

$$f = \frac{1}{t_w+t_g} \quad (6)$$

The bubble frequency predicted by this model is obviously influenced by the surface condition through its dependence on the nucleation cavity radius. The effect of the cavity radius, surface superheat and liquid subcooling on the bubble frequency of water is demonstrated by Fig. 1, where the contact angle was taken equal to 22 deg in accordance with the measurements of Shoukri [14]. It is seen that smaller nucleation cavities are able to emit vapour bubbles at higher frequency than the larger cavities in agreement with the data of Hatton and Hall [5] and that bubble frequency decreases with decreasing surface superheat and increasing liquid subcooling. Shoukri and Judd [13] showed excellent agreement between their frequency model and experimental data for both water and iso-propyl alcohol boiling on a single copper surface having different surface finishes.

2.2 Active Nucleation Site Density. The active site density is assumed to be determined by the cumulative site density distribution suggested by Brown [10] in the form,

$$(N/A)_{r_c} = C(1/r_c)^m \quad (7)$$

where $(N/A)_{r_c}$ is the active site density of those cavities having radius equal to or greater than r_c and C and m are constants characterizing the boiling surface. According to Shoukri and Judd [4], the total active site density (N/A) at a specified condition for boiling water is determined by,

$$N/A = C(1/r_{c\,min})^m \quad (8)$$

where $r_{c\,min}$ is the minimum cavity radius under the specified condition.

Lorenz, Mikic and Rohsenow [16] determined the relationship between the minimum cavity radius $r_{c\,min}$ and the effective radius of nucleation ρ to be,

Nomenclature

A = parameter $A = 2\sigma T_{sat}/\rho_v h_{fg}$
C = constant in equation (7)
C_ℓ = specific heat of the liquid
f = bubble frequency
g = gravitational acceleration
g_c = conversion factor
h_{fg} = latent heat of vapourization
Ja = Jakob number $\mathrm{Ja} = \rho_\ell C_\ell \Delta T/\rho_v h_{fg}$
m = exponent in equation (7)
N_R = dimensionless heat flux defined by equation (3)
N/A = total nucleation site density
$(N/A)_{r_c}$ = nucleation site density for cavities having radius equal to or greater than r_c
q/A = heat flux
r_c = nucleation cavity radius
T = temperature
T_∞ = bulk liquid temperature
t_g = growth period
t_w = waiting period
α = thermal diffusivity
β = contact angle
ρ = effective radius of nucleation
ρ_ℓ = liquid density
ρ_v = vapour density
σ = surface tension
ϕ = nucleation cavity conical angle
θ = temperature difference $\theta = T - T_\infty$

Subscripts

ℓ = liquid
v = vapour
w = surface
sat = saturation
∞ = bulk

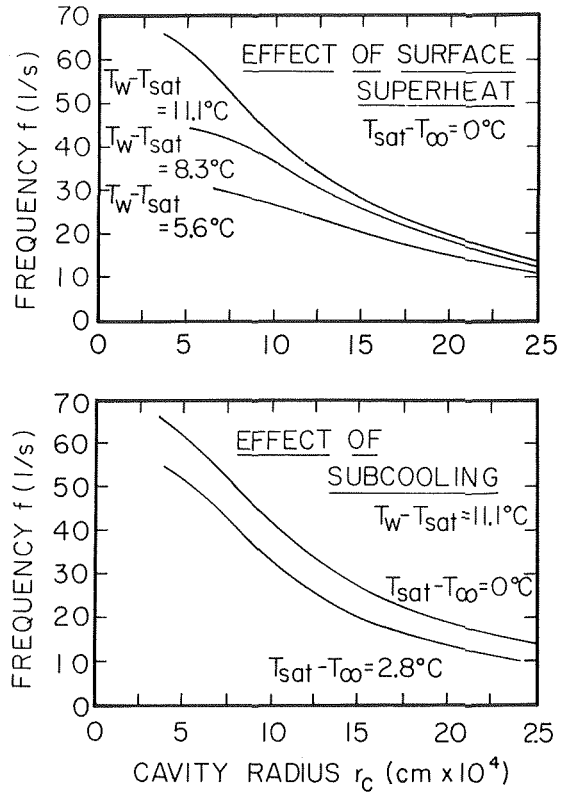

Fig. 1 The frequency model

$$\rho/r_{c\,min} = \eta(\beta, \phi) \tag{9}$$

where the function $\eta(\beta, \phi)$ is a function of the fluid contact angle β and the cavity conical angle ϕ. The function $\eta(\beta, \phi)$ is less than one for organic fluids and equals unity for boiling water. The effective radius of nucleation ρ is determined according to,

$$\rho = \frac{2\sigma T_{sat}}{\rho_v h_{fg}(T_w - T_{sat})} \tag{10}$$

Therefore, equation (8) may be written as,

$$N/A = C\left[\frac{\eta(\beta, \phi)\rho_v h_{fg}(T_w - T_{sat})}{2\sigma T_{sat}}\right]^m \tag{11}$$

which for the case of boiling water reduces to

$$N/A = C(1/\rho)^m = C\left[\frac{\rho_v h_{fg}(T_w - T_{sat})}{2\sigma T_{sat}}\right]^m \tag{12}$$

2.3 Evaluation of the Bubble Flux Density. As described earlier, under specified conditions of surface superheat and liquid subcooling, the frequency of bubble departure is a function of the nucleation cavity radius,

$$f = f(r_c) \tag{13}$$

Consequently, the bubble flux density Φ for nucleation cavities having radii in the range from r_c to $r_c + \Delta r_c$ can be determined with the help of equations (7) and (11),

$$\Delta\Phi = f(r_c)\Delta(N/A)_{r_c} \tag{14}$$

where $f(r_c)$ is the frequency of bubble departure evaluated for a cavity radius equal to r_c and $\Delta(N/A)_{r_c}$ is the active site density of the cavities having radii in the range from r_c to $r_c + \Delta r_c$. Since equation (7) predicts the number of active sites having radii equal to or larger than r_c, one may conclude that,

$$\Delta(N/A)_{r_c} = C[(1/r_c)^m - (1/r_c + \Delta r_c)^m] \tag{15}$$

which can be written in the form,

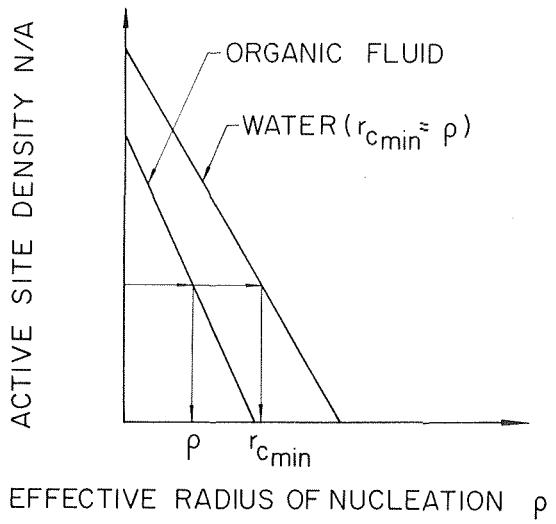

Fig. 2 Determination of the ratio ($\rho/r_{c\,min}$) for organic fluids

$$\Delta(N/A)_{r_c} = C(1/r_c)^m[1 - (1 + \Delta r_c/r_c)^{-m}] \tag{16}$$

Equation (16) may be approximated to yield,

$$\Delta(N/A)_{r_c} \simeq mC(1/r_c)^{m+1}\Delta r_c \tag{17}$$

Substituting equation (17) into (14) yields

$$\Delta\Phi = mCf(r_c)(1/r_c)^{m+1}\Delta r_c \tag{18}$$

By integrating equation (18) between the minimum and maximum radius of the nucleation cavities, the bubble flux density for specified boiling conditions is obtained,

$$\Phi = mC\int_{r_{c\,min}}^{r_{c\,max}} \frac{f(r_c)}{r_c^{m+1}}\,dr_c \tag{19}$$

where $r_{c\,min}$ is the radius of the smallest active site that could be activated for the boiling condition which is evaluated by equation (9) to yield,

$$r_{c\,min} = \frac{1}{\eta(\beta, \phi)}\frac{2\sigma T_{sat}}{\rho_v h_{fg}(T_w - T_{sat})} \tag{20}$$

and $r_{c\,max}$ is the radius of the largest cavity on the boiling surface which can be evaluated by using either of the Hsu [17] or Han and Griffith [8] nucleation models. The use of either of these models requires a knowledge of the superheated thermal layer thickness. An alternative method is to assume $r_{c\,max}$ to equal 2.5×10^{-2} mm since it is the largest natural nucleation cavity reported to exist in the literature. The bubble flux density was observed to be insensitive to the method of evaluating $r_{c\,max}$ since for large values of cavity radius both the frequency and the site density values are small and the product of frequency and site density is negligibly small.

The frequency model presented was used to predict $f(r_c)$ and numerical integration was performed to obtain the bubble flux density for specified boiling conditions according to equation (19). The constants m and C were determined experimentally by fitting experimental data of (N/A) versus ρ according to equation (11) for the particular boiling surface. For boiling water where the minimum cavity radius equaled the effective radius of nucleation, i.e., $r_{c\,min} = \rho$, the constants m and C were determined by fitting the experimental data of N/A versus ρ as determined by equation (12) since the function $\eta(\beta, \phi)$ equals unity. For the case of boiling organic fluids, it was necessary to determine the function $\eta(\beta, \phi)$. The method used for evaluating this function involved boiling both water and the organic fluid on a single surface. Then by plotting the curves of N/A versus ρ for both fluids, the ratio $(\rho/r_{c\,min})$ could be obtained for different values of N/A as shown schematically in Fig. 2.

3 Boiling Heat Flux Model

The bubble flux density as determined by equation (19) is believed to encompass all the surface effects since it is a function of the two parameters most influenced by the surface effects, i.e., the active site density and the bubble frequency. Therefore the boiling heat flux should be expected to correlate with the bubble flux density in a unified correlation independent of the surface finish.

Shoukri [19] presented a set of nucleate pool boiling data for boiling water on a copper surface having three different surface finishes. Fig. 3 shows a plot of the active site density (N/A) as a function of the effective radius of nucleation ρ. The data are fitted by the least square method to determine the constants m and C for each surface. The corresponding boiling characteristic curves for the same three surfaces are shown in Fig. 4. For each value of surface superheat, the bubble flux density is calculated using the method outlined earlier. A plot of the boiling heat flux and the corresponding bubble flux density for the three surfaces is shown in Fig. 5. A unified correlation between the bubble flux density and the boiling heat flux is seen to exist for the three surfaces. This agreement may be justified by arguing that the bubble flux density as derived by the method presented earlier encompasses all the surface effects and that a single correlation between the bubble flux density and the boiling heat flux will exist for any single liquid-solid combination.

Singh [20] also presented a set of experimental data for boiling water on a copper surface having four different surface finishes as shown in Fig. 6. The corresponding cumulative distributions for the active nucleation sites are shown in Fig. 7. By evaluating the bubble flux density at each surface superheat and plotting it versus the boiling heat flux results, the same unifying trend is apparent up to a heat flux limit of about 160 kW/m^2 as shown in Fig. 8.

The consistent agreement obtained by treating the data in the manner described above suggests that the bubble flux density as evaluated by equation (19) encompasses all the surface effects and that a unified correlation between the boiling heat flux and the bubble flux density should exist for each solid-liquid combination and solid surface geometry irrespective of the surface finish. Such a correlation is believed to be applicable in nucleate pool boiling only within the regime of isolated bubbles. This behavior can be explained physically if it is argued that in the regime of isolated bubbles under specified conditions of surface superheat and liquid subcooling, each vapour bubble is responsible for the removal of a certain amount of energy

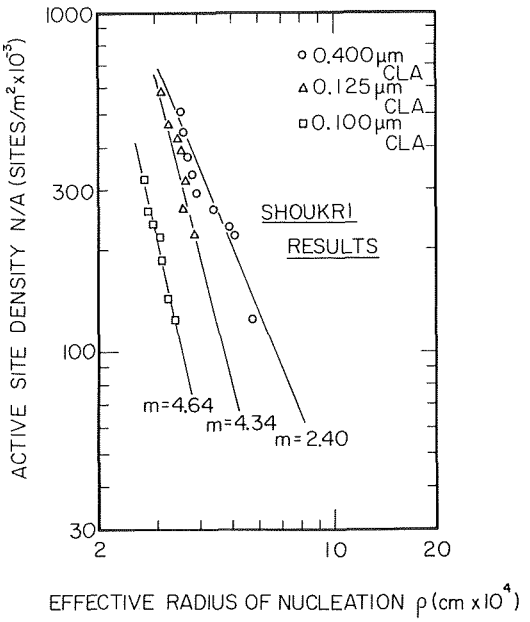

Fig. 3 Active site density versus effective radius of nucleation according to Shoukri

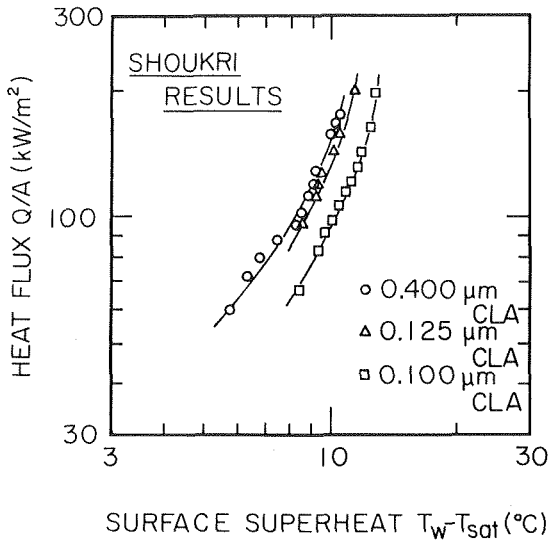

Fig. 4 Boiling characteristic curves according to Shoukri

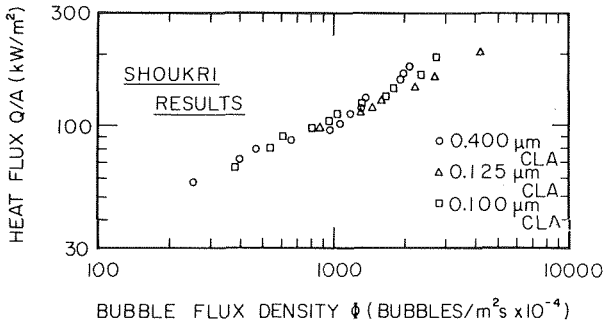

Fig. 5 Boiling heat flux versus bubble flux density for Shoukri's data

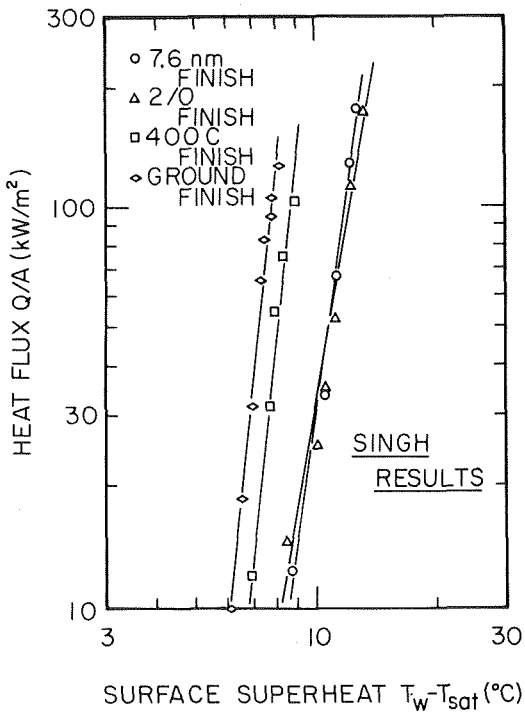

Fig. 6 Boiling curves for water according to Singh

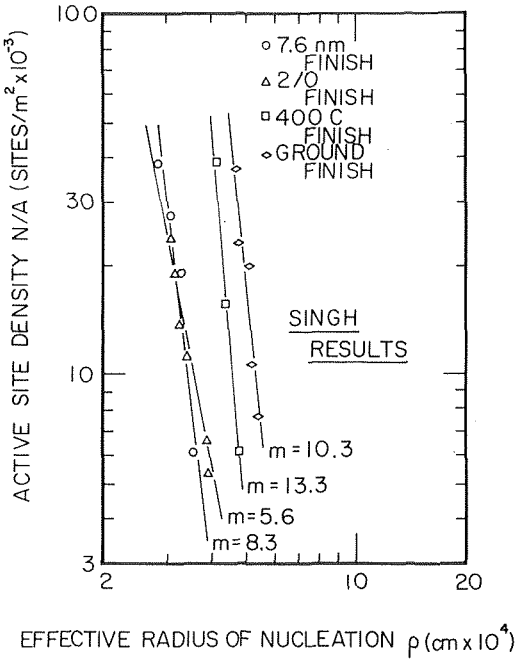

Fig. 7 Active site density versus effective radius of nucleation according to Singh

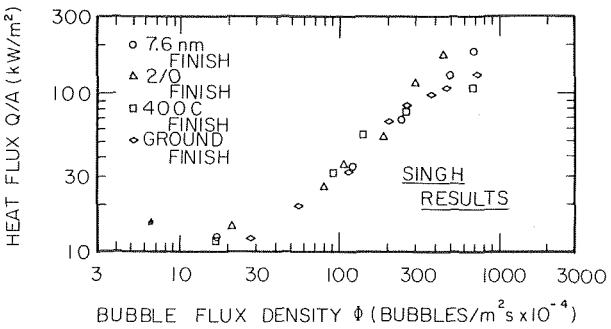

Fig. 8 Boiling heat flux versus bubble flux density for Singh's data

from the surface to the liquid bulk. Therefore, the total rate of heat removal from the surface is a direct function of the rate of bubble emission from the boiling surface, i.e., the bubble flux density. However, the mechanisms by which the energy associated with each bubble is transferred cannot be deduced from such analysis.

Although the concept presented above is believed to be valid for any solid/liquid flow combination, the data presented only confirm its validity for boiling water. Assuming that there is general validity, it should be possible to utilize this concept to develop different empirical correlations for boiling heat flux versus bubble flux density for different solid-liquid combinations to be used for design purposes. However, the need to determine the surface characteristics as described by the empirical constants m and C makes its usefulness limited at the present time unless some method becomes available to determine these constants without conducting an experiment.

4 Discussion of the Mechanisms of Nucleate Boiling

The complexity of the nucleate boiling phenomenon makes it impossible to explain it by a single mechanism. Instead, it is more realistic to consider several energy transfer mechanisms operating simultaneously. The relative importance of the contribution of each of these mechanisms to the overall heat transfer process will vary with the heat flux range, liquid subcooling and system pressure.

So far as the regime of isolated bubbles is concerned, it is reasonable to assume that there are three main mechanisms by which heat is transferred from the solid surface to the liquid:

1 Transient conduction to and subsequent replacement of the superheated liquid layer adjacent to the surface, i.e., the energy associated with the vapour-liquid mass interchange.

2 Microlayer evaporation at the growing bubble base.

3 Natural and forced convection at the areas of the heating surface outside the area of influence of each bubble.

The first two mechanisms of energy transport represent the energy associated with each bubble departing from the boiling surface which explains why the boiling heat flux is expected to be a function of the rate of bubble emission i.e., a function of the bubble flux density. As the active site density increases, most of the heating surface will be covered by the areas of influence of the vapour bubbles and the third mechanism will assume very little significance.

As a consequence of assuming the first two mechanisms to prevail, it is believed that each vapour bubble is associated with the removal of certain quantity of heat from the part of the surface influenced by it. Part of the heat is removed by transient conduction to the liquid layer replacing the departing bubble and the other part is removed by microlayer evaporation. Obviously, the first mechanism operates during the waiting period t_w, the period during which the cold liquid that rushes to the surface to replace the detaching bubble is heated enough to support the next bubble growth, whereas the microlayer evaporation mechanism operates during the bubble growth period t_g, the period during which the bubbles grow to departure size. In general, it is expected that the relative significance of these two mechanisms would depend not only on the period of time during which each of them is active but also on how efficient they are under different conditions of surface superheat, liquid subcooling and system pressure. At the moment, it is difficult to quantify the contribution of each of the two mechanisms and more work is required along this line.

As the heat flux increases beyond the range in which the individual active sites are distinguishable, very strong turbulent motion is observed to take place all over the boiling surface and the phenomenon is believed to be even more complicated. Therefore, the analysis of energy transport based on the performance of a single active site is no longer valid.

5 Conclusions

Analysis of the effect of surface conditions in nucleate boiling is introduced and the concept of the bubble flux density is presented. A method of evaluating the bubble flux density as a function of the active site density and the frequency of bubble departure is proposed which is found to encompass all the surface effects. By experimental evidence, a unified correlation between the boiling heat flux and the bubble flux density seems to exist for any particular solid-liquid combination irrespective of the surface finish. It is believed that such a correlation should be valid only in the regime of isolated bubbles.

References

1 Corty, C., Foust, A. S., "Surface Variables in Nucleate Boiling," Chem. Eng. Progress Symp., Series, 51, 1955, p. 1.

2 Clark, H. B., Strenge, P. S., Westwater, J. W., "Active Sites for Nucleate Boiling," Chem. Eng. Progress Symp., Series, 55, 1959, p. 103.

3 Griffith, P., Wallis, J. D., "The Role of Surface Conditions in Nucleate Boiling," Chem. Eng. Progress Symp., Series, 56, 1960, p. 49.

4 Shoukri, M., Judd, R. L., "Nucleation Site Activation in Saturated Boiling," ASME JOURNAL OF HEAT TRANSFER, Feb. 1975, p. 93.

5 Hatton, A. P., Hall, I. S., "Photographic Study of Boiling on Prepared Surfaces," *Proceedings of the Third International Heat Transfer Conference*, Chicago, 1966.

6 Rohsenow, W. M., "A Method of Correlating Heat Transfer Data for Surface Boiling of Liquids," TRANS. ASME, 74, 1952, p. 969.

7 Nishikawa, K., "Nucleate Boiling Heat Transfer of Water on Horizontal Roughened Surface," Mem. Fac. Engng., Kyushu, 17, 85, 1957.

8 Kurihara, H. M., Meyers, J. E., "Effect of Superheat and Surface Roughness in Nucleate Boiling," *AIChE Journal*, 6, 1960, p. 83.

9 Mikic, B. B., Rohsenow, W. M., "A New Correlation of Pool Boiling Data Including the Effect of Heating Surface Characteristics," ASME JOURNAL OF HEAT TRANSFER, May 1969, p. 245.

10 Brown, W. T., "Study of Flow Surface Boiling," Ph.D. Thesis, Mech. Eng. Dept., M.I.T., 1967.

11 Judd, R. L., Shoukri, M., "Nucleate Boiling on an Oxide Coated Glass

Surface", ASME JOURNAL OF HEAT TRANSFER, Aug. 1975, p. 494.
12 Singh, A., Mikic, B. B., Rohsenow, W. M., "Effect of Superheat and Cavity Size on Frequency of Bubble Departure in Boiling," ASME JOURNAL OF HEAT TRANSFER, May 1977, p. 246.
13 Shoukri, M. and Judd, R. L., "A Theoretical Model for the Bubble Frequency in Nucleate Pool Boiling Including Surface Effects," *Proceedings of the Sixth International Heat Transfer Conference*, Toronto, Aug. 1978.
14 Shoukri, M., "The Influence of Surface Conditions in Nucleate Boiling," Ph.D Thesis, McMaster University, 1977.
15 Staniszewski, B. B., "Nucleate Boiling Growth and Development," Tech. Report No. 16, DSR7673, Heat Transfer Lab., M.I.T., 1959.
16 Lorenz, J. J., Mikic, B. B., Rohsenow, W. M., "The Effect of Surface Conditions on Boiling Characteristics," *Proceedings of the Fifth International Heat Transfer Conference*, Japan, 1974
17 Hsu, Y. Y., "On the Size Range of Active Nucleation Cavities on a Heating Surface," ASME JOURNAL OF HEAT TRANSFER, Aug. 1962, p. 207.
18 Han, C., Griffith, P., "The Mechanism of Heat Transfer in Nucleate Pool Boiling," *Int. Journal of Heat and Mass Transfer*, 8, 1965, p 887.
19 Shoukri, M., "Nucleation Site Activation in Saturated Boiling," M. Eng. Thesis, McMaster University, 1974.
20 Singh, A., "Effect of Surface Conditions on Nucleation and Boiling Characteristics," Ph.D. Thesis, Dept. of Mech. Eng., M.I.T., 1974.

N. Seki
Professor.

S. Fukusako
Associate Professor.

K. Torikoshi[1]
Graduate Student.

Department of Mechanical Engineering,
Hokkaido University,
Sapporo 060, Japan

Experimental Study on the Effect of Orientation of Heating Circular Plate on Film Boiling Heat Transfer for Fluorocarbon Refrigerant R-11

The characteristics of film boiling heat transfer from a heated horizontal circular brass plate to a pool of fluorocarbon R-11 are examined for the case in which only the top side of the plate is in contact with the liquid (facing upward) and for the case in which the bottom side of the plate is in contact with the liquid (facing downward). It is found that the film coefficient for the facing downwards orientation of the plate was found to be closely correlated by the following:

$$\mathrm{Nu} = 0.35\ (L/C_p\Delta T)\ \mathrm{Gr}^{0.25}\cdot \mathrm{Pr}^{0.25}$$

Introduction

Film boiling heat transfer has been of interest to workers in many fields of heat engineering. Many studies have been performed by investigators since the first study by Bromley [1], but film boiling heat transfer from a horizontal surface remains uninvestigated in detail. Regarding film boiling phenomena from the upper or underside of a horizontal flat, the following characteristics have been clarified by the previous experimental investigations. The vapor film found on the underside is generally stable, as compared with that on the upper, and the vapor flows out radially along the surface of the plate. Furthermore, on the underside, the escape of vapor dome does not take place and the liquid near the vapor-liquid interface is not accelerated due to vapor dome generation while on the upperside, vapor breaks through and escapes into the bulk liquid at certain locations on the vapor-liquid interface under the influence of gravity.

An approach to evaluate the film boiling heat transfer from the upper surface of a horizontal plate has usually been based on the Taylor's instability theory. Originally, Berenson [2] predicted the theoretical film boiling heat transfer on an infinite horizontal plate facing upward by adopting the Taylor's theory under the assumptions of an infinite vapor film thickness and a two-dimensional analysis using a derivation of interfacial wavelength. His prediction gives a fairly good agreement with the experimental results at the minimum heat flux. However, it seems that his analysis had some problems as to the direct transposition of the Taylor's model to film boiling, in addition, Lao, et al. [3] pointed out that beyond the minimum heat flux, Berenson's prediction adopting Taylor's model has a disparity with the previously reported experimental results and proposed their new model, in which a liquid layer possesses a net upward momentum rising from the mean level of this layer during bubble formation. They showed that their experimental results using an aluminum plate of 7.5 cm × 7.5 cm were correlated by the following:

$$\mathrm{St}' = 75.9\ \mathrm{Re}^{-0.915} \text{ for R-11.}$$

Ishigai, et al. [4] conducted pool boiling experiments on upper surface of two kinds of circular plate of 25 mm and 50 mm in diameter, with saturated water as liquid. They concluded that the burn-out point for facing downward was to occur at a much lower heat flux than that for facing upward. Recently, Farahat, et al. [5] made an analytical investigation for facing downward and compared their predictions based on the laminar boundary layer theory with the experimental results by Ishigai, et al. [4] with saturated water. Their data for the plate of 50 mm in diameter were four or five times smaller than those by Ishigai, et al. [4].

The purpose of this study is to examine experimentally the effect of orientation of the heating surface on film boiling heat transfer of R-11 from a finite horizontal circular plate. Also, it is true that the study for facing downward in film boiling region has solely been performed by Ishigai, et al. [4] using different diameter of heater and also saturated water. Therefore, in order to compare the present results with the experimental results by Ishigai, et al. [4], a similar diameter of heater to the one adopted by them is adopted in this study.

Experimental Apparatus

The schematic diagram of the apparatus is presented in Fig. 1. In this case the plate was of brass and 30 mm in diameter. The R-11 was

[1] Present address: Daikin Kogyo Co., Ltd., Sakai, Osaka.

Contributed by the Heat Transfer Division for publication in the JOURNAL OF HEAT TRANSFER. Manuscript received by the Heat Transfer Division January 30, 1978.

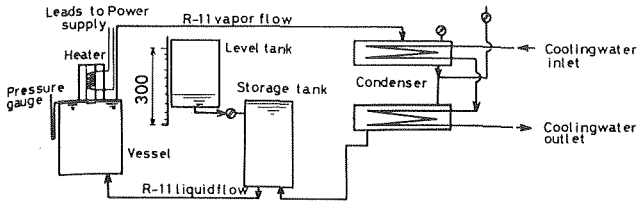

Fig. 1 Schematic diagram of experimental apparatus

contained in an open bakelite vessel, 200 mm × 200 mm in the end of which were fixed two observation windows of glass. The experiments were carried out on the upward facing of a horizontal circular plate which was immersed in R-11 liquid contained in a test vessel and supported vertically with a supporting device. The vapor generated is condensed by a two-stage condenser and returned to the test vessel by gravity. The liquid level is kept at a desired level during each run by an adjustable tank. Figs. 2(*a*) and 2(*b*) show the main test section of pool film boiling for facing downward and for facing upward respectively. The heating surface is placed at the center of the vessel. A detecting probe is traversed radially or vertically into the vessel to measure the temperature distribution of working liquid near the heating surface, and the position of the probe is monitored by a linear displacement micrometer. To hold temperature of the liquid at saturation, an auxiliary heater is used.

The heater assembly and its sectional dimension are presented in Fig. 3. This comprises a coil asbestine insulator surrounding a cylindrical brass block of 34 mm in diameter and 200 mm length, to which it is cemented with Sauereisen cement. And the main heater consists of nichrome resistance wire wounded around the whole brass cylinder. A stainless steel tube is covered on the main heater, and at its lower end, a stainless steel bushing is inserted between a stainless steel tube and the main heater. In addition, a guard heater of nichrome resistance wire is built up in the asbestine insulator surrounding the sleeve. The test specimen of 30 mm in diameter is made up at the end of the brass cylindrical block. For the downward facing experiment, in immersing the heater assembly into the test vessel, the heater assembly is supported on another upper bakelite plate. Furthermore, a teflon plate is inserted between the heater assembly and the above-memtioned bakelite plate to insulate the assembly from the heater.

For the upward facing experiment, as will be seen in Fig. 2(*b*), the heated surface is supported on a 100 mm square stainless steel space of 3 mm thickness and the stainless steel spacer whose thickness is reduced to 0.5 mm for insulation is mounted on the top end of the heater.

Flat-sided rectangular glass is employed to facilitate the visual observation. The still photographs for the illustration of the bubble behavior, vapor domes and vapor-liquid interface are taken at the exposure time of 0.002 s, by an Asahi Pentax camera.

Experimental Procedure

Prior to each run, the heating surface was prepared by polishing with emery paper, No. 3/0, then cleaned with acetone until the surface became fully shiny.

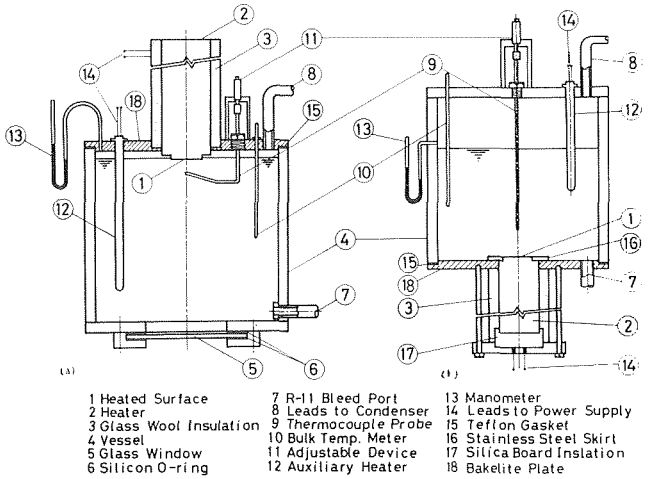

Fig. 2 Test section of boiling apparatus for facing (*a*) downward and (*b*) upward

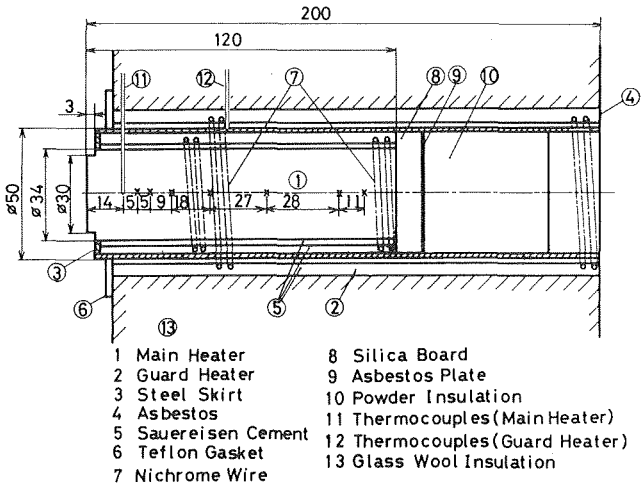

Fig. 3 Heater assembly

After this, the working liquid in the vessel was preliminary heated by an auxiliary heater immersed in the liquid (see Figs. 2(*a*) and 2(*b*)) until the liquid temperature was settled at its saturated temperature. The input power to the heater was controlled by a slidac. In order to prevent possible burnout when the temperature of the main heater passed through the maximum heat flux point, it was initially heated to a temperature sufficiently high to assure film boiling before it was immersed in the liquid. During operation, the temperature fluctuations near the heating surface were measured by traversing a thermocouple probe with a micrometer head device into the liquid.

Nomenclature

B = height of vapor path
C_p = specific heat
D = circular plate diameter
g = acceleration of gravity
Gr = Grashof number, $D^3\rho_v(\rho_l - \rho_v)\, g/\mu_v{}^2$
k = thermal conductivity
L = latent heat of vaporization
Nu = Nusselt number, $\alpha_{co}D/k$
Pr = Prandtl number, $C_p\mu/k$
q = heat flux
Re = Reynolds number, $\lambda q/4\mu L$
St′ = modified Stanton number, St $\lambda/4B$ = $(L/C_p\Delta T{\cdot}4B/\lambda)\lambda/4B = L/C_p\Delta T$
ΔT = temperature difference between surface and saturated liquid
α_{co} = convective heat transfer coefficient
λ = wavelength
μ = viscosity
ρ_l, ρ_v = saturated liquid and vapor densities, respectively

Subscripts

v or no subscript = vapor
l = liquid

The Estimation of Surface Temperature and Heat Flux

Eight chromel-alumel thermocouples (0.3 mm in dia.) are arranged axially in the body of the heater block and their positions are shown in Fig. 3. The surface temperature is estimated by extrapolating the temperature distribution indicated by five thermocouples located along the central axis of the heater.

Heat flux is evaluated by measuring the temperature gradient with thermocouples positioned in various parts of the heater, while the surface temperature is also evaluated by the extrapolation of the above-mentioned temperature gradient at the surface is also examined by subtracting the heat loss from the electric power delivered to the test section. The maximum limit of the difference between both evaluations is ascertained to be less than ±3 percent.

Although such a method of estimating the surface temperature was adopted by Hosler, et al. [6] and Ishigai, et al. [4], it might be considered that such a method to evaluate the surface temperature might not yield so large error in accuracy.

Results and Discussion

The Observation of Film Boiling Behavior on the Horizontal Surface. (1) Facing Downward. Visual observations recorded by camera are shown in Fig. 4. As shown in Fig. 4, all the photos are presented in the view oblique to the heated surface to enable observation of the whole behavior of vapor film. These photos show that the bubble behavior in the two cases-facing downward and facing upward is very different. Stages (a, b) and (c) in Fig. 4 correspond to the portions (a, b) and (c) marked in the boiling curve in Fig. 5. From these observations, the vapor-liquid interface appears to be stable over the heat flux range (a) to (c).

The motion of vapor-liquid interface has a regularity in general as predicted in the previous theoretical analyses of film boiling [2, 3] introducing a concept of wave motion based on the Taylor's instability. However, as long as the test plate is smaller than the order of critical wavelength [2], it is understood that the interfacial waviness with small amplitude, as shown in Fig. 4, may propagate over the moving interface in reality.

(2) Facing Upward. Visual observations (a′, b′) and (c′) in Fig. 4 correspond to the portions (a′, b′) and (c′) indicated on the boiling curve in Fig. 5. As the heat flux increases, the observed wave patterns of the vapor-liquid interface show the previous reported phenomena of unstable film boiling. However, Berenson [2], in predicting the wave pattern in this case, adopted an assumption that the bubble is ruptured into liquid spaced sites to make a periodical change of state. This does not appear to be supported by the observed motion in the vapor-liquid interface. It has been reported that the difference between Berenson's prediction and the actual phenomena depends mainly on the scale effect of the heater used. However, by setting an interference tube vertically on the surface, it was observed that the escape dome rose directly upward from the active heater area within the tube. It might therefore be considered that the difference between Berenson's prediction and the observed pattern is caused by the effect of induced convective flow rather than the scale effect of the heater.

The Boiling Heat Transfer Curve

Fig. 5 shows the boiling curve obtained from the present experiments. The heat flux g is here plotted against the difference between the surface and the saturation temperature ΔT through the nucleate boiling to the film boiling region. The freon would decompose to form the coke on the heating surface at ΔT = about 650°C. Therefore, it should be noted that at the start of the run the present data are obtained under the condition of mirror finish surface, while at the end of run when ΔT is close to 650°C the present data are obtained under the condition that the coke is formed on the surface. These results for saturated R-11 under the conditions of horizontal surface and atmospheric pressure are also compared in Fig. 5 with results or predictions previously reported by other investigators. For facing downward, only the data for saturated water by Ishigai, et al. [4] is ranged from the nucleate boiling to the film boiling region. The predicted results by Farahat, et al. [5] who investigated analytically the validity of the experimental results by Ishigai, et al. [4] are much lower than the experimental results by Ishigai, et al. [4]. The results by Hosler, et al. [6] for facing upward and by Anderson, et al. [7] for facing downward are also plotted in Fig. 5. The present data were the most extensive and exhibit the nucleate and film boiling region of the normal boiling curve. The differences in liquids and surface used by the several investigators must be expected to produce different results, but it is noteworthy that the data of Anderson, et al. [7] from only a slightly larger metal disk in the same liquid, show good agreement with the present results over Anderson's [7] limited range of nucleate boiling.

The Influence of Orientation of Heating Surface on Film Boiling Heat Transfer

The influence of orientation of heating surface on film boiling heat transfer is qualitatively discussed in the previous section. As can be seen from Fig. 4, it might be understood that the vapor motion between for facing downward and for facing upward is different each other. For facing downward, vapor flows out in a radial direction along the heated surface, while the vapor escapes for facing upward rise to straightly. Fig. 5 shows the saturated pool boiling heat transfer curve. As shown in this figure, it is clear that film boiling heat flux for facing upward is considerably higher than that for facing downward though the downward facing situation is considerably different from the upward facing one where the surface submerged far below liquid free surface. Generally, the difference between these two cases can be explained by differences between their interfacial wave motions. This is apparently substantiated by the visual observations recorded here. In the facing downward case, it is apparent from the visualizations that a stable wave exists at the vapor-liquid interface during film boiling, while in the facing upward case, a gigantic vapor dome is seen to be ruptured vigorously thus thinning the vapor layer. Therefore, the heat transfer for facing upward is expected to be higher than that for facing downward. This means that a difference of heat transfer coefficient between for facing downward and facing upward may be resulted from the change of mechanisms of vapor rupture motion, as shown in Fig. 4, rather than from a change of behavior of induced convective flow which Lienhard, et al. [8] and Lao, et al. [3] discussed. Fig. 6 shows the film boiling heat transfer coefficients evaluated by Bromley's equation [1] using the results of the present experiments. These are compared (Fig. 6) with the experimental results for facing upward obtained by Hosler, et al. [6] and the analytical prediction by Berenson [2] (facing upward) using a simple geometrical model based on the concept of Taylor's instability. It appears clearly that the effects of the orientation of the heating surface is considerable and that the differences between the results of the two configurations may be most early explained by the different thickness of vapor layer pertaining to the two cases.

Hosler's results [6] obtained with the same liquid can be expected to differ from the present results because of the wall effect which is effective in the present study. Also, it might be considered that this restriction of wall is effective on the present experiments using 30 mm in diameter of heater, and the effect of induced convective flow on boiling heat transfer for facing upward is one of the important problems to clarify the characteristics of the boiling heat transfer. In general, it might be understood that the induced convective flow depends on heater size, liquid level from the heater, etc. Lienhard, et al. [8] discussed the effect of the induced convective flow on boiling heat transfer by deducing only the Borishanski number in the case of nucleate pool boiling.

For facing downward, the reported experimental data of film boiling have been only data by Ishigai, et al. [4] using saturated water. These are higher than the present results. One of the possible reason is dependent on the difference between both the liquid natures, that is, the difference of physical properties between them. In Fig. 6, Berenson's prediction using the idea of hydrodynamic calculation for facing upward is demonstrated to coincide with the present experiments for facing downward. In these two different cases, this coincidence may be caused by the reason that the Berenson's prediction is

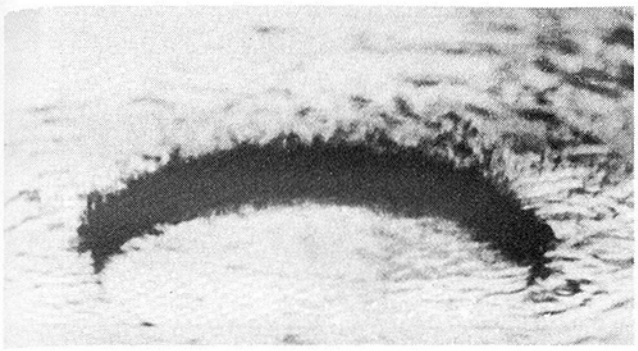

Fig. 4(*a*)

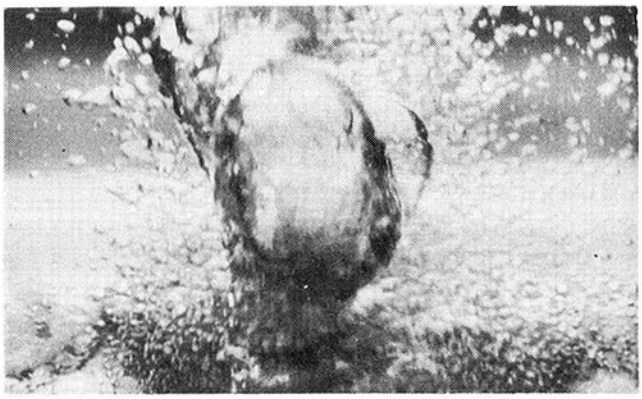

Fig. 4(*a'*)

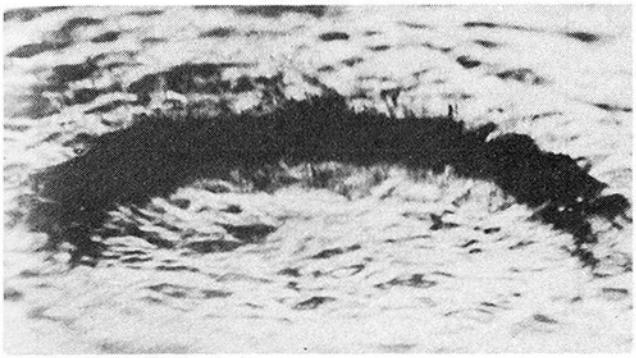

Fig. 4(*b*)

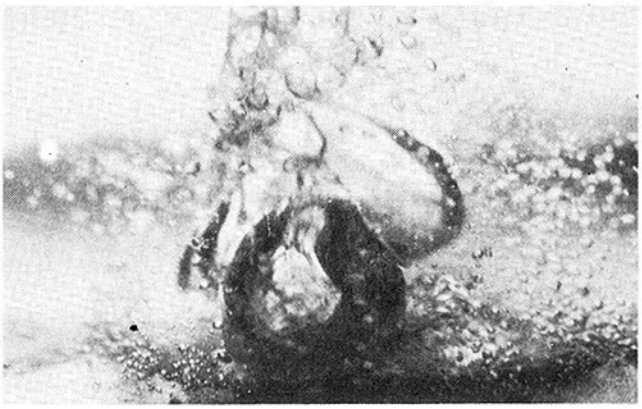

Fig. 4(*b'*)

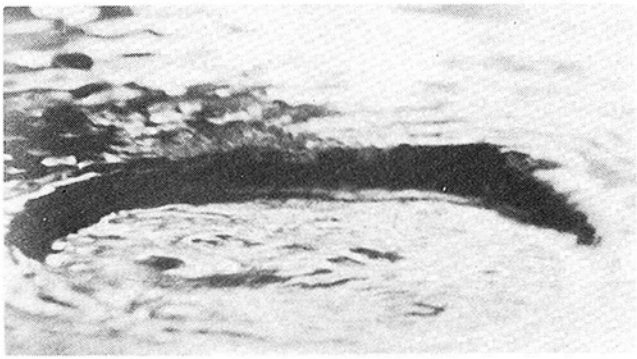

Fig. 4(*c*)

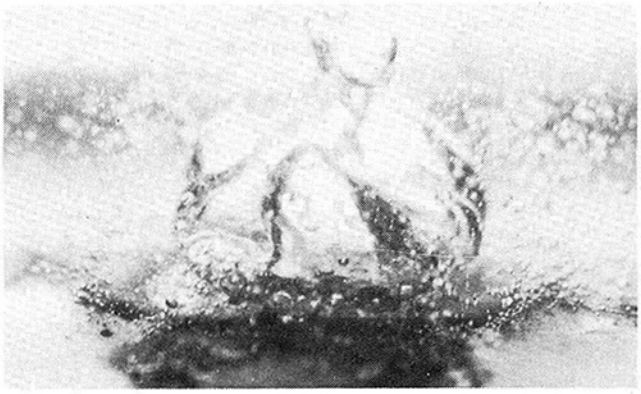

Fig. 4(*c'*)

Fig. 4 Visual observations of film boiling identified as facing downward and facing upward

idealized by wave motion at a stable vapor-liquid interface, which is similar to the vapor motion for facing downward, as shown in Figs. 4(*a'*, *b'*) and (*c'*). Also, for facing downward, both size effect and edge effect of heater on the problem of film boiling heat transfer are important problems, since the farther it has to move, the thicker the vapor layer must be at the center. Moreover, it might be considered that the vapor motion may be usually dependent on the size effect. Therefore, in the present study, the present experimental results are compared with those by Ishigai, et al. [4], whose experimental condition is similar to the present study.

$$\mathrm{Nu} = 0.35\,(L/C_p\Delta T)\,\mathrm{Gr}^{0.25}\cdot\mathrm{Pr}^{0.25}$$

The constant in the above expression is determined by the inclination of the straight line indicated in this figure, moreover it should be noted that the present correlation has a qualitatively good agreement with the results for water by Ishigai, et al. [4].

Conclusions

The present study is meant to clarify the characteristics of heat transfer of R-11 in the film boiling regions. And also, the experimental

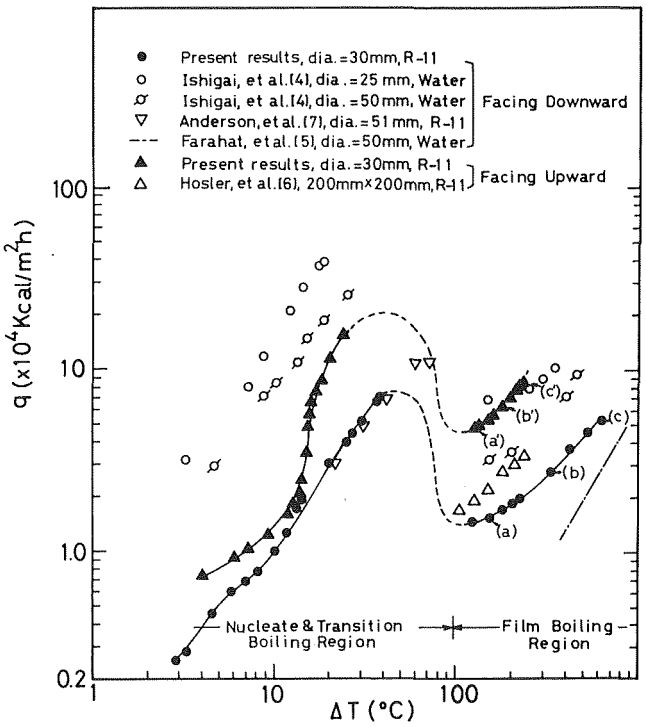

Fig. 5 Pool boiling heat transfer to saturated R-11 and saturated water on flat horizontal plates

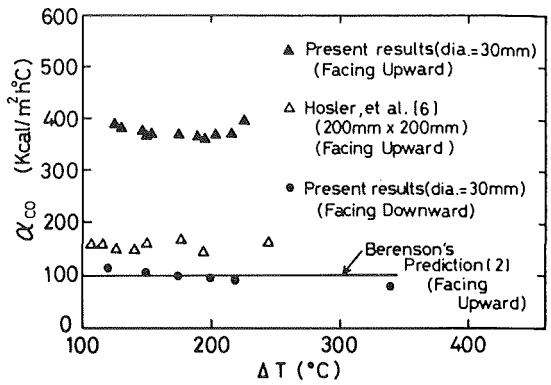

Fig. 6 Variation of average heat transfer coefficient on film boiling

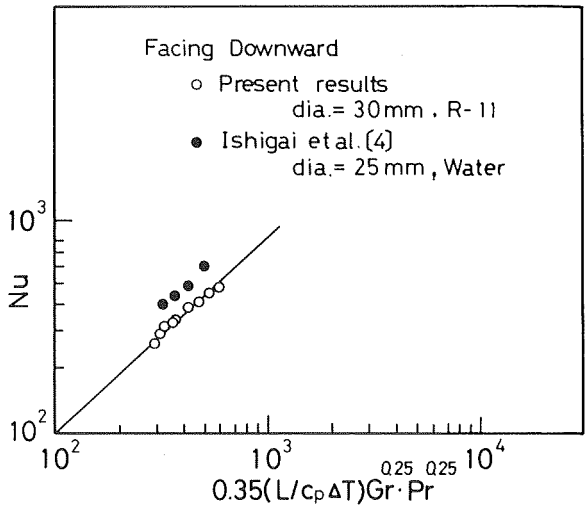

Fig. 7 A linear correlation for film boiling for facing downward

study is focused on the effect of heater orientation on the heat transfer coefficients of film boiling.

1 It is made clear that the heat transfer characteristics of film boiling depend drastically on the orientation of the heating surface, namely, facing downward or facing upward. Also, it is clear that the average convective heat transfer coefficient for facing upward is several times than that for facing downward.

2 From the present results for R-11, a correlation for facing downward can be expressed as

$$\mathrm{Nu} = 0.35\ (L/C_p\Delta T)\ \mathrm{Gr}^{0.25} \cdot \mathrm{Pr}^{0.25}.$$

It should be noted that this proposed correlation has reasonably close correspondence that is provable from the experimental results for water by Ishigai, et al. [4].

References

1 Bromley, L. A., "Heat Transfer in Film Boiling," *Chemical Engineering Progress*, Vol. 46, 1950, pp. 221–227.

2 Berenson, P. J., "Film Boiling Heat Transfer from a Horizontal Surface," ASME JOURNAL OF HEAT TRANSFER, Vol. 83, 1961, pp. 351–357.

3 Lao, Y. J., Barry, R. E., and Balzhiser, R. E., "A Study of Film Boiling on a Horizontal Plate," Fourth International Heat Transfer Conference, Vol. 5, 1970, B3-10.

4 Ishigai, S., Inoue, K., Kiwaki, Z., and Inai, T., "Heat Transfer from a Flat Surface Facing Downward," International Development in Heat Transfer Conference, Paper. 26, 1961, pp. 224–229.

5 Farahat, M. M., and Madbouly, E. E., "Stable Film Boiling Heat Transfer from Flat Horizontal Plates Facing Downwards," *International Journal of Heat and Mass Transfer*, Vol. 20, 1977, pp. 269–277.

6 Hosler, E. R., and Westwater, J. W., "Film Boiling on a Horizontal plate," *Journal of American Rocket Society*, Vol. 32, 1962, pp. 553–558.

7 Anderson, R. P., and Bova, L., "The Role of Downfacing Burnout in Post-accident Heat Removal," *Trans. Am. Nucl. Soc.*, Vol. 14, 1971, pp. 294–304.

8 Lienhard, J. H., and Kelling, K. B. Jr., "An Induced Convection Effect Upon the Peak-Boiling Heat Flux," ASME JOURNAL OF HEAT TRANSFER, Vol. 92, 1970, pp. 1–5.

M. Ünsal
Middle East Technical University
Gaziantep Campus
Gaziantep, Turkey

W. C. Thomas
Virginia Polytechnic Institute and State University
Blacksburg, Va. 24061

Linearized Stability Analysis of Film Condensation

A modified Yih analysis is used to investigate the stability of laminar film condensation on a vertical wall. The analysis presented leads to closed-form expressions for the wave amplification rate, the wave velocity, the neutral stability curve, and the critical Reynolds number. It is found that the condensation mass transfer rate has a dual role in the instability-inducing mechanism. Results indicate that surface tension, viscosity, and the overall effect of condensation mass transfer tend to stabilize while gravity tends to destabilize the flow. The critical distance predictions are an order of magnitude larger than the predictions from previous theories.

Introduction

Laminar film condensation on a cooled isothermal plate suspended in a very large volume of quiescent vapor is considered. Previous analyses which assume the condensate flow to be invariant with time conflict with experimental findings where time-dependent phenomena, namely surface ripples or waves, have been observed. Analyses have only recently been reported for determining the condition for the onset of the unstable or "disturbed" flow regime. A predictive theory and solution methodology is developed in the present paper to determine whether a small disturbance to the undisturbed flow is amplified or damped. The linear stability theory and perturbation solution method are used to yield closed-form analytical solutions. The role of phase-change mass transfer in the instability mechanism is identified. The solution for the neutral stability condition is compared with the previous formulation and numerical solution of the problem, and the reasons for the differences in results are discussed.

Film condensation on a plane surface was first analyzed by Nusselt [1]. Later, Rohsenow [2] extended Nusselt's analysis to take into account the heat convection in the condensate film. Subsequently, Sparrow and Gregg [3] solved the boundary layer equations of laminar film condensation. Two basic hypotheses exist in the boundary layer solution. One of these is the boundary layer simplification of the governing equations. By an order of magnitude analysis of the terms in the governing equations, it can be shown that the boundary layer solution is valid only in those regions where $\mathrm{Re} \gg \zeta/\mathrm{Pr}$ (the leading edge problem). It has been established that the Nusselt solution is a good approximation to the boundary-layer solution when $\zeta \ll 1$ [4]. The other hypothesis is the assumption of a steady-state undisturbed liquid film. This assumption on time-independence has been the subject of several investigations of the stability of laminar film condensation [5–9].

Bankoff [5] used a long-wave perturbation method originally developed by Yih [10] to analyze the stability problem. Without considering the temperature disturbance equation, he found that film condensation on a vertical wall is always unstable. Marschall and Lee [6, 7] employed the same method of solution but used a different interface stress condition. They accounted for disturbances in the temperature field and predicted the existence of a critical Reynolds number below which the condensate film is completely stable. For a vertical wall, their critical Reynolds number is negligibly small for all practical situations. Lee and Marschall [8] solved the stability problem formulated in [7] using a high-speed digital computer. With the aid of their numerical method, they demonstrated the shape of the neutral stability curve on the α-Re plane and presented calculations for the wave amplification rate and the wave velocities. Ünsal [9] formulated the interfacial conditions starting from first principles and noted that the interfacial normal stress condition used in [5–8] is incorrect. He also noted that the kinematic condition used in these investigations did not take into account the mass transfer across the interface.

In the present theoretical study, the derivation of the proper interfacial conditions is briefly outlined. The resulting stability problem is analyzed by a modified version of the Yih analysis to yield closed-form analytical solutions.

Formulation

The interfacial conditions between a vapor and a liquid film in the presence of heat and mass transfer across the interface have been previously formulated [11]. In the following development, it is shown, with certain simplifying assumptions, that these interfacial conditions can be reduced into a form containing only the liquid-phase variables.

Considering the two-dimensional geometry shown in Fig. 1, let

$$I(\tilde{x}, \tilde{y}, \tilde{t}) = \tilde{y} - \tilde{\eta}(\tilde{x}, \tilde{t}) = 0 \tag{1}$$

denote the equation for the phase interface where $I(\tilde{x}, \tilde{y}, \tilde{t})$ is a scalar

Contributed by the Heat Transfer Division for publication in the JOURNAL OF HEAT TRANSFER. Manuscript received by the Heat Transfer Division May 3, 1977.

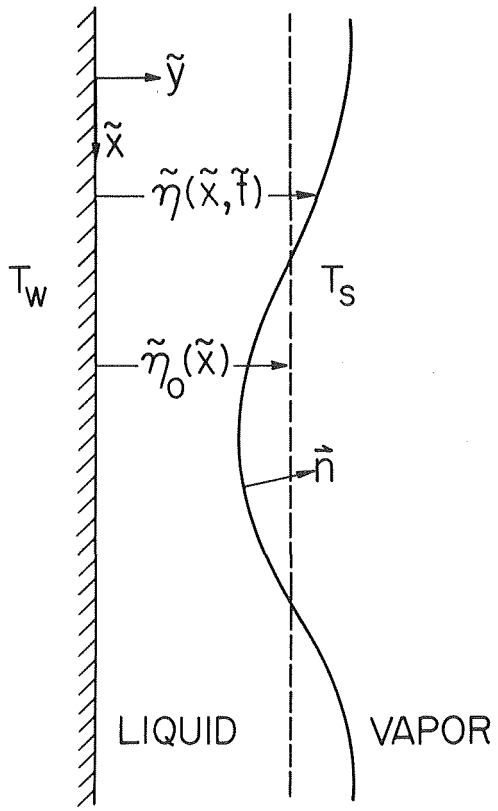

Fig. 1 Geometry of flow

point function which gives the instantaneous $\tilde{y}$-direction distance between the point $(\tilde{x}, \tilde{y})$ and a point on the interface $(\tilde{x}, \tilde{\eta})$. The unit normal to the interface, pointed into the vapor phase, is

$$\vec{n} = \nabla I/|\nabla I| \tag{2}$$

The interfacial velocity $\vec{V}_i$ is related to $I(\tilde{x}, \tilde{y}, \tilde{t})$ by taking the material time derivative of equation (1), i.e.,

$$I_{\tilde{t}} + \vec{V}_i \cdot \nabla I = 0 \tag{3}$$

Continuity of tangential velocities of the two phases at the interface can be written as

$$(\vec{V} - \vec{V}_g) \times \vec{n} = 0 \qquad \text{on } I = 0 \tag{4}$$

The liquid mass flux and the vapor mass flux across the interface are related to the velocities by

$$m = \rho(\vec{V} - \vec{V}_i) \cdot \vec{n} \qquad \text{on } I = 0$$
$$m_g = -\rho_g(\vec{V}_g - \vec{V}_i) \cdot \vec{n} \qquad \text{on } I = 0 \tag{5}$$

Mass conservation across the interface gives

$$m + m_g = 0 \qquad \text{on } I = 0 \tag{6}$$

The effect of vapor drag on laminar film condensation has been shown to be insignificant [12]. While the effect on film stability is less certain, the vapor shear stress has been neglected in previous investigations [5–9] and this simplification is retained in the present investigation. The momentum interfacial condition becomes

$$m\vec{V} + m_g\vec{V}_g - \tilde{p}_g\vec{n} - \vec{n} \cdot \Pi - \frac{\sigma}{R}\vec{n} = 0 \quad \text{on } I = 0 \tag{7}$$

In equation (7), the interfacial radius of curvature R is taken positive if the center of curvature lies on the liquid-phase side. The interfacial energy balance is obtained by equating the heat flux in the liquid film at the interface with the energy released as a result of phase change.

$$\vec{q} \cdot \vec{n} - h_{fg}m = 0 \qquad \text{on } I = 0 \tag{8}$$

(Equations (2–8) have also been derived in detail from an interfacial control volume approach [9, pp. 55–58]). Equation (8) does not contain a heat flux term for the vapor phase because the vapor is considered to be at uniform temperature. Eliminating $\vec{V}_i$ from equation (8) by using equation (3), one obtains

$$k(T_{\tilde{y}} - \tilde{\eta}_{\tilde{x}}T_{\tilde{x}}) - \rho h_{fg}(\tilde{\psi}_{\tilde{x}} + \tilde{\psi}_{\tilde{y}}\tilde{\eta}_{\tilde{x}} + \tilde{\eta}_{\tilde{t}}) = 0 \quad \text{on } I = 0 \tag{9}$$

Under the boundary layer approximations and steady-state assumption, it can be shown [9, p. 61] that equation (9) is equivalent to the overall energy balance equation given in [3]. It should be noted that the kinematic surface condition used in [5–8] is valid only when the heat flux in the liquid at the interface vanishes.

Using equations (3) and (6) and noting that (4) and (9) hold on $I = 0$, the vapor velocity and the interface velocity can be eliminated from equation (7). The normal and tangential components of (7) then become [9, pp. 58–62]

Nomenclature

c_p = liquid specific heat
$c = c_r + ic_i$ = complex wave celerity
g = gravitational acceleration
h_{fg} = latent heat
I = defined in equation (1)
k = liquid thermal conductivity
m, m_g = defined in equation (5)
$Nd = \zeta^2/\gamma \mathrm{Pr}^2$
$N_\xi = 2^{1/3}\sigma\rho^{-1}\nu^{-4/3}g^{-1/3}(1-\gamma)^{-1/3}$
$\vec{n}$ = unit normal to interface
$\tilde{p}$ = liquid pressure
$\tilde{p}_g$ = vapor pressure
$\bar{p}$ = dimensionless base flow pressure
p = dimensionless disturbance pressure
P = disturbance pressure amplitude
Pe = PrRe, local Peclet number
$\mathrm{Pr} = \rho c_p \nu/k$, Prandtl number
$\dot{q}$ = liquid heat flux
R = interface radius of curvature
$\mathrm{Re} = U_0\tilde{\eta}_0/\nu$, local Reynolds number
Re_c = critical Reynolds number
S = disturbance temperature amplitude
$\tilde{t}$ = time
t = dimensionless time
T = liquid temperature
T_s = vapor saturation temperature
T_w = wall temperature
$\Delta T = T_s - T_w$
$U_0 = \dfrac{g(1-\gamma)}{2\nu}\tilde{\eta}_0^2$, local base flow interfacial liquid $\tilde{x}$-component velocity
$\vec{V}$ = liquid velocity
$\vec{V}_g$ = vapor velocity
$\vec{V}_i$ = interface velocity
$\tilde{x}$ = parallel coordinate
$\tilde{x}_0$ = local value of parallel coordinate
$\tilde{x}_c$ = critical distance
x = dimensionless parallel coordinate
$\tilde{y}$ = normal coordinate
y = dimensionless normal coordinate
α = dimensionless wave number
$\gamma = \rho_g/\rho$
$\zeta = c_p\Delta T/h_{fg}$, heat capacity parameter
$\tilde{\eta}$ = film thickness
$\tilde{\eta}_0 = \left[\dfrac{4k\nu\Delta T\tilde{x}_0}{(1-\gamma)\rho g h_{fg}}\right]^{1/4}$ local base flow film thickness
$\bar{\eta}$ = dimensionless base flow film thickness
η = dimensionless disturbance film thickness
$\bar{\theta}$ = dimensionless base flow temperature
θ = dimensionless disturbance temperature
ν = liquid kinematic viscosity
Π = liquid stress tensor
ρ_g = vapor density
ρ = liquid density
σ = surface tension
ϕ = disturbance stream function amplitude
$\tilde{\psi}$ = liquid stream function
$\bar{\psi}$ = dimensionless base flow stream function
ψ = dimensionless distrubance stream function

Subscripts

$\tilde{x}, \tilde{y}, y, \tilde{t}$ = partial differentiation with respect to the subscript

$$\tilde{p} + 2\rho\nu\tilde{\psi}_{\tilde{x}\tilde{y}}(1+\tilde{n}_{\tilde{x}}^2)(1-\tilde{n}_{\tilde{x}}^2)^{-1} + \sigma\tilde{n}_{\tilde{x}\tilde{x}}(1+\tilde{n}_{\tilde{x}}^2)^{-3/2} + k^2 h_{fg}^{-2}\rho^{-1}\gamma^{-1}(\gamma-1)(T_{\tilde{y}} - \tilde{n}_{\tilde{x}}T_{\tilde{x}})^2(1+\tilde{n}_{\tilde{x}}^2)^{-1} = \tilde{p}_g \quad \text{on } I = 0 \tag{10}$$

$$\tilde{\psi}_{\tilde{y}\tilde{y}} - \tilde{\psi}_{\tilde{x}\tilde{x}} + 4\tilde{\eta}_{\tilde{x}}\tilde{\psi}_{\tilde{x}\tilde{y}}(\tilde{\eta}_{\tilde{x}}^2 - 1)^{-1} = 0 \quad \text{on } I = 0 \tag{11}$$

Equation (10) shows that the phase-change mass transfer increases the pressure on the liquid-phase side. In this respect, the normal stress condition in [6–8] contains a sign error. Furthermore, the vapor velocity term in the normal stress interfacial condition of [6–8] should not contain the factor ½ because momentum flux is just density times the square of the velocity.

A detailed derivation of the interfacial conditions for the linearized stability problem is given in the Appendix. The procedure is outlined as follows. The variables are separated into nondimensional base flow and disturbance quantities using the following transformations:

$$\begin{gathered}\tilde{p}/(\rho U_0^2) \to \bar{p} + p \\ \tilde{\psi}/(U_0\tilde{\eta}_0) \to \bar{\psi} + \psi \\ \tilde{\eta}/\tilde{\eta}_0 \to \bar{\eta} + \eta \\ (T - T_w)/\Delta T \to \bar{\theta} + \theta \\ \tilde{x}/\tilde{\eta}_0, \tilde{y}/\tilde{\eta}_0, \tilde{t}U_0/\tilde{\eta}_0 \to x, y, t\end{gathered} \tag{12}$$

The transformations (12) are substituted into (9–11) and the x-direction momentum equation. The base flow quantities satisfy the equations under the parallel flow approximation. The conditions are transformed onto the base flow interface by a Taylor series expansion for the disturbance film thickness. The transformed equations are linearized with respect to the disturbances. The resulting linear equations for the disturbances admit traveling wave solutions of the form

$$\begin{aligned} p &= P(y)\exp(i\alpha(x-ct)) + CC \\ \psi &= \phi(y)\exp(i\alpha(x-ct)) + CC \\ \theta &= S(y)\exp(i\alpha(x-ct)) + CC \\ \eta &= \exp(i\alpha(x-ct)) + CC \end{aligned} \tag{13}$$

where c is the complex wave celerity and CC stands for complex conjugate. The final form of the disturbance interfacial conditions is as follows:

$$\zeta S_y = i\alpha \mathrm{Pe}[\phi + (\bar{\psi}_y - c)] \qquad \text{at } y = \bar{\eta} \tag{14}$$

$$\phi_{yyy} + \alpha[(i\,\mathrm{Re}\,(c - \bar{\psi}_y) - 3\alpha)\phi_y + 2i\theta_y(\gamma-1)\,Nd\,\mathrm{Re}^{-1}S_y] - i\alpha^3 N_\xi \mathrm{Re}^{-2/3} = 0 \qquad \text{at } y = \bar{\eta} \tag{15}$$

$$\phi_{yy} + \alpha^2\phi + \bar{\psi}_{yyy} = 0 \qquad \text{at } y = \bar{\eta} \tag{16}$$

Equation (16), which represents the disturbance tangential stress condition at the interface, agrees with the results in [6–8]. The Nusselt base flow is given by

$$\begin{gathered}\bar{\psi}_y = 2\bar{\eta}y - y^2, \qquad \bar{\theta} = y/\bar{\eta}, \qquad \bar{\eta} = (\tilde{x}/\tilde{x}_0)^{1/4} \\ \bar{p} = \zeta^2(1-\gamma)\bar{\theta}_y^2/(\gamma \mathrm{P_e}^2) + \tilde{p}_g/(\rho U_0^2)\end{gathered} \tag{17}$$

The base flow pressure is equal to the vapor pressure plus the pressure increase resulting from phase change at steady state.

The formulation of the stability problem is completed by the equations governing the disturbance amplitude functions, the temperature condition at the interface, and the conditions at the wall surface. The derivation details have been previously reported [6, 9] and will be omitted. These conditions are

$$\phi_{yyyy} - 2\alpha^2\phi_{yy} + \alpha^4\phi = i\alpha\mathrm{Re}[(\bar{\psi}_y - c)(\phi_{yy} - \alpha^2\phi) - \psi_{yyy}\phi]$$

$$S_{yy} - \alpha^2 S = i\alpha\,\mathrm{Pe}\,[(\bar{\psi}_y - c)S - \bar{\theta}_y\phi]$$

$$\phi = \phi_y = S = 0 \qquad \text{at } y = 0$$

$$S = -\bar{\theta}_y \qquad \text{at } y = \bar{\eta}$$

Asymptotic Solution

Local solutions for the linearized stability problem posed by equations (14–18) are obtained by letting $\bar{\eta} = 1$ in these equations. An asymptotic solution valid for long waves is obtained by assuming the following expansions:

$$\phi = \phi_0 + \alpha\phi_1 + 0(\alpha^2), \qquad S = S_0 + \alpha S_1 + 0(\alpha^2) \tag{19}$$

Equations (19) are substituted into (15–18) and the coefficients of like powers of α are equated. Noting that N_ξ is large in situations of practical interest and taking $\alpha^2 N_\xi = 0(1)$ gives the zeroth-order problem

$$\begin{aligned} \phi_{0yyyy} &= 0 & S_{0yy} &= 0 \\ \phi_0 = \phi_{0y} &= 0 & &\text{at } y = 0 \\ \phi_{0yy} &= -\bar{\psi}_{yyy} & &\text{at } y = \bar{\eta} \\ \phi_{0yyy} &= 0 & &\text{at } y = \bar{\eta} \\ S_0 &= -\bar{\theta}_y & &\text{at } y = \bar{\eta} \end{aligned} \tag{20}$$

and the first-order problem

$$\begin{aligned} \phi_{1yyyy} &= i\,\mathrm{Re}[(\bar{\psi}_y - c)\phi_{0yy} - \bar{\psi}_{yyy}\phi_0] \\ S_{1yy} &= i\,\mathrm{Pe}\,[(\bar{\psi}_y - c)S_0 - \bar{\theta}_y\phi_0] \\ \phi_1 = \phi_{1y} = S_1 &= 0 \qquad \text{at } y = 0 \\ \phi_{1yy} = S_1 &= 0 \qquad \text{at } y = \bar{\eta} \\ \phi_{1yyy} &= i\,\mathrm{Re}\,(\bar{\psi}_y - c)\phi_{0y} + i2(1-\gamma)Nd\,\mathrm{Re}^{-1}\bar{\theta}_y S_{0y} + i\alpha^2 N_\xi\,\mathrm{Re}^{-2/3} \qquad \text{at } y = \bar{\eta} \end{aligned} \tag{21}$$

Using (17) with $\bar{\eta} = 1$, the zeroth and first-order problems are solved in succession. The solution procedure involves integration, and the results are

$$\left.\begin{aligned} S_0 &= -y, \qquad \phi_0 = y^2 \\ S_1 &= i\,\mathrm{Pe}\left[\left(\frac{1}{5} - \frac{c}{6}\right)y + \frac{c}{6}y^3 - \frac{1}{4}y^4 + \frac{1}{20}y^5\right] \\ \phi_1 &= i\,\mathrm{Re}\left[\frac{1}{30}y^5 - \frac{1}{12}cy^4\right] + \left[\frac{1}{3}i(\gamma-1)\,Nd\,\mathrm{Re}^{-1} + \frac{1}{6}i\alpha^2 N_\xi\,\mathrm{Re}^{-2/3}\right]y^3 + \left[\frac{1}{2}i\,\mathrm{Re}\left(c - \frac{2}{3}\right) + i(1-\gamma)Nd\,\mathrm{Re}^{-1} - \frac{1}{2}i\alpha^2 N_\xi\,\mathrm{Re}^{-2/3}\right]y^2 \end{aligned}\right\} \tag{22}$$

Substituting (22) into (19) and (19) into (14) with $\tilde{\eta} = 1$ yields

$$\zeta\left[-1 + \alpha i\,\mathrm{Pe}\left(\frac{c}{3} - \frac{11}{20}\right)\right] = i\alpha\,\mathrm{Pe}\left[2 - c + \alpha\left(i\,\mathrm{Re}\left(\frac{5}{12}c - \frac{3}{10}\right) + \frac{2}{3}i(1-\gamma)\,Nd\,\mathrm{Re}^{-1} - \frac{1}{3}i\alpha^2 N_\xi\,\mathrm{Re}^{-2/3}\right)\right] \tag{23}$$

Letting $c = c_r + ic_i$, equation (23) can be solved for c_r and c_i. It should be noted that an asymptotic expansion is not assumed for the wave celerity. Instead, the wave celerity is determined by letting the asymptotic solutions for ϕ and S satisfy the interfacial energy condition exactly to obtain closed-form solutions of improved accuracy. Solving equation (23), the following expressions are obtained for the dimensionless wave velocity and the dimensionless wave amplification rate

$$c_r = [(2 + 11\zeta/20)(1 + \zeta/3) + 5\mathrm{Re}(\zeta/\mathrm{Pe} + 9\alpha^2\mathrm{Re}/30 - 2\alpha^2(1-\gamma)Nd/3\mathrm{Re} + \alpha^4 N_\xi \mathrm{Re}^{-2/3}/3)/12]/[(1 + \zeta/3)^2 + 25\alpha^2\mathrm{Re}^2/144] \tag{24}$$

$$\alpha c_i = [-(1 + \zeta/3)\zeta/\mathrm{Pe} + \alpha^2((8/15 + 31\zeta/240)\mathrm{Re} + 2(1 + \zeta/3)(1-\gamma)Nd/3\mathrm{Re}) - \alpha^4(1 + \zeta/3)N_\xi \mathrm{Re}^{-2/3}/3]/[(1 + \zeta/3)^2 + 25\alpha^2\mathrm{Re}^2/144] \tag{25}$$

Discussion

Infinitesimal disturbances on the condensate film will grow or decay in amplitude depending on whether $c_i > 0$ or $c_i < 0$. The neutral sta-

bility condition ($c_i = 0$) separates stable from the unstable flow regime disturbances. The effects of different parameters on film stability is evident in equation (25). The term containing the dimensionless condensation parameter Nd has a destabilizing effect because it has a positive sign. The reason for this can be determined by noting that this term results from the condensation momentum flux term in equation (10). When the condensate film is exposed to a disturbance, the condensation rate and, consequently, the momentum flux increase at the wave troughs and decrease at the crests. Consequently, condensation mass transfer acts to create larger interfacial pressures at troughs than at crests and the effect tends to destabilize the film. This result contradicts the results in [6–8] where a stabilizing effect of Nd is predicted because of the error noted previously in their normal stress interfacial condition. In equation (25), the term containing the Peclet number shows a stabilizing effect. It exists because of the liquid heat flux term in equation (14) and accounts for a stabilizing effect of condensation mass transfer. An increased condensation rate at the wave troughs tends to decrease the wave amplitude. This effect of the condensation mass transfer, which has been neglected in the previous investigations, is strongly stabilizing as shown later in this section. It is concluded, therefore, that the phase change has a dual role in the stability mechanism with the stabilizing effect dominating over the destabilizing effect. It is clear from equation (25) that the surface tension parameter N_ξ has a stabilizing effect.

The neutral stability curve can be obtained by letting $c_i = 0$ and solving the resulting equation for $\alpha c_i = 0$, equation (25) gives

$$\alpha = ([a_2 + (a_2^2 - 4a_1a_3)^{1/2}]/2a_1)^{1/2} \tag{26}$$

where

$$a_1 = (1 + \zeta/3)N_\xi \mathrm{Re}^{1/3}/3, \qquad a_3 = (1 + \zeta/3)\zeta/\mathrm{Pr}$$

$$a_2 = ((8/15 + 31\zeta/240)\mathrm{Re}^2 + 2(1 + \zeta/3)(1 - \gamma)Nd/3)$$

When ζ/Pr is small, equation (26) identifies the *two* unstable regions as shown by the crosshatched regions in Fig. 2. The smaller region of instability near the origin results from the destabilizing effect of Nd. Mathematically, equation (26) gives two critical Reynolds numbers, Re_{c1} and Re_{c2}, and $\mathrm{Re}_{c1} < \mathrm{Re} < \mathrm{Re}_{c2}$ is the completely stable flow range.

The critical Reynolds numbers are determined by locating the zeros of the discriminant in (26), i.e.,

$$a_2 - 2(a_1a_3)^{1/2} = 0$$

Substituting for a_1, a_2, and a_3 yields

$$\left(\frac{8}{15} + \frac{31}{240}\zeta\right)\mathrm{Re}_c^2 + \frac{2}{3}\left(1 + \frac{\zeta}{3}\right)(1 - \gamma)\frac{\zeta^2}{\gamma \mathrm{Pr}^2}$$

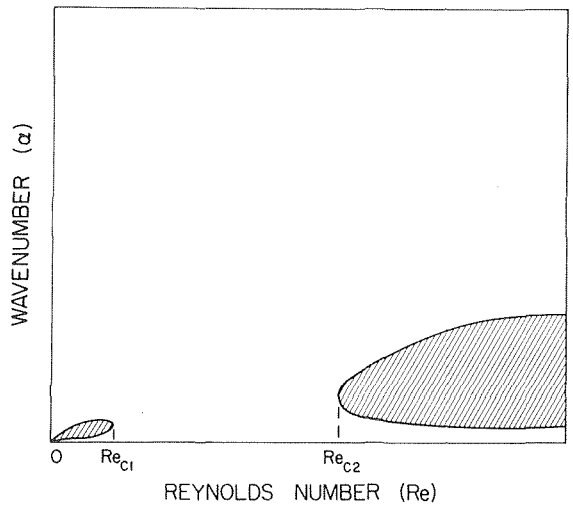

Fig. 2 Unstable regions for small ζ/Pr

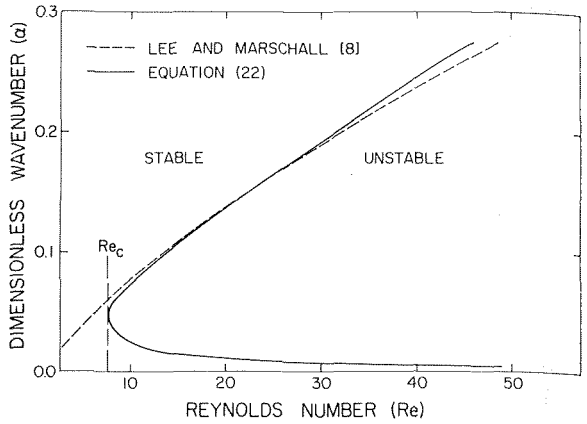

Fig. 3 Neutral stability curve for saturated steam, T_s = 373K, ΔT = 47 K

$$-2\left(1 + \frac{\zeta}{3}\right)\left(\frac{N_\xi \zeta}{3\mathrm{Pr}}\right)^{1/2}\mathrm{Re}_c^{1/6} = 0 \tag{27}$$

For small ζ/Pr, accurate approximations for Re_{c1} and Re_{c2} may be obtained by neglecting the first term or the second term, respectively, in equation (27). Hence

$$\mathrm{Re}_{c1} = \frac{1}{27}N_\xi^{-3}([1 - \gamma]/\gamma)^6(\zeta/\mathrm{Pr})^9 \tag{28}$$

$$\mathrm{Re}_{c2} = \left[\frac{15}{4}\frac{[1 + \zeta/3]}{[1 + 31\zeta/128]}\left(\frac{N_\xi \zeta}{3\,\mathrm{Pr}}\right)^{1/2}\right]^{6/11} \tag{29}$$

For practical situations (where ζ/Pr is small), Re_{c1} is quite small and, in fact, generally corresponds to locations so close to the leading edge of the plate that the boundary layer assumptions and Nusselt analysis for film condensation are invalid. Specifically, it can be shown, by an order-of-magnitude analysis of the terms in the x-direction momentum equation, that the above stability analysis is invalid when $\mathrm{Re} < \sqrt{3}\,\zeta/(2\,\mathrm{Pr})$. Consequently, discussion will be limited to regions of the α-Re plane where $\mathrm{Re} > \sqrt{3}\,\zeta/((2\,\mathrm{Pr})$ and the stability results apply. Equation (26) is presented graphically in Fig. 3 for saturated steam at 373 K with $\Delta T = 47$ K. The physical properties are evaluated at the reference temperature $T_w + \Delta T/3$ except for surface tension and latent heat which are evaluated at 373 K. For this example, $N_\xi = 12347$, $\gamma = 0.000611$, $\zeta/\mathrm{Pr} = 0.0333$, and $\zeta = 0.0872$ which gives $R_{c1} = 1.9 \times 10^{-8}$ and $R_{c2} = 7.9$. Since $\mathrm{Re}_{c1} \ll \sqrt{3}\,\zeta/(2\,\mathrm{Pr})$, the unstable region near the origin is disregarded and the critical Reynolds number below which all infinitesimal disturbances decay with time is given by Re_{c2}. The agreement with the results from [8] is good in those regions where α is large. The reason is that the effect of condensation mass transfer on the stability of the film is negligible for large wave numbers. The short wavelength disturbances in this region are stabilized solely by surface tension. The discrepancy between the two theories appears at small wave numbers. The film is stabilized at small wave numbers by the condensation mass transfer. Balancing the latent heat of the condensation rate on the interface by the heat flux in the liquid film (equation (9)) shifts the lower branch of the neutral stability curve upward from the $\alpha = 0$ axis. The destabilizing effect of condensation mass transfer through the dimensionless parameter Nd of the normal stress interfacial condition is, for all practical purposes, negligible. For small ζ, equation (29) can be further simplified with negligible loss of accuracy to

$$\mathrm{Re}_{c2} = \left[\frac{15}{4}\left(\frac{N_\xi \zeta}{3\,\mathrm{Pr}}\right)^{1/2}\right]^{6/11} \tag{30}$$

Observing that

$$\mathrm{Re} = \frac{U_0\tilde{\eta}_0}{\nu} = \frac{g(1 - \gamma)}{2\nu^2}\left[\frac{4k\nu\zeta\tilde{x}}{(1 - \gamma)\rho g c_p}\right]^{3/4} \tag{31}$$

Equations (30) and (31), when solved for the critical distance, give

Table 1 Critical distance in various experiments

Experiment	Liquid	ΔT (C)	Length of Test Section (cm)	Calculated Critical Distance, $\bar{x}_c$ (cm)
Ritani and Shekriladze	Water	$\Delta T = 1$	21.7	6.4
Walt and Kroger	Freon 12	$\Delta T = 1$	5.7	1.7
Mills and Seban	Water	$\Delta T = 4$	12.7	12.3
Slegers and Seban	n-Butyl Alcohol	$\Delta T = 30$	12.7	4.9

$$\bar{x}_c = \frac{1}{4}\left[(75\sigma)^4\left(\frac{c_p}{k\zeta}\right)^7\frac{\rho^3\nu^9}{g^5(1-\gamma)^5}\right]^{1/11} \tag{32}$$

Equations (30–32) show that it is misleading to refer to only a critical Reynolds number to ascertain the stability or instability of condensate film flow. Equation (30) shows that decreasing ζ decreases Re_c which implies a destabilizing effect. This observation is incomplete because of the functional dependence of Re on ζ as shown by (31). Equation (32) shows that the critical distance varies inversely with ζ. Consequently, decreasing ζ increases the critical distance $\bar{x}_c$ and, therefore, has a stabilizing effect. Equation (32) shows that increasing surface tension or viscosity increases the critical distance. On the other hand, increasing ΔT or gravity decreases the critical distance. The critical distances calculated from equation (32) for the experiments reported in references [13–16] are shown in Table 1. It is seen that these calculated critical distances may be small but are not negligible. Equation (32) shows that the condensate film can be completely stabilized by letting $\Delta T \to 0$. This trend is in qualitative agreement with the experimental observations where better comparison between the boundary layer solutions of laminar film condensation and experimental results are obtained for small ΔT. A reason for the deviation between theory and experiment at large ΔT can be conjectured to result, in part, from the finite amplitude surface waves on the condensate film.

References

1 Jakob, M., *Heat Transfer,* John Wiley, New York, 1967, pp. 663–667.

2 Rohsenow, W. M., "Heat Transfer and Temperature Distribution in Laminar-Film Condensation," TRANS. ASME, Vol. 78, 1956, pp. 1645–1648.

3 Sparrow, E. M., and Gregg, J. L., "A Boundary Layer Treatment of Laminar-Film Condensation," ASME JOURNAL OF HEAT TRANSFER, Vol. 81, 1959, pp. 13–18.

4 Ünsal, M., and Thomas, W. C., "Perturbation Solutions for Laminar Film Condensation on Nonisothermal Walls," ASME *Journal of Applied Mechanics,* Vol. 43, 1976, pp. 367–368.

5 Bankoff, S. G., "Stability of Liquid Flow Down a Heated Inclined Plane," *International Journal of Heat and Mass Transfer,* Vol. 14, 1971, pp. 377–385.

6 Marschall, E., and Lee, C. Y., "Stability of Condensate Flow Down a Vertical Wall," *International Journal of Heat and Mass Transfer,* Vol. 16, 1973, pp. 41–48.

7 Marschall, E., and Lee, C. Y., "Stability Characteristics of Condensate Films," *Wärme-und Stoffübertragung,* Vol. 1, 1973, pp. 32–37.

8 Lee, C. Y., and Marschall, E., "Laminar Stability Analysis of Condensate Film Flow," *Wärme-und Stoffübertragung,* Vol. 7, 1974, pp. 14–21.

9 Ünsal, M., "Stability of a Condensate Film Flowing Down a Vertical Plane," Ph.D. Thesis, Virginia Polytechnic Institute and State University, 1975.

10 Yih, C. S., "Stability of Liquid Flow Down an Inclined Plane," *Physics of Fluids,* Vol. 6, 1963, pp. 321–334.

11 Hsieh, D. Y., "Effects of Heat and Mass Transfer on Rayleigh-Taylor Instability," ASME *Journal of Basic Engineering,* Vol. 94, 1972, pp. 156–162.

12 Chen, M. M., "An Analytical Study of Laminar Film Condensation: Part 1—Flat Plates," ASME JOURNAL OF HEAT TRANSFER 83, 1961, pp. 48–54.

13 Ritani, G. V., and Shekriladze, T. G., "An Experimental Study of the Heat Exchange Process on Transition from Laminar to Turbulent Flow of the Film" *Thermal Engineering II,* 1964, pp. 101–103.

14 Walt, J. V. D., and Kröger, D. G., "Heat Transfer During Film Condensation of Saturated and Superheated Freon-12," *Progress in Heat and Mass Transfer,* Vol. 6, 1972, pp. 75–98.

15 Mills, A. F., and Seban, R. A., "The Condensation Coefficient of Water," *International Journal of Heat and Mass Transfer,* Vol. 10, 1967, pp. 1815–1826.

16 Slegers, L., and Seban, R. A., "Nusselt Condensation of n-Butyl Alcohol," *International Journal of Heat and Mass Transfer,* Vol. 12, 1969, pp. 237–239.

APPENDIX

Equations (14) and (15) are derived as follows. Substituting (12) into (9) yields

$$\zeta(\bar{\theta}_y + \theta_y - \bar{\eta}_x\bar{\theta}_x - \bar{\eta}_x\theta_x - \eta_x\bar{\theta}_x - \eta_x\theta_x) - Pe\,(\bar{\psi}_x + \psi_x + \bar{\psi}_y\bar{\eta}_x + \bar{\psi}_y\eta_x + \psi_y\bar{\eta}_x + \psi_y\eta_x + \eta_t) = 0 \qquad \text{at } y = \bar{\eta} + \eta \tag{33}$$

The following Taylor Series expansions are used to transform (33) from $y = \bar{\eta} + \eta$ to $y = \bar{\eta}$.

$$\bar{\theta}_y(x, \bar{\eta} + \eta) = \bar{\theta}_y + \eta\bar{\theta}_{yy} + \text{nonlinear terms (NTs)} \qquad \text{at } y = \bar{\eta}$$

$$\theta_y(x, \bar{\eta} + \eta, t) = \theta_y + \text{NTs} \qquad \text{at } y = \bar{\eta}$$

$$\bar{\eta}_x\bar{\theta}_x(x, \bar{\eta} + \eta) = \bar{\eta}_x\bar{\theta}_x + \eta\bar{\eta}_x\bar{\theta}_{xy} + \text{NTs} \qquad \text{at } y = \bar{\eta}$$

$$\bar{\eta}_x\theta_x(x, \bar{\eta} + \eta, t) = \bar{\eta}_x\theta_x + \text{NTs} \qquad \text{at } y = \bar{\eta}$$

$$\eta_x\bar{\theta}_x(x, \bar{\eta} + \eta) = \eta_x\bar{\theta}_x + \text{NTs} \qquad \text{at } y = \bar{\eta}$$

$$\bar{\psi}_x(x, \bar{\eta} + \eta) = \bar{\psi}_x + \eta\bar{\psi}_{xy} + \text{NTs} \qquad \text{at } y = \bar{\eta}$$

$$\psi_x(x, \bar{\eta} + \eta, t) = \psi_x + \text{NTs} \qquad \text{at } y = \bar{\eta}$$

$$\bar{\eta}_x\bar{\psi}_y(x, \bar{\eta} + \eta) = \bar{\eta}_x\bar{\psi}_y + \eta\bar{\eta}_x\bar{\psi}_{yy} + \text{NTs} \qquad \text{at } y = \bar{\eta}$$

$$\eta_x\bar{\psi}_y(x, \bar{\eta} + \eta) = \eta_x\bar{\psi}_y + \text{NTs} \qquad \text{at } y = \bar{\eta}$$

$$\bar{\eta}_x\psi_y(x, \bar{\eta} + \eta, t) = \bar{\eta}_x\psi_y + \text{NTs} \qquad \text{at } y = \bar{\eta}$$

Substituting these expansions into (33) yields

$$\zeta(\bar{\theta}_y + \eta\bar{\theta}_{yy} + \theta_y - \bar{\eta}_x\bar{\theta}_x - \eta\bar{\eta}_x\bar{\theta}_{xy} - \bar{\eta}_x\theta_x - \eta_x\bar{\theta}_x) - Pe(\bar{\psi}_x + \eta\bar{\psi}_{xy} + \psi_x + \bar{\eta}_x\bar{\psi}_y + \eta\bar{\eta}_x\bar{\psi}_{yy} + \eta_x\bar{\psi}_y + \bar{\eta}_x\psi_y + \eta_t) + \text{NTs} = 0 \qquad \text{at } y = \bar{\eta} \tag{34}$$

The base flow must satisfy the steady part of (34), so that

$$\zeta(\bar{\theta}_y - \bar{\eta}_x\bar{\theta}_x) - Pe(\bar{\psi}_x + \bar{\eta}_x\bar{\psi}_y) = 0 \qquad \text{at } y = \bar{\eta} \tag{35}$$

The Nusselt solution actually satisfies

$$\zeta\bar{\theta}_y - Pe(\bar{\psi}_y + \bar{\eta}_x\bar{\psi}_y) = 0 \qquad \text{at } y = \bar{\eta} \tag{36}$$

The term $\bar{\eta}_x\bar{\theta}_x$ in (35) is neglected (boundary layer type approximation). Taking equation (36) into account and neglecting the nonlinear terms with respect to the disturbance quantities, equation (34) becomes

$$\zeta(\theta_y + \eta\bar{\theta}_{yy} - \eta\bar{\eta}_x\bar{\theta}_{xy} - \bar{\eta}_x\theta_x - \eta_x\bar{\theta}_x) - Pe(\psi_x + \eta\bar{\psi}_{xy} + \eta\bar{\eta}_x\bar{\psi}_{yy} + \eta_x\bar{\psi}_y + \bar{\eta}_x\psi_y + \eta_t) = 0 \qquad \text{at } y = \bar{\eta}$$

Neglecting x-derivative terms with respect to the base flow quantities (parallel-flow approximation) and observing that $\bar{\theta}_{yy} = 0$ yields

$$\zeta\theta_y - Pe(\psi_x + \eta_x\bar{\psi}_y + \eta_t) = 0 \qquad \text{at } y = \bar{\eta} \tag{37}$$

Substitution of (13) into (37) yields the interfacial energy disturbance equation (14).

Substituting (12) into (10) and neglecting x-derivatives with respect to the base flow quantities (parallel-flow approximation) gives

$$\bar{p} + p + \frac{2}{\mathrm{Re}}\psi_{xy}\frac{1+\eta_x{}^2}{1-\eta_x{}^2} + N_\xi\mathrm{Re}^{-5/3}\frac{\eta_{xx}}{(1+\eta_x{}^2)^{3/2}} + \frac{\zeta^2}{Pe^2}\frac{(\gamma-1)}{\gamma}\frac{(\bar{\theta}_y + \theta_y + \eta_x\theta_x)^2}{(1-\eta_x{}^2)} = \frac{\bar{p}_g}{\rho U_0{}^2} \qquad \text{at } y = \bar{\eta} + \eta \tag{38}$$

The following Taylor series expansions are used to transform (38) from $y = \bar{\eta} + \eta$ to $y = \bar{\eta}$:

$$\bar{p}(x, \bar{\eta} + \eta) = \bar{p}(x, \bar{\eta}) + \eta\bar{p}_y(x, \bar{\eta}) + \text{NTs}$$

$$p(x, \bar{\eta} + \eta, t) = p(x, \bar{\eta}, t) + \text{NTs}$$

$$[\psi_{xy}(x, \bar{\eta} + \eta, t)]\frac{1 + \eta_x{}^2}{1 - \eta_x{}^2} = \psi_{xy}(x, \bar{\eta}, t) + \text{NTs}$$

$$\frac{(\bar{\theta}_y + \theta_y + \eta_x\theta_x)^2}{1 - \eta_x{}^2}\Bigg|_{y=\bar{\eta}+\eta} = (\bar{\theta}_y{}^2 + \eta 2\bar{\theta}_{yy} + 2\bar{\theta}_y\theta_y)\Big|_{y=\bar{\eta}} + \text{NTs}$$

Substituting these expansions into (38) and neglecting the nonlinear terms with respect to the disturbance quantities yields

$$\bar{p} + \eta\bar{p}_y + p + \frac{2}{\text{Re}}\psi_{xy} + N_\xi\,\text{Re}^{-5/3}\eta_{xx} + \frac{\zeta^2}{Pe^2}\frac{(\gamma - 1)}{\gamma}(\bar{\theta}_y{}^2 + \eta 2\bar{\theta}_{yy} + 2\bar{\theta}_y\theta_y) = \frac{\tilde{p}_g}{\rho U_0{}^2} \qquad \text{at } y = \bar{\eta} \quad (39)$$

The base flow must satisfy the steady part of equation (39), hence,

$$\bar{p} = \frac{\zeta^2}{Pe^2}\frac{(1 - \gamma)}{\gamma}\bar{\theta}_y{}^2 + \frac{\tilde{p}_g}{\rho U_0{}^2} \qquad \text{at } y = \bar{\eta} \quad (40)$$

Observing that the right-hand side of equation 40 is independent of y, one finds that $\bar{p}_y = 0$. Noting that $\bar{\theta}_{yy} = 0$ and taking equation (40) into account, equation (39) reduces to

$$p + \frac{2}{\text{Re}}\psi_{xy} + N_\xi\text{Re}^{-5/3}\eta_{xx} + 2\frac{\zeta^2}{\text{Pe}^2}\frac{(\gamma - 1)}{\gamma}\bar{\theta}_y\theta_y = 0 \qquad \text{at } y = \bar{\eta} \quad (41)$$

Substitution of (12) into the x-momentum equation for the condensate film and neglecting x-derivative terms with respect to $\bar{\psi}$ gives

$$\bar{p}_x + p_x = \frac{1}{F^2} + \frac{1}{\text{Re}}(\psi_{xxy} + \bar{\psi}_{yyy} + \psi_{yyy}) - (\bar{\psi}_y + \psi_y)\psi_{xy} + \psi_x(\bar{\psi}_{yy} + \psi_{yy}) - \psi_{yt} \quad (42)$$

where $F = U_0(g\tilde{\eta}_0).^{-1/2}$ Taking $\tilde{p}_g = \rho_g g\tilde{x}$ and neglecting the x-derivative term with respect to $\bar{\theta}_y$ equation (40) gives

$$\bar{p}_x = \frac{\gamma}{F^2}$$

Observing that the base flow must satisfy the steady part of equation (42)

$$\bar{p}_x = \frac{1}{F^2} + \frac{1}{\text{Re}}\bar{\psi}_{yyy} \quad (43)$$

Taking (43) into account and neglecting nonlinear terms with respect to the disturbance stream function ψ, equation (42) becomes

$$p_x = \frac{1}{\text{Re}}(\psi_{xxy} + \psi_{yyy}) - \bar{\psi}_y\psi_{xy} + \bar{\psi}_{yy}\psi_x - \psi_{yt} \quad (44)$$

Equation (44), being valid pointwise, is in particular valid at $y = \bar{\eta}$. Substitution of (13) into (41) and (44) yields

$$P + \frac{2}{\text{Re}}i\alpha\phi_y - N_\xi\text{Re}^{-5/3}\alpha^2 + 2\frac{\zeta^2}{\text{Pe}^2}\frac{(\gamma - 1)}{\gamma}(\bar{\theta}_y S_y + \bar{\theta}_{yy}) = 0 \qquad \text{at } y = \bar{\eta}$$

and

$$i\alpha P = \frac{1}{\text{Re}}(\phi_{yyy} - \alpha^2\phi_y) - i\alpha\bar{\psi}_y\phi_y + i\alpha\bar{\psi}_{yy} + i\alpha c\phi_y \qquad \text{at } y = \bar{\eta}$$

Eliminating P from these equations, and noting that $\bar{\theta}_{yy} = 0$ and $\bar{\psi}_{yy} = 0$ at $y = \bar{\eta}$, gives equation (15).

T. H. Kuehn
Assistant Professor.
Department of Mechanical Engineering and
Engineering Research Institute
Iowa State University
Ames, Iowa 50011

R. J. Goldstein
Professor.
Department of Mechanical Engineering
University of Minnesota
Minneapolis, Minn. 55455

An Experimental Study of Natural Convection Heat Transfer in Concentric and Eccentric Horizontal Cylindrical Annuli

An experimental study has been conducted to determine the influence of eccentricity and Rayleigh number on natural convection heat transfer through a fluid bounded by two horizontal isothermal cylinders. Eccentricity of the inner cylinder substantially alters the local heat transfer on both cylinders, but the overall heat transfer coefficients change by less than 10 percent over the range of eccentricities investigated. Heat transfer results using the concentric geometry are given for Rayleigh numbers from 2.2×10^2 to 7.7×10^7 which includes regions of conduction, laminar convection, and partially turbulent convection.

Introduction

Natural convection heat transfer continues to be an important method of energy transfer that is receiving considerable attention. Numerous applications are found in energy conversion, storage, and transmission systems. Examples of these using the horizontal coaxial cylinder geometry studied here include concentrating solar collector receiver design, initial melting of a phase change material around heating pipes in thermal storage systems, and compressed gas insulated high-voltage electric transmission cables.

Considerable experimental work has been done on the flow and overall heat transfer coefficients by natural convection between horizontal concentric cylinders. The effect of the diameter ratio on the heat transfer coefficient has been studied by several investigators including Beckmann [1], Liu, Mueller, and Landis [2], Grigull and Hauf [3], and Lis [4]. Flow patterns in air were observed by Bishop and Carley [5], Bishop, Carley, and Powe [6], Powe, Carley, and Bishop [7], and Grigull and Hauf [3]. Liu, Mueller, and Landis [2] described the effect of diameter ratio and Prandtl number on flow patterns using air, water, and silicone oil.

The influence of Prandtl number on the overall heat transfer coefficient was first studied by Kraussold [8]. Further work has been done by Liu, Mueller, and Landis [2].

Most experimental studies have been limited to the range of Rayleigh number $10^1 < \mathrm{Ra}_L < 10^6$. Koshmarov and Ivanov [9] obtained heat transfer results in gases for $10^{-9} < \mathrm{Ra}_L < 10^5$ which includes results in the rarefield gas regime. With their geometry the Rayleigh number must be less than about 10^{-2} before the heat transfer coefficient becomes significantly less than that for conduction through the gas at a pressure of one atmosphere. Lis [4] used nitrogen and sulphur hexafluoride gas under pressure to obtain overall heat transfer results up to $\mathrm{Ra}_L = 10^{10}$ where the flow is turbulent.

Other parameters that have been investigated include annulus eccentricity and the effect of fluid density inversion. Zagromov and Lyalikov [10] obtained overall heat transfer coefficients in air for various vertical and horizontal eccentricities of the inner cylinder. Experiments with water near the point of maximum density have been conducted by Seki, Fukusako, and Nakaoka [11].

The primary objective of the present experimental study is to extend knowledge of temperature distributions, flow patterns, and local and overall heat transfer coefficients to as large a Rayleigh number as possible within the limits of the existing laboratory facilities. A secondary objective is to analyze the effect of annulus eccentricity. The results of this study should help in understanding the phenomena which are necessary for the development of complete and accurate correlating equations required for engineering design.

Apparatus

Optical methods were chosen to study the temperature field between the cylinders since some results are obtained in fluctuating and turbulent flow conditions. Both instantaneous and time-averaged results can be obtained to study the flow and heat transfer coefficients. The best method of achieving a large Rayleigh number within the size constraints of the available Mach-Zehnder interferometer was to use a pressurized gas system.

The test cell described in [12] is used as the model. The test cell is placed inside a pressure tank when tests requiring nonatmospheric pressure are performed. The tank consists of a steel cylinder and two steel end plates. The end plates are tie-bolted together with the cylinder between them. Two quartz windows, 5.08 cm thick and 15.25

Contributed by the Heat Transfer Division for publication in the JOURNAL OF HEAT TRANSFER. Manuscript received by the Heat Transfer Division May 23, 1977.

cm in diameter, act as the pressure windows convering a 10.16 cm circular hole in the center of each end plate. Connections and seals for the cooling water, gas line, electric heater wires, and thermocouple wires are all located on the steel cylinder. A piston-cylinder assembly with a free floating piston was incorporated into the closed cooling water loop so that the pressure of the water can be maintained approximately equal to that of the gas in the cylinder when the gas pressure is above atmospheric. This minimizes the stress on the test cell due to the presence of the cooling water. A sketch of the test cell within the pressure tank is shown in Fig. 1. Further details of design and construction are described in [13].

A Mach-Zehnder interferometer is used to obtain interferograms of the gas within the test cell. A 5 mW He-Ne laser serves as the light source. One fringe shift is produced by a temperature difference of 35 °C using nitrogen at a pressure of 0.15 atm whereas a temperature difference of only 0.1 °C is necessary at a pressure of 35 atm.

Overall heat transfer results are obtained by measuring the total electric power supplied to the inner cylinder heater, the temperatures of the two cylinders, and the gas pressure. End losses and radiation corrections are made to determine the convective heat transfer coefficient. All fluid properties are based on the arithmetic mean temperature of the two cylinders for the overall results.

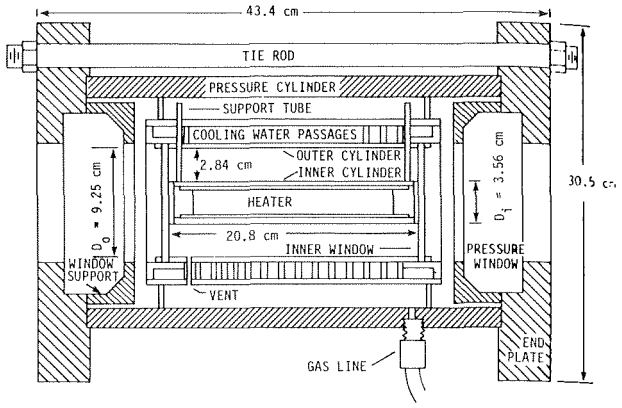

Fig. 1 Schematic cross section of test cell within the pressure tank

Results

Effect of Inner Cylinder Position. Overall heat transfer results have been obtained using air at atmospheric pressure with the inner cylinder moved below center at $\epsilon_v/L \approx -1/3$ and $-2/3$ over the range $3 \times 10^4 < \mathrm{Ra}_L < 10^5$. Virtually no difference was found between these eccentric heat transfer coefficients and those for the concentric geometry that were reported earlier [12]. Another series of tests were performed in which all parameters remained constant except the inner cylinder position so that the results could be analyzed in more detail.

The Rayleigh number based on the radius difference, Ra_L, remained near 4.8×10^4, the Prandtl number near 0.7, and the diameter ratio at 2.6. The inner cylinder was located at five different vertical positions within the outer cylinder, $\epsilon_v/L \approx 2/3$, $1/3$, 0, $-1/3$, and $-2/3$. Then the entire test cell was rotated to give results at angles of 30 deg, 60 deg, 90 deg, 120 deg, and 150 deg from the vertical position with $\epsilon/L \approx 2/3$.

Fig. 2 shows four of the interferograms obtained. In Fig. 2(*a*), (*b*), and (*c*) the fringes or isotherms are symmetric about the vertical plane passing through the centers of the cylinders. The inner cylinder is always surrounded by a thermal boundary layer while the presence of a boundary layer on the outer cylinder depends on the inner cylinder position. When the inner cylinder is near the bottom of the cavity, the outer cylinder has a boundary layer adjacent everywhere. When the inner cylinder is moved near the top, there is no boundary layer on the bottom portion of the outer cylinder. The plume rising

Nomenclature

A, B and C = constants
D_i = inner cylinder diameter
D_0 = outer cylinder diameter
g = gravitational acceleration
$\overline{h}_i$ = average inner cylinder heat transfer coefficient, $Q/\pi D_i Z(T_i - T_0)$
h_i = local heat transfer coefficient on inner cylinder, $q_{w_i}/(T_i - T_0)$
h_0 = local heat transfer coefficient on outer cylinder, $q_{w_0}/(T_i - T_0)$
$\overline{h}_i'$ = average heat transfer coefficient on inner cylinder, $Q/\pi D_i Z(T_i - \overline{T}_b)$
$\overline{h}_0'$ = average heat transfer coefficient on outer cylinder, $Q/\pi D_0 Z(\overline{T}_b - T_0)$
k = thermal conductivity
k_{eq} = local equivalent conductivity, $h_i D_i \ln(D_0/D_i)/2k$ for inner cylinder, $h_0 D_0 \ln(D_0/D_i)/2k$ for outer cylinder
$\overline{k}_{\mathrm{eq}}$ = average equivalent conductivity, $\overline{\mathrm{Nu}}/\mathrm{Nu}_{\mathrm{cond}}$
$L = R_0 - R_i$
n = index of refraction
$\overline{\mathrm{Nu}}$ = Nusselt number for conduction or convection between horizontal concentric cylinders, $\mathrm{Nu}_{\mathrm{cond}}$ or $\mathrm{Nu}_{\mathrm{conv}}$
$\mathrm{Nu}_{\mathrm{cond}}$ = Nusselt number for conduction between concentric cylinders, $2/\ln(D_0/D_i)$
$\overline{\mathrm{Nu}}_{\mathrm{conv}}$ = Nusselt number for convection between concentric cylinders, $\overline{h}_i D_i/k$
$\overline{\mathrm{Nu}}_i'$ = Nusselt number for natural convection from a horizontal cylinder to an infinite fluid, $\overline{h}_i' D_i/k$
$\overline{\mathrm{Nu}}_0'$ = Nusselt number for quasi-steady natural convection to a fluid contained within a horizontal cylinder, $\overline{h}_0' D_0/k$
P = pressure
Pr = Prandtl number, ν/α
q_w = heat flux per unit area from cylinder surface
Q = rate of total heat flow
R = radial coordinate measured from center of inner cylinder
R' = distance from center of inner cylinder to outer cylinder, used for eccentric case
R_i = inner cylinder radius
R_0 = outer cylinder radius
Ra_{D_i} = inner cylinder Rayleigh number, $g\beta D_i^3(T_i - \overline{T}_b)/\nu\alpha$
Ra_{D_0} = outer cylinder Rayleigh number, $g\beta D_0^3(\overline{T}_b - T_0)/\nu\alpha$
Ra_L = Rayleigh number based on radius difference, $g\beta L^3 \Delta T/\nu\alpha$
T = temperature
$\overline{T}_b$ = average fluid temperature between inner and outer cylinder boundary layers
T_i = temperature of inner cylinder
T_0 = temperature of outer cylinder
Z = length of cylindrical annulus (along light beam)
α = thermal diffusivity
β = thermal coefficient of volumetric expansion
ϵ = distance inner cylinder is moved from a concentric position
ϵ_v = eccentricity along vertical axis (positive upwards)
θ = angular coordinate measured from top with center of inner cylinder as origin
θ' = angle measured from top to line joining centers of inner and outer cylinders with center of outer cylinder as origin
λ = wavelength of light
ν = kinematic viscosity
ϕ = dimensionless temperature, $(T - T_0)/T_i - T_0)$
$\overline{\phi}_b$ = average dimensionless fluid temperature between inner and outer cylinder boundary layers, $(\overline{T}_b - T_0)/(T_i - T_0)$, experimental values evaluated at $R_i + L/2$
ΔF = fringe shifts
ΔT = temperature difference between cylinders, $T_i - T_0$

Subscripts

i = evaluated at inner cylinder
0 = evaluated at outer cylinder

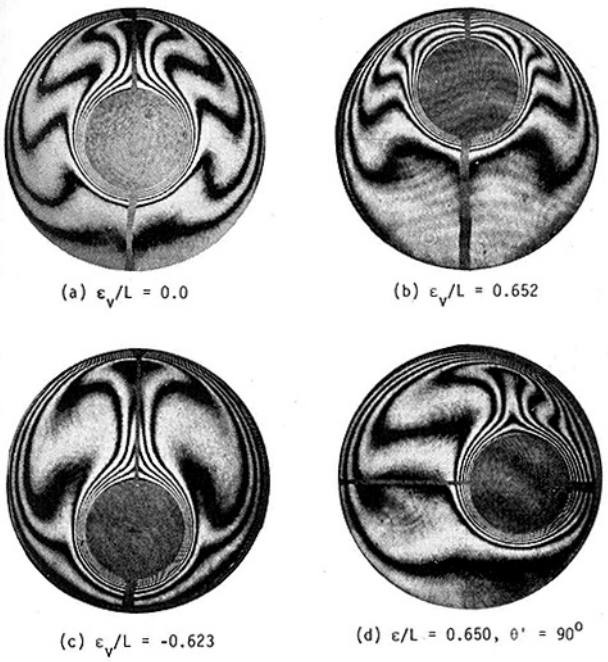

Fig. 2 Interferograms of eccentric tests using atmospheric air, $Ra_L \approx 4.8 \times 10^4$

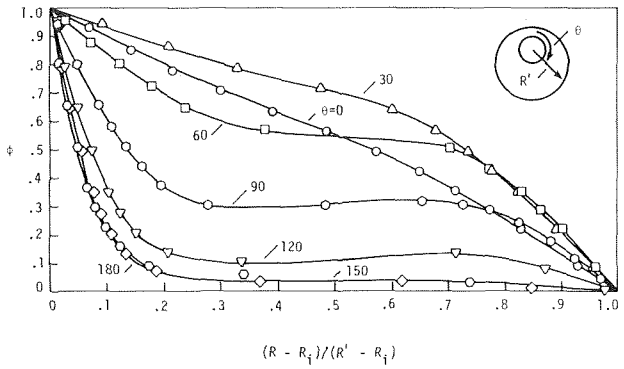

Fig. 3 Dimensionless temperature distribution for eccentric test, $\epsilon_v/L = 0.652$, $Ra_L = 4.80 \times 10^4$, Pr = 0.706

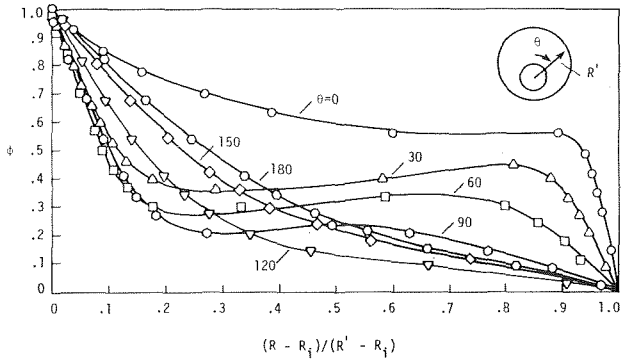

Fig. 4 Dimensionless temperature distribution for eccentric test, $\epsilon_v/L = -0.623$, $Ra_L = 4.93 \times 10^4$, Pr = 0.706

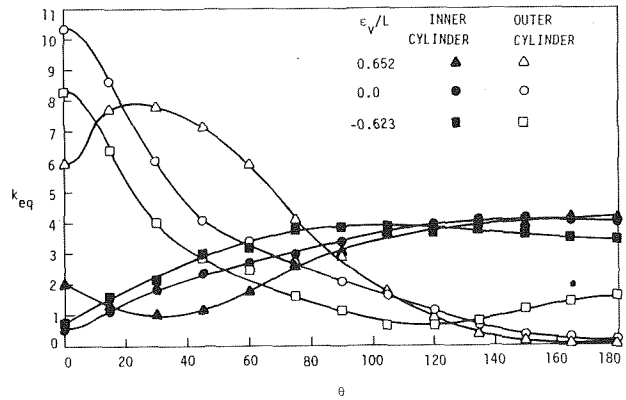

Fig. 5 Comparison of concentric and eccentric local heat transfer coefficients, $Ra_L \approx 5 \times 10^4$, Pr = 0.706

from the inner cylinder is well defined except when the inner cylinder is near the top of the cavity. In Fig. 2(*b*) there appear to be secondary cells above the inner cylinder causing a plume to separate on each side of the inner cylinder before the flow reaches the top. The plume observed in Fig. 2(*d*) does not rise vertically above the inner cylinder but deviates from the vertical. This deviation becomes more pronounced as the cylinder is moved closer to the top.

Each of the vertically eccentric interferograms has been analyzed quantitatively. The temperature distributions resulting from Fig. 2(*b*) and (*c*) are shown in Figs. 3 and 4, respectively. That corresponding to Fig. 2(*a*) was given in Fig. 15 of [12]. The distributions for angles larger than 90 deg in Fig. 3 and those less than 90 deg in Fig. 4 are similar in shape to those for the concentric case. However, the profiles in the regions where the two cylinders are close together are greatly distorted from those obtained when the cylinders are concentric. This can be seen for angles less than 90 deg in Fig. 3 and for angles larger than 90 deg in Fig. 4. This profile distortion is due primarily to the restriction of the flow in these regions which tends to result in a temperature profile closer to that for conduction between the cylinders than for a convective boundary layer.

Local heat transfer coefficients are plotted in Fig. 5 for the tests shown in Fig. 2(*a*), (*b*), and (*c*). The local values at the top of the annulus near $\theta = 0$ deviate considerably from the concentric geometry when the inner cylinder is moved up. A similar effect is seen near the bottom when the inner cylinder is moved down. One result of moving the inner cylinder down is to decrease the nonuniformity on the outer cylinder. The ratio of maximum to minimum local heat transfer coefficient on the outer cylinder is 86 when $\epsilon_v/L = \frac{2}{3}$, 80 when $\epsilon_v/L = 0$, and only 13 when $\epsilon_v/L = -\frac{2}{3}$.

The overall heat transfer coefficients for the eccentric tests were all found to be within 10 percent of that for the concentric geometry. The results tend to decrease by as much as 5 percent as the inner cylinder is moved up to $\epsilon_v/L = \frac{2}{3}$ and increase by 10 percent as the inner cylinder is moved down to $\epsilon_v/L = -\frac{2}{3}$. When the cylinders nearly touch, the large local heat transfer coefficient, due to conduction in the narrow gap, will increase the overall value considerably above that for convection in the concentric case. This will occur regardless of where the two cylinders are nearly touching. Zagromov and Lyalikov [10] found this condition when $\epsilon/L > 0.9$.

Effect of Rayleigh Number. Heat transfer results using the concentric geometry were obtained over the range $2.2 \times 10^2 \leq Ra_L \leq 7.7 \times 10^7$ using pressurized nitrogen as the test fluid. The resulting interference patterns were observed and photographed so that qualitative descriptions of the flow could be made and, in some cases, quantitative local heat transfer results could be determined.

The instantaneous interferograms shown in Fig. 6 cover much of the range of Rayleigh number studied. The progression is from nearly pure conduction in Fig. 6(*a*) to partially turbulent flow in Fig. 6(*f*).

The single fringe shift in Fig. 6(*a*) shows that the isotherms are distorted from the concentric configuration that would occur for pure conduction. The overall equivalent conductivity, $\bar{k}_{eq}$, is 1.38, which

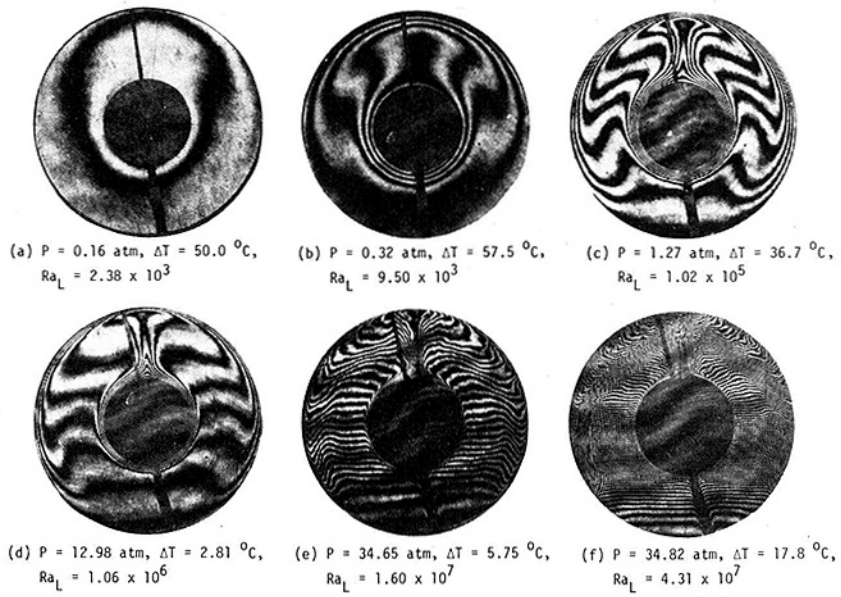

Fig. 6 Interferograms of concentric tests using pressurized nitrogen

indicates that the heat transfer is slightly larger than that of conduction.

Fig. 6(b) and (c) are in a steady laminar boundary layer regime. Thermal boundary layers can be seen adjacent to both cylinders. The temperature reversal in the central portion of the gap is caused by the strong recirculating flow pattern.

Oscillation of the plume above the inner cylinder was first observed near $Ra_L = 2 \times 10^5$. This agrees with the observations of [2, 4], and [5]. Oscillations near $Ra_L = 3 \times 10^5$ consist of an intermittent sideways swaying of the plume with no discernable regularity. Periodic fluctuations in the outer cylinder boundary layer were first observed near $Ra_L = 5 \times 10^5$. These consist of wave-like fluctuations that start near the top and travel along the outer cylinder boundary layer. The waves are attenuated as they move downward around the annulus. Fig. 6(d) shows the plume at its maximum amplitude with ripples in the outer cylinder boundary layer barely discernable in the upper half of the annulus.

Above $Ra_L = 1.5 \times 10^6$ there is no definite frequency of plume oscillation. As the Rayleigh number increases the plume tends to become more irregular, and the fluctuations in the outer cylinder boundary layer increase in intensity. The upper half of the plume appears to be turbulent in Fig. 6(e) at $Ra_L = 1.6 \times 10^7$. The irregular fringe pattern near the outer cylinder in the top half of the annulus indicates the location of turbulent flow. The lower half of the annulus remains virtually steady except for small disturbances moving downward in the outer cylinder boundary layer.

The entire plume is turbulent at $Ra_L = 2 \times 10^7$, but the remainder of the inner cylinder boundary layer is steady. As the Rayleigh number increases the turbulent portion adjacent to the inner cylinder spreads to include the top half of the inner cylinder boundary layer near $Ra_L = 8 \times 10^7$.

Quantitative results including temperature distributions and local heat transfer coefficients were obtained for $5 \times 10^4 < Ra_L < 3 \times 10^6$ using time averaged interferograms. The optical results are restricted to this range: too few fringes are obtainable at Rayleigh numbers less than this and refraction errors impose the upper limit.

Representative temperature profiles obtained near $Ra_L = 3 \times 10^6$ are given in Fig. 7. Profiles for air at $Ra_L = 5 \times 10^4$ were given in Fig. 15 of [13]. The profiles in Fig. 7 show the relatively thin boundary layers compared to the size of the gap and the continued presence of the temperature inversion in the center, although this is not as pronounced as at lower Rayleigh numbers. The average fluid temperature in the annulus is much lower than the logarithmic mean temperature.

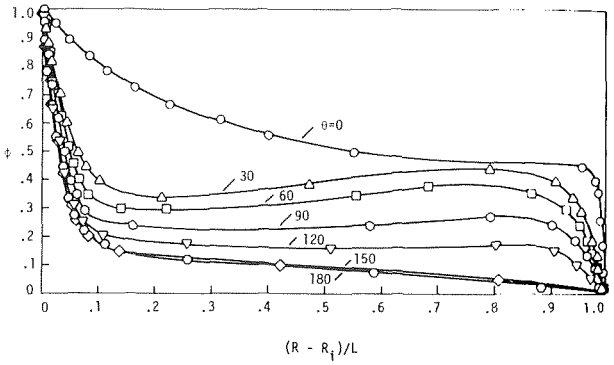

Fig. 7 Time averaged dimensionless temperature distribution at start of outer cylinder boundary layer unsteadiness, $Ra_L = 2.51 \times 10^6$

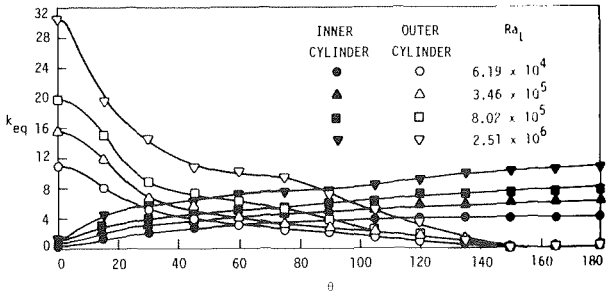

Fig. 8 Local heat transfer coefficient versus angular position at four Rayleigh numbers

This indicates that the maximum thermal resistance occurs across the inner cylinder boundary layer.

Analysis of the temperature gradients at the surface of each cylinder yields the local heat transfer coefficients. These are plotted for both cylinders versus angular position in Fig. 8 at four different Rayleigh numbers.

The heat transfer coefficients on the inner cylinder follow a distribution similar to that for a free horizontal cylinder. The maximum occurs at the stagnation point ($\theta = 180$ deg) with the minimum at the

plume separation point ($\theta = 0$ deg). The boundary layer of relatively uniform thickness that surrounds the inner cylinder gives little variation in heat transfer except near the top of the cylinder.

The situation is very different on the outer cylinder. The maximum local heat transfer coefficient is at the top due to the impinging plume. Within 30 deg of the top, the heat transfer is large. Between 30 deg and 150 deg a boundary layer exists, but the velocity decays rapidly as the flow moves toward the bottom of the annulus. The bottom portion of the gap is filled with nearly stagnant fluid. The ratio of maximum to minimum local heat transfer coefficient for the outer cylinder is approximately 100:1 whereas that for the inner cylinder is about 10:1 over the range in Rayleigh number shown in Fig. 8.

Overall heat transfer results are listed in Table 1. The maximum deviations between the overall measurements and the averaged inner cylinder optical results are 9.8 percent between the Rayleigh numbers and 7.6 percent between the averaged heat transfer coefficients. The standard deviations are approximately 3 percent for each.

The results can be well correlated by the following equations which are modified slightly from those given in [14] for Pr = 0.7.

$$\mathrm{Nu}_i' = \frac{2}{\ln\left[1 + \frac{2}{[(0.5\,\mathrm{Ra}_{D_i}{}^{1/4})^{15} + (0.12\,\mathrm{Ra}_{D_i}{}^{1/3})^{15}]^{1/15}}\right]} \tag{1a}$$

$$\mathrm{Nu}_0' = \frac{-2}{\ln\left[1 - \frac{2}{[(\mathrm{Ra}_{D_0}{}^{1/4})^{15} + (0.12\,\mathrm{Ra}_{D_0}{}^{1/3})^{15}]^{1/15}}\right]} \tag{1b}$$

$$\bar{\phi}_b = \frac{\mathrm{Nu}_i'}{\mathrm{Nu}_i' + \mathrm{Nu}_0'} \tag{1c}$$

$$\mathrm{Nu}_{\mathrm{conv}} = \left[\frac{1}{\mathrm{Nu}_i'} + \frac{1}{\mathrm{Nu}_0'}\right]^{-1} \tag{1d}$$

$$\mathrm{Nu}_{\mathrm{cond}} = 2/\ln(D_0/D_i) \tag{1e}$$

$$\mathrm{Nu} = [(\mathrm{Nu}_{\mathrm{cond}})^{15} + (\mathrm{Nu}_{\mathrm{conv}})^{15}]^{1/15} \tag{1f}$$

$$\bar{k}_{\mathrm{eq}} = \mathrm{Nu}/\mathrm{Nu}_{\mathrm{cond}} \tag{1g}$$

Equation (1) fits the data better than the general correlation given in [14] which was intended to show trends and limiting cases rather than be an accurate correlation for any one situation. The theory developed in [14] does not consider the effect of the recirculating flow on the inner cylinder boundary layer heat transfer coefficient. Flow recirculation should increase the heat transfer coefficients above those obtained for each cylinder separately. The term G in [14] accounts for this effect in laminar flow for the outer cylinder. The laminar coefficient for the inner cylinder has been increased empirically from 0.3987 to 0.5 and the coefficients for turbulent flow increased from 0.1 to 0.12 for both cylinders. The outer cylinder conduction term was removed since this simplifies the correlation without changing the results significantly. The resulting correlation fits all the present overall data with a standard deviation of 4.5 percent. The maximum error occurs near $\mathrm{Ra}_L = 10^3$ which is in the transition region from conduction to laminar convection. The standard deviation above $\mathrm{Ra}_L = 5 \times 10^3$ is 1.7 percent.

Previous experimental heat transfer correlations predict lower values of the heat transfer coefficient than obtained in the present study. The correlation of [2] gives a standard deviation of 26.1 percent for data above $\mathrm{Ra}_L = 9 \times 10^3$. The standard deviations using the correlations from [3] and [4] are 5.2 percent and 10.5 percent using data between $3 \times 10^4 < \mathrm{Ra}_L < 5 \times 10^5$ and larger than $\mathrm{Ra}_L = 6 \times 10^4$, respectively.

The dimensionless average fluid temperature near the center of the gap obtained from the present correlation agrees fairly well with the experimental results. The value of $\bar{\phi}_b$ from Fig. 7 is approximately 0.25 compared to 0.28 given by the correlation (1).

Conclusions

For natural convection heat transfer between horizontal isothermal cylinders, the overall heat transfer coefficient for an eccentric geometry with $\epsilon/L \leq 2/3$ is within 10 percent of that for the concentric case at the same Rayleigh number. However, the local coefficients on both cylinders change appreciably, particularly where the cylinders are very close. One effect of moving a heated inner cylinder below its concentric position is to make the local coefficients on the outer cylinder more uniform.

Results at large Rayleigh numbers show that the flow first becomes unsteady in the plume above the inner cylinder and that this becomes turbulent as the Rayleigh number is increased. The strong turbulence generated in the plume is convected to the outer cylinder near the plume impingement. This rapidly decays as the flow moves along the outer cylinder so that the bottom half of the annulus is virtually steady. Thus steady laminar flow and highly turbulent flow exist in the same flow loop in the cavity simultaneously. Local and overall heat transfer coefficients have been presented with a conduction film boundary layer model fitting the overall data for $\mathrm{Ra}_L > 5 \times 10^3$ with a standard deviation of 1.7 percent.

Table 1 Overall heat transfer results with horizontal concentric cylinders using pressurized nitrogen $D_0/D_1 = 2.6$

P (atm)	ΔT (°C)	$\frac{1}{2}(T_i + T_0)$ (°C)	Ra_L	Pr	$\bar{k}_{\mathrm{eq}}$
0.071	16.4	32.4	2.21×10^2	0.719	0.97
0.067	49.7	53.3	4.96×10^2	0.716	1.00
0.065	58.8	54.2	5.44×10^2	0.716	1.02
0.081	58.0	52.0	8.26×10^2	0.717	1.06
0.110	53.5	51.1	1.31×10^3	0.717	1.14
0.164	50.0	53.3	2.38×10^3	0.716	1.38
0.191	60.1	55.0	3.66×10^3	0.716	1.53
0.269	49.6	53.0	5.91×10^3	0.717	1.82
0.320	57.5	53.2	9.50×10^3	0.717	2.01
0.408	48.4	52.4	1.29×10^4	0.717	2.25
0.491	52.8	52.6	2.08×10^4	0.717	2.47
0.651	48.8	52.5	3.20×10^4	0.717	2.89
0.977	38.0	44.4	6.19×10^4	0.718	3.32
1.27	36.7	43.2	1.02×10^5	0.718	3.66
1.82	23.2	36.6	1.44×10^5	0.718	3.97
2.76	13.7	32.8	2.25×10^5	0.719	4.39
4.58	7.56	27.8	3.46×10^5	0.720	4.76
5.78	5.62	28.9	4.05×10^5	0.720	5.00
6.88	4.66	28.1	4.86×10^5	0.721	5.25
8.46	4.29	27.3	6.81×10^5	0.721	5.60
10.3	3.39	27.5	8.02×10^5	0.722	5.91
13.0	2.81	27.6	1.06×10^6	0.723	6.47
17.0	1.99	27.5	1.30×10^6	0.725	6.69
21.7	1.58	27.2	1.70×10^6	0.727	7.05
33.5	0.83	27.6	2.14×10^6	0.731	7.44
34.6	0.91	27.7	2.51×10^6	0.731	7.88
34.9	1.28	25.3	3.75×10^6	0.732	8.42
34.8	1.82	25.5	5.26×10^6	0.732	9.24
34.5	2.38	25.8	6.75×10^6	0.732	10.15
34.6	3.32	25.4	9.53×10^6	0.732	10.68
34.7	4.48	26.6	1.27×10^7	0.732	11.83
34.7	5.75	27.5	1.60×10^7	0.732	12.56
34.7	7.01	29.1	1.90×10^7	0.731	13.27
34.2	8.98	31.4	2.27×10^7	0.731	13.67
34.8	11.4	33.0	2.92×10^7	0.731	14.78
34.6	14.2	34.7	3.48×10^7	0.730	15.59
34.8	17.8	36.6	4.31×10^7	0.730	16.53
35.2	22.7	37.6	5.53×10^7	0.730	17.66
35.0	28.7	40.8	6.60×10^7	0.729	18.65
34.4	37.9	46 1	7.74×10^7	0.728	19.64

Acknowledgment

The authors wish to acknowledge the University of Minnesota Computer Center for a grant of computer time, the National Science foundation for support under Grant ENG 75-01091, an NDEA IV Fellowship for one of the authors (T.H.K.), and partial support from the Engineering Research Institute, Iowa State University.

References

1 Beckmann, W., "Die Wärmeübertragung in Zylindrischen Gasschichten bei natürlicher Konvektion," *Forschung auf dem Gebiete des Ingenieurwesens*, Bd. 2, Heft 5, 1931, pp. 165–178.

2 Liu, C. Y., Mueller, W. K., and Landis, F., "Natural Convection Heat Transfer in Long Horizontal Cylindrical Annuli," ASME *International Developments in Heat Transfer*, Pt. 4, 1961, pp. 976–984.

3 Grigull, U., and Hauf, W., "Natural Convection in Horizontal Cylindrical Annuli," Third International Heat Transfer Conference, 1966, pp. 182–195.

4 Lis, J., "Experimental Investigation of Natural Convection Heat Transfer in Simple and Obstructed Horizontal Annuli," Third International Heat Transfer Conference, 1966, pp. 196–204.

5 Bishop, E. H., and Carley, C. T., "Photographic Studies of Natural Convection Between Concentric Cylinders," *Proceedings of the 1966 Heat Transfer Fluid Mechanics Institute*, pp. 63–78.

6 Bishop, E. H., Carley, C. T., and Powe, R. E., "Natural Convective Oscillatory Flow in Cylindrical Annuli," *International Journal of Heat and Mass Transfer*, Vol. 11, 1968, pp. 1741–1752.

7 Powe, R. E., Carley, C. T., and Bishop, E. H., "Free Convective Flow Patterns in Cylindrical Annuli," ASME JOURNAL OF HEAT TRANSFER, Vol. 91, 1969, pp. 310–314.

8 Kraussold, H., "Wärmeabgabe von zylindrischen Flüssigkeitschichten bei natürlicher Konvektion," *Forschung auf dem Gebiete des Ingenieurwesens* Bd. 5, Heft 4, 1934, pp. 186–191.

9 Koshmarov, Y. A., and Ivanov, A. Y., "Experimental Study of Heat Transfer Through a Rarefield Gas Between Coaxial Cylinders," *Heat Transfer-Soviet Research*, Vol. 5, 1973, pp. 29–36.

10 Zagromov, Y. A., and Lyalikov, A. S., "Free Convection Heat Transfer in Horizontal Cylindrical Layers with Different Positions of the Heated Element," *Inzhenerno-Fizicheskii Zhurnal*, Vol. 10, 1966, pp. 577–583.

11 Seki, N., Fukusato, S., and Nakaoka, M., "An Analysis of Free Convective Heat Transfer with Density Inversion of Water Between Two Horizontal Concentric Cylinders," ASME JOURNAL OF HEAT TRANSFER, Vol. 98, 1976, pp. 670–672.

12 Kuehn, T. H., and Goldstein, R. J., "An Experimental and Theoretical Study of Natural Convection in the Annulus Between Horizontal Concentric Cylinders," *Journal of Fluid Mechanics*, vol. 74, 1976, pp. 695–719

13 Kuehn, T. H., "Natural Convection Heat Transfer from a Horizontal Circular Cylinder to a Surrounding Cylindrical Enclosure," Ph.D. Thesis, University of Minnesota, 1976.

14 Kuehn, T. H., and Goldstein, R. J., "Correlating Equations for Natural Convection Heat Transfer Between Horizontal Circular Cylinders," *International Journal of Heat and Mass Transfer*, Vol. 19, 1976, pp. 1127-1134.

A. Bejan

Assistant Professor.
Department of Mechanical Engineering,
University of Colorado,
Boulder, Colo. 80309

C. L. Tien

Professor.
Department of Mechanical Engineering,
University of California,
Berkeley, Calif. 94720

Laminar Natural Convection Heat Transfer in a Horizontal Cavity with Different End Temperatures

The heat transfer by free convection in a horizontal cavity with adiabatic horizontal walls and differentially heated end walls is studied analytically. The paper develops three models for explaining and predicting the heat transfer mechanism in a cavity with the height/length aspect ratio considerably smaller than one. The three models are: 1) the regime of vanishing Rayleigh numbers, 2) the intermediate regime, and 3) the boundary layer regime. The transition from one model to the next occurs as the Rayleigh number increases. The Nusselt number prediction based on the three-regime theory agrees very well with available numerical and experimental heat transfer data.

Introduction

As shown by Ostrach [1], the gravity-induced flow in slender horizontal enclosures exposed to axial temperature gradients has received relatively little attention in the literature. The single comprehensive treatment of a flow of this type was published only recently in a series of four articles by Cormack, Leal and Imberger [2], Cormack, Leal and Seinfeld [3], Imberger [4], and Cormack, Stone and Leal [5]. These authors investigated the flow in a shallow horizontal cavity with differentially heated end-walls with application to the convection of heat in estuaries and other shallow bodies of water used for waste heat disposal. The geometry considered in the first three articles, Fig. 1, consists of a two-dimensional cavity with a height-to-length ratio much smaller than unity, $h/L \ll 1$. The two end-walls are maintained at different temperatures, T_a and T_b, and the two horizontal walls are adiabatic. The authors studied this flow analytically [2], numerically [3], and experimentally [4]. They showed that when h/L is small, the flow pattern is composed of two major regions: 1) the core region, containing a parallel counterflow in which the warmer branch resides in the upper half of the cross-section, 2) the end region, with a length of the order of h or smaller, turning the parallel counterflow around by 180 deg. The flow pattern and the two regions of interest are shown schematically in Fig. 1.

The objective of this paper is to develop an approximate theory for predicting the net heat transfer between the two ends of the enclosure. Cormack, et al. [2] derived an asymptotic result for the overall Nusselt number valid only in the limit $h/L \to 0$. In this limit, the resistance to heat transfer is due entirely to the ideal thermal contact existing between the two branches of the core region counterflow. In the present paper we consider the more general heat transfer problem, namely, an enclosure with h/L small but finite. We show that as the Rayleigh number increases, the flow pattern changes enough so that the asymptotic Nusselt number theory [2] no longer applies. When the Rayleigh number is high enough, the main resistance to heat transfer is due to two thin boundary layers lining the end-walls. Also, there exists an intermediate regime of moderate Rayleigh numbers in which the boundary layers and the core counterflow have comparable effects on the net heat transfer rate between the two ends of the enclosure. In what follows we develop a complete set of analytical results for the Nusselt number corresponding to the three regimes. In doing so, we find excellent agreement between our theory and heat transfer data predicted numerically by Cormack, et al. [3] and measured experimentally by Imberger [4].

Mathematical Formulation

The equations governing the flow of viscous incompressible fluid in the horizontal rectangular enclosure are

$$\frac{\partial u}{\partial x} + \frac{\partial v}{\partial y} = 0 \tag{1}$$

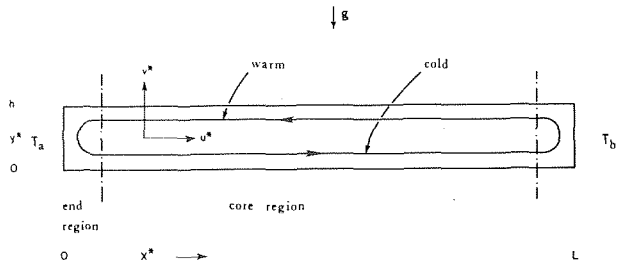

Fig. 1 Schematic of free convection pattern in horizontal cavity with different end temperatures

Contributed by the Heat Transfer Division for publication in the JOURNAL OF HEAT TRANSFER. Manuscript received by the Heat Transfer Division April 5, 1978.

$$u\frac{\partial T}{\partial x}+v\frac{\partial T}{\partial y}=\frac{\partial^2 T}{\partial x^2}+\frac{\partial^2 T}{\partial y^2} \tag{2}$$

$$\frac{1}{\mathrm{Pr}}\left(u\frac{\partial u}{\partial x}+v\frac{\partial u}{\partial y}\right)=-\frac{\partial P}{\partial x}+\frac{\partial^2 u}{\partial x^2}+\frac{\partial^2 u}{\partial y^2} \tag{3}$$

$$\frac{1}{\mathrm{Pr}}\left(u\frac{\partial v}{\partial x}+v\frac{\partial v}{\partial y}\right)=-\frac{\partial P}{\partial y}+\mathrm{Ra}\cdot T+\frac{\partial^2 v}{\partial x^2}+\frac{\partial^2 v}{\partial y^2} \tag{4}$$

Equations (1–4) have been nondimensionalized by defining x, y, u, v, T and P as

$$x=x^*/h,\quad y=y^*/h \tag{5}$$

$$u=u^*h/\alpha,\quad v=v^*h/\alpha \tag{6}$$

$$T=\frac{T^*-T_a}{T_b-T_a},\quad P=\frac{P^*h^2}{\rho\alpha\nu} \tag{7}$$

where the asterisks indicate the dimensional variables of the problem. In deriving equations (1–4) we relied on the usual Boussinesq approximation, $\rho=\rho_0[1-\beta(T^*-T_a)]$. The intensity of the free convection effect is characterized by the Rayleigh number based on height,

$$\mathrm{Ra}=\frac{g\beta h^3(T_b-T_a)}{\alpha\nu}. \tag{8}$$

Without loss of generality, it is assumed that the right end of the enclosure is warmer than the left, $T_b > T_a$, as shown by the direction of the counterflow on Fig. 1.

Equations (1–4) are to be solved subject to the following conditions which account for the four solid walls:

$$u=v=0,\quad \partial T/\partial y=0\quad \text{at } y=0,1 \tag{9}$$

$$u=v=0,\quad T=0,1\quad \text{at } x=0,L/h \tag{10}$$

The Heat Transfer Problem

As stated in the Introduction, the objective of this work is to develop analytical means for estimating the heat transfer rate in the system of Fig. 1. One can regard this system as a thermosyphon oriented horizontally between two bodies with different temperatures. Since the long horizontal walls are adiabatic, heat transfer occurs only in the horizontal direction, at a rate per unit width q(W/m) to be determined. Based on our assumption $T_b > T_a$, the heat transfer rate q is considered positive from right to left on Fig. 1.

The overall Nusselt number for net heat transfer in the horizontal direction is defined as

$$\mathrm{Nu}=\frac{q}{k(T_b-T_a)} \tag{11}$$

The magnitude of Nu can be estimated by performing an energy flux analysis over any vertical cross-section,

$$\mathrm{Nu}=\int_0^1\left(\frac{\partial T}{\partial x}-uT\right)dy,\quad x=\text{constant}. \tag{12}$$

A special form of equation (12) used later in this study comes from evaluating integral (12) over one of the two end walls, say the wall at $x = 0$,

$$\mathrm{Nu}=\int_0^1\left(\frac{\partial T}{\partial x}\right)_{x=0}dy. \tag{13}$$

As in most convective heat transfer problems, in order to calculate the Nusselt number we must first determine the velocity and temperature distribution in the fluid filling the enclosure. In the next three sections we derive the flow and temperature field for three laminar flow regimes brought on by increasing the Rayleigh number (Ra) while keeping the aspect ratio (h/L) constant and small.

The Ra → 0 Regime

Cormack, et al. [2] showed that for a slender horizontal cavity with $h/L \ll 1$ the flow in the core region is characterized by horizontal streamlines and by a constant temperature gradient in the x direction. In terms of our notation, their result is

$$u_c(y)=K_1\mathrm{Ra}\left(\frac{y^3}{6}-\frac{y^2}{4}+\frac{y}{12}\right),\quad v_c=0 \tag{14, 15}$$

$$T_c(x,y)=K_1x+K_2+K_1{}^2\mathrm{Ra}\left(\frac{y^5}{120}-\frac{y^4}{48}+\frac{y^3}{72}\right), \tag{16}$$

where subscript c stands for core solution. The two parameters K_1, K_2 are arbitrary at this point. Eventually, K_1 and K_2 will be determined from meshing the core solution with the flow and temperature pattern prevailing in the two end regions. For clarity, the velocity and temperature profiles in the core region have been reproduced on Fig. 2. The core flow constitutes a natural counterflow heat exchanger with balanced streams, hence, with constant temperature difference between streams. The warmer current occupies the upper half of the parallel-plate space and is cooled gradually as it proceeds from right to left.

The core solution (14–16) is based on an asymptotic analysis in parameter h/L small, Ra and Pr being arbitrary but fixed [2]. An interesting feature of this solution is that the velocity field is parallel, to all orders in the small parameter h/L. This means that the core flow is described by equations (14–16) as long as $h/L \ll 1$, parameters K_1 and K_2 being functions of the dimensionless groups governing the phenomenon, Ra, h/L and Pr.

Fig. 3 shows schematically the temperature distribution along the top and bottom walls of the horizontal enclosure. We see that in the core region the temperature difference in the y direction (ΔT) is constant, $\Delta T = K_1{}^2\mathrm{Ra}/720$. The unknown parameter K_1 is the horizontal temperature gradient in the core region, $\partial T_c/\partial x$. The temperature difference between the top and bottom walls ΔT increases as Ra increases. However, since ΔT cannot exceed unity, the horizontal temperature gradient K_1 must steadily decrease as Ra increases.

Using the core solution (14–16), the Nusselt number (12) can be expressed in terms of Ra and K_1,

Nomenclature

b = constant, equation (32)
g = gravitational acceleration
h = height of enclosure
k = thermal conductivity
K_1, K_2 = parameters of core flow
L = length of enclosure
$M_{b\ell}$ = boundary layer flow rate, equation (44)
M_c = core flow rate, equation (45)
Nu = Nusselt number, equation (11)
P = pressure
Pr = Prandtl number, ν/α
q = heat transfer rate per unit width
Ra = Rayleigh number, equation (8)
T = temperature
T_a, T_b = end temperature
ΔT = temperature difference between the upper and lower wall $K_1{}^2\mathrm{Ra}/720$
u = horizontal velocity
v = vertical velocity
x = horizontal coordinate
y = vertical coordinate
( )* = dimensional variables
( )$_c$ = core region
α = thermal diffusivity
β = coefficient of thermal expansion
γ = factor, equation (36)
Γ = factor, equation (34)
δ = extent of end region, Fig. 3
λ = boundary layer thickness
ν = kinematic viscosity
ρ = density

$$\mathrm{Nu} = K_1 + \frac{K_1^3 \mathrm{Ra}^2}{362880}, \tag{17}$$

which demonstrates that the ability of estimating the Nusselt number hinges on determining the horizontal temperature gradient K_1.

In the limit $\mathrm{Ra} \to 0$ the core temperature distribution is independent of y, as shown by equation (16) and Fig. 3. In this limit the temperature varies linearly between the two ends and, by writing

$$T_c = 0 \text{ at } x = 0 \quad \text{and} \quad T_c = 1 \text{ at } x = L/h \tag{18}$$

we find

$$K_1 = h/L \quad \text{and} \quad K_2 = 0. \tag{19}$$

Combining this result with equation (17) we obtain

$$\mathrm{Nu}\,\frac{L}{h} = 1 + \frac{1}{362880}\left(\mathrm{Ra}\,\frac{h}{L}\right)^2 \tag{20}$$

where the second term represents the heat transfer contribution due to free convection. The group $\mathrm{Ra}\,h/L$ which dictates the size of this contribution is the equivalent of a Rayleigh number based on the imposed horizontal temperature gradient $(T_b - T_a)/L$.

It is important to point out that the Nusselt number expression (20) is valid not only in the limit $\mathrm{Ra} \to 0$ and h/L finite, as derived. In addition, the same expression holds in the limit $h/L \to 0$ and Ra finite, which is the limit considered by Cormack, et al. [2]. Expression (20) could have been derived based on equation (16) and Fig. 3 arguing that for a fixed Ra and h/L tending to zero, the temperature gradient K_1 (hence ΔT) also approaches zero. Comparing expression (20) with the asymptotic result reported by Cormack, et al. [2] we find that $1/362880 = 2.76 \times 10^{-6}$ replaces the coefficient 2.86×10^{-6} found numerically in [2].

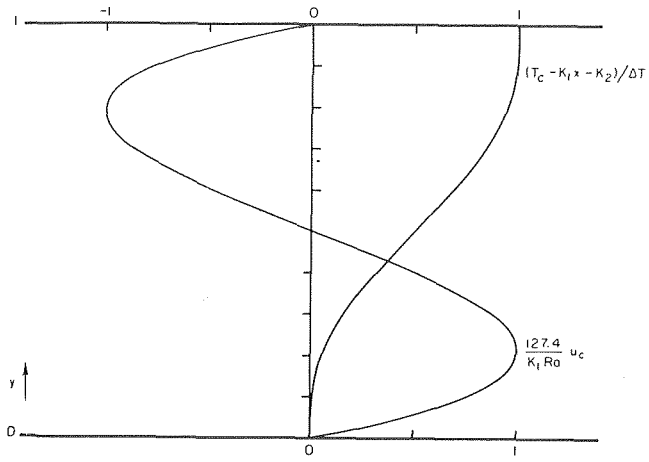

Fig. 2 Horizontal velocity profile and temperature distribution in the core region

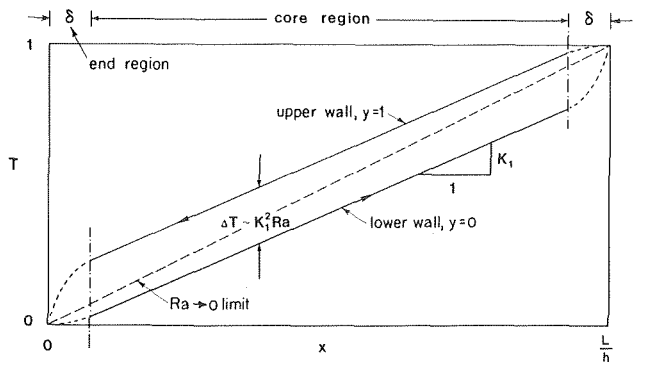

Fig. 3 Schematic of temperature distribution along the top and bottom walls of the horizontal rectangular cavity shown in Fig. 1

The Intermediate Regime

As indicated on Fig. 3, increasing the Rayleigh number accentuates the thermal stratification of the core flow. In this section we analyze the intermediate case where the ΔT between the upper and lower walls is no longer negligible but is still smaller than unity. Here we determine parameters K_1 and K_2, which define the core flow and the Nusselt number, by matching the core solution with an integral solution for the flow and temperature field in the end region. This procedure has been previously developed and used by Bejan and Tien [6] in the study of heat transfer by natural convection in a horizontal space filled with a fluid-saturated porous medium. For this reason, only the main points of this analysis are discussed.

We define the end region length δ as that segment of the horizontal enclosure within which the core solution (14–16) breaks down. Inside the end region, $0 < x < \delta$, the flow is turned around and cooled as it comes in contact with the vertical wall at $x = 0$. We seek integral constraints for the unknown parameters K_1 and K_2. The energy constraint is obtained by integrating equation (2) twice, the first time from $y = 0$ to $y = 1$ and the second time from $x = \delta$ to $x = \delta$. For the momentum integral constraint we first eliminate the pressure terms between equations (3) and (4). The resulting equation is then integrated twice, like the energy equation. The energy and momentum equations are

$$\int_0^1 \left|\frac{\partial T}{\partial x}\right|_{x=0} dy = K_1 - \int_0^1 |uT|_{x=\delta}\, dy \tag{21}$$

$$\mathrm{Ra}\left|\int_0^1 T dy\right|_{x=0}^{x=\delta} = \int_0^\delta \left|\frac{\partial^2 u}{\partial y^2}\right|_{y=0}^{y=1} dx - \left|\frac{d^2}{dx^2}\int_0^1 v dy\right|_{x=0}^{x=\delta} \tag{22}$$

The next step is the selection of reasonable profiles for the velocity and temperature distribution inside the end region. The general rule in performing this operation is to select profiles which satisfy the boundary conditions along the solid walls $y = 0, 1$, $x = 0$ and match the value and slope of the core profiles at $x = \delta$ as shown on Fig. 4. Thus, the chosen profiles are

$$u = K_1 \mathrm{Ra}\left(\frac{x}{\delta}\right)^2\left[6 - 8\frac{x}{\delta} + 3\left(\frac{x}{\delta}\right)^2\right]\left(\frac{y^3}{6} - \frac{y^2}{4} + \frac{y}{12}\right) \tag{23}$$

$$v = \frac{-K_1 \mathrm{Ra}}{\delta}\left(\frac{x}{\delta}\right)\left(1 - \frac{x}{\delta}\right)^2\left(\frac{y^4}{2} - y^3 + \frac{y^2}{2}\right) \tag{24}$$

$$T = (T_c - \delta K_1)\left[2\frac{x}{\delta} - \left(\frac{x}{\delta}\right)^2\right] + K_1 x. \tag{25}$$

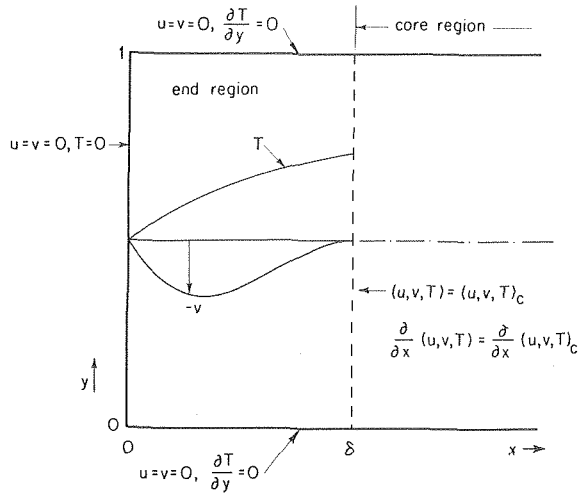

Fig. 4 Boundary and matching conditions for integral analysis of the end region

where u and v also satisfy the continuity equation (1) at any given point inside the end region. The core temperature T_c appearing in equation (25) is given by equation (16). Substituting expressions (23-25) into the integral constraints (21, 22) yields

$$\frac{K_1^3 \mathrm{Ra}^2 \delta}{725760} = K_2 + \frac{K_1^2 \mathrm{Ra}}{1440} \tag{26}$$

$$\frac{2}{5} K_1 \delta \left(\frac{1}{4\delta^4} - 1 \right) = K_2 + \frac{K_1^2 \mathrm{Ra}}{1440}, \tag{27}$$

showing $\delta \to 1/\sqrt{2}$ as $\mathrm{Ra} \to 0$ and also $\delta < 1/\sqrt{2}$ for any Ra finite. Thus, we obtained two equations (26, 27) for K_1 and K_2 in terms of Ra and the new unknown δ. The third equation necessary for uniquely determining parameters K_1 and K_2 comes from accounting for the flow around the $x = L/h$ end. This task is equivalent to noticing that the flow in the entire cavity is symmetric about the center of the cavity. The centrosymmetry condition can also be expressed as

$$T_c \left(\frac{L}{2h}, \frac{1}{2} \right) = \frac{1}{2}, \tag{28}$$

i.e., the temperature in the center is the arithmetic mean of the two end temperatures.

Equations (26–28) constitute the needed set of conditions for determining K_1, K_2 and δ as functions of Ra and h/L. Based on this result and equation (17), the Nusselt number calculation becomes straightforward. However, the Nusselt number relationship is implicit and cannot be reported in the form of a simple algebraic expression. Instead, the Nusselt number was plotted directly on Fig. 5 as the solid lines along with the numerical results of Cormack, et al. [3] and the experimental data reported by Imberger [4]. The agreement between our theory and the numerical Nusselt number estimates [3] is excellent. The experimental data [4] fall within 30 percent of our prediction. It is shown in the next section that Imberger's experimental results [4] which correspond to relatively high Rayleigh numbers (10^7–10^8) are better correlated by a boundary layer theory. In fact, the solid lines of Fig. 5 show the gradual transition from a Nusselt number dominated by the long counterflow thermal resistance, as in the $\mathrm{Ra} \to 0$ limit or the $h/L \to 0$ limit expressed by equation (20) where $\mathrm{Nu} \sim \mathrm{Ra}^2$, to a boundary layer heat transfer regime where, as shown below, $\mathrm{Nu} \sim \mathrm{Ra}^{1/5}$.

The Boundary Layer Regime

We consider now the high Rayleigh number range when the temperature difference between the top and bottom walls, ΔT, is comparable with unity. As shown by the experiments performed by Imberger [4] on water-filled enclosures with aspect ratios 1/100 and 1/50,

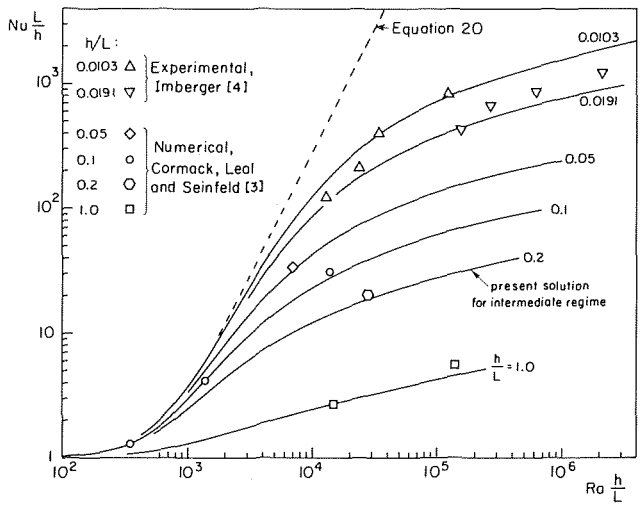

Fig. 5 Nusselt number chart showing the present theory for the intermediate regime vis-a-vis published numerical and experimental heat transfer data

in the high Ra range the horizontal temperature gradient K_1 can become at least one order of magnitude smaller than h/L. The strong temperature variation is confined to two very thin layers of fluid adjacent to the end walls. The boundary layers are similar to the ones occurring in vertical enclosures with different vertical wall temperatures, as discussed by Elder [7] and Gill [8], and recently by Quon [9]. One noteworthy feature of this type of boundary layer is that it is driven not by the imposed temperature difference between the vertical walls, but by the difference between each vertical wall and the thermally stratified fluid filling the core region. Another important feature is that at midheight, $y = 1/2$, the boundary layer exhibits no entrainment of core fluid, i.e., the horizontal velocity component u is zero across the boundary layer. Below, we will use these observations in developing a boundary layer theory for heat transfer in the horizontal enclosure with different end temperatures.

Specifically, we match the core solution (14–16) with a boundary layer solution in a region situated around the midheight point $y = 1/2$. Now, for the boundary layer solution consider the $x = 0$ vertical layer of thickness λ, where the horizontal length scale λ is considerably smaller than the cavity height h. It is shown later that λ/h is considerably smaller than unity provided the Rayleigh number is high enough [see equation (41)]. Consequently, equations (1–4) can be simplified by neglecting the $\partial^2/\partial y^2$ terms in favor of the $\partial^2/\partial x^2$ terms. Using the zero entrainment condition $u = 0$, the boundary layer equations become

$$\partial v/\partial y = 0, \quad v \frac{\partial T}{\partial y} = \frac{\partial^2 T}{\partial x^2} \tag{29, 30}$$

$$\mathrm{Ra} \frac{\partial T}{\partial x} + \frac{\partial^3 v}{\partial x^3} = 0 \tag{31}$$

Proceeding on a path similar to Gill's boundary layer solution for vertical cavities [8], we regard $\partial T/\partial y$ appearing in equation (30) as a known constant

$$\partial T/\partial y = b^4/\mathrm{Ra} \tag{32}$$

We later relate this constant to the vertical temperature gradient present outside the boundary layer, in the core region. Substituting constant (32) into equation (30), and eliminating the temperature between equations (30) and (31) we obtain a single equation for $v(x)$

$$\partial^4 v/\partial y^4 + b^4 v = 0. \tag{33}$$

The solution satisfying the $v(0) = \lim_{bx \to \infty} v = 0$ conditions is

$$v = -\Gamma \sin \frac{bx}{\sqrt{2}} e^{-bx/\sqrt{2}}, \tag{34}$$

Γ being an arbitrary constant. Substituting expression (34) back into equation (31), integrating once and setting $T(0) = 0$ we find

$$T = \frac{\Gamma b^2}{\mathrm{Ra}} \left[1 - \cos \frac{bx}{\sqrt{2}} e^{-bx/\sqrt{2}} \right]. \tag{35}$$

The boundary layer solution (34, 35) depends on two arbitrary parameters, b and Γ. Fig. 6 presents a sketch of v/Γ and $T\mathrm{Ra}/(2\Gamma b^2)$ in the vicinity of the vertical wall. We recognize now that the inverse of b plays the role of dimensionless boundary layer thickness, i.e., λ/h.

The unknowns b and Γ are determined from matching the boundary layer solution (34, 35) with the core solution at $y \approx 1/2$. For the vertical temperature gradient constant we write

$$\frac{\partial T}{\partial y} = \gamma \left(\frac{\partial T_c}{\partial y} \right)_{y=1/2}, \tag{36}$$

in which γ is a number of the order of 1/2 accounting for the fact that across the boundary layer $\partial T/\partial y$ varies from 0 at the wall to a maximum $\partial T_c/\partial y$ in the core region. A second matching condition results from the observation that in the boundary layer regime the temperature in the core region at mid-height is nearly isothermal approaching $(T_a + T_b)/2$. This observation is supported strongly by Imberger's

temperature measurements [4]. We write then

$$\lim_{bx \to \infty} T = \frac{1}{2}. \tag{37}$$

In conclusion, the matching conditions (36, 37) yield

$$\frac{b^4}{\mathrm{Ra}} = \frac{\gamma}{384} K_1{}^2 \mathrm{Ra} \quad \text{and} \quad \frac{\Gamma b^2}{\mathrm{Ra}} = \frac{1}{2}. \tag{38, 39}$$

The solution is still incomplete since K_1 appearing in equation (38) is unknown. One last equation, sufficient for determining K_1, results from an energy conservation argument in the horizontal direction. Combining equations (35) and (13) and setting the calculated Nusselt number equal to the core solution-based expression (17), we find

$$\mathrm{Nu} = \frac{\Gamma b^3}{\mathrm{Ra}\sqrt{2}} = \frac{K_1{}^3 \mathrm{Ra}^2}{362880}. \tag{40}$$

In reproducing expression (17) as the right hand side of equation (40) we neglected K_1 relative to the convective term $K_1{}^3\mathrm{Ra}^2/362880$. Finally, combining equations (38–40) we obtain

$$b^{-1} = 0.567\, \gamma^{-3/10}\, \mathrm{Ra}^{-1/5} \sim \lambda/h \tag{41}$$

$$K_1 = 60.93\, \gamma^{1/10}\, \mathrm{Ra}^{-3/5} \tag{42}$$

$$\mathrm{Nu} = 0.623\, \gamma^{3/10}\, \mathrm{Ra}^{1/5} \tag{43}$$

The unknown γ introduced by assumption (36) plays only a minor role if its approximate value is indeed 1/2, or larger, perhaps. We learn more about the value of γ by considering the net flowrate carried upward in the $x = 0$ boundary layer and comparing it with the flowrate in one branch of the core region counterflow. Calculating

$$M_{b\ell} = -\int_0^\infty v\,dx \quad \text{and} \quad M_c = \int_0^{1/2} u\,dy \tag{44, 45}$$

we find

$$\gamma = 0.405 \frac{M_c}{M_{b\ell}}. \tag{46}$$

Result (46) demonstrates that γ is greater than 0.405 since, as shown by Imberger [3], in the boundary layer regime the core flow gradually departs from the parallel counterflow structure sketched in Fig. 1. When Ra exceeds 10^7–10^8, the core streamlines situated about $y = 1/2$ close inside the core region without ever entering the boundary layer. This observation suggests that $M_c/M_{b\ell}$ is actually greater than unity. For all practical purposes it is then reasonable to replace the γ terms by unity in equations (41–43).

Fig. 7 shows the boundary layer Nusselt number

$$\mathrm{Nu} \simeq 0.623\, \mathrm{Ra}^{1/5} \tag{47}$$

vis-a-vis Imberger's experimental results [4]. The experimental data, obtained in two different cavity geometries, fall on the same curve asymptotically approaching the theoretical Nu (47). One interesting feature of this result is that the heat transfer rate is independent of the aspect ratio h/L.

Fig. 8 presents a similar comparisón between the measured horizontal temperature gradient K_1 and the theoretical result

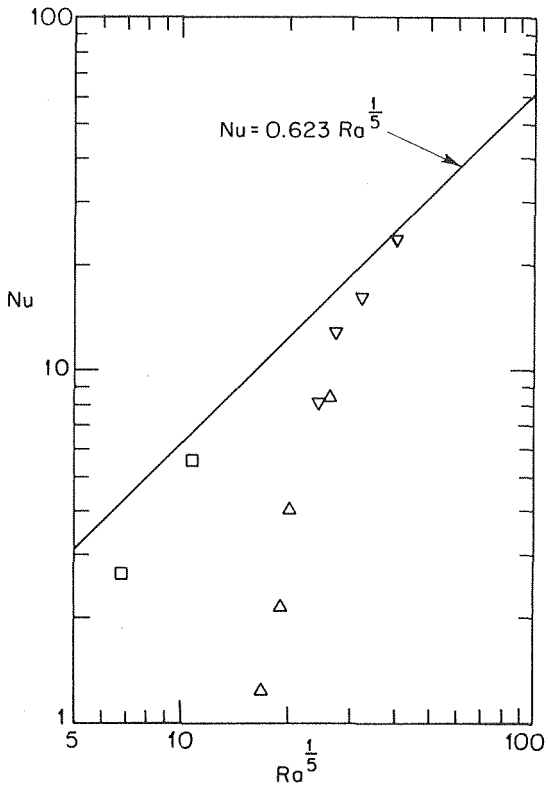

Fig. 7 Nusselt number chart comparing the present result for the boundary layer regime, equation (47), with Imberger's experimental data [4] and the numerical simulation for a square cavity [3]. For legend see Figs. 5, and 9.

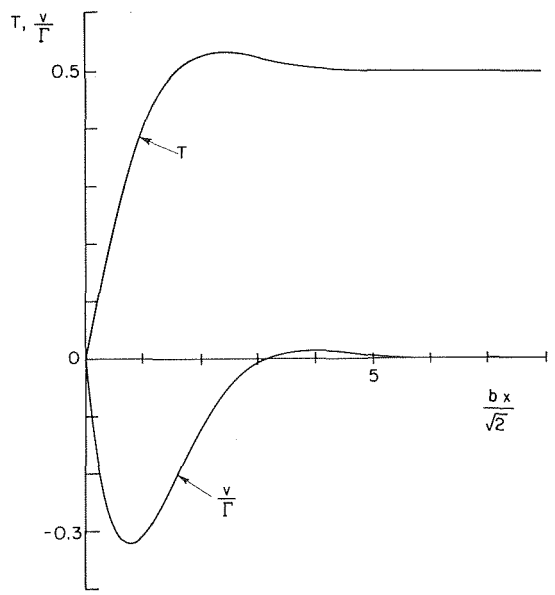

Fig. 6 Velocity and temperature distribution in the cold end boundary layer near $y = 1/2$

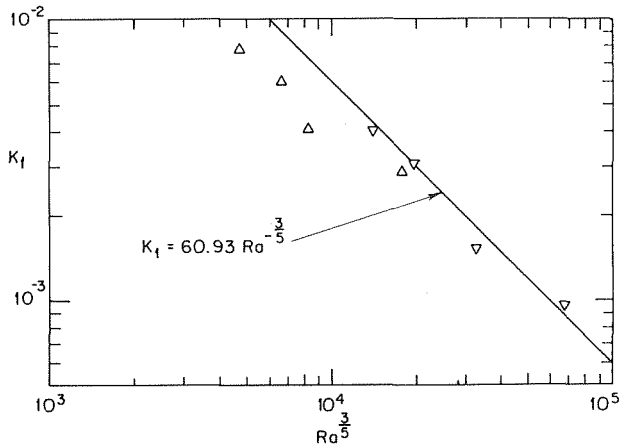

Fig. 8 The horizontal temperature gradient K_1 predicted by the boundary layer theory, equation (48), versus the measurements reported by Imberger [4]

$$K_1 \simeq 60.93\ \mathrm{Ra}^{3/5}. \tag{48}$$

The agreement is very good, particularly when the Rayleigh number is in excess of approximately 10^7.

It is worth commenting on the validity of the zero entrainment approximation which led to the boundary layer solution derived above. This approximation allowed us to neglect the $u\ \partial T/\partial x$ term in favor of the $v\ \partial T/\partial y$ term in the energy equation (2). Using the boundary layer solution (34–43) we find that the two terms are actually of the same order of magnitude. For example, $0(v\ \partial T/\partial y) = 0(\Gamma) = \mathrm{Ra}^{3/5}$, while $0(u\ \partial T/\partial x) = 0(u_c h/\lambda) = \mathrm{Ra}^{3/5}$. Therefore, the zero entrainment solution is valid only *locally* near $y = 1/2$ where, due to the centrosymmetry the cavity flow, the horizontal velocity is zero. The situation is similar to the one encountered by Gill in vertical cavities [8]: Gill showed that the Nusselt number derived based on a zero entrainment approximation is very close to a considerably more accurate Nusselt number result averaged over the whole side wall of the vertical cavity.

Summary of Results

We developed an approximate picture for the heat transfer by laminar free convection in a horizontal cavity. The heat transfer problem was analyzed based on three models, the Ra → 0 regime, the intermediate regime and the boundary layer regime. It is important to conclude this presentation with a summary of our results and a chart indicating for what combinations (Ra, h/L) each of the three regimes represents the best model for predicting the Nusselt number.

A frontier separating the Ra → 0 regime from the intermediate regime is found by comparing the size of the temperature difference between the top and bottom walls ΔT with the end-to-end temperature difference which is one. We recall now that in the Ra → 0 regime ΔT is much smaller than unity. Then, we can regard $\Delta T < 1/10$ as a sufficient requirement for the low Ra regime's presence. Since in the Ra → 0 regime $K_1 = h/L$ and, from the core solution, $\Delta T = K_1{}^2\mathrm{Ra}/720$, the $\Delta T < 1/10$ requirement states

$$\mathrm{Ra} < 72 \left(\frac{h}{L}\right)^{-2}. \tag{49}$$

This relation is sketched on Fig. 9 and divides the h/L − Ra plane into two sections.

If condition (49) is not fulfilled, the intermediate model or the boundary layer model may constitute a better description of the heat transfer mechanism in the cavity. Which model is better depends on how high the Rayleigh number. We find a second frontier separating the boundary layer regime from the intermediate regime by recalling that in the boundary layer regime the core temperature gradient K_1 is very small. Aided by Fig. 8, we argue that the boundary layer regime extends beyond the point where K_1 is smaller than one tenth of its maximum value, i.e., $K_1 < (h/L)/10$. With K_1 given by equation (48), this criterion requires

$$\mathrm{Ra} > 4.4\ 10^4\ (h/L)^{-5/3}. \tag{50}$$

Criterion (90) is shown traced on Fig. 9.

The numerical and experimental cases [3, 4] used for comparison throughout this study were projected onto the same field, h/L − Ra. Although frontiers (49, 50) can only be regarded as diffuse or approximate, we see that the data base covers all three regimes, the bulk of the data corresponding to the intermediate regime. Interestingly enough, the lone numerical simulation for a square cavity in the boundary layer regime ($h/L = 1$, $\mathrm{Ra} = 1.4 \times 10^5$) reports a Nusselt number which is only 18 percent lower than the value predicted by equation (47). The theoretical results developed in this paper agree very well with the heat transfer information available in the literature.

Another important observation concerns the absence of a Prandtl number effect on the Nusselt number results obtained here. In the Ra → 0 regime, the heat transfer is governed by the counterflow described by the core solution (14–16). However, the flow is fully developed (independent of x) and the inertia terms appearing in equations (3, 4) drop out. Consequently, in the Ra → 0 regime the Nusselt number as well as other aspects of the flow are independent of Pr. In the boundary layer limit, the Prandtl number effect drops out as a result of the zero entrainment approximation, $u = 0$; this becomes evident if we compare the boundary layer equations (29–31) with the complete equations (1–4). Since the zero entrainment assumption is valid only locally (around $y = 1/2$), the absence of a Prandtl number effect in the boundary layer regime can only be regarded as an approximation. However, we can safely conclude that for laminar free convection in horizontal cavities with different end temperatures the Prandtl number effect is minor. More experimental evidence is needed in order to fully elucidate this effect.

We point out that in the Ra → 0 regime displayed on Fig. 9 the horizontal heat transfer is not necessarily by conduction as the Ra → 0 limit tends to suggest. Consider the Nusselt number formula (20) for this regime: if $\mathrm{Ra}\ h/L > (362880)^{1/2} = 602.4$ and if the aspect ratio is small, say $h/L < 0.01$, the heat tranfer is convection dominated. Such cases clearly reside within the Ra → 0 domain of Fig. 9. The fact that equation (20) can describe the heat transfer in convection dominated cases ($\mathrm{Nu}\ L/h \gg 1$) is supported also by the evidence gathered on Fig. 5. Cormack, et al. [2] did not recognize that in the h/L → 0 limit, with Ra arbitrary but fixed, the horizontal heat transfer may be due entirely to the free convection mechanism and not to conduction.

We conclude this presentation with a theoretical Nusselt number correlation which covers all three laminar regimes shown on Fig. 9. Although in this study we already developed formulas for calculating Nu for each regime separately, a general expression condensing all three results into one is more often more valuable for practical engineering calculations. The following correlation is based on the method of Churchill and Usagi [10]. We seek a Nusselt number expression effecting a smooth transition from the Ra → 0 limit, equation (20), to the boundary layer limit, equation (47). This correlation is

$$\mathrm{Nu}\,\frac{L}{h} = 1 + \left\{\left[\frac{(\mathrm{Ra}\ h/L)^2}{362880}\right]^n + \left(0.623\ \mathrm{Ra}^{1/5}\,\frac{L}{h}\right)^n\right\}^{1/n}, \tag{51}$$

where exponent n is determined from substituting the Nusselt number data of Fig. 5 into expression (51) and solving for n. Averaging the values obtained for n we find

$$n = -0.386 \tag{52}$$

with a standard deviation of only 8 percent. In conclusion, we recommend the use of correlation (51, 52) for evaluating the net heat transfer rate in a horizontal enclosure with different end temperatures, provided the flow is laminar. This correlation as well as the rest of the theoretical results developed in this paper should hold as long as the Rayleigh number is less than approximately 10^9. Above $\mathrm{Ra} \simeq 10^9$, we expect the flow to become turbulent along the two vertical ends of the enclosure, by analogy with the transition to turbulence in free convection along a vertical isothermal plate suspended in an isothermal fluid [11].

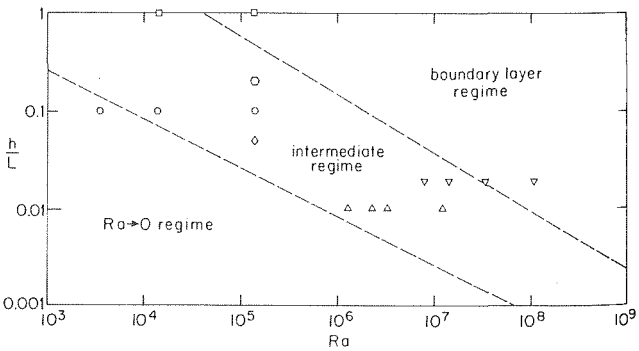

Fig. 9 Summary of the three laminar free convection regimes covered by the present theory. The h/L − Ra field contains also the experimental and numerical data used for comparison throughout this study (same data as on Fig. 5).

Acknowledgment

The authors thank Professor J. Imberger of the Civil Engineering Department, University of California, Berkeley, for many precious comments. The authors also thank Professor S. Ostrach, Case Western Reserve University, for bringing references [2–5] to their attention in the early stages of this study. The authors thank Professor A. Campo, University of Puerto Rico, for pointing out reference [10]. This work was supported in part by a postdoctoral fellowship awarded to A. Bejan by the Miller Institute for Basic Research in Science, University of California, Berkeley.

References

1 Ostrach, S., "Natural Convection in Enclosures," *Advances in Heat Transfer,* Vol. 8, 1972, pp. 161–227.

2 Cormack, D. E., Leal, L. G., and Imberger, J., "Natural Convection in a Shallow Cavity with Differentially Heated End Walls. Part 1. Asymptotic Theory," *Journal of Fluid Mechanics,* Vol. 65, 1974, pp. 209–229.

3 Cormack, D. E., Leal, L. G., and Seinfeld, J. H., "Natural Convection in a Shallow Cavity with Differentially Heated End Walls. Part 2. Numerical Solutions," *Journal of Fluid Mechanics,* Vol. 65, 1974, pp. 231–246.

4 Imberger, J., "Natural Convection in a Shallow Cavity with Differentially Heated End Walls. Part 3. Experimental Results," *Journal of Fluid Mechanics,* Vol. 65, 1974, pp. 247–260.

5 Cormack, D. E., Stone, G. P., and Leal, L. G., "The Effect of Upper Surface Conditions on Convection in a Shallow Cavity with Differentially Heated End Walls," *International Journal of Heat and Mass Transfer,* Vol. 18, 1975, pp. 635.

6 Bejan, A., and Tien, C. L., "Natural Convection in a Horizontal Porous Medium Subjected to and End-to-End Temperature Difference," ASME JOURNAL OF HEAT TRANSFER, Vol. 100, No. 2, pp 191–198.

7 Elder, J. W., "Laminar Free Convection in a Vertical Slot," *Journal of Fluid Mechanics,* Vol. 23, 1965, pp. 77–98.

8 Gill, A. E., "The Boundary-Layer Regime for Convection in a Rectangular Cavity," *Journal of Fluid Mechanics,* Vol. 26, 1966, pp. 515–536.

9 Quon, C., "Free Convection in an Enclosure Revisited," ASME JOURNAL OF HEAT TRANSFER, Vol. 99, No. 2, 1977, pp. 340–342.

10 Churchill, S. W., and Usagi, R., "A General Expression for the Correlation of Rates of Transfer and Other Phenomena," *AIChE Journal,* Vol. 18, 1972, pp. 1121–1128

11 Schlichting, H., *Boundary Layer Theory,* McGraw-Hill, 1960, pp. 334.

P. A. Iyer
Senior Research Engineer.
General Atomic Corp.,
San Diego, Calif.

R. E. Kelly
Professor.
Mechanics and Structures Department,
University of California,
Los Angeles, Calif. 90024
Mem. ASME

Supercritical Solutions for the Buoyancy Boundary Layer

Two-dimensional, finite amplitude solutions for the Prandtl buoyancy boundary layer are obtained for Reynolds numbers close to the critical values by an expansion in terms of disturbance amplitude. Supercritical nonlinear wave solutions are found to occur, rather than subcritical instabilities. The dependence of the wave amplitude and Nusselt number upon wall inclination, relative wall temperature, and Prandtl number is discussed.

Introduction

The Prandtl buoyancy boundary layer solution [1, 2] describes the buoyancy-induced flow adjacent to an infinite wall which is inclined at some angle from the horizontal and whose temperature is raised or lowered by a constant amount relative to a stably stratified ambient fluid. A Boussinesq fluid is assumed, and the density in the ambient fluid is taken to vary linearly in the vertical (z_d) direction so that the Brunt-Väisälä frequency, N_B, is constant there. A schematic of the situation is shown in Fig. 1, where we note that n_d and s_d are dimensional coordinates normal to and along the wall, respectively. The wall inclination angle, θ, is measured from the vertical.

The governing equations are

$$\frac{\partial \mathbf{V}}{\partial t} + (\mathbf{V}\cdot\nabla)\mathbf{V} = -\nabla(p/\rho_0) + (\rho/\rho_0)\mathbf{g} + \nu\nabla^2\mathbf{V}, \tag{1}$$

$$\frac{\partial T}{\partial t} + (\mathbf{V}\cdot\nabla)T = \kappa\nabla^2 T, \tag{2}$$

$$\nabla\cdot\mathbf{V} = 0, \quad \rho = \rho_0[1-\beta(T-T_0)], \tag{3}$$

where ρ_0 is a reference density corresponding to T_0 and ν, κ, and β are taken to be constant. Outside the wall boundary layer, the fluid is in hydrostatic equilibrium with a temperature given by $T_{amb} = T_0(1 + z_d/H)$ so that $N_B{}^2 = -(g/\rho_0)(d\rho/dz_d) = g\beta T_0/H$ there. The buoyancy layer solution to equations (1–3) is given by

$$\overline{T} = T_0(1 + z_d/H) + \Delta T_w e^{-n}\cos n, \tag{4a}$$

$$\mathbf{V} = \mathbf{i}_s V_0 e^{-n}\sin n, \tag{4b}$$

where n is the nondimensional coordinate (n_d/δ) and

$$\delta = \{4\nu\kappa H/\beta g T_0\cos^2\theta\}^{1/4}, \quad V_0 = \Delta T_w\{\beta\kappa g H/T_0\nu\}^{1/2} \tag{5}$$

We can also express the characteristic boundary layer thickness δ as $\delta = \{4\nu\kappa/(N_B\cos\theta)^2\}^{1/2}$ or $(\delta/H) = (\mathrm{Ra}_H\cos^2\theta/4)^{-1/4}$, where Ra_H is a Rayleigh number based on the scale height H and T_0. Note that δ is independent of s_d and ΔT_w, whereas V_0 is independent of s_d and θ. The functions appearing in equations (4*a*,*b*) are plotted in Fig. 2. Note that the oscillatory nature of the solutions can give a region of relatively cold fluid (for $\Delta T_w > 0$) as well as backflow at the edge of the boundary layer.

Prandtl used his solution to shed light upon the characteristics of mountain-valley winds. Later, Phillips [3] discussed an oceanic application of the case corresponding to an adiabatic wall temperature, and Gill [4] demonstrated how the buoyancy layer concept is pertinent to the emergence of boundary layers in convection within a rectangular cavity. For the case of an isothermal wall, of course, the present solution does not apply, and the actual boundary layer solution then depends on s_d, as discussed in [5]. From the viewpoint of stability theory, the Prandtl solution is attractive for this very reason, because the problem of "nonparallel flow corrections" does not arise.

The present paper concerns the weakly nonlinear stability of the flow described by equations (4*a*,*b*). Previous linear stability analyses [6, 7] have given fairly complete information regarding the dependence of the neutral stability boundaries upon the characteristic Reynolds number ($\mathrm{Re}_\delta = |V_0|\delta/\nu$), Prandtl number, and angle of inclination. In particular, Iyer [7] has shown that the preferred mode of instability, for a range of Pr near unity, consists of two-dimensional waves which propagate parallel to the wall for the cases of both relatively cold and hot walls. For the case of a hot, upwards facing wall, one might expect a thermal instability to occur in the form of spanwise periodic, longitudinal vortices, such as found for the case of an inclined slot [8]. As shown in Fig. 5 of [7], however, the wave-type mode of instability sets in first for all angles of inclination (for Pr = 0.72) in the present case of a fluid unbounded from above. For this reason, only two-dimensional waves will be considered in the nonlinear analysis. Nonlinear aspects of the longitudinal vortices for the case of a slot have recently been discussed in great detail in [9].

Our method of analysis consists of an expansion in terms of the disturbance amplitude in a region close to the critical Reynolds number for a given disturbance. Another method of investigating finite amplitude effects is the energy method [10], by which a Reynolds number (Re_E) is determined below which all disturbances decay, regardless of amplitude (global stability). Dudis and Davis [11] applied the energy method to the buoyancy layer for the case of a vertical

Contributed by the Heat Transfer Division of THE AMERICAN SOCIETY OF MECHANICAL ENGINEERS, and presented at the AIAA/ASME Thermophysics and Heat Transfer Conference, Palo Alto, Cal. May 25–26, 1978. Manuscript received by the Heat Transfer Division January 20, 1978. Paper No. 78-HT-38.

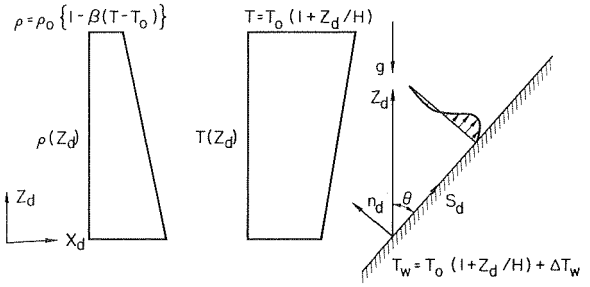

Fig. 1 Schematic of the flow field

wall and found that Re_E was well below the critical Reynolds number ($Re_{\delta,0}$) obtained from linear theory ($Re_E = 19.7\ Re_{\delta,0} = 101$ for Pr = 0.72). A possibility therefore exists that subcritical instability occurs for the buoyancy layer when finite amplitude effects are considered, and part of the motivation for the present analysis was to explore this possibility further. We shall return to this matter in the concluding section, after our results are discussed.

Analysis

We introduce a two-dimensional perturbation to the flow so that the overall temperature and stream function are given by

$$T(n, s, t) = T_0(1 + z_d/H) + \Delta T_w\{\Theta(n) + T'(n, s, t)\} \quad (6a)$$

$$\psi(n, s, t) = V_0\delta\{\Psi(n) + \psi'(n, s, t)\}, \quad (6b)$$

where Θ and Ψ represent the buoyancy layer solutions and T' and ψ' represent the disturbance. Because we are interested in the possibility of neutrally stable, finite amplitude waves, it is convenient to reduce the problem to a steady one by using a frame of reference which moves with the wave. Hence, we introduce the new variable

$$r = s - ct \quad (7)$$

and look for solutions of the form $T' = T'(n, r)$, $\psi' = \psi'(n, r)$. The equations for T' and ψ' are obtained from equations (1–3), after substituting equations (6a,b), subtracting out the mean flow terms, and eliminating pressure, as

$$\mathrm{Re}_\delta\left[(D\Psi - c)\frac{\partial}{\partial r}\nabla^2\psi' - D^3\Psi\frac{\partial\psi'}{\partial r} + \left(\frac{\partial\psi'}{\partial n}\frac{\partial}{\partial r} - \frac{\partial\psi'}{\partial r}\frac{\partial}{\partial n}\right)\nabla^2\psi'\right]$$
$$= \nabla^4\psi' + 2\left(\frac{\partial T'}{\partial n} - \frac{\partial T'}{\partial r}\tan\theta\right), \quad (8)$$

$$\mathrm{Re}_\delta\mathrm{Pr}\left[(D\Psi - c)\frac{\partial T'}{\partial r} - D\Theta\frac{\partial\psi'}{\partial r} + \left(\frac{\partial\psi'}{\partial n}\frac{\partial}{\partial r} - \frac{\partial\psi'}{\partial r}\frac{\partial}{\partial n}\right)T'\right]$$

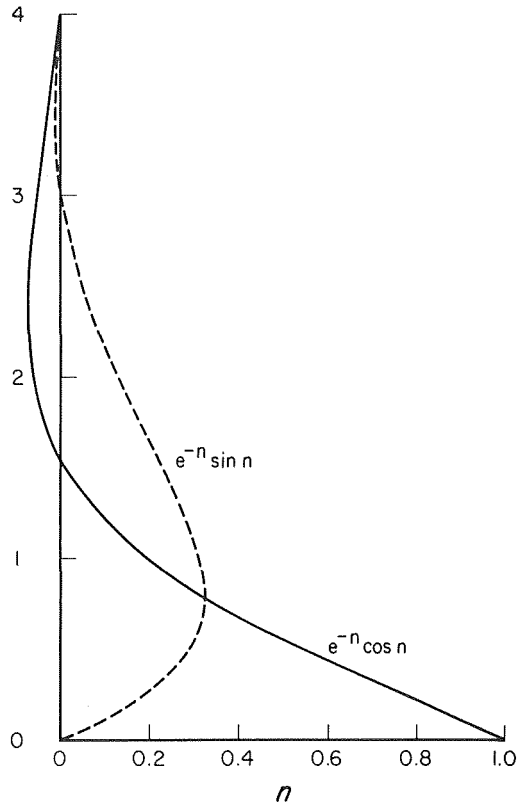

Fig. 2 The boundary layer functions: (—), e^{-n} cos (n); (- - -), e^{-n} sin (n)

$$+ 2\frac{\partial\psi'}{\partial n} - 2\tan\theta\frac{\partial\psi'}{\partial r} = \nabla^2 T'. \quad (9)$$

We seek solutions by expanding in terms of the disturbance amplitude ϵ, viz.

$$\psi' = \sum_{n=1}\epsilon^n\psi_n, \quad T' = \sum_{n=1}\epsilon^n T_n, \quad (10a)$$

$$c = c_0 + \sum_{n=1}\epsilon^n c_n \quad (10b)$$

$$\mathrm{Re}_\delta = \mathrm{Re}_{\delta,0} + \sum_{n=1}\epsilon^n\mathrm{Re}_{\delta,n} \quad (10c)$$

and substituting the expansions into equations (8) and (9). In the above, the c_n represent nonlinear corrections to the wavespeed,

Nomenclature

c = wavespeed
$D = d/dn$
g = gravitational acceleration
H = scale height
$i = \sqrt{-1}$
$\mathbf{i}$ = unit vector
n = coordinate normal to the wall
N_B = Brunt-Väisälä frequency
Nu = Nusselt number
p = pressure
Pr = Prandtl number
$r = s - ct$
Ra = Rayleigh number
Re = Reynolds number
s = coordinate parallel to wall
t = time
T = temperature
V = velocity
z = coordinate in vertical direction
A, B, C, D = numerical constants
L, M, N, P = linear operators
α = wavenumber
β = coefficient of volumetric expansion
δ = characteristic boundary layer thickness
Δ = difference
ϵ = disturbance amplitude
ζ = eigenfunction for temperature
θ = angle of inclination from vertical
Θ = basic temperature distribution
κ = thermal diffusivity
ν = kinematic viscosity
ρ = density
ϕ = eigenfunction for streamfunction
ψ, Ψ = streamfunction

Subscripts

d = dimensional
0 = reference value
amb = ambient value
w = wall value
n = nth term in expansion
ℓ = laminar value
E = value based on energy theory
δ = value based on boundary layer thickness

Superscripts

$\bar{}$ = mean in direction of s
$'$ = disturbance quantity
$*$ = adjoint quantity
$\tilde{}$ = complex conjugate

whereas the $\mathrm{Re}_{\delta,n}$ allow us to relate ϵ to a value of Re_δ different from the linear, critical value ($\mathrm{Re}_{\delta,0}$). This relationship emerges first when terms of $0(\epsilon^3)$ are considered. At $0(\epsilon)$, the linear stability equations are obtained, namely

$$\mathrm{Re}_{\delta,0}\left[(D\Psi - c_0)\frac{\partial}{\partial r}\nabla^2\psi_1 - D^3\Psi\frac{\partial\psi_1}{\partial r}\right] = \nabla^4\psi_1 + 2\left(\frac{\partial T_1}{\partial n} - \frac{\partial T_1}{\partial r}\tan\theta\right), \quad (11)$$

$$\mathrm{Re}_{\delta,0}\mathrm{Pr}\left[(D\Psi - c_0)\frac{\partial T_1}{\partial r} - D\Theta\frac{\partial\psi_1}{\partial r}\right] + 2\frac{\partial\psi_1}{\partial n} - 2\tan\theta\frac{\partial\psi_1}{\partial r} = \nabla^2 T_1 \quad (12)$$

Neutral solutions are obtained by taking the disturbance of the form

$$\psi_1(n, r) = \phi_{11}(n)e^{i\alpha r} + \tilde{\phi}_{11}(n)e^{-i\alpha r} \quad (13a)$$

$$T_1(n, r) = \zeta_{11}(n)e^{i\alpha r} + \tilde{\zeta}_{11}(n)e^{-i\alpha r} \quad (13b)$$

The eigenvalue problem consists of solving the following ordinary differential equations

$$L(\phi_{11}) + M(\zeta_{11}) + i\alpha\mathrm{Re}_{\delta,0}c_0(D^2 - \alpha^2)\phi_{11} = 0, \quad (14a)$$

$$N(\zeta_{11}) + P(\phi_{11}) + i\alpha\mathrm{Re}_{\delta,0}c_0\zeta_{11} = 0, \quad (14b)$$

where the linear operators L, M, N and P are defined as

$$L = (D^2 - \alpha^2)^2 + i\alpha\mathrm{Re}_{\delta,0}D^3\Psi - i\alpha\mathrm{Re}_{\delta,0}D\Psi(D^2 - \alpha^2) \quad (15a)$$

$$M = 2(D - i\alpha\tan\theta) \quad (15b)$$

$$N = (D^2 - \alpha^2) - i\alpha\mathrm{Re}_{\delta,0}\mathrm{Pr}D\Psi \quad (15c)$$

$$P = -2(D - i\alpha\tan\theta) + i\alpha\mathrm{Re}_{\delta,0}\mathrm{Pr}D\Theta \quad (15d)$$

The boundary conditions are

$$\phi_{11}(0) = D\phi_{11}(0) = \zeta_{11}(0) = 0 \quad (16a)$$

$$\delta_{11}, D\phi_{11}, \zeta_{11} \text{ bounded as } n \to \infty. \quad (16b)$$

The neutral solutions to equations (14a,b) have been described in detail elsewhere [7] and will not be discussed here. However, the neutral stability curves for the case of a heated wall with Pr = 0.72 are shown in Fig. 3 for future reference. The linear solutions are normalized on the basis that

$$\int_0^\infty [\phi_{11}^*(D^2 - \alpha^2)\phi_{11} + \mathrm{Pr}\zeta_{11}^*\zeta_{11}]dn = 1.0 \quad (17)$$

where an asterisk denotes a solution to the system adjoint to equations (14a,b). This condition follows from the orthogonality condition governing solutions to the linear equations (cf. [12]).

The next steps in the analysis involve a procedure which is now fairly standard (e.g., see [10], sections 10–13) but which involves very complicated equations for the present flow. For reasons of space, these equations will not be presented here completely; for full details of the equations and the analysis, the reader is referred to the thesis by Iyer [12]. At $0(\epsilon^2)$, the solution for ψ_2 and T_2 consists of a harmonic term and distortion of the mean profiles and is of the form

$$\psi_2(n, r) = \phi_{22}(n)e^{2i\alpha r} + \tilde{\phi}_{22}(n)e^{-2i\alpha r} + \phi_{20}(n), \quad (18a)$$

$$T_2(n, r) = \zeta_{22}(n)e^{2i\alpha r} + \tilde{\zeta}_{22}(n)e^{-2i\alpha r} + \zeta_{20}(n). \quad (18b)$$

As can be shown, a necessary condition to obtain a solution at this order is that $c_1 = 0$, $\mathrm{Re}_{\delta,1} = 0$. The equations for the mean terms are

$$\frac{d^4\phi_{20}}{dn^4} + 2\frac{d\zeta_{20}}{dn} = i\alpha\mathrm{Re}_{\delta,0}\frac{d^2}{dn^2}\left(\tilde{\phi}_{11}\frac{d\phi_{11}}{dn} - \phi_{11}\frac{d\tilde{\phi}_{11}}{dn}\right), \quad (19a)$$

$$\frac{d^2\zeta_{20}}{dn^2} - 2\frac{d\phi_{20}}{dn} = i\alpha\mathrm{Re}_{\delta,0}\mathrm{Pr}\frac{d}{dn}(\tilde{\phi}_{11}\zeta_{11} - \phi_{11}\tilde{\zeta}_{11}). \quad (19b)$$

The equation for ϕ_{20} can be integrated once, with the constant of integration being set equal to zero corresponding to zero mean pressure gradient. The equations are then solved numerically, subject to homogeneous boundary conditions of the form given by equations (16a,b). The solutions for ϕ_{20} and ζ_{20} are shown in Fig. 4 for Pr = 0.72 and θ = 40 deg for the case of a relatively hot wall. The composite nondimensional mean velocity, given to this order by

$$(V_0)^{-1}\frac{d\bar{\Psi}}{dn} = \frac{d\Psi}{dn} + \epsilon^2\frac{d\phi_{20}}{dn}, \quad (20)$$

is shown in Fig. 5 for ϵ = 0.1. The maximum velocity is reduced somewhat in the wall region. Nonetheless, the heat transfer from the hot wall can be increased due to the instability, as shown later in Fig. 6, due to the nonhomogeneous terms occurring in equation (19b). The maximum percentage change in the mean quantities occurs at the

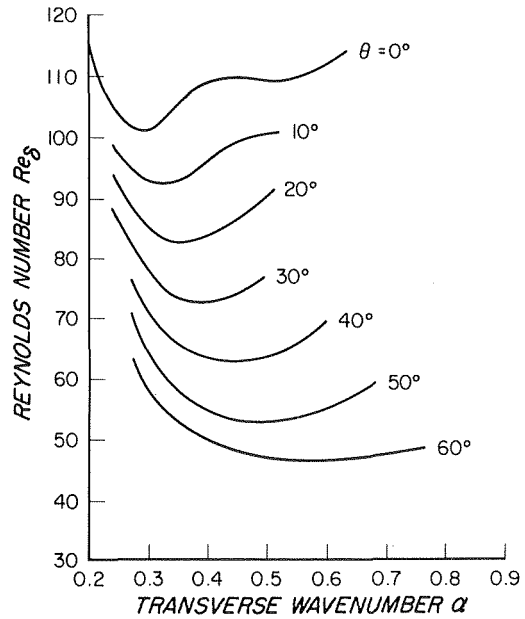

Fig. 3 Linear neutral stability curves for two-dimensional waves (heated wall case with Pr = 0.72)

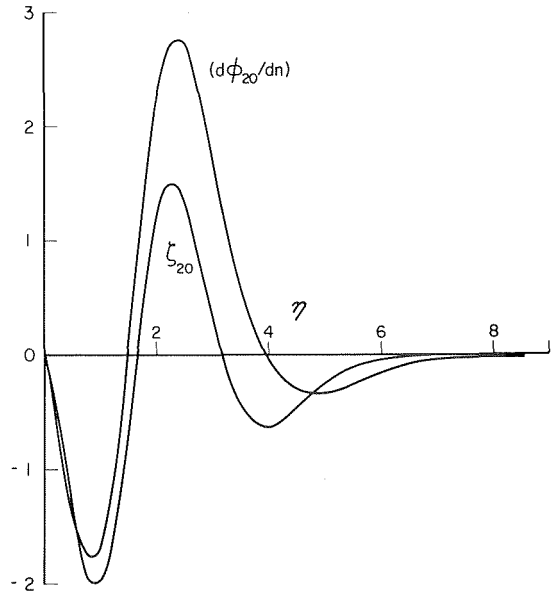

Fig. 4 The second-order distortions to the mean temperature (ζ_{20}) and mean velocity ($d\phi_{20}/dn$) for θ = 40 deg, heated wall case, Pr = 0.72

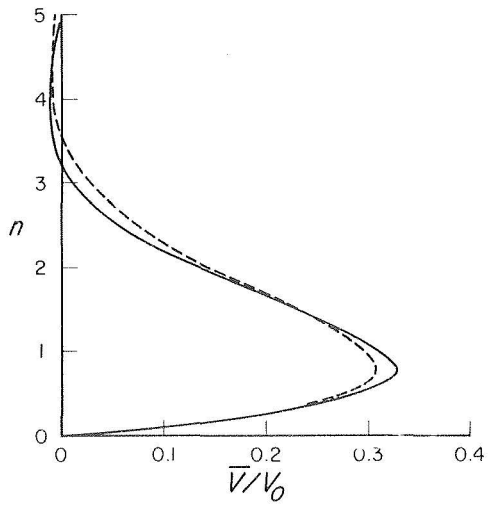

Fig. 5 The mean velocity for laminar flow (—) and for slightly supercritical flow (- - -) with $\epsilon = 0.1$, $\theta = 40$ deg, heated wall case, Pr = 0.72

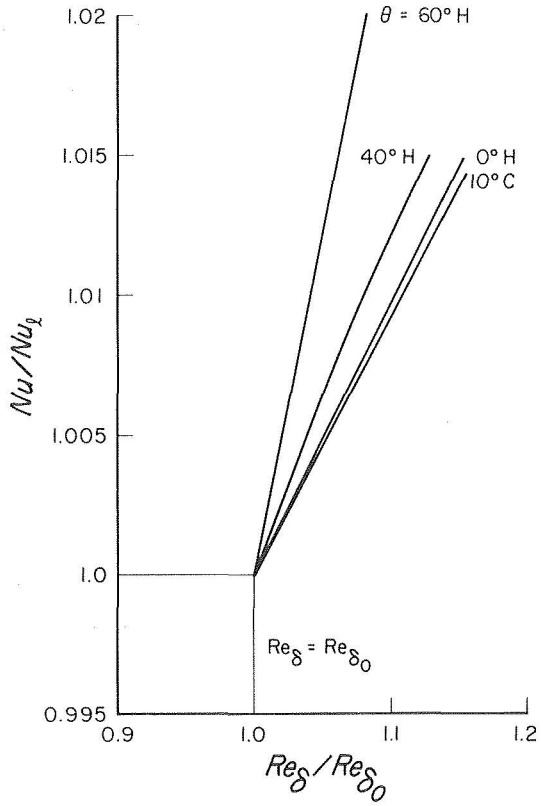

Fig. 6 The ratio of Nusselt number for supercritical flow to the Nusselt number for laminar flow for Pr = 0.72 (*H*: heated wall, *C*: cooled wall)

edge of the boundary layer, due to the relatively slow decay of the disturbance functions.

At $0(\epsilon^3)$, the solution has the form

$$\psi_3(n, r) = \phi_{31}(n)e^{i\alpha r} + \tilde{\phi}_{31}(n)e^{-i\alpha r} + \phi_{33}(n)e^{3i\alpha r} + \tilde{\phi}_{33}(n)e^{-3i\alpha r} \quad (21)$$

The harmonic terms in equation (21) are not of special interest, but the first two terms represent a modification of the fundamental. They arise from interaction of the mean distortion with the fundamental and also interaction between the fundamental and the first harmonic. A type of resonance therefore arises, and a solution is obtained only if a certain solvability condition is satisfied ([10], section 12). It is this condition which allows us to relate ϵ to $(\mathrm{Re}_\delta - \mathrm{Re}_{\delta,0})$ and which now will be obtained. The equations for ϕ_{31} and ζ_{31} are

$$L(\phi_{31}) + M(\zeta_{31}) + i\mathrm{Re}_{\delta,0}c_0(D^2 - \alpha^2)\phi_{31} = i\alpha\mathrm{Re}_{\delta,2}F_1(n) + i\alpha\mathrm{Re}_{\delta,0}F_2(n) - i\alpha c_2\mathrm{Re}_{\delta,0}(D^2\phi_{11} - \alpha^2\phi_{11}), \quad (22)$$

$$N(\zeta_{31}) + P(\phi_{31}) + i\alpha\mathrm{Re}_{\delta,0}c_0\mathrm{Pr}\zeta_{31} = i\alpha\mathrm{Re}_{\delta,2}\mathrm{Pr}G_1(n) + i\alpha\mathrm{Re}_{\delta,0}G_2(n) - i\alpha c_2\mathrm{Re}_{\delta,0}\mathrm{Pr}\zeta_{11}, \quad (23)$$

where F_1, F_2, G_1, G_2 are complicated functions of ϕ_{11}, ϕ_{20}, ϕ_{22}, ζ_{11}, ζ_{20}, ζ_{22} and are given in [12]. Homogeneous boundary conditions again occur. If equation (22) is multiplied by ϕ_{11}^*, equation (23) by ζ_{11}^*, the results then integrated over all n and added, we obtain the solvability condition in the form

$$i\alpha c_2\mathrm{Re}_{\delta,0} = \mathrm{Re}_{\delta,2}(A + iB) - (C + iD) \quad (24)$$

where A, B, C, D are numerical constants arising from the integration. For neutrally stable solutions, c_2 must be real. After separating out the real and imaginary parts of equation (24), we obtain

$$\mathrm{Re}_{\delta,2} = C/A, \quad c_2 = (B\mathrm{Re}_{\delta,2} - D)/(\alpha\mathrm{Re}_{\delta,0}) \quad (25)$$

The first relation allows us to determine the wave amplitude, ϵ. This result follows from truncating the expansion (10*c*) at $0(\epsilon^2)$ and rewriting it as

$$\epsilon^2 = \frac{\mathrm{Re}_\delta - \mathrm{Re}_{\delta,0}}{\mathrm{Re}_{\delta,2}} = \left(\frac{\mathrm{Re}_\delta - \mathrm{Re}_{\delta,0}}{\mathrm{Re}_{\delta,0}}\right)\left(\frac{A\mathrm{Re}_{\delta,0}}{C}\right) \quad (26)$$

If $(A/C) > 0$, then ϵ is a real quantity for $\mathrm{Re} > \mathrm{Re}_{\delta,0}$, i.e., supercritical, finite amplitude wave solutions are obtained. If (A/C) were less than zero, then such solutions would occur for $\mathrm{Re} < \mathrm{Re}_{\delta,0}$, and subcritical instability would occur. We have found that $(A/C) > 0$ for all cases considered, so that supercritical solutions are obtained. The resulting value of ϵ is given in Table 1 for a 10 percent change in Re_δ, i.e., $(\mathrm{Re}_\delta - \mathrm{Re}_{\delta,0})/\mathrm{Re}_{\delta,0} = 0.1$. The results given there correspond to the critical wavenumber for each case, i.e., the minimum value of $\mathrm{Re}_{\delta,0}$ (cf. Fig. 3). However, additional calculations were made for the case of a vertical wall with Pr = 0.72 for a range of wavenumbers spanning the "nose" of the neutral curve for that case ($0.25 \le \alpha \le 0.5$). Again, only supercritical solutions were found. It was found easier to compute numerically solutions for an inclined hot wall rather than for a cold wall, due to the larger values of $\mathrm{Re}_{\delta,0}$ occurring in the latter case. The cold wall results are therefore limited to $\theta \le 10$ deg. The results indicate that, for Pr = 0.72, the wave amplitude increases continuously

Table 1 The Wave Amplitude for $(\mathrm{Re}_\delta - \mathrm{Re}_{\delta,0})/\mathrm{Re}_{\delta,0} = 0.1$

Wall Condition	Pr	θ	$\mathrm{Re}_{\delta,0}$	$\mathrm{Re}_{\delta,2}$	c_0	c_2	ϵ
Hot	0.72	60 deg	46.3	647.5	0.266	−3.17	0.0846
Hot	0.72	40 deg	62.86	2080	0.255	−2.04	0.0550
—	0.72	0 deg	101.0	5620	0.281	−4.62	0.0425
Cold	0.72	10 deg	110.48	6950	0.283	−6.22	0.0399
—	0.1	0 deg	108.54	2360	0.172	−1.62	0.0678
—	1.0	0 deg	76.11	5000	0.312	−6.35	0.0390

as we go from the case of a cold wall with $\theta = 10$ deg to the case of a hot wall with $\theta = 60$ deg, whereas for $\theta = 0$ deg (vertical case), the amplitude increases as Pr decreases. The correction to the wavespeed is also shown and compared to c_0, where it is understood that positive c implies wave propagation in the direction of the mean flow. For all cases considered, finite amplitude effects tend to decrease c and therefore slow down the wave.

The Nusselt number can now be calculated for the same percentage increase in Re_δ. The mean Nusselt number is given by

$$\mathrm{Nu} = 1 - \frac{2\tan\theta}{\mathrm{Re}_\delta \mathrm{Pr}} - \epsilon^2 D\zeta_{20}(0) \tag{27}$$

where the first two terms correspond to the basic laminar state, i.e.,

$$\mathrm{Nu}_\ell = 1 - \frac{2\tan\theta}{\mathrm{Re}_\delta \mathrm{Pr}} \tag{28}$$

In order to convey the effects of the instability, we have plotted $(\mathrm{Nu}/\mathrm{Nu}_\ell)$ as a function of $\mathrm{Re}_\delta/\mathrm{Re}_{\delta,0}$ in Fig. 6 for $\mathrm{Pr} = 0.72$ and various angles of inclination. As might have been anticipated from the comments concerning the wave amplitude, the ratio is greater for the case of a hot wall with nonzero θ than for the case of a cold wall. However, the ratio is always greater than unity for supercritical Re_δ, as one would expect intuitively. For small Pr, however, this need not be the case, as Fig. 7 indicates for the case of a vertical wall. Although $(\mathrm{Nu}/\mathrm{Nu}_\ell) > 1$ for $\mathrm{Pr} = 0.72$ and unity, it is less than unity for $\mathrm{Pr} = 0.1$. Physically, this is due to the reduction in the mean velocity close to the wall as shown in Fig. 5, which is not offset by the nonlinear disturbance terms on the right-hand side of equation (19b) for the case of small Pr. Of course, this result is valid only within the limits of the present analysis. For still larger Re_δ, further terms in the expansion would be required, and the Nusselt number would presumably then begin to increase with Re_δ.

In some nonlinear stability analyses, use is made of the "Stuart shape assumption" [13], in which only the fundamental and the distortion of the mean profile are considered, i.e., the generation of harmonic terms is ignored. Calculations were also made for the present problem on this basis. Although the conclusion concerning the existence of supercritical states was unchanged, the numerical value of ϵ, etc., was affected significantly. This approach is therefore not recommended for the present type of stability problem.

Conclusions

We have found in this analysis that only supercritical, finite amplitude wave solutions are obtained when the expansion is carried out to the present order for the cases considered. We have also found that the wave amplitude and Nusselt number depends upon angle of inclination and whether the wall is hot or cold on a relative basis, as well as upon Reynolds and Prandtl numbers.

As mentioned in the introduction, energy theory [11] yields the results that the Reynolds number required for the decay of an arbitrary disturbance is well below the linear critical value, thereby allowing the existence of subcritical instabilities. The results of energy theory analysis and the present amplitude expansion analysis are therefore qualitatively different. This is in contrast to the case of classical Rayleigh-Benard convection, for which both approaches predict that no subcritical instability is possible, as well as to the case of instability in shear flows of the plane Poiseuille type, for which both approaches predict subcritical instability (to the order considered in the present expansion analysis and for two-dimensional disturbances). The present flow is different from plane Poiseuille flow in that the basic velocity profile has points of inflection and also in that the basic instability can be driven by the streamwise density variations. It would be interesting to see whether or not the same qualitative difference arises in other flows with such characteristics.

It should be remembered, of course, that we have not eliminated the possibility of subcritical instability, in that we have considered only two-dimensional disturbances and have ignored higher order terms in the amplitude expansion. Subcritical instability might still arise if such effects are considered. If they must be included to obtain subcritical instability, however, the situation would still be qualitatively different from that characteristic of plane Poiseuille flow.

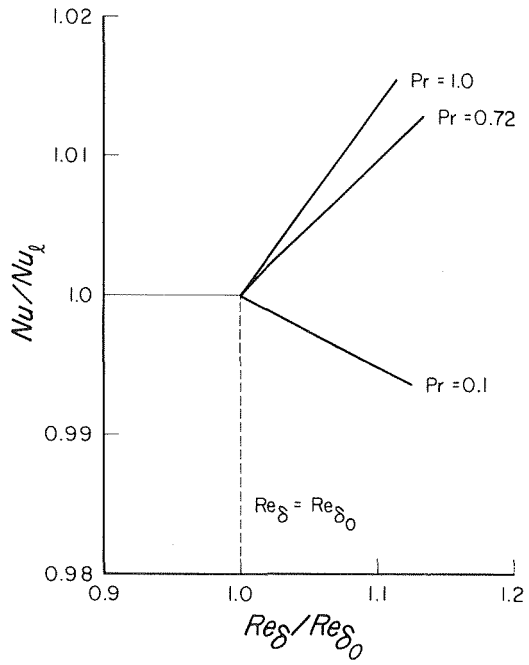

Fig. 7 The ratio of Nusselt number for supercritical flow to the Nusselt number for laminar flow for the case of a vertical, heated wall and various values of Prandtl number

Acknowledgment

This research was supported by the N.S.F. under Grant GA-31247. The authors appreciate the comments of S.H. Davis concerning the results.

References

1 Prandtl, L., *Essentials of Fluid Dynamics*, Hafner Publ. Co., New York, 1952, pp. 422–425.

2 Turner, J. S., *Buoyancy Effects in Fluids*, Cambridge Univ. Press, 1973, pp. 243–245.

3 Phillips, O. M., "On Flows Induced by Diffusion in a Stably Stratified Fluid," *Deep-Sea Research*, Vol. 17, 1970, pp. 435–443.

4 Gill, A. E., "The Boundary Layer Regime for Convection in a Rectangular Cavity," *Journal of Fluid Mechanics*, Vol. 26, 1966, pp. 515–536.

5 Chen, C. C., and Eichhorn, R., "Natural Convection from a Vertical Surface to a Thermally Stratified Fluid," ASME JOURNAL OF HEAT TRANSFER, Vol. 98, 1976, pp. 446–451.

6 Gill, A. E. and Davey, A., "Instabilities of a Buoyancy-Driven System," *Journal of Fluid Mechanics*, Vol. 35, 1969, pp. 775–798.

7 Iyer, P. A., "Instabilities in Buoyancy-Driven Boundary-Layer Flows in a Stably Stratified Medium," *Boundary-Layer Metereorology*, Vol. 5, 1973, pp. 53–66.

8 Hart, J. E., "The Stability of Flow in a Differentially Heated Inclined Box," *Journal of Fluid Mechanics*, Vol. 47, 1971, pp. 547–576.

9 Clever, R. M., and Busse, F. H., "Instabilities of Longitudinal Convection Rolls in an Inclined Layer," *Journal of Fluid Mechanics*, Vol. p. 81, 1977. 107–127.

10 Joseph, D. D., *Stability of Fluid Motions*, Vol. 1, Springer-Verlag, Berlin, 1976.

11 Dudis, J. J. and Davis, S. H., "Energy Stability of the Buoyancy Boundary Layer," *Journal of Fluid Mechanics*, Vol. 47, 1971, pp. 381–403.

12 Iyer, P. A., *Instabilities in Buoyancy-Driven Boundary Layer Flows over Inclined Surfaces*, Ph.D. thesis, School of Engineering and Applied Science, University of California, Los Angeles, 1973.

13 Stuart, J. T., "On the Non-Linear Mechanics of Hydrodynamic Stability," *Journal of Fluid Mechanics*, Vol. 4, 1958, pp. 1–21.

C. F. Chen

Department of Mechanical, Industrial, & Aerospace Engineering,
Rutgers University,
New Brunswick, N. J. 08903

Time-Dependent Double-Diffusive Instability in a Density-Stratified Fluid along a Heated Inclined Wall

We consider a stably stratified fluid contained between two parallel sloping plates. At t = 0, the lower plate is given a step increase in temperature; a time-dependent convective flow is generated. Stability of such a flow with respect to double-diffusive mechanism is analyzed. The method is the same one used by Chen [6] in treating a similar problem with vertical walls. The predicted critical values of Rayleigh number and wavelength compare favorably with those observed experimentally. No overstability is encountered up to 75 deg of inclination of the heating wall to the vertical. For a horizontal layer, however, instability starts in an overstable mode. The frequency of the overstable mode compares favorably with that predicted by Veronis [7] for a free-free layer.

1 Introduction

Consider a fluid whose density is stably stratified by a solute in the presence of a sloping wall which is impervious to solute diffusion. The normal derivative of the solute must vanish at such a boundary. The constant density lines which are horizontal in the main body of the fluid must bend to meet the boundary normally. This curving of the constant density lines creates a buoyancy force which drives a thin layer of fluid upward slowly along the slope [1, 2]. Now if the wall is heated, the fluid would acquire an additional convective velocity along the wall which is usually much larger than that in the buoyancy layer. It is generally true that the diffusivity of heat is much larger than that of the solute. Thus the constant solute lines will be lifted upward by the convective motion. Any lateral motion of a parcel of fluid will bring it into a surrounding which is cooler and contains less solute. The temperature equilibrates in a comparatively short time thus releasing the potential energy of the solute contained in the parcel. The parcel sinks thus creating a vortex motion. In a physical experiment, this double-diffusive instability manifests itself as an array of vortices which eventually develops into nearly horizontal cellular motion. Of course such instability only occurs if convection due to heating exceeds certain critical magnitude.

Recently, we completed a series of experiments investigating such instabilities [3]. The experiments were carried out in a gradient of sugar solution contained in a test tank in which the heating wall could be set at any angle of inclination from the vertical. The heat transfer walls were made of thick aluminum plates through which water passages were machined. Constant temperatures for both walls were maintained by circulating water heated by two Haake baths. The desired density gradient was obtained by filling the tank by a modified two-bucket method [3]. Before the start of each experiment, the temperature of the Haake bath for the heating wall was set at a predetermined level, while the other was set at the room temperature. When the two baths came up to their respective temperatures, valves were opened to let the water circulate through the two walls. This marked the start of the experiment. If the temperature difference between the heating wall and the ambient were supercritical, an array of vortices would appear along the heating wall in a matter of minutes.

Since the tank was wide, being approximately 12 cm at its narrowest part, the presence of the cold wall was not felt by the fluid near the heating wall at the time of onset of instabilities. The natural length scale h for the problem is then the rise of a heated parcel of fluid in the stratified surroundings [4]

$$h = \frac{\alpha \Delta T}{-\frac{1}{\rho}\left(\frac{\partial \rho}{\partial \zeta}\right)_0} \tag{1}$$

The governing parameter for this problem is the Rayleigh number based on h

$$\mathrm{R} = g\alpha \Delta T h^3/(\kappa \nu) \tag{2}$$

The experimentally determined stability boundary is shown in Fig. 1. The unflagged data points were obtained by Chen, Paliwal and Wong [4], and the flagged points were obtained by Chen and Skok [5].

Contributed by the Heat Transfer Division of THE AMERICAN SOCIETY OF MECHANICAL ENGINEERS and presented at the AIAA/ASME Thermophysics and Heat Transfer Conference, Palo Alto, California, May 25-26, 1978. Manuscript received by the Heat Transfer Division January 20, 1978. Paper No. 78-HT-43.

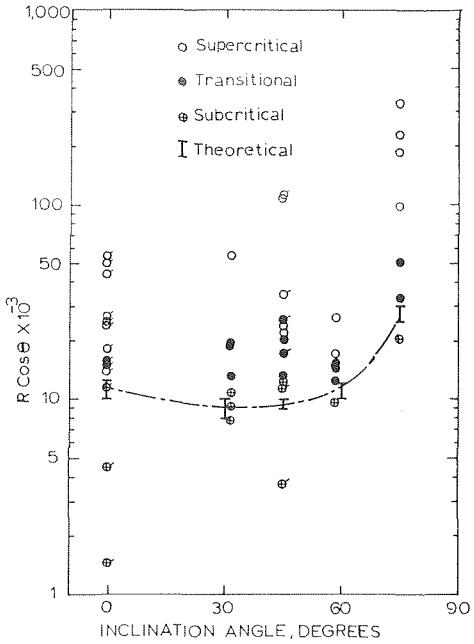

Fig. 1 Effect of inclination angle on the transitional characteristics

The different symbols denote the subcritical, transitional and supercritical flow regimes.

In the subcritical state, fluid is convected slowly along the wall. In the supercritical state, vortices or convection rolls spontaneously occur all along the heating wall. In the transitional state, convection rolls propagate from the two ends. It is seen that by using R cos θ to account for the reduced gravity, the transition regime is correlated rather well up to $\theta = 60$ deg. Beyond this point, the flow becomes increasingly stable.

In this paper, we use the linear stability approach to analyze the problem. The method consists of initially distributing small random perturbations of given wavelength in the fluid. The subsequent motion of the fluid is obtained by numerically integrating the linearized equation of motion. The kinetic energy of the perturbations is monitored at all times. The flow is considered stable or unstable according to the decay or growth of the perturbation kinetic energy. The critical wavelength is determined by the fastest growing mode. This method was used successfully in calculating the stability of a stratified fluid when subjected to lateral heating from a vertical wall [6]. For the present case of inclined wall, the predicted transition regime and critical wavelengths agree rather well with the experimental results. The results also show that there is no overstability for θ up to 75 deg.

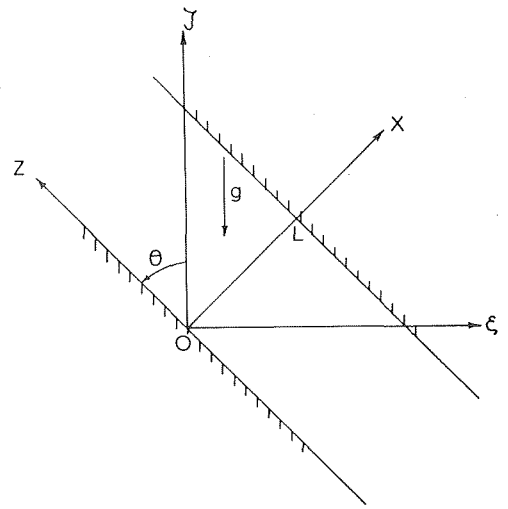

Fig. 2 Coordinate system

For the case of a horizontal layer, $\theta = 90$ deg, the instability exhibits overstable mode at a frequency close to that given by Veronis [7].

2 Basic and Perturbation Equations

Consider a stably stratified fluid contained within two parallel sloping walls of infinite extent. Let the density of the fluid be approximated by

$$\rho = \rho_0(1 - \alpha(T - T_0) + \beta(S - S_0)) \tag{3}$$

Let (ξ, ζ) be the horizontal and vertical coordinates; let z be aligned with the lower sloping wall and x pointing across the gap as shown in Fig. 2. For a two-dimensional motion, the vorticity equation in the Boussinesq approximation is

$$\frac{1}{\mathrm{P_r}}\frac{D\omega}{Dt} = \nabla^2\omega - \mathrm{R}\cos\theta(T_x - S_x) + \mathrm{R}\sin\theta(T_z - S_z) \tag{4}$$

in which D/DT denotes substantial derivative and the subscripts denote partial differentiation. The heat and solute diffusion equations are

$$\frac{DT}{Dt} = \nabla^2 T \text{ and } \frac{DS}{Dt} = \tau\nabla^2 S \tag{5) \& (6}$$

The relationship between the vorticity and the stream function is

$$\nabla^2\psi = \omega \tag{7}$$

Nomenclature

E = perturbation kinetic energy normalized with respect to its initial value

E_B = nondimensional kinetic energy of the basic flow

f_{cr} = critical frequency, s^{-1}

g = gravitational acceleration, cm/s^2

h = natural length scale defined by equation (1)

K = nondimensional wave number

L = nondimensional tank width

N = Brunt-Väisälä frequency

$\mathrm{P_r}$ = Prandtl number = ν/κ

R = Rayleigh number defined by equation (2)

S = nondimensional solute concentration

T = nondimensional temperature

T_p = nondimensional period of oscillation

ΔT = temperature difference, °C

t = nondimensional time

u, w = nondimensional velocity components in (x, z) directions

x, z = nondimensional coordinate system defined along the tank. See Fig. 2

$\alpha = -\frac{1}{\rho}\frac{\partial\rho}{\partial \mathrm{T}}$, $^\circ\mathrm{C}^{-1}$

$\beta = \frac{1}{\rho}\frac{\partial\rho}{\partial \mathrm{S}}$, $(wt \text{ percent})^{-1}$

θ = inclination of the heated wall from the vertical wall, deg.

κ = thermal diffusivity, cm^2/s

κ_s = solute diffusivity, cm^2/s

λ_{cr} = cricital wavelength, cm

ν = kinematic viscosity, cm^2/s

(ξ, ζ) = nondimensional horizontal and vertical coordinate system. See Fig. 2

ρ = density, gm/cm^3

$\tau = \kappa_s/\kappa$

ψ = nondimensional stream function

ω = nondimensional vorticity

ω_r, ω_i = real and imaginary parts of ω

Subscripts

0 = the reference state

1 = the basic flow state

′ = perturbation quantity

The definition of ψ is

$$\frac{\partial \psi}{\partial z} = u, \frac{\partial \psi}{\partial x} = -w \tag{8}$$

These equations have been nondimensionalized by the use of characteristic length h and characteristic time h^2/κ. Temperature difference from T_0 is nondimensionalized by ΔT; solute difference from S_0 is nondimensionalized by $-h(\partial S/\partial \zeta)_0$.

The initial conditions are

$$\begin{gathered} t < 0 \quad T = 0 \text{ throughout} \\ t \leq 0 \quad S = S_0 - z \cos\theta - x \sin\theta \\ t = 0 \quad T = 1 \text{ at } x = 0 \end{gathered} \tag{9}$$

The boundary conditions are

$$\begin{gathered} u = w = \frac{\partial S}{\partial x} = 0, \quad \text{at } x = 0 \text{ and } L \\ T = 1 \text{ at } x = 0, \quad \text{and } T = 0 \text{ at } x = L \end{gathered} \tag{10}$$

In order to simulate the physical experiments, L must be large compared to h so that the presence of the opposite cold wall does not affect the results. This can be achieved if $L \geq 8$ [6].

We now seek a basic time-dependent solution which is parallel to the sloping walls, thus

$$u_1 = 0, \quad w_1 = w_1(x, t), \quad \omega_1 = \omega_1(x, t), \text{ etc.}$$

The solute distribution is written as

$$S = S_0 - z \cos\theta + S_1(x, t) \tag{11}$$

so that the initial condition on $S_1(x, t)$ is

$$S_1(x, 0) = -x \sin\theta \tag{12}$$

The equations for the basic flow become

$$\frac{1}{\mathrm{Pr}} \frac{\partial \omega_1}{\partial t} = \frac{\partial^2 \omega_1}{\partial x^2} - \mathrm{R} \cos\theta \left[\frac{\partial T_1}{\partial x} - \frac{\partial S_1}{\partial x} \right] + \mathrm{R} \sin\theta \cos\theta \tag{13}$$

$$\frac{\partial T_1}{\partial t} = \frac{\partial^2 T_1}{\partial x^2} \tag{14}$$

$$\frac{\partial S_1}{\partial t} = w_1 \cos\theta + \tau \frac{\partial^2 S_1}{\partial x^2} \tag{15}$$

$$\nabla^2 \psi_1 = \omega_1 \tag{16}$$

The same initial and boundary conditions (9) and (10) apply except for S_1 as noted above.

Let now the flow be disturbed by small perturbations

$$\begin{gathered} S = S_0 - z \cos\theta + S_1(x, t) + S'(x, z, t) \\ T = T_1(x, t) + T'(x, z, t) \\ u = u'(x, z, t) \\ w = w_1(x, t) + w'(x, z, t). \text{ etc.} \end{gathered}$$

The linearized equations are:

$$\frac{1}{\mathrm{P_r}} \frac{\partial \omega'}{\partial t} = \frac{\partial^2 \omega'}{\partial x^2} - \mathrm{R} \cos\theta (T'_x - S'_x) + \mathrm{R} \sin\theta (T'_z - S'_z) - \frac{1}{\mathrm{Pr}} \left(u' \frac{\partial \omega_1}{\partial x} - w_1 \frac{\partial \omega'}{\partial_z} \right) \tag{17}$$

$$\frac{\partial T'}{\partial t} = \nabla^2 T' - u' \frac{\partial T_1}{\partial x} - w_1 \frac{\partial T'}{\partial z} \tag{18}$$

$$\frac{\partial S'}{\partial t} = \tau \nabla^2 S' + w' \cos\theta - w_1 \frac{\partial S'}{\partial z} - u' \frac{\partial S_1}{\partial x} \tag{19}$$

$$\nabla^2 \psi' = \omega' \tag{20}$$

with boundary conditions

$$T' = u' = w' = \partial S'/\partial x = 0 \quad \text{at } x = 0 \text{ and } L \tag{21}$$

Earlier experiments show that the secondary flow is periodic in z; we therefore assume that the perturbations have the following form

$$\omega' = [\omega_r(x, t) + i\omega_i(x, t)] \exp(iKz), \text{ etc.} \tag{22}$$

When these are substituted into equations (17)–(20) and real and imaginary parts are separated, we obtain eight equations, six of which describe the time evolution of T', S', and ω', and two of which relate ω' to ψ'. It is to be noted that only real quantities have physical meaning.

3 Method of Solution

The basic and perturbation equations are integrated forward in time simultaneously. In the basic flow, the sudden elevation of the boundary temperature and the switching-on of diffusivities at $t = 0$ induce an upward flow along the slope. For the perturbed flow, small random disturbances in ω are distributed initially throughout the flow field. It was found in [6] that initial disturbances either in ω, T, or S would yield the same result. The random disturbances are generated by IBM subroutine RANDU with their magnitude limited between $\pm 0.5 \times 10^{-4}$. With such an assumption, the initial kinetic energy of the perturbations is of the order 10^{-10} while that of the basic flow is of order one.

The diffusion equations are written in finite-difference form using forward time differences and central space differences. To insure stability of the numerical scheme, the time step is chosen such that $\Delta t = 0.35\ \Delta x^2/\mathrm{P_r}$.

The equation relating ψ and ω when written in finite difference form becomes tridiagonal, which can be solved by Gaussian elimination. The perturbation kinetic energy which is calculated according to the expression given in [6] is evaluated at each time step. The wavenumber K is systematically varied to obtain the fastest growing wave. All calculations are made with $\mathrm{P_r} = 7.0$ and $\tau = 0.0033$ which are appropriate for a sugar solution. Δx is set at 0.05, a value which was shown by [6] to be adequate.

4 Results and Discussion

4.1 Inclined Geometry. It is assumed that the width of the tank is $8h$. Since for a given initial density gradient, the characteristic length h varies as $\mathrm{R}^{1/4}$, there will be a small variation in the physical size of the tank as the Rayleigh number is varied. To fix ideas, the values of h and ΔT are shown in Table 1 with increasing values of θ for $\mathrm{R} \cos\theta = 10^5$ for a density gradient of -0.27×10^{-2} cm^{-1}. To obtain these values, we assumed that $\nu = 1.05 \times 10^{-2}$ cm^2/s, $\kappa = 1.5 \times 10^{-3}$ cm^2/s, and $\alpha = 3.06 \times 10^{-4}$ °C^{-1}. It is seen that h increases from 0.88 cm to 1.23 cm as θ increases 0 deg to 75 deg. This increase in the physical size of the tank will not materially affect the stability results since at the time of onset of instabilities, the effect of the opposite wall is negligible.

The basic time-dependent convective flow exhibits an interesting behavior. The step increase in temperature along one of the sloping walls induces a convective velocity of large magnitude. As a result, fluid is brought upward into a region where it becomes heavier than its surroundings. The fluid parcel experiences a negative buoyancy force and decelerates. It overcompensates and becomes buoyant again, and thus accelerates. The velocity profile oscillates about a mean which decays slowly towards the steady state value. The kinetic energy of the basic flow E_B oscillates at the Brunt-Väisälä frequency characterized by the gravity component and the density gradient along the wall. This is exhibited in Fig. 3 in which E_B is shown for $\theta = 30$ deg

Table 1 Values of h and ΔT for $\mathrm{R} \cos\Theta = 10^5$ with initial density gradient $= -0.27 \times 10^{-2}$ cm^{-1}

θ	h, cm	ΔT, °C
0 deg	0.878	7.75
30 deg	0.911	8.03
45 deg	0.958	8.45
60 deg	1.045	9.22
75 deg	1.231	10.86

and 75 deg. The nondimensional period of oscillation T_p is given by

$$T_p = \frac{2\pi}{(\mathrm{P_r R}\cos^2\theta)^{1/2}}$$

The appropriate periods of oscillations for these two cases are shown in the figure. As the angle of inclination of the wall decreases toward zero, both the density gradient and the component of gravity along the wall increase. This in effect increases the spring constant resulting in an oscillation of higher frequency or lower period. At later times, the amplitude of oscillations decreases and E_B approaches the steady state value. For $h = 1$ cm, $t = 1$ corresponds to approximately 670 s.

Vertical velocity distributions for $\theta = 30$ deg at times corresponding to a local maximum and minimum in E_B are shown in Fig. 4. In general, there is upward flow near the heating wall and a slow return flow in the rest of the tank as required by continuity. The physical velocity is extremely small. For $w = 1$, it corresponds to a velocity of 1.65×10^{-2} cm/s. Velocity distributions at other angles have the same characteristics. The magnitude of the maximum velocity increases with angle of inclination.

The time-evolution of the perturbation kinetic energy is shown in Fig. 5 for $\mathrm{R}\cos\theta = 10^5$. The kinetic energy of the perturbations normalized with respect to its initial value, E, is shown as a function of time. Initially there is a rather sharp decay of the perturbed motion due to viscous damping. If the Rayleigh number is supercritical, as is true in the present case, the decay is halted and E assumes exponential growth. During the decay phase, the perturbation kinetic energy also exhibits oscillations at large inclination angles. Its frequency, however, is twice the Brunt-Väisälä frequency characterized by the gravity component and density gradient *normal* to the wall. Since in this case, the velocity components oscillate about zero rather than a finite mean value, the energy, being the square of the velocity, will exhibit a frequency twice that of the velocity oscillations. These oscillations are not detected for $\theta \leq 30$ deg. It becomes noticeable at $\theta = 45$ deg, and becomes increasingly prominent at higher angles. The amplitude of oscillations, being quite large initially at $\theta = 75$ deg, decays and finally disappears when exponential growth takes place.

The occurrence of oscillations in E as a function of the inclination angle can be explained in terms of the relative directions of the solute gradient and the temperature gradient in the fluid. In the case of vertical walls, $\theta = 0$ deg, the solute gradient is essentially vertical and the temperature gradient horizontal. Oscillation of the perturbation motion in the direction of the solute gradient will be quickly damped as there is negligible release of potential energy. However, if the solute and temperature gradients are in the same direction as in the case of a horizontal layer, then oscillations in the direction of the solute gradient will be accompanied by the release of potential energy as the fluid parcel is moving in a temperature gradient. As the angle of inclination is reduced, this effect becomes smaller.

It is seen from these curves that the growth of E becomes less rapid as the angle of inclination is increased while $\mathrm{R}\cos\theta$ is kept at 10^5. All curves shown are for the critical wavelengths; the growth of E for other wavelengths is less rapid. The predicted values of the critical wavelengths are compared with the experimentally observed values in Table 2. The agreement is better at larger angles. This may be attributed to the cell erosion process discussed in [3] and [4]. At lower values of θ, the critical wavelengths are small and there are many

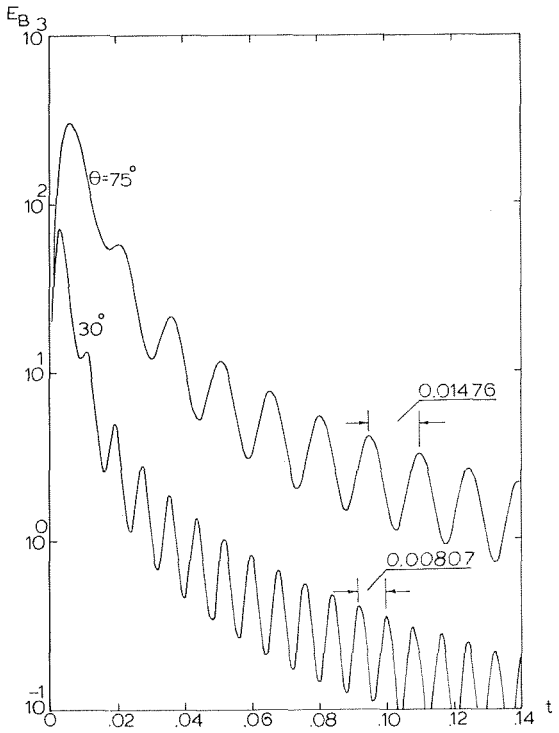

Fig. 3 Variation of kinetic energy of the basic flow for R cos Θ = 10^5

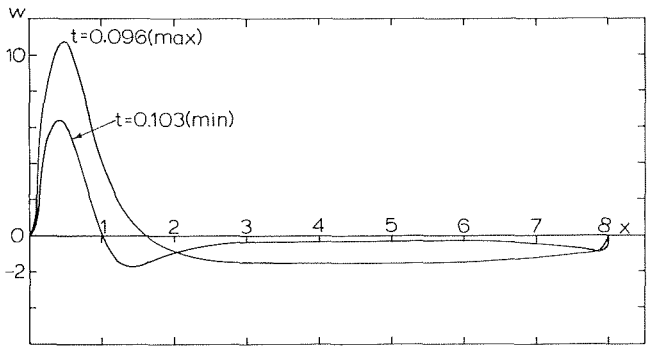

Fig. 4 Vertical velocity distribution for Θ = 30 deg

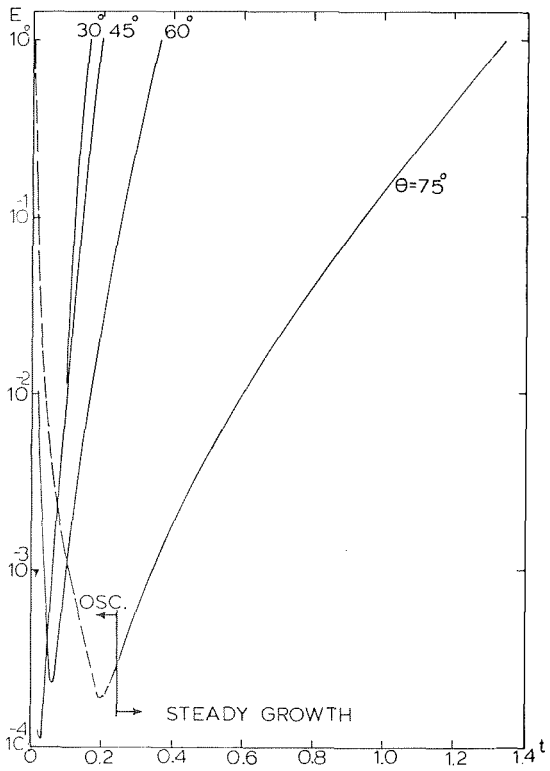

Fig. 5 Growth of perturbation kinetic energy at R cos Θ = 10^5

Table 2 Comparison of predicted and observed critical wavelengths in the vertical direction

θ	$\lambda_{cr} \cos\theta$, cm Predicted	Observed
0 deg [6]	0.49	0.59–0.85
30 deg	0.583	0.80
45 deg	0.657	0.84
60 deg	0.809	0.79
75 deg	1.261	1.30

convection rolls along the heating wall. Erosion process takes place shortly after the rolls are formed. As the angle is increased, the rolls become larger, and the erosion process takes longer time. For $\theta \leq 45$ deg, the predicted wavelength is about 70–80 percent of that observed, indicating, perhaps, at the time of observation some erosion has taken place already.

At each angle, calculations are repeated as the value of R cos θ is reduced in discrete steps while keeping the same critical wavelength. The growth of the perturbation kinetic energy becomes slower and slower. When the value of the Rayleigh number is reduced below the critical value, the perturbation kinetic energy decays steadily. Since the value of R cos θ is varied in steps, what we obtain is a critical Rayleigh number range. These are shown in Fig. 1 by a symbol I indicating the two limits, and are connected by a chain-dot line. There is shallow minimum around $\theta = 30$ deg. In general the predicted critical Rayleigh numbers form the lower limit of the transitional regime of the experimental data. It may be concluded that up to $\theta =$ 60 deg the critical state is $(R \cos\theta)_{cr} \simeq 10^4$. Beyond $\theta = 60$ deg, the critical Rayleigh number increases; at $\theta = 75$ deg, it is almost three times as large.

4.2 Horizontal Geometry. It is realized that the character of the basic state in a horizontal geometry is completely different from that in an inclined geometry. For angles of inclination different from 90 deg, however small the difference, the basic state consists of a time-dependent convective flow. When $\theta = 90$ deg, the source term in the vorticity equation (13) for the basic flow vanishes. The basic state is that of a stratified layer of quiescient fluid with heat slowly being diffused from the lower wall. It is a reasonable expectation then that the critical Rayleigh number varies smoothly with θ until $\theta = 90$ deg, where it may experience a discontinuity.

For the horizontal geometry the problem becomes that of impulsively heating from below a stably stratified layer. The stability of such a layer with free-free boundary conditions and a steady linear temperature profile has been considered by Veronis [7]. The layer becomes unstable in an overstable mode with the frequency of the most unstable mode given by

$$f_{cr} = \left[\frac{1-\tau}{3(1+P_r)}\right]^{1/2} N \tag{23}$$

when N is the Brunt-Väisälä frequency.

The results of our calculations for the impulsive heating of a horizontal layer at $R = 10^5$ are shown in Fig. 6. The perturbation kinetic energy first decays with an oscillation at twice the Brunt-Väisälä frequency. At $t = 0.047$, it starts to grow with a slow modulation. For the three complete cycles calculated, the periods are 0.040, 0.317, and 0.0293. The period of the most unstable mode calculated according to (23) is 0.036, which is not too far from the values obtained. When the Rayleigh number is reduced to 10^4, the perturbation kinetic energy decays steadily, indicating stability. It is noted that with our method of scaling the tank width is always $8h$. With such a wide tank and given density gradient, the steady-state temperature gradient is always below the critical value for instability. What we calculate for here is the time-dependent case. As the temperature diffuses upward from the boundary, it may exceed the critical value within a thin layer near the heated wall. Once the fluid overturns, successive layers will be generated as demonstrated by Turner [8].

4.3 Streamline Pattern. Perturbation streamlines have been obtained through the use of a computer plotter routine. In Fig. 7 we show the streamline pattern for the case $\theta = 45$ deg, R cos $\theta = 10^5$ and $t = 0.4$. Values of stream functions shown are $\psi'/\psi'_{max} = \pm 0.2, \pm 0.4, \pm 0.6, \pm 0.8$. The hot wall is at $x = 0$. The nondimensional width of the tank is eight; only half of the tank is shown. The elongated vortices are set approximately 45 deg with respect to the wall, and they are of alternate signs. Little or no motion is found beyond $x = 3$. Streamline patterns for a horizontal layer at $R = 10^5$ are shown in Figs. 8 and 9. The gravity vector in this case is the negative x − direction. The Streamlines at $t = 0.137$, which corresponds to a relative maximum of the perturbation kinetic energy (cf. Fig. 6) are shown in Fig. 8. The pattern shows a regular array of vortices. At a relative minimum of the perturbation kinetic energy at $t = 0.148$, the pattern consists of vortices with double peaks as shown in Fig. 9. Further study is needed to ascertain the evolution of these vortices through successive maxima and minima.

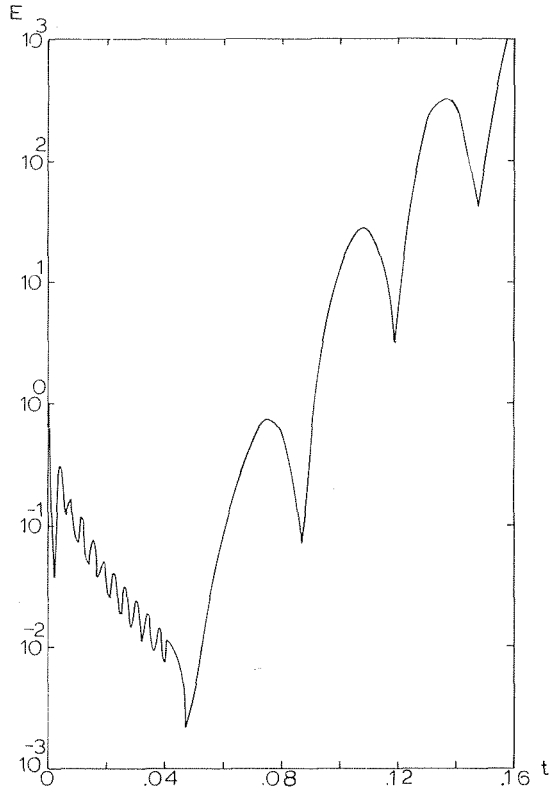

Fig. 6 Growth of perturbation kinetic energy in a horizontal layer at R = 10^5

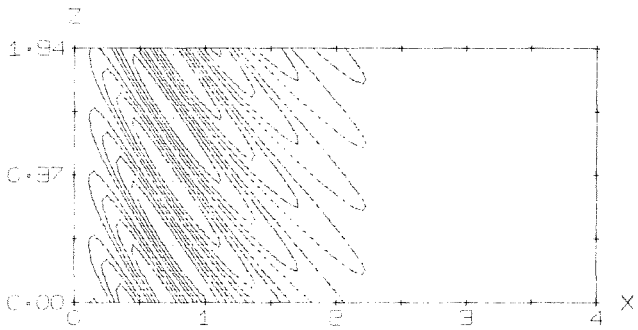

Fig. 7 Streamline pattern for Θ = 45 deg, R cos Θ = 10^5, and $t = 0.4$

5 Conclusions

a) The effect of heating from a sloping wall on the onset of instabilities in a stably stratified fluid can be correlated very well by the Rayleigh number with reduced gravity, R cos θ, up to $\theta = 60$ deg. Within this range the critical value of R cos θ is approximately 10^4.

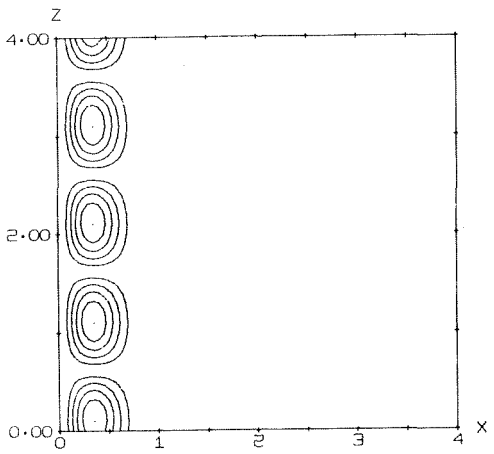

Fig. 8 Streamline pattern for $\Theta = 90$ deg, $R = 10^5$, and $t = 0.137$

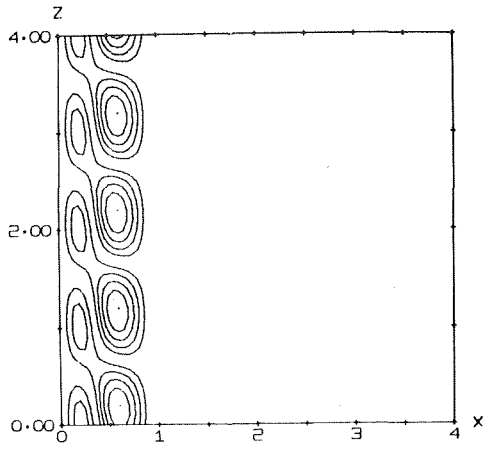

Fig. 9 Streamline pattern for $\Theta = 90$ deg, $R = 10^5$, and $t = 0.148$

b) Beyond $\theta = 60$ deg, the effect of heating from below becomes important, and $(R \cos \theta)_{cr}$ becomes larger. At $\theta = 75$ deg $(R \cos \theta)_{cr} \simeq 2.5 \times 10^4$.

c) No overstability is encountered for $0 \leq \theta \leq 75$ deg. For a horizontal layer, $\theta = 90$ deg, however, instability onsets in an overstable mode at a frequency close to that given by Veronis [6]. This conclusion agrees with the findings of Paliwal and Chen [9] for the stability of steady convection of a stably stratified fluid in a heated inclined slot.

d) The method of analysis yields values of critical Rayleigh numbers and critical wavelengths which are in reasonable agreement with previous experimental results.

Acknowledgment

The financial support of the National Science Foundation through Grant ENG-73-03534-A01 is gratefully acknowledged.

References

1 Wunsch, C., "On Oceanic Boundary Mixing," *Deep-Sea Res.*, Vol. 17, 1970, pp. 293–301.

2 Phillips, O. M., "On Flows Induced by Diffusion in a Stably Stratified Fluid," *Deep-Sea Res.*, Vol. 17, 1970, pp. 435–443.

3 Chen, C. F., Paliwal, R. C., and Wong, S. B., "Cellular Convection in a Density-Stratified Fluid: Effect of Inclination of the Heated Wall," *1976 Heat Transf. Fluid Mech. Inst.*, pp. 18–32, Stanford University Press.

4 Chen, C. F., Briggs, D. G., and Wirtz, R. A., "Stability of Thermal Convection in a Salinity Gradient Due to Lateral Heating," *Int. J. Heat Mass Transf.*, Vol. 14, 1971, pp. 57–66.

5 Chen, C. F. and M. W. Skok, "Cellular Convection in a Salinity Gradient Along a Heated Inclined Wall," *Int. J. Heat Mass Transf.*, Vol. 17, 1974, pp. 51–60.

6 Chen, C. F., "Onset of Cellular Convection in a Salinity Gradient Due to a Lateral Temperature Gradient," *J. Fluid Mech.*, Vol. 63, 1974, pp. 563–576.

7 Veronis, G., "On Finite Amplitude Instability in Thermohaline Convection," *J. Mar. Res.*, Vol. 23, 1965, pp. 1–17.

8 Turner, J. S., "The Behaviour of a Stable Salinity Gradient Heated from Below," *J. Fluid Mech.*, Vol. 33, 1968, pp. 183–200.

9 Paliwal, R. C. and Chen, C. F., "Stability of Motion of a Density-Stratified Fluid in a Differentially Heated Inclined Slot", *Bull. Am. Phys. Soc.*, Vol. 22, 1977, p. 1276.

F. Tamanini

Senior Research Scientist,
Factory Mutual Research Corporation,
Factory Mutual System,
Norwood, Mass. 02062

The Effect of Buoyancy on the Turbulence Structure of Vertical Round Jets

The paper presents an application of the algebraic stress modeling (ASM) technique to the prediction of the flow in a turbulent round buoyant jet. In the ASM approach, algebraic formulas are obtained for the Reynolds stresses, $\overline{u_i u_j}$, and for the components of the turbulent heat flux, $\overline{tu_i}$. In the model used here, transport equations are solved for the turbulence kinetic energy, k, its dissipation, ϵ, and the mean square temperature fluctuations, g. The study shows that buoyancy increases the rate of dissipation of g above the values indicated by previous recommendations for the modeling of that quantity. As a possible explanation for this result it is suggested that buoyancy introduces anisotropy in the fluctuations at the dissipation scale. The study shows that the contribution from the secondary components of the strain tensor to the production of k is non-negligible. In addition, between 12 and 17 percent of the longitudinal enthalpy flux is contributed by the turbulent fluctuations.

Finally, it is observed that the modeling of buoyant flows still presents uncertainties and that additional work is necessary to properly account for the effect of buoyancy on the production of ϵ and the dissipation of g.

Introduction

Over the past ten years significant progress has been made in the development of turbulence models which are suitable for engineering applications [1]. In current practice, much popularity is enjoyed by so-called two-equation models, where the turbulent transport is evaluated from an algebraic formula involving two properties of the turbulence; these in turn are obtained by finding the solution to a modeled form of their transport equations. The turbulence kinetic energy, k, and its dissipation, ϵ, are often selected as the two properties which characterize the turbulence field [2]. In situations where it is necessary to estimate the level of fluctuations of a scalar quantity, an additional model transport equation is introduced for the mean square fluctuations, g, of temperature or concentrations.

A higher level of sophistication is achieved by Reynolds-stress models in which equations are solved for all second-order correlations among velocity components and scalar quantities. The drawback of this approach lies in the increased complexity of the formulation and consequent increased computer time required to obtain solutions [2, 3]. In this study, we have preferred to follow a suggestion for algebraic stress modeling (ASM) originally made by Rodi [4] and later extended to the components of the turbulent heat flux by Gibson and Launder [5]. The final scheme amounts to an improved version of the k-ϵ-g formulation, where the improvement is represented by the fact that the large-scale anisotropy of the flow is taken into account through the replacement of some of the constants of the standard k-ϵ-g model with known functions of gradients of the mean velocity and temperature fields and ratios of production and dissipation of k and g. Meroney [6], in his study of stratified turbulent shear flows, has shown that the ASM approach is much more economical than a full Reynolds-stress model, while sacrificing little in terms of accuracy.

In this paper we present an application of the ASM technique to the case of axisymmetric thermal plumes; the results from a comparison with experimental data are used to: 1) emphasize the limitations of the model in its present form; and 2) discuss the modifications in the structure of the flow induced by the presence of buoyancy.

Theoretical Model

The equations used by the model and details on their derivation can be found in [7]. In the following sections we will simply highlight the deviations from standard practice. A complete list of symbols is given in the nomenclature. It should be noted that capital letters or overbars indicate mean quantities, while lower case letters or primes refer to fluctuating components.

Mass, Momentum and Energy. Conservation of mass, momentum and energy is imposed by writing the boundary layer form of the appropriate conservation equations, which were obtained by neglecting turbulent correlations involving density fluctuations. The turbulent shear stress in the momentum equation and the radial

Contributed by the Heat Transfer Division for publication in the JOURNAL OF HEAT TRANSFER. Manuscript received by the Heat Transfer Division August 19, 1977.

turbulent heat flux in the energy equation are left in their exact form, in anticipation of the fact that model expressions for all second-order correlations will be available.

In what might appear to be inconsistent with the boundary layer assumption, we have retained the longitudinal gradients of the quantity $\overline{u_x}^2 - \overline{u_r}^2$ in the x-momentum equation:

$$(C - D)_{U_x} = -\partial/\partial x(\bar{\rho}(\overline{u_x}^2 - \overline{u_r}^2)) + a_g(\rho_0 - \bar{\rho}) \quad (1)$$

and of the longitudinal heat flux, $\overline{tu_x}$, in the energy equation:

$$(C - D)_T = -\partial/\partial x(\bar{\rho}\,\overline{tu_x}) \quad (2)$$

where C and D indicate, respectively, the convective and diffusive term of the quantity indicated as a subscript. The reason for retaining these terms will be further discussed later: at this point, it is sufficient to state that in a thermal plume $\overline{tu_x}$ gives a non-negligible contribution to the total energy flux. Even though the corresponding term in the momentum equation is not as important, overall consistency of the model motivates its retention.

Turbulent Correlations. Transport equations are solved for three quantities: turbulence kinetic energy, k, dissipation of turbulence kinetic energy, ϵ, and mean square temperature fluctuations, $g \equiv \overline{t}^2$. The structure of the model equations is the same for all three quantities and is given by:

$$(C - D)_\gamma = \bar{\rho}(P_\gamma - \epsilon_\gamma) \quad (3)$$

where P_γ and ϵ_γ represent production and dissipation of the variable in question ($\gamma = k, \epsilon$ or g).

For the modeling of turbulent diffusion we have relied on a proposal for gradient-driven diffusion made by Launder, et al. [8]. We believe that this choice is appropriate for the flow modeled in this study, even though it is understood that, for more complex situations, the direct effect of buoyancy on turbulent transport may have to be included [3].

With regard to the terms representing production (P_γ) and dissipation (ϵ_γ), some require modeling, while some can be treated exactly as indicated in the following sections.

Turbulence Kinetic Energy (k). The dissipation of k is ϵ by definition: the problems related to its modeling are, therefore, shifted to the ϵ-equation. The production P_k is also treated exactly because it involves calculable correlations and mean field gradients. The source P_k is evaluated by the model as:

$$P_k = 1/2 \sum_i P_{ii} \quad (4)$$

where the sources of the Reynolds stresses $\overline{u_x}^2$, $\overline{u_r}^2$, $\overline{u_\theta}^2$ are given by:

$$P_{xx} = -2\overline{u_x}^2(\partial U_x/\partial x) - 2\overline{u_x u_r}(\partial U_x/\partial r) - 2a_g\overline{\rho' u_x}/\bar{\rho} \quad (5)$$

$$P_{rr} = -2\overline{u_r}^2(\partial U_r/\partial r);\ P_{\theta\theta} = -2\overline{u_\theta}^2 U_r/r \quad (6, 7)$$

Note the presence of the last term in equation (5) representing production of $\overline{u_x}^2$ due to buoyancy.

Equations (5)–(7) are written by neglecting the component $\partial U_r/\partial x$ of the strain tensor. In a departure from the common practice of boundary layer treatments, we have kept the terms involving $\partial U_x/\partial x$ and $\partial U_r/\partial r$ even though they should be small with respect to $\partial U_x/\partial r$. It will be shown that quantities containing these terms give rise to production of k which is by no means negligible.

Because of the cylindrical geometry, a term involving a third-order correlation, $2\overline{u_r u_\theta}^2/r$, should appear in P_{rr} and, with the opposite sign, in $P_{\theta\theta}$. We have neglected these higher order correlations but without being too confident that it is appropriate to do so. A clarification of this issue should not be postponed, particularly considering the fact that the k-ϵ model is known to require special adjustments when applied to axisymmetric forced jets [2].

Dissipation of Turbulence Kinetic Energy (ϵ). In dealing with the terms P_ϵ and ϵ_ϵ representing production and dissipation of ϵ, both of which require modeling, we follow standard k-ϵ practice [2, 8] and write:

$$P_\epsilon = \epsilon(c_{\epsilon 1}P_k - (c_{\epsilon 3} - c_{\epsilon 1})a_g\overline{\rho' u_x}/\bar{\rho})/k \quad (8)$$

$$\epsilon_\epsilon = c_{\epsilon 2}\epsilon^2/k \quad (9)$$

The above expressions are based on little more than dimensional analysis; therefore, one should not be excessively optimistic in estimating their performance in a buoyant flow.

The second term in brackets is introduced for the sake of generality, since there is no a priori argument saying that the sources of k associated with mean strain and buoyancy should appear in the ϵ-equation with the same weighing factor. In fact, Hossain and Rodi [9] have observed that different values of $c_{\epsilon 3}$ are required to match experimental data on horizontal and vertical buoyant jets. The choice, made in this study, to set $c_{\epsilon 3} = c_{\epsilon 1}$ should be regarded as subject to possible revision as more information becomes available on the performance of the model in different situations involving buoyant flows.

Mean Square Temperature Fluctuations (g). The source of temperature fluctuations is given by:

$$P_g = -2\overline{tu_x}(\partial T/\partial x) - 2\overline{tu_r}(\partial T/\partial r) \quad (10)$$

As for the case of P_k, no modeling is necessary since the terms appearing in the definition of P_g are all calculable. Note that the contribution from the longitudinal component of the turbulent heat flux is taken into account.

Nomenclature

a_g = acceleration of gravity, m/s^2
A_u, A_t, B_u, B_t = constants in equations (18) and (19)
c_{g2}, $c_{\epsilon 1}$, $c_{\epsilon 2}$, $c_{\epsilon 3}$ = model constants
C = convection term
D = diffusion term
f_i = "memory" factor in equation (12)
F_0 = buoyancy flux, m^4/s^3
g = mean square temperature fluctuations, (K)^2
H = enthalpy flux defined by equation (20), J/s
k = turbulence kinetic energy, m^2/s^2
K = entrainment coefficient defined in equation (21)
$\dot{M}$ = total mass flux, kg/s
P_γ = rate of production of γ per unit mass of fluid
r = radial coordinate, m
T, t = mean and fluctuating temperature, K
U_i, u_i = mean and fluctuating velocity components in the i-direction, m/s
W = jet momentum, kg m/s^2
x = longitudinal coordinate, m
γ = dummy variable, represents k, ϵ or g
ΔT = excess temperature above ambient ($T - T_0$), K
ϵ = dissipation of turbulence kinetic energy, m^2/s^3
ϵ_γ = rate of dissipation of γ per unit mass of fluid
ρ = density, kg/m^3

Subscripts

c = centerline
i, j = indexes referring to coordinate axes
is = isotropic
x, r, θ = longitudinal, radial, tangential component
1 = nozzle fluid conditions
0 = room conditions

Superscripts

$\bar{}$ indicates time average
$'$ indicates fluctuating component

In the modeling of the dissipation, ϵ_g, we follow the standard k-ϵ-g approach, as proposed by Spalding [10]:

$$\epsilon_g = c_{g2} g \epsilon / k \tag{11}$$

There is indication that equation (11) may not be adequate to model ϵ_g; the unusually high value (2.80) adopted in this work for the constant c_{g2} tends to confirm that opinion. In [7] we suggest the possibility that the increase in the value of c_{g2} is due to the fact that buoyancy distorts the turbulence all the way down to the dissipation scale. To account for such effect we proposed to write [7]:

$$c_{g2} = c_{g2,is} \frac{8}{81} \sum_i f_i^{-2} (\overline{u_i^2}/k)^{-3} \tag{12}$$

where the constant $c_{g2,is}$ can be obtained from data on the decay of temperature fluctuations in isotropic turbulence. The functions f_i (for $i = x, r, \theta$) are memory factors, which are as yet unknown, but probably depend on the flux Richardson number, R_f, and the ratios, P_k/ϵ and P_g/ϵ_g.

The proposal of equation (12) is still at an early stage of development; it might turn out that the modeling of the functions f_i is so complex as to make the solution of a separate transport equation for ϵ_g a more attractive alternative. It should be mentioned that Zeman and Lumley [3] and Meroney [6] have already undertaken the latter approach and that Launder [11] also argues for it.

Reynolds Stresses ($\overline{u_i u_j}$). The starting point for the modeling of the Reynolds stresses is represented by the transport equation for $\overline{u_i u_j}$ developed by Launder, et al. [8]. Rodi's proposal [4] for algebraic stress modeling eliminates from the equation the terms containing derivatives of $\overline{u_i u_j}$ by assuming:

$$(C - D)_{\overline{u_i u_j}} = \frac{\overline{u_i u_j}}{k} (C - D)_k \tag{13}$$

After some algebra, the introduction of the above assumption in the model equation for $\overline{u_i u_j}$ leads to an algebraic formula for $\overline{u_i u_j}$ [5, 7].

As anticipated in the introduction, the model can now account in some approximate way for the anisotropic distribution of turbulence kinetic energy among its components as well as for the direct effect of buoyancy on the shear stress.

Turbulent Heat Flux Components ($\overline{tu_i}$). In order to obtain expressions for the correlations $\overline{tu_i}$ we start from the model transport equation for these quantities proposed by Launder [12], and apply Rodi's concept for algebraic stress modeling in the form suggested by Gibson and Launder [5]:

$$(C - D)_{\overline{tu_i}} = \overline{tu_i} \left(\frac{1}{2\overline{u_i^2}} (C - D)_{\overline{u_i^2}} + \frac{1}{2\overline{t^2}} (C - D)_{\overline{t^2}} \right) \tag{14}$$

Following a procedure analogous to that adopted in the case of $\overline{u_i u_j}$, we obtain a formula for $\overline{tu_i}$ [7] which differs from that used by Gibson and Launder [5] only in the fact that we have not made the assumption $P_g = \epsilon_g$.

Choice of Model Constants. The model outlined in the preceding sections contains 11 constants, for which values must be selected. In our earlier work [7] we have not undertaken a systematic optimization effort, since we have considered only a limited number of flows, namely, forced and buoyant axisymmetric jets. As a general rule, we have adopted the values which users of k-ϵ-g or Reynolds stress techniques seem to agree upon and we have made changes only where strictly necessary. The complete set used for the calculations performed in the course of this study is given in [7].

We found that, of all the constants, c_{g2} is the only one requiring a value significantly different from those that have appeared in the literature. Spalding [10] for his predictions of concentration fluctuations in a round forced jet adopted $c_{g2} = 1.79$ and recently [9, 12] there has been a tendency toward the use of values as low as 1.25. We have already commented on the possibility that small-scale anisotropy is responsible for the spread among the values for c_{g2}; however, we did not make use of equation (12) in this study.

Another problem arises in relation to our choice of 1.92 for $c_{\epsilon 2}$. It is known [2] that the k-ϵ model is anomalous with regard to the case of forced round jets, in the sense that the adoption of the standard value for $c_{\epsilon 2}$, i.e., 1.92 when $c_{\epsilon 1} = 1.44$, leads to a predicted rate of spread which is too high. In fact, in our own calculations of round forced jets [7] we corrected for this effect by setting $c_{\epsilon 2} = 1.74$. The anomalous behavior of the forced jet could be due to the very rapid decay of the velocity ($\propto x^{-1}$); in that case, the thermal plume should be a normal flow with respect to the modeling of ϵ, since the velocity decay is much slower ($U_x \propto x^{-1/3}$). On the basis of this argument, we have finally chosen $c_{\epsilon 1} = 1.44$ and $c_{\epsilon 2} = 1.92$, i.e., the standard values. The presence of the additional parameter, $c_{\epsilon 3}$ (set equal to $c_{\epsilon 1}$ in the model) prevents us from reaching a definite conclusion on the appropriate value for $c_{\epsilon 2}$. The fact that we could also obtain agreement with thermal plume data using $c_{\epsilon 2} = 1.74$ and a lower value for $c_{\epsilon 3}$ ($\cong 0.9$), indicates that the issue is far from being resolved.

Boundary and Initial Conditions. Five differential equations for U_x, T, k, ϵ and g are solved using the Patankar-Spalding method [13] for parabolic flows. The transverse velocity U_r is obtained from the continuity equation. In the case of the round buoyant jet predicted here the dependent variables assume the ambient values ($U_x = k = \epsilon = g = 0$, $T = T_0 = 302$ K) at the outer edge of the initial shear layer and the nozzle values ($U_x = U_{x,1} \simeq 0.674$ m/s, $T = T_1 = 573$ K) at the inner edge. When the inner edge reaches the jet axis, the symmetry condition is imposed on the radial derivatives of the variables.

Establishing a set of initial conditions is easy for velocity and temperature (top-hat profiles were selected in the nozzle flow) but presents problems with regard to the turbulence quantities. The turbulence model used here cannot cope with low-Reynolds number turbulence, much less transition. Therefore, to be rigorous one should use the model starting at a station where the turbulence is fully developed and where radial profiles of k, ϵ and g are available. We follow the practice to begin the calculation at the rozzle lip by assuming laminar flow. Turbulence is then "turned on" at an arbitrary distance from the nozzle by selecting initial profiles for k, ϵ and g given by:

$$k = 10^{-4} U_x^2 \tag{15}$$

$$\epsilon = k^{3/2}/r_1 \tag{16}$$

$$g = 10^{-4}(T_1 - T)(T - T_0) \tag{17}$$

where r_1 (=0.0318 m) is the nozzle radius. The location for the beginning of the turbulent calculation is then adjusted so that the virtual origin of the computed flow matches that given by the experiment.

Experimental Data

Recently there has been renewed interest in turbulent buoyant jets and experimental investigations of the structure of the turbulence in axisymmetric plumes have finally appeared [14, 15]. This follows a 20 year interval during which Yih's measurements [16] for the profiles of mean temperature and vertical velocity have remained practically unchallenged. In the present study we have used the data by George, et al. [14], since we believe them to be more reliable. To justify this choice, however, we will describe the points on which the three cited studies agree and try to explain the differences.

The profiles of mean excess (over the ambient) temperature (ΔT) and vertical velocity (U_x) are usually presented in dimensionless form by giving their Gaussian fits:

$$(x/F_0)^{1/3} U_x = A_u \exp(-B_u (r/x)^2) \tag{18}$$

$$a_g (x^5/F_0^2)^{1/3} \frac{\Delta T}{T} = A_t \exp(-B_t (r/x)^2) \tag{19}$$

where the buoyancy flux F_0 is related by $F_0 = a_g H/(c_p \rho_0 T_0)$ to the enthalpy flux, H, which in turn is given by:

$$H = 2\pi c_p \int_0^\infty \bar{\rho} U_x \Delta T [1 + \overline{tu_x}/(U_x \Delta T)] r dr \tag{20}$$

The following values are reported for the four constants A_u, B_u, A_t and B_t by [14]–[16]:

	A_u	B_u	A_t	B_t
George, et al. [14]	3.4	55	9.1	65
Nakagome and Hirata [15]	—	39	—	63
Yih [16]	4.7	96	11	71

The three sets of data are in substantial agreement only with reference to the rate of spread of the temperature profile (constant B_t). Part of the difference between the values for A_t reported by George, et al. [14] and Yih [16] is due to the fact that the former evaluated H and, therefore, F_0 including the turbulent contribution (cf. equation (20)) while the latter did not. If tu_x is neglected, the F_0 associated with George, et al.'s data is reduced by 17 percent and the fit to the temperature data requires $A_t = 10.3$ instead of 9.1. One can conclude that the mean temperature profile is well established.

The situation is quite different for the velocity measurements. Yih's [16] measurements, which were obtained using a fan anemometer, imply that the velocity profile is narrower than the temperature profile. The other two studies [14, 15] come to the opposite result. In our opinion these are closer to the truth, since they involved a more reliable technique based on hot-wire anemometry with a procedure for the interpretation of the signal, which accounts for the instantaneous value of the temperature. Note that what is given by George, et al. [14] for B_u is a "recommended" value, which takes into account the possible overestimate of the one-wire probe near the edges of the plume. A fit through the actual data points would give $B_u = 45$, which is in good agreement with the value reported by Nakagome and Hirata [15].

Even though a final judgment probably must wait for measurements obtained with a velocity probe which does not suffer directional ambiguity, the above considerations are the basis for our choice of George, et al.'s results for the comparisons with the model predictions discussed in the following section.

Numerical Predictions

Radial Profiles of Mean and Fluctuating Velocity and Temperature. The model predictions for the radial profiles of mean and fluctuating components of vertical velocity and temperature are shown in dimensionless form in Figs. 1–4. As can be seen, there is overall good agreement between theory and experiment for all four quantities. The calculated profiles of mean variables essentially reach the self-preserving state at about eight diameters, while those of the fluctuating components require more time. The model predicts that at the last station at which measurements were made by George, et al. [14], i.e., 16 diameters from the source, all profiles are self-preserving. However, since the theory is not capable of accurately modeling the initial growth of the turbulence, the departure, which we believe to be small, of the conditions of the experiment from self-preservation should be judged on the basis of the data themselves and not on the results of the prediction.

The calculated profile of shear stress implies that the turbulent transport of momentum is greater than that calculated and measured for a round forced jet by about 45 and 90 percent respectively [7]. This result is contrasted by the observation that the longitudinal component of the turbulence intensity is of similar magnitude in the two cases: $(\overline{u_x^2})^{1/2}/U_{x,c} \cong 0.28$ on the axis of both flows and the rest of the radial profiles are also very similar. It is reasonable to infer that the action of buoyancy probably does not have a very strong effect on the level of the components of the turbulence kinetic energy.

The situation is quite different with reference to the temperature field. The relative intensity of temperature fluctuations, $(\overline{t^2})^{1/2}/\Delta T$, is measured by George, et al. [14] as being about 0.38 on the axis, while forced jet data for the same quantity seem to indicate a much lower value (~0.22, cf. [7]). This result is particularly remarkable, since buoyancy does not enter directly in the g-equation and should be evaluated by remembering the unusually large value of dissipation ($c_{g2} = 2.8$ in equation (11)), which is required to obtain a predicted level of temperature fluctuations in line with the experiment. With regard to the temperature fluctuations, it should be mentioned that Chen and Rodi [17] have calculated $(\overline{t^2})^{1/2}/\Delta T = 0.82$ on the plume axis using $c_{g2} = 1.25$; the disagreement between their prediction and experiment further confirms our finding for a need to increase c_{g2}.

Entrainment. An indication of more vigorous lateral transport in the buoyant jet than in the forced jet is given by the magnitude of the entrainment at the free boundary. We have chosen to present these results by using the entrainment coefficient K, defined by Ricou and Spalding [18] as:

$$K = \frac{d\dot{M}}{dx}/(\rho_0 W)^{1/2} \tag{21}$$

where $\dot{M}$ is the mass flux in the plume and W is the total momentum.

The value of K calculated for the thermal plume is about 0.55. If one neglects the turbulent contribution to W, which amounts to 8.3 percent of the total momentum, the asymptotic value of K is about 0.57. The results for the forced jet, taken from [7], indicate in that case a much lower value of $K = 0.29$ and, therefore, a difference of almost

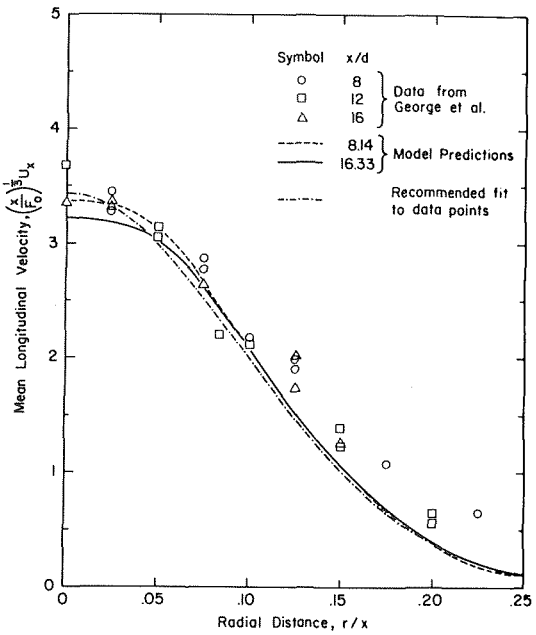

Fig. 1 Radial distribution of mean vertical velocity

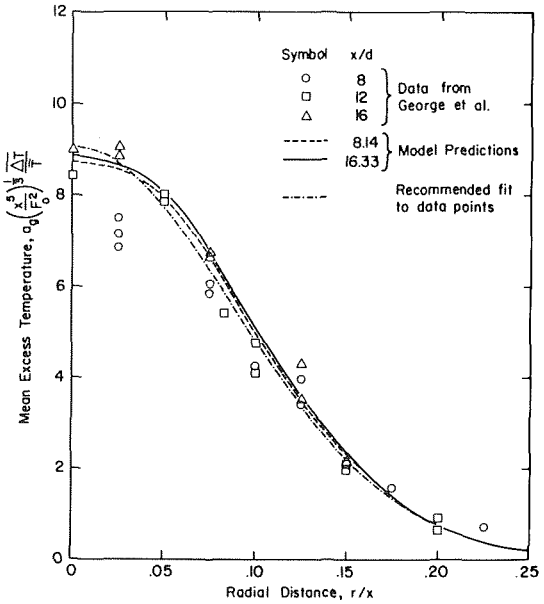

Fig. 2 Radial distribution of mean excess temperature

a factor of two. This result points to the fact that alterations of the turbulence structure due to buoyancy can have a profound impact on overall characteristics of the flow, even though other indicators of the intensity of the fluctuations are less dramatically affected.

Longitudinal Enthalpy Flux. Since turbulence is "stretched" by gravity in the longitudinal direction, one would expect temperature and velocity fluctuations in that direction to be highly correlated. Therefore, a quantity of interest is the longitudinal component of the turbulent heat flux. The prediction of the model, presented in the form of a correlation coefficient, is shown in Fig. 5. The data by George, et al. [14] indicate that this coefficient is roughly constant and equal to ~0.67, while the data by Nakagome and Hirata [15], which have more scatter, imply a value of about 0.5. As can be seen, the numerical predictions fall somewhere between these two sets of data. Selecting a value of 0.3, instead of 0.5, for one of the model constants (c_{t2}, see [5, 7]) would make the calculated correlation coefficient agree almost exactly with George et al.'s measurements. This indication is in agreement with the recommendations contained in the recent review by Launder [11] and suggests that only 30, instead of 50 percent, of the heat flux generated by mean strain and buoyancy is directly removed by the pressure fluctuations.

Note that the numerical model predicts that 12 percent (the data of George, et al. would indicate 17 percent) of the total longitudinal heat flux is contributed by the turbulent fluctuations. If the corresponding turbulent term in the energy equation were neglected, the calculated mean temperatures would be too large by 10–20 percent, because the total heat flux, H, is conserved in the thermal plume and there is no contribution to H due to turbulence at the beginning of the calculation, where the flow is assumed to be laminar.

Terms in k and g-Balance. Before concluding, it is appropriate to consider the relative magnitudes of the different terms entering in the transport equations for k and g. We will do so by discussing the profiles in Figs. 6 and 7 and by making reference to the forced jet case, studied elsewhere [7]. With regard to the balance for turbulence kinetic energy (Fig. 6), the results in [7] show that the normalized magnitude of the dissipation in the thermal plume is very close to that obtained for the forced jet. The production terms, however, are quite different: the total k-production is some 20 percent lower than the total dissipation for the forced jet, 30 percent higher for the buoyant jet.

The interesting result is that direct buoyancy effects, through the term $-a_g\overline{\rho' u_x}/\bar{\rho}$, are only partially responsible for the excess production of k; the rest of this excess comes from higher levels of shear. In addition, there is a non-negligible effect due to the secondary components of the strain tensor. The term $-\overline{u_x}^2(\partial U_x/\partial x)$, for example, has an overall negative contribution which amounts to 17 percent of the total production of k. When one considers that the contribution due to buoyancy is of the order of 23 percent, it is clear that it is not appropriate to discriminate against the contributions from the secondary components of strain by neglecting them. This is true, even though these terms almost cancel each other out, if one is interested in making a more accurate estimate of the repartition of k among its components.

The profiles of the terms entering the balance in the g-equation are shown in Fig. 7. The plot is analogous to the one referring to the forced jet case except for two details. The magnitude of the production and dissipation of g in the buoyant flow is almost 2.5 times as large as in the forced case. Furthermore, the production of g due to the longi-

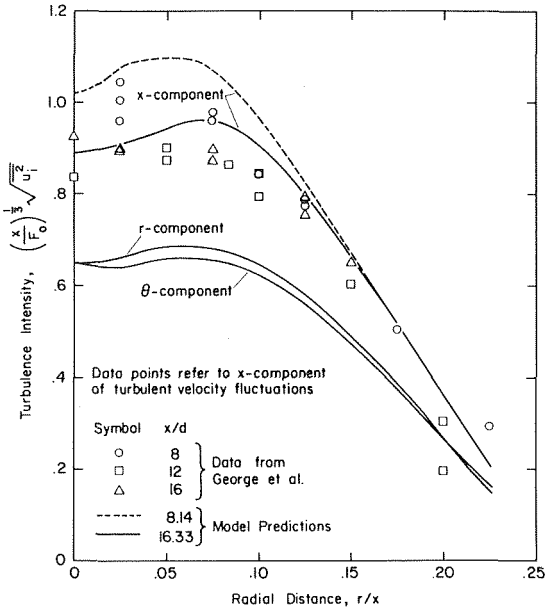

Fig. 3 Radial profiles of three components of turbulence intensity

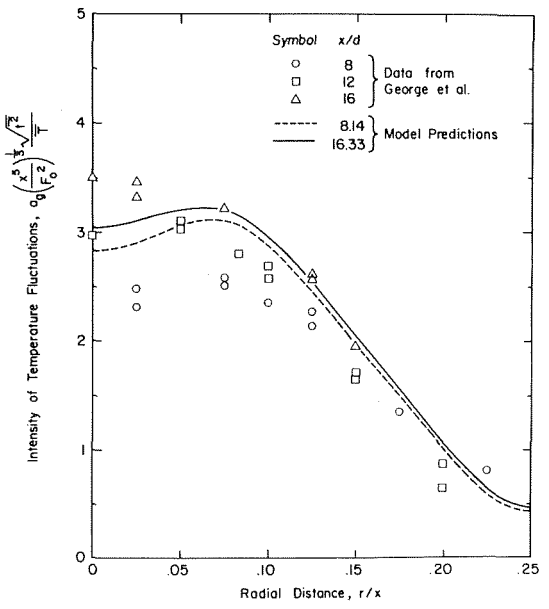

Fig. 4 Radial profiles of the intensity of temperature fluctuations

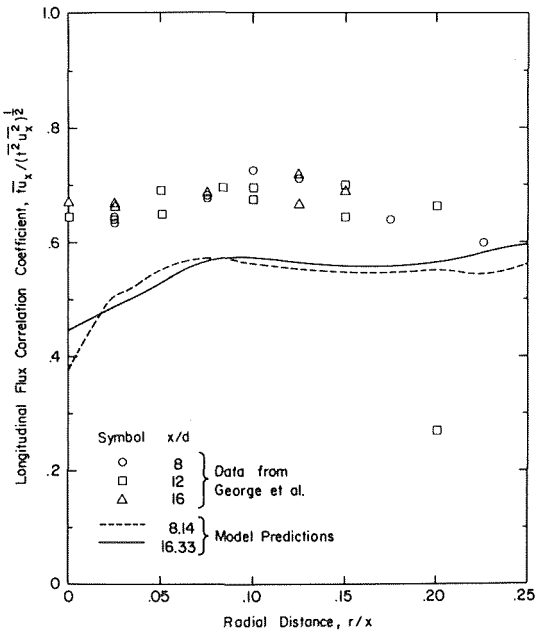

Fig. 5 Radial profile of vertical component of turbulent heat flux

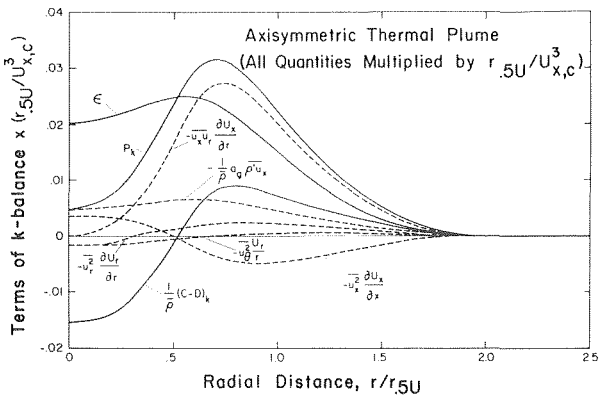

Fig. 6 Radial distribution of production/dissipation terms in the k-equation. The radius $r_{0.5U}$ represents the distance from the axis at which the vertical velocity U_x reaches half its centerline value

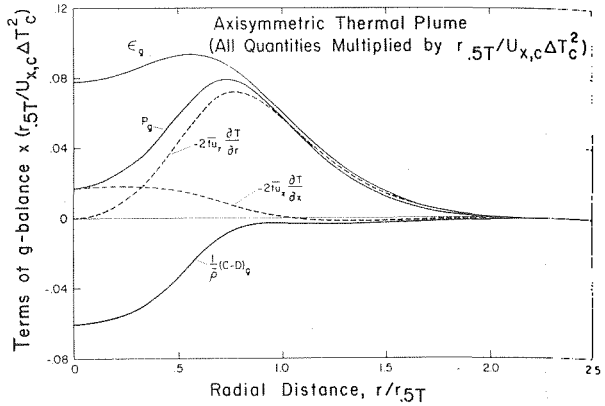

Fig. 7 Radial distribution of production/dissipation terms in the g-equation. The radius $r_{0.5T}$ represents the distance from the axis at which the excess temperature ΔT reaches half its centerline value

tudinal component of the turbulent heat flux, while negligible in the forced jet, gives a more significant contribution in the buoyant case. It should be pointed out, though, that the overall magnitude of such contribution, which is 6.3 percent of the total, is not as large as one might infer from Fig. 7, since the largest values occur near the axis. Despite this result, which shows the overall effect not to be too important, we would argue that the term may be more significant in buoyant flows other than the one examined here, and should be included, particularly considering that the quantity in question can be evaluated using the ASM approach with very little effort.

Conclusions

By using a modified version of the k-ϵ-g technique we have been able, with little computational effort, to retain in the model, terms which are usually neglected. As a result, we have found that in asymptotic round thermal plumes:

1 The longitudinal component of the turbulent heat flux accounts for 12–17 percent of the total heat flux in the plume;

2 the secondary components of the strain tensor give a significant contribution to the production of turbulence kinetic energy;

3 the source of temperature fluctuations associated with the longitudinal turbulent heat flux, while only 6.3 percent of the total in the case considered, can be of greater importance in other situations.

Somewhat unexpected was the need to increase the magnitude of the dissipation of temperature fluctuations by choosing a large value (2.80) for the constant c_{g2}. We postulate that part of such increase is due to buoyancy-induced anisotropy at the scale, where dissipation takes place. Related to this question is the modeling of the term representing production of ϵ due to buoyancy; it is not clear at this point to what extent the alleged small-scale anisotropy affects that quantity and whether new modeling schemes for P_ϵ should account for it. Hopefully, the results from this work on the effect of buoyancy for the case of round jets will help the process of a major rethinking of the treatment of the dissipation.

Acknowledgments

The author is grateful to John de Ris of Factory Mutual Research Corporation for continuous advice and encouragement. The study was internally sponsored and the support of the Research Corporation is acknowledged.

References

1 Launder, B. E. and Spalding, D. B., *Mathematical Models of Turbulence,* Academic Press, London and New York, 1972.

2 Launder, B. E., Morse, A., Rodi, W. and Spalding, D. B., "Prediction of Free Shear Flows-A Comparison of the Performance of Six Turbulence Models," *Proceedings Of The Conference On Turbulent Shear Flows,* NASA Langley Research Center, NASA SP-321 (N73-28154-173), July 1972, pp. 361–426.

3 Zeman, O. and Lumley, J. L., "A Second-Order Model for Buoyancy-Driven Mixed Layers," *Proceedings of the International Seminar on Turbulent Buoyant Convection,* Dubrovnik, Yugoslavia, 1976, pp. 65–76.

4 Rodi, W., "A New Algebraic Relation for Calculating the Reynolds Stresses," *Zeitschrift für Angewandte Mathematik and Mechanik,* Vol. 56, 1976, pp. 219–221.

5 Gibson, M. M. and Launder, B. E., "On the Calculation of Horizontal Turbulent, Free Shear Flows under Gravitational Influence," ASME JOURNAL OF HEAT TRANSFER, Vol. 98C, 1976, pp. 81–87.

6 Meroney, R. N., "An Algegraic Stress Model for Stratified Turbulent Shear Flows," *Computers and Fluids,* Vol. 4, 1976, pp. 93–107.

7 Tamanini, F., "An Improved Version of the k-ϵ-g Model of Turbulence and Its Application to Axisymmetric Forced and Buoyant Jets," FMRC Technical Report No. 22360-4, RC-B-63, Feb. 1977, Factory Mutual Research Corp., Norwood, Massachusetts.

8 Launder, B. E., Reece, G. J. and Rodi, W., "Progress in the Development of a Reynolds-Stress Turbulence Closure," *Journal of Fluid Mechanics,* Vol. 68, Part 3, 1975, pp. 537–566.

9 Hossain, M. S. and Rodi, W., "Influence of Buoyancy on the Turbulence Intensities in Horizontal and Vertical Jets," *Proceedings of the International Seminar on Turbulent Buoyant Convection,* Dubrovnik, Yugoslavia, 1976, pp. 39–51.

10 Spalding, D. B., "Concentration Fluctuations in a Round Turbulent Free Jet," *Chemical Engineering Science,* Vol. 26, 1971, pp. 95–107.

11 Launder, B. E., "Heat and Mass Transport by Turbulence," Chapter 6 in *Topics in Applied Physics—Turbulence,* P. Bradshaw ed., Springer, 1976.

12 Launder, B. E., "On the Effect of a Gravitational Field on the Turbulent Transport of Heat and Momentum," *Journal of Fluid Mechanics,* Vol. 67, Part 3, 1975, pp. 569–581.

13 Patankar, S. V. and Spalding, D. B., *Heat and Mass Transfer in Boundary Layers. A General Calculation Procedure,* 2nd ed., Intertext Books, London, 1970.

14 George, W. K., Alpert, R. L. and Tamanini, F., "Turbulence Measurements in an Axisymmetric Buoyant Plume," *International Journal Heat Mass Transfer, 20,* No. 11, 1977, pp. 1145–1154.

15 Nakagome, H. and Hirata, M., "The Structure of Turbulent Diffusion in an Axi-symmetrical Thermal Plume," *Proceedings of the International Seminar on Turbulent Buoyant Convection,* Dubrovnik, Yugoslavia, 1976, pp. 361–372.

16 Yih, C. S., "Free Convection Due to a Point Soruce of Heat," *Proceedings of the First U.S. National Congress of Applied Mechanics,* 1952, pp. 941–947.

17 Chen, C. J. and Rodi, W., "A Mathematical Model for Stratified Turbulent Flows and its Application to Buoyant Jets," *XVIth Congress, International Association for Hydraulic Research,* São Paolo, 1975.

18 Ricou, F. P. and Spalding, D. B., "Measurements of Entrainment by Axisymmetrical Turbulant Jets," *Journal of Fluid Mechanics,* Vol. 11, 1961, pp. 21–32.

R. O. Buckius
Assistant Professor.

D. C. Hwang
Graduate Research Assistant.

Department of Mechanical and Industrial Engineering, University of Illinois at Urbana-Champaign, Urbana, Ill.

Conservative Anisotropic Scattering in a Planar Medium with Collimated Radiation

The directional hemispherical and bidirectional reflectance and transmittance are presented for a conservative anisotropic scattering medium. Collimated incident radiation and linear anisotropic scattering are considered so that the azimuthal dependence must be retained. The effects of optical thickness, anisotropic scattering, incident angle, polar angle, and azimuthal angle are presented in a closed-form approximate solution. Comparisons with exact solutions are also presented.

Introduction

Anisotropic scattering is of considerable interest in many practical engineering problems. The radiant transfer contribution can be significant in problems of energy transport in particulate clouds, planetary atmospheres, porous materials, and pigment coatings. Many previous studies have employed numerical techniques in the solutions to such scattering problems. Chandrasekhar [1] has presented exact numerical solutions for the transmitted and reflected energy in a finite slab with isotropic scattering. Numerical results have also been obtained for nonconservative and conservative isotropic scatter in a finite medium [2]. Evans, Chu, and Churchill [3] have computed the transmittance and reflectance of a collimated beam incident upon a nonconservative anisotropically scattering slab. Numerical results for semi-infinite media have also been obtained [1, 4]. These results indicate the considerable differences between anisotropic and isotropic scattering problems.

The exact solutions to conservative scattering problems are complex and necessarily require large computing efforts. Various approximate techniques have been proposed to solve scattering problems with collimated incident radiation. Irvine [5–7] has discussed many of the standard approximations for the transmitted and reflected flux in finite and semi-infinite media. Armaly and Lam [8] have investigated collimated radiation incident on a semi-infinite medium and the effect of interface reflection and refraction. Since isotropic scattering was considered, the source function is independent of the azimuthal angle. Approximate results have also been presented by Wang [9] for anisotropic scattering with azimuthally symmetric radiation fields. Closed-form solutions [10, 11] have been obtained for anisotropically scattering finite media with diffuse walls and, therefore, are independent of the azimuthal angle.

The purpose of the present work is to study radiative transfer with anisotropic scattering in a finite medium. The solutions for the conservative case with a collimated incident beam are presented in an approximate closed form. Expressions for the bidirectional and directional hemispherical reflectance and transmittance are developed. The azimuthal dependence of the incident beam and the linear anisotropic phase function are included.

Formulation

The system under consideration is a planar medium which does not reflect or reradiate at the boundaries. A collimated beam is incident at an angle of (θ_0, ϕ_0). The medium scatters anisotropically and emission from medium is neglected. The medium properties and the incident beam are interpreted as being monochromatic or as being independent of wavelength.

The radiation intensity for this one-dimensional medium is characterized by the equation of transfer given as

$$\mu \frac{d\hat{i}(\kappa, \mu, \phi)}{d\kappa} + \hat{i}(\kappa, \mu, \phi) = \frac{1}{4\pi} \int_0^{2\pi} \int_{-1}^{1} \hat{i}(\kappa, \mu', \phi') \cdot p(\mu, \phi; \mu', \phi') d\mu' d\phi' = S(\kappa, \mu, \phi). \quad (1)$$

The phase function is represented in the linear anisotropic form as

$$p(\mu, \phi; \mu', \phi') = 1 + a_1 \mu\mu' + a_1 (1 - \mu^2)^{1/2} \cdot (1 - \mu'^2)^{1/2} \cos(\phi - \phi') \quad (2)$$

This phase function is a first-order approximation of an infinite Legendre series. It describes forward, isotropic, and backward scattering by $a_1 = +1, 0, -1$, respectively. Comparisons of this phase function with more detailed and computationally complex representations indicate the usefulness of this approximation in atmospheric calculations [7] and in directional hemispherical property determinations [3]. The boundary conditions are given by

$$\hat{i}^+(0, \mu, \phi) = 0, \quad \mu > 0$$
$$\hat{i}^-(\kappa_L, \mu, \phi) = i_d \delta(\mu - \mu_0)\delta(\phi - \phi_0), \quad \mu < 0 \quad (3)$$

where $\mu_0 = \cos\theta_0$ and is positive. The resulting expressions for the

Contributed by the Heat Transfer Division of THE AMERICAN SOCIETY OF MECHANICAL ENGINEERS and presented at the AIAA/ASME Thermophysics and Heat Transfer Conference, Palo Alto, California, May 25–26, 1978. Manuscript received by the Heat Transfer Division May 22, 1978. Paper No. 78-HT-17.

positive and negative directed intensities subject to these boundary conditions are

$$\hat{i}^+(\kappa, \mu, \phi) = \int_0^{\kappa} S(\kappa', \mu, \phi) \exp[-(\kappa - \kappa')/\mu]\, d\kappa'/\mu, \quad \mu > 0$$

$$\hat{i}^-(\kappa, \mu, \phi) = i_d \delta(\mu - \mu_0)\delta(\phi - \phi_0) \cdot \exp[(\kappa_L - \kappa)/\mu] - \int_{\kappa}^{\kappa_L} S(\kappa', \mu, \phi) \cdot \exp[-(\kappa - \kappa')/\mu] d\kappa'/\mu, \quad \mu < 0. \quad (4)$$

This problem is separated into the collimated portion, $\hat{i}_c(\kappa, \mu, \phi)$, and the scattered portion, $\hat{i}_s(\kappa, \mu, \phi)$. The collimated solution is then substituted into the scattered portion resulting in a new source function for the scattered portion. The solution to the collimated portion is given as

$$\hat{i}_c^+(\kappa, \mu, \phi) = 0, \quad \mu > 0$$

$$\hat{i}_c^-(\kappa, \mu, \phi) = i_d \delta(\mu - \mu_0)\delta(\phi - \phi_0) \exp[(\kappa_L - \kappa)/\mu], \quad \mu < 0. \quad (5)$$

The equation of transfer for the scattered component of the intensity is then given by

$$\mu \frac{d\hat{i}_s(\kappa, \mu, \phi)}{d\kappa} + \hat{i}_s(\kappa, \mu, \phi) = \frac{i_d}{4\pi} p(\mu, \phi; -\mu_0, \phi_0) \cdot \exp[-(\kappa_L - \kappa)/\mu_0] + \frac{1}{4\pi} \int_0^{2\pi} \int_{-1}^{1} \hat{i}_s(\kappa, \mu', \phi') \cdot p(\mu, \phi; \mu', \phi') d\mu' d\phi'. \quad (6)$$

The resulting boundary conditions for the scattered intensity are

$$\hat{i}_s^+(0, \mu, \phi) = 0, \quad \mu > 0$$

$$\hat{i}_s^-(\kappa_L, \mu, \phi) = 0, \quad \mu < 0. \quad (7)$$

Thus, the complete solution is the sum of the solution for the scattered portion given by equation (6) subject to equation (7) and the results for the collimated portion given in equation (5).

The intensity for the scattered component can be expressed in a two-term cosine series expression for the phase function given in equation (2) as

$$\hat{i}_s(\kappa, \mu, \phi) = i_{s0}(\kappa, \mu) + i_{s1}(\kappa, \mu) \cos(\phi - \phi_0). \quad (8)$$

The problem reduces to two azimuthally independent integro-differential equations and their boundary conditions. They are given as

$$\mu \frac{di_{s0}(\kappa, \mu)}{d\kappa} + i_{s0}(\kappa, \mu) = \frac{i_d}{4\pi}(1 - a_1\mu\mu_0) \cdot \exp[-(\kappa_L - \kappa)/\mu_0] + \frac{G_s(\kappa)}{4\pi} + \frac{a_1\mu}{4\pi} q_s(\kappa) \quad (9)$$

with

$$i_{s0}^+(0, \mu) = i_{s0}^-(\kappa_L, \mu) = 0 \quad (10)$$

and

$$\mu \frac{di_{s1}(\kappa, \mu)}{d\kappa} + i_{s1}(\kappa, \mu) = \frac{i_d}{4\pi} a_1(1 - \mu^2)^{1/2} \cdot (1 - \mu_0^2)^{1/2} \exp[-(\kappa_L - \kappa)/\mu_0] + \frac{a_1}{4\pi}(1 - \mu^2)^{1/2} D_s(\kappa) \quad (11)$$

with

$$i_{s1}^+(0, \mu) = i_{s1}^-(\kappa_L, \mu) = 0 \quad (12)$$

where

$$G_s(\kappa) = 2\pi \int_{-1}^{1} i_{s0}(\kappa, \mu') d\mu' \quad (13a)$$

$$q_s(\kappa) = 2\pi \int_{-1}^{1} i_{s0}(\kappa, \mu')\mu' d\mu' \quad (13b)$$

and

$$D_s(\kappa) = \pi \int_{-1}^{1} i_{s1}(\kappa, \mu')(1 - \mu'^2)^{1/2} d\mu'. \quad (13c)$$

The scattered incident energy per unit area is represented by $G_s(\kappa)$ and the scattered radiant heat flux is given by $q_s(\kappa)$.

The solutions for the coefficients of the cosine series expansions are substituted into equation (13) which results in a set of three integral equations. New variables defined as

$$G(\kappa) = G_s(\kappa) + i_d \exp[-(\kappa_L - \kappa)/\mu_0] \quad (14a)$$

$$q(\kappa) = q_s(\kappa) - i_d\mu_0 \exp[-(\kappa_L - \kappa)/\mu_0] \quad (14b)$$

and

$$D(\kappa) = D_s(\kappa) + i_d(1 - \mu_0^2)^{1/2} \exp[-(\kappa_L - \kappa)/\mu_0] \quad (14c)$$

are introduced into these integral equations. These variables represent the contributions to the incident intensity per unit area, $G(\kappa)$, the radiant heat flux, $q(\kappa)$, and $D(\kappa)$ from both the collimated and the scattered components. The heat flux is independent of κ for conservative scattering and is hereafter denoted by q. The resulting governing equations are

$$\frac{G(\kappa)}{2\pi} = \frac{i_d}{2\pi} \exp[-(\kappa_L - \kappa)/\mu_0] + \int_0^{\kappa_L}$$

Nomenclature

A_1, A_2 = coefficients defined in equation (26)
a_1 = anisotropic scattering coefficient defined by equation (2)
a, b, c = coefficients defined in equation (21)
B_1, B_2 = coefficients defined in equation (27)
$D(\kappa)$ = defined in equation (14c)
$E_n(x)$ = exponential integral function of argument x
$G(\kappa)$ = average incident intensity per unit area
i = intensity
i_d = incident collimated intensity
$p(\mu, \phi; \mu', \phi')$ = phase function
q = radiative heat flux
$S(\kappa, \mu, \phi)$ = source function
y_1, y_2, z_1, z_2 = defined in equation (28)
δ = Dirac delta function
η = defined in equation (23)
θ = polar angle
θ_0 = incident polar angle
κ = optical depth
$\mu = \cos\theta$
$\mu_0 = \cos\theta_0$
$\rho'(\mu_0)$ = directional hemispherical reflectance
$\rho''(\mu_0, \phi_0; \mu, \phi)$ = bidirectional reflectance
$\tau'(\mu_0)$ = directional hemispherical transmittance
$\tau''(\mu_0, \phi_0; \mu, \phi)$ = bidirectional transmittance
$\tau_s''(\mu_0, \phi_0; \mu, \phi)$ = scattered component of the bidirectional transmittance
ϕ = azimuthal angle
ϕ_0 = incident azimuthal angle

Superscripts

$\wedge$ = azimuthally dependent quantities
$+$ = positive direction
$-$ = negative direction

Subscripts

c = collimated
L = layer thickness
s = scattered

$$\cdot\left[\frac{G(\kappa')}{4\pi}E_1(|\kappa-\kappa'|)+\frac{a_1 q}{4\pi}sgn(\kappa-\kappa')E_2(|\kappa-\kappa'|)\right]d\kappa' \quad (15a)$$

$$\frac{q}{2\pi}=-\frac{i_d\mu_0}{2\pi}\exp[-(\kappa_L-\kappa)/\mu_0]+\int_0^{\kappa_L}\cdot\left[\frac{G(\kappa')}{4\pi}sgn(\kappa-\kappa')E_2(|\kappa-\kappa'|)+\frac{a_1 q}{4\pi}E_3(|\kappa-\kappa'|)\right]d\kappa' \quad (15b)$$

$$D(\kappa)=i_d(1-\mu_0^2)^{1/2}\exp[-(\kappa_L-\kappa)/\mu_0]+\frac{a_1}{4}\cdot\int_0^{\kappa_L}D(\kappa')[E_1(|\kappa-\kappa'|)-E_3(|\kappa-\kappa'|)]d\kappa' \quad (15c)$$

where $E_n(x)$ denotes the exponential integral function of argument x. Equations (15a) and (15b) are a coupled set of linear integral equations for $G(\kappa)$ and q and equation (15c) is an independent equation for $D(\kappa)$. Thus, if the radiant heat flux is desired, then only the set of equations (15a) and (15b) needs to be solved and if the intensity is required, then equation (15c) must also be solved.

The directional hemispherical reflectance is defined as the ratio of the reflected energy in all directions and the incident energy in a single direction. This is expressed as

$$\rho'(\mu_0)=1+\frac{q}{i_d\mu_0}. \quad (16)$$

This is also termed the albedo of a finite planar medium. The directional hemispherical transmittance is similarly defined as the ratio of the transmitted energy in all directions to the incident energy in a single direction. For a conservative medium, this is simply

$$\tau'(\mu_0)=1-\rho'(\mu_0). \quad (17)$$

Bidirectional properties retain the azimuthal dependence since they depend upon the intensity. The bidirectional reflectance is defined as

$$\rho''(\mu_0,\phi_0;\mu,\phi)=\frac{\pi\hat{i}^+(\kappa_L,\mu,\phi)}{i_d\mu_0}=\frac{\pi}{i_d\mu_0}\cdot[i_{s0}^+(\kappa_L,\mu)+i_{s1}^+(\kappa_L,\mu)\cos(\phi-\phi_0)] \quad (18)$$

where equations (5) and (8) have been combined. The bidirectional transmittance is given by

$$\tau''(\mu_0,\phi_0;\mu,\phi)=\frac{\pi\hat{i}^-(0,\mu,\phi)}{i_d\mu_0}=\frac{\pi}{i_d\mu_0}[i_c^-(0,\mu,\phi)+i_{s0}^-(0,\mu)+i_{s1}^-(0,\mu)\cos(\phi-\phi_0)]. \quad (19)$$

The scattered portion of the bidirectional transmittance is denoted by $\tau_s''(\mu_0,\phi_0;\mu,\phi)$ and includes the last two terms on the right-hand side of the last equation. Once these bidirectional properties are determined, it is also possible to obtain the hemispherical properties defined above.

Approximate Solution

The kernel substitution method [10, 12] is used to obtain an approximate closed-form solution to the governing equations. In the solution of equations (15a) and (15b) for $G(\kappa)$ and q, the dependence of the exponential integrals is taken as

$$E_2(t)=\exp(-at) \quad (20a)$$

and the dependence taken in the solution of equation (15c) to $D(\kappa)$ is

$$E_1(t)-E_3(t)=b\exp(-ct). \quad (20b)$$

Various authors have recommended different values for the coefficients of the exponential functions [9, 12]. Comparisons between the approximate closed-form solutions given below and available exact solutions have been made and the recommended values are

$$a=2;\quad b=16/9;\quad c=8/3. \quad (21)$$

The values of b and c were obtained by equating the zeroth and first moments of equation (20b).

These approximate forms of the exponential integral functions are substituted into equations (15). The integrals are eliminated by double differentiation and the equations for $G(\kappa)$ and q are decoupled. The resulting differential equations are

$$\frac{d^2G(\kappa)}{d\kappa^2}=i_d\left(\frac{1}{\mu_0^2}-a^2\right)\exp[-(\kappa_L-\kappa)/\mu_0] \quad (22a)$$

$$\frac{dq}{d\kappa}=0 \quad (22b)$$

$$\frac{d^2D(\kappa)}{d\kappa^2}-\eta^2D(\kappa)=i_d(1-\mu_0^2)^{1/2}\left(\frac{1}{\mu_0^2}-c^2\right)\cdot\exp[-(\kappa_L-\kappa)/\mu_0] \quad (22c)$$

where

$$\eta^2=c\left(c-\frac{a_1 b}{2}\right). \quad (23)$$

The solutions are expressed as

$$G(\kappa)=i_d(1-a^2\mu_0^2)\exp[-(\kappa_L-\kappa)/\mu_0]+A_1\kappa+A_2 \quad (24a)$$

$$D(\kappa)=i_d\frac{(1-\mu_0^2)^{1/2}(1/\mu_0^2-c^2)}{\frac{1}{\mu_0^2}-\eta^2}\cdot\exp[-(\kappa_L-\kappa)/\mu_0]+B_1\exp(-\eta\kappa)+B_2\cdot\exp[-\eta(\kappa_L-\kappa)] \quad (24b)$$

and q is an unknown constant. The unknown coefficients in equations (24) and q are obtained from the boundary conditions contained in equations (15) by substituting these equations back into equations (15) and equating the various powers of κ. The resulting expressions for the five constants are

$$q=-\frac{2i_d(1-4\mu_0^2)}{(4+4\kappa_L-a_1\kappa_L)}\left[\frac{1}{\frac{1}{\mu_0}-2}+\frac{\exp(-\kappa_L/\mu_0)}{\frac{1}{\mu_0}+2}\right] \quad (25)$$

$$A_1=(a_1-4)q$$

$$A_2=-2[q+i_d(1-4\mu_0^2)\exp(-\kappa_L/\mu_0)/(1/\mu_0+2)] \quad (26)$$

$$B_1=-\frac{i_d(1-\mu_0^2)^{1/2}(y_1z_1+y_2z_2)}{\left(\frac{1}{\mu_0^2}-\eta^2\right)(y_1^2-y_2^2)}$$

$$B_2=\frac{i_d(1-\mu_0^2)^{1/2}(y_1z_2+y_2z_1)}{\left(\frac{1}{\mu_0^2}-\eta^2\right)(y_1^2-y_2^2)} \quad (27)$$

where

$$y_1=1/(8/3-\eta),$$

$$y_2=\exp(-\eta\kappa_L)/(8/3+\eta),$$

$$z_1=(1/\mu_0-8/3)\exp(-\kappa_L/\mu_0),\quad \text{and}$$

$$z_2=(1/\mu_0+8/3). \quad (28)$$

In many problems, the directional hemispherical reflectance (or albedo) and transmittance are of primary importance. The result of the present method is

$$\rho'(\mu_0)=1-\tau'(\mu_0)=1+\frac{q}{\mu_0 i_d} \quad (29)$$

where q is given in equation (25). The bidirectional properties are functions of the intensity in the positive and negative directions. The intensity is a sum of the results for the collimated portion given in equation (5) and the scattered portion given in equation (8). From the equations of transfer for the azimuthally independent equation (equations (9–12)), the scattered intensities are obtained. The positive scattered intensity is

$$\hat{i}_s^+(\kappa, \mu, \phi) = i_{s0}^+(\kappa, \mu) + i_{s1}^+(\kappa, \mu)\cos(\phi - \phi_0), \quad \mu > 0 \quad (30)$$

with

$$i_{s0}^+(\kappa, \mu) = \frac{i_d(1 - 4\mu_0^2)}{4\pi\mu\left(\frac{1}{\mu} + \frac{1}{\mu_0}\right)}\{\exp[(\kappa - \kappa_L)/\mu_0] - \exp(-\kappa_L/\mu_0 - \kappa/\mu)\} + \frac{\mu}{4\pi} \cdot [1 - \exp(-\kappa/\mu)]\left(a_1 q - A_1 + \frac{A_2}{\mu}\right) + \frac{A_1}{4\pi}\kappa, \quad \mu > 0 \quad (31)$$

$$i_{s1}^+(\kappa, \mu) = \frac{i_d a_1(1 - \mu^2)^{1/2}(1 - \mu_0^2)^{1/2} z_1 z_2}{4\pi\left(\frac{1}{\mu_0^2} - \eta^2\right)\mu\left(\frac{1}{\mu} + \frac{1}{\mu_0}\right)} \cdot [\exp(\kappa/\mu_0) - \exp(-\kappa/\mu)] + \frac{B_1 a_1(1 - \mu^2)^{1/2}}{4\pi(1 - \eta\mu)} \cdot [\exp(-\eta\kappa) - \exp(-\kappa/\mu)] + \frac{B_2 a_1(1 - \mu^2)^{1/2}}{4\pi(1 + \eta\mu)}\{\exp[\eta(\kappa - \kappa_L)] - \exp[-\eta\kappa_L - \kappa/\mu]\}, \quad \mu > 0 \quad (32)$$

and the bidirectional reflectance is obtained from these expressions with $\kappa = \kappa_L$ (equation (18)). The negative scattered intensity is

$$\hat{i}_s^-(\kappa, \mu, \phi) = i_{s0}^-(\kappa, \mu) + i_{s1}^-(\kappa, \mu)\cos(\phi - \phi_0), \quad \mu < 0 \quad (33)$$

with

$$i_{s0}^-(\kappa, \mu) = -\frac{i_d(1 - 4\mu_0^2)}{4\pi\mu\left(\frac{1}{\mu_0} + \frac{1}{\mu}\right)}\{\exp[(\kappa_L - \kappa)/\mu] - \exp[(\kappa - \kappa_L)/\mu_0]\} - \frac{\mu}{4\pi}\{1 - \exp[(\kappa_L - \kappa)/\mu]\} \cdot (A_1 - a_1 q - A_2/\mu) + (A_1/4\pi)\{\kappa - \kappa_L \exp[(\kappa_L - \kappa)/\mu]\}, \quad \mu < 0 \quad (34)$$

$$i_{s1}^-(\kappa, \mu) = -\frac{i_d a_1(1 - \mu^2)^{1/2}(1 - \mu_0^2)^{1/2}(1/\mu_0^2 - 64/9)}{4\pi\left(\frac{1}{\mu_0^2} - \eta^2\right)\mu\left(\frac{1}{\mu_0} + \frac{1}{\mu}\right)} \cdot \{\exp[(\kappa_L - \kappa)/\mu] - \exp[(\kappa - \kappa_L)/\mu_0]\} - \frac{B_1 a_1(1 - \mu^2)^{1/2}}{4\pi(1 - \eta\mu)}\{\exp[-\kappa/\mu - (\eta - 1/\mu)\kappa_L] - \exp(-\eta\kappa)\} - \frac{B_2 a_1(1 - \mu^2)^{1/2}}{4\pi(1 + \eta\mu)} \cdot \{\exp[(\kappa_L - \kappa)/\mu] - \exp[\eta(\kappa - \kappa_L)]\}, \quad \mu < 0 \quad (35)$$

where the bidirectional transmittance is obtained from these expression with $\kappa = 0$ and equation (5) (see equation (19)).

Results and Discussion

The results for the directional hemispherical reflectance are presented in Fig. 1 with the exact solutions for isotropic scattering [2]. Eddington's approximation [7] is also shown which is the same as the solution given by Wang [9] for isotropic scattering. The two stream approximation and modified two stream approximation have not been plotted in this figure since the error is much greater primarily at large incident angles. A summary of these approximations is given in [5, 6]. The results for isotropic scattering indicate that the present results and Eddington's approximation are both quite accurate with the present model being more accurate at large incident angles. Comparisons of the present expression with the exact forward scattering result ($a_1 = 1$) for normal incidence ($\mu_0 = 1$) given by Busbridge [4] shows that the Eddington and modified two stream results are slightly more accurate than the present result with the maximum error of the present model being no greater than 7 percent. Other incident angles were not presented for comparison by Busbridge.

The anisotropic scattering effects are clearly exhibited in this figure. The back scattering reflectance ($a_1 = -1$) always yields the largest directional hemispherical reflectance with the forward scattering reflectance the minimum. Significant differences between the isotropic and anisotropic phase functions are shown principally at moderate optical depths. At the limits of large and small optical depths, the anisotropic scattering effects are significantly reduced. The anisotropic scattering effects are also shown to be more pronounced at small angles of incidence.

The bidirectional results are shown in Figs. 2–6. These results were obtained from the intensity expressions given in equations (30–35). Since the general phase function considered here is of the linear anisotropic form and the incident radiation is collimated, the azimuthal dependence must be considered. These figures, except Fig. 2, present the results for two values of ϕ in the plane of incidence—forward directions ($\phi_0 - \phi = 0$ deg) and backward directions ($\phi_0 - \phi = 180$ deg)—while other azimuthal directions are related by the cosine dependence of this phase function. Fig. 2 presents the results for isotropic scattering which are independent of ϕ and are, therefore, valid for all azimuthal angles. Also note that only the scattered component of the bidirectional transmittance is presented in these figures.

The effects of optical depth on the bidirectional reflectance and transmittance for isotropic scattering are shown in Fig. 2. There is an increase in the reflectance as the polar angle (θ) increases for small optical depths. This is a result of the larger optical paths observed for small optical depths and larger polar angles. As the optical depth increases, this increase in reflectance is diminished to such an extent that when the optical depth becomes large, there is a decrease in reflectance with increasing angle. Similar results for the scattered portion of the bidirectional transmittance are shown. The exact solutions [1] are also included and the dependencies of the bidirectional properties with optical depth and polar angle are shown to be accurately predicted by the present closed-form solution.

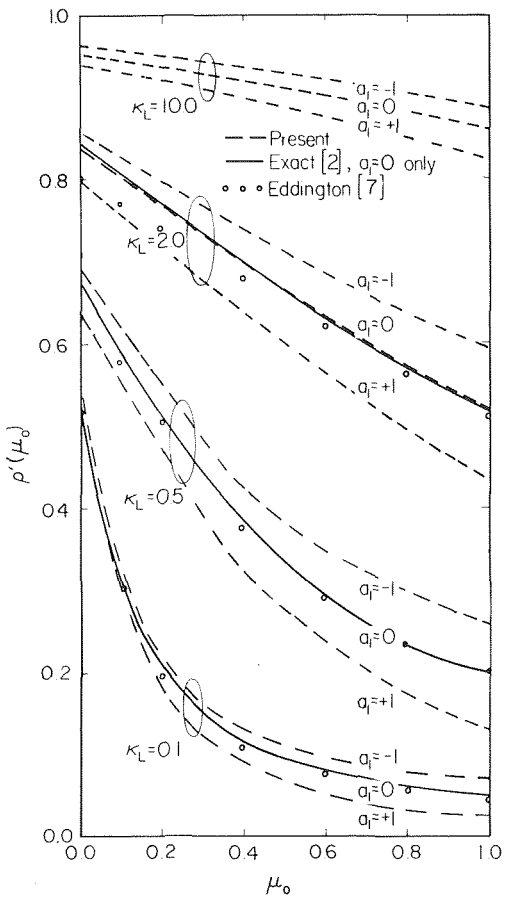

Fig. 1 Directional hemispherical reflectance versus incident angle

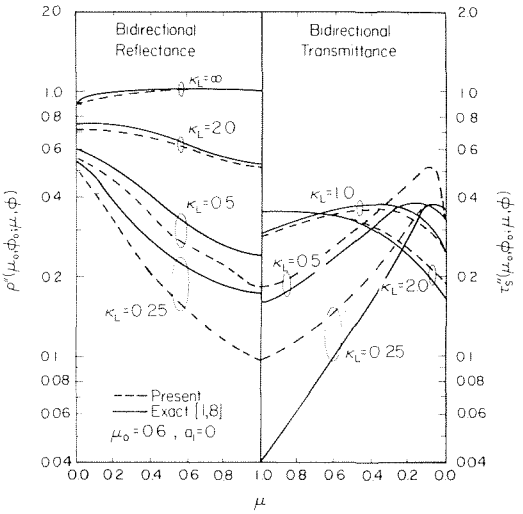

Fig. 2 Effect of optical depth on bidirectional reflectance and scattered component of the bidirectional transmittance for isotropic scattering (μ_0 = 0.6)

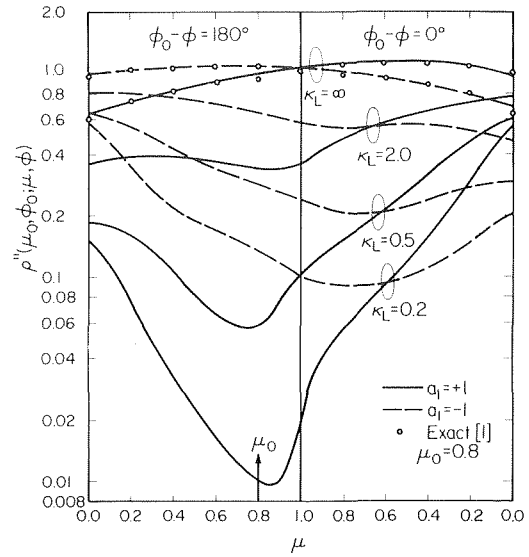

Fig. 3. Effect of anisotropic scattering and optical depth on bidirectional reflectance (μ_0 = 0.8)

The anisotropic scattering results for $\mu_0 = 0.8$ are presented in Figs. 3 and 4. The decreasing dependence of the reflectance on the polar angle as the optical depth is increased is also exhibited in anisotropic scattering but the effect is much more pronounced. The forward scattering reflectance is generally larger in the forward directions with significant differences between the forward and back scattering occurring at moderate and small optical depths. Note that the integrated reflectance (directional hemispherical reflectance in Fig. 1) for small optical depths is smaller for the forward scattering medium. The bidirectional transmittance indicates a shift of maximum intensity from large polar angles to small polar angles. This is much the same as for isotropic scattering yet the variation in magnitude is much greater for anisotropic scattering. Also presented are the exact solutions for linear anisotropic scattering without azimuthal symmetry. The agreement between the closed-form approximate results and the exact results is quite good.

The effect of incident angle can be determined from Figs. 5 and 6 for $\mu_0 = 0.2$. The incident angle significantly effects the bidirectional reflectance for all optical depths. The differences between forward and back scattering are increased at large polar angles for small optical depths. These differences in magnitudes are also seen for the scattered portion of the bidirectional transmittance but the effect is not as great. The results for normal incidence ($\mu_0 = 1$) have not been presented since all the resultant bidirectional reflectances and transmittances are independent of ϕ.

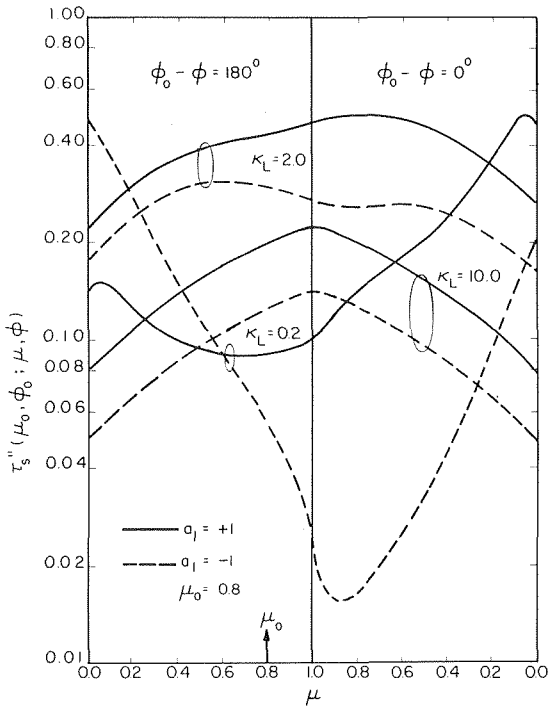

Fig. 4 Effect of anisotropic scattering and optical depth on the scattered component of the bidirectional transmittance (μ_0 = 0.8)

Conclusions

The effects of conservative anisotropic scattering for a finite medium have been presented. The effect of anisotropic scattering on the directional hemispherical reflectance is shown to be of principle importance at moderate optical depths and small incident angles. Bidirectional properties have been shown to have similar results with a much more pronounced effect for anisotropic scattering. Closed-form solutions have been presented for the intensity, bidirectional properties, and the hemispherical directional properties. Comparisons with exact solutions indicate that the dependences with polar angle, azimuthal angle, angle of incidence, optical depth, and linear anisotropic scattering are accurately predicted.

Acknowledgment

This work was supported in part by the National Science Foundation under Grant ENG 76-09851.

References

1 Chandrasekhar, S., *Radiative Transfer*, Dover, New York, 1960.

2 Hottel, H. C., Sarofim, A. F., and Sze, D. K., "Radiative Transfer in an Absorbing-Scattering Medium," *Proc., 3rd Int. Heat Transfer Conf.*, AIChE, Vol. 5, 1966, pp. 112–21.

3 Evans, L. B., Chu, C. M., and Churchill, S. W., "The Effect of Anisotropic Scattering on Radiant Transport," ASME JOURNAL OF HEAT TRANSFER, Aug. 1965, pp. 381–7.

4 Busbridge, I. W., and Orchard, S. E., "Reflection and Transmission of Light by a Thick Atmosphere according to a Phase Function: 1 + x cos θ," *Astrophysical J.*, Vol. 149, Sept. 1967, pp. 655–64.

5 Irvine, W. M., "Multiple Scattering by Large Particles II. Optically Thick Layers," *Astrophysical J.*, Vol. 152, June 1968, pp. 823–34.

6 Kawata, Y., and Irvine, W. M., "The Eddington Approximation for

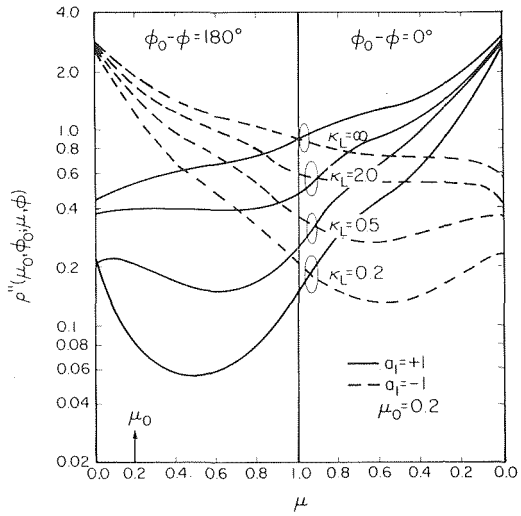

Fig. 5 Effect of anisotropic scattering and optical depth on bidirectional reflectance ($\mu_0 = 0.2$)

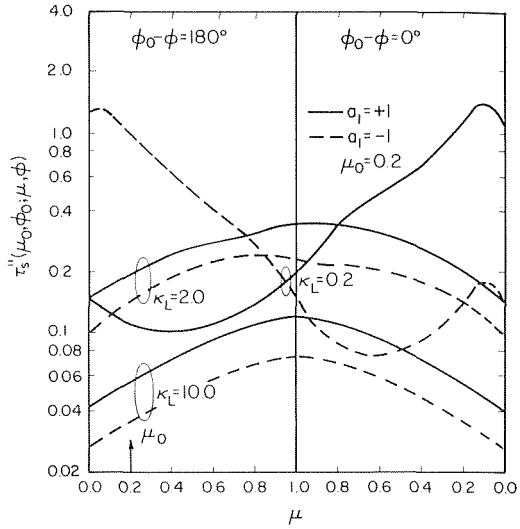

Fig. 6 Effect of anisotropic scattering and optical depth on the scattered component of the bidirectional transmittance ($\mu_0 = 0.2$)

Planetary Atmospheres," *Astrophysical J.*, Vol. 160, May 1970, pp. 787–90.

7 Irvine, W. M., "Multiple Scattering by Large Particles," *Astrophysical J.*, Vol. 142, 1965, pp. 1563–75.

8 Armaly, B. F., and Lam, T. T., "Influence of Refractive Index on Reflectance from Semi-infinite Absorbing-Scattering Medium with Collimated Incident Radiation," *Int. J. Heat and Mass Transfer*, Vol. 18, 1975, pp. 893–900.

9 Wang, L. S., "Anisotropic Nonconservative Scattering in a Semi-infinite Medium," *Astrophysical J.*, Vol. 174, June 1972, pp. 671–8.

10 Dayan, A., and Tien, C. L., "Heat Transfer in a Gray Planar Medium with Linear Anisotropic Scattering," ASME JOURNAL OF HEAT TRANSFER, Aug. 1975, pp. 391–6.

11 Dayan, A., and Tien, C. L., "Radiative Transfer with Anisotropic Scattering in an Isothermal Slab," *J. Quant. Spectrosc. Radiat. Transfer*, Vol. 16, 1976, pp. 113–25.

12 Armaly, B. F., and Lam, T. T., "A Note on the Exponential Kernel Approximation," *J. Quant. Spectrosc. Radiat. Transfer*, Vol. 14, 1974, pp. 651–6.

J. C. Simonich[1]
Graduate Student.

P. Bradshaw
Reader in Fluid Dynamics.

Department of Aeronautics,
Imperial College,
London, England

Effect of Free-Stream Turbulence on Heat Transfer through a Turbulent Boundary Layer

Measurements in a boundary layer in zero pressure gradient show that the effect of grid-generated free-stream turbulence is to increase heat transfer by about five percent for each one percent rms increase of the longitudinal intensity. In fact, even a Reynolds analogy factor, 2 × (Stanton number)/(skin-friction coefficient), increases significantly. It is suggested that the irreconcilable differences between previous measurements are attributable mainly to the low Reynolds numbers of most of those measurements. The present measurements attained a momentum-thickness Reynolds number of 6500 (chord Reynolds number approximately 6.3 × 10^6) and are thought to be typical of high-Reynolds-number flows.

Introduction

If Reynolds' analogy were exact, one would expect the percentage increase in turbulent heat transfer caused by free-stream turbulence to be the same as the percentage increase in surface shear stress. Measurements of surface shear stress by various workers give values on the order of three for the coefficient A in the formula

$$\frac{c_f}{c_{f0}} = 1 + A\frac{(\overline{u_e^2})^{1/2}}{U_e} \tag{1}$$

expressing the effect of free-stream turbulence, with an integral length scale of the order of the boundary layer thickness, on the skin friction coefficient at given $U_e\theta/\nu$ in a constant-pressure turbulent boundary layer. The coefficient A depends rather strongly on the length scale. Measurements of heat transfer, on the other hand, are in strong disagreement: four of the six relevant experiments in the literature suggest that heat transfer (Stanton number) is not significantly affected by free-stream turbulence, which is contrary to intuition. It would require the Reynolds analogy factor $\mathrm{St}/(0.5\,c_f)$ to obey a formula like equation (1) but with an equal and opposite value of A. It would also be contrary to the common belief among engineers who use turbulence promoters to increase heat transfer through turbulent boundary layers or duct flows.

The present experiment was designed to investigate the effect of nearly isotropic grid turbulence on heat transfer through a constant-pressure boundary layer on a slightly-heated surface. Specifically, it was designed to measure the coefficient A_θ in the Stanton-number formula corresponding to equation (1),

$$\frac{\mathrm{St}}{\mathrm{St}_0} = 1 + A_\theta\frac{(\overline{u_e^2})^{1/2}}{U_e}. \tag{2}$$

As the coefficient A in equation (1) is uncertain to ±25 percent at least, it was thought unrealistic to attempt to determine A_θ to much better accuracy than this. The experiment was therefore arranged to measure *changes* in heat transfer, resulting from the insertion or removal of turbulence grids in the flow, to an accuracy of the order of ±20 percent of the change. The apparatus and techniques used are therefore not the optimum for *absolute* measurements of heat transfer, but we felt that the contradictions in previous experiments on the effect of free-stream turbulence probably resulted from attempts to obtain absolute, rather than comparative measurements to good accuracy. In fact, the absolute accuracy of Stanton number measurement in the present experiment seems to be good; values of St_0 lie within ten percent of the mean of previous data and well within the scatter. This gives confidence in the reliability of the values of A_θ.

The results show that A_θ is about five. The difference between A_θ and A is barely significant but suggests that the Reynolds analogy factor increases slightly in the presence of free-stream turbulence.

Previous Work

Table 1 summarizes previous experiments on the effect of free-stream turbulence on heat transfer from turbulent boundary layers in substantially zero pressure gradient. In some of these cases deductions about free-stream turbulence effects were made as a by-product of the main result and in others the techniques were open to criticism. The two experiments which seem most reliable for the present purpose are those of Kestin, et al. [1, 5, 6] and Junkhan and Serovy [8]. Both experiments were done at rather low Reynolds number, and both indicated negligible effect of free-stream turbulence

[1] Now at Aerothermodynamics Research Department, Detroit Diesel Allison Division, General Motors, Indianapolis, Indiana 46206

Contributed by the Heat Transfer Division for publication in the JOURNAL OF HEAT TRANSFER, Manuscript received by the Heat Transfer Division May 25, 1978.

Table 1 Summary of past research

Author	Date	Ref	Re_x	$\sqrt{\overline{u_e^2}}/U_e$	Increase in Nu?
Sugawara, et al.	1953	2	$4.2 \times 10^3 - 3.2 \times 10^5$	0.7 – 8.3	Yes
Edwards and Furber	1956	3	$6.1 \times 10^4 - 2.5 \times 10^6$	1.5 –5.0	No
Reynolds, Kays, and Kline	1958	4	$2.6 \times 10^5 - 3.5 \times 10^6$	2.0 – 5.0	No
Kestin, et al.	1961	1, 5, 6	$4.3 \times 10^4 - 6.1 \times 10^5$	0.7 – 3.8	No
Feiler and Yeager	1962	7	$2.7 \times 10^4 - 1.2 \times 10^5$	9 – 10	Yes
Junkhan and Serovy	1967	8	$3.9 \times 10^4 - 3.7 \times 10^5$	0.4 – 8.3	No

on heat transfer in zero pressure gradient. Kestin, et al. found a small increase in heat transfer in a flow with pressure gradient, while Junkhan and Serovy found none. Therefore, whether one relies on these two experiments or accepts a majority verdict from the authors cited in Table 1, the conclusion from previous work is that free-stream turbulence does not influence heat transfer through a turbulent boundary layer in zero pressure gradient. Such an influence is not positively precluded, however, because most of the experiments were done at such a low Reynolds number that transitional or post-transitional effects may have been present. The implication from the results of Reynolds, et al. [4] that there is no influence is insecure because they did not do a low-turbulence check experiment (their free-stream turbulence was that naturally occurring in their wind tunnel). The thermal boundary layer of Edwards and Furber [5] was confined to the inner part of the velocity boundary layer. A more detailed review is given by Simonich [9].

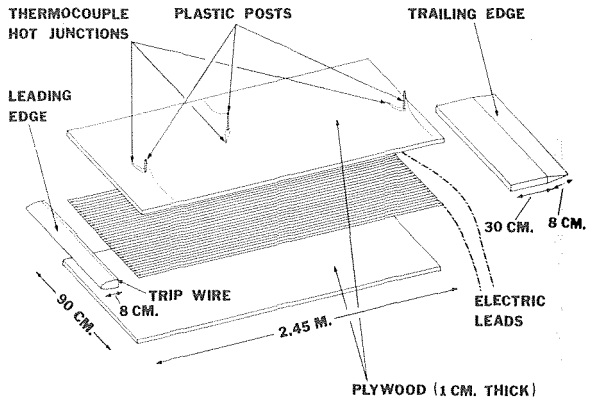

Fig. 1 Exploded view of the experimental heat transfer plate

Apparatus and Techniques

All the measurements reported here were made in the 3 ft × 3 ft (90 cm × 90 cm) closed-circuit wind tunnel of the Department of Aeronautics. The tunnel has a background turbulence level of about 0.03 percent. Two sets of heat transfer and skin-friction measurements were made at free-stream speeds of 16 and 21 ms^{-1}.

The test plate was mounted horizontally in the tunnel working section with its leading edge 1.9 m from the turbulence grid position. An exploded view of the plate assembly is shown in Fig. 1. The heated portion was made by gluing 30 pieces of 0.05 mm × 2.5 cm steel shim strips lengthwise, at 2.8 cm spanwise pitch, to a sheet of 1 cm plywood 90 cm wide and 2.45 m long, and then gluing a second plywood sheet over the strips to produce a symmetrical model. The 2.5 cm wide strips were connected in series by wires embedded in the front and rear ends of the sandwich. A leading-edge fairing 8 cm long, with a longitudinal section like a slightly pointed half ellipse, was added. Smoke-tunnel tests by P. E. Hancock (unpublished) showed that this shape appeared to be free of flow separation for longitudinal-component intensities up to at least four percent. A trip wire 1.2 mm in diameter was fixed to the surface at the rear of the unheated leading-edge fairing so that the origins of the turbulent boundary layer and the thermal boundary layer were nearly the same. The unheated trailing edge fairing consisted of a parallel section 30 cm long, to minimize pressure gradients at the aft measuring station, followed by a straight tapered portion 8 cm long.

The heating element, whose resistance was about 8 Ω, was supplied from an autotransformer, the current (up to 20A) and voltage being measured by separate Avo Model 8 multimeters. The manufacturer's quoted accuracy for this type of multimeter is three percent of full scale. The meters were not calibrated individually, but their function was checked by interchanging the current and voltage meters without noticeable change in the readings. It was assumed that the inductance of the plane heating element was negligible so that the power dissipated was equal to the product of current and voltage. The surface heat transfer rate was taken as half the power, divided by the plane area of the heated part of the plate, less a correction for radiation

Nomenclature

A, A_θ = empirical constants, equations (1, 2)
b = grid bar thickness
C, C_θ = empirical constants, equations (4, 5)
c_f = skin-friction coefficient, $\tau_w/(0.5\ \rho U_e^2)$
c_p = specific heat at constant pressure
K, K_θ = empirical constants, equations (4, 5)
L_x = longitudinal–integral length scale
L_ϵ = dissipation length scale, defined by equation (3*b*)
M = grid mesh width
Q = heat transfer per unit area per unit time
$\overline{q^2} = \overline{u^2} + \overline{v^2} + \overline{w^2}$
Re_θ = momentum-thickness Reynolds number, $U_e\ \theta/\nu$
St = Stanton number, $Q_w/[\rho c_p\ U_e\ (T_w - T_e)]$
T = temperature
T_τ = friction temperature, $Q_w/c_p u_\tau$
u, v, w = fluctuating velocity components in x, y, z directions
U, V, W = mean velocity components in x, y, z directions
u_τ = friction velocity, $(\tau_w/\rho)^{1/2}$
X = distance from grid
x, y, z = coordinates with origin at origin of boundary layer: x streamwise, y normal to surface
δ = boundary layer thickness (distance from surface at which $U = 0.995\ U_e$)
ϵ = turbulent energy dissipation rate
θ = momentum thickness
ν = kinematic viscosity
Π, Π_θ = wake parameters, equations (6*b*, 7*b*)
ρ = density
τ = shear stress

Subscripts

e = value at boundary layer edge
0 = value with low free-stream turbulence
w = value at surface ("wall")

losses estimated at between 7 and 15 percent of the heat transfer rate. (See Appendix for radiation loss calculation.)

The temperature difference between the plate surface and the free-stream, $T_w - T_e$, roughly 2 °C, was measured at three stations 0.32, 1.08 and 2.46 m from the leading edge (2.22, 2.98 and 4.36 m from the position of the turbulence grids). Chromel-alumel thermocouples welded from 0.025 mm wires were used. The "hot" junctions and several cm of the adjacent wires were fixed to the plate, with the junction at the centerline, using polyurethane varnish as the adhesive; the surface near the junction was effectively smooth. The "cold" junctions, between the two thermocouple wires and copper leads, were made at the top of 3 mm dia posts, fixed to the plate about 15 cm from the center line and protruding well outside the boundary layer. The copper leads were then continued without further joins to the input terminals of the amplifier/voltmeter (Comark Electronics Ltd) used to measure the temperature difference.

Temperature-profile measurements were made by attaching the two cold junctions of a similar thermocouple to the front of a pitot-like probe about 1 mm in diameter, the junction protruding about 3 mm forward of the probe body. Again, the hot junction was fixed to the plate surface.

The thermal time constant of the plate (the time taken to cool to $1/e$ times the initial temperature difference) was calculated as about 200 s, while the conduction time constant (the time taken for the surface temperature to rise to $1 - 1/e$ times the heater element temperature after the latter was first switched on) was about 270 s, neglecting external heat transfer. The settling time required after a change in turbulence level or heating rate was determined mainly by the characteristic time scale of free-stream temperature drift in the closed-circuit wind tunnel. The procedure adopted was to run the tunnel for about 30 min and then monitor $T_w - T_e$ at 5 min intervals until it ceased to change, typically after a further 20–40 min. This does not, strictly, define a steady state since T_e (and T_w) continue to increase, and the convective heat transfer is less than the apparent value by $mc\ d\ T_w/dt$ where m and c are the mass and specific heat of the plate. However since the thermal time constant of the tunnel is much larger than that of the plate, the error is small.

Velocity profiles were measured with pitot tubes and skin friction with Preston (surface pitot) tubes. Preston-tube values of c_f agreed to within five percent of deductions from logarithmic plots of the velocity profiles. An average of the two methods was used in the data analysis.

The turbulence grids had mesh widths, M, of 1½, 3 and 6 in. (3.8, 7.6 and 15.2 cm), with bar widths, b, close to the classical value of $^3/_{16}$ of the mesh width used by Batchelor and Townsend at Cambridge (M/b = 4.17, 6.0 and 4.8, respectively). The bars of the two smaller grids were of square cross section and arranged in a biplanar array at right angles. The largest grid had square bars in a monoplane array. Other users of this grid have found traces of unsteady or inhomogeneous flow, absent in square-bar biplane grids; the present results obtained with it are generally more scattered than results of tests using the smaller grids, but are not thought to be seriously atypical. The longitudinal-component turbulence levels, measured about half way between the test plate and the tunnel roof, are shown in Fig. 2, the change in percentage intensity between the two operating speeds of 16 and 21 ms^{-1} being negligible.

Spectra and length scales were not measured directly. However, defining a dissipation length scale L as $(\overline{q^2})^{3/2}/\epsilon$, the turbulent energy equation for decaying homogeneous turbulence can be written as

$$\frac{1}{2}U\frac{\overline{dq^2}}{dx} = -\epsilon = \frac{(\overline{q^2})^{3/2}}{L} \tag{3a}$$

and in grid turbulence L is about 1.1 times the longitudinal integral scale L_x. In the present work we have deduced a slightly different scale, from the equation

$$U\frac{\overline{du^2}}{dx} = \frac{(\overline{u^2})^{3/2}}{L_\epsilon} \tag{3b}$$

This scale has the advantage that it can be deduced from u-component measurements only. If the turbulence is isotropic ($\overline{q^2} = 3\overline{u^2}$),

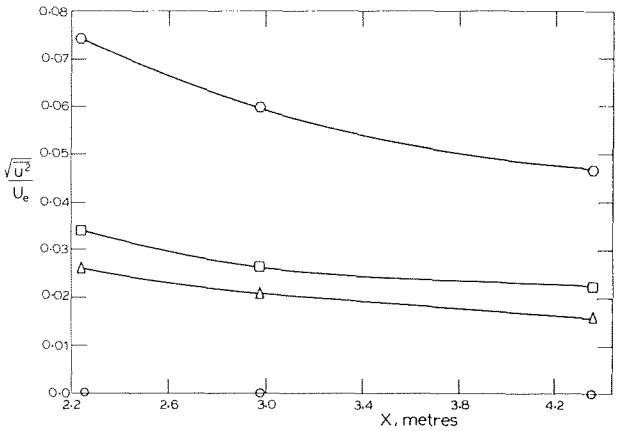

Fig. 2 Component of longitudinal turbulence intensity versus distance downstream of the grid, X. ○ no grid, △, 1½ in. grid; □ 3 in. grid; ○ 6 in. grid

$$L_\epsilon = L/(2\sqrt{3})$$

The distance from the grid to the first measuring station, 2.22 m, was nearly 15 times the mesh width of the largest grid so that in this and all other cases a good approximation to homogeneity should have been attained.

Experimental Accuracy

The object of the experiment was to measure *changes* of 10–20 percent in St to an accuracy (at 20:1 odds) of ±20 percent of the change, i.e. ±2–4 percent of St itself. To achieve this, the *absolute* accuracy of St need be no better than the above mentioned ±20 percent. For instance, *consistent* errors of 20 percent in tunnel speed, temperature difference or heat transfer rate would have been acceptable as long as short-term repeatability was within two to four percent. The spatial uniformity of the heat flux from the electric heaters to the surface of the plywood was checked by measuring the spanwise variation of an approximation to $T_w - T_e$ with a 2 mm dia. bead thermocouple traversed across the surface. The temperature difference was uniform to within the instrument resolution of about three percent of the temperature difference. Spanwise uniformity of the velocity was satisfactorily checked independently, and the effect of the sidewall boundary layer displacement thickness (less than 1 cm) was evidently confined to the generation of a very weak longitudinal pressure gradient, secondary flows being important only very close to the side walls.

The temperature difference $T_w - T_e$ was roughly 2 °C, and was recorded to an accuracy of .025 °C. As the kinematic viscosity of air changes by about 0.6 percent per °C and c_f or St vary as about the $(-1/4)$ power of local Reynolds number, Re_θ, any temperature difference much larger than those used here would result in noticeable changes in c_f or St, perhaps of the order of those caused by free-stream turbulence, with resulting confusion in the interpretation of the results. It should be noted that up to 20 percent consistent error in $T_w - T_e$ can be accepted for present purposes, and the correspondence between readings of the different thermocouples was much better than this as can be seen from the plots of St against Re_θ.

To summarize, the absolute accuracy of St measurement aimed for was ±20 percent, the error residing almost entirely in $T_w - T_e$. We estimate the St accuracy actually achieved at about ±10 percent, while the changes in St required to evaluate A_θ appear to be accurate to about ±20 percent on the average. Other quantities such as c_f or Re_θ are estimated to be accurate to five percent or better.

Boundary Layer Scaling

It is generally accepted that the effect of free-stream turbulence is likely to be felt mainly in the outer layer of a boundary layer, and that the law of the wall is no more likely to be affected by free-stream

turbulence than by changes in turbulence within the boundary layer. In the present work we have assumed, with self consistent results, that this conclusion applies to the law of the wall for temperature as well as that for velocity. The following scaling analysis is given in some detail because of the prevalence in the heat transfer literature of simplified versions, incorporating hidden assumptions of equality between constants or scaling functions for the velocity and temperature fields. Such assumptions would lead to confusion in the present work where the distinction between A and A_θ must be maintained unless it is shown to be small experimentally.

The present analysis is a rearrangement and extension of that given by Kader and Yaglom [10]. In the logarithmic regions at a distance from the surface small compared to the thickness of the boundary layer but large compared to the thickness of the sublayers adjacent to the surface, in which viscous or conductive effects are important, we have

$$\frac{U}{u_\tau} = \frac{1}{K} \ln \frac{u_\tau y}{\nu} + C \tag{4}$$

and

$$\frac{T_w - T}{T_\tau} = \frac{1}{K_\theta} \ln \frac{u_\tau y}{\nu} + C_\theta \tag{5}$$

where T_τ is called the friction temperature and C_θ, though not K_θ, depends on Pr. In the whole region between the sublayers and the boundary layer edge, including the regions of validity of equation (4) and equation (5), the "defect" laws

$$\frac{U_e - U}{u_\tau} = f(y/\delta) \tag{6a}$$

and

$$\frac{T - T_e}{T_\tau} = f_\theta(y/\delta) \tag{7a}$$

are expected to apply if the origin of the thermal boundary layer is at the leading edge. The instantaneous edge of the thermal boundary layer coincides almost exactly with the instantaneous edge of the velocity boundary layer if Pr is close to unity. The mean thicknesses are therefore related so that δ can be used for both. Also the thickness of the conductive sublayer is nearly the same as the thickness of the viscous sublayer, $30\ \nu/u_\tau$ say, if Pr is near unity.

In the regions of validity of both equation (4) and equation (5) from $u_\tau\ y/\nu \approx 30$ to $y \approx .2\delta$, compatibility requires equation (6a) and equation (7a) to take the special forms

$$\frac{U_e - U}{u_\tau} = -\frac{1}{K} \ln \frac{y}{\delta} + \frac{2\pi}{K} \tag{6b}$$

$$\frac{T - T_e}{T_\tau} = -\frac{1}{K_\theta} \ln \frac{y}{\delta} + \frac{2\pi_\theta}{K_\theta} \tag{7b}$$

where Π and Π_θ are called the "wake parameters." In constant-pressure boundary layers beneath low-turbulence streams, f and f_θ are functions of y/δ only, and Π and Π_θ are constants, except at low Reynolds number. In principle the decay rate, as well as the local properties, of the free-stream turbulence may affect the functions and the wake parameters, but if the free-stream turbulence can be described locally by one velocity scale and one length scale the decay rate follows from the turbulent energy equation and need not be included explicitly. Taking the representative scales as the u-component-root-mean square intensity $(\overline{u_e^2})^{1/2}$ and the dissipation length scale L_ϵ, we expect Π and Π_θ to depend on $(\overline{u_e^2})^{1/2}/u_\tau$ and L_ϵ/δ.

Now adding equation (4) to equation (6b) and equation (5) to equation (7b) gives

$$\frac{U_e}{u_\tau} = \frac{1}{K} \ln \frac{u_\tau \delta}{\nu} + C + \frac{2\Pi}{K} \tag{8}$$

and

$$\frac{T_w - T_e}{T_\tau} = \frac{1}{K_\theta} \ln \frac{u_\tau \delta}{\nu} + C_\theta + \frac{2\Pi_\theta}{K_\theta} \tag{9}$$

where the first two terms on the right of each equation are the right-hand sides of equation (4) and equation (5) evaluated at $y = \delta$ and the third terms are the deviations of the actual profiles from the logarithmic laws. Since by definition $c_f = 2(u_\tau/U_e)^2$ and $\mathrm{St} = (u_\tau/U_e) \times (T_\tau/(T_w - T_e))$, elimination of $u_\tau\delta/\nu$ between equation (8) and equation (9) gives

$$\frac{\mathrm{St}}{0.5\ c_f} = \frac{K_\theta/K}{1 + \sqrt{\frac{c_f}{2}} \left[\frac{C_\theta K_\theta - CK + 2\ (\Pi_\theta - \Pi)}{K} \right]} \tag{10}$$

where $\mathrm{St}/(0.5\ c_f)$ is commonly called the Reynolds analogy factor. Most of the common formulae for Reynolds analogy factor are special cases of equation (10). With the values $K = 0.40$, $K_\theta = 0.47$, $C = 5.0$, $C_\theta = 3.8$ (for air), $2\Pi/K = 2.35$, $2\Pi_\theta/K_\theta = 2.35$, as recommended by Kader and Yaglom [10] for a low-turbulence stream, we have

$$\frac{\mathrm{St}}{0.5 c_f} = \frac{1.18}{1 - 0.098 \sqrt{(0.5\ c_f)}} \tag{11}$$

This is an unusually low value of the coefficient of $(0.5\ c_f)^{1/2}$, which is the small difference of large quantities. Changing $2\Pi_\theta/K_\theta$ to the value of about 2.0 found in the present work increases the coefficient from -0.098 to -1.8. von Kärmän's formula has a coefficient of -2.7 but a numerator of unity. The values of $\mathrm{St}/(0.5\ c_f)$ predicted by these three versions of equation (10) when $c_f = 0.0030$ ($U_e\ \theta/\nu \approx 5000$, a value typical of the data below) are 1.19, 1.27, 1.11. The experimental value at this Reynolds number is 1.19.

The effects of free-stream turbulence on the mean velocity profile include a decrease in Π, and therefore, from equation (8), an increase in u_τ/U_e and c_f at a given value of $u_\tau\delta/\nu$. If the consensus of previous data, that free-stream turbulence does not affect Stanton number, were correct, $(T_w - T_e)/T_\tau$ would have to increase in proportion to u_τ/U_e, and equation (9) shows that this could happen only if Π_θ increased. Thus, we cannot simultaneously have an unaffected Stanton number and an unaffected temperature profile, so that free-stream turbulence must have some effect on the thermal boundary layer. If Π_θ decreased by the same amount as Π, equation (10) shows that the Reynolds-analogy factor would be unaltered. That is, the qualitative ideas of Reynolds' analogy suggest that $\Pi_\theta - \Pi$ will alter less than Π_θ or Π separately. The results presented below indicate that $\mathrm{St}/(0.5\ c_f)$ increases with free-stream turbulence level, implying that Π_θ decreases more than Π. We note that if Π and Π_θ vary linearly with $(\overline{u_e^2})^{1/2}/u_\tau$, the turbulence dependent term in the denominator of equation (10) is proportional to $(\overline{u_e^2})^{1/2}/U_e$. Similar analyses [11] for equation (8) and equation (9) separately justify the forms equation (1) and equation (2), and we therefore plot the results presented below against $(\overline{u^2})^{1/2}/U_e$ rather than the parameter $(\overline{u_e^2})^{1/2}/u_\tau$ on which Π and Π_θ depend. This should reduce the dependence of the plotted quantities on c_{f_0}, although the assumption of linear variation of Π and Π_θ is possible only for $(\overline{u_e^2})^{1/2}/U_e < 0.05$, say, and Meier [12] has recently shown that for very small values of $(\overline{u_e^2})^{1/2}/U_e$, less than about 0.01, c_f/c_{f_0} (and by implication Π) varies as $\overline{u_e^2}$.

Strictly, the changes in St, c_f and profile parameters should be evaluated at a constant value of $u_\tau\delta/\nu$ for compatibility with the similarity analysis above. In practice comparisons at constant momentum-thickness Reynolds number are more convenient, and are made exclusively below. The use of $U_e x/\nu$ as a correlating parameter for heat transfer, or anything else, simply introduces uncertainties about transition effects, and may be responsible for some of the confusion documented in Table 1.

Results and Discussion

Figs. 3 and 4 show the variation of skin-friction coefficient and Stanton number with momentum-thickness Reynolds number Re_θ in the clean tunnel and behind three different turbulence grids. Later analysis is based on the smooth curves shown in those figures. The clean-tunnel results for skin friction agree fairly well with the results of Weighardt, quoted in [13], except at the low-Reynolds-number end. The Reynolds-analogy factor in the clean tunnel (Fig. 5) decreases slightly with increasing Re_θ to a value of about 1.20 at the upper end

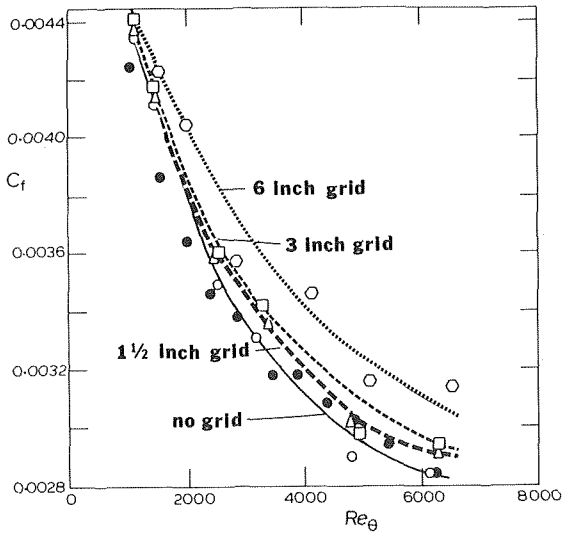

Fig. 3 Skin-friction coefficient versus momentum-thickness Reynolds number. ●, Wieghardt [13]; other symbols as in Fig. 2

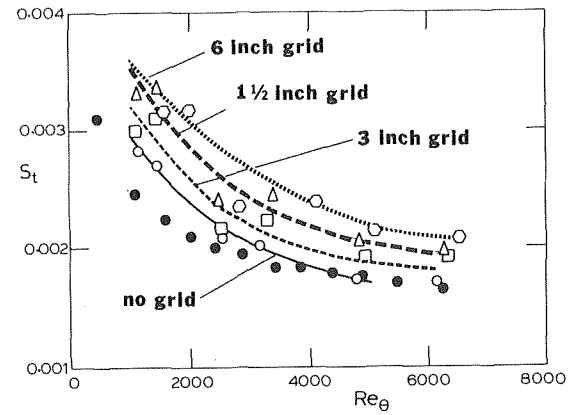

Fig. 4 Stanton number versus momentum-thickness Reynolds number. ●, 1.16 × Wieghardt c_f; other symbols as in Fig. 2

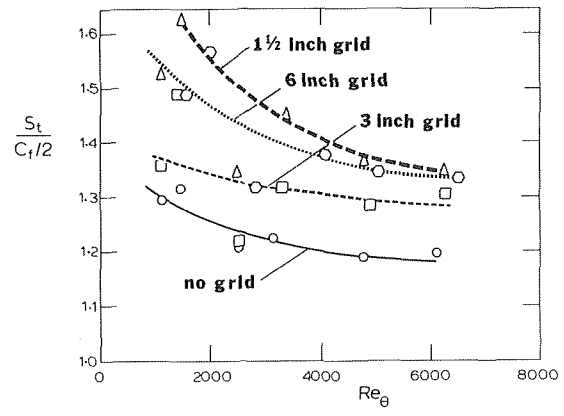

Fig. 5 Reynolds-analogy factor versus momentum-thickness Reynolds number. Symbols as in Fig. 2

of the range. If Weighardt's values of c_f were used the latter value would be about 1.16, the Reynolds-analogy factor recommended by Chi [14] as a fit to all high-Reynolds-number data. Note that free-stream turbulence length scale, as well as intensity, varies with grid size so that a simple trend in Fig. 5 is not necessarily to be expected.

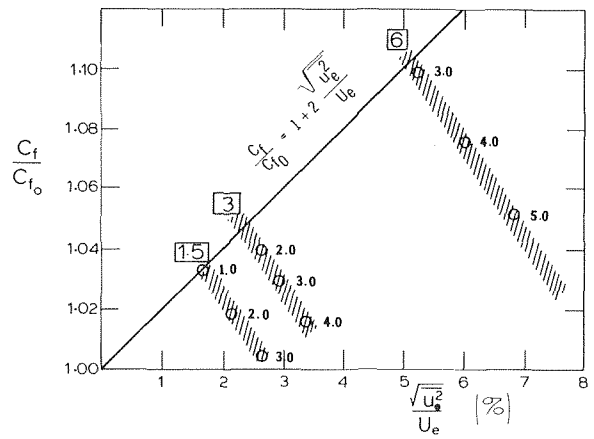

Fig. 6 Factor of increase in skin-friction coefficient at given R_θ, versus free-stream turbulence intensity crossplot from Fig. 2; width of shaded regions indicates scatter, boxed labels show grid size in inches, numbers near shaded regions are approximate values of L_ϵ/δ at the points shown.

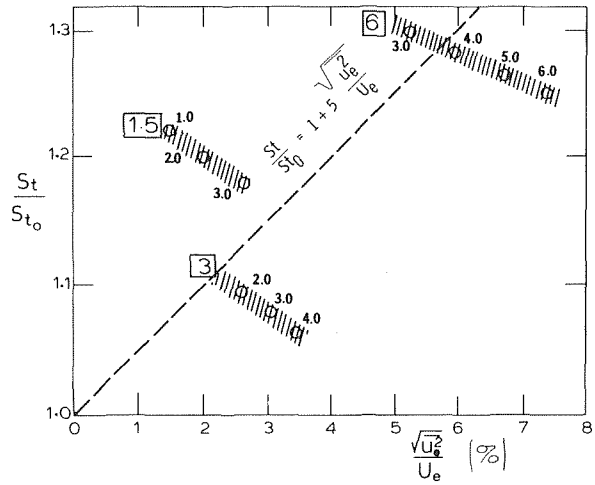

Fig. 7 Factor of increase in Stanton number at given Re_θ, versus free-stream turbulence intensity. Crossplot from Fig. 3; key as in Fig. 6

When the skin-friction coefficient and Stanton number are replotted as c_f/c_{f_0} and St/St_0 against root-mean-square turbulence intensity $(\overline{u_e^2})^{1/2}/U_e$, (Figs. 6 and 7) it can be seen that the rate of increase of Stanton number is larger than that of skin-friction coefficient and that in both cases individual data points from each grid cross the general trend.

Hancock [15] has systematically investigated the effect of length scale L_ϵ, as well as intensity, on c_f/c_{f_0}, using both his own results and those of previous investigators. He finds that for given $\overline{u_e^2}$ the value of c_f/c_{f_0} decreases strongly with increasing value of L_ϵ/δ. One explanation for the decrease in effect of free-stream turbulence with increase in L_ϵ/δ is that [16] the condition $V = 0$ at the solid surface reduces the normal-component intensity of the free-stream turbulence for $y < 2\,L_\epsilon$ approximately. Thus, if $L_\epsilon > 0.5\,\delta$ the free-stream turbulence that affects the flow near $y = \delta$ is weaker than the nominal value of $\overline{u_e^2}$ measured far from the surface. Fig. 7 shows that St/St_0 also decreases with increasing L_ϵ/δ at given $\overline{u_e^2}$ although the effect appears to be less severe than in the case of c_f. Therefore, the form of equation (2), with $A_\theta = 5$ independent of L_ϵ/δ, should be adequate for interim use until more data are available. The present c_f data, supported by Hancock show that the assumption of constant A is *not* adequate. However, even the largest value of A deducible from the present results ($L_\epsilon/\delta > 1.0$) is only about 2 and therefore significantly

smaller than the best fit value of A_θ. Qualitatively, it appears that St not only increases with free-stream turbulence level but actually increases faster than c_f.

At low Reynolds number II, and presumably II_θ, decreases and it is possible that the ability of free-stream turbulence to reduce π is itself reduced. However, the variation of II with Re_θ for each grid (Fig. 8) seems consistent. The values for the 6 in. grid are uncertain because of the residual inhomogeneity of the mean flow. II and II_θ are plotted against $(u_e^2)^{1/2}/U_e$ at the aft station ($Re_\theta \approx 6000$) in Fig. 9 to illustrate the behavior at high Reynolds number. These are the only values of II_θ measured during the experiment, the corresponding profiles being shown in Fig. 10. The values of C_θ implied by the measured temperature profiles and heat-transfer rates were scattered about the value of 3.8 recommended by Kader and Yaglom and the profiles were arbitrarily shifted along the T axis to match $C_\theta = 3.8$. The percentage uncertainty thus introduced into II_θ is no greater than the percentage uncertainty in St.

Conclusions

A simple application of similarity analysis shows that free-stream turbulence must affect either the Stanton number or the shape of the temperature profile plotted in inner layer coordinates (or both). It is therefore not possible for the temperature field to be completely unaffected by free-stream turbulence. Previous experimental work at low Reynolds numbers suggests, but not very conclusively, that the Stanton number is unaffected.

The present measurements, at momentum-thickness Reynolds numbers up to 6000 and with grid-produced turbulence intensities up to seven percent, appear to show conclusively that the Stanton number increases with increasing free-stream turbulence, by about five percent for each percent of rms intensity. This rate of increase of St is rather larger than the consensus value for the rate of increase of c_f (and considerably larger than the rate of increase of c_f measured in the present work), which implies that the Reynolds-analogy factor increases. In the range of free-stream turbulence length scale explored here, the Stanton number at given turbulence intensity decreases as the length scale increases, although the range of measurements was not sufficient to rule out the possibility of this decrease being a Reynolds-number effect since large ratios of length scale to boundary layer thickness were obtained only at low Reynolds numbers.

Acknowledgments

John Simonich's work was supported by a General Motors Fellowship. We are grateful to Dr. P. E. Hancock for many helpful discussions.

APPENDIX

Radiation Losses. The radiative heat transfer was estimated by the formula

$$Q_r = \epsilon\, \sigma\, A\, (T_w^4 - T_s^4) \tag{1}$$

where ϵ is the emissivity of a wooden surface, taken as .935 in the present case, σ is the Stefan-Boltzmann constant, 5.67×10^{-11} $kWm^{-2}\,K^{-4}$, A is the plate area, and T_w and T_s are the absolute temperatures of the plate and of the tunnel walls. A good approximation for small temperature differences is

$$Q_r = 4\, \sigma\, A\, T_w^3\, \Delta T \tag{2}$$

where $\Delta T = T_w - T_s$, so the contribution of radiative heat transfer to the Stanton number is

$$\mathrm{St}_r = \frac{4\sigma\, T_w^3}{\rho c_p U_e} \tag{3}$$

which becomes large at low velocities. With $\rho = 1.2$ kg m^{-3}, $c_p = 1\ kW$ kg$^{-1}\,K^{-1}$, $T_w = 288K$,

$$\mathrm{St}_r = 4.6 \times 10^{-3}/U_e \tag{4}$$

and taking $U_e = 20$ ms^{-1} gives $\mathrm{St}_r = 2.3 \times 10^{-4}$ or roughly ten percent of the convective contribution. This is a surprisingly high figure, but equation (4) applies to any low-speed air flow with a small temperature difference and an emissivity close to unity. The emissivity is, of course, uncertain but since $0 < \epsilon < 1$ the worst possible error in any of the Stanton-number results, or in A_θ itself, is no more than ten percent.

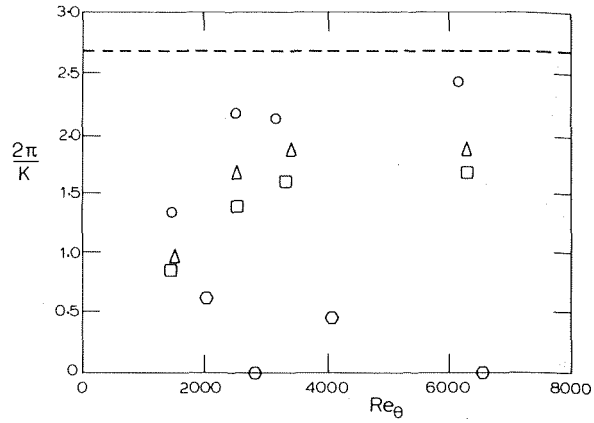

Fig. 8 Variation of wake strength with Re_θ for each grid. Note that free-stream turbulence intensity decreases as Re_θ increases. Symbols as in Fig. 2. Dotted line is the high Reynolds number equilibrium value suggested by Coles.

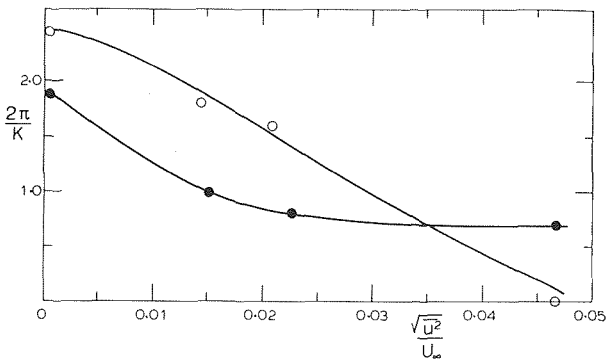

Fig. 9 Variation of wake strength th free-stream turbulence intensity at x = 2.46 *m*, U_e = 22 ms^{-1} ($Re_\theta \simeq 6000$) ○, velocity profile; ●, temperature profile

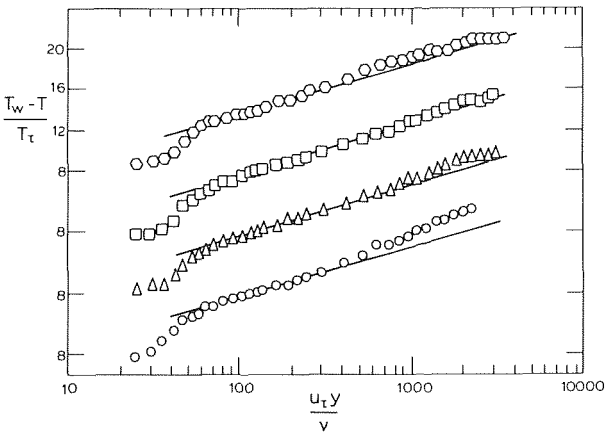

Fig. 10 Temperature difference nondimensionalized by friction temperature, versus $u_\tau y/\nu$. Symbols as in Fig. 2

References

1 Kestin, J., "The Effect of Free-Stream Turbulence on Heat Transfer Rates," *Advances in Heat Transfer*, Vol. 3, ed. by T. F. Irvine, Jr. and J. P. Hartnett, Academic Press, London 1966.

2 Sugawara, S., Sato, T., Hirosyasa, K., Osaka, H., "The Effect of Free-Stream Turbulence on Heat Transfer from a Flat Plate," NACA Tech. Memo 1441, 1958.

3 Edwards, A., Furber, B. N., "The Influence of Free-Stream Turbulence on Heat Transfer by Convection from an Isolated Region on a Plane Surface in Parallel Air Flow," *Proc. Inst. Mech. Engrs.*, London, Vol. 1970, 1956, p. 941.

4 Reynolds, W. C., Kays, W. M., Kline, S. J., "Heat Transfer in the Turbulent Incompressible Boundary Layer-1-Constant Wall Temperature," NASA Memo 12-1-58W, 1958.

5 Kestin, J., Maeder, P. F., Wang, H. E., "Influence of Turbulence on the Transfer of Heat from Plates with and without a Pressure Gradient," *International Developments in Heat Transfer*, International Heat Transfer Conference, University of Colorado and London, England, ASME, 1961, p. 432.

6 Büyüktür, A. R., Kestin, J., Maeder, P. F., "Influence of Combined Pressure Gradient and Turbulence on the Transfer of Heat from a Plate," *Int. J. Heat Mass Transfer*, Vol. 7, 1964, p. 1175.

7 Feiler, C. E., Yaeger, E. B., "Effect of Large-Amplitude Oscillations on Heat Transfer," NASA Tech. Report R-142, 1962.

8 Junkhan, G. H., Serovy, G. K., "Effects of Free-Stream Turbulence and Pressure Gradient on Flat-Plate Boundary-Layer Velocity Profiles and on Heat Transfer," ASME JOURNAL OF HEAT TRANSFER, Vol. 89, 1967, p. 169.

9 Simonich, J. C., "Heat Transfer from a Turbulent Boundary Layer in a Zero Pressure Gradient," M.Sc Project Report, Imperial College, London, 1976.

10 Kader, B. A., Yaglom, A. M., "Heat and Mass Transfer Laws for Fully Turbulent Wall Flows," *Int. J. Heat Mass Transfer*, Vol. 15, 1972, p. 2329.

11 Bradshaw, P., "Effect of Free-Stream Turbulence on Turbulent Shear Layers," Aeronautical Research Council, paper 35648, 1974.

12 Meier, H. U., "The Response of Turbulent Boundary Layers to Small Turbulence Levels in the External Free-Stream," DFVLR Interner Bericht, 251-76A17, 1976, presented at the 10th Congress of International Council of the Aeronautical Sciences (ICAS), Ottawa, Canada, Oct. 3, 1976, ICAS Paper 76-05.

13 Coles, D., Hirst, E. A., *Proceedings AFOSR-IFP*-Stanford Conference on Computation of Turbulent Boundary Layers, Vol. 2, Stanford University, 1968.

14 Chi, S. W., "Friction and Heat Transfer in a Compressible Turbulent Boundary Layer on a Smooth Flat Plate," Ph.D. Thesis, Imperial College, University of London, 1965.

15 Hancock, P. E., "Effect of Free-Stream Turbulence on Turbulent Boundary Layers," Ph.D. Thesis, Imperial College, University of London, 1978.

16 Thomas, N. H., Hancock, P. E., "Grid Turbulence Near a Moving Wall," *J. Fluid Mech.*, Vol. 82, 1977, p. 481.

A. Polak
Professor.

M. J. Werle[1]
Professor.
Mem. ASME

Department of Aerospace Engineering and Applied Mechanics
University of Cincinnati,
Cincinnati, Oh. 45221

Interacting Turbulent Boundary Layer over a Wavy Wall

This paper is concerned with the two-dimensional supersonic flow of a thick turbulent boundary layer over a train of relatively small wave-like protuberances. The flow conditions and the geometry are such that there exists a strong interaction between the viscous and inviscid flow. Here the interacting boundary layer equations are solved numerically using a time-like relaxation method with turbulence effects represented by the inclusion of the eddy viscosity model of Cebeci and Smith. Results are presented for flow over a train of up to six waves for Mach numbers of 2.5 and 3.5, Reynolds numbers of 10 and 32 $\times 10^6$/meter, and wall temperature ratios T_w/T_0 of 0.4 and 0.8. Limited comparisons with independent experimental and analytical results are also given.

Introduction

This paper is concerned with the two-dimensional supersonic flow of thick turbulent boundary layers over a train of relatively small wave-like protuberances. Interest in this subject arises from the need to predict the extent to which an initially flat plate boundary layer has been disturbed by a regular corrugation in the wall surface. The flow conditions and the geometry considered here are such that a strong interaction exists between the viscous and inviscid flow. The problem cannot be solved without including interaction effects because classical boundary layer methods would terminate in a separation point singularity.

To handle the present subject by boundary-layer methods, a technique for treatment of the interacting boundary layer equations as well as models for turbulence and for the viscous-inviscid interaction process must be available. A numerical method for addressing closed bubble separation regions was developed by Werle and Vatsa [1]. It was applied to a number of laminar separated flow problems including flow over a train of sine-wave protuberances [2]. This method uses the interacting boundary layer equations with a time-like relaxation concept which accounts for the boundary-value nature of the problem. This approach is adopted in the present study with the inclusion of the eddy viscosity model of Cebeci and Smith into the solution scheme. The present form of the numerical algorithm includes several modifications to that of the earlier work [2, 3] in order to accommodate the turbulent nature of the flow, the thick boundary layer, and the rather dramatic geometry variations of the wavy wall.

It was found that the method was capable of handling the interacting turbulent flows of present interest. Solutions were obtained for flow of thick turbulent boundary layers over a train of waves. The results are presented in terms of surface pressure, skin friction and heat transfer distributions. The predicted trends are compared with available analytical results based on small disturbance theory and with experimental data.

Governing Equations

1 Boundary Layer Equations in Physical Coordinates. The suitability of the interacting boundary layer equations for describing the relatively strong streamwise variations in the boundary layer characteristics due to sudden changes in the body geometry has been, at least for the laminar case, verified earlier [1, 2]. This approach is used in the present study in which Prandtl's classical boundary layer equations are adopted with the only modification being that the pressure variation was not prescribed but calculated simultaneously from a viscous-inviscid interaction model.

The boundary layer approximation in two-dimensional viscous flow problems implies that the pressure variation is assumed to occur only along one coordinate, taken in the general direction of the wall shear layer. The degree of this approximation depends on the choice of the coordinate system. While for very thin boundary layers over a corrugated wall, or thick boundary layers over a relatively flat wall, surface coordinates were suitable (see [3]), for thick boundary layers flowing over a small amplitude wavy wall, Cartesian coordinates were found to be more appropriate. Accordingly, the governing equations will first be written to apply to both the usual surface coordinates (s^*, n^*) and the Cartesian coordinates (x^*, y^*) using the notation (x_1^*, x_2^*) to denote either of these. Nondimensional variables of order one are now defined according to the scheme

$$x_1 = x_1^*/L^*, \qquad x_2 = \mathrm{Re}_r^{1/2} x_2^*/L^* \tag{1a}$$

$$u = u^*/u_\infty^*, \qquad v = \mathrm{Re}_r^{1/2} v^*/u_\infty^*, \qquad p = p^*/\rho_\infty^* u_\infty^{*2},$$

$$\rho = \rho^*/\rho_\infty^*, \qquad T = C_p^* T^*/u_\infty^{*2} \tag{1b}$$

with

$$\mathrm{Re}_r \equiv \rho_\infty^* u_\infty^* L^*/\mu_r^* (u_\infty^{*2}/C_p^*) \tag{1c}$$

[1] Current affiliation: United Technology Research Center, East Hartford, Conn.

Contributed by the Heat Transfer Division for publication in the JOURNAL OF HEAT TRANSFER. Manuscript received by the Heat Transfer Division January 30, 1978

and u^*, v^*, p^*, ρ^* and T^* represent the mean velocities, pressure, density and temperature respectively.

The turbulent layer equations in these variables are:

Continuity Equation

$$\frac{\partial}{\partial x_1}(\rho u) + \frac{\partial}{\partial x_2}(\rho v) = 0 \tag{2}$$

Momentum Equation

$$\rho\left(u\frac{\partial u}{\partial x_1} + v\frac{\partial u}{\partial x_2}\right) = \rho_e u_e \frac{du_e}{dx_1} + \frac{\partial}{\partial x_2}\left(\mu\frac{\partial u}{\partial x_2} + \tau_T\right) \tag{3}$$

Energy Equation

$$\rho\left(u\frac{\partial T}{\partial x_1} + v\frac{\partial T}{\partial x_2}\right) = -\rho_e u_e \frac{du_e}{dx_1}u + \frac{\partial u}{\partial x_2}\left(\mu\frac{\partial u}{\partial x_2} + \tau_T\right) + \frac{\partial}{\partial x_2}\left(\frac{\mu}{\mathrm{Pr}}\frac{\partial T}{\partial x_2} + q_T\right), \tag{4}$$

where τ_T and q_T are the nondimensional turbulent stress and turbulent heat flux respectively.

The gas is assumed to be air with constant specific heats and constant Prandtl number, Pr = 0.72 with the perfect gas law,

State Equation

$$p = \frac{\gamma - 1}{\gamma}\rho T \tag{5}$$

Boundary Conditions

$$u(x_1, x_{2_w}) = 0, \qquad v(x_1, x_{2_w}) = 0, \qquad T(x_1, x_{2_w}) = T_w(x_1)$$

and

$$u(x_1, \infty) = u_e(x_1), \qquad T(x_1, \infty) = T_e(x_1) \tag{6}$$

where $x_{2_w}(x_1)$ describes the body surface contour ($x_{2_w} = 0$ in surface coordinates, $x_{2_w} = y_w(x)$ for Cartesian coordinates).

2 Turbulence Model. To obtain closure of the system of equations (2–6), models for the turbulent stress and turbulent heat flux terms are needed. The eddy viscosity concept used in conjunction with Prandtl's mixing length hypothesis for the wall layer region is the most widely used algebraic model for turbulent stress. A well known representation is the two layer eddy viscosity model of Cebeci and Smith which has been very successful in modeling turbulence effects for flat plate boundary layers and other attached boundary layers with moderate pressure gradients. Less favorable results are obtained when using this model for strongly interacting and separated flow regions where it appears to fail conceptually.

In an effort to better align the predictions for separated flows with experimental data, previous investigators (see [4] and [5] for examples) have empirically modified the equilibrium eddy viscosity model to account for the history effect. Thus "frozen," "relaxation," and other models were devised and successfully applied in several separated flow predictions. One of the present authors [6] also used the frozen and relaxation models in the interacting boundary layer equations for separated flows with no significant improvements in the predicted results over those obtained with the basic eddy-viscosity model. In [6] it was concluded that the eddy viscosity model failed in the problem of supersonic flow past compression ramps because of the ramp induced shock penetration into the boundary layer, resulting locally in large longitudinal gradients. In the present problem, with continuous surface curvature and a thick boundary layer ($a/\delta \ll 1$) the interaction effects tend to reduce longitudinal gradients. Therefore, the eddy viscosity model was considered acceptable. Thus we take

$$\tau_T = \epsilon\frac{\partial u}{\partial x_2} \tag{7a}$$

and relate q_T to τ_T by turbulent Prandtl number as

$$\mathrm{Pr}_T \equiv \left(\tau_T \Big/ \frac{\partial u}{\partial x_2}\right) \Big/ \left(q_T \Big/ \frac{\partial T}{\partial x_2}\right). \tag{7b}$$

The turbulent Prandtl number is here taken constant, $\mathrm{Pr}_T = 0.90$. The two layer (outer and inner region) Cebeci-Smith model is then given as:

Inner Region

$$(\epsilon/\mu)_i = \frac{\rho^*\bar{\ell}^{*2}}{\mu^*}\left|\frac{\partial u^*}{\partial x_2{}^*}\right| \tag{8a}$$

where

$$\ell^* = K_1 x_2{}^*[1 - \exp(-x_2{}^*/A^*)] \tag{8b}$$

with $K_1 = 0.40$ and

$$A^* = 26(\mu^*/\rho^*)\left(\mu_w{}^*\left|\frac{\partial u^*}{\partial x_2{}^*}\right|_w \Big/ \rho^*\right)^{-1/2} \tag{8c}$$

where the absolute value of $\partial u^*/\partial x_2{}^*$ has been introduced in equation (8c) as a modification of the Cebeci-Smith model for reverse flows.

Outer region

$$(\epsilon/\mu)_0 = \frac{\rho^* u_e{}^*}{\mu^*}K_2\bar{\gamma}\delta_{\mathrm{kinc}} \tag{9a}$$

where $\bar{\gamma}$ is the transverse intermittency function

$$\bar{\gamma} = \{1 - \mathrm{erf}\,[5(x_2/x_{2_e} - 0.78]\}/2 \tag{9b}$$

The variable x_{2_e} is the value of x_2 at which $u/u_e = 0.995$, and δ_{kinc} is the incompressible displacement thickness.

3 Boundary Layer Equations in Transformed Variables. First, the boundary layer equations given in Section 1 are here recast using the Levy-Lees transformation. Then, the Prandtl's transposition theorem is applied, which makes the form of the wall boundary conditions for both the surface coordinates and the Cartesian coordinates identical. Accordingly, the new independent variables are defined by

$$\xi = \int_0^{x_1} \rho_e\mu_e\mu_e\, dx_1, \qquad \eta = \frac{u_e}{\sqrt{2\xi}}\int_{x_{2w}}^{x_2}\rho\, dx_2 \tag{10a,b}$$

Nomenclature

a = amplitude

C_f = skin friction coefficient, $\tau_w{}^*/\rho_\infty{}^*u_\infty{}^{*2}/2$

C_p = constant pressure specific heat

h = heat transfer coefficient

H = nondimensional total enthalpy, $H = H^*/u_\infty{}^{*2}$

L^* = reference length

M = Mach number

Re_∞ = Reynolds number based on free stream viscosity, $\mathrm{Re}_\infty = \rho_\infty{}^*u_\infty{}^*L^*/\mu_\infty{}^*$

t = time

V = transformed v velocity in the boundary-layer

γ = ratio of specific heats, C_p/C_v

δ = nondimensional displacement thickness

δ_{kinc} = incompressible displacement thickness

δ_T = displacement body height

ϵ = eddy viscosity

θ_T = surface inclination of the displacement body

μ = nondimensional viscosity, $\mu = \mu^*/\mu_r{}^*(u_\infty{}^{*2}/C_p{}^*)$

Subscripts

e = conditions evaluated on the displacement body or at the outer edge of the boundary layer

$f.p.$ = flat plate value

w = conditions evaluated at the wall

∞ = conditions evaluated in the upstream freestream

Superscripts

$*$ = denotes dimensional quantities

Normalized dependent variables F, θ, and g, for the velocity, static enthalpy, and total enthalpy are now introduced by

$$F = u/u_e, \qquad \theta = T/T_e, \qquad g = H/H_e \tag{11a,b,c}$$

and equations (2–4) become

Continuity equation

$$\frac{\partial V}{\partial \eta} + 2\xi \frac{\partial F}{\partial \xi} + F = 0 \tag{12}$$

Momentum equation

$$2\xi F \frac{\partial F}{\partial \xi} + V \frac{\partial F}{\partial \eta} = \beta(\theta - F^2) + \frac{\partial}{\partial \eta}\left(\ell\bar{\epsilon}\frac{\partial F}{\partial \eta}\right) \tag{13a}$$

or

$$2\xi F \frac{\partial F}{\partial \xi} + V \frac{\partial F}{\partial \eta} = \left(1 + \frac{\alpha}{2}\right)\beta(g - F^2) + \frac{\partial}{\partial \eta}\left(\ell\bar{\epsilon}\frac{\partial F}{\partial \eta}\right) \tag{13b}$$

Static temperature energy equation

$$2\xi F \frac{\partial \theta}{\partial \xi} + V \frac{\partial \theta}{\partial \eta} = \alpha\ell\bar{\epsilon}\left(\frac{\partial F}{\partial \eta}\right)^2 + \frac{\partial}{\partial \eta}\left(\ell\frac{\hat{\epsilon}}{\mathrm{Pr}}\frac{\partial \theta}{\partial \eta}\right) \tag{14a}$$

Total temperature energy equation

$$2\xi F \frac{\partial g}{\partial \xi} + V \frac{\partial g}{\partial \eta} = \frac{2\alpha}{2+\alpha}\left[\ell(\bar{\epsilon} - \hat{\epsilon}/\mathrm{Pr})F\frac{\partial F}{\partial \eta}\right] + \frac{\partial}{\partial \eta}\left(\frac{\ell\hat{\epsilon}}{\mathrm{Pr}}\frac{\partial g}{\partial \eta}\right), \tag{14b}$$

where ℓ is the viscosity parameter defined by

$$\ell = \rho\mu/\rho_e\mu_e \tag{15}$$

with μ given from Sutherlands viscosity law and the turbulent parameters, $\bar{\epsilon}$ and $\hat{\epsilon}$ are defined as

$$\bar{\epsilon} = 1 + (\epsilon/\mu)\Gamma, \quad \hat{\epsilon} = 1 + (\epsilon/\mu)\frac{\mathrm{Pr}}{\mathrm{Pr}_T}\Gamma \tag{16a,b}$$

where Γ is the streamwise intermittency function: for fully laminar flow $\Gamma = 0$ and for fully turbulent flow $\Gamma = 1$, while for the transitional region its value varies smoothly from zero to one. The parameters α and β are obtained from the local inviscid flow as

$$\alpha = {u_e}^2/T_e, \quad \beta = \frac{2\xi}{u_e}\frac{du_e}{d\xi} \tag{17a,b}$$

State equation

$$\rho_e/\rho = \theta, \quad \text{or } \rho_e/\rho = \frac{\alpha}{{u_e}^2}\left(H - \frac{{u_e}^2}{2}F^2\right) \tag{18a,b}$$

Boundary conditions

$$F(\xi, 0) = 0, \quad V(\xi, 0) = 0, \quad \theta(\xi, 0) = T_w/T_e \quad \text{or } g(\xi, 0) = H_w/H_e \tag{19a}$$

and

$$F(\xi, \infty) = 1, \quad \theta(\xi, \infty) = 1 \text{ or } g(\xi, \infty) = 1 \tag{19b}$$

The turbulence relations given in Section 2 can be expressed in transformed variables as:

Inner region

$$(\epsilon/\mu)_i = \sqrt{\mathrm{Re}_r}\frac{{\rho_e}^2{u_e}^2K_1^2x_2^2{\pi_1}^2}{\mu_e\sqrt{2\xi}\ell\theta^3}\left|\frac{\partial F}{\partial \eta}\right| \tag{20a}$$

where

$$\pi_1 = 1 - \exp(-\pi_2) \tag{20b}$$

$$\pi_2 = \frac{x_2\rho_e u_e}{26\ell\theta^2\mu_e}\left(\theta\sqrt{\mathrm{Re}_r}\frac{\mu_e\ell_w}{\sqrt{2\xi}}\left|\frac{\partial F}{\partial \eta}\right|_w\right)^{1/2} \tag{20c}$$

Outer region

$$(\epsilon/\mu)_0 = \frac{\rho_e u_e}{\mu_e}\mathrm{Re}_r K_2 \frac{\bar{\gamma}\delta_{\mathrm{kinc}}}{\ell\theta^2} \tag{20d}$$

$$\delta_{\mathrm{kinc}} = \frac{\sqrt{2\xi}}{\sqrt{\mathrm{Re}_r}\rho_e u_e}\int_0^{\eta_e}\theta(1 - F)\,d\eta \tag{20e}$$

The interacting boundary layer calculations require an initial velocity and temperature profile at some station ahead of the effective interaction region (see Fig. 1). This profile was obtained here from a noninteracting two dimensional laminar-transitional-turbulent boundary layer calculation by an ordinary marching technique using a prescribed pressure distribution. In the examples shown in this paper, the boundary layer thickness is considerably larger than the wave amplitude. This fact in combination with the shape of the surface geometry has led us to adopt the Cartesian coordinate system.

4 **Inviscid/Viscous Interaction Model.** The interaction of the boundary layer with the isentropic supersonic inviscid flow is modeled in the pressure gradient parameter β by coupling it to the inclination θ_T of the total displacement body δ_T. The edge pressure is obtained from the Prandtl-Meyer relation approximated here to second order in terms of θ_T as

$$p_e = \frac{1}{\gamma {\mathrm{M}_\infty}^2} + \frac{\theta_T}{\sqrt{{\mathrm{M}_\infty}^2 - 1}} + \frac{({\mathrm{M}_\infty}^2 - 2)^2 + \gamma {\mathrm{M}_\infty}^4}{4({\mathrm{M}_\infty}^2 - 1)^2}{\theta_T}^2 \tag{21}$$

where

$$\theta_T = \tan^{-1}(d\delta_T/dx), \quad \delta_T = y_w + \delta \tag{22a,b}$$

$$\delta = \mathrm{Re}_r^{-1/2}\int_{x_{2w}}^{\infty}\left(1 - \frac{\rho u}{\rho_e u_e}\right)dx_2 \tag{22c}$$

Once p_e is obtained the isentropic relations and Euler's equation are used to obtain β in equation (17*b*). Thus, the inviscid and viscous flows must be solved simultaneously since they are directly connected through the displacement thickness given in equation (22*c*).

Numerical Method of Solution

The numerical method used is an implicit finite difference scheme written for the similarity form of the governing equations that marches from some initial station along the surface to the terminal point of interest. To account for the boundary value nature of the problem, Werle and Vatsa [1] have added the time dependent concept, similar to the one used for the solution of elliptic partial differential equations. This results in modification of only the momentum equation (13) by replacing the pressure parameter β with $\bar{\beta}$ defined as

$$\bar{\beta} = \beta + \frac{\partial \delta}{\partial t} \tag{23}$$

This method has been successfully applied to laminar separated flow

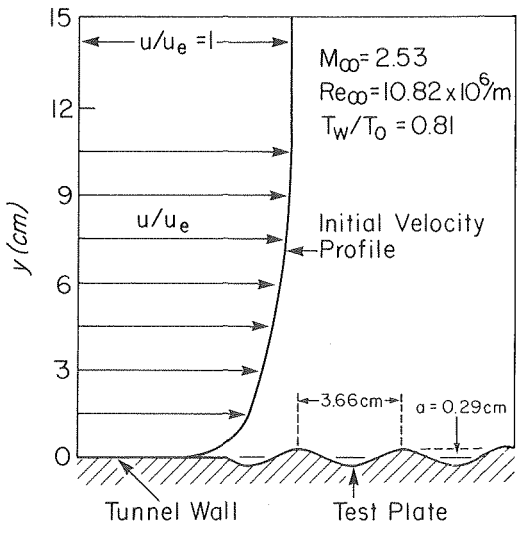

Fig. 1 Flow geometry

problems with various flow configurations including one with multiple interacting regions [2, 3]. The extension of this approach to turbulent boundary layers involves, aside from inclusion of the eddy viscosity model into the solution scheme, a number of modifications (see [7] for details).

For reasons of efficiency and accuracy a variable mesh size in the η direction is used in solving most turbulent boundary layers. A mesh growing in size from the wall as a geometric progression is used in the present algorithm. The governing equations were linearized and the partial derivatives were replaced by finite differences. The eddy viscosity term ϵ/μ, appearing as a nonlinear term in the governing equations, is approximated by its previous station value. Central differences were used to represent partials with respect to η (except where upwind differencing for F_η was required in the outer region of the boundary layer) as well as for the streamwise derivatives of the displacement body height, δ_T. Upwind differencing was used in the convection terms in the momentum and energy equations and forward differencing with respect to δ in the continuity equation.

In the present calculations the initial conditions were set by taking the zero time displacement body to correspond to a flat plate boundary layer and the surface protuberance to be of zero height. Subsequent time sweeps are conducted with the wave amplitude increasing gradually by a small amount. After the desired geometry is reached (after the first 10–15 sweeps) the time-like relaxation process is continued until the flow properties are relaxed to their final value. The convergence criteria used in this relaxation procedure was that the skin friction coefficient varies at most in the fourth significant figure. For a train of six waves, with 55 normal grid points and 111 longitudinal grid points, the calculation was performed in about 15 min of computer time on the IBM 376-168.

Results and Discussion

A major interest of the present investigation is in the numerical predictions for thick turbulent boundary layers over a wavy wall, as those in the experiments of [8]. The geometry and the flow conditions were therefore chosen to coincide with those given in [8]. The amplitude and wave length are $a^* = 0.29$ cm, $w^* = 3.66$ cm, respectively. A reference length, $L = 15.25$ cm, was chosen. The base flow conditions are defined by $M_\infty = 2.53$, $Re_\infty = 10.82 \times 10^6$/m, $T_\infty = 174$ K and $T_w/T_0 = 0.81$. Henceforth, we will refer to these conditions as standard flow conditions.

To obtain the present results it is first necessary to generate initial profiles at some point ahead of the first protuberance-flat plate juncture. For the standard flow conditions this station was taken at $x = 72.90$ (i.e., $x^* = L^*x = 11.12$ m), where the initial profiles were obtained from a noninteracting calculation to correspond to the boundary layer as it develops along the wall of the UPWT Langley Wind Tunnel [8]. The interacting algorithm was subsequently employed between this initial station and a downstream station past the last protuberance. The problem was first formulated and solved in the customary surface coordinates. It turned out that the geometry extremes make the use of the Cartesian coordinates version of the boundary layer equations more reasonable. The results of the calculations shown here were performed with a longitudinal step size $\Delta x = 0.02$, and a 55 point grid across the boundary layer.

Examples from the calculated results are presented for flow over a train of up to six waves, for Mach numbers $M_\infty = 2.5$ and 3.5, for Reynolds numbers $Re_\infty = 10.82 \times 10^6$/m and 32.46×10^6/m and for wall to total temperature ratios $T_w/T_0 = 0.40$ and 0.81.

Fig. 2 shows the contour of a train of six waves, the displacement body and the interacting and inviscid pressure distributions for the standard flow conditions. The difference in the inviscid and interacting pressures dramatically shows the effect and need for interaction. The pressure is calculated from an approximation to the Prandtl-Meyer relation, accurate to second order in flow inclination angle. The inviscid pressure is calculated using the local body slope, whereas the interacting pressure is obtained by using the slope of the displacement body ($= \delta_T = y_w + \delta$). The difference in the interacting and inviscid pressure is due to the difference in amplitudes of the actual and displacement body. It is interesting to observe that the interacting pressure is almost periodic even though the average displacement thickness decreases. Fig. 3 shows with the distribution of pressure the corresponding distribution of surface heat transfer and skin friction at the same base flow conditions. The pressure peaks and peaks in heating occur at about the same location ahead of the body surface peak. The peak in skin friction is shifted in the opposite direction. While the pressure distribution is nearly periodic, the heating levels and the skin friction peaks rise in the downstream direction. The rate of rise in peak heating is decreasing very slowly. These results are in contradistinction to our similar study [3] of thin laminar flow over a train of sine-waves, where the peaks in heating decreased rapidly in the steamwise direction.

To demonstrate the effect on surface properties due to Mach number, wall temperature, the Reynolds number, three additional cases are shown in Figs. 4–6. The increase of Mach number (Fig. 4) from 2.5 to 3.5 causes a decrease in the ratio of $h_{max}/h_{f.p.}$. As in the standard flow case, the location at which the first wave was placed was chosen in such a way that the flat plate boundary layer displacement thickness was about the same as in the companion experimental study of [8].

The lowering of wall temperature to $T_w/T_0 = 0.40$ (Fig. 5) shows a similar trend in $h_{max}/h_{f.p.}$ as for the increase in Mach number. But the absolute rate of surface heating is much higher than in the previous case. Interestingly, the $h/h_{f.p.}$ curve is smoother here than in other cases.

Lastly, an increase in Reynolds number, shown in Fig. 6, is seen to cause an increase in the ratio of peak heating.

An interesting aspect of the present results is the location of the peaks in pressure, heat transfer and shear. The present predictions show the peaks in pressure and heating to occur at about the same location. This is in agreement with experimental observations [8]. The location of the peak pressure in the present results is shifted to the right of the location of the inviscid peak pressure location (at $y \approx 0$) by a phase angle of about 60 deg. Theoretical studies by Inger and

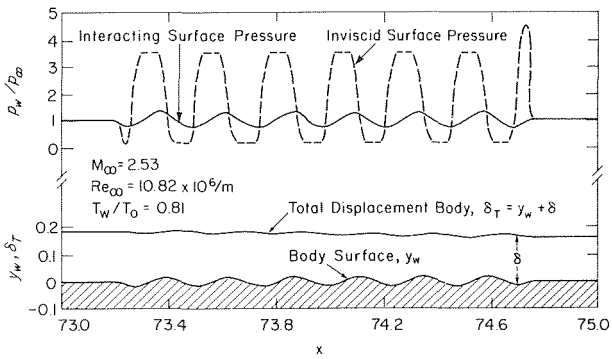

Fig. 2 Displacement body and surface pressure—standard case

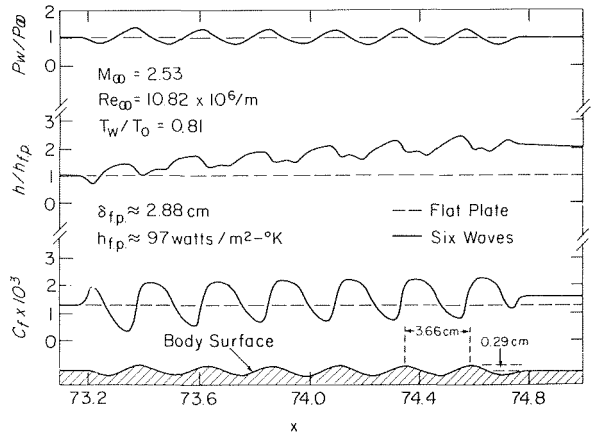

Fig. 3 Surface properties—standard case

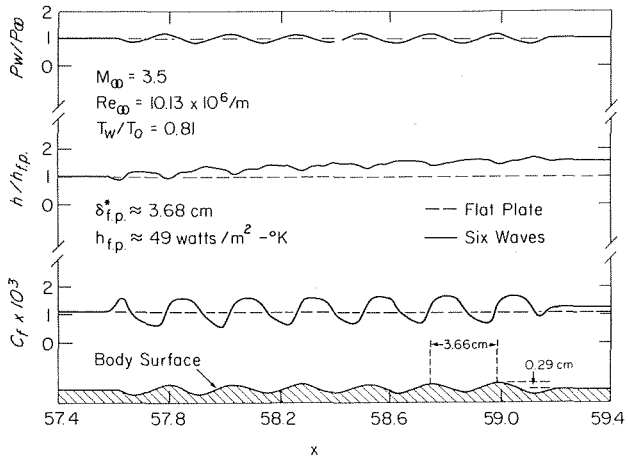

Fig. 4 Mach number effect on surface properties

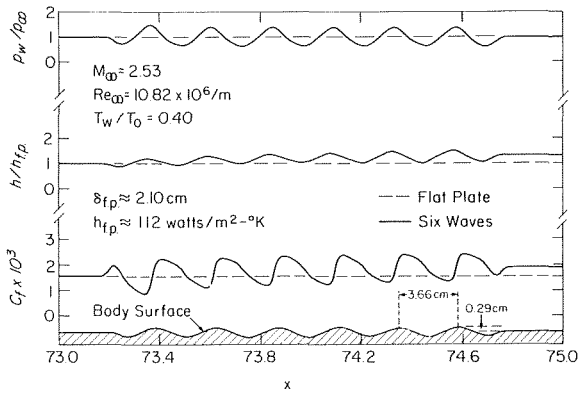

Fig. 5 Wall temperature effect on surface properties

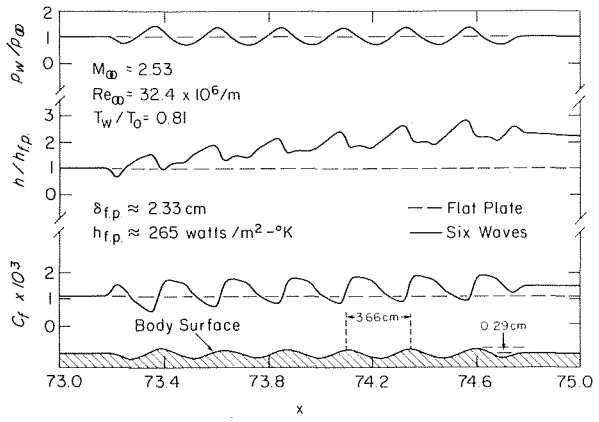

Fig. 6 Reynolds number effect on surface properties

Williams [9] and by Lekoudis, et al. [10] predict such a shift. Data from these studies given up to $M_\infty = 2.0$ show a shift to the left which drops off quickly towards zero at $M_\infty \simeq 2$. It is therefore possible to expect a phase angle in the opposite sense for $M_\infty > 2$, as is the case in present results. Although the present results and those in [9] and [10] were obtained by different methods, there is similarity in trends for the pressure phase shift. In the present formulation $\partial p/\partial y = 0$ and the pressure phase shift is entirely due to the x-directional shift of the total displacement body with respect to the surface profile (Fig. 2), while in the analytical studies of [9] and [10] the pressure phase shift is due to the perturbation pressure in the y-direction, inherent in the formulation of the problem. The maximum wall shear location ob-

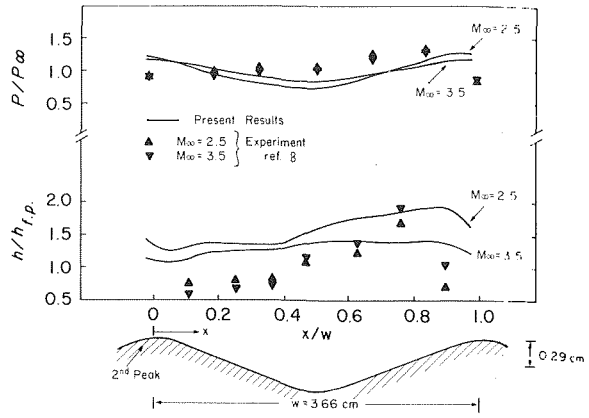

Fig. 7 Mach number effect on surface properties; comparison with experimental data

tained from present calculations is shifted to the right of the peaks in pressure and surface heating by about 60 deg. According to theoretical predictions [10] qualitatively such a shift is expected. Experimental data available at the same flow conditions [8] show a periodic trend in surface pressure as well as in the surface heating distribution. The periodic trend in surface pressure is observed also in the present predictions with peak values of $p_{max}/p_{f.p.} = 1.3$ at $M_\infty = 2.5$ and $p_{max}/p_{f.p.} = 1.2$ at $M_\infty = 3.5$. In [8] the peak values for pressure are given at $M_\infty = 3.5$ as $p_{max}/p_{f.p.} = 1.3$. The distribution of pressure and heating values between the second and third peak are compared to experimental data [8] in Fig. 7. While the heating distributions in the experiments of [8] are nearly repetitive over consecutive waves (with $h_{max}/h_{f.p.} = 1.9$ at $M_\infty = 2.5$ and $h_{max}/h_{f.p.} = 2.2$ at $M_\infty = 3.5$), the present predictions show a continuous increase over the length of the waves. Note though that in the experimental study there is also an indication that separation occurs, while a lack of separation is observed in the analytical results of Fig. 3. The cause of this disagreement is not certain but it could well be due to our choice of turbulence model[2] or in the fact that the present calculations do not simulate all the test conditions well enough (three-dimensional effects or boundary layer development on the tunnel wall). Note the calculated boundary layer displacement thickness of the initial profile at station $x = 72.90$ is 2.86 cm, close to the value given in [8]. However the predicted surface heating value at this station is too high when compared to experimental data of [8] (The predicted value is $h_{f.p.} = 96.5$ watts/m^2 K vs 62.5 watts/m^2 K in experiments). Other prediction methods also typically over predict to about the same level the heat transfer rates for boundary layers developing along the wind tunnel walls [12] thus indicating that some final adjustments may be needed in the turbulence model for these flows.

Conclusions

A numerical method capable of handling multiple interacting flow regions was adapted to the problem of thick turbulent boundary layer over a wavy wall.

The results of calculations presented in terms of surface pressure, skin friction, and heat transfer distributions disclose features distinctly different from the laminar case. The present results show a shift in the location of the viscous pressure peaks relative to the peaks in the inviscid pressure and to the peaks in the wall shear. These phase shifts are in qualitative agreement with theoretical predictions based on small disturbance theory. The location of peaks in interacting pressure and heat transfer coincide, and the longitudinal pressure

[2] It is possible that the streamline curvature with its delaying effect on the turbulence structure [11] is responsible for this discrepancy between the experimental data and present predictions. A test calculation has shown that Bradshaw's correction for the longitudinal curvature effect aligns the predictions closer to experimental data.

variation is periodic. This is in agreement with the experimental data. The experiments also show periodicity in surface heating distribution, while the present results predict a continuous increase in heating indicating a possible weakness in the turbulence model for a surface with rapidly varying curvature.

Acknowledgments

This work was supported by NASA under Grant NSG 1208 with Mr. James Dunavant of the Langley Research Center as Technical Monitor. In addition, the authors wish to gratefully acknowledge the continued interest and technical guidance of Professor R. T. Davis of the University of Cincinnati.

References

1 Werle, M. J. and Vatsa, V. N., "A New Method for Supersonic Boundary Layer Separations," *AIAA Journal*, Vol. 12, 1974, pp. 1491–1497.

2 Werle, M. J., Polak, A., Vatsa, V. N. and Bertke, S. D., "Finite Difference Solutions for Supersonic Separated Flows," appearing in *Flow Separation*, AGARD CP 168, 1975.

3 Polak, A., Werle, M. J., Vatsa, V. N. and Bertke, S. D., "Numerical Study of Separated Laminar Boundary Layers Over Multiple Sine-Wave Protuberances," *Journal of Spacecraft and Rockets*, Vol. 13, 1976, pp. 168–173.

4 Shang, J. S. and Hankey, W. L., Jr., "Numerical Solution for Supersonic Turbulent Flow Over a Compressible Ramp," *AIAA Journal*, Vol. 13, 1975, pp. 1368–1374.

5 Horstman, C. C., Hung, C. M., Settles, G. S., Vas, I. E. and Bogdonoff, S. M., "Reynolds Number Effects on Shock-Wave Turbulent Boundary Layer Interactions—A Comparison of Numerical and Experimental Results," AIAA Paper 77-42, presented at the AIAA 15th Aerospace Sciences Meeting, January 24–26, 1977, Los Angeles, California.

6 Werle, M. J. and Bertke, S. D., "Application of an Interacting Boundary Layer Model to the Supersonic Turbulent Separation Problem," Report No. AFL 76-4-21, August 1976, Dept. of Aerospace Engineering, University of Cincinnati, Cincinnati, Ohio.

7 Polak, A. and Werle, M. J., "Supersonic Separated Turbulent Boundary-Layer Over a Wavy Wall," Report No. AFL 77-11-36, November 1977, Dept. of Aerospace Engineering, University of Cincinnati, Cincinnati, Ohio.

8 Brandon, A. J., Masek, R. V. and Dunavant, J. C., "Aerodynamic Heating to Corrugation Stiffened Structures in Thick Turbulent Boundary Layers," *AIAA Journal*, Vol. 13, 1975, pp. 1460–1466.

9 Inger, G. R. and Williams, E. P., "Subsonic Supersonic Boundary-Layer Flow Past a Wavy Wall," *AIAA Journal*, Vol. 10, 1972, pp. 636–642.

10 Lekoudis, S. G., Nayfeh, A. H. and Saric, W. S., "Compressible Boundary Layer Over Wavy Walls," *The Physics of Fluids*, Vol. 19, 1976, pp. 514–519.

11 Bradshaw, P., "Effects of Streamline Curvature on Turbulent Flow," AGARDograph No. 169, 1973.

12 Couch, L. M. and Stallings, R. O., Jr., "Heat Transfer Measurements on a Flat Plate with Attached Protuberances in a Turbulent Boundary Layer at Mach Numbers of 2.49, 3.51, and 4.44," NASA TND-376, 1966.

U. C. Saxena
Engineer,
General Electric Company,
San Jose, Calif.,
Asso. Mem. ASME

A. D. K. Laird
Professor,
Department of Mechanical Engineering,
University of California,
Berkeley, Calif. 94720,
Mem. ASME

Heat Transfer from a Cylinder Oscillating in a Cross-Flow

This paper presents data on the effects of transverse oscillations on local heat transfer rates from a 7/8 in. (22 mm) diameter vertical circular cylinder, with an internal heater, subjected to cross-flow at a Reynolds number of 3500 in an open water channel during forced oscillations. The amplitude was varied from 0.89 to 1.99 times the diameter of the cylinder and the frequency from 0.4 to 1.2 Hz. The amplitude and frequency contributed about equally to the increases in local heat transfer coefficients. The increases in some cases were up to 60 percent, and were as much as 15 percent larger on the back than on the front of the cylinder. Motion pictures showed that the larger increases generally coincided with the larger flow disturbances that result from wake capture.

Introduction

Heat transfer from oscillating cylinders is an important technological problem involving many scientifically interesting phenomena. Although it has received considerable attention in recent years, there is a dearth of information and there are some apparently conflicting data. The problems stem largely from the influence of the oscillations of the cylinder upon the surrounding fluid flow. Certainly, if the flow is not significantly altered by the oscillations in a manner conducive to changing heat transfer, little effect will be noticed. Martinelli and Boelter [1] obtained increases up to 500 percent for free convection heat transfer by vibrating a 0.75 in. (19 mm) diameter cylinder in water. Other investigators [2, 3, 4, 5, 6] have also reported increases in heat transfer in the presence of oscillations. Sreenivasan and Ramachandran [7] found no appreciable effect on heat transfer rate from a horizontal cylinder. Kezios and Prasanna [8] reported a 20 percent increase in the average heat transfer coefficient from a cylinder vibrating transversely in cross-flow. However, Mori and Tokuda [9] who studied the heat transfer from an isothermal circular cylinder vibrating with small vibrational velocities in the direction of an oncoming flow, reported no increase in heat transfer rate for the forward portion of the cylinder; effects on the rear side of the cylinder were not reported. Scanlan [10], who investigated the effects on laminar forced-convection heat transfer of the vibration of a plane 1 in. (25.4 mm) square heating surface, vibrating normal to itself in water, found a maximum increase of 175 percent. Kestin and Maeder [11], investigating the effect of free stream turbulence, hypothesized that these effects are connected with the fact that a quasi-steady turbulent stream is essentially an oscillating stream with average amplitude of oscillation roughly proportional to the intensity of turbulence in the free stream.

During exploratory tests in connection with the present study, it was found that slow oscillations did not cause significant increases in heat transfer, nor did rapid, small-amplitude oscillations of approximately 2 mm at 30 Hz. The effects on the flow pattern around the cylinder apparently were too small to affect the heat transfer.

It is well known that vigorous oscillations of cylinders have a pronounced effect on the fluid flow around the cylinder, and there is a voluminous literature. Several reviews are available, for example, Morkovin, 1964 [12] and Laird, 1965 [13]. The greatest effect caused by cylinder oscillations in the Reynolds number range in which laminar boundary layers normally exist on the cylinders occurs in the band of frequencies and amplitudes that tend to force eddies to be shed at oscillating frequencies. This phenomenon, often referred to as wake capture, was documented by Bishop and Hassan, 1964 [14] and has been the subject of numerous studies.

In order to establish the magnitude of the increase of heat transfer during vigorous oscillations, the practically important case of wake capture was considered in the present study. Lienhard's group [15, 16] had shown that forced oscillations could be used to simulate wake capture flow conditions and that much economy of experimentation could result. They also showed that wake capture effects were similar over a wide range of combinations of Reynolds number and oscillation parameters. Consequently, forced oscillations were chosen for this study. Preliminary experiments showed that heat transfer effects were similar over a range of wake capture conditions attainable with the available equipment. Therefore, the study concentrated on one set of conditions that gave the best combination of heat transfer measurement, smooth flow in the channel and adequate photographic conditions, within the reliable operating range of the drive mechanism.

Specifically, the local heat transfer rates from a vertically mounted, internally heated, rigid, circular cylinder undergoing forced oscillations transverse to the main stream in an open flow water channel were experimentally investigated at one mainstream velocity of 0.5

Contributed by the Heat Transfer Division for publication in the JOURNAL OF HEAT TRANSFER. Manuscript received by the Heat Transfer Division April 19, 1978.

ft. s^{-1} (0.15 m s^{-1}) and Reynolds number of 3500, amplitude to diameter ratios $0.89 \leq AD^{-1} \leq 1.99$ and frequencies from 0.4 to 1.2 Hz.

Apparatus and Procedures

Details of the experimentation sketched briefly below are described more fully in [17].

The test cylinder was a 7/8 in. (22.2 mm) diameter, 1/8 in. (3.18 mm) thick and 2-15/16 in. (74.6 mm) long copper tube. A 2-9/16 in. (65.1 mm) long, 5/8 in. (15.9 mm) diameter cartridge heater was fitted inside, as shown in Fig. 1. The cylinder was provided with phenol-formaldehyde covers at both ends (with an additional methacrylate extension piece for the bottom end) to reduce the axial heat conduction losses.

The cylinder was supported in a vertical position with its bottom 1/16 in. (1.6 mm) above the bottom of the 4.5 in. (114 mm) deep by 44 in. (1.1 m) wide channel by means of a vertical 1/8 in. (3.18 mm) diameter steel rod which was clamped to a rigid fixture above the water channel. The fixture was equipped with strain gauges and a calibrated oscillograph for recording frequency, f, and amplitude, A. As a check, the frequency was also calculated from a magnetic pickup record, and by timing a number of oscillations with a stopwatch. The three methods were in good agreement.

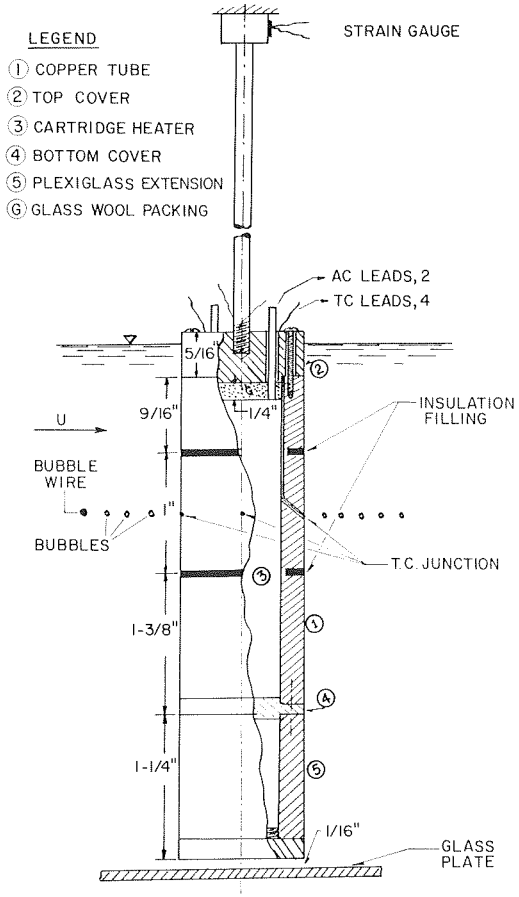

Fig. 1 Constructional details of test cylinder

Four 30-gauge copper-constantan thermocouples equally spaced circumferentially in a horizontal plane, and located flush with the outer surface of the cylinder, were used to measure the surface temperature of the cylinder. The EMF differences between these and another thermocouple in the water upstream from the cylinder were recorded on a second oscillograph, which was calibrated against a standard potentiometer. Temperatures at various angular locations on the cylinder surface relative to the main flow were measured by rotating the cylinder in the horizontal plane. Angular positions, θ, of the thermocouples were determined from a semicircular plate, graduated in degrees from 0–180, that was aligned with the axis of the cylinder and positioned so that a pointer attached to the cylinder support rod rotated over the graduations.

The difference, ΔT, between surface temperature, T_s, and the main stream temperature, T_m, at a selected thermocouple location on the stationary cylinder at a given angular position was recorded on the oscillograph while the cylinder was stationary. Then, by using the zero-offset control, the trace of ΔT was made to coincide with the temperature datum line (established during the calibration of the oscillograph) and the gain of the amplifier was increased. The cylinder was then oscillated and the change in surface temperature was recorded. This procedure was repeated at the same angular setting of the cylinder for the three other thermocouple locations 90 deg. apart on the cylinder surface. In this manner, temperature data were recorded for all chosen angular positions on each side of the cylinder. Heat input was determined and controlled by the electrical energy input to the heaters as calculated from ammeter and voltmeter readings.

To check the output of the thermocouples, the average heat flux at the outer surface was determined for the stationary cylinder case in two ways: a) by measuring heater power input, and b) by calculating the loss to the water by means of the equation

$$Q = \sum_{i=1}^{N} S_i [h(T_s - T_m)]_i \tag{1}$$

where S_i is the incremental cylinder surface area centered on the angular position, and h is the time-average local heat transfer coefficient evaluated with the aid of [18 and 19].

For $0 \leq \theta \leq 80$ deg, from [19],

$$h = 1.14 \frac{k_f}{D} \left(\frac{UD}{\nu_f}\right)^{0.5} \mathrm{Pr}^{0.4} \left[1 - \left(\frac{\theta}{90}\right)^3\right] \tag{2}$$

with θ measured in degrees from the upstream extremity of the cylinder and properties evaluated at the film temperature, which is the average of T_s and T_m. Pr is the Prandtl number, k_f the thermal conductivity, and ν_f the kinematic viscosity.

For $80 < \theta \leq 120$, h can be read from Fig. 9–9, page 410, of [19].

For $120 < \theta \leq 180$ deg, (19) gives:

$$h = 0.229 \frac{k_f}{D} \left(\frac{UD}{\nu_f}\right)^{0.63} \mathrm{Pr}^{0.4} \left[1 - \left(\frac{180 - \theta}{90}\right)^2\right] \tag{3}$$

Axial heat conduction losses were negligible due to the construction of the cylinder [17]. The results of (a) and (b) were found to be in good agreement, within about 4 percent, for four heating rates, as shown

Nomenclature

A = amplitude of cylinder oscillation from mean position.
D = diameter of the cylinder.
f = frequency of oscillation, Hz.
h = heat transfer coefficient based on film properties.
k = thermal conductivity coefficient.
N = number of angular positions.
Pr = Prandtl number.
Q = total heat transfer rate from cylinder to water.
S_i = surface increment centered on angular position i.
T = temperature.
U = cross-flow velocity, that is, mainstream velocity.
ΔT = temperature difference between cylinder surface and mainstream.
θ = angular location, measured from the front of the cylinder surface.
ν = kinematic viscosity.

Subscripts

avg = average
e = eddy shedding.
f = property evaluated at film temperature, $(T_m + T_s)/2$.
m = in the mainstream.
o = with oscillation.
s = cylinder surface, local value at any given θ.

in Table 1.

The increases in local heat transfer coefficients during oscillation were calculated from the local temperature differences between the cylinder surface and the mainstream temperatures during oscillations and while the cylinder was at rest. Because the difference is small between local circumferential heat transfer rates when the cylinder is at rest and when it is oscillating, the increase of local heat transfer coefficient with oscillations is given to a good approximation by

$$\frac{h_o}{h} \doteq \frac{\Delta T}{\Delta T_o} \tag{4}$$

Since the increase of heat transfer depends on the intensity of the fluid motions close to the cylinder, and these motions tend to be greatest during wake capture, transverse velocities, represented by Af, were chosen to include the practical range of natural oscillations during wake capture by varying f from 0.4 to 1.2 Hz and the A/D ratio from 0.89 to 1.99. These conditions were produced by moving the cylinder transversely by means of a crank mechanism operating on the support rod about 4 in. (0.1 m) above the top of the cylinder. Amplitudes were determined by the crank eccentricity which was calibrated with measured deflections of the cylinder.

The hydrogen bubble technique [20] was employed to make the flow around the cylinder clearly visible. Since no appreciable difference in the flow was detected regardless of the depth (from just below the surface to just above the channel bottom) at which the horizontal transverse bubble-generating wire was placed (upstream of the cylinder), the flow around the cylinder was considered uniform from surface to bottom and two-dimensional in horizontal planes. A glass sheet forming the bottom of the channel facilitated photographing the flow field from below with a 16 mm motion-picture camera. The flow velocity was obtained from motion pictures of the hydrogen bubbles moving between two fixed points on the glass plate. Because of variations in viscosity due to small changes in water temperature, the Reynolds number for the flow past the cylinder varied ±2 percent from the mean value of 3500.

Table 1 Check on cylinder surface temperatures by comparison of calculated and measured heat transfer rates from cylinder at rest

Calculated watt	Measured watt	Difference percent
110	115	4.3
136	142	4.1
217	225	3.7
261	271	3.6

Results and Discussion

The time-average percentage increases in local heat transfer resulting from oscillation over those when the cylinder was fixed are listed in Table 2, which also includes the temperature distribution around the fixed cylinder, as ΔT, referred to the mainstream temperature. The mean ΔT is based on sixteen sets of measurements taken as part of the procedure for collecting the data at A/D ratios from 0.89 to 1.55. Similar ΔT's were found for the remainder of the runs. The mid-mean values, calculated by suppressing the highest and lowest quarter of the values so as to eliminate possible mis-readings or instrument malfunctions, were the same as the mean values within the experimental accuracy of these means, which is indicated by the standard error of the mean listed. It was not possible to ascertain what part of the apparent disparities in the local heat transfer rate increases resulted from local changes in the flow at the different stages of wake capture and which were caused by inaccuracies in the data because of the small (about 1 to 5°C) decreases in local surface temperatures due to the oscillations. However, the principal effects are clear.

Table 2 Local fixed cylinder temperature minus water temperature (ΔT) and percentage increase in local heat transfer rate during oscillation

	θdeg	0	5	20	35	50	65	80	90	95	110	125	140	155	170	180	Average increase due to oscillation exclusive of 90 degree values	
Mean ΔT, °F		16.4	16.6	16.5	17.1	16.5	17.1	17.8	18.0	18.1	18.9	18.7	18.1	18.0	17.7	17.8		
Std Error of Mean		0.32	0.26	0.46	0.24	0.42	0.38	0.36	1.38	0.30	0.99	0.22	0.63	0.65	0.43	0.43		
Midmean ΔT, °F		16.4	16.7	16.6	17.2	16.9	17.4	18.0	18.1	18.1	18.7	18.7	18.6	18.5	17.8	17.9		
Std Error of Mean		0.28	0.14	0.20	0.09	0.29	0.18	0.13	0.48	0.10	0.38	0.11	0.25	0.57	0.20	0.29		
	f/f_e	f Hz															Front	Back
A=0.89D	0.47	0.68	9.1	8.2	7.3	7.2	6.8	7.9	12.6	9.3	13.2	9.2	13.0	13.7	14.1	13.0	10.2	8	12
	0.64	0.92	15.8	18.0	16.3	16.3	15.1	18.6	19.5	21.7	25.1	22.1	24.8	22.0	24.5	26.8	27.5	17	25
	0.72	1.04	20.9	21.3	22.2	20.6	23.3	27.8	27.8	27.7	32.0	30.7	30.5	37.1	40.5	39.9	39.9	23	36
	0.83	1.20	24.7	22.9	21.2	22.5	26.1	28.6	31.0	35.7	35.7	33.8	37.5	39.6	42.4	32.9	41.3	25	38
A=1.11D	0.38	0.54	10.9	8.7	7.5	7.0	10.4	13.0	11.3	12.9	11.7	9.4	7.4	18.2	15.3	19.1	15.3	10	14
	0.49	0.70	11.0	10.5	10.4	10.6	8.7	9.8	10.1	15.8	14.6	14.2	17.1	15.4	11.0	10.9	15.1	10	14
	0.63	0.90	18.5	15.0	17.6	14.5	18.9	20.5	25.8	25.8	25.6	24.4	25.4	28.2	30.3	33.7	32.0	19	29
	0.72	1.04	19.7	22.7	19.6	21.9	22.6	24.3	27.3	29.9	35.0	31.8	34.8	36.0	38.1	40.8	38.4	23	36
	0.83	1.20	23.6	24.8	24.8	25.8	33.5	36.9	40.7	37.9	35.7	37.9	43.4	54.5	58.8	62.3	47.3	30	49
A=1.55D	0.38	0.54	14.2	12.8	14.4	14.1	12.9	16.3	23.5	20.7	20.3	20.4	19.7	26.8	28.6	27.5	26.2	15	24
	0.61	0.87	24.4	19.5	23.3	20.7	27.8	30.0	35.5	34.0	33.6	30.9	34.8	39.6	45.4	43.1	43.8	26	39
	0.83	1.20	31.8	29.7	30.4	41.9	34.2	39.0	43.9	46.9	46.6	45.8	49.8	55.7	55.5	58.6	59.2	36	53
	f/f_e	θ deg	0		15	30	45	60	75	90		105	120	135	150	165	180		
A=1.77D	0.37	0.53	14.0		13.6	12.0	14.8	17.5	18.6	20.9		19.9	19.6	24.3	31.0	23.8	26.9	15	24
	0.49	0.70	20.7		19.9	19.6	23.3	26.4	30.9	31.3		36.0	28.4	43.0	49.6	44.0	40.8	23	40
	0.61	0.87	26.5		25.5	23.3	33.2	36.6	42.5	44.0		41.9	40.9	60.0	60.8	59.4	57.8	31	53
	f/f_e	θ deg	0		15			55	75	90		105			145	165	180		
A=1.99D	0.28	0.40	6.8		12.9			11.9	11.0	15.3		14.5			17.3	14.2	14.3	11	15
	0.49	0.70	20.6		27.1			33.7	26.3	44.5		37.9			48.4	41.6	37.0	27	41
	0.73	1.05	35.0		41.6			48.4	47.4	55.0		51.3			51.7	49.1	52.0	43	51

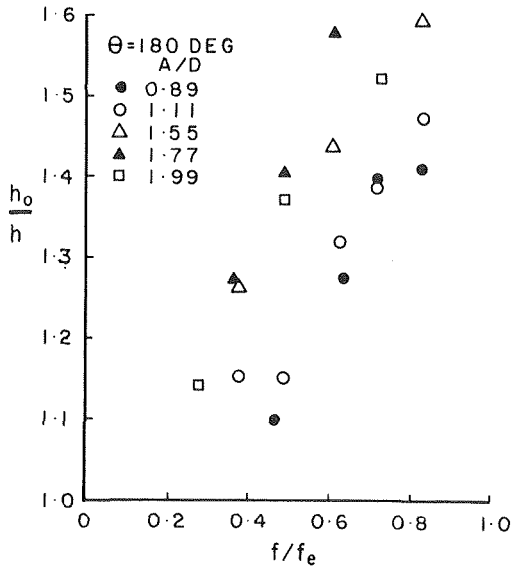

Fig. 2 Ratio of local heat transfer coefficient during oscillation to that for the fixed cylinder, h_o/h, as a function of the ratio of oscillation frequency to eddy shedding frequency, f/f_e, with amplitude to diameter ratio, A/D, as parameter, at the downstream extremity of the cylinder, $\theta = 180$ deg

Table 3 The separate influence of angular position on the increase of heat transfer coefficient, normalized on 90 deg

Position, Degrees+	$h_o/(h_o)_{90\ \mathrm{deg}}$
0	0.93
5–25	0.93
30–50	0.94
55–65	0.97
70–80	0.98
(90)	(1.00)
95–110	1.00
115–135	1.00
140–155	1.05
160–175	1.05
180	1.05

Fig. 2 shows h_o/h, the ratio of local heat transfer coefficients with and without oscillation, as a function of the ratio of oscillation frequency to fixed-cylinder eddy shedding frequency, f/f_e, with A/D as parameter. The trends are typical of all the data in Table 2. The dependencies of h_o/h on f/f_e and A/D are of about the same order of magnitude and vary somewhat with angular position as shown in Table 3, tending to be larger on the rear than on the front of the cylinder. Generally, the average heat transfer on the back increased significantly more than on the front at all amplitudes and frequencies, the average increases on the back being some 5 to 15 percent larger than on the front and tending to be larger at larger frequencies and amplitudes. Average values of percentage increases on the front and back are listed on the right side of Table 2.

Increases in local heat transfer coefficient of about 50 to 60 percent occurred on the back of the cylinder at the higher frequencies and amplitudes. At the smaller frequencies and amplitudes, increases of 10 to 20 percent were common.

Motion pictures taken simultaneously with the heat transfer data and visual observations showed that, as expected, the eddies were shed at the same frequency as the oscillation during wake capture and that, in general, the larger the disturbance induced in the near wake, the larger was the increase in heat transfer. However, at the highest frequencies and amplitudes, heat transfer augmentation decreased.

The combined influence of frequency and amplitude is shown in Fig. 3 in which the average heat transfer coefficient $(h_o/h)_{\mathrm{avg}}$ as a function of Af is plotted for the front and back separately. The ratio of maximum transverse velocity, $2\pi Af$, of the cylinder to the main stream velocity, U, is also given because of its importance in wake capture. Since the velocity in the tests was 0.5 ft/s^{-1}, Af is twice the parameter Af/U which, by factoring in Strouhal number, $\mathrm{St} = f_eD/U$, can be transformed into another parameter $\mathrm{St}(f/f_e)(A/D)$ which involves the influences of the oscillation to eddy shedding frequency ratio and the amplitude to diameter ratio.

Figs. 2 and 3 show that there is some minimum value of f/f_e and of A/D [through $2\pi Af/U = 2\pi\mathrm{St}(f/f_e)(A/D)$] below which heat transfer increases are minor. There is also an upper limit to both these ratios beyond which heat transfer ceases to increase significantly more than that which could be expected because of the increase in relative velocity of the cylinder and the water resulting from oscillations. In these data, the upper limit is shown to occur, for example, in Table 2 at $A/D = 1.99$ and $f/f_e = 0.73$, and in Fig. 3 in which the three highest data points show a decrease rather than a continued increase with increasing A/D and Af. The existence of limitations on the range of f/f_e and A/D values that cause the higher heat transfer coefficients can be attributed to wake capture that exists over a similar range of these ratios.

Increased heat transfer during oscillations results from increased intensity of fluid motion that tends to be greatest during wake capture. A major part of the requirement for wake capture is that $2\pi Af/U$ must be sufficiently large to cause eddies to form close behind the cylinder. The other principal part is that f must be close enough to f_e so that eddies form readily at the frequency of the oscillation. Large self-excited oscillations tend to occur near natural frequencies of cylinder systems, apparently because the larger amplitudes associated with an approach to resonance are required in order for the minimum A/D ratios needed for the initiation of wake capture to be reached. However, the similarity between the resonance and the wake capture phenomena appears to be coincidental. Further involvement of the resonance of the spring mass cylinder system in the ordinary sense does not seem to occur because a phase shift between the fluid force and the cylinder "response" is not observed [21]. In addition, wake capture tends to occur well below the natural frequency of the cylinder in vacuum. The fact that wake capture occurs during forced oscillations also supports the lack of involvement of true resonance.

The relative magnitudes of the influences of the system parameters on the increase of heat transfer were of interest. Consequently, although it is evident in some cases that other factors dependent on details of the flow were significant, an estimate was made of the approximate magnitudes of the influences of the principle parameters (frequency, amplitude and angular position) on the local heat transfer coefficient by a simplified correlation procedure. First, the slopes of logarithmic plots of h_0/h, averaged separately over the ranges of angular position $0 \le \theta \le 90$ and $\le \theta \le 180$ deg as functions of f/f_e (f_e = 1.44 Hz) for each A/d ratio were found and averaged. Then for each value of A/D, all h_o/h values divided by f/f_e raised to the corresponding exponent for the front and back of the cylinder were plotted

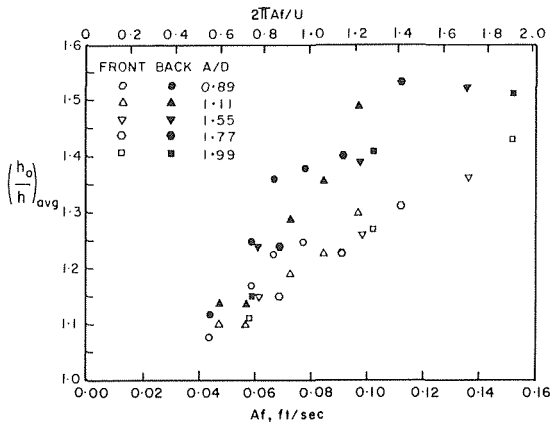

Fig. 3 Ratios of heat transfer coefficients averaged over the front and over the back of the cylinder separated, $(h_o/h)_{\mathrm{avg}}$, as functions of the product Af, and the ratio of maximum transverse velocity to mainstream velocity, $2\pi AF/U$, with amplitude to diameter ratio as parameter

Table 4 Exponents of variables from logarithmic plots

	A/D = 0.89	1.11	1.55	1.77	1.99		
Slope, (h_o/h) versus (f/f_e)						Average	Std. Dev.
Front	.28	.28	.19	.27	.28	0.26	0.04
Back	.36	.44	.33	.44	.30	0.37	0.06
Average values							
$(h_o/h)(f/f_e)^{-0.26}$	1.21	1.24	1.33	1.38	1.43	Slope = 0.20	
$(h_o/h)(f/f_e)^{-0.37}$	1.46	1.56	1.70	1.83	1.80	Slope = 0.29	

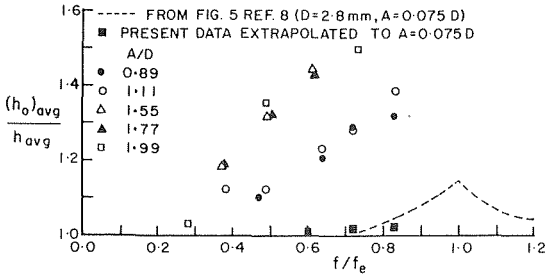

Fig. 4 Ratio of average heat transfer coefficients over the entire cylinder surface while oscillating and when fixed, $(h_o)_{avg}/h_{avg}$, as a function of frequency ratio, f/f_e, with amplitude to diameter ratio as parameter

as functions of A/D on logarithmic paper, and the slopes of straight lines through the points were obtained over the front and the back of the cylinder separately. The steps in the calculation and the resulting exponents, or slopes, are summarized in Table 4.

This calculation shows that, for this system over the range of variables tested, h_o/h is approximately proportional to $(f/f_e)^{0.26}$ and $(A/D)^{0.20}$ on the front, and to $(f/f_e)^{0.37}$ and $(A/D)^{0.29}$ on the back of the cylinder.

The separate influence of angular position was estimated by dividing all values of h_o/h by the products:

$$(f/f_e)^{0.26}(A/D)^{0.20} \text{ for } 0 \leq \theta \leq 90 \text{ deg}$$

$$(f/f_e)^{0.37}(A/D)^{0.29} \text{ for } 90 \text{ deg} \leq \theta \leq 180 \text{ deg}$$

The resulting quotients were averaged and normalized on the 90 deg value for ranges of angular position as shown in Table 3.

Since data from directly comparable systems could not be found in the literature, two that seemed to have more in common with the present system were chosen to check trends. Increases in average heat transfer of up to approximately one-fifth, as a result of standing waves producing maximum velocities normal to the mainstream velocity up to one-quarter of the mainstream velocity, were reported in [5]. Although the 3/4 in. (19 mm) cylinder diameter was about the same as in this study, and the Reynolds numbers of approximately 9000 to 10,000 were in the range producing laminar boundary layers on the cylinder, the flow used in [5] could not have been in the wake capture regime because the f/f_e ratio was fifteen rather than being of the order of unity or somewhat less as required for onset of normal wake capture. However, the reported increase in heat transfer, which must have been due to increased fluid motions about the cylinder, were comparable to those found in this study.

In the other system [8] considered, D and A/D were much smaller but the f/f_e range coincided with the present range from about 0.7 to 0.8 as shown in Fig. 4 on which results from Fig. 5 of [8] are reproduced. The present data extrapolated at three values of f/f_e as shown by the solid squares in Fig. 4 agree reasonably well. However, the small A/D values suggest that the flows involved were not similar.

Although these data can be correlated by the parameter Af/U, extrapolations to other values of Af/U should not be made without prior knowledge that valid results will be obtained because the magnitude of the product Af is not sufficient to specify the flow regime at a given value of U. Also, for different systems, the same values of Af/U may not give the same results because A/D and f/f_e must both be in the proper ranges for wake capture to occur. As extreme examples, a very large amplitude and very low frequency may produce results equivalent to steady cross flow, and minute amplitudes at large frequencies may scarcely disturb the flow enough to affect the heat transfer.

Conclusions

For the range of conditions of this investigation, some local heat transfer coefficients were up to about 60 percent larger during oscillations than when the cylinder was at rest. The largest increases occurred on the back of the cylinder at the largest amplitudes and frequencies.

At the A/D and f/f_e ratios of this study, the amplitude and frequency are the major factors in the increase of heat transfer, being about equally influential.

The increase of heat transfer coefficient with angular position is small relative to the increases due to amplitude and frequency. However, on the average, the increases on the back of the cylinder were some 15 percent larger than on the front.

Acknowledgments

This investigation was supported by the Sea Water Conversion Laboratory of the University of California, Berkeley, and the National Science Foundation.

References

1 Martinelli, R. C., Boelter, L. M. K., "The Effect of Vibration on Heat Transfer by Free Convection from a Horizontal Cylinder," *Proc. 5th International Congress*, Applied Mechanics, 1938, p. 578.

2 Lemlich, R., "Effect of Vibration on Natural Convection Heat Transfer," *Ind. Engrg. Chemistry*, Vol. 47, 1175, 1955.

3 Fand, R. M. and Kaye, J. P., "The Influence of Vertical Vibrations on Heat Transfer by Free Convection from a Horizontal Cylinder," *Intl. Dev. Heat Transfer*, 490, 1961.

4 Fand, R. M. and Peebles, E. M., "A Comparison of the Influence of Mechanical and Acoustical Vibrations on Free Convection from a Horizontal Cylinder," ASME JOURNAL HEAT TRANSFER, Vol. 84, 1962, p. 268.

5 Fand, R. M. and Cheng, P., "The Influence of Sound on Heat Transfer from a Cylinder in Crossflow," *Int. Journal of Heat and Mass Transfer*, Vol. 6, No. 7, July 1963, pp. 571–596.

6 Lemlich, R. and Rao, M. A., "The Effect of Transverse Vibration on Free Convection from a Horizontal Cylinder," *Intl. J. of Heat and Mass Transfer*, Vol. 8, No. 27, 1965.

7 Sreenivasan, K. and Ramachandran, A., "Effect of Vibration on Heat Transfer from a Horizontal Cylinder to a Normal Air Stream," *Intl. Journal of Heat and Mass Transfer*, Vol. 3, 1961, pp. 60–67.

8 Kezios, S. P. and Prasanna, K. V., "Effect of Vibration on Heat Transfer from a Cylinder in Normal Flow," ASME Paper No. 66-WA/HT-43, 1966.

9 Mori, Y. and Tokuda, S., "The Effect of Oscillation on Instantaneous Local Heat Transfer in Forced Convection from a Cylinder," *Proc. Third International Heat Transfer Conference*, Chicago, Aug. 1966, Vol. III, pp. 49–56.

10 Scanlan, J. A., "Effect of Normal Surface Vibration on Laminar Forced Convective Heat Transfer," *Ind. Engrg. Chemistry*, Vol. 50, 1958, pp. 1565–1568.

11 Kestin, J. and Maeder, P. F., "Influence of Turbulence on Transfer of Heat from Cylinders," NACA, TN, 4018 (1957).

12 Morkovin, M. V., "Flow around Circular Cylinder—A Kaleidoscope of Challenging Fluid Phenomena," Symposium on Fully Separated Flows, Philadelphia, PA, 1964.

13 Laird, A. D. K., "Forces on a Flexible Pile," *Proc. ASCE Specialty Conference on Coastal Engineering*, Santa Barbara, Oct. 1965, pp. 249–268.

14 Bishop, R. E. D., and Hassan, A. Y., "The Lift and Drag Forces on a Circular Cylinder in a Flowing Fluid," *Proceedings of the Royal Society of London*, Vol. 277, Series A, 1964, pp. 51–75.

15 Lienhard, J. H., "Synopsis of Lift, Drag, and Vortex Frequency Data for Rigid Circular Cylinders," Washington State University, Bulletin 300, 1966.

16 Liu, L. W. and Lienhard, J. H., "Locked in Vortex Shedding Behind Circular Cylinders, with Application to Transmission Lines," ASME Preprint, 67-FE-24, Fluids Engr. Conf., Chicago, Ill., May 1967.

17 Saxena, U. C., "Effects of Transverse Oscillations upon the Local Convective Heat Transfer Coefficient for Circular Cylinder with Cross-Flow," Ph.D. Dissertation, University of California, Berkeley, 1973.

18 Kreith, Frank, *Principles of Heat Transfer*, International Textbook Company, Scranton, Pennsylvania, 1965, pp. 408–410.

19 Matsui, Hiroshi, "Heat Transfer Phenomenon in Wake Flow of Cylinder," *Heat Transfer 1970* (Papers presented at the Fourth International Heat

Transfer Conference, Paris—Versailles 1970) Elsevier Publishing Company, Amsterdam, 1970, Vol. II, FC 5.9.

20 Schraub, F. A., et al., "Use of Hydrogen Bubbles for Quantitative Determination of Time Dependent Velocity Field in Low Speed Water Flows," Rep. MD-10, Thermoscience Division, Department of Mech. Engrg., Stanford University, Feb. 1964.

21 Laird, A. D. K., "Wave Forces on Piling," University of California Institute of Engineering Research, Report No. HPS-64-1, p. 25, Contract No. MBY-32233 U.S. Naval Civil Engineering Laboratory, Port Hueneme, Calif., 1964.

ERRATA

Erratum: T. C. Hsieh, A. Hashemi and R. Greif, "Shock Tube Measurements of the Emission of Carbon Dioxide in the 2.7 Micron Region," published in the August, 1975 issue of the JOURNAL OF HEAT TRANSER, pp. 397–399.

The correct versions of Figs. 4 and 5 are presented below. At 1800 K, $P_{CO_2} L$ = 3,440 N/m = 3.44 atm cm, P_{CO_2} = 48,500, N/m^2 = 0.485 atm and p_{total} = 194,000 N/m^2 = 1.94 atm; at 2500 K, p_{CO_2L} = 4,290 N/m = 4.29 atm cm, p_{CO_2} = 60,500 N/m^2 = 0.605 atm and p_{total} = 242,000 N/m^2 = 2.42 atm.

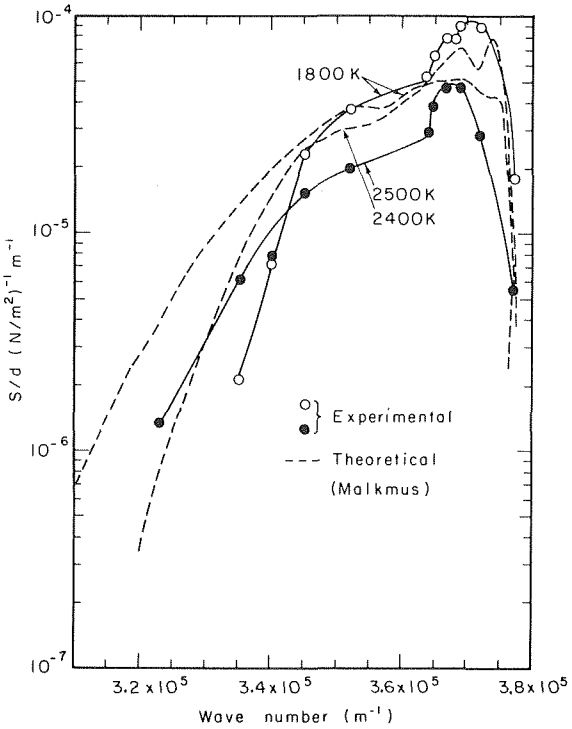

Fig. 4 Results for mean absorption coefficient

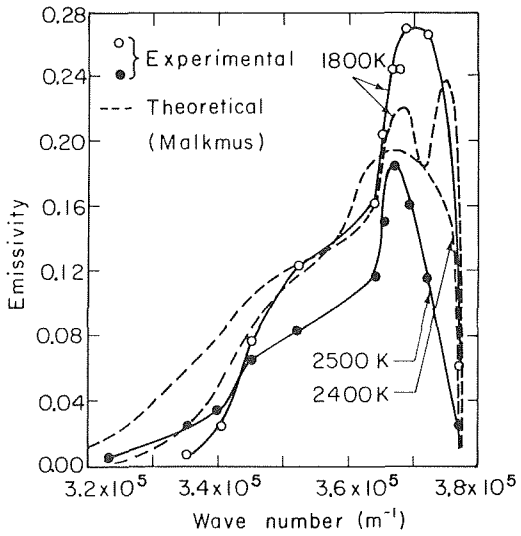

Fig. 5 Results for emissivity

A. D. Anderson
Staff Engineer.

T. J. Dahm
Senior Staff Engineer.

Aerotherm Division of Acurex Corporation, Mountain View, CA.

Boundary Layer Closure and Heat Transfer in Constant Base Pressure and Simple Wave Guns[1]

Solutions of the two-dimensional, unsteady integral momentum equation are obtained via the method of characteristics for two limiting modes of light gas launcher operation, the "constant base pressure gun" and the "simple wave gun." Example predictions of boundary layer thickness and heat transfer are presented for a particular 1 in. hydrogen gun operated in each of these modes. Results for the constant base pressure gun are also presented in an approximate, more general form.

Introduction

The prediction of boundary layer closure, which delimits the regime of ideal gun performance, and heat transfer, which may cause melting, are important considerations in the design of high velocity light gas launchers such as those used in ballistic ranges. In order to improve performance, that is, to increase muzzle velocity or projectile mass per unit area, it is necessary to increase gas pressures and probably also gas temperatures (sound speed). Although this implies thinner boundary layers and therefore less severe closure problems it leads to extremely large heat transfer rates. Thus, a better understanding of boundary layer phenomena would be very useful in any attempt to extend light gas launcher performance beyond presently accepted limits.

Heat transfer rates in gun tubes are very high, to the point of being very difficult, if not impossible, to measure. As a consequence, no data exist upon which to base predictions of heat transfer behavior under increasingly intense conditions. The parent research program has an objective to launch models at high velocity, with launch masses two to three times greater than permitted using conventional technology. It is crucial that the launch tube heat transfer aspect of launcher performance be characterized and dealt with if the program is to be a success.

A procedure for predicting nonsteady laminar and turbulent boundary layer behavior is outlined in [1], based on finite differences of the boundary layer differential equations of motion. Although the basic procedure can be developed to consider the current problem, time and cost considerations indicate the use of a simpler, more approximate analysis procedure.

This paper extends the gun barrel two-dimensional boundary layer integral momentum analysis of [2] to consider ballistic cycles appropriate to light gas launchers. The analysis of [2] has been verified for laminar conditions in [1], based on excellent comparisons with the exact nonsteady momentum boundary layer results. In the current paper, the boundary layer is assumed to be turbulent (Reynolds numbers are extremely large). Relationships approximately valid for steady flow are utilized to describe boundary layer profiles and the skin friction. After solution of the unsteady integral momentum equation by the method of characteristics, the heat transfer is estimated using Reynolds analogy.

Although the boundary layer analysis is applicable to the wider class of inviscid flows, the results presented herein are restricted to two particular perfect gas internal ballistic cycles which can be described analytically. These are the "constant base pressure gun" (CBPG) and the "simple wave gun" (SWG), both described in detail in a later section. For a given areal mass density, barrel length and muzzle velocity, these two modes of gun operation bracket practical ideal ballistic cycles in many important ways. Predictions for the two cycles analyzed should therefore also be useful in making engineering estimates for other cycles.

Unsteady Integral Momentum Analysis

The planar-two-dimensional,[2] unsteady boundary layer integral momentum equation was developed in a very general form in [2]. Three integral parameters arise in this equation, the familiar momentum and displacement thickness as well as a density integral. The momentum thickness is defined as

$$\theta = \int_0^\infty \frac{\rho u}{\rho_i u_i}\left(1 - \frac{u}{u_i}\right) dy \tag{1}$$

[1] This analysis was done under the sponsorship of the Defense Nuclear Agency, Contract No. DNA001-76-C-0407.

Contributed by the Heat Transfer Division for publication in the JOURNAL OF HEAT TRANSFER. Manuscript received by the Heat Transfer Division August 26, 1977.

[2] Application to gun barrels implies neglect of transverse curvature effects.

where i denotes the inviscid flow outside the boundary layer. The displacement thickness and density integrals appear in shape factors

$$H = \frac{\int_0^\infty \left(1 - \frac{\rho u}{\rho_i u_i}\right) dy}{\theta} \tag{2}$$

and

$$G = H - \frac{\int_0^\infty \left(1 - \frac{\rho}{\rho_i}\right) dy}{\theta} \tag{3}$$

It is convenient to use the momentum flux deficit

$$F = \rho_i u_i \theta \tag{4}$$

as the dependent variable. In that case, the unsteady integral momentum equation given in [2] becomes (assuming no mass transfer from the wall)

$$\frac{\partial F}{\partial t} + \frac{u_i}{G}\frac{\partial F}{\partial x} + \left\{\frac{1}{G}\frac{\partial G}{\partial x} + \frac{(H-G)}{G u_i}\frac{\partial u_i}{\partial t} + \frac{(1+H)}{G}\frac{\partial u_i}{\partial x}\right\} F = \frac{\tau_w}{G} \tag{5}$$

Since Reynolds numbers in the barrels of high-speed guns are extremely large, the boundary layer is certainly turbulent. The wall shear may therefore be approximated by (see [3])

$$\tau_w = 0.0128\, I_p \rho_i u_i^2 \left(\frac{F}{\mu_i}\right)^{-1/4} \tag{6}$$

where I_p represents the variable property effect usually evaluated by a reference enthalpy technique. In this study a constant representative value of $I_p = 1.5$ is assumed, which is correct for wall temperature to edge temperature ratios of about 0.2 (see [4]).

The shape factors, H and G, have been evaluated following the technique outlined in [4]. A 1/7 power velocity profile was assumed together with a modified Crocco approximation to the enthalpy profile.

$$\frac{h + (u^2/2) - h_w}{h_i + (u_i^2/2) - h_w} = \left(\frac{u}{u_i}\right)^2 \tag{7}$$

These shape factors are shown in Fig. 1 as a function of wall temperature ratio. G is approximately equal to 1.3, independent of wall temperature and that value is assumed here. In what follows, H is also assumed constant in any particular solution. In a later section, it is shown numerically that the results are relatively insensitive to the choice of H. The ratio of the boundary layer thickness, δ, to momentum thickness, which is required in closure calculations, is also shown in Fig. 1.

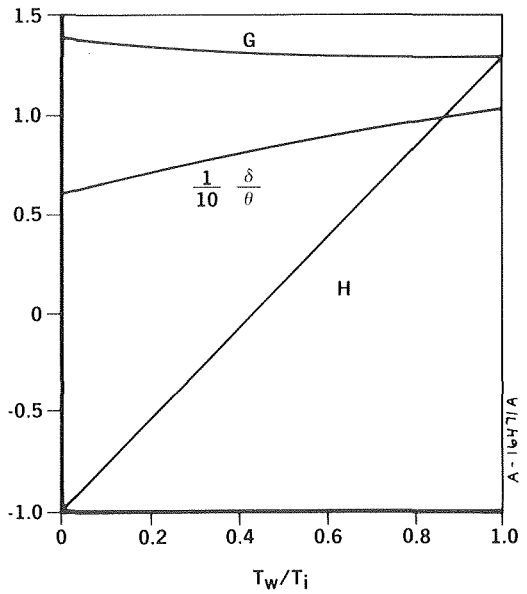

Fig. 1 Turbulent Boundary layer shape factors, 1/7 power velocity profile

Equation (5) is well suited to solution by the method of characteristics. With the choice of t as the independent variable, derivatives of F and u_i along the characteristics are

$$\left.\frac{dF}{dt}\right|_c = \frac{\partial F}{\partial x}\left.\frac{dx}{dt}\right|_c + \frac{\partial F}{\partial t} \tag{8}$$

and

$$\left.\frac{du_i}{dt}\right|_c = \frac{\partial u_i}{\partial x}\left.\frac{dx}{dt}\right|_c + \frac{\partial u_i}{\partial t} \tag{9}$$

Partial derivatives with respect to t may be eliminated from equation (5) by substitution of these expressions. Then with the choice of characteristic direction of

$$\left.\frac{dx}{dt}\right|_c = \frac{u_i}{G} \tag{10}$$

the derivative $\partial F/\partial x$ is eliminated and equation (5) becomes

$$\left.\frac{dF}{dt}\right|_c + \left\{\frac{(H-G)}{G u_i}\left.\frac{du_i}{dt}\right|_c + \frac{2G + H(G-1)}{G^2}\frac{\partial u_i}{\partial x}\right\} F = 0.0148\, \mu_i^{1/4} \rho_i u_i^2 F^{-1/4} \tag{11}$$

Nomenclature

A = barrel area
a = sound speed
D = barrel diameter
D_c = chamber diameter
F = momentum flux deficit, equation (4)
G = boundary layer shape factor, equation (3)
H = boundary layer shape factor, equation (2)
H = heat transfer coefficient, equation (44)
h = enthalpy
I_p = coefficient representing variable property effects
L = barrel length
L_c = chamber length
M = projectile mass
P = pressure
$\dot{Q}$ = heat flux
T = temperature
t = time variable
t^* = dimensionless time variable for SWG, equation (23)
U = muzzle velocity
u = streamwise velocity
u^* = dimensionless streamwise velocity for SWG, equation (25)
X = magnitude of heat transfer coefficient for CBPG, equation (45)
x = streamwise coordinate
x^* = dimensionless streamwise coordinate for SWG, equation (24)
y = surface normal coordinate
α = initial projectile acceleration
γ = ratio of specific heats
δ = boundary layer thickness
θ = momentum thickness, equation (1)
μ = dynamic viscosity
ξ = function defined for inviscid flows linear in x, equation (12)
ρ = mass density
τ = dimensionless time variable for CBPG, equation (17)
τ_w = wall shear stress
Ψ = distribution of heat transfer coefficient for CBPG, equation (46)
ω = temperature exponent in viscosity relation

Subscripts

c = along characteristic
i = inviscid flow outside boundary layer
0 = initial chamber conditions
p = projectile
r = recovery
w = wall
1 = beginning of characteristics

This equation is of the Bernoulli type and is easily linearized and solved formally.

Further analysis will be restricted to inviscid flows in which the velocity is linear in x. The two ballistic cycles analyzed below are included in this class. For these flows, it is permissible to write

$$\frac{\partial u_i}{\partial x} = \frac{d\ ln\xi}{dt} \tag{12}$$

Now, with H and G constant and the initial condition that the boundary layer thickness is zero at the origin of characteristics ($t = t_1$), integration of equation (11) yields

$$F = \left\{\frac{5}{4} \times 0.0148\, u_i^{-B_1} \xi^{-B_2} \int_{t_1}^{t} u_i^{B_1+2} \xi^{B_2} \rho_i \mu_i^{1/4} dt\right\}^{4/5} \tag{13}$$

where

$$B_1 = \frac{5(H-G)}{4G} \quad \text{and} \quad B_2 = \frac{5(2G + H(G-1))}{4G^2} \tag{14}$$

The integration in equation (13) must be performed along characteristic lines, that is, along solutions to equation (10) for the particular flow in question.

Internal Ballistic Cycles

Fig. 2 indicates the nomenclature used to describe gun geometry. The approximate shape of the boundary layer is indicated by the dashed curves.

Two limiting idealized cycles are considered. In either case, the propulsion gas is assumed to be a perfect gas with constant specific heat and a viscosity relation of the form $\mu = \mu_0(T/T_0)^\omega$. The subscript 0 denotes initial chamber conditions. All processes in the core flow are considered to be isentropic so that $P/P_0 = (\rho/\rho_0)^\gamma = (T/T_0)^{\gamma/(\gamma-1)}$.

The Constant Base Pressure Gun. The CBPG is a chambered gun ($D_c > D$) in which a scheduled compression by a piston in the chamber causes a certain history of thermodynamic property variation at the chambrage plane, described below, which in turn leads to constant base pressure.

The projectile motion and inviscid flowfield for the CBPG are given in [5]. Projectile acceleration is constant:

$$\alpha = \frac{P_0 A}{M} \tag{15}$$

The muzzle velocity is

$$U = \sqrt{2\alpha L} \tag{16}$$

The time variable is conveniently normalized as

$$\tau = \frac{U}{2L} t \tag{17}$$

so that

$$x_p = L\tau^2 \tag{18}$$

and

$$u_p = U\tau \tag{19}$$

The infinitesimal layer of gas at the base of the projectile remains at constant pressure and entropy during the cycle. The density of this gas is therefore constant so that the layer occupies constant volume and moves with the velocity of the projectile. To the second layer of gas, the first layer appears to be part of an enlarged projectile of constant volume undergoing constant acceleration. The pressure (and density) of the second layer must therefore also be a constant. Repetition of this argument leads to the conclusion that each element of fluid remains at constant density as it moves down the barrel, so that $D\rho/Dt = 0$. Continuity then requires that the velocity be independent of x at any particular time, that is,

$$u_i = U\tau \tag{20}$$

Solution of the momentum equation yields the temperature distribution,

$$\frac{T_i}{T_0} = 1 + \epsilon\left(\tau^2 - \frac{x}{L}\right) \tag{21}$$

where

$$\epsilon = \frac{U^2}{2C_p T_0} \tag{22}$$

The required history of thermodynamic properties at the chambrage plane ($x = 0$) is given by equation (21). For any particular muzzle velocity, a higher initial chamber temperature implies that less compression is required in the chamber during the cycle.

The Simple Wave Gun. The SWG is a constant diameter gun ($D_c = D$) in which the propellant gas expands from rest in a constant volume chamber. Upon release of the projectile, the initial expansion wave moves upstream and is reflected from $x = -L_c$. The inviscid flow solution presented below is restricted to the simple wave region between the projectile and the first reflected wave.

A description of the projectile motion in a SWG is developed in [5] and outlined below. It is most convenient to write this description in terms of the following dimensionless variables:

$$t^* = \frac{\alpha(\gamma+1)}{2a_0} t, \quad x^* = \frac{\alpha(\gamma+1)}{2a_0^2} x, \quad u^* = \frac{(\gamma+1)}{2a_0} u \tag{23, 24, 25}$$

In a simple wave region, the temperature is related to the velocity by

$$\frac{T_i}{T_0} = \left(1 - \frac{(\gamma-1)}{(\gamma+1)} u_1^*\right)^2 \tag{26}$$

This expression is converted to a pressure ratio and substituted into the equation for projectile motion, which is then integrated with the results

$$u_p^* = \frac{\gamma+1}{\gamma-1}\left[1 - (1+t^*)^{-\frac{\gamma-1}{\gamma+1}}\right] \tag{27}$$

and

$$x_p^* = 1 + \frac{2(1+t^*)}{\gamma-1} - \frac{\gamma+1}{\gamma-1}(1+t^*)^{2/(\gamma+1)} \tag{28}$$

Equations (27) and (28) can be combined into the form

$$u_p^* = \frac{x_p^* + t^*}{1+t^*} \tag{29}$$

This equation describes the motion of the gas at the base of the projectile and, in fact, is the correct form for the inviscid velocity throughout the simple wave region, that is

$$u_i^* = \frac{x^* + t^*}{1+t^*} \tag{30}$$

Note that the velocity is zero on the initial upstream expansion wave ($x^* = -t^*$) and also that the position where $u_i^* = 1.0$ (sonic velocity, $u_i = a_i = 2a_0/(\gamma+1)$, from equation (26)) is fixed at $x^* = 1.0$.

Ballistic Performance Comparison. The purpose of this section is to provide some indication that analyses of the CBPG and the SWG are useful in a practical sense. Since projectiles are necessarily somewhat fragile, the peak base pressure must be held below a certain limit. Within such a limitation, the CBPG gives the maximum possible muzzle velocity for fixed barrel geometry and projectile mass. An

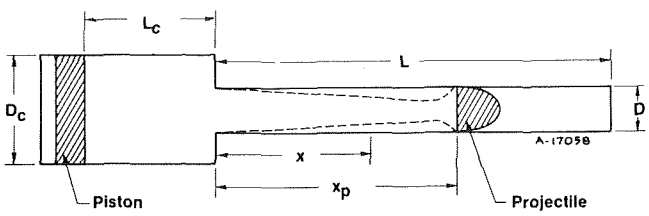

Fig. 2 Gun geometry

SWG, on the other hand, gives a lower muzzle velocity than the CBPG for the same peak (initial) pressure. Also, it is not practical to build a true SWG as a launcher because of the excessive chamber length and associated propellant gas. The SWG, should, however, provide a reasonable approximation to the flow in the barrel of chambered guns in which no compression occurs during the cycle. In a later section it will be shown that the CBPG suffers extremely high heating rates near the chamber in comparison to the SWG (for the same muzzle velocity, barrel geometry and projectile mass). Design trade-offs will therefore probably be appropriate so that both the high performance CBPG and the relatively low performance SWG are of interest.

The performance of the two cycles can be conveniently compared in terms of the dimensionless variables defined earlier for the SWG. However, the isentropic index γ remains as a parameter. This comparison is shown in Fig. 3 for $\gamma = 1.4$. For very large sound speeds (that is, $u_p^* \to 0$) the SWG approaches the performance of a CBPG. At finite sound speeds, for any particular muzzle velocity and barrel length, the initial acceleration, α, is of course larger for the SWG than for the CBPG.

Also shown on Fig. 3 are ballistic performance calculations for several practical hydrogen cycles in which there is no compression in the chamber during the cycle (see [6]). As expected, almost all of these results fall between those for the two idealized cycles, but nearer those for the SWG. This is an indication that the boundary layer closure and heat transfer results obtained below for the idealized cycles should be useful in estimating boundary layer effects in practical guns.

Prior to boundary layer closure, projectile base pressure will be influenced for any cycle by boundary layer displacement effects, and thermal radiation from the inviscid core. The latter quantity in many cases is small compared to other energy transfers, and will be ignored here. Displacement effects depend on boundary layer displacement thickness, which is small for low wall to edge temperature ratios typical of launch tubes (Fig. 1). Thus, one expects that an isentropic inviscid analysis will accurately predict core and projectile behavior prior to boundary layer closure. Thereafter, both the convective heat and momentum transfers degrade projectile base pressure. Thus, boundary layer closure limits the regime of isentropic behavior of the gun internal ballistics, and the useful length of launch tube. In the boundary layer analyses that follow, the inviscid property variations from the relations above will be used with the expectation of high accuracy prior to boundary layer closure.

Analytic Results for the CBPG

The solution of equation (10) for the characteristic lines, subject to equation (20), is

$$\frac{x_c}{L} = \frac{x_1}{L} + \frac{1}{G}(\tau^2 - \tau_1^2) \tag{31}$$

The characteristics are chosen to originate at a location, (x_1, τ_1), where the boundary layer thickness is zero. This is a natural boundary condition at the base of the projectile, since all fluid particles except those on the wall are moving at projectile velocity. Consequently, characteristics are being continuously originated at the projectile base as it moves down the barrel, $x_1(\tau_1) = L\tau_1^2$. The chambrage plane boundary layer thickness is zero only at zero time, and its subsequent growth depends upon characteristics that originate at zero time in the chamber. A detailed and general analysis of the chamber fluid mechanics is beyond the scope of the present paper. However, one would expect at least that the boundary layer is quite thin at the chambrage plane due to the high upstream accelerations. In terms of heat transfer it is conservative to assume zero boundary layer thickness at the chambrage plane at all times, $x_1(\tau_1) = 0$, akin to the boundary condition at the leading edge of a sharp flat-plate. This simplification is invoked in the remainder of the analysis, so that characteristics are also being originated continuously at the chambrage plane during the ballistic event. For either type of characteristic,

$$\frac{x_c}{L} = \frac{1}{G}(\tau^2 - \tau_1^2) + (1 - \delta_{j0})\tau_1^2 \tag{32}$$

where

$$\delta_{j0} = \begin{cases} 0 \text{ for projectile characteristics} \\ 1 \text{ for chambrage plane characteristics} \end{cases}$$

Fig. 4 shows some of these characteristic lines.

Since u_i is independent of x, ξ (equation (12)) is constant and does not influence the solution. Also, further analysis of the CBPG is restricted to $H = 0.2\ G$,[3] which allows integration of equation (13) in closed form. The gas properties in the integrand may be written as

$$\rho_i \mu_i^{1/4} = \rho_0 \mu_0^{1/4} \left(\frac{T_i}{T_0}\right)^{\lambda} \tag{33}$$

where

$$\lambda = \frac{1}{\gamma - 1} + \frac{\omega}{4} \tag{34}$$

The temperature along a characteristic is

$$\frac{T_i}{T_0} = 1 + \epsilon[b(\tau^2 - \tau_1^2) + \delta_{j0}\tau_1^2] \tag{35}$$

where

$$b = \frac{(G-1)}{G} \tag{36}$$

[3] The influence of H upon the solution is investigated numerically for the SWG in the next section.

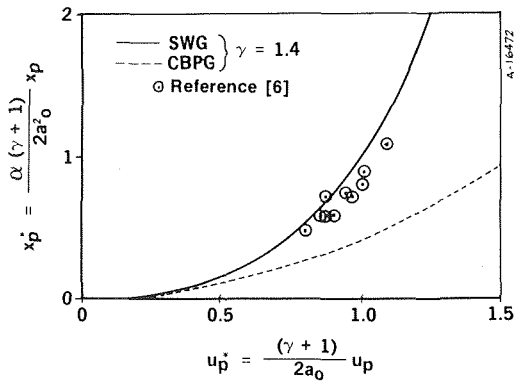

Fig. 3 Generalized ballistic performance

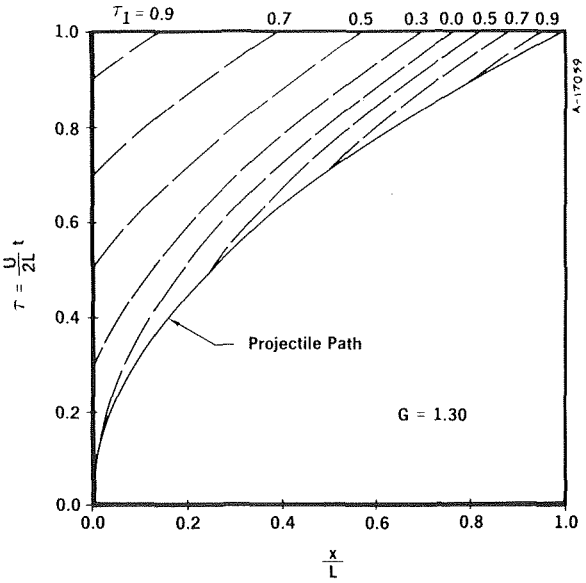

Fig. 4 Boundary layer characteristics for a CBPG

Equation (13) may now be integrated, with the result

$$F = \left[\frac{5}{4} \times 0.0148 \rho_0 \mu_0^{1/4} U L \tau g(T_i, T_1)\right]^{4/5} \tag{37}$$

where

$$g(T_i, T_1) = \frac{\left(\frac{T_i}{T_0}\right)^{\lambda+1} - \left(\frac{T_1}{T_0}\right)^{\lambda+1}}{b\epsilon(\lambda+1)} \tag{38}$$

The dimensionless momentum thickness may now be written as

$$\frac{\theta}{L} = 0.041 \left(\frac{\rho_0 UL}{\mu_0}\right)^{-1/5} \tau^{-1/5} g^{4/5} \left(\frac{T_i}{T_0}\right)^{-1/(\gamma-1)} \tag{39}$$

Since ϵ is a small parameter, a series expansion of the temperature dependent terms is of interest. The first two terms are

$$g^{4/5}\left(\frac{T_i}{T_0}\right)^{-1/(\gamma-1)} = (\tau^2 - \tau_1{}^2)^{4/5}\left\{1 + \epsilon\left[\left(\frac{\omega}{10} - \frac{3}{5(\gamma-1)}\right) \times b(\tau^2 - \tau_1{}^2) + \left(\frac{\omega}{5} - \frac{1}{5(\gamma-1)}\right)\delta_{j0}\tau_1{}^2\right]\right\} \tag{40}$$

For values of ϵ of interst, ($\epsilon < 0.25$), the first term of this expansion is accurate to within about ten percent. With this approximation,

$$\frac{\theta}{L} \approx 0.041 \left(\frac{\rho_0 UL}{\mu_0}\right)^{-1/5} \tau^{-1/5}(\tau^2 - \tau_1{}^2)^{4/5} \tag{41}$$

From this expression it is apparent that the maximum boundary layer thickness occurs, at any time, very near the common characteristic ($\tau_1 = 0$). This provides a convenient means for estimating boundary layer closure—that is, when the boundary layer thickness is equal to the barrel radius. Assuming $T_w/T_i = 0.55$ (for which $H = 0.2G$), Fig. 1 indicates $\delta/\theta = 8.6$. Using equations (18) and (41) the projectile location at closure is estimated to be

$$\left(\frac{x_p}{D}\right)_{\text{closure}} = 35.6 \left(\frac{\theta}{\delta}\right)^{10/7} \left(\frac{D}{L}\right)^{3/7} \left(\frac{\rho_0 UL}{\mu_0}\right)^{2/7} \tag{42}$$

In the next section this expression will be compared to some numerical results for the SWG.

Heat transfer can be estimated using Reynolds analogy, that is,

$$\frac{\dot{Q}}{\rho_i u_i (h_r - h_w)} = \frac{\tau_w}{\rho_i u_i{}^2} \tag{43}$$

where h_r is the recovery enthalpy which is taken here as equal to the total enthalpy, $h_i + u_i{}^2/2$. Using equation (6) with $I_p = 1.5$, the heat transfer coefficient can be written as

$$\mathbf{H} = \frac{\dot{Q}}{(h_r - h_w)} = 0.0192\, \rho_i u_i \mu_i{}^{1/4} F^{-1/4} \tag{44}$$

Substituting the solution for F, equations (37) and (38), the heat transfer coefficient is now written as a magnitude times a distribution. The magnitude is defined to be

$$X = 0.043 \left(\frac{\rho_0 UL}{\mu_0}\right)^{-1/5} \rho_0 U \tag{45}$$

and the distribution is

$$\Psi = \tau^{4/5} \left(\frac{T_i}{T_0}\right)^{\lambda} g^{-1/5} \tag{46}$$

The magnitude of the heat transfer coefficient depends strongly on the muzzle velocity U. Consider, for simplicity, that T_0 and L are fixed. Initial chamber pressure and therefore density are proportional to U^2 (see equations (15) and (16)), so that

$$X \sim U^{12/5} \tag{47}$$

Doubling the muzzle velocity will thus increase the heat transfer rate by a factor greater than five.

The distribution of the heat transfer coefficient at any given time has a minimum near the characteristic that begins at $\tau_1 = 0$, $x_1 = 0$, that is, near the position of maximum momentum thickness. At the chambrage plane and at the projectile base, where the momentum thicknesses are zero, the heat transfer coefficient is predicted to be infinite. Since the projectile is moving, it is the region near the chambrage plane which suffers the highest sustained heating rates. Example time histories of heat transfer coefficients at fixed location for the CBPG are compared with similar results for the SWG in the next section.

Numerical Results for the SWG

In what follows, the SWG flowfield is regarded as a reasonable approximation to the flow downstream of $x = 0$ in a chambered gun. The initial condition of zero momentum thickness is therefore applied at $x = 0$ (and at the projectile) as in a CBPG.[4]

Upon substitution of equation (30), equation (10) may be written as

$$\frac{d}{dt^*}(1 - x_c{}^*) - \frac{(1 - x_c{}^*)}{\beta(1 + t^*)} = -\frac{1}{\beta} \tag{48}$$

where

$$\beta = \frac{(\gamma+1)G}{2} \tag{49}$$

The solution to equation (48) is

$$x_c{}^* = 1 + \frac{(1+t^*)}{(\beta-1)} - \left(1 - x_1{}^* + \frac{1 + t_1{}^*}{(\beta-1)}\right)\left(\frac{1+t^*}{1+t_1{}^*}\right)^{1/\beta} \tag{50}$$

For chambrage plane characteristics, $x_1{}^* = 0$, while for projectile characteristics, $x_1{}^*$ is given by equation (28). The characteristic lines have roughly the same general shape as those shown for the CBPG in Fig. 4.

For the SWG inviscid flowfield (equation (30)), equation (12) yields

$$\xi = (1 + t^*)^{2/(\gamma+1)} \tag{51}$$

In normalized form, equation (13) becomes for the SWG

$$F = \left\{\frac{5}{4} \times \frac{0.0148 \rho_0 \mu_0{}^{1/4}}{\alpha}\left(\frac{2a_0}{\gamma+1}\right)^3 \left(\frac{x_c{}^* + t^*}{1+t^*}\right)^{-B_1} (1+t^*)^{-2B_2/(\gamma+1)} \times \int_{t_1{}^*}^{t^*} \left(\frac{x_c{}^* + t^*}{1+t^*}\right)^{B_1} (1+t^*)^{2B_2/(\gamma+1)} \left(\frac{T_i}{T_0}\right)^{\lambda} dt^*\right\}^{4/5} \tag{52}$$

Numerical evaluations of F (and other variables) were generated by computer for certain sample problems. All cases were for a 2.54-cm bore gun with $L/D = 300$ and a projectile mass to area ratio of $M/A = 17.0$ gm/cm^2. Hydrogen was assumed as the propellant gas with $\gamma = 1.4$ and $\mu = 1.137 \times 10^{-6}\,(T/\text{K})^{\omega}$ gm/(cm·s), $\omega = 0.75$. The initial chamber temperature was taken to be 5000 K.

For a muzzle velocity of 6 km/s, SWG boundary layer solutions were generated for values of H of 0.0, 0.2G, and 0.4G. The results for maximum momentum thickness as a function of projectile location are shown in Fig. 5. The parameter H apparently has only a small influence on boundary layer thickness. If δ/θ is considered to be a function of H (Fig. 1), then closure position is almost independent of H.

Results for a CBPG with the same geometry and muzzle velocity are also shown. There is little difference between the exact solution (from equation (39)) and the approximate expression (from equation (41)). For a given projectile position, the boundary layer is thicker in a CBPG than in an SWG. This is because projectile velocities and gas densities are higher and viscosities are lower in an SWG, therefore, core Reynolds numbers at the position of maximum boundary layer thickness are higher.

Sample closure results for the SWG are compared with the approximate expression (equation (42)) for the CBPG in Fig. 6. The results for the SWG in Fig. 6 show a greater sensitivity of closure to muzzle velocity than the CBPG does. The dependence on barrel length and initial chamber temperature are also indicated for the CBPG.

[4] In a true SWG, the initial condition would be applied on the initial upstream expansion wave, $x^* = -t^*$, rather than at $x = 0$.

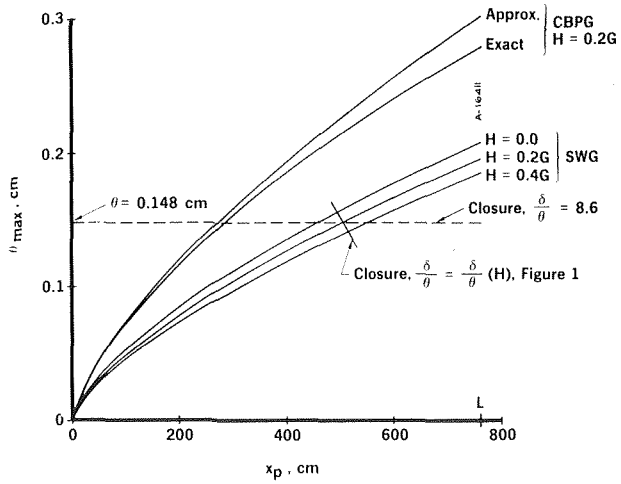

Fig. 5 Growth of maximum boundary layer momentum thickness. $U = 6$ km/s, gun description follows equation (52)

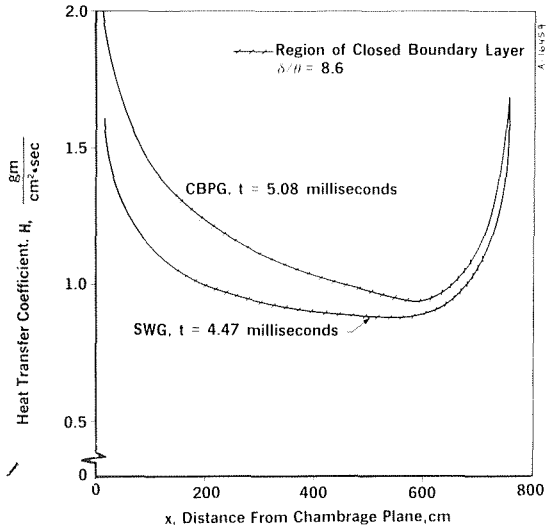

Fig. 7 Axial distribution of heat transfer coefficient at the time of projectile expulsion. $U = 3$ km/s, gun description follows equation (52)

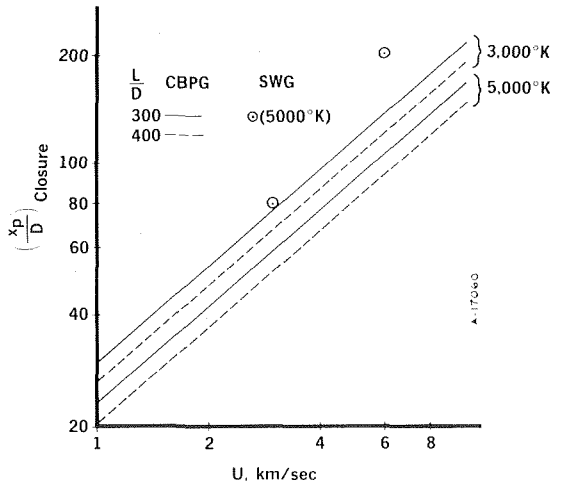

Fig. 6 Projectile locations at the time of boundary layer closure. $\delta/\theta = 8.6$, gun description follows equation (52)

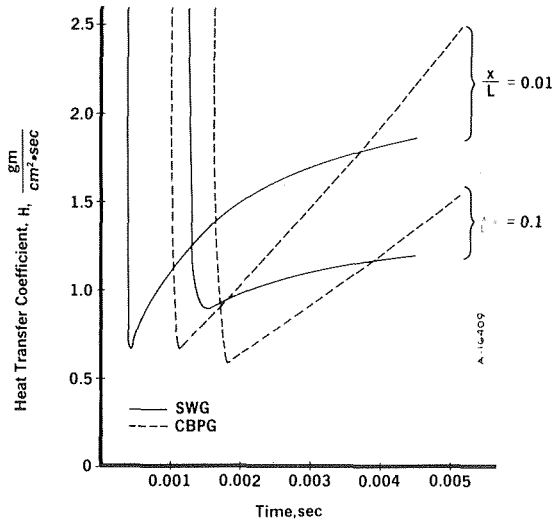

Fig. 8 Time histories of heat transfer coefficient. $U = 3$ km/s, gun description follows equation (52)

Distributions of heat transfer coefficients at the time of projectile expulsion are shown in Fig. 7 for a SWG and a CBPG operating at the same muzzle velocity, 3 km/s. Near the chambrage plane, the CBPG has higher density and velocity. In addition to these effects, the heat transfer is also higher for the CBPG because it has increasing total enthalpies with time while those for the SWG are decreasing. These effects are all more pronounced at higher muzzle velocities.

Time histories of heat transfer coefficients at two locations are shown in Fig. 8 for the two types of guns operating at 3 km/s. Pulse lengths and heat transfer coefficient levels are quite similar for the two guns; however, the CBPG will experience significantly higher heating levels late in the cycle because of higher total enthalpies as well as the higher heat transfer coefficient shown.

Example material response evaluations were performed using the one-dimensional "Aerotherm Charring Material Thermal Response and Ablation Program" (CMA, [7]). Input to the CMA code includes pressure and recovery enthalpy histories from the ballistic cycle, and the heat transfer coefficient distribution from the boundary layer calculations. This code uses real gas thermochemistry (in this case, for hydrogen) generated with the "Aerotherm Chemical Equilibrium" (ACE, [8]) code, to determine the wall enthalpy, h_w, as a function of wall temperature and pressure. The transient internal conduction computation uses a numerical finite difference procedure.

Material response predictions for steel and copper (see [6]) for the subject hydrogen gun indicated melting near the chambrage plane at a muzzle velocity of 3 km/s in the CBPG, in agreement with early launcher development experience [9]. These materials were therefore eliminated from consideration at higher muzzle velocities.

Tungsten thermal response predictions were performed for a 6 km/s muzzle velocity at $x/L = 0.01$[5] in the gun under consideration operating either as a CBPG or as a SWG. The heat transfer coefficient histories are similar in shape to those shown in Fig. 8, but have a magnitude five or six times as large. The thermal response predictions, which are displayed in Fig. 9, indicate that tungsten will melt in a CBPG at these conditions but will not melt in a SWG. The reason for the vast difference between the predictions for the two cycles is apparent from the total enthalpy distributions, also shown in Fig. 9.

At the time the projectile leaves the muzzle, the velocity at the

[5] Results very near the chambrage plane are inaccurate based on the assumption of zero boundary layer thickness there. The position chosen for analysis may experience some heat transfer prediction errors, but not to an extent sufficient to change the conclusions from the analysis concerning melting.

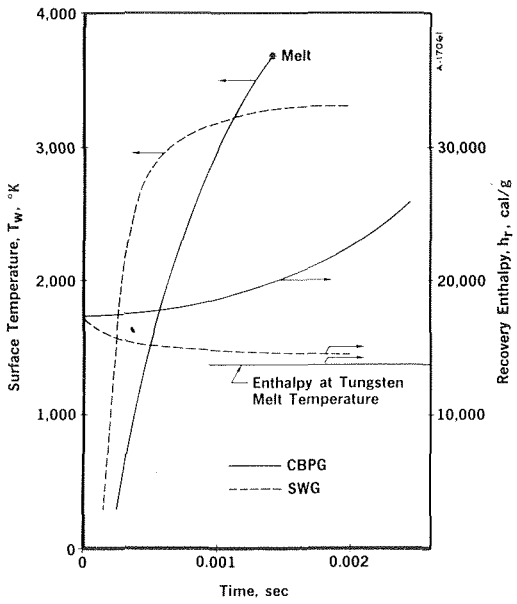

Fig. 9 Tungsten thermal response and recovery enthalpy history. $U = 6$ km/s, $x = 0.01$ L, gun description follows equation (52)

chambrage plane is 6 km/s in the CBPG and only 3.5 km/s in the SWG. Also, the local temperature increases in a CBPG and decreases in a SWG. The net result is that at muzzle time the ratio of total enthalpies for the two cycles is about 1.8. Since the enthalpy of hydrogen at the melting temperature of tungsten is almost as large as the SWG total enthalpy, the difference in total enthalpy between the two cycles has a drastic effect on heat transfer.

Although the SWG results appear encouraging from a material protection point of view, it must be kept in mind that base pressures are prohibitively high at early times in this mode of operation. The CBPG provides the best ballistic performance for a given base pressure, but has prohibitively high heat transfer rates. Thus, it is apparent that alterations to a given cycle which tend to solve one of these problems will tend to aggravate the other.

Conclusions

- A simplified prediction technique has been developed for boundary layer closure and heat transfer in light gas guns
- Tungsten is far superior to steel as a heat sink material in high performance launchers

References

1 Bartlett, E. P., Anderson, L. W., and Kendall, R. M., "Time-Dependent Boundary Layers With Application To Gun Barrel Heat Transfer," Heat Transfer and Fluid Mechanics Institute, p. 263, 1972.

2 Dahm, T. J., and Anderson, L. W., "Propellant Gas Convective Heat Transfer in Gun Barrels," Aerotherm Final Report 70-18, Aerotherm Division/Acurex Corporation, Aug. 1970.

3 Kays, W. M., *Convective Heat and Mass Transfer*, McGraw-Hill, New York, p. 94, 1966.

4 Dahm, T. J., et al., "Inviscid Flow and Heat Transfer Modeling for Reentry Vehicle Nosetips," Aerotherm Final Report 76-224, Aerotherm Division/Acurex Corporation, October 1976.

5 Seigel, A. E., "The Theory of High Speed Guns," AGARDograph 91, North Atlantic Treaty Organization Advisory Group for Aerospace Research and Development, May 1965.

6 Cohen, L. M., et al., "Feasibility of a Hybrid Hypervelocity Launcher," Aerotherm. TR-77-238, Aerotherm Division/Acurex Corporation, Jan. 1977.

7 Wool, M. R., "User's Manual Aerotherm Charring Material Thermal Response and Ablation Program, Version 3," Aerotherm Report UM-70-14, Aerotherm Division/Acurex Corporation, April 1970.

8 Powars, C. A., and Kendall, R. M., "User's Manual Aerotherm Chemical Equilibrium (ACE) Computer Program," Aerotherm Report UM-69-7, Aerotherm Division/Acurex Corporation, May 1969.

9 Seifert, K., "Hypervelocity Launcher Design," Physics International Final Report PIFR-708, p. 14, December 1975.

J. R. Ward
Research Chemist.

T. L. Brosseau
Mechanical Engineer

US Army Ballistic Research Laboratory
Aberdeen Proving Ground, MD 21005

Reduction of Heat Transfer to High Velocity Gun Barrels by Wear-Reducing Additives

In order to understand how wear-reducing additives such as TiO_2/wax and polyurethane foam liners reduce erosion, a series of gun firings was made in a 105 mm tank cannon equipped with thermocouples to measure the heat transferred to the gun barrel both in the presence and in the absence of the additives. Four thin thermocouples (0.13 mm diameter) were placed at different radial distances from the bore surface. Each thermocouple was placed at the same axial distance along the gun barrel. From the temperature distribution measured 100 milliseconds after propellant ignition, the total heat transferred in the gun barrel was determined. On the basis of single shot measurements, both the polyurethane foam and the TiO_2/wax liner reduced the heat transferred to the gun barrel by ten percent. Repeated firings with TiO_2/wax liners afforded steadily increasing reduction in heat transfer which was attributed to the formation of an insulating layer of TiO_2 and unreacted wax on the bore surface. This also accounts for the twenty-five fold increase in wear life of the M68 tank cannon firing rounds equipped with TiO_2/wax liners.

This thermocouple technique is now used to design optimum weight and location of wear-reducing additives in other gun systems, since the efficacy of the wear-reducing liner can be deduced from a few shots.

Introduction

Wear-reducing additives such as polyurethane foam and titanium dioxide/wax (TiO_2/wax) liners have been in the U. S. Army inventory for over a decade, yet the mechanism by which the additives reduce erosion is uncertain [1]. Fig. 1 contrasts the wear profile and wear rate of the M68 tank cannon firing APDS (Armor-piercing, discarding sabot) rounds equipped with and without wear-reducing additives. The wear test results clearly show the superiority of the TiO_2/wax liner over the polyurethane foam liner. Recent heat transfer measurements in a 37 mm gun barrel [2] concluded that the polyurethane foam liner reduced heat input to the barrel to the same extent as the TiO_2/wax liner as long as the additives were employed in the same configuration. Similar findings were reported from erosion measurements in a 37 mm vented chamber made from the same 37 mm gun [3]. In the wear test depicted in Fig. 1, only the TiO_2/wax liners were equipped with flaps. The presence of such flaps was the configuration that gave the maximum heat transfer reduction [2, 3]. In order to see if the superiority of the TiO_2/wax liner in the M68 tank cannon was solely a question of its configuration, heat transfer measurements were conducted in an M68 tank cannon. Secondary objectives were to demonstrate that the heat transfer measurements could be correlated to erosion and to test a recent hypothesis [4] that the "secondary" wear peak for polyurethane foam at 76 cm RFT (measured from

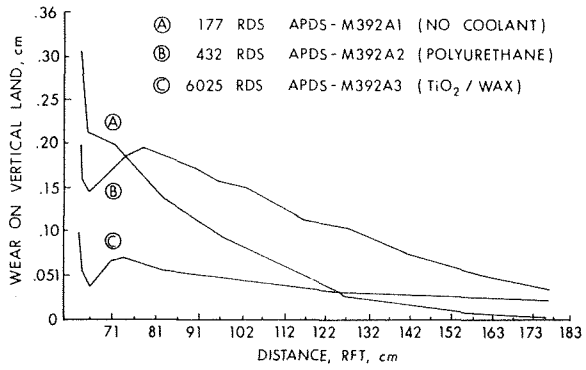

Fig. 1 Wear profile of M68 tank cannon firing APDS rounds equipped with and without wear-reducing liners

Contributed by the Heat Transfer Division of THE AMERICAN SOCIETY OF MECHANICAL ENGINEERS and presented at the AICHE/ASME Heat Transfer Conference, Salt Lake City, Utah, August 15–17, 1977. Manuscript received by the Heat Transfer Division January 25, 1978. Paper No. 77-HT-19

the rear face of the tube) in Fig. 1 was caused by the additive acting only at the origin of rifling and losing its down-bore effectiveness.

Experimental

Thermocouples were applied to an M68, 106 mm gun tube using the same techniques developed and described in [5]. The thermocouples were each located over a groove so that erosion of the bore surface beneath the thermocouples would be negligible during the firing sequence. The outside diameter of the gun tube was not concentric with the inside bore diameter; however, the gun tube was too long and too heavy to use the technique described in [5] for determining the concentricity between the outside diameter and the bore diameter. Therefore, holes were drilled through the gun tube 12.7 mm in front of each thermocouple location and in the same groove as each thermocouple location. A spring-loaded plug was used to define the inner surface of the barrel, and the depth micrometer described in [5] was used to measure the thickness of the gun tube at each location. From these measurements, the concentricity between the outside diameter and the bore diameter, and the distances from each thermocouple location to the bore surface were determined.

Temperatures at four different radial positions were measured at two locations along the length of the gun tube. The temperatures at each position were measured as continuous functions of time, and from these measurements temperature distributions were obtained from the 100 ms time interval. The radial positions and locations along the length of the gun tube are shown in Fig. 2. Chamber pressure was measured in the cartridge case by using an internal ferrule pressure gage.

The temperatures and chamber pressures were recorded simultaneously on a Honeywell magnetic tape recording system in the same manner as reported previously [2, 5]. In this test, however, the Neff amplifiers were maintained at 294 K in an air-conditioned trailer that was located close to the firing barricade. This kept the length of the leads over which the small thermocouple signals had to travel to a minimum.

Rounds fired in the test consisted of a model number M392 APDS projectile, M80A1 primer, and 5.48 kg of seven perforated, 1.14 mm web M30 propellant (Lot No. RAD 67877). Polyurethane foam and TiO_2/wax liners, as used with the M392 APDS round, were used in several different configurations, and locations of the liners within the cartridge case are summarized in Figs. 4–11. The TiO_2/wax liner without flaps is used in the M456 HEAT round.

A "clean-out" round was fired with no wear-reducing additive following rounds fired with TiO_2/wax liners to remove any traces of TiO_2 or wax that might be left on the barrel [6]. One series of firings was then made without firing clean-out rounds.

Results

Fig. 12 depicts temperature versus time at each thermocouple for a round fired with no wear-reducing additive.

Table 1 summarizes temperature rises recorded at 100 ms after propellant ignition for five rounds fired this way in order to estimate the net heat input. At this time the propellant gases are no longer measurably heating the barrel and axial conduction should be negligible.

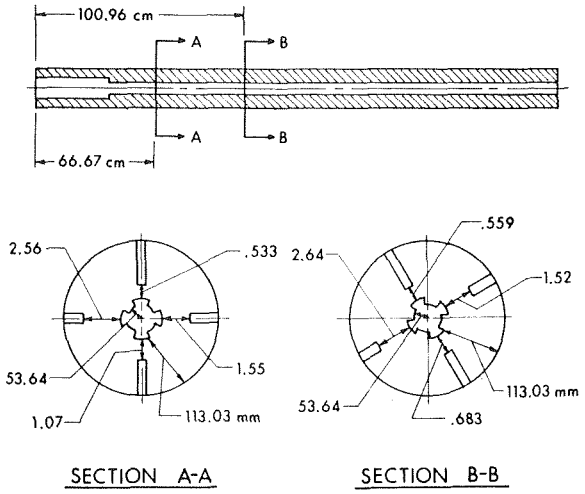

Fig. 2 Location of thermocouples in 105 mm M68 gun tube

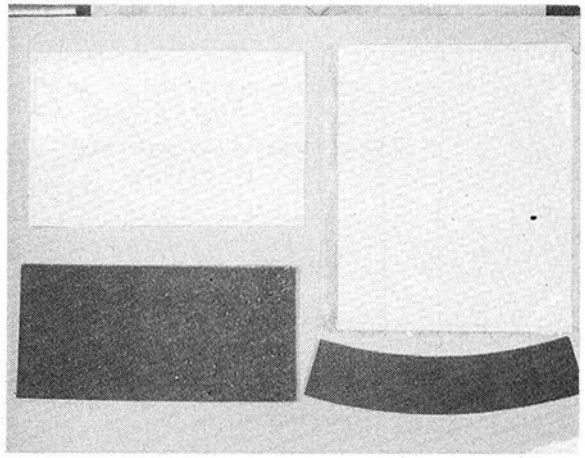

Fig. 3 Standard wear-reducing liners used in the 105 mm M68 tank gun

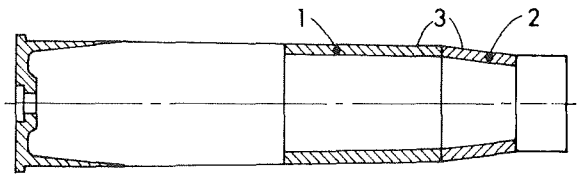

1. LARGE POLYURETHANE (.087 kg)
2. SMALL POLYURETHANE (.027 kg)
3. GLUED

Fig. 4 Two-piece polyurethane liner

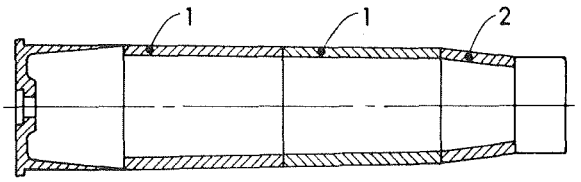

1. LARGE POLYURETHANE (.087 kg)
2. SMALL POLYURETHANE (.027 kg)

Fig. 5 Three-piece polyurethane liner

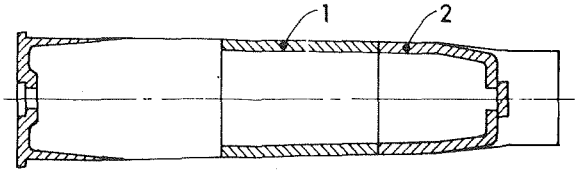

1. LARGE POLYURETHANE (.087 kg)
2. LARGE POLYURETHANE WITH FLAPS (.087 kg)

Fig. 6 Polyurethane liner with flaps

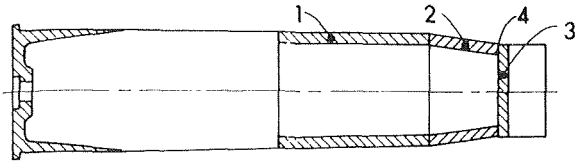

1. LARGE POLYURETHANE (.087 kg)
2. SMALL POLYURETHANE (.027 kg)
3. POLYURETHANE DISK
4. GLUED

Fig. 7 Two-piece polyurethane liner with disk

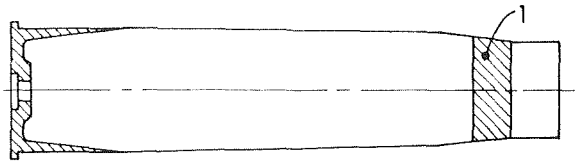

1. 13 GLUED POLYURETHANE DISKS (.154 kg)

Fig. 8 Stack of 13 glued disks

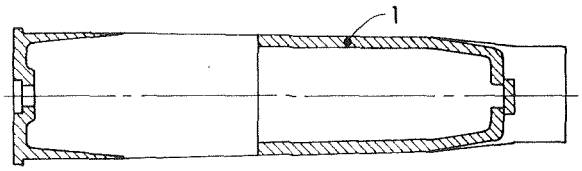

1. TiO_2/WAX WITH FLAPS (.141 kg)

Fig. 9 TiO_2/wax liner with flaps

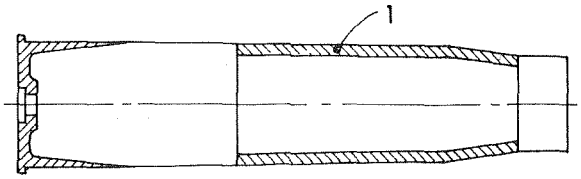

1. Ti O_2/WAX (.141 kg)

Fig. 10 TiO_2/wax liner without flaps and positioned at front of cartridge case

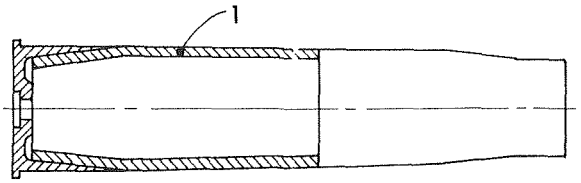

1. Ti O_2/WAX (.141 kg)

Fig. 11 TiO_2/wax liner without flaps and positioned at rear of cartridge case

The total heat in a given volume of the gun barrel is given by

$$Q = \rho C V \Delta T, \tag{1}$$

where Q = heat input into the barrel, ρ = density of gun steel, C = specific heat of gun steel, V = volume, ΔT = temperature rise of gun steel in volume element, V.

Since the temperature in the gun barrel at this time varies only with radial distance into the gun tube, the net heat input into the gun barrel is computed as follows. Equation (1) is recast in differential form as:

$$dQ = \rho C \Delta T dV. \tag{2}$$

For a unit axial length of one millimeter,

$$dQ = \rho C l \Delta T dA. \tag{3}$$

For a hollow cylinder of unit axial length,

$$dQ = \rho C 2\pi r \Delta T dr, \tag{4}$$

and

$$Q = 2\pi\rho C \int_{r_i}^{r_0} r \Delta T dr,$$

where r_i and r_0 are the inside radius and outside radius of the gun barrel, respectively, and ΔT is the temperature rise at a distance r into the tube wall. The integral in equation (5) is solved graphically by visually fitting a smooth curve through the four available values of $r\Delta T$ versus r, and then measuring the area under the curve. By placing the thermocouples around the barrel, it is inherently assumed that heat input to the barrel is radially uniform. Since the smooth curve fit to the four values of $r\Delta T$ passes through each point within the uncertainty of the temperature measurement, any error in assuming uniform radial heat input should be within the uncertainty in the temperature measurement.

The density and specific heat of gun steel (SAE 4140) are 7.85 g/cm^3 and 0.419 J/g-K [7], respectively.

Table 2 summarizes the heat inputs computed from the temperature measurements for each configuration of additive.

Discussion

As the results clearly indicate, the total heat input to the barrel is

Table 1 Example of temperature rises recorded without additive at 100 ms after propellant ignition[a,b]

Thermocouple Depth, mm	66.7cm RFT[c]	101cm RFT[c]
0.53	502 ± 0.6[d]	473 ± 0.6
1.07	454 ± 0.4	463 ± 0.5
1.55	405 ± 0.3	394 ± 0.4
2.56	331 ± 0.2	319 ± 0.2

a = Temperature rise in K. *b* = Five round replicates. *c* = Axial location of thermocouples measured from the rear face of the tube (RFT). *d* = One standard deviation from the mean.

Table 2 Heat transfer determined from 100 ms temperature measurements[a]

Additive and Configuration	66.7cm RFT	101cm RFT
No additive	426	359
Two-Piece Polyurethane Glued	372	326
Three-Piece Polyurethane	370	319
Polyurethane with Flaps	375	321
Two-Piece Polyurethane with Disk	401	342
Stack of 13 Glued Disks	425	356
TiO_2/Wax with Flaps	380	321
TiO_2/Wax Forward	396	334
TiO_2/Wax Rearward	414	346
TiO_2/Wax with Flaps (Sixth in Series with No Clean-Out Rounds)	358	298

a = Heat transfer measured in Joules/mm.

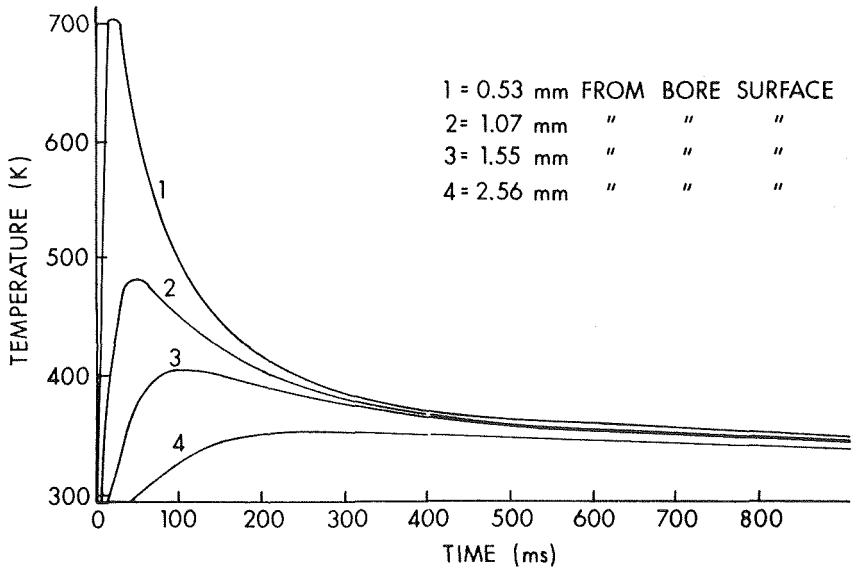

Fig. 12 Temperature versus time at 66.7 cm location in 105 mm gun tube using no additive

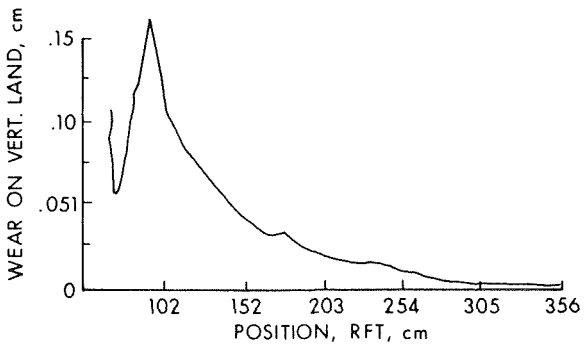

Fig. 13 Wear profile of M68 tank cannon firing M456 HEAT round with TiO_2/wax liner without flaps

reduced by the wear-reducing additives in various amounts depending on composition and configuration within the cartridge case. The addition of flaps enhances the heat transfer reduction for either polyurethane foam or TiO_2/wax which is consistent with observations made in the 37 mm firings. The major difference between the TiO_2/wax and the polyurethane foam liner is the added protection to the barrel afforded by repeated firings of TiO_2/wax (380 J/mm versus 358 J/mm after six consecutive shots). Hence, the difference between the polyurethane foam wear curve in Fig. 1 and the TiO_2/wax wear curve can be attributed to both the flaps on the TiO_2/wax liner and the insulating effect of repeated firings with TiO_2/wax. Since the heat input is smaller for sequential TiO_2/wax firings (358 J/mm) than for polyurethane foam with flaps (375 J/mm), one would conclude that TiO_2/wax with flaps is the additive of choice for tank ammunition.

No attempt was made during these tests to characterize any layer deposited on the barrel by the TiO_2/wax liner. A bore residue was removed from the M68 cannon during early trials of the TiO_2/wax additive [6]. The chemical analysis of that residue is listed in Table 3 which shows TiO_2 to be the major constituent. Russell [8] recently estimated that an insulating coating of TiO_2 as thin as 10μm could significantly reduce heat transfer to the gun barrel surface.

The down-bore temperature measurements also show that the effectiveness of the polyurethane foam diminishes rapidly in contrast to the still significant heat transfer reduction down-bore for TiO_2/wax liners with flaps fired sequentially. This, too, is consistent with the wear profile in Fig. 1 in which wear at the origin of rifling and at the secondary wear peak is reduced by TiO_2/wax liners with flaps. The

Table 3 Analysis of Bore Residue From Rounds With TiO_2/Wax Liners

Compound	Percent by Weight
TiO_2	77.4
Paraffin Wax	7.1
Silica	2.6
Organic Residue	7.7
Inorganic Residue	5.2

two rounds causing secondary wear in the field are the APDS round with polyurethane foam (Fig. 1) and the M456 HEAT round. The HEAT round has a TiO_2/wax liner without flaps as in Fig. 10. The wear profile for this round is shown in Fig. 13. The heat transfer results and the wear profile in Fig. 1 suggest that secondary wear can be mitigated by use of TiO_2/wax with flaps for all projectiles fired from the M68 tank cannon. The down-bore temperature measurements are consistent with the hypothesis [4] that the secondary wear is the result of the polyurethane foam's capability to reduce heat transfer to the gun steel diminishing rapidly away from the origin of rifling region.

A startling observation was the effect of gluing the polyurethane foam to the cartridge case wall. The glued liner was nearly twice as effective as the unglued liner. In practice the polyurethane foam liner is glued to preclude the liner from falling toward the rear of the cartridge case when the propellant is loaded into the case.

The polyurethane foam liner with a disk in place of flaps failed to reduce significantly heat transfer in comparison to the unglued, two-piece liner. This contradicts claims by the United Kingdom that the use of a disk improves the wear-reducing ability of polyurethane foam [1]. The new FH70 155 mm howitzer developed in part by the UK uses a polyurethane foam liner with disk as depicted in Fig. 7.

The results for the three-piece polyurethane foam liner suggest that lengthening the liner contributes slightly to reducing heat input. Lengthening the TiO_2/wax liner would appear to offer no benefit, since the less flammable TiO_2/wax liner placed at the rear of the cartridge case left unacceptable residue in the gun chamber in the form of unburned fragments of liner.

Since it appeared that the more additive placed near the projectile the better the erosion reduction, a test was conducted with a plug made from thirteen polyurethane foam liners glued together. No reduction in heat transfer occurred. Presumably the plug was blown through the tube without being consumed by the propellant combustion gases.

The results also show that wear-reducing additives can be designed without resorting to wear tests expending hundreds of rounds. One conclusion of these tests is that polyurethane foam with flaps would not be as effective in the M392 projectile as the TiO_2/wax liner. Assuming polyurethane foam with flaps performs significantly better than the standard polyurethane liner, well over 400 rounds need to be fired to determine where the wear curve for polyurethane foam with flaps would fall on Fig. 1 relative to TiO_2/wax with flaps.

Conclusions

1 Heat transfer in the M68 tank cannon is reduced by wear-reducing additives.

2 The reduction in heat transfer is strongly a function of the configuration and location of the additive with respect to the propellant and to the projectile. Positioning the additive near the forward end of the cartridge case is more effective in reducing the heat input to the gun tube than positioning the additive near the rearward end of the cartridge case. The use of flaps at the forward end of both types of liners increases the reduction of the heat input to the gun tube.

3 For polyurethane foam and TiO_2/wax liners, the reduction of heat transfer to the gun tube was the same on a single-shot basis if they were positioned alike.

4 The film left by sequentially firing rounds with the TiO_2/wax liner with flaps appears to be the main reason for its superiority over the two-piece, glued polyurethane liner in the M68 tank cannon.

5 A polyurethane foam disk glued to the front of the polyurethane liner is not as effective in reducing heat to the gun tube as performed flaps on the front of the polyurethane liner.

6 This heat transfer technique can be used to evaluate different designs instead of expending hundreds of rounds for each design test.

References

1 A. A. Alkidas, M. S. Summérfield, and J. R. Ward, "Survey of Wear-Reducing Additives," BRL Memorandum Report No. 2603, March 1976 (AD #B010280L).

2 T. L. Brosseau and J. R. Ward, "Reduction of Heat Transfer to Gun Barrels by Wear-Reducing Additives," ASME JOURNAL OF HEAT TRANSFER, Vol. 97, 1975, pp. 610–614.

3 M. A. Schroeder and M. Inatome, "The Relationship Between Chemical Composition and Wear-Reducing Effectiveness of Some Laminar Additives for Gun Propellants: Polyvinyltetrazole," BRL Memorandum Report No. 2512, Aug. 1975 (AD #B007029L).

4 J. R. Ward, "Proposed Mechanism for the Formation of Secondary Wear in the M68 Tank Cannon," BRL Memorandum Report No. 2557, Nov. 1975 (AD #B008040L).

5 T. L. Brosseau, "An Experimental Method for Accurately Determining the Temperature Distribution and the Heat Transferred in Gun Barrels," BRL Report No. 1740, Sept. 1974 (AD #B000171L).

6 R. O. Wolff, "Reduction of Gun Erosion, Part II. Barrel Wear-Reducing Additive," Picatinny arsenal Technical Report No. 3096, Aug. 1963.

7 R. N. Jones and S. Breitbart, "A Thermal Theory for Erosion of Guns by Powder Gases," BRL Report No. 747, Jan. 1951.

8 L. H. Russell, "Simplified Analysis of the Bore Surface Heat Transfer Reduction in Gun Barrels as Achieved by Using Wear-Reducing Additives," NSWC/DL TR-3378, Oct. 1975.

T. E. Laskaris

Rotating Machinery Unit,
General Electric Company,
Corporate Research and Development Center,
Schenectady, N. Y. 12301

Transient Thermal Analysis of Epoxy-Impregnated Superconducting Windings in Linearly Ramped Fields

Heat is generated in superconducting windings whenever the magnetic field changes. During these transient periods, the current carrying capability of the superconductor is limited by the temperature distribution inside the winding, especially in epoxy-impregnated winding composites that have limited thermal conductance. A finite-difference transient thermal analysis of a superconducting winding composite is presented. The analysis is employed to predict the critical current of a cylindrical coil and a modular racetrack winding under linear ramping of the magnetic field, when eddy current losses and hysteresis losses prevail. The dependence of these losses on the magnetic field and temperature is properly accounted for. The analytical predictions are compared to experimental data and the agreement is excellent.

Introduction

Transient thermal analysis of epoxy-impregnated windings is of considerable interest in a variety of superconducting devices, such as proton accelerator superconducting magnets and superconducting a-c generators. To achieve high-energy magnetic fields, superconducting windings are often designed to operate at high current densities consistent with the critical current density of the superconductor, thus leaving a narrow margin for transient heating.

Transient heating of the superconducting winding occurs whenever the magnetic field changes. The field winding of a superconducting generator, for example, will experience heating in response to unbalance of the three phases, when the field current changes during rotor oscillations, or when residual magnetic flux penetrates the rotor electromagnetic shield following a fault in the power system. During these transient periods, the current carrying capability of the superconductor is limited by the temperature distribution inside the winding, especially in epoxy-impregnated winding composites that have limited thermal conductance. Evidently the winding temperature at any given point must be maintained below the corresponding critical temperature of the superconductor at the point. The latter is dependent upon the local magnetic flux density and current.

Despite the widespread interest in the transient behavior of winding composites, there is relatively little applicable analysis in the literature. This is apparently due to the poor characterization of these composites or the limited availability of thermal properties at low temperature. Murphy, Walker, and Carr [1–3] have addressed the problem of superconductor losses using a continuous model of anisotropic electrical conductivities. Hust [4], and Collings, et al. [5] measured the thermal properties of a specific winding composite at low temperatures.

The purpose of the present investigation is to consider linearly ramped fields in epoxy-impregnated windings and predict the location and instant at which the temperature, current, and flux density first reach their critical values.

Superconducting Winding Composite

As part of an investigation concerning the development of epoxy-impregnated windings, a number of cylindrical coils and racetrack windings were constructed and tested by the author's company [6]. These windings have consistently attained the critical current predicted by testing a short sample of superconductor when the current was ramped slowly.

The winding modules were wound of copper-stabilized niobium-titanium multifilamentary superconductor, arranged in several layers of approximately equal numbers of turns per layer. Around each layer of the winding, a complete turn of glass woven fabric is applied as interlayer insulation. The winding section is then impregnated with epoxy by a controlled vacuum process, to prevent the formation of voids in the winding composite. Fig. 1 illustrates the cross-sectional view of a cylindrical coil and a racetrack winding module that were wound with the same rectangular *NbTi* superconductor. The specification of this superconductor is summarized in Table 1.

The logitudinal and trasverse thermal conductivities of similar

Contributed by the Heat Transfer Division of THE AMERICAN SOCIETY OF MECHANICAL ENGINEERS and presented at the AIChE-ASME Heat Transfer Conference, Salt Lake City, Utah, August 15–17, 1977. Revised Manuscript received by the Heat Transfer Division January 20, 1978. Paper No. 77-HT-77.

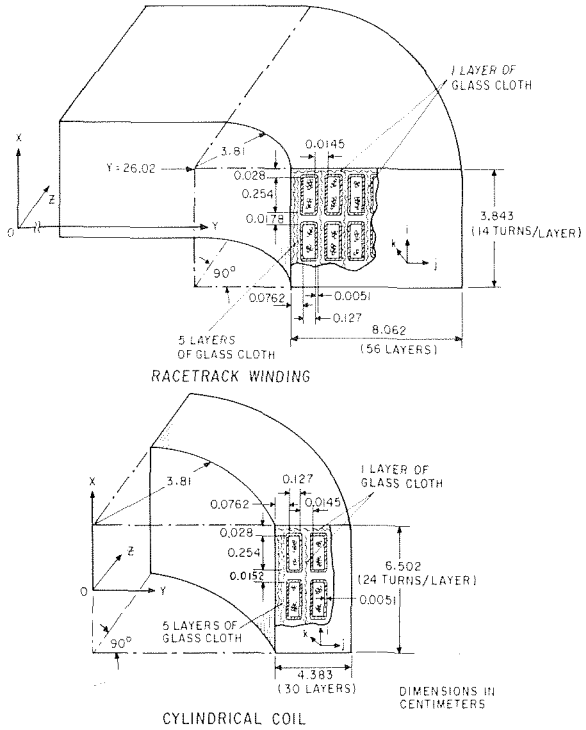

Fig. 1 Geometry of cylindrical coil and racetrack winding

Table 1 Niobium-Titanium superconductor specifications

Characteristic	Specification
Stabilizer matrix to superconductor ratio	1.6/1
Filament 360 deg twist pitch (cm)	1.5
Number of filaments	1531
Cross section	
—shape	Rectangular
—width (cm)	0.254
—height (cm)	0.127
Stabilizer matrix	
—material	Copper
—resistivity ratio at zero field	160
—low temperature resistivity*, ρ, (ohm-cm) versus flux density, B, (Telsa)	$\rho = (0.9 + 0.421\ B) 10^{-8}$, $1 \leqq B \leqq 7$
Superconductor filament average diameter (cm)	0.0034
Wire insulation	
—material	Polyvinyl formal
—thickness (cm)	0.00508
Critical current**, I_0, (A) at 4.22 K versus flux denisty, B, (Telsa)	$I_0 = 1.30952\ B^2 - 302.262\ B + 2983.57$, $4 \leqq B \leqq 7$
Critical flux density***, B_0, (Tesla) at zero current versus temperature, T, (K)	$B_0 = -0.103715\ T^2 - 0.740336\ T + 15.3147$, $4.22 \leqq T \leqq 8$

* Linear approximation of Kohler plot [9] (error <1 percent)
** Curve fitting to measured data by superconductor manufacturer (error <1 percent)
*** Curve fitting to data by Hampshire, et al. [10]

epoxy-impregnated winding composites were measured by Hust [4]. The measured data reported agree reasonably well with the values calculated on the basis of the component conductivities of the composite.

Consider the local coordinate system i, j, k of Fig. 1. According to Hust [4], the thermal conductivity of the composite parallel to the j-axis can be evaluated by considering two parallel segments of the composite. The first is the epoxy-polyvinyl-formal strip parallel to the j-axis, and the second comprises the wires and epoxy-polyvinyl-formal strips (perpendicular to the j-axis) arranged in series with the heat flow in that direction.

The conductivity of the composite parallel to the j-axis is then obtained by summing the effective conductivities of the parallel segments, weighted by their respective relative areas:

$$K_j = \left[t_{ej} K_{ep} + t_{wj} \frac{(t_{ei} + t_{wi})}{\left(\frac{t_{ei}}{K_{ep}} + \frac{t_{wi}}{K_w}\right)} \right] \frac{1}{(t_{ej} + t_{wj})} \tag{1}$$

The logitudinal thermal conductivity is obtained by summing the area-weighted conductivities of *Cu, NbTi,* and epoxy-polyvinyl-formal.

In the temperature region of interest (4.2 –7.5 K), the thermal conductivity of the epoxy-polyvinyl-formal insulation is considered approximately constant. An estimated value, $K_{ep} = 0.0003$ W/cm-K, of the thermal conductivity of the epoxy-polyvinyl-formal was obtained from Childs, et al. [7], using polyvinyl acetate in place of polyvinyl formal. The same value of thermal conductivity is also used for the sidelong boundary layers of insulation, since these layers contain a negligible amount of glass reinforcement. The inner and outer boundary layers of insulation, however, are reinforced with sufficient glass-woven fabric to yield a higher value of thermal conductivity, $K_{eg} = 0.00085$ W/cm-K, according to measurements by Hertz and Haskins [8]. Because of the insufficient characterization of the wire cross section (such as the configuration of filments in the matrix), a rough estimate is made [4] of the transverse conductivity of the Cu/NbTi wire; namely, $K_w = 0.1$ W/cm-K.

The calculated thermal conductivities of the winding composites

Nomenclature

A_{sc} = area of superconductor
$B, \dot{B}$ = magnetic flux density, and flux density rate of change
C_p = specific heat
d = superconductor filament diameter
h = convective-pool-boiling heat transfer coefficient
$I, \dot{I}$ = current, and current ramping rate
J_c = critical current density of superconductor
K_{ep} = thermal conductivity of epoxy-polyvinyl-formal
K_j = thermal conductivity of composite parallel to j-axis
K_{eg} = thermal conductivity of epoxy-glass
K_w = transverse thermal conductivity of wire
ℓ = 360 deg twist pitch of superconductor filaments
L = element circumference at point $P_{i,j}$ (Fig. 3)
L_1 = element circumference at midpoint of line $P_{i-1,j}, P_{i,j}$ (Fig. 3)
L_2 = element circumference at midpoint of line $P_{i+1,j}, P_{i,j}$ (Fig. 3)
P_e, P_h = eddy current and hysteresis losses per unit volume of wire
R = radius at point $P_{i,j}$
s = volume fraction of bare wires in composite
$T_{i,j}{}^n, T_f$ = temperature of point $P_{i,j}$ at time $n\Delta t$, and surrounding fluid
t_{ej}, t_{wj} = thickness of epoxy-polyvinyl-formal, and wire along j-axis
t = time
U_x, U_y = overall heat transfer coefficients to liquid helium
λ = volume fraction of superconductor in wire
ρ = density of composite
ρ_{Cu} = electrical resistivity of copper matrix

of Fig. 1 are tabulated in Table 2. The results indicate that the longitudinal thermal conductivity of the winding composite is more than 300 times larger than the transverse thermal conductivities. Further, the variation of the superconductor losses of the racetrack winding in the circumferential direction, typically, does not exceed 25 percent of the average value. Consequently, a two-dimensional heat transfer model of the racetrack winding would be sufficient to predict the performance of the winding under transient heating.

Collings and Jelinek [5] have performed an experimental investigation of the low-temperature specific heat of an epoxy-impregnated superconducting composite, similar in composition to the winding composites of Fig. 1. The experimental data [5] are used in the form of the expression

$$\rho C_p(T) = 5.5\ 10^{-5}\ T^{2.7} \quad \text{J/cm}^3\text{-K} \tag{2}$$

where T is the kelvin (K). Equation (2) is valid in the temperature range 4.2 to 8 K.

Superconductor Losses

Losses are generated in the superconductor as a result of exposure to a changing magnetic field environment. Two types of losses are generally encountered in multifilamentary superconductors: eddy current losses, and hysteresis losses.

Consider a rectangular multifilamentary superconductor. The eddy current losses produced by ramped magnetic fields or low-frequency alternating fields can be calculated by means of a continuum model of the conductor with anisotropic electrical conductivities [1, 2, 3]. For the case of a linearly ramped transverse magnetic field, $\dot{B}$, the eddy current losses per unit volume are approximated by the relation that applies to cylindrical conductors:

$$P_e = \frac{1-\lambda}{1+\lambda}\frac{1}{\rho_{Cu}(B)}\left(\frac{\ell\dot{B}}{2\pi}\right)^2 \tag{3}$$

The resistivity of copper, $\rho_{Cu}(B)$, at low temperature [9] is expressed in Table 1 as a linear function of the local magnetic flux density, B.

The full penetration, filamentary hysteresis losses per unit volume during field ramping from B_1 to B_2 in time Δt, are evaluated on the basis that the filaments are carrying the transport current. It follows that

$$P_h = \frac{\lambda d}{2\Delta t}\left|\int_{B_1}^{B_2} J_c(B, T)dB\right| \tag{4}$$

The critical current density $J_c(B, T)$ of the superconductor filaments can be expressed as a function of the magnetic flux density, B, and the temperature, T. At any given temperature, T, the critical flux density $B_0(T)$, at which the critical current is zero, was derived by Hampshire, et al. [10] for a NbTi superconductor. Since J_c varies linearly with temperature over the useful range of flux densities [10], the critical current density is approximately determined at any flux density and temperature using the experimental function $I_0(B)$ at 4.2 K in conjunction with the function $B_0(T)$. It follows that

$$J_c(B, T) = I_0(B + B_0(4.2) - B_0(T))\frac{1}{A_{sc}} \tag{5}$$

The functions $B_0(T)$ and $I_0(B)$ are given in Table 1.

It is evident from equations (3–5) that the superconductor losses depend strongly upon the rate of change as well as the magnitude of the magnetic field. Therefore, the three-dimensional magnetic flux density vector must be computed in the space of the winding. The computation of the field at a given point in space can be performed by subdividing the winding into a number of straight wire segments. The Biot-Savart law can then be employed to compute the ontribution of each wire segment to the magnetic flux density vector. The vectorial sum of all such contributions from the wire segments in the winding yields the flux density vector at the point under condiseration.

Fig. 2 displays the computed flux density, B_x, on the plane of symmetry of the windings, perpendicular to the pole axis ($x = 0$). The field of both windings is evaluated at the critical current of the superconductor, $I_c = 942\ A$ at 7 Tesla and 4.22 K. In this particular case, both windings have the same peak field at the inner radius.

Finite Difference Formulation

The winding module is subdivided into elements, of similar shape and rectangular cross section, to form a regular network. The intersections of networks, called nodal points, are identified by two subscripts, say i and j, to indicate the row and column of the point. Fig. 3 is a schematic diagram of the element subdivisions that illustrates the control volume about typical and boundary nodal points. The temperature of the point $B_{i,j}$ at time $n\Delta t$ is represented by $T_{i,j}^n$.

The first law of thermodynamics is applied to the control volume about a nodal point, say $B_{i,j}$, and Fourier's law of heat conduction is employed to relate the heat fluxes to the nodal temperatures. The finite difference equation of the nodal point $B_{i,j}$ follows:

Table 2 Computed thermal conductivities of winding composite*

Winding Composite	Racetrack Winding	Cylindrical Coil
Transverse conductivity K_i, (W/cm-K)	0.00398	0.00413
Transverse conductivity K_j, (W/cm-K)	0.00269	0.00269
Longitudinal conductivity K_k, (W/cm-K)	1.497	1.511

* Values are applicable to temperatures from 4.2 K to 7.5 K.

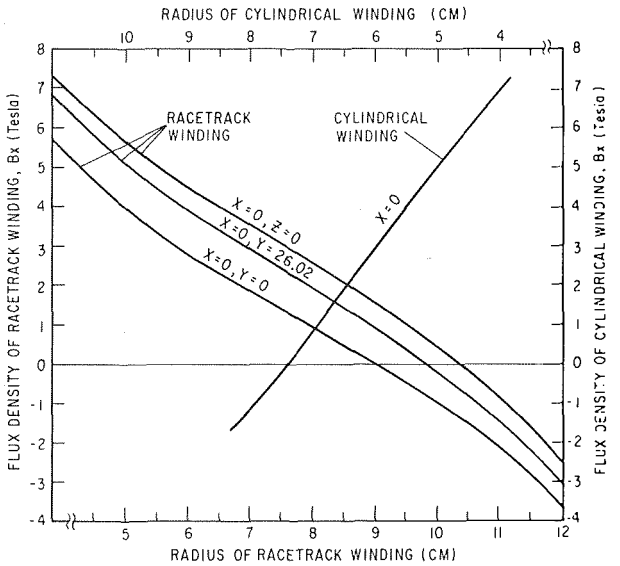

Fig. 2 Flux density of cylindrical coil and racetrack winding at current of 942 A

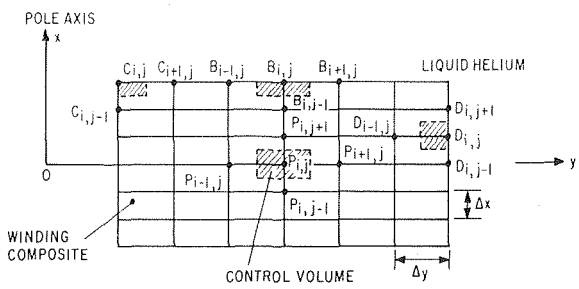

Fig. 3 Finite difference schematic

$$T_{i,j}^{n} = \left\{ K_y \frac{\Delta x}{2\Delta y} L_1 T_{i-1,j}^{n} + K_y \frac{\Delta x}{2\Delta y} L_2 T_{i+1,j}^{n} + K_x \frac{\Delta y}{\Delta x} L\, T_{i,j-1}^{n} + U_x T_f \Delta y\, L + \left[\frac{1-\lambda}{1+\lambda} \frac{1}{\rho_{Cu}(n\dot{B}\Delta t)} \left(\frac{\dot{B}\ell}{2\pi}\right)^2 + \frac{\lambda d}{2\Delta t} \left| \int_{(n-1)\dot{B}\Delta t}^{n\dot{B}\Delta t} J_c(B, T_{i,j}^{n}) dB \right| \right] \times \frac{\Delta x \Delta y}{2} Ls + \rho C_p \left(T_{i,j}^{n-1}\right) \frac{\Delta x \Delta y}{2\Delta t} L T_{i,j}^{n-1} \right\} \left[\rho C_p \left(T_{i,j}^{n-1}\right) \frac{\Delta x \Delta y}{2\Delta t} L + U_x \Delta y L + K_y \frac{\Delta x}{2\Delta y} \times (L_1 + L_2) + K_x \frac{\Delta y}{\Delta x} L \right]^{-1} \quad (6)$$

The finite difference equations of the inner points, $P_{i,j}$, and boundary points, $D_{i,j}$ or $C_{i,j}$, are derived in a straightforward manner.

To avoid problems of numerical instability associated with explicit formulations of the finite difference equations, the derivation of equation (6) was carried out using backward differences in time. The resulting implicit difference equations are known to be unconditionally stable.

When the windings are tested, they are fully immersed in liquid helium. Thus, the overall heat transfer coefficients U_x, U_y depend on the convective-pool-boiling heat transfer coefficient, h, in liquid helium, and the corresponding thicknesses t_x, t_y of the external layers of insulation, namely

$$\frac{1}{U_x} = \frac{1}{h} + \frac{t_x}{K_{ep}}, \frac{1}{U_y} = \frac{1}{h} + \frac{t_y}{K_{eg}} \quad (7)$$

Since the heat transfer coefficient, h, is many orders of magnitude larger than the conductance of the insulation layer, the heat transfer coefficients U_x and U_y depend primarily on the insulation thicknesses t_x and t_y, respectively. Typical values of U_x, U_y for the winding composites of Fig. 1 are 0.0105 W/cm-K and 0.0109 W/cm-K, respectively.

The finite difference equations involve the computation of the rate of change of flux density, $\dot{B}$, at each nodal point of the two-dimensional heat transfer model of the winding. In the case of the cylindrical coil, one needs to evaluate $\dot{B}$ at all the nodal points of only one arbitrarily chosen cross section, because of the rotational symmetry. The circumferential field distribution of the racetrack winding, however, requires averaging at each nodal point. The field is computed for that purpose at three cross sections of the winding. The first is at the winding centroid and perpendicular to the y-axis; the second is at the end of the straight section and perpendicular to the y-axis; the third is at the end winding, and coplanar with the x-axis and the y-axis.

At each time step, Δt, the system of simultaneous finite difference equations is solved for the nodal temperatures by employing a matrix inversion technique.

Linearly Ramped Field

The thermal transient to be studied comprises ramping of the magnetic field, linearly. The windings are initially at a uniform temperature of 4.2 K. The superconductor losses are then imposed stepwise at time zero, and vary thereafter according to the local flux density and temperature. As the temperature distribution of the winding is changing with time, its current and corresponding flux density distribution are also increasing monotonically with time. At lower magnetic fields, both the eddy current losses and hysteresis losses are higher, because the magnetoresistance of copper at low temperatures is directly proportional to the flux density, and the critical current of the superconductor is higher. Consequently, the superconductor losses are decreasing with time.

Physically, there is an instant when the critical current, temperature, and magnetic flux density are reached at a specific point within the winding. At that point and instant, the superconductor reverts to its normal state.

The specific objective of the present investigation is to predict the location and instant at which the temperature, current, and flux density first reach their critical values. It is evident that the point where transition first occurs will always lie on the y-axis of the windings, since both the flux density and the temperature attain their maximum values on the y-axis.

Fig. 4 depicts the transient temperature profiles in the y-axis of the cylindrical coil for several ramping rates. The temperature profile initially increases with time, reaches a peak, and subsequently decreases. The initial increase is the typical response to suddenly applied internal heat generation. By virtue of the decreasing superconductor losses, shown in Fig. 4, the temperature profile is expected to attain a peak and then decrease.

The superconductor losses and the transient temperature profiles in the y-axis of the racetrack windings are plotted in Fig. 5 for current ramping rates of 31.4 A/sec, and 62.8 A/sec. As before, the temperature profile increases rapidly with time, to reach its peak in about three seconds, and then decreases slowly as the superconductor losses decrease. As a result of this temperature variation with time, it is anticipated that for sufficiently high field ramping rates, the critical temperature of the composite will be reached in less than about 3 seconds; that is, before the peak temperature profile is reached. Conversely, for sufficiently low field ramping rates, the winding will reach the critical temperature in more than about 3 seconds; that is, after the temperature profile peaks.

The fractional ramping rates, $\dot{I}$, of Figs. 4 and 5 were chosen to be close to the experimental values for direct comparison.

The superconductor characteristic curves $I_c(B, T)$ are plotted in Fig. 6 for several temperatures from 4.22 K to 7.4 K. The family of short-sample characteristic curves is constructed from the manufacturer's measured values of I_c versus B at 4.22 K in conjunction with the experimental data of Hampshire, et al. [10]. Equation (5) is not used in the process, because it is valid in a narrow domain.

The family of curves of current versus magnetic flux density (load lines) are presented in Fig. 6 for several nodal points along the y-axis of the windings. The temperature at these points is taken from Figs. 4 and 5, and the temperature profile at a given instant is plotted in Fig. 6 versus the load line coordinates. The temperature scale used is the one of the superconductor critical temperature, T_c, as indicated on the characteristic curves of Fig. 6. Clearly, the temperature profile plotted in this manner defines the critical current of the points in the y-axis at that instant. The point of minimum cirtical current is the location at which normal transition occurs at the instant when the charging current coincides with the minimum critical current. Since that instant is not known in advance, the temperature profile in the y-axis must be plotted in Fig. 6 at several time intervals, to determine the minimum critical current versus time and compare it with the charging current.

The temperature profiles of Fig. 6 are drawn at the instant when the charging current coincides with the minimum critical current. The point of minimum current is then identified as the point of normal transition. The y-coordinate of that point is found by interpolation between the y-coordinates of the adjacent load lines. It should be emphasized that the peak temperatures of Fig. 5 do not necessarily correspond to the minimum current values of Fig. 6.

As might be anticipated, the critical current at low current ramping rates is reached at the inner surface of the winding, where the magnetic field peaks. At higher current ramping rates, however, the incipience of normal transition occurs at points within the winding composite.

The computed values of critical current versus the current ramping rate are compared in Fig. 7 to the experimental data [6], and the agreement is excellent.

Fig. 6 shows that, at low ramping rates, the points of normal transition of the racetrack winding are close but not identical to the corresponding points of the cylindrical coil.

The experimental data of Fig. 7 were obtained by applying a constant voltage across the winding terminals and allowing the current to increase linearly. The maximum current that is attained in the linear portion of the curve of current versus time defines the critical current of the winding. Fig. 8 illustrates typical curves of current versus time that were obtained by testing the racetrack winding. The

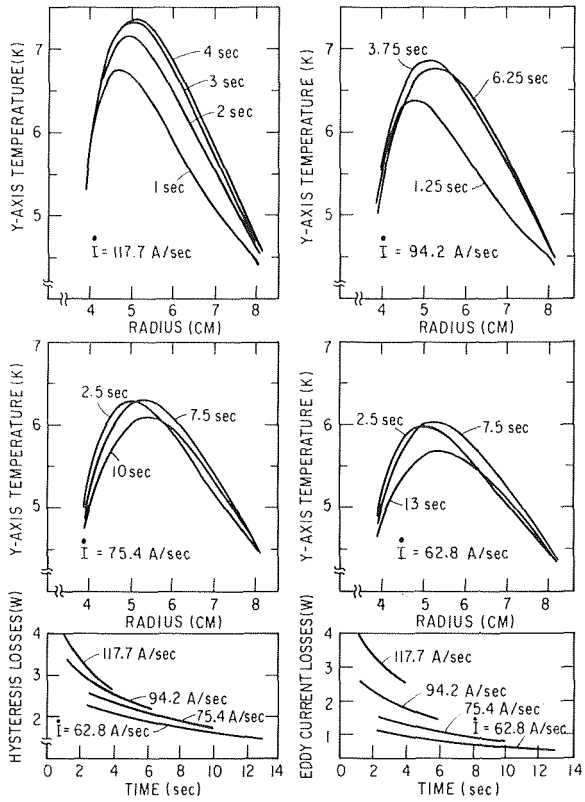

Fig. 4 Transient temperature profiles and superconductor losses of cylindrical coil

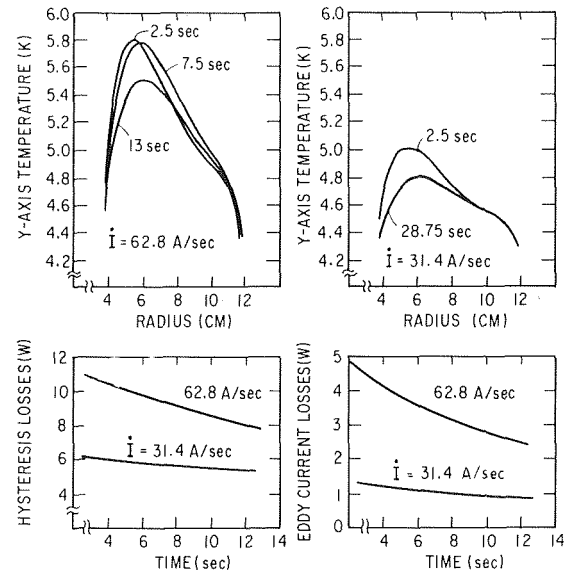

Fig. 5 Transient temperature profiles and superconductor losses of racetrack winding

transition current shown in Fig. 8 was obtained by a digital voltmeter that was connected across a 0.00005 ohm shunt. The test data were repeated with error that is generally less than 0.005. The measured self-inductance of the racetrack winding is 0.32 H.

Concluding Remarks

A finite-difference transient thermal analysis of a superconducting winding composite is presented. The analysis is employed to predict the critical currents of a cylindrical coil and a modular racetrack

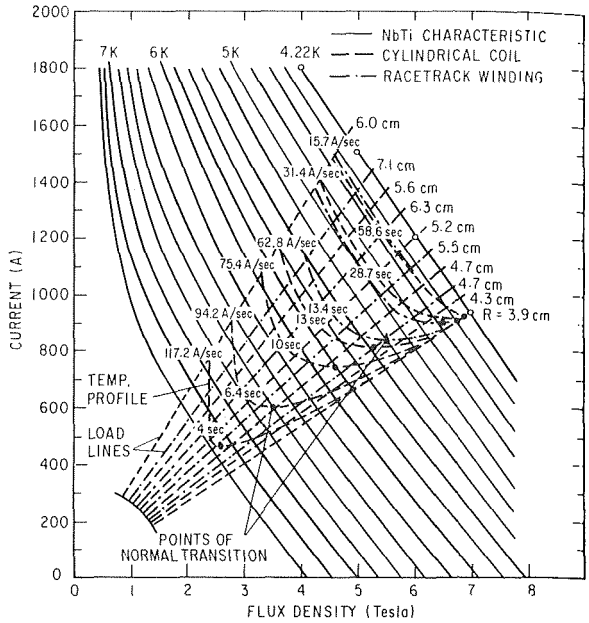

Fig. 6 Winding normal transition characteristics during field ramping

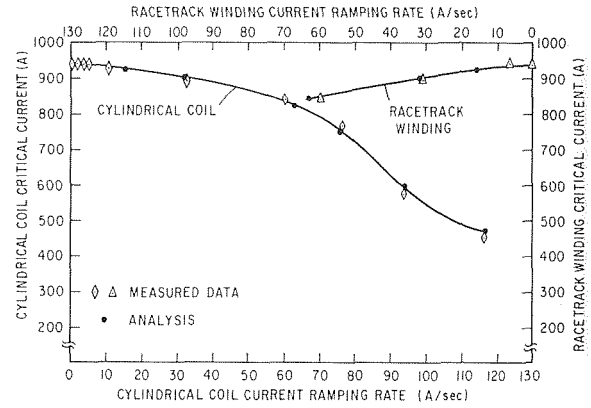

Fig. 7 Critical current of windings versus current ramping rate

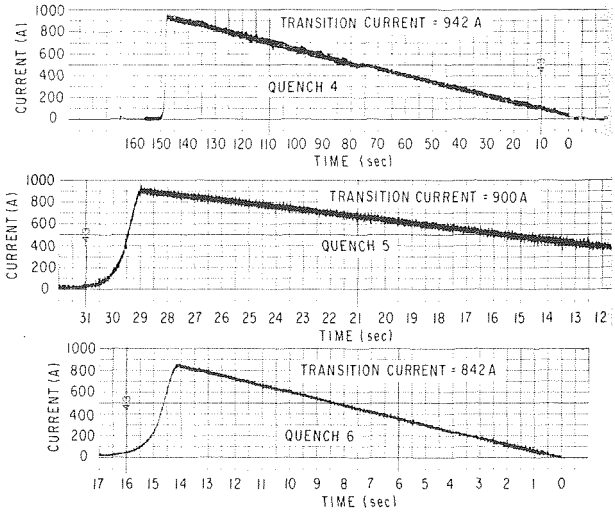

Fig. 8 Current ramping and transient decay of racetrack winding (winding self-inductance is 0.32 *H*)

winding under linear ramping of the magnetic field, when eddy current losses and hysteresis losses prevail. The dependence of these losses on the magnetic field and temperature is properly accounted for. The analytical predictions are in excellent agreement with the experimental data.

The present method of analysis permits a prediction of the safety margin that exists between the operating current of an epoxy-impregnated, superconducting winding and the critical current, when transient heating of the winding occurs as a result of ramping or low-frequency oscillations of the magnetic field. Thus, the superconducting winding can be designed to operate safely at the highest allowable field and current density consistent with the transient magnetic field requirements.

References

1 Carr, W. J., Jr., Walker, M. S., and Murphy, J. H., "Alternating Field Loss in a Multifilament Superconducting Wire for Weak A C Fields Superposed on a Constant Bias," *Journal of Applied Physics,* Vol. 46, No. 9, 1975, pp. 4048–4052.

2 Walker, M. S., Murphy, J. H., and Carr, W. J., Jr., "Alternating Field Losses in Mixed Matrix Multifilament Superconductors," *IEEE Transactions on Magnetics,* Vol. MAG-11, No. 2, 1975, pp. 309–312.

3 Murphy, J. H., Walker, M. S., and Carr, W. J., Jr., "Alternating Field Losses in a Rectangular Multifilamentary NbTi Superconductor," *IEEE Transactions on Magnetics,* Vol. MAG-11, No. 2, 1975, pp. 313–316.

4 Hust, J. G., "Low Temperature Thermal Conductivity Measurements on Longitudinal and Transverse Sections of a Superconducting Coil," *Cryogenics,* Jan. 1975, pp. 8–11.

5 Collings, E. W. and Jelinek, F. J., "Low Temperature Thermal Expansion and Specific Heat Properties of Structural Materials," *NBS-ARPA Materials Research for Superconducting Machinery III,* Semiannual Technical Report, April 1975.

6 Jefferies, M. J., and Laskaris, E. T., "Rotor Winding Development for a 20-MVA Superconducting A-C Generator," *Proceedings of Conference on Technical Applications of Superconductivity,* Alushta, U.S.S.R., September 16–19, 1975.

7 Childs, G. E., Ericks, L. J., and Powell, R. L., "Thermal Conductivity of Solids at Room Temperature and Below," *NBS Monograph 131,* pp. 533–543.

8 Hertz, J. and Haskins, J. F., "Thermal Conductivity of Reinforced Plastics at Cryogenic Temperatures," *Advances in Cryogenic Engineering,* Vol. 10, Plenum Press, New York, 1964, pp. 163–170.

9 Benz, M. G., "Magnetoresistance of Copper at 4.2 K in Transverse Fields up to 100 KG," *Journal of Applied Physics,* Vol. 40, No. 5, 1969, pp. 2003–2005.

10 Hampshire, R. G., Sutton, J., and Taylor, M. T., "Effect of Temperature on the Critical Current Density of Nb-44%Ti Alloy," *Proceedings of Conference on Low Temperatures and Electric Power,* March 24–26, 1969, pp. 251–257.

A. Bejan

Assistant Professor.
Department of Mechanical Engineering,
University of Colorado, Boulder, Colorado 80309

Two Thermodynamic Optima in the Design of Sensible Heat Units for Energy Storage

The paper presents a treatment of sensible heat energy storage units as systems intended to store useful work. An analysis of the thermodynamic irreversibilities associated with storing energy from a hot gas source as sensible heat in huge liquid baths points out two important trade-offs: 1. There exists an optimum, well-defined quantity of hot gas to be used in order to maximize the useful work stored in the liquid bath. Using more than this optimum quantity in the hope of maximizing the amount of thermal energy stored as sensible heat leads to severe thermodynamics losses. 2. There exists an optimum relationship among the gas-liquid heat exchanger design parameters which minimizes the system irreversibility while maximizing its capability of storing useful work. This relationship provides a procedure for estimating the heat exchanger optimum number of transfer units (N_{tu}). Increasing the N_{tu} above the optimum in order to upgrade the heat exchanger effectiveness and the thermal energy storage capability leads to prohibitive losses due to fluid friction in the heat exchanger channels. The existence of the two optima demonstrates that designing sensible heat units for maximum thermal energy storage does not necessarily amount to thermodynamically optimizing such systems.

Introduction

Storing energy efficiently is an important contemporary problem. Efficient storage systems for thermal energy are needed in a wide variety of applications. In general, it is advantageous and often possible to store the heat rejected by one thermodynamic process and use it later as part of the energy input for the same process or an entirely different one. As shown in [1], thermal energy storage units can be used in peak power shaving operations: electric power companies are eager for efficient methods to store the power generated during slack periods to ease the strain on heavy demand periods.

Of the many possible ways of storing energy for later use, energy storage in the form of sensible heat is attractive from economic considerations. For peak power shaving applications in particular, heating large tanks of water or oil and recovering the thermal energy to generate electricity during maximum demand periods seems the most attractive alternative [1].

Traditionally, the thermal design and optimization of a sensible heat storage unit and the associated heat exchanger relies on the view that the system thermal performance can be assessed in terms of how much thermal energy the unit can store. In short, a unit is considered more effective than another if—for the same heat input and the same amount of storage material—it is capable of storing more thermal energy. For example, this point of view served as basis for a recent proposal for testing the thermal performance of sensible heat (fluid & solid) storage units [2].

The objective of this article is to analyze the performance of sensible heat storage units by treating them as systems designed to store *useful* work, the function they perform in most applications. The paper develops the thermal design and optimization of a fluid sensible heat storage unit and its related heat exchanger based on minimizing the waste of useful work (irreversibility, entropy generation) present in the unit during the storage process. As a prelude to the conclusions reached in this study it is shown that, depending on the circumstances, storing the maximum possible amount of thermal energy may come in direct conflict with the real task of maximizing the storage of useful work.

It is important to recognize that there exists a great variety of considerations which must be accounted for in the design of a "good" storage system. Most of these considerations are either thermodynamic or economic in nature. The present work addresses only the thermodynamic side of the design philosophy. We attempt in this paper to clarify the importance of not disregarding the irreversibility (second law) aspect associated with the basic storage process.

Contributed by the Heat Transfer Division for publication in the JOURNAL OF HEAT TRANSFER. Manuscript received by the Heat Transfer Division October 28, 1977.

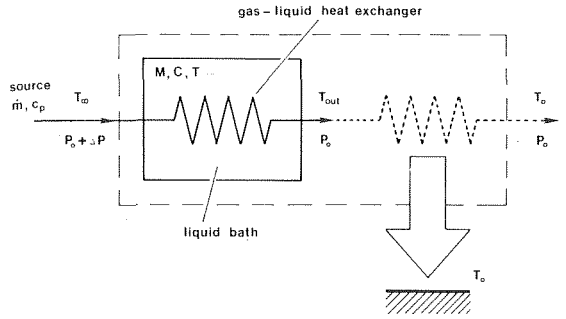

Fig. 1 Schematic of hot gas-liquid bath system for energy storage as sensible heat

For the sake of clarity in illustrating the concepts of useful work and irreversibility, we will employ as working example a very simple class of sensible heat systems used for energy storage. The basic element is presented in detail in the next section.

Element for Sensible Heat Storage in Liquid Pools

Consider the storage system shown schematically on Fig. 1. It consists of a large liquid bath of mass M and specific heat C placed in an insulated vessel. Hot gas enters the system through one port, is cooled by flowing through a heat exchanger immersed in the bath and is eventually discharged into the atmosphere. Gradually, the bath temperature T as well as the gas outlet temperature T_{out} rise, approaching the hot gas inlet temperature T_∞.

The bath is filled with an incompressible liquid such as water or oil. The stream $\dot{m}$ carries an ideal gas, for example high temperature steam or air.

It is assumed that initially the bath temperature equals the environment temperature T_0. The stream of hot gas $\dot{m}$ is supplied continuously at T_∞, P_0 by an energy source or the exhaust from another thermodynamic process. The pressure of the hot gas supply must be raised slightly above atmospheric, $P_0 + \Delta P$, so that the gas stream can overcome the pressure drop caused by friction in the heat exchanger.

The time dependence of the bath temperature and the gas outlet temperature during the storage process can be derived analytically. The final result is available in the engineering literature and can be written as [3]

$$\frac{T - T_0}{T_\infty - T_0} = 1 - e^{-\theta y} \tag{1}$$

$$\frac{T_{out} - T_0}{T_\infty - T_0} = 1 - ye^{-\theta y} \tag{2}$$

where θ represents dimensionless time or the amount of hot gas used from the source until time t,

$$\theta = \frac{\dot{m}c_p t}{MC}, \tag{3}$$

and y is a parameter characterizing the gas-liquid heat exchanger,

$$y = 1 - e^{-N_{tu}}. \tag{4}$$

The number of transfer units N_{tu} appearing in equation (4) is defined as

$$N_{tu} = \frac{UA}{\dot{m}c_p}, \tag{5}$$

where A is the total heat transfer area on the gas side and U is the overall heat transfer coefficient based on A.

In addition to the system features mentioned in the beginning of this section, the following simplifying assumptions were needed for deriving equations (1) and (2). It was assumed that: c_p and C are constant, there is no condensation or vaporization during the process, the liquid bath is well mixed (isothermal), the overall heat transfer coefficient U is constant and, finally, the heat capacity of the gas instantly trapped in the heat exchanger is much smaller than the bath heat capacity MC.

Upon examining expression (1), we see that the ability to store thermal energy in the system of Fig. 1, $T - T_0$, simply increases with increasing the charging time θ and/or the number of transfer units N_{tu}. It will be shown in what follows that, from the point of view of maximizing the storage of useful work, there exist two very important thermodynamic trade-offs (optima):

- an optimum charging time θ_{opt}, beyond which the loss of useful work associated with steadily discharging the T_{out} gas into the atmosphere becomes dominant.
- an optimum number of transfer units $N_{tu,opt}$, above which the loss of useful work due to friction ΔP in the gas-liquid heat exchanger becomes dominant.

Dissipation of Useful Work during the Energy Storage Process

The energy storage process illustrated in Fig. 1 has three inherently lossy (irreversible) features. First, the heat transfer between the hot gas and the liquid bath always takes place across a finite ΔT. Second, the gas stream discharged into the atmosphere is eventually cooled down to T_0, again by heat transfer across a finite ΔT. Third, the gas flow requires a net ΔP across the heat exchanger to overcome friction.

The combined effect of all three irreversibilities makes up a basic characteristic of all sensible heat storage systems, namely, only a fraction of the total useful work carried by the supply stream is eventually stored in the storage element. The remaining fraction is dissipated (wasted) through the thermodynamic irreversibilities present in the system.

Nomenclature

A = heat transfer area, gas side
c_p = specific heat at constant pressure
C = specific heat of liquid bath
f = friction factor
G = mass velocity
I = irreversibility, dissipated useful work, (J)
$\dot{I}$ = irreversibility rate, dissipated useful mechanical power, (W)
L = flow length
$\dot{m}$ = mass flow rate
M = mass of liquid bath
N_{Re} = Reynolds number
N_{St} = Stanton number
N_{tu} = number of transfer units
P_0 = atmospheric pressure, absolute
ΔP = pressure drop
r_h = hydraulic radius
R = ideal gas constant
s = specific entropy
S = entropy production, (J/K)
$\dot{S}$ = rate of entropy production, (W/K)
t = time
T = liquid bath temperature, absolute
T_0 = environment temperature, absolute
T_{out} = gas outlet temperature, absolute
T_∞ = gas inlet temperature, absolute
ΔT = temperature difference
u = specific internal energy
U = overall heat transfer coefficient
v = specific volume
W_{max} = maximum useful work
y = heat exchanger parameter, equation (4)
θ = charging time, spent quantity of hot gas
ρ = gas density
τ = temperature difference, equation (9)
ϕ = specific availability

Subscripts

min = minimum
opt = optimum

Quantitatively, the instantaneous rate of useful work dissipation or irreversibility rate $\dot{I}$ equals the system rate of entropy generation $\dot{S}$ times the environment absolute temperature [4],

$$\dot{I} = \dot{S}T_0. \tag{6}$$

Performing a second law analysis, the net rate of entropy production in the system surrounded by a dashed line on Fig. 1 is

$$\dot{S} = \dot{m}c_p \ln\frac{T_0}{T_\infty} + \dot{m}R \ln\left(1 + \frac{\Delta P}{P_0}\right) + \frac{d}{dt}\left(MC \ln\frac{T}{T_0}\right) + \frac{1}{T_0}\dot{m}c_p(T_{\text{out}} - T_0) \tag{7}$$

where the first two terms represent the entropy change experienced by the ideal gas stream from inlet to outlet, the third term stands for the time rate of change of the liquid bath entropy, and the last term accounts for the entropy flux by heat transfer to the environment at temperature T_0.

The total entropy generated from the beginning of the charging process until some instant t is obtained by integrating expression (7) in time from zero to t. Writing $S = \int_0^t \dot{S}\,dt$ and using equations (1) and (2) we obtain

$$\frac{S}{\dot{m}c_p t} = \frac{R}{c_p}\ln\left(1 + \frac{\Delta P}{P_0}\right) + \tau - \ln(1+\tau) + \frac{1}{\theta}\{\ln[1 + \tau(1 - e^{-y\theta})] - \tau(1 - e^{-y\theta})\} \tag{8}$$

where τ is a dimensionless way of expressing the characteristic temperature difference of the problem,

$$\tau = \frac{T_\infty - T_0}{T_0}. \tag{9}$$

Expression (8) shows that the losses accumulated from time zero to t depend on three factors, the temperature difference (τ), the duration of the energy storage process (θ) and the heat exchanger design (y and $\Delta P/P_0$). The product $\dot{m}t$ used in normalizing expression (8) is the total amount of hot gas used from time zero to t. One can easily combine equations (8) and (6) to estimate the useful work dissipated during this time interval, i.e., $I = ST_0$.

We can now compare the dissipated (wasted) fraction ST_0 with the maximum useful work $W_{\max}$ contained by the hot gas used from time zero to t. To calculate $W_{\max}$ we imagine that the mass of hot gas $\dot{m}t$ is processed by one or a succession of reversible devices until its temperature T_∞ is lowered to the environment temperature level T_0. The maximum work produced in this manner equals the drop in gas availability [5]

$$W_{\max} = \dot{m}t(\phi_\infty - \phi_0) \tag{10}$$

where $\phi = u + P_0 v - T_0 s$ is the specific availability relative to the (P_0, T_0) environment. Properties u, v and s are defined in the nomenclature. The net result is

$$W_{\max} = \dot{m}tc_pT_0[\tau - \ln(1+\tau)] \tag{11}$$

Combining equations (11) and (8) we arrive at an expression for the relative fraction of useful work dissipated during the storage process

$$\frac{I}{W_{\max}} = \left(\frac{R}{c_p}\right)\frac{\ln(1 + \Delta P/P_0)}{\tau - \ln(1+\tau)} + 1 - \frac{\tau(1 - e^{-y\theta}) - \ln[1 + \tau(1 - e^{-y\theta})]}{\theta[\tau - \ln(1+\tau)]} \tag{12}$$

The first term on the right hand side is the contribution due to fluid friction ΔP in the heat exchanger. The remaining two terms account for losses due to heat transfer across a finite ΔT. Therefore expression (12) can be viewed as

$$\frac{I}{W_{\max}} = \left(\frac{I}{W_{\max}}\right)_{\Delta P} + \left(\frac{I}{W_{\max}}\right)_{\Delta T} \tag{13}$$

Equations (12) and (13) are the necessary analytical tools for pointing out the optimum set of conditions for minimizing the waste of useful working during the storage process.

Before proceeding with the analysis it is worth pointing out that the ratio $I/W_{\max}$, equations (12) and (13), is in effect a **Number of Irreversibility Units N_I** which quantizes the thermodynamic performance of the whole storage system. This concept is similar to the **Number of Entropy Generation Units N_S** introduced first by this author in the development of the N_S design method for heat exchanger thermodynamic optimization [7, 8].

Optimum Charging Time, θ_{opt}

The time θ, i.e., the amount of high temperature gas used for charging the storage element, plays a major role in determining the loss of useful work due to heat transfer across a finite temperature difference. The $(I/W_{\max})_{\Delta T}$ contribution was plotted on Fig. 2 as a function of θ for discrete values of τ and N_{tu}. It is apparent that for a given τ and N_{tu} there exists an optimum θ when the ΔT losses reach a minimum. Away from this minimum, $(I/W_{\max})_{\Delta T}$ tends to unity. In the $\theta \to 0$ limit, the entire useful work content of the hot stream is dissipated by heat transfer to the liquid bath which is initially at atmospheric temperature. In the $\theta \to \infty$ limit, the gas stream exits the heat exchanger as hot as it enters; its useful work content is again dissipated entirely by direct heat transfer to atmospheric temperature.

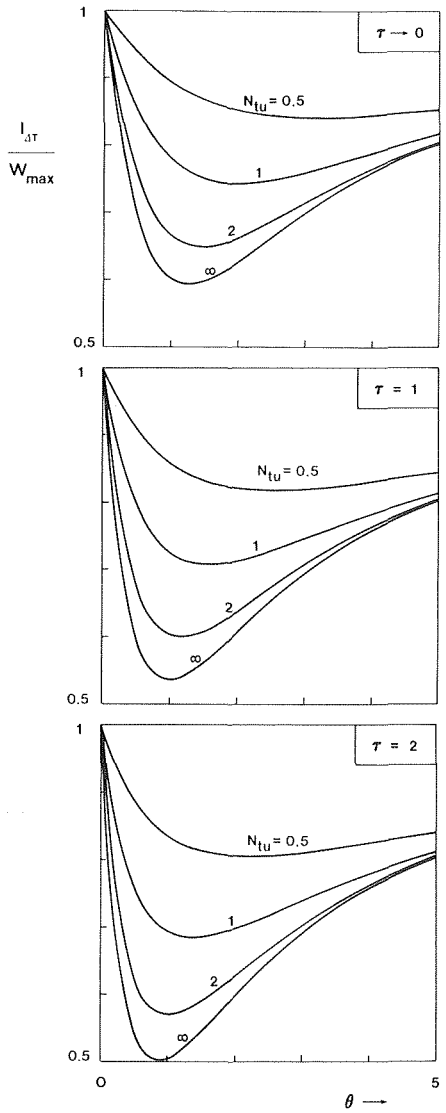

Fig. 2 Fraction of useful work dissipated by heat transfer across a finite temperature difference

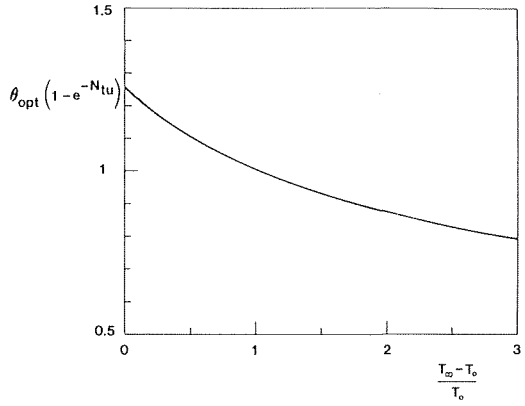

Fig. 3 Optimum amounts of hot gas (charging time) θ_{opt} for minimum irreversibility due to heat transfer across a finite ΔT

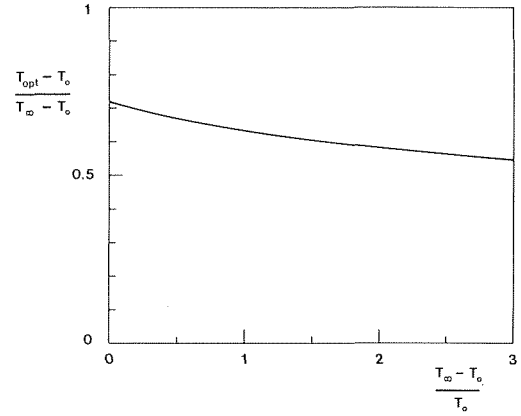

Fig. 5 Optimum amount of thermal energy stored as sensible heat corresponding to maximum storage of useful work

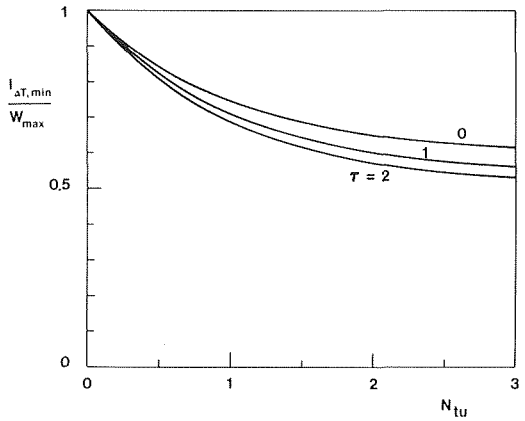

Fig. 4 Minimum fraction of useful work dissipated by heat transfer across a finite ΔT

An implicit equation for θ_{opt} can be derived by locating the θ minimum of expression (12). This equation was solved numerically and the result is shown on Fig. 3. The optimum quantity of hot gas used for charging the sensible heat storage element, θ_{opt}, is a weak function of the temperature difference τ and a relatively stronger function of N_{tu}.

At the optimum, $\theta = \theta_{opt}$, the loss of useful work due to heat transfer across a finite ΔT assumes the minimum value shown in Fig. 4. Of the two parameters τ and N_{tu}, the number of transfer units has a more sizeable impact on $(I/W_{max})_{\Delta T,min}$. We see now that for practical values of τ and N_{tu} the minimum fraction of useful work dissipated by heat transfer across a finite ΔT is consistently greater than 50 percent. According to expression (13), the ΔP loss is always added to the minimum ΔT loss of Fig. 4. Hence, the storage technique shown in Fig. 1 always dissipates at least half of the useful work potential provided by the energy source.

If the storage unit operates in the optimum regime, the total amount of thermal energy stored as sensible heat at the end of the charging process, $MC(T_{opt} - T_0)$, is far from the maximum storage capability of the liquid bath, $MC(T_\infty - T_0)$. The optimum thermal energy storage corresponding the maximum storage of useful work is shown in Fig. 5. In accordance with Fig. 2 and expression (12), if one seeks to heat the liquid bath until the stored thermal energy reaches its maximum, $T = T_\infty$, one runs the risk of storing none or a very small fraction of the useful work drawn from the high temperature source.

Heat Exchanger Optimum Number of Transfer Units $N_{tu,opt}$

The irreversibility analysis presented above makes it possible to identify an important trade-off relevant to optimizing the gas-liquid heat exchanger of Fig. 1. In expression (13) the ΔT contribution to the dissipation of useful work always decreases as the heat exchanger N_{tu} increases. At the same time the ΔP contribution increases with N_{tu}. Thus, it is possible to determine an optimum number of transfer units which minimizes I/W_{max}. The optimum N_{tu} is derived purely from thermodynamic considerations before proceeding with the actual heat exchanger design. This is the same thermodynamic trade-off employed by McClintock [6] and Bejan [7] in optimizing counterflow heat exchangers as well as heat exchanger with prescribed heat flux distribution [8].

To illustrate this point, consider the following set of limiting assumptions. First, assume that the overall N_{tu} is practically equal to the N_{tu} for the gas side of the heat exchanger. This is the case where the thermal resistance between gas stream and liquid bath is dominated by resistance to heat transfer from the stream to the heat exchanger wall. Under these circumstances, the ratio $\Delta P/P_0$ is directly proportional to the number of transfer units

$$\frac{\Delta P}{P_0} = \left(\frac{f}{N_{St}}\frac{G^2}{2\rho P_0}\right)N_{tu} \tag{14}$$

where f, N_{St} and G are, respectively, the friction factor, Stanton number and mass velocity for the gas side. Expression (14) was obtained by eliminating the length to hydraulic radius ratio L/r_n from the relations defining N_{tu} and friction factor [9],

$$N_{tu} = (L/r_n)N_{St} \tag{15}$$

and

$$\Delta P/P_0 = f(L/r_n)G^2/(2\rho P_0) \tag{16}$$

The second limiting assumption is $\Delta P/P_0 \ll 1$, allowing us to approximate $\ln(1 + \Delta P/P_0)$ by $\Delta P/P_0$ in equation (12). Combining this assumption with equation (14) we have shown that the ΔP contribution to lost useful work is directly proportional to the heat exchanger N_{tu},

$$\left(\frac{I}{W_{max}}\right)_{\Delta P} \simeq \left(\frac{R/c_p}{\tau - \ln(1+\tau)}\frac{f}{N_{St}}\frac{G^2}{2\rho P_0}\right)N_{tu} \tag{17}$$

By substituting expression (17) in place of the ΔP term of equation (12) we can now derive an expression for the optimum number of transfer units for which I/W_{max} is a minimum. The result can be written as

$$N_{tu,opt} = \ln\left[\frac{e^{-y\theta}\tau^2(1-e^{-y\theta})}{\tau(1-e^{-y\theta})+1}\right] - \ln\left[\frac{G^2}{2\rho P_0}\frac{f}{N_{St}}\frac{R}{c_p}\right] \tag{18}$$

If the storage element operates in the optimum regime described in the preceeding section, the first term appearing in expression (18) depends only on τ ($y\theta_{opt}$ is given as a function of τ in Fig. 3). This simple result was plotted on Fig. 6, the optimum number of transfer units decreasing as the mass velocity G increases.

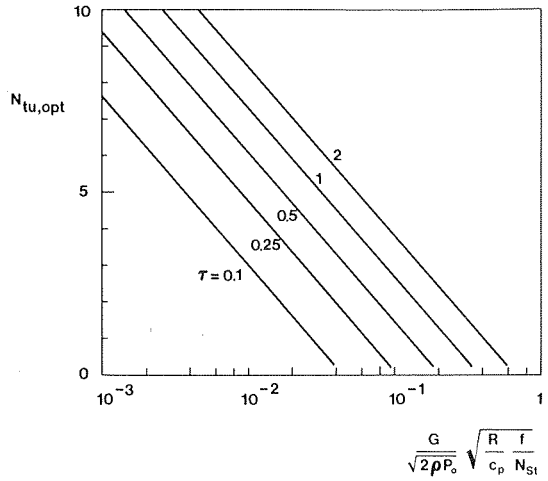

Fig. 6 Optimum relationship between parameters N_{tu}, $G/(2\rho P_0)^{1/2}$ and N_{Re} for minimum irreversibility in the gas-liquid heat exchanger

Although it is beyond the stated objective of the present treatment to numerically design a heat exchanger using the chart of Fig. 6, a few observations may prove instructive. Upon examining equations (15) and (16), the heat exchanger design rests on selecting three design parameters, for example N_{tu}, $G/(2\rho P_0)^{1/2}$ and the Reynolds number N_{Re} which determines both f and N_{St}. Equation (18) and Fig. 6 provide an optimum relationship between the three parameters. However, since for most heat exchanger surfaces the ratio f/N_{St} is a very weak function of N_{Re} [7], the optimum relationship is actually a one-to-one dependence between N_{tu} and G which, if obeyed, automatically leads to a highly desirable thermodynamic optimum. With this relationship plus the fact that the selection of N_{Re} has little impact on optimum thermodynamic performance, the heat exchanger design becomes a considerably more straightforward procedure.

Concluding Remarks

By analyzing the irreversibility associated with storing energy as sensible heat we have been able to show two important trade-offs relevant to optimizing this class of thermal systems. We first saw the optimum amount of high temperature fluid θ_{opt} which leads to the maximum storage of useful work in the sensible heat storage unit. Going beyond this optimum "time of exposure" in the hope of maximizing the amount of thermal energy stored as sensible heat is counter-productive. In fact, the thermal energy stored at the time of maximum useful work storage is only 50 to 70 percent of the maximum energy storage capability (Fig. 5).

The irreversibility analysis also pointed out the characteristically lossy features which accompany the technique of storing energy as sensible heat. Even under the most efficient operating conditions, $\theta = \theta_{opt}$ and using a pressure drop-free heat exchanger, the unit stores less than 50 percent of the useful work potential delivered by the high temperature source.

Finally, the irreversibility analysis revealed once again the heat exchanger trade-off between losses due to fluid friction ΔP and heat transfer across a finite ΔT. This trade-off was translated into a direct way of calculating the heat exchanger number of transfer units $N_{tu,opt}$ in terms of other system parameters in order to maximize the fraction of useful work stored.

As was pointed out in the very beginning, in order to be able to develop the irreversibility analysis and its conclusions we focused on probably the simplest class of sensible heat storage units. The basic element was described in detail in the first section of this article (Fig. 1). However, the thermodynamic features of this simple system are also present in more complex versions of the sensible heat energy storage technique. This is to say that the thermodynamic treatment of, for example, sensible heat storage in huge liquid pools from a stream of condensing vapor would unquestionably have led to the same trade-offs and a similar set of conclusions. Solid units for sensible heat storage could also be optimized according to the method outlined in this article; the final design conclusions would qualitatively match the conclusions reached in this study.

Furthermore, consider the process or set of processes by which, later on, the stored energy is drained from the storage system. It is evident that the drainage process carries with it many of the irreversible features present in the initial storage phase. Therefore, as a suggestion for further work, it would be interesting and worthwhile to apply the present irreversibility minimization approach to the thermodynamic optimization of the drainage process.

Acknowledgment

The author wishes to thank Professor C. L. Tien, Chairman, Department of Mechanical Engineering, University of California, Berkeley, for many useful comments and words of encouragement. This work was supported by a postdoctoral fellowship awarded by the Miller Institute for Basic Research in Science at the University of California, Berkeley.

References

1 "Shaving the Power Peak," *Technology Review,* Vol. 79, No. 8, July–Aug. 1977, pp. 68.

2 Kelly, G. E., and Hill, J. E., "Method of Testing for Rating Thermal Storage Devices Based on Thermal Performance," Report NBS IR-74-634, May 1975.

3 Mueller, A. C., "Heat Exchangers" in *Handbook of Heat Transfer,* Rohsenow, W. M., and Hartnett, J. P., Editors, McGraw-Hill, New York, 1973, pp. 18–31, 18–34.

4 Van Wylen, G. J., and Sonntag, R. E., *Fundamentals of Classical Thermodynamics,* Wiley, New York, 1973, pp. 276, 277.

5 Keenan, J. H., *Thermodynamics,* MIT Press, Cambridge, Mass. 1970, pp. 289.

6 McClintock, F. A., "The Design of Heat Exchanger for Minimum Irreversibility," Paper No. 51-A-108, presented at the 1951 ASME Annual Meeting.

7 Bejan, A., "The Concept of Irreversibility in Heat Exchanger Design: Counterflow Heat Exchangers for Gas-to-Gas Applications," ASME JOURNAL OF HEAT TRANSFER, Vol. 99, No. 3, pp. 374–380.

8 Bejan, A., "General Criterion for Rating Heat Exchanger Performance," to appear in the *International Journal of Heat and Mass Transfer,* Vol. 21, 1978.

9 Kays, W. M., and London, A. L., *Compact Heat Exchangers,* McGraw-Hill, New York, 1964, pp. 33, 35.

D. B. Kreitlow[1]
Graduate Student.
Student Mem. ASME.

G. M. Reistad
Associate Professor.
Mem. ASME.

C. R. Miles
Graduate Student.
Department of Mechanical Engineering,
Oregon State University,
Corvallis, Oregon

G. G. Culver
Associate Professor and Head.
Department of Mechanical Engineering Technology,
Oregon Institute of Technology,
Klamath Falls, Oregon
Assoc. Mem. ASME.

Thermosyphon Models for Downhole Heat Exchanger Applications in Shallow Geothermal Systems

The analysis of downhole heat exchangers used to extract energy from relatively shallow geothermal wells leads to the consideration of several interesting problems of buoyancy-driven heat transfer in enclosures. This paper considers thermosyphoning through and around the wellbore casing which is perforated at two or more depths. Analytical models are developed for thermosyphoning in the cased well both with and without a heat exchanger installed. Theoretical results are compared with experimental values. These comparisons show that the observed energy extraction rates and flow rates through the well casing are possible with thermosyphoning as the only circulation mechanism within the well bore. The model with a heat exchanger installed is parametrically evaluated to illustrate the sensitivity of the model to estimated parameters and the effect of changes in design variables or constraints.

Introduction

At the present time, downhole heat exchangers (DHEs) are widely used for extracting geothermal energy from the shallow, low temperature geothermal resource at Klamath Falls, Oregon [1]. Although there are many installations of these devices, they have not really been analyzed, but rather built and somewhat improved in a trial and error process. This work considers thermosyphon-type heat transfer models that have arisen in analyzing the present type installations to determine how they can be improved.

Fig. 1 shows a typical installation of a DHE. It consists of (1) the wellbore, generally 15 to 36 cm in diameter and drilled with a cable rig, (2) a casing sealed to the well bore at the top end for a distance of about six m and perforated at two levels, at the hot water strata level (well bottom) and just below the standing water level, and (3) an unfinned U-shaped heat exchanger made from bare steel pipe.

The analysis here considers two configurations:

A The cased wellbore: (no heat exchanger)

B The cased wellbore with heat exchanger

Before examining each of these individually, consider the results of several preliminary experiments that have influenced the selection of heat transfer models for both configurations. Bulk fluid flow

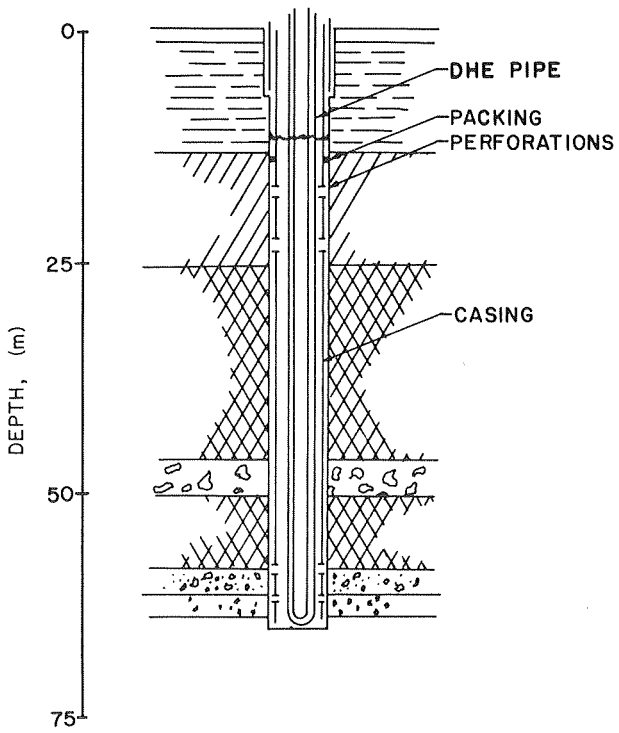

Fig. 1 Typical DHE installation

[1] Presently at Tektronix Inc., Beaverton, Oregon.

Contributed by the Heat Transfer Division for publication in the JOURNAL OF HEAT TRANSFER. Manuscript received by the Heat Transfer Division January 26, 1978.

measurements with a vane anemometer (spinner) on seven wells indicated little or no vertical flow in the uncased well and a substantial vertical flow (up to about seven cm/s average velocity) between the perforations in the cased well. Flow measurement equipment small enough to be lowered into a well with a DHE installed was not available at the time of testing so no flow measurements were taken for this configuration. Temperature measurements for each situation are shown in Fig. 2. The uncased wells have a substantial temperature gradient with the hottest temperature at the bottom and considerably lower temperatures at the static water level. The cased well, with the DHE not operating, on the other hand, exhibits an essentially constant temperature from the water level to the bottom inside the casing. For the configuration with the downhole heat exchanger installed and operating, the temperatures of the well fluid are highest at the water level and decrease with depth.

These results by themselves indicate the following heat transfer situations corresponding to A and B above:

A Thermosyphoning up the inside of the well casing and down the annular space between the casing and the wellbore.

B Thermosyphoning up through the annular space between the casing and the wellbore and down the inside of the casing.

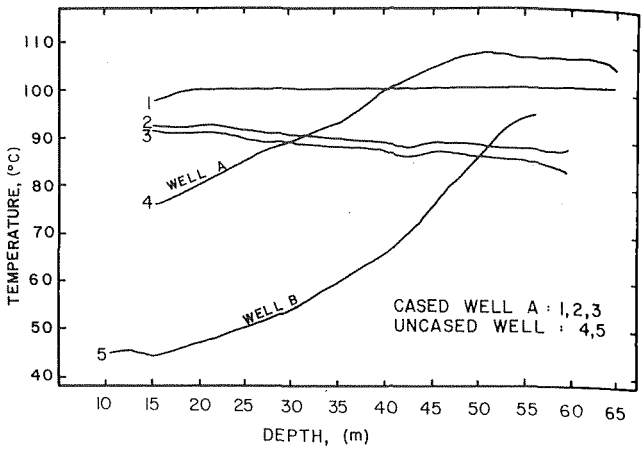

Fig. 2 Measured temperature profile of cased and uncased wells. (Values are inside the casing of the cased well.)

Cased Well Without Heat Exchanger

The measurement of a significant vertical flow (seven cm/s) in the cased well without heat exchanger when no flow was found in the uncased well led to modeling of the thermosyphoning believed to be responsible. This was done for three reasons: (1) to determine if thermosyphoning alone is sufficient to account for the observed flow rate, (2) to determine the effect of various parameters on the mass flow rate and temperature profile, so that potential methods of increasing the heat transfer to a downhole heat exchanger can be identified and (3) to provide a check on the validity of this type of model, since measurements are much more easily obtained from the well when it is uncluttered by heat exchanger pipes that twist around inside the casing rather than hanging straight down.

The simplified physical model shown in Fig. 3 for this configuration consists of a vertical impermeable cylindrical tube located concentrically within a vertical cylindrical hole in an infinite impermeable medium of finite thickness. The inner cylinder represents the casing while the cylindrical hole in the medium represents the wellbore and surrounding earth. The inner cylinder, being smaller than the wellbore, forms a vertical annulus between it and the earth in which flow can take place. At the bottom of the cylinders (both at the same depth) an open aquifer is assumed at temperature T_b. Water fills the inner cylinder and annulus to a level just below the top of the cylinders. Just below the water level, the casing has perforations that allow fluid to flow from inside the casing to the annulus or vice versa. The medium

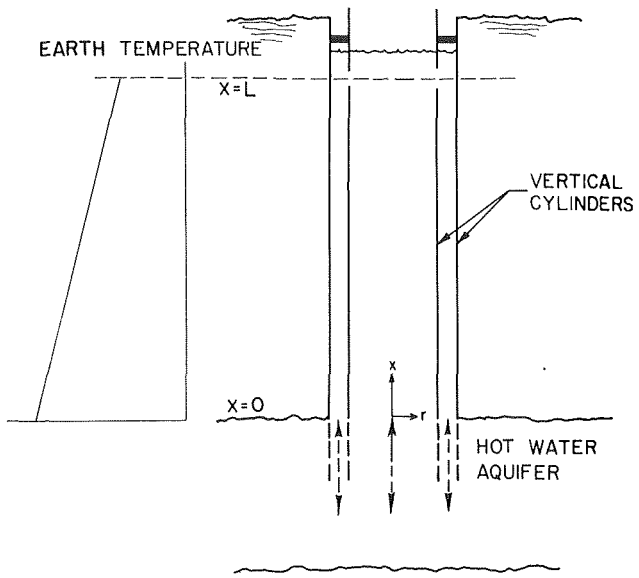

Fig. 3 Simplified physical model of cased well without heat exchanger

Nomenclature

$\overline{A}$ = earth temperature gradient
A_i = cross-sectional area inside the casing
A_0 = cross-sectional area, outer annulus
c_p = specific heat at constant pressure
D_H = diameter of heat exchanger pipe
D_i = inside diameter of casing
D_w = diameter of wellbore
De_i = hydraulic diameter of inside the casing
De_0 = hydraulic diameter of annulus outside the casing
D/e = one over the relative roughness
f_{fi} = Fanning friction factor for inside of casing
f_{f0} = Fanning friction factor for outer annulus
g = acceleration due to gravity
k = thermal conductivity
k_g = thermal conductivity of earth
L = length of well (between perforation levels for the cased well)
$\dot{m}$ = mass flow rate through casing
$\dot{m}_H$ = mass flow rate through heat exchanger
Pr = Prandtl number = $\nu/\alpha = \mu c_p/k$
$\dot{Q}_H$ = energy extraction rate through heat exchanger
r_w = wellbore radius
R = radial distance from center line of well
Re = Reynolds number
t = time since start of given mode of thermosyphoning
T = temperature
T_b = temperature of reservoir
T_g = earth temperature
T_i = water temperature inside the casing
T_0 = water temperature outside the casing
T_1 = water temperature in entering leg of heat exchanger
T_2 = water temperature in leaving leg of heat exchanger
T_w = well wall temperature
U_H = overall heat transfer coefficient through heat exchanger
U_i = overall heat transfer coefficient through the casing
U_w = overall heat transfer coefficient to well wall
x = distance upward from bottom perforations of well casing for the cased well
XL = length of heat exchanger below top perforation
α = thermal diffusivity
β = thermal expansion coefficient
ρ_i = density inside casing
ρ_0 = density in annulus outside of casing
ρ_r = density at reference temperature T_b

is assumed to have a temperature which increases linearly with depth and at time zero has the same temperature at all values of radius at a fixed depth. Furthermore, at $x = 0$, its temperature is T_b and the gradient is $\overline{A}$, so the initial ground temperature is $T_g = T_b - \overline{A}x$.

The driving force for thermosyphoning in this configuration comes from the hot reservoir fluid and the relatively cooler well walls. The casing of the well serves to isolate the upward and downward flows which results in greatly increased bulk fluid flow, relative to the uncased situation, and a nearly uniform temperature profile inside the casing. Because both the well walls and the casing are assumed impermeable, except for the perforations, the mass flow rate through the casing is the same as that through the annulus but in the opposite direction. Since the well walls are providing the cooling, the flow in this configuration is expected to be up the inside of the casing and down the annulus.

This model can be treated by a one-dimensional analysis where the fluid properties are assumed to vary only in the vertical direction, both inside the casing and in the annulus, and heat transfer occurs only in the radial direction. The governing equations are the continuity, energy and momentum equations. As indicated above, the continuity equation requires that the mass flow rate ($\dot{m} = \rho VA$) be constant everywhere in the system. The energy and momentum equations are coupled because the circulation is buoyancy driven, with the flow rate being the one that will balance the frictional head loss against the net buoyancy head. The flow may be laminar or turbulent both inside the casing and in the annulus, and care must be taken to use the appropriate heat transfer and friction coefficients. In this work, the friction factors are obtained from the equations:

For laminar flow (Re < 2300)

$$f_f = \frac{16}{\mathrm{Re}}$$

For turbulent flow (rough pipe, $(D/e)/\mathrm{Re}\sqrt{f_f} > 0.01$)

$$\frac{1}{\sqrt{f_f}} = 4.0 \log_{10} \frac{D}{e} + 2.28$$

And for transition flow

$$\frac{1}{\sqrt{f_f}} = 4 \log_{10} \frac{D}{e} + 2.28 - 4 \log_{10} \left(4.67 \frac{D/e}{\mathrm{Re}\sqrt{f_f}} + 1\right)$$

The convective heat transfer coefficients for the casing, well walls and heat exchanger pipes were obtained from the Prandtl analogy.

The energy equation restrictions can be formulated by making energy balances between positions x and $x + \Delta x$ both in the casing and in the annulus and letting Δx approach zero. This energy equation for the fluid inside the casing yields a differential equation in terms of the temperatures in the annulus and casing and the mass flow rate,

$$\frac{dT_i}{dx} = \frac{U_i \pi D_i}{\dot{m}\, c_p} (T_0 - T_i) \tag{1}$$

where the subscripts i and 0 refer to inside the casing and outside the casing (inside the annulus) respectively.

The energy balance on the fluid in the annulus is not as simple in that it must include a term to account for the transient heat transfer to the wall. A number of authors [2, 3, 4] have approximated this term with a line source solution. The approach here is to take the method of Ramey [2], which relies on the work of Carslaw and Jaegar [5]. Ramey defines an $f(t)$ by the following equation where $d\dot{q}$ is the rate of heat transfer through the wall of height dx to the surrounding earth at time (t):

$$d\dot{q} = \frac{2\pi k_g (T_w - T_g)}{f(t)} dx \tag{2}$$

where T_w and T_g are the wall and undisturbed earth temperature at level x, respectively. The parameter $f(t)$ is given in Fig. 4. Several curves for $f(t)$ are illustrated, those for (1) constant wall temperature, (2) constant heat flux and (3) a radiation boundary condition. All three converge for long times. For short times, the "radiation boundary condition" should be used with $r = r_w$, $U = U_w$, $k = k_g$, and T_w in

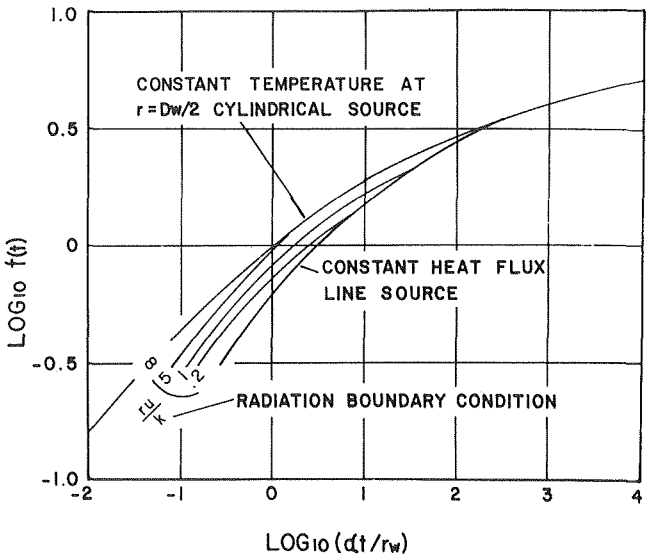

Fig. 4 The function $f(t)$ defined by equation (2), from Ramey [2]

equation (2) replaced with T_0 (2). The energy balance on the fluid in the annulus then yields

$$\frac{dT_0}{dx} = \frac{2\pi k_g}{f(t)\dot{m}c_p} (t_0 - T_g) + \frac{U_i \pi D_i}{\dot{m} c_p} (T_0 - T_i) \tag{3}$$

Equations (1) and (3) have the unknowns $T_0(x)$, $T_i(x)$, $\dot{m}$, U_i, and $f(t)$. The function $f(t)$ in turn depends on U_w and therefore $\dot{m}$. To carry the analysis a step further in closed form, neglect the variation of U_i and U_w in the x direction. Then, at a specified time (t), equations (1) and (2) can be integrated in terms of the constants $f(t)$, $\dot{m}$ and U_i to get expressions for the temperature profiles in the annulus and casing. With the boundary conditions

$$T_i(0) = T_b \quad \text{and} \quad T_0(L) = T_i(L) \tag{4}$$

to be discussed later, the resulting temperature profiles are

$$T_i(x) = B_1 e^{\lambda_1 x} + B_2 e^{\lambda_2 x} + \frac{\overline{A}}{C_1} \dot{m} + T_b - \overline{A}x \tag{5}$$

$$T_0(x) = T_i(x) + \dot{m}/C_1 (B_1 \lambda_1 e^{\lambda_1 x} + B_2 \lambda_2 e^{\lambda_2 x} - \overline{A}) \tag{6}$$

where

$$\lambda_1 = \frac{C_2 + (C_2^2 + 4C_1C_2)^{1/2}}{2\dot{m}}, \quad \lambda_2 = \frac{C_2 - (C_2^2 + 4C_1C_2)^{1/2}}{2\dot{m}}$$

$$C_1 = \frac{U_i \pi D_i}{c_p}, \quad C_2 = \frac{2\pi k_g}{f(t) c_p}$$

and

$$B_1 = \frac{-\overline{A}\left[1 + \frac{\dot{m}}{C_1}\lambda_2 e^{\lambda_2 L}\right]}{\lambda_2 e^{\lambda_2 L} - \lambda_1 e^{\lambda_1 L}}, \quad B_2 = \frac{\overline{A}\left[1 + \frac{\dot{m}}{C_1}\lambda_1 e^{\lambda_1 L}\right]}{\lambda_2 e^{\lambda_2 L} - \lambda_1 e^{\lambda_1 L}}$$

Note that if $\dot{m}$ is specified, U_i and U_w could be calculated, $f(t)$ could be obtained from Fig. 4 and the temperature profiles numerically evaluated. The remaining relationship to specify the $\dot{m}$ is obtained by integrating the density along the height of each column of fluid to get an expression for the buoyant head, and setting this equal to the head loss due to friction at the same mass flow rate.

The available buoyant head is

$$h_{\mathrm{Buoy}} = g \int_0^L (\rho_0 - \rho_i) dx \tag{7}$$

In terms of the thermal expansion coefficient, this becomes

$$h_{\mathrm{Buoy}} = \rho_r g \beta \int_0^L (T_i(x) - T_0(x)) dx \tag{8}$$

Equations (1) and (5) allow this integration to be carried out:

$$h_{\text{Buoy}} = -\frac{\rho_r g \dot{m}}{C_1}[B_1(e^{\lambda_1 L} - 1) + B_2(e^{\lambda_2 L} - 1) - \overline{A}L] \quad (9)$$

The friction head loss is approximated as that due to the friction along the walls only and is separated into two components, that inside the casing and that in the annulus.

$$h_{\text{Loss}} = 2f_{fi}\frac{L}{De_i}V_i^2 + 2f_{f0}\frac{L}{De_0}V_0^2$$

$$= 2L\dot{m}^2\left[\frac{f_{fi}}{\rho A_i^2 De_i} + \frac{f_{f0}}{\rho A_0^2 De_0}\right] \quad (10)$$

Equating h_{Buoy} to h_{Loss} yields the equation that can be solved iteratively for the mass flow rate:

$$\dot{m} - \frac{\rho^2 g\beta}{2C_1 L\left(\frac{f_{fi}}{A_i^2 De_i} + \frac{f_{f0}}{A_0^2 De_0}\right)}\{B_1(1 - e^{\lambda_1 L}) + B_2(1 - e^{\lambda_2 L}) + \overline{A}L\} = 0 \quad (11)$$

The model results for vertical mass flow rate through the well of varying (1) D/e (1/the relative roughness) for the annulus, (2) well diameter, (3) earth temperature gradient, and (4) time, are presented in Fig. 5. The results are presented for parameter variations about a standard set presented in Table 1, at two different values of time. These curves show that the predicted flow rate is very dependent on the value of time when time is less than several hours, but not very dependent for values of time larger than this. Since all well testing occurred at times at least several hours after casing installation, time does not have a large influence on predicted values and dashed lines in Figs. 5(*a*), (*b*), and (*d*) and the upper portion of the solid line in Fig. 5(*c*) are the appropriate values to compare with. Note, however, that here time includes the influence of the conductivity of the earth, and impermeable ground with a thermal conductivity of 0.78 W/mK was assumed. The presence of cool ground water near the wellbore could significantly alter the situation and would cause greater $\dot{m}$ values than those predicted from the above analysis.

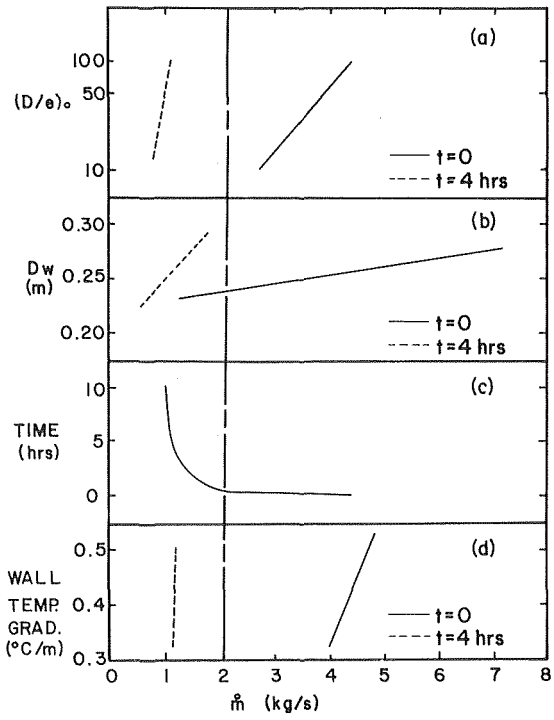

Fig. 5 Mass flow rate for various parameter variations about the standard set (see Table 1.) Experimental value for actual well with physical characteristics of well specified in Table 1, and tested several days after casing installation

Table 1 Test well characteristics and standard parameter set

General Characteristics
- D_w = 0.254 m
- D_H = 0.060 m
- Static Water Level—14 m
- Perforation Levels: 17 to 12 m and 57 to 65 m
- Temperature at bottom of well = 100°C

Standard Parameter Set
- D_w = 0.254 m
- D_i = 0.203 m
- $(D/e)_0$ = 100
- Earth Temperature Gradient = 0.42 K/m
- L for cased well = 50 m
- t = 4 hours

Fig. 5 also shows that the wellbore diameter has substantial influence on the predicted flow rate. The wellbore diameter probably varies substantially from top to bottom due to washing and sloughing, and an accurate value is difficult to predict. An average of value two to five cm larger than that drilled seemed reasonable to the authors.

The relative roughness of the annulus, again difficult to predict accurately, has a ten to 20 percent influence on $\dot{m}$ over the range of its expected value. The earth temperature gradient has little influence when varied over its expected range.

Overall, the results, presented in Fig. 5, show that the thermosyphoning model presented above predicts flows of the same order of magnitude, but somewhat less than those experimentally observed. The influence of the wall boundary condition as previously discussed is the probable reason for observed rates being larger than those predicted from the model here.

It must be noted that the model here does not consider mixing at the bottom of the two cylinders. The aquifer fluid at T_b is assumed to enter into the casing and the fluid flowing down the annulus goes freely into the aquifer. From the temperature profiles 1 and 4 in Fig. 2 it appears there is some mixing. However, the amount of mixing must be substantially below 100 percent recirculation because of experimental results from heat exchanger tests. Thus in the absence of evaluated amounts of mixing the apparently closest approximation is nonmixing as selected in the boundary condition of equation (4).

Cased Well With DHE

Early wells used for DHEs at Klamath Falls were not cased except for a short length near the ground surface. Later it was discovered that casing the well appreciably extends its life. Some wells that were not originally cased have been cleaned out and a casing installed. This resulted in significantly increased heat exchanger output but it was not clear how much of this was due to the casing and how much was due to the cleaning [1]. The preliminary measurements shown in Fig. 6 indicate that the output of a well can be nearly doubled by the installation of a slotted casing. Thus the slotted casing plays a major role in efforts to increase the effectiveness of downhole heat exchangers for these applications.

The model for the cased well was extended to include a downhole heat exchanger with flow inside the casing downward. This results in four differential equations rather than the two of (1) and (3) above:

$$\frac{dT_0}{dx} = -\left[\frac{2\pi k_g}{f(t)c_p}(T_0 - T_w) + \frac{U_i \pi D_i}{c_p}(T_0 - T_i)\right]\Big/\dot{m} \quad (12)$$

$$\frac{dT_i}{dx} = -\left[\frac{U_i \pi D_i}{c_p}(T_0 - T_i) + \frac{U_H \pi D_H}{c_p}(T_1 + T_2 - 2T_i)\right]\Big/\dot{m} \quad (13)$$

$$\frac{dT_1}{dx} = \frac{U_H \pi D_H}{c_p \dot{m}_H}(T_1 - T_i) \quad (14)$$

$$\frac{dT_2}{dx} = \frac{U_H \pi D_H}{c_p \dot{m}_H}(T_i - T_2) \quad (15)$$

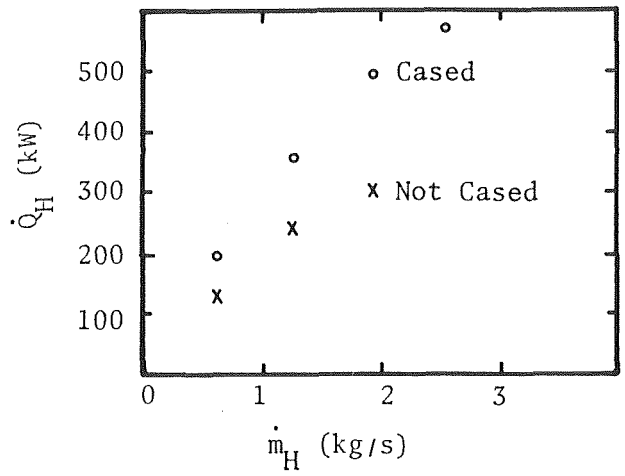

Fig. 6 Experimental energy extraction rates for well of Table 1, both cased and not cased

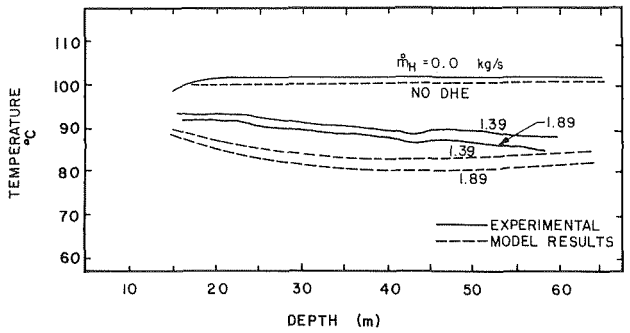

Fig. 7 Experimental and model predicted temperature profiles for several heat exchanger flow rates. Model values for standard parameter set (Table 1). Water inlet temperature for the heat exchanger is 21.1°C.

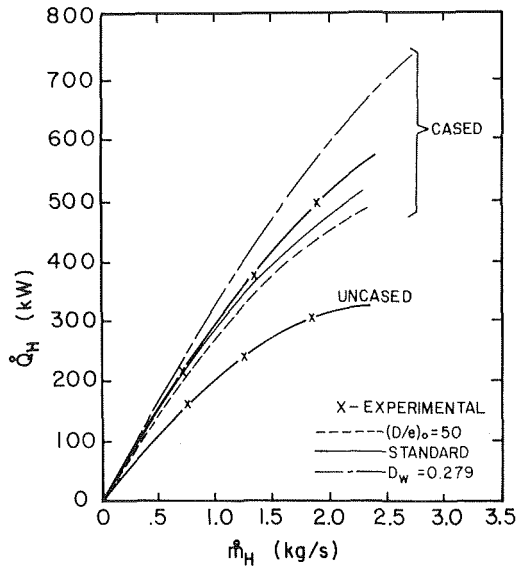

Fig. 8 Experimental and model results for energy extraction as a function of flow rate through the heat exchanger for well indicated in Table 1

where subscripts are as above and subscripts 1 and 2 refer to the entering and leaving legs of the heat exchanger, and subscript H refers to the heat exchanger.

The boundary conditions are

(1) $T_0(0) = T_b$
(2) $T_0(L) = T_i(L)$
(3) $T_1(0) = T_2(0)$
(4) $T_1(L) = T_{in}$

These correspond to (1) the temperature of the reservoir (assumed known), (2) temperatures of the water inside and outside the casing are equal at the top perforation level, (3) the temperatures in the two legs of the heat exchanger are equal at the bottom where they join, and (4) the temperature of the water entering the downhole heat exchanger (assumed known). These equations were solved numerically, iterating on the mass flow rate. The mass flow rate is again determined by setting the head due to the density difference between the outside and the inside of the casing equal to the frictional loss.

Fig. 7 shows the temperature profile inside the casing for the model and one experimental well. Results for two nonzero flow rates through the heat exchanger are shown in addition to results for the cased well with no heat exchanger discussed earlier. The experimental results for the nonzero mass flow rates indicate a flow up in the annulus and down the inside of the casing. The analytical results, with boundary conditions, set to correspond to the indicated flow directions, compare quite well in trends with the experimental results.

The influence of the three estimated parameters that are not accurately known, $(D/e)_0$, D_w, and earth temperature gradient, and time were also investigated for the cased well with a heat exchanger. Unlike the cased well with no heat exchanger, here the time and earth temperature gradient have little effect on the model results. This is because the energy exchange through the heat exchanger is much much larger than that by conduction through the well walls for the range of outputs and well lengths considered here particularly after several hours of operation. The influence of D_w and $(D/e)_0$ are illustrated in Fig. 8 where several model result curves are presented in comparison to the experimental results of the well specified in Table 1. This figure shows that both the well diameter and the well-wall roughness substantially affect the model results, with the well diameter having the major influence. As discussed above, the range of these two variables presented in Fig. 8 could be expected for any specific application.

The comparisons of Fig. 8 show that the thermosyphoning can account for the energy extraction rates that are experimentally measured. Furthermore, they show that the model can predict the output within about 15 percent for reasonable estimated parameters. Consequently, the authors feel that thermosyphoning is the major mechanism for heat transfer in the wells and furthermore that while it must be recognized that application of this model has some uncertainty due to the selected values of well diameter and D/e, the model allows the effect of design variables or design constraints of specific applications to be evaluated.

Influence of Design Variables and Constraints. There are many variables to be considered: those associated with (1) the well—D_i, D_w, T_b, and L; (2) the heat exchanger design—D_H, XL, and the number of loops; and (3) the heat exchanger fluid (compressed water) characteristics, entering temperature and $\dot{m}_H$. Figs. 9, 10, and 11 show the energy extraction rate as a function of each of these variables. The curves are based on changes of only the variables indicated on the curve about the "standard value" indicated in Table 1, with all of the other variables held at their standard value.

Several of the curves are indicated as "new" or "scaled." New indicates that the heat exchanger tubes and the well casing have not been fouled and the heat transfer fouling resistance is zero. Scaled refers to the condition when both the heat exchanger tubes and the well casing have been fouled by the geothermal fluids and the fouling coefficient is specified as 850 W/m^2 K [6].

Well Characteristics. Figs. 9(*a*), (*b*), (*c*), and (*d*) show the influence of the well characteristics, length (L), diameter (D_w), casing diameter (D_i), and source temperature (T_b). Increases in T_b or D_w both provide increased energy extraction rates. The increase from D_w starts to level out quite rapidly while the increase due to T_b continues linearly to temperatures beyond 200°C. The length L and well casing diameter on the other hand both show an optimum value where the maximum energy extraction rate occurs. The influence of the casing diameter is particularly interesting: in usual applications where the

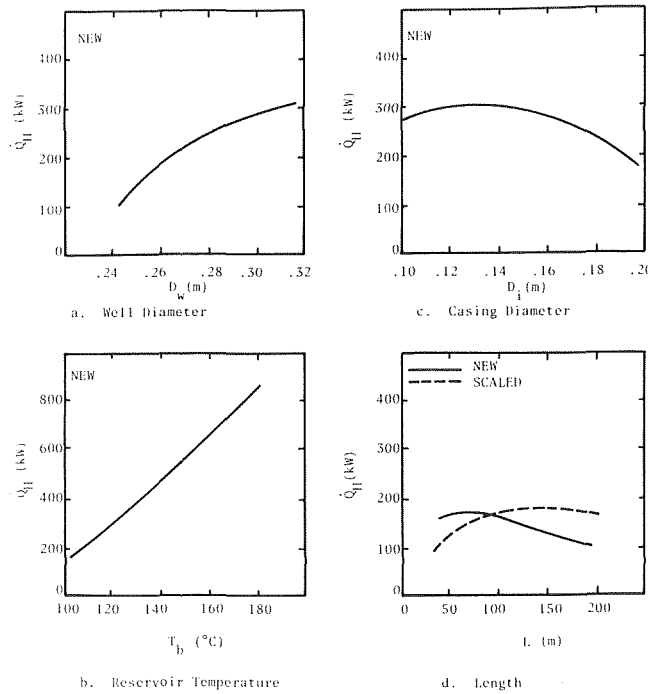

Fig. 9 Energy extraction rate as a function of well variables

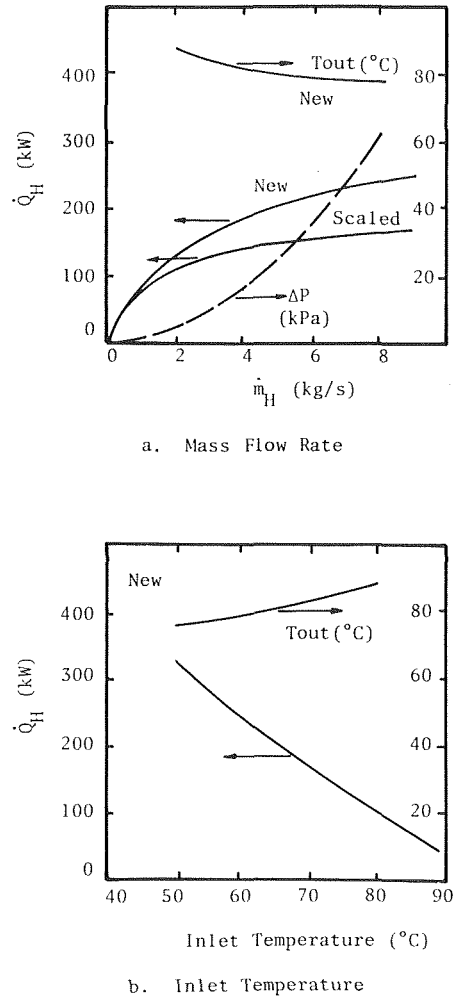

Fig. 11 Performance of the "standard case" DHE as a function of heat exchanger fluid flow rate and inlet temperature

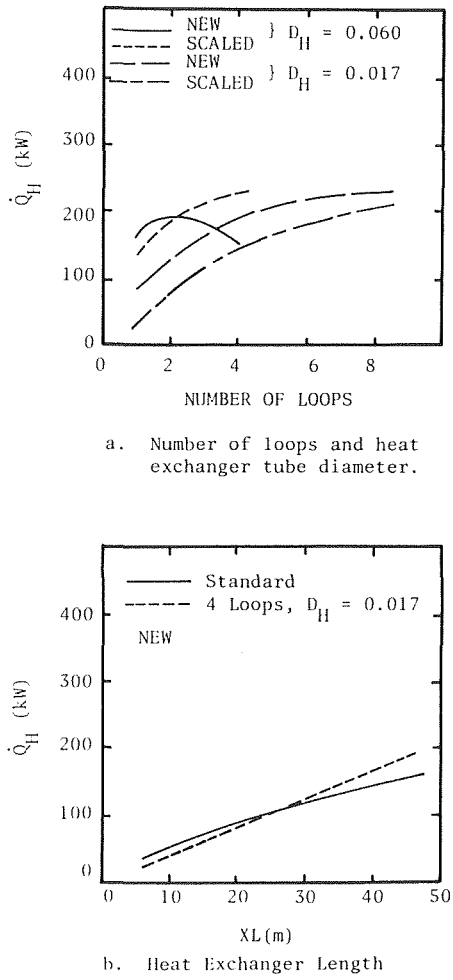

Fig. 10 Energy extraction rate as a function of heat exchanger design variables

well is 0.254 m in diameter the casing is 0.203 m; this curve shows that roughly 50% higher heat transfer rates can be expected with a smaller casing. The length is not nearly as controllable as the casing diameter since it is dictated to a large extent by the depth of the hot water strata. However, in some instances locating the top perforations at a lower level could prove beneficial. Note that in the scaled condition, the peak is not nearly as sharp and that greater heat transfer rates can occur than in the unscaled condition. The reason is that the fouled casing serves to insulate the cooled column of fluid from the hot fluid in the annulus and increases the thermosyphoning rate.

Heat Exchanger Design Variables. Figs. 10(*a*) and (*b*) show the effect of heat exchanger diameter (D_H), number of heat exchanger loops, and the length of the heat exchanger (XL). In Fig. 10(*a*) the energy extraction rate is seen to increase as the number of loops of heat exchanger (number of U-tubes in parallel) increases for each of the cases shown except for the unfouled, larger diameter heat exchanger. As the number of loops increases, if the mass flow through the well were constant, the heat transfer coefficient for the casing would increase because of increased velocity inside the casing. Similarly, the film coefficient on the outside of the heat exchanger tubes would increase, but the film coefficient on the inside of the heat exchanger would decrease. Also friction losses would be greater. For the unfouled 0.060 m heat exchanger, the friction losses, increased casing coefficient (which tends to decrease thermosyphoning) and decreased inside heat exchanger film coefficient apparently dominate. For the other cases, the increased area and outside heat exchanger film coefficient override these decreases for the range of tubes shown. Where the scaled 0.060 m heat exchanger has greater energy extrac-

tion rate than the unscaled one, the cause is, as explained before, due to the scaling on the casing increasing the thermosyphoning.

The heat exchanger length (XL) may be less than the length between perforations in the casing. Fig. 10(b) shows that for the standard case, changes in the heat exchanger length are almost directly proportional to changes in the energy extraction rate.

Heat Transfer Fluid Variables. Here the only fluid considered in the heat exchanger is compressed water. As a result, the major variables are mass flow rate ($\dot{m}_H$) and inlet temperature. Figs. 11(a) and (b) show their influence. Increasing $\dot{m}_H$ increases the energy extraction rate, but also increases pressure drop and outlet temperature. Increased pressure drops will require larger circulation pumps and lowered outlet temperatures will affect process design. Decreasing the inlet temperature markedly increases the energy extraction rate but also decreases the outlet temperature.

Conclusion

Cased wells with perforations at the shallow hot water level and just below the static water level, both with and without a DHE, have been modeled as thermosyphoning problems. The models developed predict results comparable in magnitude and trends to those measured for physical parameter values that are assumed to be representative of expected values. The results show that the thermosyphoning can account for the energy extraction rates experimentally observed. Furthermore, the models can be used to predict the effects of changes in well characteristics, heat exchanger design and heat exchanger fluid variables. Results are presented for variation about a standard design. Results show that the energy output is quite sensitive to changes in a number of the variables. Minor design changes can increase output by over 50 percent.

It must be noted that the models do not take into account any mixing that occurs at the bottom of the well, or any limitations on fresh flow of hot fluid into the well and as such the results must be viewed with caution for application to either new wells or energy extraction rates substantially out of the range for which tests have been made.

Acknowledgment

This work has been supported under U. S. Energy Research and Development Administration (now Department of Energy) Contract number EY-76-S-06-2429.

References

1 Culver, G. G., Lund, J. W., and Svanevik, L. S., "Klamath Falls Hot Water Well Study," UCRL-13614, 1974, Lawrence Livermore Laboratory, Livermore, Ca.

2 Ramey, H. J., Jr., "Well-bore Heat Transmission," *Journal of Petroleum Technology*, Vol. 225, 1962.

3 Boldizar, T., "The Distribution of Temperature in Flowing Wells," *American Journal of Science*, Vol. 256, 1958.

4 Birch, F., "Temperature and Heat Flow in a Well Near Colorado Springs," *American Journal of Science*, Vol. 245, 1947.

5 Carslaw, H. S. and Jaegar, J. C., *Conductions of Heat in Solids*, Oxford U. Press, Amen House, London, 1950.

6 *Mark's Mechanical Engineers' Handbook*, Edited by T. Baumeister, Sixth Edition, 1958, p. 4–106.

T. Y. R. Lee[1]
R. E. Taylor

Properties Research Laboratory,
School of Mechanical Engineering,
Purdue University,
West Lafayette, Ind. 47907

Thermal Diffusivity of Dispersed Materials

Measurements have been made of the effective thermal diffusivity at room temperature of composites consisting of one phase randomly dispersed in a second phase. The method is based on the flash technique. Data are presented for four types of composites ranging in particle-to-matrix diffusivity ratios from 0.48 to 1137, in volume specific heat ratios 0.04 to 1.16, and in volume fraction of dispersed particle from zero up to 34 percent. The results show that the limitations of the concept of an effective thermal diffusivity are far beyond the situations to which it is currently applied in the transient state heat conduction problems. Values of effective diffusivities derived from values of the effective thermal conductivity calculated from the Bruggeman variable-dispersion equation are found to agree well with the measured diffusivity values.

Introduction

In many cases of dispersed composites, it can be assumed that heterogeneous materials may be described adequately as consisting of a homogeneous and isotropic matrix in which particles of a second homogeneous and isotropic phase are dispersed. Assuming that the volume concentration of the dispersed particles is constant and that the material may be described as quasi-homogeneous and quasi-isotropic, it should be possible to calculate the properties of the composite material given the properties of the matrix and the dispersed particles.

Unfortunately there are comparatively few cases where such calculations can be made rigorously. Furthermore, attempts to derive generalized formulae require confirmation with well-defined experimental systems, and these are generally lacking. One of the complications is the extremely wide range of variables which must be considered before any generalized formulation can be expected. These variables include:

1 The geometry of the dispersed phase(s):
   (a) Shape of particles,
   (b) Size and size distribution of particles,
   (c) Concentration and concentration distribution of particles,
   (d) Orientation of particles,
2 The state of matter of the dispersed phase(s),
3 The composition of the dispersed phase(s),
4 The composition of the continuous phase.

It is a difficult task to describe the geometry of the dispersed phase, since the geometry of the individual particles as well as the arrangement in space of the particles in relation to each other have to be considered. Thus, shape, size, and size distribution are properties of the particles while orientation and concentration are features of the system.

The shape of many dispersed phases encountered in materials technology can be considered to be approximately spheres or cylinders. Depending on the height/diameter ratio, the cylinders may in turn be platelets at one extreme or rods at the other. The orientation of the particles may affect the isotropy of the system.

The size and size distribution of the particles are important variables since they basically control the texture of the material. Together with volume fraction, they also determine the interfacial area, which plays a large part in determining the magnitude of the interaction between the dispersed phase (or phases) and the continuous phase.

Concentration is usually measured in terms of volume or weight fraction. The concentration distribution describes the extent to which the phases are mixed and is the most important single measure of the homogeneity of the system.

In the usual derivation of the differential equation describing heat conduction the assumption of homogeneity is made without providing any criterion to determine when this assumption is valid:

$$\frac{\partial T}{\partial t} = \alpha \nabla^2 T, \tag{1}$$

where

$$\alpha = \frac{k}{\rho C} \tag{2}$$

is called the thermal diffusivity, k is the thermal conductivity, ρ is the density and C is the specific heat at constant pressure. Although numerous unsteady-state measurements of the thermal diffusivity of heterogeneous materials have been made, the relationship of the thermal diffusivity of the heterogeneous system to that of the individual phases is not clear. In fact, strictly speaking, one cannot speak of the thermal diffusivity as a characteristic property of a heteroge-

[1] Present address: Dyess Air Force Base, TX 79607

Contributed by the Heat Transfer Division for publication in the JOURNAL OF HEAT TRANSFER. Manuscript received by the Heat Transfer Division November 23, 1977.

neous material since the differential equation in which the thermal diffusivity appears as a characteristic constant applies only to "homogeneous" materials. In some practical problems, however, the concept of an "effective thermal diffusivity" which controls the gross temperature at some specified boundary appears to be useful.

The concept of the thermal diffusivity as a characteristic constant of a heterogeneous material was examined by Kerrisk [1, 2]. He obtained criteria for nonhomogeneity of the material under certain transient conditions including those normally encountered in the flash diffusivity technique [3]. The criterion limits the practical size of the particulate phase to be much smaller than the sample thickness for the sample to be considered sufficiently homogeneous so that the usual relation between the thermal diffusivity and thermal conductivity holds. Lee and Taylor [4] successfully measured the thermal diffusivity of samples containing particles whose diameter was 50 times Kerrisk's upper limit. Their results showed that the concept of an effective thermal diffusivity is valid at least for particle-to-matrix diffusivity ratios between 1 and 3.5 and volume specific heat ratios between 0.02 to 0.63 in randomly dispersed composites containing up to 30 volume percent of dispersed particles.

The advantage of considering a heterogeneous material as homogeneous for a transient thermal problem is that the concept of thermal diffusivity $\alpha = k/\rho C$, can be applied. Since the thermal diffusivity is inherently much easier to measure than thermal conductivity, this is an important advantage from the experimenter's viewpoint. Theories and models exist for calculating steady-state properties including the thermal conductivity [5, 6] of heterogeneous materials; thus, the validity of an effective thermal diffusivity in the unsteady-state heat transfer problem in a heterogeneous material can be tested.

The purpose of the present study in this area is to investigate dispersed systems by measuring the thermal diffusivity using the flash method in order to explore the limitations of the concept of effective thermal diffusivity as a characteristic constant of a heterogeneous material in terms of the volume fraction of particles, particle geometry, particle size, and ratios of the property values of the particles and matrix.

Experimental Method and Apparatus

The flash (pulse) method [3] of measuring thermal diffusivity was employed. A small, uniform, thermally-insulated sample initially at a constant temperature receives a very short burst of radiant energy at one (front) surface and the transient temperature history of the opposite (back) surface is recorded, the resulting data contain information related to the thermal diffusivity of the sample. The source of the radiant energy is a laser and irradiation times are of the order of one ms or less. Experimentally, the flash method is characterized by its great simplicity, by requiring only a small amount of sample material, and by being readily extended to high temperatures.

The effective thermal diffusivity (α_e) of the sample could be determined from the following equation [7]:

$$\alpha_e = \frac{K_x \ell^2}{t_x} \tag{3}$$

where ℓ is the thickness of the sample, t_x is the time from the initiation of the pulse until the rear face temperature rise reaches x percent of its maximum value and K_x is a constant. For $t_x = t_{1/2}$, $K_x = 0.1389$ [3]. The experimental data (temperature versus elapsed time) were collected using an analog-to-digital converter and a minicomputer-based digital data acquisition system. Values of α were calculated at various percent rises and the experimental data were nondimensionalized and compared on-line to the mathematical model to insure that the initial and boundary conditions were adequately satisfied. A copy of a typical on-line display for an epoxy-copper sphere sample is given in Fig. 1. The ordinate is normalized temperature (temperature rise/maximum temperature rise) expressed in percent. The abscissa is normalized time (elapsed time/time to reach one-half maximum temperature rise). The smooth solid line represents the mathematical model in which there are no heat losses, the sample is uniformly heated, and the heat flow is one-dimensional. The actual experimental data are shown by the closely spaced dots up to about $3\frac{1}{2}$ halftimes and by the widely spaced dots thereafter. The close agreement between the experimental data and the mathematical model during the first two halftimes (over 80 percent of the temperature rise) shows that the experiment is valid, i.e., the boundary conditions are being adequately met. This is confirmed by the calculated values of α from 10 to 80 percent which were all within 3 percent of each other. For this particular sample the halftime was 2.7730 s (Fig. 1) so that the laser pulse duration (0.6 ms) is completely negligible. After about 6 s heat losses to the surroundings become significant as shown by the deviation of the dots from the mathematical model, but since the diffusivity values are all calculated within the first 5 s, this deviation has no significance. The situation illustrated in Fig. 1 was observed for all experimental data observed as part of this paper. A critical evaluation of the errors associated with the flash method has been given by Taylor [7].

The experimental apparatus for the flash method has been described elsewhere [8]. For the temperature measurement at the rear face of the sample, a plate containing the sample holder was attached to a single spring-loaded thermocouple assembly. The spring-loaded thermocouple assembly was movable horizontally so as to press the probe of the thermocouple against the sample surface or to remove it. Also, the sample holder in the plate was adjustable; therefore, the probe could be positioned at any desired position on the rear sample surface. The output of the thermocouple detector was connected to an oscilloscope for visual checking and was also connected to an analog-to-digital converter which, in turn, was connected to the digital data acquisition system. The time response of the thermocouple and its associated electronics was checked and found to be less than 20 ms for the present samples.

The experimentally measured values of effective thermal diffusivity $(\alpha_e)_{\text{exp}}$ for the dispersed samples were obtained by averaging the diffusivity values measured by a thermocouple placed at different locations on the sample's rear surface. These locations were based on a hexagonal pattern and at the center location on the back face of the samples. The thermal diffusivity value for each run was obtained using Taylor's extrapolation method [8]: calculations of α values similar to the usual calculations based on the half-time, $t_{0.5}$ (the time required for the temperature response of the back surface to reach half its maximum value, 0.5 $T_{\max}$) were made for $T = 0.2\ T_{\max}$, $T = 0.3\ T_{\max}$, . . . $T = 0.8\ T_{\max}$. The resulting seven values of α were graphed versus the fractional temperature rise and extrapolated back to $T = 0.0\ T_{\max}$, the zero percentage rise, to obtain an improved value of diffusivity.

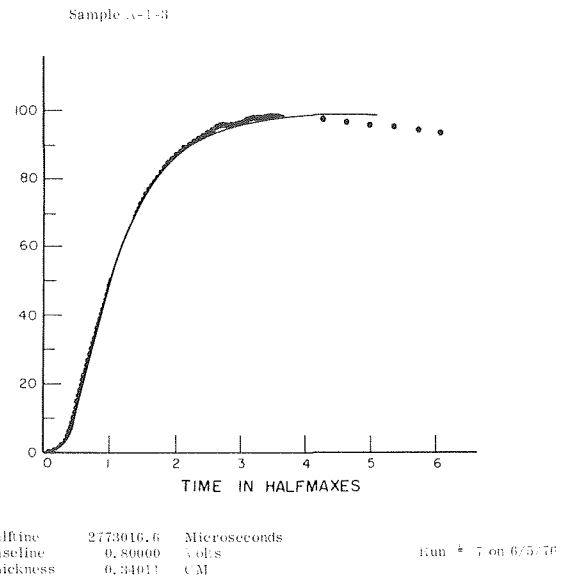

Fig. 1 Comparison of experimental data to mathematical model (sample A-1-3)

The seven measured α values used to obtain an averaged α for samples were always within ±5 percent and usually within ±3 percent of the averaged values.

Sample Descriptions

We shall designate Type A for copper spheres with diameter sized from 250 to 595 μm dispersed in epoxy resin, Type B, for steel shot with diameter sizes from 279 to 584 μm dispersed in epoxy resin, Type C, for copper spheres with diameter sizes from 250 to 595 μm dispersed in Indalloy No. 8, and Type D, for steel shot with diameter sizes from 432 to 584 μm dispersed in Indalloy No. 8. The epoxy resin was fabricated by mixing two parts resin 600 with one part hardener No. 66 and five weight percent black color paste 502 and curing for two days. Indalloy No. 8 is a fusible alloy, which is composed of 44 In, 42 Sn, 14 Cd, all in weight percent and has an eutectic point at 93°C. The properties of the sample materials are given in Table 1. The samples are described in detail elsewhere [9]. All samples were 1.27 cm dia and from 0.25 to 0.40 cm thick. The volume fraction of copper spheres in the epoxy matrix ranged from 1.8 to 28.6 percent; and in the indalloy matrix they ranged from 1.9 to 29.8 percent. The volume fraction of steel shot in the epoxy matrix ranged from 2.1 to 33.2 percent and in the indalloy matrix they ranged from 5.6 to 35.0 percent. The particles were reasonably uniform in diameter. Techniques were developed using clear epoxy to insure random particle dispersion in the epoxy-based samples and solidification occurred so rapidly in the indalloy-based samples that randomness was assured.

Experimental Results

Two calculated values of effective thermal diffusivities $(\alpha_e)_{cal}$ of the samples were obtained from $\alpha_e = k_e/C_e\rho_e$ where the subscript e represents the effective properties, one using the calculated effective thermal conductivity from the Rayleigh-Maxwell equation [10, 11]:

$$\frac{k_e}{k_c} = \frac{2 - 2v_d + (1 + v_d)k_d/d_c}{2 + v_d + (1 - v_d)k_d/k_c}, \tag{4}$$

and one from the Bruggeman variable-dispersion equation [12]:

$$\frac{k_e - k_d}{k_c - k_d}\left(\frac{k_c}{k_e}\right)^{1/3} = 1 - v_d, \tag{5}$$

along with the calculated effective volumetric heat capacity,

$$C_e\rho_e = v_cC_c\rho_c + v_dC_d\rho_d \tag{6}$$

where v is the volume fraction, the subscript c represents the continuous phase, and the subscript d represents the dispersed particles.

Figs. 2–5 show the plot of experimentally measured thermal diffusivity values for Types A–D composites versus volume percent of dispersed particles. In these figures, there are curves for the calculated effective thermal diffusivity values based on the Rayleigh-Maxwell equation (equation [4]), and on the Bruggeman Variable-dispersion equation (equation [5]).

Table 1 Thermophysical properties of matrix and particles at 300 K

Material Property	Copper	Steel† Shot	Epoxy Resin	Indalloy No. 8
Density (g cm^{-3})	8.94	7.801	1.13	7.45
Specific heat (Jg^{-1} K^{-1})	0.384	0.473	1.46	0.231
Thermal Conductivity (W cm^{-1} K^{-1})	3.982	0.430	0.00168	0.419
Thermal Diffusivity (cm^2 s^{-1})	1.16	0.116	0.00102	0.243

† Literature values; other values were measured.

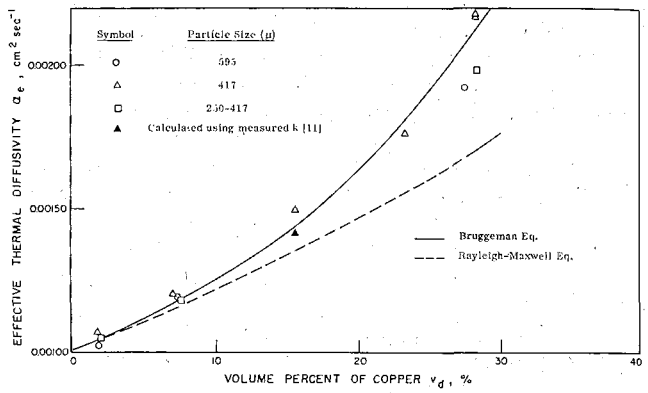

Fig. 2 Effective thermal diffusivity of copper sphere—epoxy resin composites (type A) versus volume percent of copper

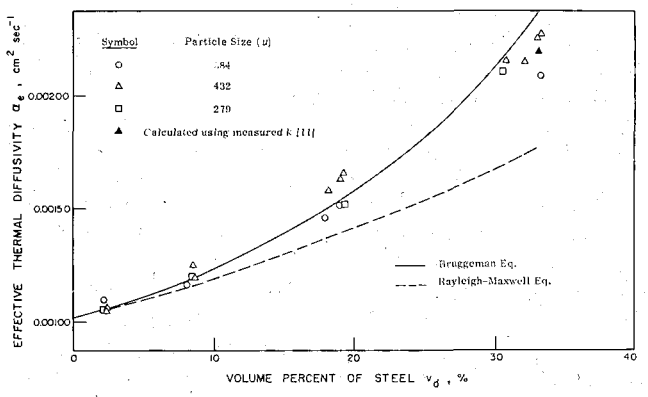

Fig. 3 Effective thermal diffusivity of steel shot—epoxy resin composites (type B) versus volume percent of steel

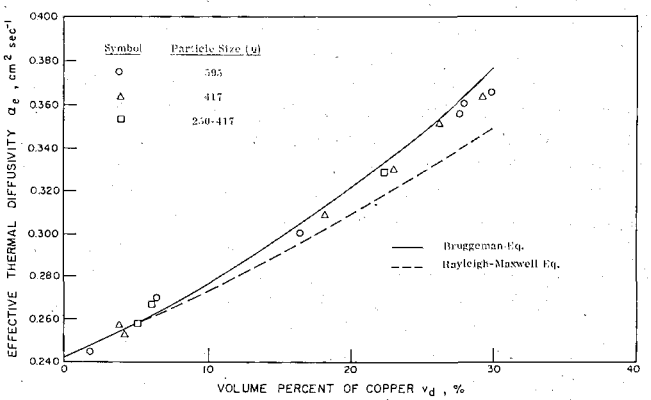

Fig. 4 Effective thermal diffusivity of copper sphere—indalloy No. 8 composites (type C) versus volume percent of copper

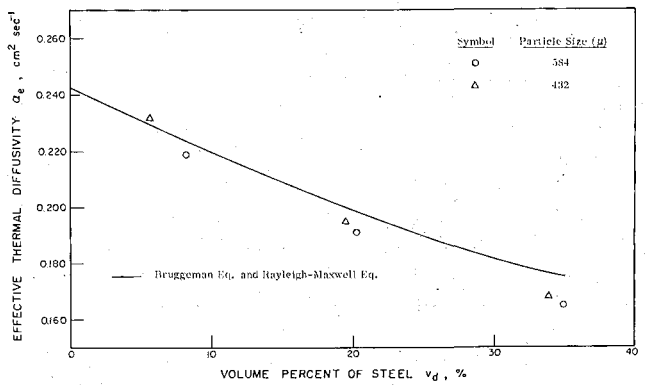

Fig. 5 Effective thermal diffusivity of steel shot—indalloy No. 8 composites (type D) versus volume percent of steel

The effective thermal conductivity of three samples were measured by using a steady-state hot plate method [14]. These samples were 15.74 and 28.55 percent volume fraction of 417 μm dia copper sphere-epoxy resin, and 33.06 percent volume fraction of 432 μm dia steel shot-epoxy resin composites. The deviations[2] of thermal diffusivity calculated from these measured conductivity values and effective values of C_e and ρ_e, from the directly measured effective thermal diffusivity are 5.3, −0.5, and 3.1 percent, respectively. These results are also shown in Figs. 2 and 3 as solid triangles.

Conclusion

The effective thermal diffusivities at room temperature of all the dispersed samples of four different types were successfully measured using the flash method. This conclusion is based on the close agreement between the experimental values measured at seven different positions on the rear face of each sample as well as the general trend of the data as a function of increasing volumes of dispersed phase. This conclusion was confirmed independently by measuring values of the effective thermal conductivity using a hot-plate apparatus. Therefore, these nonhomogeneous samples may be considered homogeneous for transient state heat conduction problems.

The experimental values were compared to those calculated using the Raleigh-Maxwell and Bruggeman-variable dispersion equations. These two equations give similar results at small particle volume fractions. At a particle volume fraction greater than 10 percent, the Bruggeman-variable-dispersion equation gives a better prediction of the effective thermal diffusivity values.

From the present experimental data and the previous studies [1, 2, 4], the criteria for the homogeneity of the heterogeneous material can be represented in terms of the property ratio of particle-to-matrix, such as α_d/α_c; k_d/k_c; and $(\rho_d C_d v_d)/(\rho_c C_c v_c)$, geometrical ratio, such as ℓ/D; nD/ℓ, where n is the total number of particles in the sample thickness direction and D is the diameter of the particle, and the concentration of the particles, such as volume fraction of the dispersed particle v_d. Values of the various ratios investigated are given in Table 2. The present work combined with previous results show that the concept of effective thermal diffusivity is valid for ratios of 0.48–1137 for α_d/α_c; 0.02–1.16 for $(\rho_d C_d v_d)/(\rho_c C_c v_c)$; 3.8–2857 for ℓ/D; 0.23–0.88 for nD/ℓ and 0.12–34 for v_d. It should be noted that these ranges of the variables are not necessarily the lower and upper bounds for heterogeneous materials to be considered as being homogeneous. In any event the degree of nonhomogeneity which can be tolerated and still yield meaningful thermal diffusivity values by using the flash method is far beyond the situations in which it is currently being applied. A three-dimensional representation of the magnitude of the variables studied is drawn in Fig. 6 using log (α_d/α_c), nD/ℓ, and $(\rho_d C_d v_d)/(\rho_c C_c v_c)$ as the orthogonal axes. All the volume represented by the box meets the criteria for sufficient homogeneity for effective diffusivity to be meaningful.

The dependence of the effective thermal diffusivity on the volume fraction of the dispersed particle is quite obvious from the results. For the solid dispersed phase, the effective thermal diffusivity increases as the volume fraction of particle increases when the property ratio α_d/α_c is larger than 1.0 (Figs. 2–4). On the other hand, the effective thermal diffusivity decreases as the volume fraction of particle increase α_d/α_c is less than 1.0 (Fig. 5). The rate of increase or decrease is dependent upon the magnitude of α_d/α_c.

The fact that the particle size and shape have no influence at room temperature on the effective thermal diffusivity is confirmed by the present work (various diameter particle) and by Lee and Taylor's [4] results (various shape particles). It should be noted that this observation would not be valid at cryogenic temperatures where particle size and shape are important [14] because the phonon mean free path becomes limited by the particle boundary.

Acknowledgments

The authors would like to express their thanks to Weldon Vaughn for machining samples. They also wish to acknowledge the help of Hans Groot in the experimental work. This work was performed as part of an NSF grant administered by the Engineering Division.

References

1 Kerrisk, J. F., "Thermal Diffusivity of Heterogeneous Materials," *Journal of Applied Physics*, Vol. 42, No. 1, Jan. 1971, pp. 267–271.

2 Kerrisk, J. F., "Thermal Diffusivity of Heterogeneous Materials II. Limits of the Steady-State Approximation," *Journal of Applied Physics*, Vol. 43, No. 1, Jan. 1972, pp. 112–117.

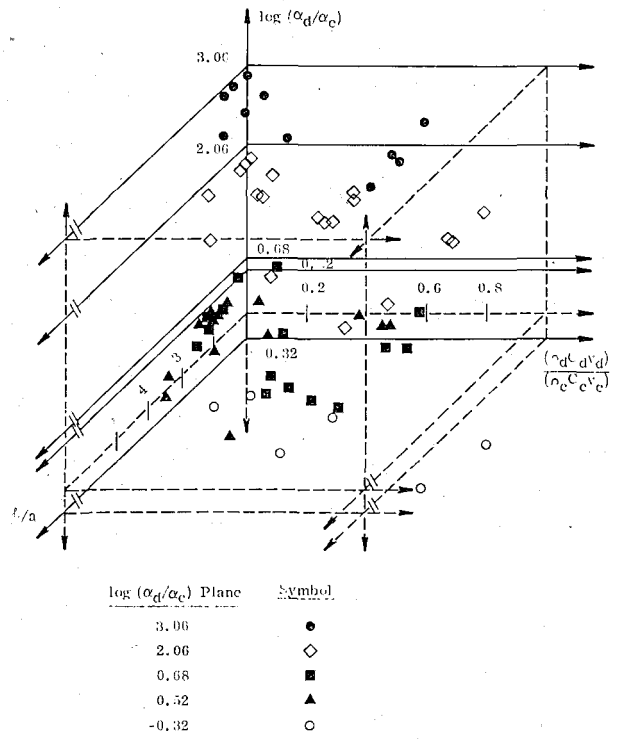

Fig. 6 Three-dimensional representation for criteria of homogeneity

[2] Deviation, percent $= \frac{(\alpha_e)_{exp} - (\alpha_e)_{cal}}{(\alpha_e)_{cal}} \times 100.$

Table 2 Ratios of various properties considered for flash diffusivity samples

Investigators	α_d/α_c	k_d/k_c	$(\rho_d C_d v_d)/(\rho_c C_c v_c)$	ℓ/D	$*nD/\ell$	v_d, percent
Kerrisk [1, 2]	—	—	—	200–2857	0.46–0.58	5–10
Lee and Taylor [4]	3.3	5.1	0.02–0.63	3.8–11.6	0.23–0.82	0.12–29
Hanley [14]	—	—	—	3–38	—	—
Present study	0.48–1137	9.5–2370	0.04–1.16	4.3–10.3	0.32–0.88	0.18–34

* $n = \left[\frac{v_d \ell^3}{(4/3)\pi(D/2)^2}\right]^{1/3}$: total number of particles in the sample thickness direction.

3 Parker, W. J., Jenkins, R. J., Butler, C. P., and Abbott, G. L., "Flash Method of Determining Thermal Diffusivity, Heat Capacity, and Thermal Conductivity," *Journal of Applied Physics,* Vol. 32, No. 9, Sept. 1961, pp. 1679–84.

4 Lee, H. J., and Taylor, R. E., "Thermal Diffusivity of Dispersed Composites," *Journal of Applied Physics,* Vol. 47, No. 1, Jan. 1976, pp. 148–151.

5 Flynn, D. R., "Mechanical and Thermal Properties of Ceramics," National Bureau of Standards Special Publication No. 303, 1969, pp. 63.

6 Powers, A. E., "Conductivity in Aggregates," Knolls Atomic Power Report KAPL 2145, General Electric Company, March 6, 1961.

7 Taylor, R. E., "Critical Evaluation of Flash Method for Measuring Thermal Diffusivity," *Revue Internationale des Hautes Temperatures et des Refractaires,* Vol. 12, No. 2, 1975, pp. 141–145.

8 Taylor, R. E., "Improvements in Data Reduction for the Flash Diffusivity Method," *Advances in Thermal Conductivity,* University of Missouri, Rolla, (publisher), Reisbig, R. L., and Sauer, H. J., ed., 1974, pp. 416–23.

9 Lee, T. Y. R., "Thermal Diffusivity of Dispersed and Layered Composites," Ph.D. Thesis, School of Mechanical Engineering, Purdue University, Aug. 1977.

10 Rayleigh, L., "On the Influence of Obstacle Arranged in Rectangular Order Upon the Properties of a Medium," *Philosphical Magazine,* Vol. 34, Series 6, Dec. 1892, pp. 481–502.

11 Maxwell, J. C., "*A Treatise on Electricity and Magnetism*," 3rd ed., Oxford University Press, Oxford, England, 1904, pp. 435–40.

12 Bruggeman, D. A. G., "Berechnung verschiedener physikalischer Konstanten von heterogenen Substanzen, I. Dielektrizitatskonstanten und Leitfahigkeiten der Mischkorper aus isotropen Substanzen" *Annalen der Physik,* Band 24, 5 Folge, Nov. 1935, pp. 636–664.

13 Cunnington, G. R., Private Communication, Palo Alto Research Laboratory, Lockheed Space and Missile Company, Palo Alto, Calif. March 1977.

14 Hanley, E. J., DeWitt, D. P., and Taylor, R. E., "The Thermal Transport Properties at Normal and Elevated Temperature of Eight Representative Rocks," *Proceedings of the Seventh Symposium on Thermophysical Properties,* ASME Cezairliyan, A., ed., in publication.

15 Garrett, K. W., and Rosenburg, H. M., "The Thermal Conductivity of Epoxy-Resin/Powder Composite Material," *Journal of Physics D. Applied Physics,* Vol. 7., No. 9, 1974, pp. 1247–1258.

journal of heat transfer

technical notes

This section contains shorter technical papers. These shorter papers will be subjected to the same review process as that for full papers.

Laminar Free Convection Heat Transfer through Horizontal Duct Connecting Two Fluid Reservoirs at Different Temperatures

A. Bejan[1] and C. L. Tien[2]

This technical note develops an analytical result for heat transfer by laminar free convection in a long horizontal parallel-plate channel connecting two reservoirs containing the same fluid but kept at different temperatures. The analysis is based on the integral method. The Nusselt number result is presented in chart form in terms of the Rayleigh number based on height, Ra, and the height/length aspect ratio, h/L.

Introduction

Elsewhere in this issue [1] we discussed the free convection heat transfer mechanism in a rectangular horizontal enclosure with the long boundaries insulated and the two vertical end-walls maintained at different temperatures. The purpose of this brief technical note is to cast some light on a related phenomenon which occurs in a slightly different geometry, namely, a long horizontal duct connecting two reservoirs which contain the same fluid but are at different temperatures. To these authors' knowledge, this phenomenon has not been dealt with in the literature. However, it is encountered in cryogenic engineering where heat leaks by free convection or other mechanisms constitute a major concern. To avoid heat leaks by free convection between fluid reservoirs at sharply different temperatures, the duct connecting the two spaces is oriented vertically with the warmer space positioned on top whenever possible. As a result, the fluid column filling the duct is thermally stratified. This is the case of most fill and vent tubes of storages vessels for cryogenic liquids. There are cases, however, when the link between the two reservoirs cannot be positioned any way but horizontally. In such cases, the horizontal duct may serve as thermosiphon between the two reservoirs, the avenue for substantial convective heat transfer. An example of such a system is the fill and vent ducting for liquid helium filled spaces provided for rotating superconducting windings [2]. The ducting in such systems is usually positioned parallel to the axis of rotation, which is equivalent to a horizontal orientation in a strong gravitational field.

In what follows, we examine the heat transfer by laminar natural convection between two reservoirs linked via a two-dimensional, parallel-plate, channel with the top and bottom walls insulated (see Fig. 1). For brevity, we found it convenient to tie this presentation to our work on horizontal enclosures [1]. For this reason we shall frequently refer to the nomenclature and mathematical apparatus used in [1] without repeating it here.

The Ra → O Regime

We begin with the observation that as Ra → 0, the heat transfer rate through the channel of Fig. 1 is also given by equation (20) derived in [1]. We recall now that the Ra → 0 regime is characterized by a very small temperature variation in the vertical direction, $\Delta T \ll 1$. The free convection pattern sketched in Fig. 1 is independent on whether or not the extreme ends are open or closed as in [1]. The important feature of the Ra → 0 limit is that the heat transfer rate through the channel is limited by the excellent thermal contact present between the upper and lower branches of the counterflow.

The question we address analytically in the following section is what changes might occur in the counterflow of Fig. 1 if, for fixed h/L, the Rayleigh number increases. It is easy to foresee that the higher the Rayleigh number, the more evident will be the presence of open ends at $x^* = 0, L$. Specifically, we foresee entrance regions developing near the two diametrically opposed entrance corners, ($x = 0, y = 0$) and ($x = L, y = h$). In these regions, the fluid entering from one reservoir or the other will remain isothermal for some length before feeling the effect of thermal diffusion in the y-direction, across the counterflow.

The Flow in the Open End Region

Consider the cold end region shown in Fig. 1. We are interested in estimating the extent of the entrance region Δ, i.e. the point beyond which the core regime (equations (14–16) in [1]) is valid. The analysis proceeds on a path similar to the integral method employed in the "intermediate regime" section of [1]. Integrating the energy and momentum equations once, from $y = 0$ to $y = 1$, we find

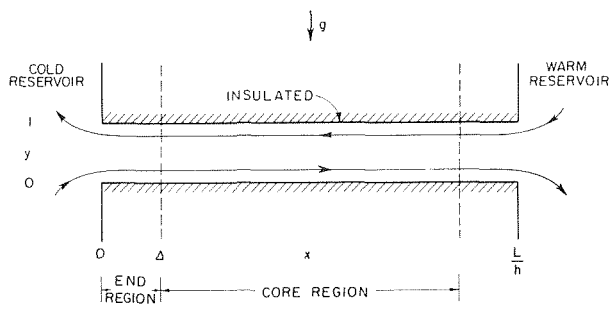

Fig. 1 Schematic of counterflow pattern in horizontal parallel plate channel connecting two differentially heated fluid reservoirs

[1] Assistant Professor. Department of Mechanical Engineering, University of Colorado, Boulder, Colo. 80309.

[2] Professor, Department of Mechanical Engineering, University of California, Berkeley, Calif. 94720.

Contributed by the Heat Transfer Division for publication in the JOURNAL OF HEAT TRANSFER. Manuscript received by the Heat Transfer Division, April 5, 1978.

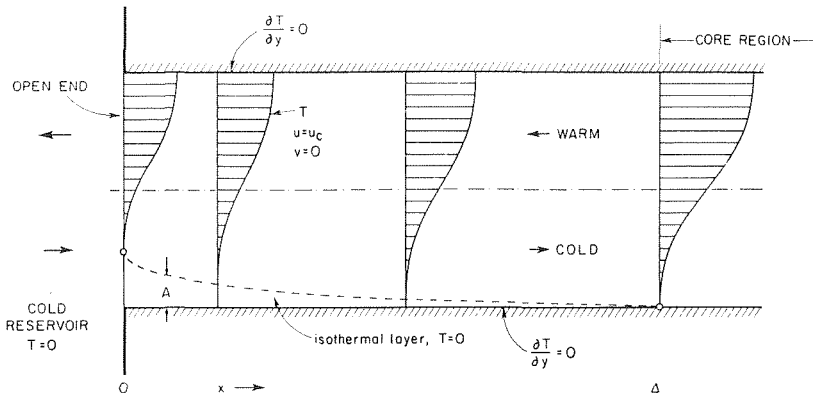

Fig. 2 Developing temperature profile in the open end region located near the cold reservoir

$$\frac{d}{dx}\int_0^1 uT\,dy = \frac{d^2}{dx^2}\int_0^1 T\,dy \tag{1}$$

$$\left|\frac{\partial^2 u}{\partial y^2}\right|_{y=0}^{y=1} = \mathrm{Ra}\frac{d}{dx}\int_0^1 T\,dy \tag{2}$$

Equations (1, 2) constitute the two integral constraints, energy and momentum, to be satisfied by the flow and temperature field at any x in the open end region. In writing these equations, we have already assumed that the flow in this region is parallel, i.e., $v = 0$. The next step consists of substituting reasonable u and T profiles into equations (1, 2). This procedure is similar to the integral method of solution developed by Lighthill for free convection in vertical tubes with the top end cooler than the bottom end [3].

Our choice of axial velocity and temperature profiles is better explained with the help of Fig. 2, which shows the open end located at the low temperature extremity of the channel, $x = 0$. The sketch shows also a layer of isothermal fluid ($T = 0$) whose thickness $A(x)$ gradually decreases as the cold stream advances from left to right towards the core region. The isothermal layer represents that portion of the entering branch which has not been effected by the warmer stream running in counterflow above it. A temperature distribution which embodies this feature along with the adiabatic wall conditions at $y = 0, 1$ is

$$T = \begin{cases} B(x)\cdot F\left(\dfrac{y-A}{1-A}\right), & A < y < 1 \\ 0 \qquad\qquad , & 0 < y < A \end{cases}, \tag{3}$$

where $F(z) = z^5/120 - z^4/48 + z^3/72$ is the function expressing the y dependence of the temperature profile in the core region, equation (16) in [1]. The unknown function $B(x)$ is proportional to the temperature along the top wall of the open end region. The temperature profile was chosen so that at the end of the developing region, $x = \Delta$, it matches the core distribution

$$B = K_1^2\mathrm{Ra},\ A = 0,\ K_1\Delta + K_2 = 0, \text{ when } x = \Delta. \tag{4, 5, 6}$$

Regarding the interaction between the channel flow and the flow in the infinite reservoir, it is assumed that the isothermal thickness A begins to decrease infinitely fast right at mouth of the channel, i.e.,

$$dA/dx \to -\infty \text{ as } x \to 0. \tag{7}$$

Selection of the axial velocity profile relies on limiting the discussion to fluids with Prandtl numbers of the order of unity or greater. We notice that the velocity boundary layer developing along the $y = 0$ wall of the channel has to grow to a thickness of roughly $h/4$ before the core velocity distribution is achieved. At the same time, the thermal boundary layer must grow twice as much, i.e., to approximately $h/2$. This observation, added to the limitation regarding the Prandtl numbers of interest, suggests that the open-end length is dictated by the thermal entrance length Δ. For all practical purposes, the flow in the end region is a shear flow confined between two parallel plates with an axial velocity distribution well approximated by the core velocity profile, equation (14) in [1].

Based on the above choice of u and T profiles, the integral conditions (1) and (2) provide a system of differential equations for $A(x)$ and $B(x)$, namely

$$\frac{d}{dx}\left[B(1-A)^2\left(1 + 13A - \frac{37}{2}A^2\right)\right] = 0 \tag{8}$$

$$\frac{d}{dx}\left[B(1-A)\right] = 1440\,K_1. \tag{9}$$

We are primarily interested in the unknown function $A(x)$ in order to determine the extent of the entrance region, Δ. Using conditions (4, 5) and (7) to eliminate the two constants resulting from integrating (8) and (9) we obtain finally

$$(1-A)\left(1 + 13A - \frac{37}{2}A^2\right) = \left[\frac{1440x}{K_1\mathrm{Ra}} + 0.431\right]^{-1}. \tag{10}$$

Setting $A(\Delta) = 0$ and $x = \Delta$ in equation (10) yields the entrance region length

$$\Delta = 0.569\frac{K_1\mathrm{Ra}}{1440}. \tag{11}$$

Result (10) has already been sketched on Fig. 2 which presents a succession of temperature profiles at various locations along the end region. The isothermal layer thickness $A(x)$ has the maximum $A = 0.242$ at $x = 0$, about half the value we would have expected. The discrepancy is due to the temperature profile chosen, equation (3), which for all x's is very flat ($\partial^2 T/\partial y^2 = 0$) right above $y = A$. In spite of this discrepancy, at the mouth $x = 0$ the isothermal layer practically fills the entire bottom half of the channel.

The entrance region length Δ, equation (11), increases as the Rayleigh number increases. Since the overall length L is fixed, the length filled by the core regime gradually diminishes. There comes a point where the Rayleigh number is so high that the left and right end regions completely do away with the core. This condition is reached when

$$\Delta > \frac{1}{2}\cdot\frac{L}{h}. \tag{12}$$

The Nusselt Number

We can now estimate the heat transfer rate through the channel when Ra is high enough so that entrance region length Δ is no longer negligible as in the Ra $\to$ 0 regime. The information required for estimating the Nusselt number, equation (17) in [1], was already developed in the preceeding section. Parameters K_1, K_2 and Δ are

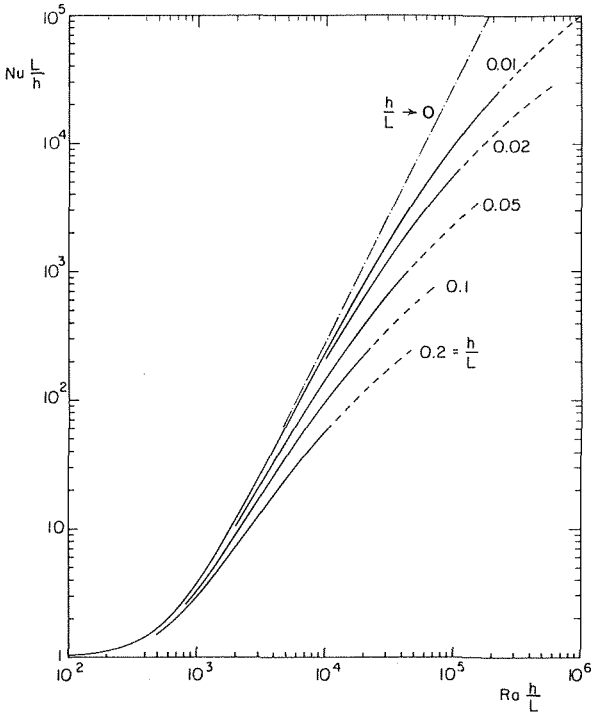

Fig. 3 Chart showing the Nusselt number as a function of Ra and h/L

uniquely determined from equations (6) and (11) plus the centrosymmetry conditions, equation (28) in [1]. Skipping the algebra associated with finding K_1 as a function of h/L and Ra and using this result in the Nusselt number formula (17) of [1], in Fig. 3 we show the resulting Nu (h/L, Ra) chart. As we might have expected, for the same Ra and h/L, the Nusselt number is consistently higher than for a shallow cavity (Fig. 5 in [1]). This is due to the absence of the two vertical walls and the boundary-layer thermal resistance associated with them.

The limitation concerning the end region length Δ, equation (12), is also indicated on Fig. 3. The h/L-Ra domain where the core regime ceases to exist in the middle portion of the channel is shown by dotted lines.

The analytical results reported in this note depend on the validity of the flow pattern assumed for this study and sketched on Fig. 1. As mentioned earlier, no experimental data exist on this free convection phenomenon. However, there exists sufficient evidence derived from related phenomena to suggest that the laminar counterflow of Fig. 1 is realistic. For example, the numerical simulations of Cormack, et al. [4] and the experimental results reported by Imberger [5] for free convection in horizontal cavities with different end temperatures proved conclusively that when the Rayleigh number is small, the horizontal space is filled by a parallel counterflow structure. In this limit, the end flow effect is unimportant, the core flow being driven by the longitudinal temperature (density) gradient established in the fluid. Regarding the counterflow pattern through the open end region, Figs. 1 and 2, the situation is similar to the counterflow through an open window of a room on fire. Considerable experimental and theoretical work on this phenomenon was conducted by Brown and Solvason [6].

Acknowledgment

This work was supported in part by a postdoctoral fellowship awarded to A. Bejan by the Miller Institute for Basic Research in Science, University of California, Berkeley.

References

1 Bejan, A., Tien, C. L., "Laminar Natural Convection Heat Transfer in a Horizontal Cavity with Different End Temperatures," ASME JOURNAL OF HEAT TRANSFER, Vol. 100, 1978.

2 Bejan, A., "Refrigeration for Rotating Superconducting Windings of Large AC Electric Machines," *Cryogenics*, Vol. 16, 1976, pp. 153–159.

3 Lighthill, M. J., "Theoretical Considerations on Free Convection in Tubes," *Journal of Mechanics and Applied Mathematics*, Vol. 6, 1953, pp. 398–439.

4 Cormack, D. E., Leal, L. G., Seinfeld, J. H., "Natural Convection in a Shallow Cavity with Differentially Heated End Walls. Part 2. Numerical Solutions," *Journal of Fluid Mechanics*, Vol. 65, 1974, pp. 231–246.

5 Imberger, J., "Natural Convection in a Shallow Cavity with Differentially Heated End Walls, Part 3. Experimental Results," *Journal of Fluid Mechanics*, Vol. 65, 1974, pp. 247–260.

6 Brown, W. G., Solvason, K. R., "Natural Convection through Rectangular Openings in Partitions—1. Vertical Partitions," *International Journal of Heat and Mass Transfer*, Vol. 5, 1962, pp. 859–868.

Turbulent Heat Transfer by Free Convection from a Rough Surface

K. Ramakrishna[1], K. N. Seetharamu[2] and P. K. Sarma[3]

Nomenclature

C_1, C_2, n, p = constants in equations (11) and (12)
C_3 = constant in equation (17)
C_p = specific heat of the fluid at constant pressure
e = absolute roughness
f = nondimensional friction factor = $\tau_w/1/2\rho u_1{}^2$
g = acceleration due to gravity
h = heat transfer coefficient

$$\text{Gr} = \text{Grashof number} = \left(\frac{g\beta\Delta T x^3}{\nu^2}\right)$$

K = thermal conductivity of the fluid
L = length of the pipe

$$\text{Nu} = \text{Nusselt number} = \frac{hx}{K}$$

Pr = Prandtl number
q = heat flux
T = temperature
ΔT = temperature difference ($T - T_\infty$)
u = velocity of the fluid in x-direction
u_1 = representative velocity of the fluid
v = velocity of the fluid in y-direction
x = distance in the direction parallel to the surface from the leading edge
y = coordinate perpendicular to x-direction
β = coefficient of volumetric expansion
τ = shear stress
ρ = density of the fluid

$$\theta = \text{nondimensional temperature} = \frac{(T - T_\infty)}{(T_w - T_\infty)}$$

α = thermal diffusivity
δ = boundary layer thickness
ν = kinematic viscosity

[1] No. 2 Evans Apt., 1429 Laramie, Manhattan, KS 66502
[2] Heat Transfer and Thermal Power Laboratory, Department of Mechanical Engineering, Indian Institute of Technology, Madras-600 036, India
[3] Department of Mechanical Engineering, High Petroleum Institute, Tobruk. Libya

Contributed by the Heat Transfer Division for publication in the JOURNAL OF HEAT TRANSFER. Manuscript received by the Heat Transfer Division May 10, 1977.

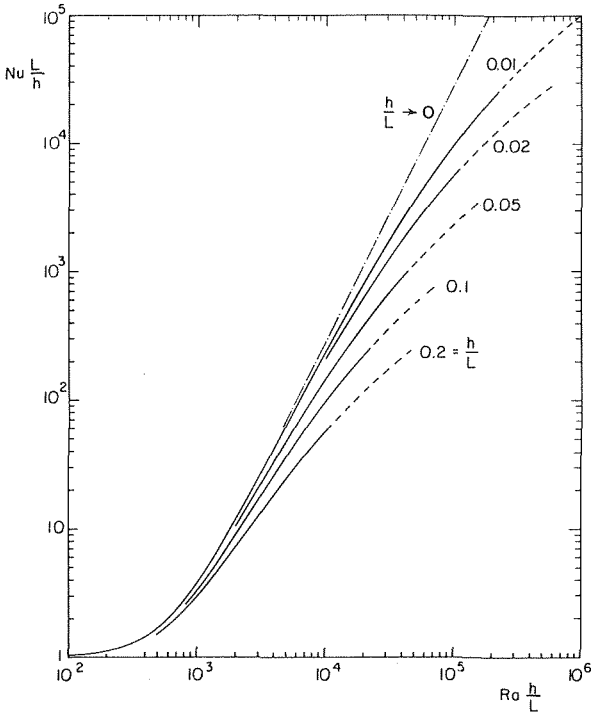

Fig. 3 Chart showing the Nusselt number as a function of Ra and h/L

uniquely determined from equations (6) and (11) plus the centrosymmetry conditions, equation (28) in [1]. Skipping the algebra associated with finding K_1 as a function of h/L and Ra and using this result in the Nusselt number formula (17) of [1], in Fig. 3 we show the resulting Nu (h/L, Ra) chart. As we might have expected, for the same Ra and h/L, the Nusselt number is consistently higher than for a shallow cavity (Fig. 5 in [1]). This is due to the absence of the two vertical walls and the boundary-layer thermal resistance associated with them.

The limitation concerning the end region length Δ, equation (12), is also indicated on Fig. 3. The h/L-Ra domain where the core regime ceases to exist in the middle portion of the channel is shown by dotted lines.

The analytical results reported in this note depend on the validity of the flow pattern assumed for this study and sketched on Fig. 1. As mentioned earlier, no experimental data exist on this free convection phenomenon. However, there exists sufficient evidence derived from related phenomena to suggest that the laminar counterflow of Fig. 1 is realistic. For example, the numerical simulations of Cormack, et al. [4] and the experimental results reported by Imberger [5] for free convection in horizontal cavities with different end temperatures proved conclusively that when the Rayleigh number is small, the horizontal space is filled by a parallel counterflow structure. In this limit, the end flow effect is unimportant, the core flow being driven by the longitudinal temperature (density) gradient established in the fluid. Regarding the counterflow pattern through the open end region, Figs. 1 and 2, the situation is similar to the counterflow through an open window of a room on fire. Considerable experimental and theoretical work on this phenomenon was conducted by Brown and Solvason [6].

Acknowledgment

This work was supported in part by a postdoctoral fellowship awarded to A. Bejan by the Miller Institute for Basic Research in Science, University of California, Berkeley.

References

1 Bejan, A., Tien, C. L., "Laminar Natural Convection Heat Transfer in a Horizontal Cavity with Different End Temperatures," ASME JOURNAL OF HEAT TRANSFER, Vol. 100, 1978.

2 Bejan, A., "Refrigeration for Rotating Superconducting Windings of Large AC Electric Machines," *Cryogenics*, Vol. 16, 1976, pp. 153–159.

3 Lighthill, M. J., "Theoretical Considerations on Free Convection in Tubes," *Journal of Mechanics and Applied Mathematics*, Vol. 6, 1953, pp. 398–439.

4 Cormack, D. E., Leal, L. G., Seinfeld, J. H., "Natural Convection in a Shallow Cavity with Differentially Heated End Walls. Part 2. Numerical Solutions," *Journal of Fluid Mechanics*, Vol. 65, 1974, pp. 231–246.

5 Imberger, J., "Natural Convection in a Shallow Cavity with Differentially Heated End Walls, Part 3. Experimental Results," *Journal of Fluid Mechanics*, Vol. 65, 1974, pp. 247–260.

6 Brown, W. G., Solvason, K. R., "Natural Convection through Rectangular Openings in Partitions—1. Vertical Partitions," *International Journal of Heat and Mass Transfer*, Vol. 5, 1962, pp. 859–868.

Turbulent Heat Transfer by Free Convection from a Rough Surface

K. Ramakrishna[1], K. N. Seetharamu[2] and P. K. Sarma[3]

Nomenclature

C_1, C_2, n, p = constants in equations (11) and (12)
C_3 = constant in equation (17)
C_p = specific heat of the fluid at constant pressure
e = absolute roughness
f = nondimensional friction factor = $\tau_w/1/2\rho u_1{}^2$
g = acceleration due to gravity
h = heat transfer coefficient

$$\text{Gr} = \text{Grashof number} = \left(\frac{g\beta\Delta T x^3}{\nu^2}\right)$$

K = thermal conductivity of the fluid
L = length of the pipe

$$\text{Nu} = \text{Nusselt number} = \frac{hx}{K}$$

Pr = Prandtl number
q = heat flux
T = temperature
ΔT = temperature difference ($T - T_\infty$)
u = velocity of the fluid in x-direction
u_1 = representative velocity of the fluid
v = velocity of the fluid in y-direction
x = distance in the direction parallel to the surface from the leading edge
y = coordinate perpendicular to x-direction
β = coefficient of volumetric expansion
τ = shear stress
ρ = density of the fluid

$$\theta = \text{nondimensional temperature} = \frac{(T - T_\infty)}{(T_w - T_\infty)}$$

α = thermal diffusivity
δ = boundary layer thickness
ν = kinematic viscosity

[1] No. 2 Evans Apt., 1429 Laramie, Manhattan, KS 66502
[2] Heat Transfer and Thermal Power Laboratory, Department of Mechanical Engineering, Indian Institute of Technology, Madras-600 036, India
[3] Department of Mechanical Engineering, High Petroleum Institute, Tobruk. Libya

Contributed by the Heat Transfer Division for publication in the JOURNAL OF HEAT TRANSFER. Manuscript received by the Heat Transfer Division May 10, 1977.

Subscripts

w = wall
∞ = infinity
L = mean

Introduction

It has been widely observed that in forced convective flows the roughness of a surface augments heat transfer from the surface. The investigations in this direction in free convection are very few and are either experimental [1] or semi-theoretical [2] in nature. In [2] though a semi-theoretical approach is adopted, no attempt has been made to correlate the experimental data with the theoretical predictions.

In this paper a theoretical analysis is carried out for the prediction of heat transfer from an isothermal, rough, vertical surface through the introduction of a friction factor. A correlation is presented for this friction factor in terms of absolute roughness from the experimental data of [2].

Formulation and Solution

The conservation equations for mass, momentum and energy, applied to a constant property boundary layer are:

$$\frac{\partial u}{\partial x} + \frac{\partial v}{\partial y} = 0 \tag{1}$$

$$\rho\left(u\frac{\partial u}{\partial x} + v\frac{\partial u}{\partial y}\right) = \frac{\partial \tau}{\partial y} + \rho g\beta\Delta T \tag{2}$$

$$u\frac{\partial T}{\partial x} + v\frac{\partial T}{\partial y} = \alpha\frac{\partial^2 T}{\partial y^2} \tag{3}$$

Equations (2) and (3) can be reduced to the integral form along with equation (1).

$$\frac{d}{dx}\int_0^\delta u^2 dy = -\frac{\tau_w}{\rho} + g\beta\Delta T_w\int_0^\delta \theta\, dy \tag{4}$$

$$\frac{d}{dx}\int_0^\delta u\,\theta\, dy = \frac{q_w}{\rho C_p \Delta T_w} \tag{5}$$

The velocity and temperature profiles are chosen as suggested by Eckert and Jackson [3] and are

$$\frac{u}{u_1} = \left(\frac{y}{\delta}\right)^{1/7}[1 - (y/\delta)]^4 \tag{6}$$

$$\theta = [1 - (y/\delta)^{1/7}] \tag{7}$$

From Reynolds analogy we have the following relationship:

$$\frac{q_w}{\tau_w} = \frac{C_p\Delta T_w\,\mathrm{Pr}^{-2/3}}{u_1} \tag{8}$$

where $\tau_w = \frac{1}{2} f\rho u_1^2$. Substitution of equations (6, 7) and (8) in equations (4) and (5) gives

$$0.4185\frac{d}{dx}(u_1^2\delta) = -4\,u_1^2 f + g\beta\Delta T_w\delta \tag{9}$$

$$0.0733\frac{d}{dx}(u_1\delta) = f\,u_1\mathrm{Pr}^{-2/3} \tag{10}$$

The friction factor f can be assumed to be independent of x [4]. In addition to this the following relationships are assumed for u_1 and δ.

$$u_1 = C_1 x^n \tag{11}$$

$$\delta = C_2 x^p \tag{12}$$

The exponents n and p and the constants C_1 and C_2 in equations (11) and (12) are determined using equations (9) and (10) as

$$n = 0.5 \quad \text{and} \quad p = 1.0 \tag{13}$$

$$C_1 = \left[\frac{g\beta\Delta T_w\,\mathrm{Pr}^{-2/3}}{0.837\,\mathrm{Pr}^{-2/3} + 0.439}\right]^{1/2} \tag{14}$$

and

$$C_2 = 9.1\,f\,\mathrm{Pr}^{-2/3} \tag{15}$$

The use of $q_w = h_x\Delta T_w$ and Reynolds analogy gives the following relationship for local heat transfer

$$\mathrm{Nu}_x = 0.754\,f\left[\frac{\mathrm{Gr}_x}{1.904\,\mathrm{Pr}^{-2/3} + 1}\right]^{0.5} \tag{16}$$

Thus the mean value of the Nusselt number can be expressed as

$$\frac{\mathrm{Nu}_L}{f} = C_3\,\mathrm{Gr}_L{}^{0.5} \tag{17}$$

The constant C_3 is a function of Prandtl number alone.

Results and Discussion

The present analysis shows that Nu_L is proportional to $\mathrm{Gr}_L{}^{0.5}$. The analysis of Eckert and Jackson [3] shows that Nu_L is proportional to $\mathrm{Gr}_L{}^{0.4}$ for smooth surface. In view of this the present prediction seems to be reasonable.

The experimental data of [2] are used to obtain correlation between f and (e/L). The relationship is given as

$$f = 0.044\,(e/L)^{0.051} \tag{18}$$

for the range and type of roughness investigated.

Regarding the general applicability of equation (18) nothing much can be said at present in view of limited experimental data available.

When the experimentally obtained values of Nusselt number are combined with the values of f, as obtained from equation (18), and plotted against Gr_L, the results coincide with the theoretical line with practically no scatter as shown in Fig. 1.

Since the Reynolds analogy is used in the derivation of equation (17), it can be used for fluids whose Prandtl numbers are close to unity.

The heat transfer rates increase by about 50 percent for rough surfaces over the smooth ones.

Conclusion

The heat transfer from a rough surface in turbulent free convection can be calculated by equation (17) for any type of roughness. In particular for the type of roughness investigated [2] the value of f can be obtained from equation (18) for a given value of (e/L). It can be used in turn to get heat transfer coefficient from equation (17).

References

1 Fujii, T., Fugii, M., Takeuchi, M., "Influence of Various Surface Roughness on Natural Convection," *International Journal of Heat and Mass Transfer*, Vol. 16, 1973, pp. 629.

2 Sastry, C. V. S. N., Murty, V. N., Sarma, P. K., "Effect of Discrete Wall

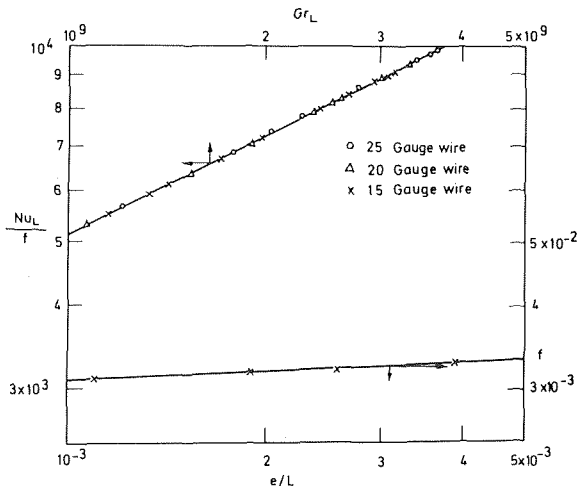

Fig. 1 Skin friction and heat transfer results

Roughness on Free Convective Heat Transfer from a Vertical Tube," Paper presented at ICHMT on Turbulent Buoyant Convection, Dubrovnik, Yugoslavia, 1976.
3 Eckert E. R. G., Jackson T. W., NACA Report 1015, 1951.
4 Nikuradse J., *Laws of Flows in Pipes*, VDI Forsch Heft 361 1933.

Hydrodynamic Stability in Horizontal Fluid Layers with Uniform Volumetric Energy Sources

K. S. Ning,[1] R. E. Faw,[1] and T. W. Lester[1]

Nomenclature

C_v = specific heat at constant volume
g = gravitational acceleration
k = thermal conductivity
L = total fluid layer depth
P = pressure
q = volumetric heat generation rate
t = time
T = temperature
V = velocity
x = spatial coordinate
X = body force term
α = thermal diffusivity
β = coefficient of volumetric expansion
ν = kinematic viscosity
ϕ = dissipation function
ρ = density

Subscripts

0 = evaluated at lower boundary
1 = evaluated at upper boundary

Introduction

The determination of criteria for the onset of convective motion in fluid layers has been the subject of numerous investigations [1–5] and a recent comprehensive review [6]. Attention has been given recently to the stability of liquid layers experiencing internal heating, a topic of importance in meteorology and geophysics as well as in engineering problems associated with the containment of liquids heated by radioactive decay. In certain design problems associated with nuclear reactor safety, stability criteria are of interest in fluids with Rayleigh numbers in excess of 10^{10} [7]. This work deals with stability criteria for internally heated fluid layers and extends previous work to cover different boundary conditions as well as a higher range of Rayleigh numbers.

Consider a horizontal fluid layer of depth L with the lower and upper surfaces fixed respectively at temperatures T_0 and T_1. The layer experiences uniform internal heating at a volumetric rate q. Two dimensionless parameters describe the state of the system with respect to the onset of convective motion. These are the external Rayleigh number and the internal Rayleigh number [9], defined respectively as:

$$\mathrm{Ra}_E = g\beta L^3(T_0 - T_1)/\alpha\nu, \tag{1}$$

$$\mathrm{Ra}_{KG} = g\beta q L^5/64\alpha\nu k. \tag{2}$$

Inasmuch as the external Rayleigh number characterizes the destabilizing influence of an externally imposed temperature difference, and the internal Rayleigh number represents the destabilizing influence on the layer by the internal heat generation, one may expect critical values of these two Rayleigh numbers to define conditions at which the layer undergoes a transition from conduction to convection heat transfer.

The purpose of this work was to calculate the critical external Rayleigh number, Ra_{EC}, for two cases; both bounding surfaces rigid and isothermal; and the upper surface free, lower surface rigid, both isothermal. The present work represents an extension of a previous analysis by Sparrow, et al., [8] to include critical internal and external Rayleigh numbers as high as 10^{10}. The results at these higher Rayleigh numbers for the case of both surfaces rigid substantiate the semi-empirical predictions of Baker, et al. [7].

Analysis

To describe the problem completely, three conservation equations and one state equation are required [8]. These equations, as expressed in tensor form, are:

$$\rho\frac{D}{Dt}V_i = \rho X_i - \frac{\partial}{\partial x_i}P + \nu\rho\nabla^2 V_i, \tag{3}$$

$$\frac{\partial\rho}{\partial t} + \frac{\partial}{\partial x_i}(\rho V_i) = 0 \tag{4}$$

$$\rho = \rho_0[1 - \beta(T - T_0)] \tag{5}$$

$$\rho V_i\frac{\partial}{\partial x_i}C_v T + \rho\frac{\partial}{\partial t}C_v T = k\nabla^2 T - P\frac{\partial Vi}{\partial x_i} + q + \phi. \tag{6}$$

Application of linear perturbation theory and the Boussinesq approximation [2–5, 8] leads to the following differential equation for the perturbation function $F(Z)$, applicable at the threshold of instability.

$$\frac{d^6F(Z)}{dZ^6} - 3\lambda^2\frac{d^4F(Z)}{dZ^4} + 3\lambda^4\frac{d^2F(Z)}{dZ^2} - \lambda^2[\lambda^4 - \mathrm{Ra}_E + 32\mathrm{Ra}_{KG}(1 - 2Z)]F(Z) = 0 \tag{7}$$

in which λ is a dimensionless factor arising from the separation of variables and Z is the ratio of the vertical coordinate to the layer thickness. Following [8], the solution of this equation can be expressed by a summation of six different series with six arbitrary constants,

$$F(Z) = \sum_{i=0}^{5} C_i f^{(i)}(Z), \tag{8}$$

in which the $f^{(i)}(Z)$ are convergent power series.

There are two hydrodynamic and one thermal boundary condition that are of interest: either a rigid or a free upper surface in combination with a rigid lower surface—both isothermal. In practice, the lower bounding surface of the fluid layer will necessarily be a rigid surface. On such a surface, all the velocity components vanish identically ("no slip"),

$$F(Z) = \frac{dF(Z)}{dZ} = 0. \tag{9}$$

The upper surface can be either rigid or free. A surface is called "free" when it is not constrained by a rigid boundary. On a free surface, it is assumed that the vertical velocity component vanishes and that the tangential shear is equal to zero,

$$F(Z) = \frac{d^2F(Z)}{dZ^2} = 0. \tag{10}$$

Thermally both upper and lower surface temperatures are assumed to be constant, but not necessarily equal. Introduction of the boundary conditions leads to a set of four linear homogeneous algebraic equations from which four of the six constants can be determined. The

[1] Department of Nuclear Engineering, Kansas State University, Manhattan, KS 66506.

[2] The heat transfer correlation derived by Baker, et al. was based on experimental data for convective heat transfer and did not explicitly account for the critical Rayleigh numbers at the onset of instability Nevertheless, implied by their correlation is an expression similar to equation (13) except that the constant 3.8311 is replaced by 4.128.

Contributed by the Heat Transfer Division for publication in the JOURNAL OF HEAT TRANSFER. Manuscript received by the Heat Transfer Division May 3, 1978.

Roughness on Free Convective Heat Transfer from a Vertical Tube," Paper presented at ICHMT on Turbulent Buoyant Convection, Dubrovnik, Yugoslavia, 1976.
3 Eckert E. R. G., Jackson T. W., NACA Report 1015, 1951.
4 Nikuradse J., *Laws of Flows in Pipes*, VDI Forsch Heft 361 1933.

Hydrodynamic Stability in Horizontal Fluid Layers with Uniform Volumetric Energy Sources

K. S. Ning,[1] R. E. Faw,[1] and T. W. Lester[1]

Nomenclature

C_v = specific heat at constant volume
g = gravitational acceleration
k = thermal conductivity
L = total fluid layer depth
P = pressure
q = volumetric heat generation rate
t = time
T = temperature
V = velocity
x = spatial coordinate
X = body force term
α = thermal diffusivity
β = coefficient of volumetric expansion
ν = kinematic viscosity
ϕ = dissipation function
ρ = density

Subscripts

0 = evaluated at lower boundary
1 = evaluated at upper boundary

Introduction

The determination of criteria for the onset of convective motion in fluid layers has been the subject of numerous investigations [1–5] and a recent comprehensive review [6]. Attention has been given recently to the stability of liquid layers experiencing internal heating, a topic of importance in meteorology and geophysics as well as in engineering problems associated with the containment of liquids heated by radioactive decay. In certain design problems associated with nuclear reactor safety, stability criteria are of interest in fluids with Rayleigh numbers in excess of 10^{10} [7]. This work deals with stability criteria for internally heated fluid layers and extends previous work to cover different boundary conditions as well as a higher range of Rayleigh numbers.

Consider a horizontal fluid layer of depth L with the lower and upper surfaces fixed respectively at temperatures T_0 and T_1. The layer experiences uniform internal heating at a volumetric rate q. Two dimensionless parameters describe the state of the system with respect to the onset of convective motion. These are the external Rayleigh number and the internal Rayleigh number [9], defined respectively as:

$$\mathrm{Ra}_E = g\beta L^3(T_0 - T_1)/\alpha\nu, \tag{1}$$

$$\mathrm{Ra}_{KG} = g\beta q L^5/64\alpha\nu k. \tag{2}$$

Inasmuch as the external Rayleigh number characterizes the destabilizing influence of an externally imposed temperature difference, and the internal Rayleigh number represents the destabilizing influence on the layer by the internal heat generation, one may expect critical values of these two Rayleigh numbers to define conditions at which the layer undergoes a transition from conduction to convection heat transfer.

The purpose of this work was to calculate the critical external Rayleigh number, Ra_{EC}, for two cases; both bounding surfaces rigid and isothermal; and the upper surface free, lower surface rigid, both isothermal. The present work represents an extension of a previous analysis by Sparrow, et al., [8] to include critical internal and external Rayleigh numbers as high as 10^{10}. The results at these higher Rayleigh numbers for the case of both surfaces rigid substantiate the semi-empirical predictions of Baker, et al. [7].

Analysis

To describe the problem completely, three conservation equations and one state equation are required [8]. These equations, as expressed in tensor form, are:

$$\rho\frac{D}{Dt}V_i = \rho X_i - \frac{\partial}{\partial x_i}P + \nu\rho\nabla^2 V_i, \tag{3}$$

$$\frac{\partial\rho}{\partial t} + \frac{\partial}{\partial x_i}(\rho V_i) = 0 \tag{4}$$

$$\rho = \rho_0[1 - \beta(T - T_0)] \tag{5}$$

$$\rho V_i\frac{\partial}{\partial x_i}C_v T + \rho\frac{\partial}{\partial t}C_v T = k\nabla^2 T - P\frac{\partial Vi}{\partial x_i} + q + \phi. \tag{6}$$

Application of linear perturbation theory and the Boussinesq approximation [2–5, 8] leads to the following differential equation for the perturbation function $F(Z)$, applicable at the threshold of instability.

$$\frac{d^6F(Z)}{dZ^6} - 3\lambda^2\frac{d^4F(Z)}{dZ^4} + 3\lambda^4\frac{d^2F(Z)}{dZ^2} - \lambda^2[\lambda^4 - \mathrm{Ra}_E + 32\mathrm{Ra}_{KG}(1 - 2Z)]F(Z) = 0 \tag{7}$$

in which λ is a dimensionless factor arising from the separation of variables and Z is the ratio of the vertical coordinate to the layer thickness. Following [8], the solution of this equation can be expressed by a summation of six different series with six arbitrary constants,

$$F(Z) = \sum_{i=0}^{5} C_i f^{(i)}(Z), \tag{8}$$

in which the $f^{(i)}(Z)$ are convergent power series.

There are two hydrodynamic and one thermal boundary condition that are of interest: either a rigid or a free upper surface in combination with a rigid lower surface—both isothermal. In practice, the lower bounding surface of the fluid layer will necessarily be a rigid surface. On such a surface, all the velocity components vanish identically ("no slip"),

$$F(Z) = \frac{dF(Z)}{dZ} = 0. \tag{9}$$

The upper surface can be either rigid or free. A surface is called "free" when it is not constrained by a rigid boundary. On a free surface, it is assumed that the vertical velocity component vanishes and that the tangential shear is equal to zero,

$$F(Z) = \frac{d^2F(Z)}{dZ^2} = 0. \tag{10}$$

Thermally both upper and lower surface temperatures are assumed to be constant, but not necessarily equal. Introduction of the boundary conditions leads to a set of four linear homogeneous algebraic equations from which four of the six constants can be determined. The

[1] Department of Nuclear Engineering, Kansas State University, Manhattan, KS 66506.

[2] The heat transfer correlation derived by Baker, et al. was based on experimental data for convective heat transfer and did not explicitly account for the critical Rayleigh numbers at the onset of instability Nevertheless, implied by their correlation is an expression similar to equation (13) except that the constant 3.8311 is replaced by 4.128.

Contributed by the Heat Transfer Division for publication in the JOURNAL OF HEAT TRANSFER. Manuscript received by the Heat Transfer Division May 3, 1978.

other two constants are zero. A nontrivial solution exists if and only if the determinant of the coefficient matrix vanishes. The value of the determinant depends on three parameters, the internal Rayleigh number, the external Rayleigh number, and a constant λ which arises from the separation of variables. For every λ value and internal Rayleigh number, an external Rayleigh number exists that causes the determinant of the cofficient matrix to be zero. Moreover, it is found that for a particular λ, there is a corresponding external Rayleigh number which is smaller than that for any other λ. A solution for the disturbance equation cannot be obtained for any external Rayleigh number below this value. Physically, this means that the quiescent state is stable because no perturbation function can be found. Therefore, the aforementioned minimum external Rayleigh number corresponds to the onset of instability. This is generally called the critical external Rayleigh number.

Results and Discussion

A semi-empirical correlation has been derived by Baker, et al. [7] for heat transfer under conditions where both surfaces are rigid and isothermal. Conceptually, they divided the fluid layer at the plane of maximum temperature into two sublayers: an upper sublayer with an insulated, free lower boundary and a lower sublayer with an insulated, free upper boundary. These same concepts may be invoked to drive an approximate relationship between critical internal and external Rayleigh numbers. With a stabilizing temperature gradient, i.e., $Ra_E < 0$, it may be assumed that the onset of instability occurs in the upper sublayer. For such a layer, with a rigid upper boundary and a free, insulated lower boundary, Kulacki [5] has computed a critical external Rayleigh number of 25.7899 based on the upper sublayer thickness. In terms of Ra_{KGC}, the critical external Rayleigh number based on the full layer thickness,

$$Ra_{KGC}(1 - L_0/L)^5 = 25.7899, \tag{11}$$

in which L_0 is the thickness of the lower sublayer. But, at the onset of instability, the temperature profile in the full layer is governed by conductive heat transfer, for which case

$$L_0/L = {}^1/_2 + k(T_1 - T_0)/qL^2 = {}^1/_2 - Ra_{EC}/64Ra_{KGC}. \tag{12}$$

Elimination of L_0/L in the above two equations leads to the result

$$Ra_{EC} = -32Ra_{KGC}(1 - 3.8311Ra_{KGC}{}^{-0.2}). \tag{13}$$

This equation would not be expected to hold for small negative values of Ra_{EC}, for which cases the upper and lower sublayers would approach equal thickness and the stabilizing effect of a negative external temperature gradient would be minimized. Indeed, equation (13) predicts a value of $Ra_{KGC} = 825.3$ for the case $Ra_{EC} = 0$ whereas the correct value should be 583.2 [5, 8].

Heretofore, theoretical justification of the approximate relationship, equation (13), has been provided by Sparrow, et al., [8] for external Rayleigh numbers up to 10^5 and by Catton and Suo-Antilla [11] for external Rayleigh numbers up to 10^8. The comparison of these previous analytical studies with equation (13) as well as the predictions from the present work in the extended Rayleigh number range are provided in Fig. 1. Agreement among the various results is entirely satisfactory except for $Ra_E > -10^6$ where the semi-empirical relation over-predicts, with respect to the analytical expressions, the critical internal Rayleigh number. This agreement also supports the conceptual approach taken by Baker, et al. [7] in deriving their semi-empirical heat transfer correlation.[2]

The critical external Rayleigh numbers are also shown for the case of a free upper surface and rigid lower surface. In the range of external Rayleigh numbers studied, the free-rigid layer is less stable than the rigid-rigid. This result agrees with the earlier analysis of Sparrow, et al., [8] for horizontal fluid layers without heat sources.

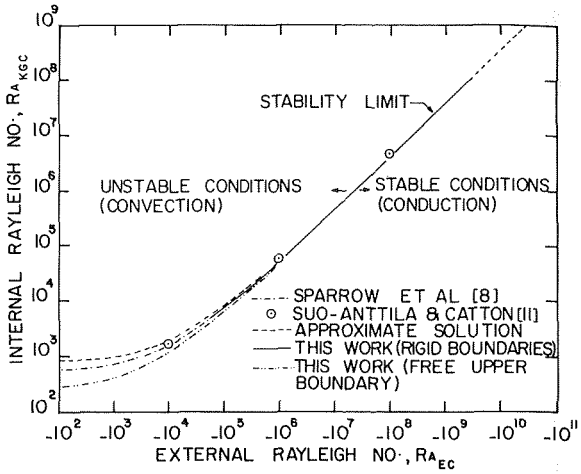

Fig. 1 Comparison of theoretical and approximate predictions of instability limit in a horizontal fluid layer with internal heat generation.

Summary and Conclusions

Hydrodynamic instability in a fluid layer has been investigated analytically in the range of Rayleigh numbers important in nuclear reactor safety analysis. The stability of free-rigid layers was also explored and the results compared to the rigid-rigid case. The free-rigid layer was observed to be less stable than the rigid-rigid system.

Acknowledgments

The authors wish to express appreciation to Drs. P. Boon-Long and F. Kulacki for helpful discussions during this study. One of us (K.S.N.) was supported by the Kansas Engineering Experiment Station as a research assistant.

References

1 Lord Rayleigh, "On Convective Currents in a Horizontal Layer of Fluid when the Higher Temperature is on the Underside," *Philosophical Magazine and Journal of Science*, Vol. 32, 1916, pp. 529–546.

2 Pellew, A., Southwell, R. V., "On Maintained Convective Motion in a Fluid Heated from Below," *Proceedings of the Royal Society of London*, Series A, Vol. 176, 1940, pp. 312–343.

3 Lin, C. C., *The Theory of Hydrodynamic Stability*, Cambridge University Press, 1951, pp. 106–109.

4 Chandrasekhar, S., *Hydrodynamic and Hydromagnetic Stability*, Oxford University Press, London, 1961, pp. 10–22.

5 Kulacki, F. A., "Thermal Convection in a Horizontal Fluid Layer with Uniform Volumetric Energy Sources," Ph.D. Dissertation in Mechanical Engineering, University of Minnesota, 1971, pp. 10–30.

6 Normand, C., Pomeau, C., Velarde, M. G., "Convective Instability: A Physicist's Approach," *Reviews of Modern Physics*, Vol. 49, 1977, pp. 581–624.

7 Baker, L. Jr., Faw, R. E., Kulacki, F. A., "Postaccident Heat Removal 1: Heat Transfer within an Internally Heated, Nonboiling Liquid Layer," *Nuclear Science and Engineering*, Vol. 61, March 1976, pp. 222–230.

8 Sparrow, E. M., Goldstein, R. J. Jonsson, V. K., "Thermal Instability in a Horizontal Fluid Layer, Effect of Boundary Conditions and Nonlinear Temperature Profile," *Journal of Fluid Mechanics*, Vol. 18, Oct. 1963, pp. 513–528.

9 Kulacki, F. A., and Goldstein, R. J., "Thermal Convection ina Horizontal Fluid Layer with Uniform Volumetric Energy Sources," *Journal of Fluid Mechanics*, Vol. 55, Part 2, 1972, pp. 271–280.

10 Kulacki, F. A., and Emara, A. A., "High Rayleigh Number Convection in Enclosed Fluid Layers with Internal Heat Sources," *Transcations of the American Nuclear Society*, Vol. 22, 1975, p. 447.

11 Suo-Anttila, A. J. and Catton, I., "The Effect of a Stabilizing Temperature Gradient on Heat Transfer from a Molten Fuel Layer with Volumetric Heating," ASME JOURNAL OF HEAT TRANSFER, Vol. 97, 1975, pp. 544–548.

Leading Edge Effects in Transient Natural Convection Flow adjacent to a Vertical Surface

R. L. Mahajan[1] and B. Gebhart[2]

Nomenclature

a = parameter determining division of thermal energy input between the wall and the fluid
$= (\rho c_p k)^{1/2}/c''$

β^* = characteristic frequency $= 2\pi f \left(\frac{g\beta q''}{k}\right)^{1/2}$

C_r = disturbance phase velocity
c'' = thermal capacity of the plate per unit surface area
f = disturbance frequency

G^* = modified flux Grashof number $= 5\left(\frac{Gr^*}{5}\right)^{1/5}$

Gr^* = flux Grashof number $= \frac{g\beta q'' x^4}{k\nu^2}$

U = characteristic base flow velocity $= \frac{\nu G^{*2}}{5x}$

Introduction

The initial part of the transient natural convection flow over a vertical surface, subject to a step change in temperature or in heat generation is known to be well described by the one-dimensional transient conduction solution for a doubly infinite vertical surface in an infinite fluid medium [1–5]. As in [5], one may estimate from such calculations the distance $x_{p,\max}$ of the propagation of a leading edge effect which terminates this pure conduction phase on a surface of finite length, where

$$x_{p,\max} = \text{maximum value of } \int_0^t u(t)dt \tag{1}$$

This distance is then used to estimate the time interval for which the conduction solution might be expected to apply locally, before true convection effects are felt.

The calculated values of $x_{p,\max}$, for a step change in surface temperature or surface flux, are given in [5], for a range of Prandtl numbers. A convenient form of equation (1) in x', given by Gebhart and Dring [6], is

$$x' = \frac{ka^5}{g\beta q''\sqrt{\alpha}} - x_{p,\max} = (t')^5 f(t') F(\mathrm{Pr}) \tag{2}$$

where $t' = a\sqrt{t}$, $f(t')$ is a t' dependent function and is the number in $x_{p,\max}$ in Table 1 in [5], and $F(\mathrm{Pr})$ is the Prandtl number effect on the integral in (1) above.

Using an interferometer, Gebhart and Dring [6] and Mollendorf and Gebhart [7] investigated these effects for the transient flow generated over a surface of finite thermal capacity, subject to a step change in input heat flux. The results indicated that the leading edge effects travelled up the plate about 20 percent faster than predicted in [5].

Mollendorf and Gebhart [7] also made some interesting observations regarding the behavior of the disturbances associated with the leading edge propagation effect. An important result of their data was that these disturbances were observed to lie in a narrow range of frequencies. Their data plotted on the stability plane are shown in Fig. 3. The conclusion was that the filtering characteristics predicted by linear stability calculations for steady laminar boundary layer flow perhaps also applied to transient flows. Further, they hypothesized that the leading edge disturbance acted as a moving boundary layer trip to trigger the flow from laminar flow to turbulence. This conjecture was based on the then quite incomplete linear stability calculations for Pr = 6.7 which showed that the disturbances having the highest amplification rates were propagated at a velocity very close to the maximum base flow velocity. Since the leading edge disturbances were postulated in the calculation to move at the maximum of the local base flow velocity, it was argued that the two effects are tied together.

However, since these data were in pressurized N_2, Pr = 0.72, for which the disturbance amplification characteristics were not known in detail, the above speculations were not definitive and have remained so far untested.

In this note, we present some new measurements of the flow and the temperature fields. These are the first taken with local sensors during the initial transient period of a starting flow, in this instance, adjacent to a uniform flux vertical surface, in pressurized nitrogen, Pr = 0.72. We then re-examine the above unresolved questions in light of the very extensive linear stability theory calculations now known for a fluid of this Prandtl number.

Experimental

The uniform flux surface was a stretched 0.00254 cm thick inconel-600 foil, 15.25 cm wide and 38.5 cm high. The foil was positioned in a large insulated pressure chamber. The ambient fluid was pressurized dry nitrogen. An energy generation step was approximated by subjecting the foil to a step in current. Transient response of the temperature and the velocity fields were measured using a 5.08×10^{-3} cm diameter copper-constantan thermocouple and a 5 μm Disa miniature probe. For further details of the experiment and the range of experimental conditions, see Mahajan and Gebhart [8].

Transient data were taken at a given downstream location x, for different values of pressure p and heat flux q'', by noting the response of the thermocouple and the hot-wire probes on two channels of a Beckman recorder. The two probes were positioned normal to the surface at a distance y corresponding to the value $\zeta_{\max}$ where $\zeta_{\max}$ is the value of $y = yG^*/5x$ for maximum velocity disturbance amplification according to the theoretical stability calculations for steady flow. See disturbance profiles in [9] for $\zeta_{\max}$. Our exploratory measurements taken with the probes at different y locations indicated this value to be a reasonable guess for maximum leading edge disturbance amplitude across the flow thickness. Note, however, that the position of the probes in y is not critical to the results of this investigation, since both the disturbance frequency and the time taken by the disturbance to propagate up the surface—the quantities of interest in this work—were found to be essentially constant across the flow thickness.

Typical analog records are seen in Fig. 1. The beginning of the transient, following a step increase in current to the foil, is indicated by a sudden excursion of the pens recording the temperature and the velocity outputs on the chart recorder, see Fig. 1. A step increase in the foil current is accompanied by a surge in the generation of electro-magnetic radiations which, picked up by the amplifier circuit of the recorder, result in an excursion of the pens. The time lapse (t) between the start of the transient and the first observed disturbance was read from such chart records and was found to be the same, within the accuracy of measurement (to 0.02 s) for both the temperature and the velocity fields. The data were taken at different downstream locations x, for various values of p and q'' in the range, $13.2 \le x \le 33$ cm, $1 \le p \le 15.92$ atm and $5 < q'' < 330$ watts/m^2. The data were reproducible to within ±3 percent.

Results and Discussion

Propagation Rate. The recorded time (t) and the distance (x) are plotted in Fig. 2 in terms of nondimensional variables t' and x',

[1] Engineering Research Center, Western Electric, P. O. Box 900, Princeton, N.J, 08540.
[2] Professor and Chairman, Mechanical Engineering Department, State University of New York at Buffalo, Amherst, NY, 14260
Contributed by the Heat Transfer Division for publication in the JOURNAL OF HEAT TRANSFER. Manuscript received by the Heat Transfer Division March 20, 1978.

respectively. The theoretical prediction of Goldstein and Briggs [5] and the experimental data of Gebhart and Dring [6] and of Mollendorf and Gebhart [7] are also plotted for comparison. We first note from Fig. 2 that the slope of the line correlating our data is the same as in [5, 6] and [7] indicating that the data are associated with the propagating leading edge effect. However, as in [6] and [7], the leading edge effects are observed earlier at a given x, than the prediction of [5]. No certain explanation is yet known for this discrepancy. A possible reason could be neglecting the convective and pressure effects across the leading edge disturbance wave in the analysis. This, as pointed out in [5], could cause the leading edge effects to be felt at an earlier time. Also, the discrepancy could be due to the unaccounted effects in the theoretical analysis of [5] of the not yet satisfactorily assessed characteristics of the leading edge region flow.

Further, we see that the present data, based on measurements with local sensors, indicate even earlier arrival of the leading edge disturbance than did the inteferometric data of [6] and [7]. The best fit through the interferometric data of [6] and [7] (all of their data points not shown in Fig. 2) indicate about 20 percent faster propagation than given in [5]. However, our results indicate about 50 percent faster rate. Such a delay in the detection of disturbances by interferometry is now well known [8, 9]. It is due to the insensitivity of the interferometer to local disturbances.

An important implication of these results is that the length of time for which one-dimensional conduction solution can be used to calculate the transport coefficients is about two-thirds of the theoretical prediction of Goldstein and Briggs [5].

Disturbance Frequency. We note from the analog records that the leading edge disturbances carried by the local flow are approximately periodic. These frequencies, when converted to B^*, are also plotted on the stability plane in Fig. 3. This plane is from [8], supplemented by additional amplitude ratio contours at higher values of G*. Recall that this plane results from linear theory stability for *steady flows*. The following points are of interest:

1 The observed disturbances are seen to be scattered, in a narrow band of frequencies, around the path of $C_r = 0.9\ U_{max}$. The leading edge effects are calculated to propagate at maximum base flow velocity. However, since these effects were found to travel faster than the predicted, the disturbances might be expected to lie in the region of $C_r > U_{max}$. The above results, however, lie in the region $C_r < U_{max}$. Noting that the stability calculations are for steady flow and not for the transients considered here, the above disagreement is not surprising. The stability calculations for the transient flow are not yet known.

However, from these results we can make some conjectures about the paths of $C_r = U_{max}$ for the transient and the steady flows. For the transient data to lie in the region $C_r < U_{max}$, the path of $C_r = U_{max}$ calculated for the transient flow should lie above the experimental data points of $B^* - G^*$ plane and thus also above $C_r = U_{max}$ path for

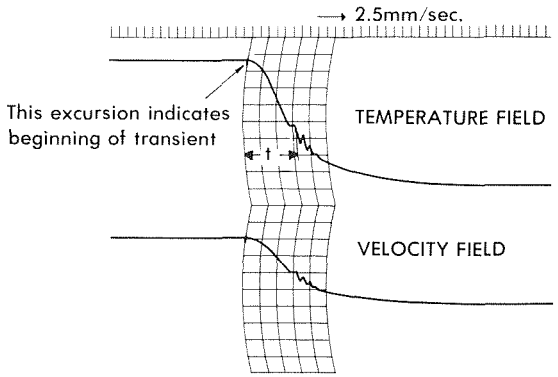

Fig. 1 Traces of temperature and velocity fields during initial transient

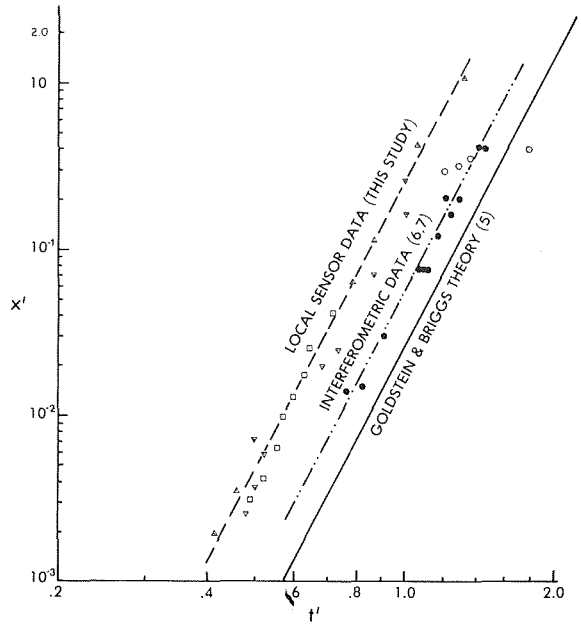

Fig. 2 Comparison of first observed waves to the leading edge propagation rate theory and other data: ●, Gebhart and Dring [6], ○, Mollendorf and Gebhart [7], present data, ▽, x = 13.2 cm, □, x = 22 cm, △, x = 33 cm

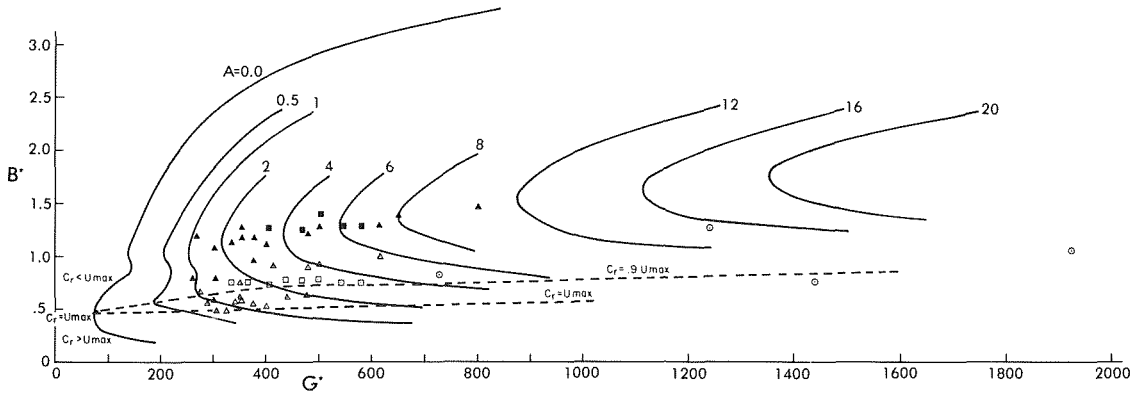

Fig. 3 Comparison of leading edge effect frequency data in transient flow (open symbols) with the most amplified disturbance frequency data in unstable steady laminar flow (filled symbols). The amplitude curves and the data for steady flow data taken from [8]. Transient data: this study, ▽, x = 13.2 cm, □, x = 22 cm, △, x = 33 cm, Mollendorf and Gebhart [7], ○

the steady flow, see Fig. 3. This suggests that the associated disturbance frequency values along $C_r = U_{max}$ path are higher for transient flow stability calculations than for the steady flow.

2 The leading edge disturbances are not the same as the most amplified disturbances associated with the breakdown of the flow from laminar to turbulent, as was conjectured in [7] on the basis of the very incomplete stability planes available at that time. This can can be seen from Fig. 3, where the most amplified disturbance data from [8] for unstable laminar flow or for locally laminar portions of the turbulent flow, are also plotted. The data in [8] are for the steady flow following the transients of this experiment. Clearly, the frequencies of the leading edge disturbances are lower than the most amplified. The data of Mollendorf and Gebhart [7], in light of the more recent stability calculations for Pr = 0.72, also supports our conclusion, see Fig. 3. That is, their data points lie well below the path of most amplified disturbance.

Acknowledgments

The authors wish to acknowledge the support of the National Science Foundation under grant ENG 7522623 and of Donna George for typing the manuscript.

References

1 Siegel, R., "Transient Free Convection from a Vertical Flat Plate," Trans. ASME, Vol. 80, 1958, pp. 347.

2 Schetz, J. A. and Eichhron, R., "Unsteady Natural Convection in the Vicinity of a Doubly Infinite Vertical Plate," ASME JOURNAL OF HEAT TRANSFER, Vol. 84, 1962, p. 334.

3 Menold, E. R. and Yang, K., "Asymptotic Solutions for Unsteady Laminar Free Convection on a Vertical Plate," ASME, *Journal of App. Mech.*, Vol. 29, No. 84, 1962, p. 124.

4 Gebhart, B., "Transient Natural Convection from Vertical Elements," ASME JOURNAL OF HEAT TRANSFER, Vol. 83, No. 1, Feb. 1961, p. 61.

5 Goldstein, R. J. and Briggs, D. G., "Transient Free Convection about Vertical Plates and Circular Cylinders," ASME JOURNAL OF HEAT TRANSFER, Vol. 86, No. 4, Nov. 1964, p. 490.

6 Gebhart, B. and Dring, R. P., "The Leading Edge Effect in Transient Natural Convection Flow From a Vertical Plate," ASME JOURNAL OF HEAT TRANSFER, Vol. 89, No. 5, Aug. 1967, p. 24.

7 Mollendorf, J. C. and Gebhart, B., "An Experimental Study of Vigorous Transient Natural Convection," ASME JOURNAL OF HEAT TRANSFER, Vol. 92, Nov. 1970, p. 628.

8 Mahajan, R. L. and Gebhart, B., "An Experimental Investigation of Transition Limits in Natural Convection Flows," accepted for publication by JFM.

9 Mahajan, R. L., "Higher Order Effects, Stability and Transition in Vertical Natural Convection Flows," Ph.D. Thesis, Cornell University.

10 Bill. R. G., Jr. and Gebhart, B., "The Transition of Plane Plumes," *Int. Journal Heat Mass Trans.*, Vol. 18, 1975, p. 513.

On the Mikic-Rohsenow Pool Boiling Correlation

P. R. Sharma[1] and B. S. Varshney[2]

Nomenclature

g = acceleration of gravity
m = constant, 2.5 for water and 3.0 for organic fluids
q = heat flux
T = temperature
ΔT = wall superheat, $T_w - T_{sat}$
λ = latent heat of evaporation
μ = coefficient of viscosity
ρ = density of fluids
Φ = parameter defined by equation (14) of [1]

Subscripts

b = boiling
l = liquid
v = vapor
w = wall

Following the mechanism of transient heat conduction to, and subsequent replacement of, the superheated layer around the heating surface, Mikic and Rohsenow [1] have derived a new correlation for the calculation of heat flux in nucleate pool boiling. This correlation satisfactorily correlates the experimental data of Addoms [2] for distilled water and of Cichelli and Bonilla [3] for three organic liquids for the pressures greater than atmospheric ranging from 101.3 kN/m^2 to 13,680 kN/m^2. The aim of this technical brief is to report the generality of the above correlation to the experimental data even for the pressures smaller than the atmospheric.

In the present investigation the range of pressure was from 11.33 kN/m^2 to 98.44 kN/m^2 and that of the heat flux from 3.3 kW/m^2 to 41.73 kW/m^2. The data were for the transfer of heat from a horizontal cylinder of 410 ASIS stainless steel to the boiling pool of pure liquids: distilled water, isopropanol, ethanol and methanol. The test cylinder was heated by a cartridge type electric heater placed in it. The power input to the heater was modulated by an auto-transformer and was measured by means of an ammeter and a voltmeter of the precision grade. The calibrated copper constantan thermocouples measured the temperature of the heating surface and the boiling liquids. The heating surface temperature was measured circumferentially at three locations—at the top, at the side and at the bottom and the liquid temperature corresponding to these surface thermocouples. Mechanical quadrature technique was used to obtain the average values of the wall superheat, ΔT. The experimental setup used for the present investigation is described elsewhere [4, 5].

The results which have been correlated by the Mikic-Rohsenow correlation are shown in Figs. 1–4. The pressure range for the individual liquid is indicated in these figures. It appears from these figures that this correlation satisfactorily correlates the present experimental data for all the four liquids investigated. All these figures show a similar trend but different intercepts. As a matter of fact, the intercept

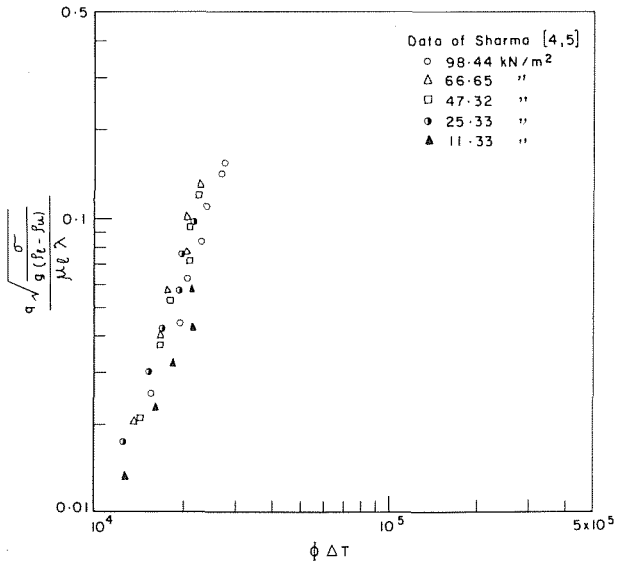

Fig. 1 Nucleate pool boiling data for water correlated by Mikic-Rohsenow correlation [1]

[1] Research Associate, Department of Chemical Engineering, University of Roorkee, Roorkee-247672, India.

[2] Professor, Department of Chemical Engineering, University of Roorkee, Roorkee-247672, India.

Contributed by the Heat Transfer Division for publication in the JOURNAL OF HEAT TRANSFER. Manuscript received by the Heat Transfer Division April 3, 1978.

the steady flow, see Fig. 3. This suggests that the associated disturbance frequency values along $C_r = U_{max}$ path are higher for transient flow stability calculations than for the steady flow.

2 The leading edge disturbances are not the same as the most amplified disturbances associated with the breakdown of the flow from laminar to turbulent, as was conjectured in [7] on the basis of the very incomplete stability planes available at that time. This can can be seen from Fig. 3, where the most amplified disturbance data from [8] for unstable laminar flow or for locally laminar portions of the turbulent flow, are also plotted. The data in [8] are for the steady flow following the transients of this experiment. Clearly, the frequencies of the leading edge disturbances are lower than the most amplified. The data of Mollendorf and Gebhart [7], in light of the more recent stability calculations for Pr = 0.72, also supports our conclusion, see Fig. 3. That is, their data points lie well below the path of most amplified disturbance.

Acknowledgments

The authors wish to acknowledge the support of the National Science Foundation under grant ENG 7522623 and of Donna George for typing the manuscript.

References

1 Siegel, R., "Transient Free Convection from a Vertical Flat Plate," Trans. ASME, Vol. 80, 1958, pp. 347.

2 Schetz, J. A. and Eichhron, R., "Unsteady Natural Convection in the Vicinity of a Doubly Infinite Vertical Plate," ASME JOURNAL OF HEAT TRANSFER, Vol. 84, 1962, p. 334.

3 Menold, E. R. and Yang, K., "Asymptotic Solutions for Unsteady Laminar Free Convection on a Vertical Plate," ASME, *Journal of App. Mech.*, Vol. 29, No. 84, 1962, p. 124.

4 Gebhart, B., "Transient Natural Convection from Vertical Elements," ASME JOURNAL OF HEAT TRANSFER, Vol. 83, No. 1, Feb. 1961, p. 61.

5 Goldstein, R. J. and Briggs, D. G., "Transient Free Convection about Vertical Plates and Circular Cylinders," ASME JOURNAL OF HEAT TRANSFER, Vol. 86, No. 4, Nov. 1964, p. 490.

6 Gebhart, B. and Dring, R. P., "The Leading Edge Effect in Transient Natural Convection Flow From a Vertical Plate," ASME JOURNAL OF HEAT TRANSFER, Vol. 89, No. 5, Aug. 1967, p. 24.

7 Mollendorf, J. C. and Gebhart, B., "An Experimental Study of Vigorous Transient Natural Convection," ASME JOURNAL OF HEAT TRANSFER, Vol. 92, Nov. 1970, p. 628.

8 Mahajan, R. L. and Gebhart, B., "An Experimental Investigation of Transition Limits in Natural Convection Flows," accepted for publication by JFM.

9 Mahajan, R. L., "Higher Order Effects, Stability and Transition in Vertical Natural Convection Flows," Ph.D. Thesis, Cornell University.

10 Bill. R. G., Jr. and Gebhart, B., "The Transition of Plane Plumes," *Int. Journal Heat Mass Trans.*, Vol. 18, 1975, p. 513.

On the Mikic-Rohsenow Pool Boiling Correlation

P. R. Sharma[1] and B. S. Varshney[2]

Nomenclature

g = acceleration of gravity
m = constant, 2.5 for water and 3.0 for organic fluids
q = heat flux
T = temperature
ΔT = wall superheat, $T_w - T_{sat}$
λ = latent heat of evaporation
μ = coefficient of viscosity
ρ = density of fluids
Φ = parameter defined by equation (14) of [1]

Subscripts

b = boiling
l = liquid
v = vapor
w = wall

Following the mechanism of transient heat conduction to, and subsequent replacement of, the superheated layer around the heating surface, Mikic and Rohsenow [1] have derived a new correlation for the calculation of heat flux in nucleate pool boiling. This correlation satisfactorily correlates the experimental data of Addoms [2] for distilled water and of Cichelli and Bonilla [3] for three organic liquids for the pressures greater than atmospheric ranging from 101.3 kN/m^2 to 13,680 kN/m^2. The aim of this technical brief is to report the generality of the above correlation to the experimental data even for the pressures smaller than the atmospheric.

In the present investigation the range of pressure was from 11.33 kN/m^2 to 98.44 kN/m^2 and that of the heat flux from 3.3 kW/m^2 to 41.73 kW/m^2. The data were for the transfer of heat from a horizontal cylinder of 410 ASIS stainless steel to the boiling pool of pure liquids: distilled water, isopropanol, ethanol and methanol. The test cylinder was heated by a cartridge type electric heater placed in it. The power input to the heater was modulated by an auto-transformer and was measured by means of an ammeter and a voltmeter of the precision grade. The calibrated copper constantan thermocouples measured the temperature of the heating surface and the boiling liquids. The heating surface temperature was measured circumferentially at three locations—at the top, at the side and at the bottom and the liquid temperature corresponding to these surface thermocouples. Mechanical quadrature technique was used to obtain the average values of the wall superheat, ΔT. The experimental setup used for the present investigation is described elsewhere [4, 5].

The results which have been correlated by the Mikic-Rohsenow correlation are shown in Figs. 1–4. The pressure range for the individual liquid is indicated in these figures. It appears from these figures that this correlation satisfactorily correlates the present experimental data for all the four liquids investigated. All these figures show a similar trend but different intercepts. As a matter of fact, the intercept

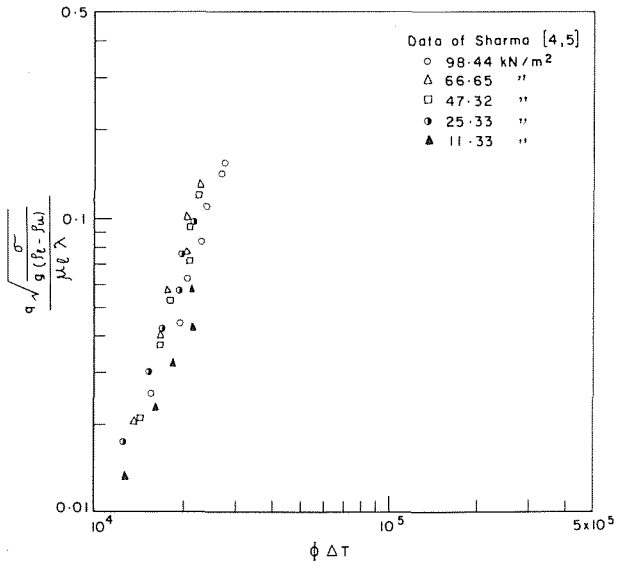

Fig. 1 Nucleate pool boiling data for water correlated by Mikic-Rohsenow correlation [1]

[1] Research Associate, Department of Chemical Engineering, University of Roorkee, Roorkee-247672, India.

[2] Professor, Department of Chemical Engineering, University of Roorkee, Roorkee-247672, India.

Contributed by the Heat Transfer Division for publication in the JOURNAL OF HEAT TRANSFER. Manuscript received by the Heat Transfer Division April 3, 1978.

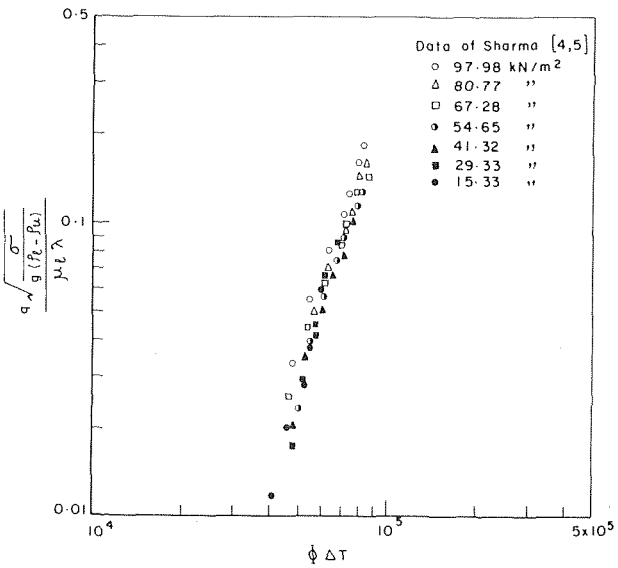

Fig. 2 Nucleate pool boiling data for isopropanol correlated by Mikic-Rohsenow correlation [1]

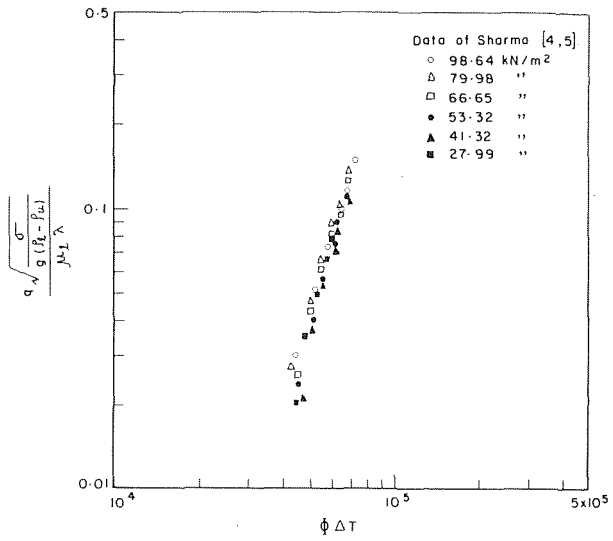

Fig. 4 Nucleate pool boiling data for methanol correlated by Mikic-Rohsenow correlation [1]

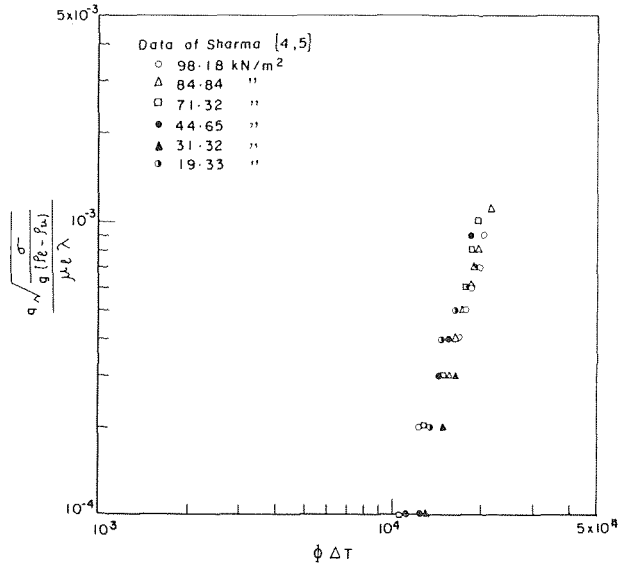

Fig. 3 Nucleate pool boiling data for ethanol correlated by Mikic-Rohsenow correlation [1]

accounts for the surface-liquid combination. Therefore, the different values of the intercept is an expected behaviour.

In summary, the Mikic-Rohsenow correlation is found to be consistent with the nucleate pool boiling data of present investigation which are for subatmospheric pressures.

References

1 Mikic, B. B. and Rohsenow, W. M., "A New Correlation of Pool-Boiling Data Including the Effect of Heating Surface Characteristics," ASME JOURNAL OF HEAT TRANSFER, May 1969, pp. 245–250.

2 Addoms, J. N., "Heat Transfer at High Rates to Water Boiling Outside Cylinders." D.Sc. Thesis, Department of Chemical Engineering, MIT, 1948.

3 Cichelli, M. T. and Bonilla, C. F., "Heat Transfer to Liquid Boiling Under Pressure," *Trans. AIChE.*, Vol. 41, 1945, pp. 755–787.

4 Sharma, P. R., "Heat Transfer Studies in Pool Boiling of Liquids," Ph.D. Thesis, Department of Chemical Engineering, University of Roorkee, Roorkee, April 1977.

5 Sharma, P. R., Kumar, P., Gupta, S. C. and Varshney, B. S., "Nucleate Pool Boiling of Liquids from Horizontal Cylinder under Subatmospheric Pressure," *Proceedings of IV National Heat and Mass Transfer Conference*, University of Roorkee, Roorkee, Paper No. 4 HMT 47, Nov. 1977, pp. 423–433.

On the Thermodynamic Superheat Limit for Liquid Metals and Its Relation to the Leidenfrost Temperature[1]

F. S. Gunnerson[2] and A. W. Cronenberg[3]

Introduction

The onset of stable film boiling plays an important role in the transient behavior of systems which incorporate exceedingly high heat transfer rates, such as nuclear reactors, rocket engines and cryogenic devices. The minimum heater surface temperature required to just sustain the stable film boiling process is defined as the Leidenfrost temperature T_{LEID}. Since the Leidenfrost temperature has become an increasingly important parameter in nuclear safety analysis, particularly with respect to the understanding of vapor explosion phenomena (where molten metals are often considered), its accurate prediction is of importance.

Predictions of the heater surface temperature at which stable film boiling commences have been attempted previously based on hydrodynamic theory [1, 2, 3], empirical fit to experimental data [4] and thermodynamic theory [5, 6]. In general, the hydrodynamic predictions yield poor results for liquid metals, while the empirical correlation, which generally yields good results, provides little insight into

[1] This work was supported by the U. S. Nuclear Regulatory Commission, Division of Fast Reactor Safety Research.

[2] Department of Chemical and Nuclear Engineering, The University of New Mexico, Albuquerque, N. M. 87131.

[3] EG&G Idaho, Inc., Idaho Falls, Idaho 83401.

Contributed by the Heat Transfer Division for publication in the JOURNAL OF HEAT TRANSFER. Manuscript received by the Heat Transfer Division February 16, 1978.

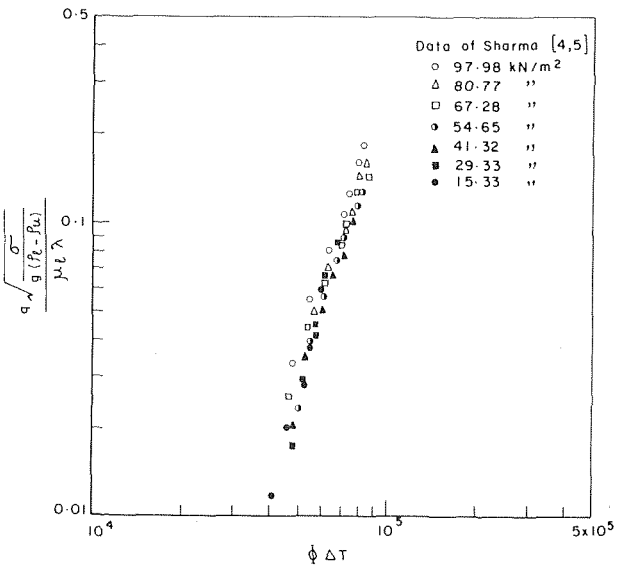

Fig. 2 Nucleate pool boiling data for isopropanol correlated by Mikic-Rohsenow correlation [1]

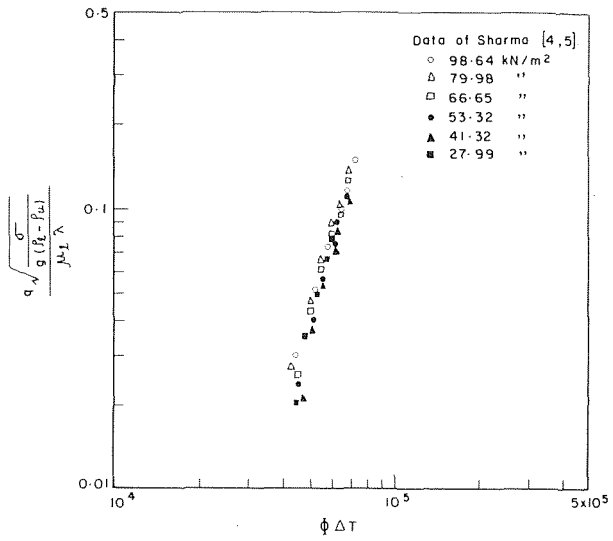

Fig. 4 Nucleate pool boiling data for methanol correlated by Mikic-Rohsenow correlation [1]

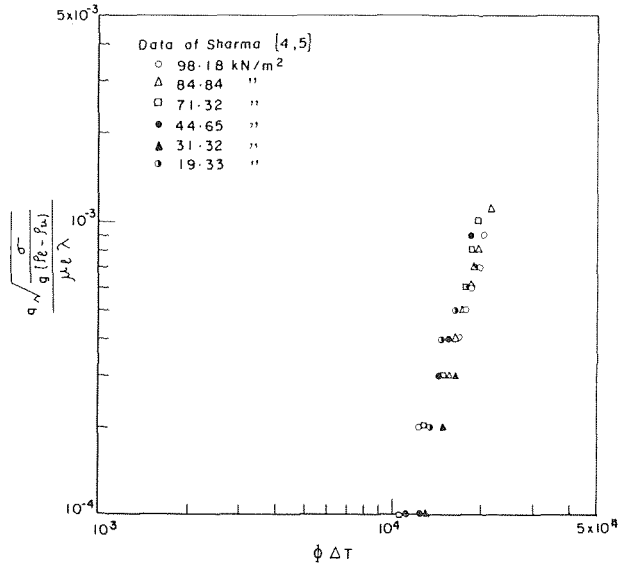

Fig. 3 Nucleate pool boiling data for ethanol correlated by Mikic-Rohsenow correlation [1]

accounts for the surface-liquid combination. Therefore, the different values of the intercept is an expected behaviour.

In summary, the Mikic-Rohsenow correlation is found to be consistent with the nucleate pool boiling data of present investigation which are for subatmospheric pressures.

References

1 Mikic, B. B. and Rohsenow, W. M., "A New Correlation of Pool-Boiling Data Including the Effect of Heating Surface Characteristics," ASME JOURNAL OF HEAT TRANSFER, May 1969, pp. 245–250.

2 Addoms, J. N., "Heat Transfer at High Rates to Water Boiling Outside Cylinders." D.Sc. Thesis, Department of Chemical Engineering, MIT, 1948.

3 Cichelli, M. T. and Bonilla, C. F., "Heat Transfer to Liquid Boiling Under Pressure," *Trans. AIChE.*, Vol. 41, 1945, pp. 755–787.

4 Sharma, P. R., "Heat Transfer Studies in Pool Boiling of Liquids," Ph.D. Thesis, Department of Chemical Engineering, University of Roorkee, Roorkee, April 1977.

5 Sharma, P. R., Kumar, P., Gupta, S. C. and Varshney, B. S., "Nucleate Pool Boiling of Liquids from Horizontal Cylinder under Subatmospheric Pressure," *Proceedings of IV National Heat and Mass Transfer Conference*, University of Roorkee, Roorkee, Paper No. 4 HMT 47, Nov. 1977, pp. 423–433.

On the Thermodynamic Superheat Limit for Liquid Metals and Its Relation to the Leidenfrost Temperature[1]

F. S. Gunnerson[2] and A. W. Cronenberg[3]

Introduction

The onset of stable film boiling plays an important role in the transient behavior of systems which incorporate exceedingly high heat transfer rates, such as nuclear reactors, rocket engines and cryogenic devices. The minimum heater surface temperature required to just sustain the stable film boiling process is defined as the Leidenfrost temperature T_{LEID}. Since the Leidenfrost temperature has become an increasingly important parameter in nuclear safety analysis, particularly with respect to the understanding of vapor explosion phenomena (where molten metals are often considered), its accurate prediction is of importance.

Predictions of the heater surface temperature at which stable film boiling commences have been attempted previously based on hydrodynamic theory [1, 2, 3], empirical fit to experimental data [4] and thermodynamic theory [5, 6]. In general, the hydrodynamic predictions yield poor results for liquid metals, while the empirical correlation, which generally yields good results, provides little insight into

[1] This work was supported by the U. S. Nuclear Regulatory Commission, Division of Fast Reactor Safety Research.

[2] Department of Chemical and Nuclear Engineering, The University of New Mexico, Albuquerque, N. M. 87131.

[3] EG&G Idaho, Inc., Idaho Falls, Idaho 83401.

Contributed by the Heat Transfer Division for publication in the JOURNAL OF HEAT TRANSFER. Manuscript received by the Heat Transfer Division February 16, 1978.

the basic phenomenon and requires prior experimental data of the variables sought. The thermodynamic approach, which incorporates simple equations of state (EOS) such as the van der Waals EOS, yields good results for the cryogens and simple fluids, but provides poor approximations for the more complex liquid metals.

Spiegler, et al. [6] suggested that the Leidenfrost temperature is a thermodynamic property of the fluid alone, independent of the substratum. They presumed that T_{LEID} is numerically equivalent to the liquid's maximum, metastable superheat temperature, and calculated that

$$T_{\mathrm{LEID}} = T_{\mathrm{MAX},S} = (27/32)\, T_c \tag{1}$$

for fluids which obey the van der Waals EOS. Experimental evidence, however, indicates that such is not always the case, in that periodic liquid-solid contact, known to exist at the Leidenfrost point under most experimental conditions, may have a pronounced effect on the location of the Leidenfrost temperature [1, 2, 4]. Thus, measured Leidenfrost data span a wide range. In general, better wetting (larger contact area) requires a higher heater surface temperature to sustain the film boiling process [2, 7]. Similarly, poor wetting limits interfacial contact area, and hence, a lower wall temperature is required to sustain film boiling. Therefore, the thermophysical nature of the heating surface normally should be considered when predicting the Leidenfrost temperature.

To assess the effect of contact on T_{LEID}, the heat transfer process between the heater and coolant is considered in the manner which follows. When two semi-infinite slabs of constant properties and different uniform temperatures are brought into intimate contact, the interface rapidly achieves a temperature which is invarient with time [8]. For the case of a solid wall and a stationary liquid (a situation common to most Leidenfrost experiments) the interface temperature has a steady-state value given by [8]

$$T_I = \frac{T_w(k/\sqrt{\alpha})_w + T_L(k/\sqrt{\alpha})_L}{(k/\sqrt{\alpha})_w + (k/\sqrt{\alpha})_L} \tag{2}$$

where T_w and T_L are the initial, precontact temperatures of the wall and liquid, α the thermal diffusivity and k the thermal conductivity. Equation (2) is also approximately valid for finite heater-coolant geometries when the contacting period is sufficiently short so that the thermal penetration distance is much less than the characteristic dimension of either the heater or liquid. Since the Leidenfrost temperature is defined as the minimum wall temperature for film boiling, T_w in equation (2) may also be viewed as a Leidenfrost temperature. When the interface is "perfect", that is, complete wetting, free from impurities and favorable sites for vapor nucleation, the maximum permissible interface temperature without vapor formation can be considered that of the liquid's maximum metastable superheat temperature, $T_{\mathrm{MAX},S}$. Therefore, if the instantaneous contact interface temperature T_I is greater than $T_{\mathrm{MAX},S}$, vapor formation is inevitable and film boiling initiated. If the interface is not perfect, that is, partial or no wetting, with nucleation sites and/or impurities, then film boiling or liquid superheating may commence at a temperature considerably less than $T_{\mathrm{MAX},S}$, and may approach the liquid's saturation temperature. If the interface temperature upon contact is less than the liquid's saturation temperature, interfacial vapor formation becomes impossible. Thus, to just sustain the film boiling process, the interfacial contact temperature is bounded by

$$T_{\mathrm{SAT}} < T_I \leq T_{\mathrm{MAX},S} \tag{3}$$

Solving equation (2) for the wall temperature just prior to contact ($T_w \approx T_{\mathrm{LEID}}$) and inserting the maximum and minimum interface and liquid temperatures yields:

$$T_{\mathrm{SAT}} < T_{\mathrm{LEID}} \leq \frac{T_{\mathrm{MAX},S}[(k/\sqrt{\alpha})_w + (k/\sqrt{\alpha})_L] - T_{MP^*}\,(k/\sqrt{\alpha})_L}{(k/\sqrt{\alpha})_w} \tag{4}$$

where T_{SAT} is the liquid's saturation temperature, $T_{\mathrm{MAX},S}$ the maximum allowable liquid superheat temperature, T_{MP} the lowest possible liquid temperature (that of its melting point) and the superscript * indicates (for convenience) no liquid subcooling below its melting point. If $k_W/k_L \gg 1$, equation (4) reduces to

$$T_{\mathrm{SAT}} < T_{\mathrm{LEID}} \lesssim T_{\mathrm{MAX},S} \tag{5}$$

Considering such arguments, it can be seen that the relationship originally proposed by Spiegler, et al. [6] (equation (1)) may be most accurate for well wetted Leidenfrost-type-boiling situations where the thermal conductivity of the wall is much greater than that of the liquid, such as cryogens on a copper surface, etc. Also, the lower limit of the Leidenfrost temperature being that of the liquid's saturation temperature (equations (4) and (5)) is consistent with that concluded by Baumeister, Hendricks and Hamill [9].

Prediction of the Maximum Metastable Superheat

For a liquid which obeys the van der Waals EOS (and at a zero reduced pressure), Spiegler, et al. [6] calculated the maximum, metastable superheat, $T_{\mathrm{MAX},S}$, to be that given by equation (1).

Leinhard [10] combined the Van der Waals EOS with Maxwell's criterion[4] and obtained the following Maxwell-van der Waals prediction for the maximum superheat

$$\frac{T_{\mathrm{MAX},S} - T_{\mathrm{SAT}}}{T_c} = \left(1 - \frac{T_{\mathrm{SAT}}}{T_c}\right) - \frac{7}{32}\left[1 - \left(\frac{T_{\mathrm{SAT}}}{T_c}\right)^{5.16}\right] \tag{6}$$

However, when compared to experimental data, equation (6) produces results that are somewhat low [10]. Based on experimental values of $T_{\mathrm{MAX},S}$, for non-metals [11] Leinhard [10] modified equation (6) and showed that the relation

$$\frac{T_{\mathrm{MAX},S} - T_{\mathrm{SAT}}}{T_c} = \left(1 - \frac{T_{\mathrm{SAT}}}{T_c}\right) - 0.905\left[1 - \left(\frac{T_{\mathrm{SAT}}}{T_c}\right)^{8}\right] \tag{7}$$

better correlates experimental data for $T_{\mathrm{MAX},S}$.

Fig. 1 illustrates the results of equations (1, 6) and (7) for $T_{\mathrm{MAX},S}$, and compares them with experimental Leidenfrost data. As shown, such equations are accurate in predicting the upper limit of the experimental Leidenfrost temperature for the cryogens and simple fliuds, but a large discrepancy exists for the liquid metals. This error

[4] Maxwell's Criterion or Equal Area Rule states that the integral of the differential Gibbs function along an isotherm between the saturated liquid and vapor states, i.e., $\int_l^v v\,dp$, equals zero.

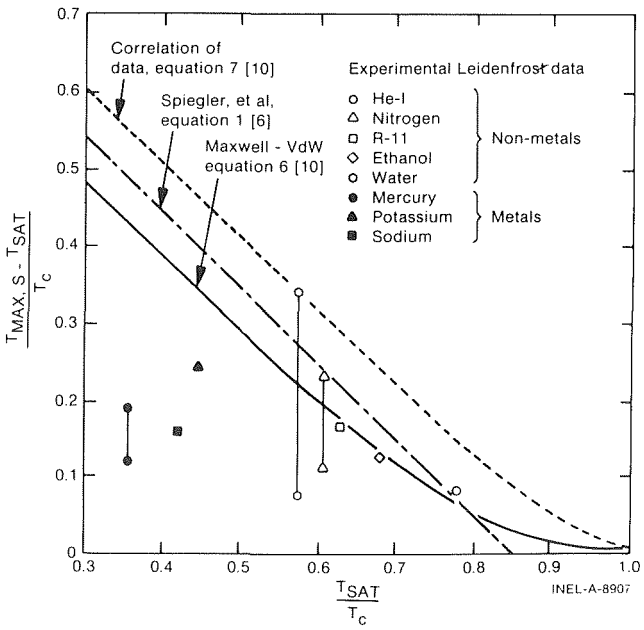

Fig. 1 Comparison of maximum superheat correlations with experimental Leidenfrost data (at 1 atm)

may arise because the simple van der Waals EOS (basis of equations (1) and (6)) fails to model the more complex structure of these liquids and/or the effects of the heating surface are not included. Similarly, the experimental correlation (equation (7)) does not incorporate liquid metal data. Thus, equations (1, 6) and (7) can produce erroneous Leidenfrost results if applied to situations where k_w/k_L is not much greater than unity, such as boiling of liquid metals on metallic-like surfaces.

Liquid Metals

To more accurately assess the maximum, metastable superheat $T_{MAX,S}$ for liquid metals from thermodynamic considerations, the modified rigid sphere equation of state developed by Young and Alder [12] is applied, the governing EOS being of the form:

$$P = P_0 - a/v^2 \tag{8}$$

where the rigid sphere pressure, P_0, is that originally proposed by Carnahan and Starling [13]:

$$P_0 = \frac{NkT}{v}\left[\frac{1 + \zeta + \zeta^2 - \zeta^3}{(1-\zeta)^3}\right] \tag{9}$$

where $\zeta = \pi N\sigma^3/6V$, σ = hard sphere diameter and P_0 the hard sphere pressure. The last term of equation (8) approximates the attractive potential found in liquid metals where the constant a is equal to $-E_0V_0$ with E_0 being the molar cohesive energy and V_0 the molar volume of the metal. The most reliable data for E_0 and V_0 for metals are available in the solid state [14]. Young and Alder [12] note that the use of solid state data is justified since the value of the constant, a, shows no significant difference between solid and liquid mercury. Also, the use of solid state data for E_0 and V_0 is not surprising since the behavior of liquid metals near their melting points is not too different from that of the corresponding solids, and it can be seen that the parameters appearing in the model potential for the liquid state are often derived from solid state data [15]. Equation (8) has been shown to accurately predict the critical temperature of liquid metals, and to a lesser extent the critical volume and pressure [12].

Combining equations (8) and (9), we express the reduced EOS for metals as

$$P_r = A(B/V_r + CB^2/V_r^2 + C^2B^3/V_r^3 - C^3B^4/V_r^4) \times (1 - CB/V_r)^{-3} - a\,B^2/P_cV_r^2 \tag{10}$$

where:

$$A = R\,T_r\,T_c/P_c,\ B = V_c^{-1},\ C = N\pi\sigma^3/6,\ a = -E_0V_0$$

and the subscripts r and c refer to reduced and critical properties respectively.

An expression for the maximum superheat, $T_{MAX,S}$, is thus found for liquid metals by applying a method parallel to that of Spiegler, et al., [6].[5] From equation (10) the maximum metastable superheat for *liquid metals* becomes

$$T_{MAX,S} = \frac{(0.50136)\,(-E_0V_0)}{N\pi R\sigma^3} \tag{11}$$

It should be noted that $T_{MAX,S}$ in equation (11) is sensitive to the accuracy of the atomic diameter, σ, which is a difficult property to determine. Values differing by ±30 percent for σ are common to the literature. An average value of σ was used in the results presented in Table 1.

Table 1 lists the thermophysical properties and calculated maximum, metastable superheat temperatures for several liquid metals. Unfortunately, no experimental maximum superheat data, for liquid metals, are available for comparison. Table 2 shows a comparison of theory with experimental Leidenfrost data. As can be seen, in virtually all cases, the range of Leidenfrost temperatures as predicted from theory (equation (4)) encompass the experimentally determined values. Also shown in Table 2 are calculated homogeneous nucleation temperatures, T_{HN}, as predicted from the kinetic theory of nucleation (see [16]). Since $T_{MAX,S}$ and T_{HN} both physically quantify the liquid's upper superheat limit, without spontaneous vapor formation, their approximate parity (Table 2) is not surprising.

It is interesting to note that Schins [32] demonstrated that the Leidenfrost temperature for water and sodium corresponds to the homogeneous nucleation temperature calculated by the Döring formula.

Application to Vapor Explosion

A point of controversy [26] in nuclear reactor safety is the interpretation of experimental results (Freon/water [27], Freon/oil [28]) where a rapid pressurization (vapor explosion) is observed in a range of contact interface temperatures somewhat below the critical temperature of the working fluid. In [29] this temperature is assessed in terms of nucleation kinetics only; that is, for well wetted systems the temperature condition is considered to be T_{HN} (assessed from kinetic theory, see [16]). For imperfect wetting, a lower temperature, called the spontaneous nucleation temperature ($T_{SAT} < T_{SN} < T_{HN}$) is considered as the threshold temperature for an explosion [30]. However, others [27, 31] have interpreted such experiments in terms of film boiling destabilization, such that vapor collapse leads to a violent nucleate boiling process with attendant fragmentation into a surface area, large enough to cause explosive vaporization and pressurization. The range of interfacial contact temperatures at film boiling destabilization (equation (3)) span the majority of the spontaneous nucleation temperature range ($T_{SAT} < T_{SN} < T_{HN}$) and closely approach the homogeneous nucleation temperature in the upper limit ($T_{MAX,S} \approx T_{HN}$, see Table 2). Thus, experimental results producing an ex-

Table 1 Thermophysical properties and calculated maximum, metastable superheat temperatures for liquid metals

Metal	$-E_0$ (kcal/mole) [14]	V_0 (cc/mole) [14]	σ^* (Å)	$T_{MAX,S}$ (K) (equation (11))
Na	26.02	23.79	3.38	2140
Hg	15.41	14.09	3.01	1060
K	21.69	45.61	4.36	1590
Cs	19.22	69.19	5.02	1400
Rb	20.20	56.07	4.70	1450
Cd	26.80	13.00	2.93	1850
Li	38.20	13.02	3.03	2380
Zn	31.00	9.17	2.63	2080
Mg	35.30	14.00	3.05	2320

* Averaged value of atomic diameters common to the literature.

Table 2 Comparison of homogeneous nucleation, maximum, metastable superheat and leidenfrost temperatures

FLUID	T_{HN}[9] (K)	$T_{MAX,S}$ (K)	$T_{LEID} = T_{HEATER\ SURFACE}$ (K) Theory	Experiment
He-I	—	4.43[1]	4.07–4.43[3]	4.51 [17][2]
Nitrogen	—	106[1]	77–106[3]	91 [18]–106 [19]
Freon-22	326	311[1]	232–311[3]	—
Freon-11	—	397[1]	297–397[3]	375 [20]
n-pentane	421	396[1]	309–396[3]	368 [2]
n-hexane	457	428[1]	342–428[3]	—
Ethanol	468	435[1]	351–435[3]	428 [21]
Water	575	578[4]	373–636[5]	537 [21][5]–593 [21][5]
Sodium	2300	2140[6]	1154–3000[7]	1594 [22][7]
Potassium	—	1590[6]	1030–1950[7]	1588 [23][7]
Mercury	—	1060[6]	630–1550[8]	967 [24][8]

1 Calculated from equation (1).
2 Estimated from constant heat flux data.
3 From equation (5), where $T_{MAX,S}$ is given by equation (1).
4 From [25], based on significant structure theory (SST) EOS.
5 Stainless steel surface.
6 From equation (11).
7 Tantalum surface.
8 Copper surface.
9 See [16] for equation.

[5] $(\partial P_r/\partial V_r) = 0$ at constant temperature evaluated at $P_r = P/P_c = 0$. This method of evaluating $T_{MAX,S}$ at $P_r = 0$ invokes little error since for liquid metals the left hand side of equation (10) (differentiated) is approximately five orders of magnitude less than the right hand side. For example, P_r (1 atm) for N_a is approximately 0.00245.

plosion which have been interpreted in terms of the kinetic theory of nucleation can likewise be viewed in terms of film boiling destabilization with attendant fine scale fragmentation of the hot material.

Conclusions

1 The upper and lower *limits of the Leidenfrost temperature* T_{LEID} can be approximated by equation (4), with the upper limit requiring a knowledge of the liquid's maximum, metastable superheat temperature.

2 The maximum, metastable superheat temperature $T_{MAX,S}$ for *liquid metals* is derived from a modified, rigid sphere equation of state and may be approximated by equation (11). For *nonmetals,* particularly those which obey a van der Waals EOS, equations (1, 6) or (7) provide a better estimate of $T_{MAX,S}$.

3 The interfacial temperature requirement for a vapor explosion from kinetic nucleation theory is similar to the minimum interfacial temperature requirement for film boiling, equation (3). Thus, experimental vapor explosion results which have been interpreted in terms of the kinetic theory of nucleation can likewise be viewed in terms of film boiling destabilization.

References

1 Berenson, P. J., ASME JOURNAL OF HEAT TRANSFER, Vol. 83, Aug. 1961, pp. 351–358.

2 Berenson, P. J., Tech. Rep. No. 17, NP-8415, Massachusetts Institute of Technology, Cambridge, Mass., 1960.

3 Gunnerson, F. S., Cronenberg, A. W., *Proc. Annual ANS Meeting,* New York, N.Y., June 1977, pp. 381–383.

4 Henry, R. E., *Trans. AiChE*—14th Heat Trans. Conf., Atlanta, Georgia, Aug. 5–8, 1973.

5 Baumeister, K. J., Simon, F. F., ASME JOURNAL OF HEAT TRANSFER, May 1973, pp. 166–173.

6 Spiegler, P., Hopenfeld, J., Silberberg, M., Bumpus, C. F., Norman, A., *International Journal of Heat and Mass Transfer,* Vol. 6, 1963, pp. 987–994.

7 Dwyer, O. E., ANS Monograph Series on Nuclear Science and Technology, ANS, Hinsdale, Ill. 1976.

8 Carslaw, H. S., Jaeger, J. C., second ed., Oxford Press, 1959.

9 Baumeister, K. J., Hendricks, R. C., & Hamill, T. D., NASA TN D-3226, 1966.

10 Leinhard, J. H., *Chemical Engineering Science,* Vol. 31, No. 9, 1976, pp. 847–849.

11 Skripov, V. P., Pavlov, P. A., *High Temperature,* (translated from Russian), Vol. 8, No. 4, 1970, pp. 782–787.

12 Young, D. A., Alder, B. J., *Physical Review* A, Vol. 3, No. 1, Jan. 1971, pp. 364–371.

13 Carnahan, N. F., Starling, K. E., *Journal of Chemical Physics,* Vol. 51, No. 2, July 1969, pp. 635–636.

14 Gschneidner, K. A., *Solid State Physics,* Vol. 16, Academic Press, New York, 1964, pp. 275–426.

15 Watts, R. O., McGee, I. J., John Wiley & Sons, New York, N.Y., 1976, p. 291.

16 Volmer, M., Z. *Electrochemie,* Vol. 35, 1929, p. 555.

17 Goodling, J. S., Irey, R. K., *Advances in Cryogenic Engineering,* Vol. 14, Plenum, N. Y., 1969, pp. 159–169.

18 Kershock, E. G., Bell, K. J., *Advances in Cryogenic Engineering,* Vol. 15, Plenum, N.Y., 1970, pp. 271–282.

19 Merte, H., Clark, J. A., *Advances in Cryogenic Engineering,* Vol. 7, Plenum, N. Y., 1962, pp. 546–550.

20 Stock, B. J., ANL-6175, Argonne National Laboratory, Argonne, Ill., June 1960

21 Godliski, E. S., Bell, K. J., *Proceedings of the Third International Heat Transfer Conference,* Vol. 4, AIChE, New York, N. Y., 1966, pp. 51–58.

22 Farahat, M., PhD Thesis, Northwestern University, Evanston, Ill., 1971, also ANL-7909.

23 Poppendiek, H. F., et al., GLR-42, SAN-409-29, Geoscience, Ltd., Solana Beach, Calif., Jan. 1966.

24 Popoendiek, H. F., et al., GLR-55, SAN-677-15, Geoscience, Ltd., Solana Beach, Calif., June 1967.

25 Eberhart, J. G., Schnyders, H. C., *Journal of Physical Chemistry,* Vol. 77, No. 23, 1973, pp. 2730–2736.

26 Cronenberg, A. W., Benz, R., to be published, Advances in Nuclear Science and Technology, 1978.

27 Anderson, R. P., Armstrong, D. R., ASME Meeting on Nuclear Reactor Safety Heat Transfer, Atlanta, Ga., Nov. 1977.

28 Henry, R. E., Fauske, H. K., McUmber, L. M., *Proceedings of ANS Conference on Fast Reactor Safety,* Chicago, Ill. (Oct. 1976).

29 Fauske, H. K., *Nuclear Science and Engineering,* Vol. 51, 1973, pp. 95–101.

30 Fauske, H. K., *Reactor Technology,* Vol. 15, No. 4, 1972–1973, pp. 278–302.

31 Board, S. J., Hall, R. W., 3rd Specialist Meeting on Na-Fuel Interaction in Fast Reactors, Tokyo, March 1976.

32 Schins, H. E. J., *Atomkernerqie,* Bd. 26, 1975, pp. 48–52.

Transient Response of a Hollow Cylindrical-Cross-Section Solid Sensible Heat: Storage Unit—Single Fluid

F. W. Schmidt[1] and J. Szego[2]

Nomenclature

A = cross-sectional area of the flow channel
c = specific heat at constant pressure
h = convective film coefficient
k = thermal conductivity
L = length of the unit
$\dot{m}$ = mass flow rate of fluid
P = heated perimeter in contact with fluid
Q = total heat stored
Q_{max} = maximum heat storage
r = radial coordinate
r_i = inner radius of annulus
r_0 = outer radius of annulus
t = temperature
$\bar{t}$ = mean temperature
V = volume of storage material
v = fluid velocity
x = axial coordinate
α = thermal diffusivity
ρ = density
θ = time.

Subscripts

a = adiabatic surface
f = fluid
fi = fluid at entrance to unit
fo = fluid at outlet of unit
m = storage material
o = initial condition
w = surface in contact with fluid

Introduction

Although many different methods have been proposed for the storage of thermal energy, the methods most extensively used at the present time utilize sensible heat storage. A review of previous published work on the prediction of the transient response of these units under single blow operating conditions was presented by Szego and Schmidt [1].

The objective of this work is to determine the transient response of a solid sensible heat storage unit having a hollow cylindrical cross section and operating under single-blow conditions. The finite-conductivity model will be used to obtain the results for two flow configurations. In the first case, the fluid flows through the channel formed by the inner surface of the hollow cylinder while the outer surface is considered to be adiabatic. In the second case, the fluid flows axially over the outer surface while the inner surface is considered to be adiabatic.

The results obtained for the aforementioned problems can be extended to predict the performance of several heat storage unit configurations. For instance, the response of a storage unit composed of a series of equally spaced circular channels, through which the energy transporting fluid flows in parallel, may be approximated by a unit

[1] Department of Mechanical Engineering, The Pennsylvania State University, University Park, PA, 16802. Mem. ASME

[2] Department of Mechanical Engineering, The Pennsylvania State University, University Park, PA, 16802. Assoc. Mem. ASME.

Contributed by the Heat Transfer Division for publication in the JOURNAL OF HEAT TRANSFER. Manuscript received by the Heat Transfer Division April 27, 1978.

plosion which have been interpreted in terms of the kinetic theory of nucleation can likewise be viewed in terms of film boiling destabilization with attendant fine scale fragmentation of the hot material.

Conclusions

1 The upper and lower *limits of the Leidenfrost temperature* T_{LEID} can be approximated by equation (4), with the upper limit requiring a knowledge of the liquid's maximum, metastable superheat temperature.

2 The maximum, metastable superheat temperature $T_{MAX,S}$ for *liquid metals* is derived from a modified, rigid sphere equation of state and may be approximated by equation (11). For *nonmetals,* particularly those which obey a van der Waals EOS, equations (1, 6) or (7) provide a better estimate of $T_{MAX,S}$.

3 The interfacial temperature requirement for a vapor explosion from kinetic nucleation theory is similar to the minimum interfacial temperature requirement for film boiling, equation (3). Thus, experimental vapor explosion results which have been interpreted in terms of the kinetic theory of nucleation can likewise be viewed in terms of film boiling destabilization.

References

1 Berenson, P. J., ASME JOURNAL OF HEAT TRANSFER, Vol. 83, Aug. 1961, pp. 351–358.

2 Berenson, P. J., Tech. Rep. No. 17, NP-8415, Massachusetts Institute of Technology, Cambridge, Mass., 1960.

3 Gunnerson, F. S., Cronenberg, A. W., *Proc. Annual ANS Meeting,* New York, N.Y., June 1977, pp. 381–383.

4 Henry, R. E., *Trans. AiChE*—14th Heat Trans. Conf., Atlanta, Georgia, Aug. 5–8, 1973.

5 Baumeister, K. J., Simon, F. F., ASME JOURNAL OF HEAT TRANSFER, May 1973, pp. 166–173.

6 Spiegler, P., Hopenfeld, J., Silberberg, M., Bumpus, C. F., Norman, A., *International Journal of Heat and Mass Transfer,* Vol. 6, 1963, pp. 987–994.

7 Dwyer, O. E., ANS Monograph Series on Nuclear Science and Technology, ANS, Hinsdale, Ill. 1976.

8 Carslaw, H. S., Jaeger, J. C., second ed., Oxford Press, 1959.

9 Baumeister, K. J., Hendricks, R. C., & Hamill, T. D., NASA TN D-3226, 1966.

10 Leinhard, J. H., *Chemical Engineering Science,* Vol. 31, No. 9, 1976, pp. 847–849.

11 Skripov, V. P., Pavlov, P. A., *High Temperature,* (translated from Russian), Vol. 8, No. 4, 1970, pp. 782–787.

12 Young, D. A., Alder, B. J., *Physical Review* A, Vol. 3, No. 1, Jan. 1971, pp. 364–371.

13 Carnahan, N. F., Starling, K. E., *Journal of Chemical Physics,* Vol. 51, No. 2, July 1969, pp. 635–636.

14 Gschneidner, K. A., *Solid State Physics,* Vol. 16, Academic Press, New York, 1964, pp. 275–426.

15 Watts, R. O., McGee, I. J., John Wiley & Sons, New York, N.Y., 1976, p. 291.

16 Volmer, M., Z. *Electrochemie,* Vol. 35, 1929, p. 555.

17 Goodling, J. S., Irey, R. K., *Advances in Cryogenic Engineering,* Vol. 14, Plenum, N. Y., 1969, pp. 159–169.

18 Kershock, E. G., Bell, K. J., *Advances in Cryogenic Engineering,* Vol. 15, Plenum, N.Y., 1970, pp. 271–282.

19 Merte, H., Clark, J. A., *Advances in Cryogenic Engineering,* Vol. 7, Plenum, N. Y., 1962, pp. 546–550.

20 Stock, B. J., ANL-6175, Argonne National Laboratory, Argonne, Ill., June 1960

21 Godliski, E. S., Bell, K. J., *Proceedings of the Third International Heat Transfer Conference,* Vol. 4, AIChE, New York, N. Y., 1966, pp. 51–58.

22 Farahat, M., PhD Thesis, Northwestern University, Evanston, Ill., 1971, also ANL-7909.

23 Poppendiek, H. F., et al., GLR-42, SAN-409-29, Geoscience, Ltd., Solana Beach, Calif., Jan. 1966.

24 Popoendiek, H. F., et al., GLR-55, SAN-677-15, Geoscience, Ltd., Solana Beach, Calif., June 1967.

25 Eberhart, J. G., Schnyders, H. C., *Journal of Physical Chemistry,* Vol. 77, No. 23, 1973, pp. 2730–2736.

26 Cronenberg, A. W., Benz, R., to be published, Advances in Nuclear Science and Technology, 1978.

27 Anderson, R. P., Armstrong, D. R., ASME Meeting on Nuclear Reactor Safety Heat Transfer, Atlanta, Ga., Nov. 1977.

28 Henry, R. E., Fauske, H. K., McUmber, L. M., *Proceedings of ANS Conference on Fast Reactor Safety,* Chicago, Ill. (Oct. 1976).

29 Fauske, H. K., *Nuclear Science and Engineering,* Vol. 51, 1973, pp. 95–101.

30 Fauske, H. K., *Reactor Technology,* Vol. 15, No. 4, 1972–1973, pp. 278–302.

31 Board, S. J., Hall, R. W., 3rd Specialist Meeting on Na-Fuel Interaction in Fast Reactors, Tokyo, March 1976.

32 Schins, H. E. J., *Atomkernerqie,* Bd. 26, 1975, pp. 48–52.

Transient Response of a Hollow Cylindrical-Cross-Section Solid Sensible Heat: Storage Unit—Single Fluid

F. W. Schmidt[1] and J. Szego[2]

Nomenclature

A = cross-sectional area of the flow channel
c = specific heat at constant pressure
h = convective film coefficient
k = thermal conductivity
L = length of the unit
$\dot{m}$ = mass flow rate of fluid
P = heated perimeter in contact with fluid
Q = total heat stored
Q_{max} = maximum heat storage
r = radial coordinate
r_i = inner radius of annulus
r_0 = outer radius of annulus
t = temperature
$\bar{t}$ = mean temperature
V = volume of storage material
v = fluid velocity
x = axial coordinate
α = thermal diffusivity
ρ = density
θ = time.

Subscripts

a = adiabatic surface
f = fluid
fi = fluid at entrance to unit
fo = fluid at outlet of unit
m = storage material
o = initial condition
w = surface in contact with fluid

Introduction

Although many different methods have been proposed for the storage of thermal energy, the methods most extensively used at the present time utilize sensible heat storage. A review of previous published work on the prediction of the transient response of these units under single blow operating conditions was presented by Szego and Schmidt [1].

The objective of this work is to determine the transient response of a solid sensible heat storage unit having a hollow cylindrical cross section and operating under single-blow conditions. The finite-conductivity model will be used to obtain the results for two flow configurations. In the first case, the fluid flows through the channel formed by the inner surface of the hollow cylinder while the outer surface is considered to be adiabatic. In the second case, the fluid flows axially over the outer surface while the inner surface is considered to be adiabatic.

The results obtained for the aforementioned problems can be extended to predict the performance of several heat storage unit configurations. For instance, the response of a storage unit composed of a series of equally spaced circular channels, through which the energy transporting fluid flows in parallel, may be approximated by a unit

[1] Department of Mechanical Engineering, The Pennsylvania State University, University Park, PA, 16802. Mem. ASME

[2] Department of Mechanical Engineering, The Pennsylvania State University, University Park, PA, 16802. Assoc. Mem. ASME.

Contributed by the Heat Transfer Division for publication in the JOURNAL OF HEAT TRANSFER. Manuscript received by the Heat Transfer Division April 27, 1978.

consisting of a series of hollow cylinders with their outer surfaces adiabatic and the fluid flowing through the inner channel, Fig. 1(*a*). In a heat storage exchanger built in a shell and tube configuration, a possible mode of operation would be when the inner fluid was still, the inner surface essentially adiabatic, and the energy transporting fluid flows over the outer surface parallel to the axis of the hollow cylinder. Such a configuration is shown in Fig. 1(*b*). A complementary case would be when the outer fluid is stationary and the energy transporting fluid flows through the inner channel.

Mathematical Model

The transient response of these two storage unit configurations is described by the energy equation for the flowing fluid and the transient conduction equation for the storage material. The following assumptions have been made: a) constant fluid and material properties, b) uniform heat transfer coefficients, c) the initial temperature distribution in the storage material is uniform, d) a step change in the inlet fluid temperature is imposed at the start of the storage process, e) two-dimensional heat conduction in the storage material, f) constant fluid velocity.

The governing differential equations are:
moving fluid:

$$\rho_f c_f \left[\frac{\partial t_f}{\partial \theta} + v \frac{\partial t_f}{\partial x} \right] = hP(t_m - t_f) \tag{1}$$

storage material:

$$\frac{1}{\alpha_m} \frac{\partial t_m}{\partial \theta} = \frac{\partial^2 t_m}{\partial r^2} + \frac{1}{r} \frac{\partial t_m}{\partial r} + \frac{\partial^2 t_m}{\partial x^2}. \tag{2}$$

The initial conditions are

$$\theta = 0 \quad t_f = t_m = t_0$$

and the boundary conditions:

$$\theta > 0 \quad x = 0 \quad t_f = t_{fi} \quad \frac{\partial t_m}{\partial x} = 0 \quad r_i < r < r_0$$

$$x = L \quad \frac{\partial t_m}{\partial x} = 0 \quad r_i < r < r_0$$

fluid in contact with inner surface

$$r = r_i \quad h(t_m - t_f) = k_m \frac{\partial t_m}{\partial r}$$

$$r = r_i \quad \frac{\partial t_m}{\partial r} = 0$$

fluid in contact with outer surface

$$r = r_0 \quad \frac{\partial t_m}{\partial r} = 0$$

$$r = r_0 \quad h(t_f - t_m) = k_m \frac{\partial t_m}{\partial r}.$$

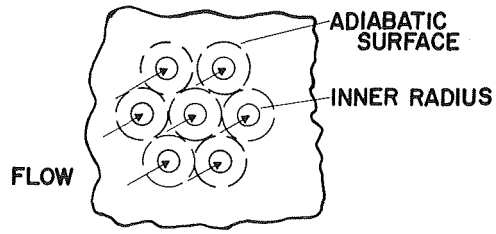

(a) CIRCULAR HOLES IN SOLID STORAGE MATERIAL

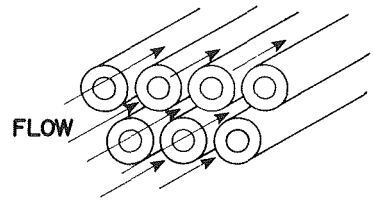

(b) FLOW OUTSIDE HOLLOW CYLINDERS

Fig. 1 Heat storage unit configurations

As shown by Schmidt and Szego [2], the transient term in equation (1), $\rho_f c_f A \, \partial t_f / \partial \theta$, can be neglected.

These equations can be placed in nondimensional form using the following variables:

$$Bi \equiv \frac{h(r_0 - r_i)}{k_m} \qquad R \equiv \frac{r}{r_0 - r_i}$$

$$V^+ \equiv \frac{r_0 - r_i}{L} \qquad U^+ \equiv \frac{r_w}{r_a}$$

$$T_f \equiv \frac{t_f - t_0}{t_{fi} - t_0} \qquad T_m \equiv \frac{t_m - t_0}{t_{fi} - t_0}$$

$$\xi = \frac{h(2\pi r_w)x}{\dot{m}_f c_f} \qquad \lambda = \frac{h(2\pi r_w)L}{\dot{m}_f c_f}$$

$$\eta \equiv \frac{h(2\pi r_w)\theta}{\pi(r_0^2 - r_i^2)\rho_m c_m} = \frac{h\theta}{(r_0 - r_i)\rho_m c_m} \left[\frac{2U^+}{1 + U^+} \right]$$

The radius of the surface in contact with the energy transporting fluid is denoted by r_w.

The nondimensional equations become:
moving fluid:

$$\frac{\partial T_f}{\partial \xi} = T_m - T_f \tag{3}$$

storage material:

$$\frac{\partial T_m}{\partial \eta} = C^* \left[\frac{1 + U^+}{2U^+} \right] \frac{\partial^2 T_m}{\partial \xi^2} + \left[\frac{1 + U^+}{2U^+} \right] \frac{1}{Bi} \left[\frac{\partial^2 T_m}{\partial R^2} + \frac{1}{R} \frac{\partial T_m}{\partial R} \right]. \tag{4}$$

where $C^* = (\lambda V^+)^2/\mathrm{Bi}$.
The initial conditions are:

$$\eta = 0 \quad T_m = T_f = 0$$

and the boundary conditions:

$$\xi = 0 \qquad T_f = 1 \qquad \frac{\partial T_m}{\partial \xi} = 0$$

$$\xi = \lambda \qquad \frac{\partial T_m}{\partial \xi} = 0$$

$$R = \frac{1}{|1 - U^+|} \qquad \frac{\partial T_m}{\partial R} = 0$$

$$R = \frac{U^+}{|1 - U^+|} \qquad \frac{\partial T_m}{\partial R} = \pm \mathrm{Bi}(T_f - T_m)$$

where + indicates that the outer surface is in contact with the fluid and − indicates that the inner surface is in contact with the fluid.

The solution of the mathematical model was obtained using a finite difference technique similar to that described in [2]. In order to reduce the discretization errors, the spacial derivatives were approximated by finite difference expressions using a modification of the method originally proposed by De Allen [3]. All results presented in this paper were obtained with a value of $V^+ = 0.01$ in order to minimize the effects of axial conduction on the results. The computer program, of course, imposes no restrictions on the value of V^+.

The amount of heat stored is determined directly from the temperature distribution in the storage material. The expression used is

$$Q = \rho_m c_m V(\bar{t}_m - t_0) \tag{5}$$

where V is the volume of the storage material and $\bar{t}_m$ is the mean temperature of the storage material. The maximum amount of heat is stored when the storage material reaches a uniform temperature equal to the inlet fluid temperature. The nondimensional heat storage, Q^+, is the ratio of the actual heat stored to the maximum possible heat storage and can be expressed as

$$Q^+ = \frac{Q}{Q_{\max}} = \frac{\bar{t}_m - t_0}{t_{fi} - t_0} \tag{6}$$

Discussion of Results

It has been shown by Szego and Schmidt [1] that for small Biot numbers, Bi $\leq$ 0.1, a simplified model can be used to determine the transient response of a heat storage unit composed of flat slabs of the storage material operating under single blow conditions. This model is based on the assumptions of infinite thermal conductivity for the storage material in the transverse direction, and zero thermal conductivity in the axial direction, indicating that the major resistance to the transfer of heat is located at the fluid-solid interface. Consequently, this model neglects thermal gradients normal to the flow direction, hence it is not directly influenced by the cross-sectional shape of the storage material. As a result, an insignificant error will be introduced in the determination of the transient response of the hollow cylindrical cross section storage unit using the simplified model, for Bi $\leq$ 0.1.

As the Biot number increases the finite conductivity model must be used and the effect of storage material geometry evaluated. In Fig. 2 the transient response of three geometrically different heat storage units are presented for a Biot number equal to 2.0. One unit is the flat slab, $U^+ = 1$, and the other two units have an annular cross section where the outer radius is ten times larger than the inner radius. When $U^+ = 0.1$ the fluid is in contact with the inner surface while for a $U^+ = 10$ the fluid is in contact with the outer surface of the hollow cylinder. The transient response as indicated by the nondimensional temperature of the fluid leaving and the fraction of the maximum heat storage appears to be nearly independent of the geometry of the storage unit. As the value of λ decreases, usually a result of an increase in the heat capacity of the energy transporting fluid $\dot{m}_f c_f$ and/or decrease in the length of the unit, the differences become larger. However, the differences still remain relatively small throughout the physically practical range for heat storage units. It is therefore recommended that if 0.1 < Bi $\leq$ 2, the effects of geometry may be neglected and the results for the flat slab presented in [2] for the finite conductivity model be used to predict the transient response of hollow cylindrical cross section solid sensible heat storage units.

If the Biot number is greater than 2, a condition usually encountered when the energy transporting fluid is a liquid, curvature effects must be considered. The transient response of the different storage units for Biot numbers of 10 and 30 are presented in Figs. 3 and 4. The curvature effect can be detected for all values of λ, thus it is recommended that the response of units operating under these conditions be determined using these curves. A more complete set of tabulated data for the case where the Biot number is greater than 2 has been presented in [4].

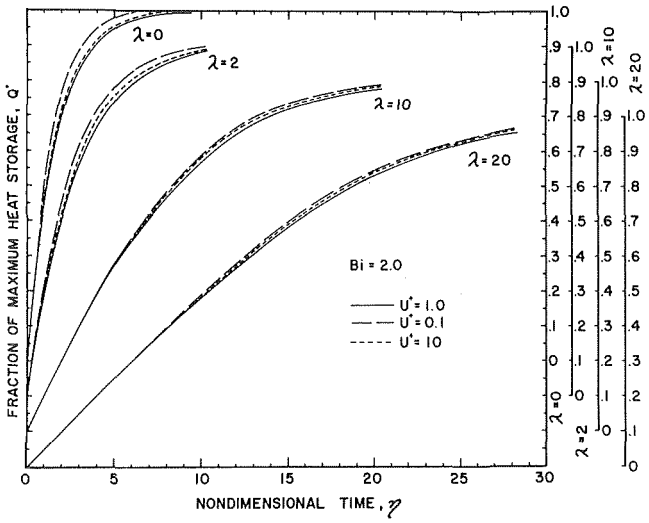

Fig. 2 Fraction of maximum heat storage, Bi = 2.0

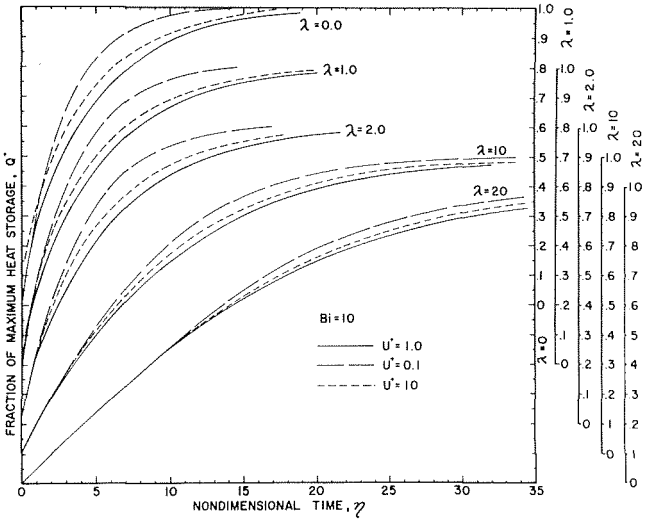

Fig. 3 Fraction of maximum heat storage, Bi = 10.0

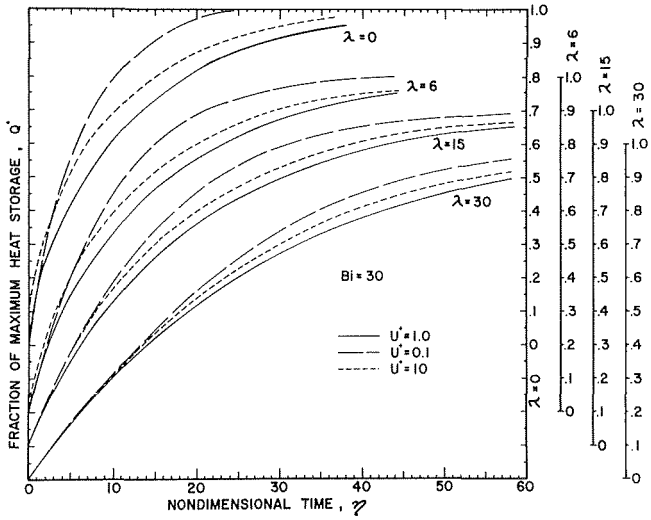

Fig. 4 Fraction of maximum heat storage, Bi = 30.0

Acknowledgment

The authors wish to acknowledge that this work was performed under NSF-RANN-AER-75-16216. The technical oversight of this grant is provided by DOE, Division of Conservation, Oak Ridge, Tenn.

References

1 Szego, J. Schmidt, F. W., "Analysis of the Effect of Finite Conductivity in the Single Blow Heat Storage Unit," submitted for publication, ASME JOURNAL HEAT TRANSFER, 1978.

2 Schmidt, F. W., Szego, J., "Transient Response of Solid Sensible Heat Thermal Storage Units—Single Fluid," ASME JOURNAL HEAT TRANSFER, Vol. 98, p. 471, 1976.

3 De Allen, D. N., Southwell, R. V., "Relaxation Methods Applied to Determine the Motion in Two Dimensions of a Viscous Fluid Past a Fixed Cylinder," *Quart. Journal Mech. and Appl. Math.*, Vol. 8, pt. 2, p. 129, 1955.

4 Schmidt, F. W., "Prediction of the Performance of Solid Sensible Heat Thermal Storage Units," NTIS Report NSF-RANN-AER-75-16216, 1978.

Analysis of the Effects of Finite Conductivity in the Single Blow Heat Storage Unit

J. Szego[1] and F. W. Schmidt[2]

Nomenclature

Bi = Biot number, hw/k_m
c = specific heat at constant pressure
d = semi-thickness of flow channel
G^+ = nondimensional parameter, $Pk_m/\dot{m}_f c_f$
h = convective film coefficient
k = thermal conductivity
L = length of the unit
$\dot{m}$ = mass flow rate of fluid
P = heated perimeter in contact with fluid
Q = total heat stored
Q_{max} = maximum heat storage
S = heat transfer surface area
t = temperature
$\bar{t}$ = mean temperature
V = volume of storage material
V^+ = characteristic length ratio, w/L
w = semi-thickness of storage material
X = nondimensional length, x/L
x = axial coordinate
Y = nondimensional transverse coordinate, y/w
y = transverse coordinate
α = thermal diffusivity of storage material
ρ = density
τ = time

Subscripts

f = fluid
fi = fluid at entrance of unit
fo = fluid exit of unit
m = storage material
o = initial condition

Introduction

For efficient use of many of the alternative energy sources as well as of waste heat, a means of storing thermal energy is needed. This paper will be restricted to solid sensible heat storage units of a rectangular cross section as shown in Fig. 1(a). The unit is initially at a uniform temperature, t_0, and the inlet fluid temperature experiences a step change. These operating conditions are frequently referred to as the "single blow" problem.

The individual channels and storage elements of the heat storage unit shown in Fig. 1(a) are considered to be identical and the unit to be perfectly insulated. If the mass flow rates of the fluids in each channel are equal, lines of symmetry will exist at the midpoints of the storage material and flow channel. The section to be analyzed can then be reduced to that shown in Fig. 1(b). The following assumptions have been made for all the models to be presented: a) constant fluid and material properties, b) uniform heat transfer coefficients, c) the initial temperature distribution in the storage material is uniform, d) a step change in the inlet fluid temperature is imposed at the start of the storage process, e) constant fluid velocity, f) thermal radiation negligible.

The first solutions to the single blow problem were based upon the assumption that the thermal conductivity of the storage material in the direction of the flow was zero while that in the transverse direction was infinite. This will be referred to as the simplified model. Solutions for this problem have been presented by Anzelius [1], Nusselt [2], Hausen [3, 4], Schumann [5], Larsen [6] and Klinkenberg [7]. Axial conduction was considered in a paper by Handley and Heggs [8], although the assumption of infinite thermal conductivity in the transverse direction was retained. In 1976, Schmidt and Szego [9] obtained a solution for the case where the thermal conductivity in both the axial and transverse directions was finite.

If the heat capacity rate of the fluid is infinite, the temperature of the fluid remains constant as it moves through the heat storage unit. Under these conditions, the temperature distribution in the storage material is one dimensional and the solution has been presented by Gröber, et al. [10].

The objective of this study is to define the regions of the independent variables where the various assumptions can be made without introducing appreciable errors in the prediction of the transient behavior of thermal energy storage units. The discussion will be restricted to the case of the single blow operating mode. The single blow solution can then be employed using the method of superposition, to determine the transient behavior of thermal energy storage units having time varying inlet fluid temperatures and mass flow rates.

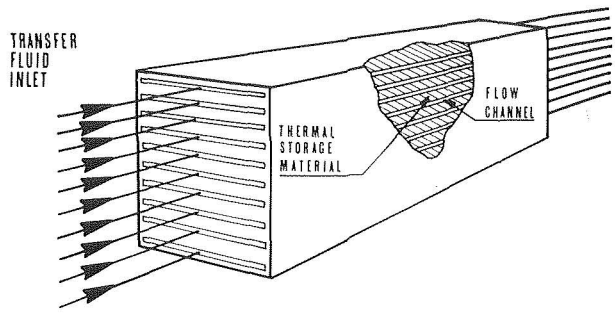

SINGLE FLUID FLAT-SLAB THERMAL STORAGE UNIT

Fig. 1 (a) Storage unit configuration

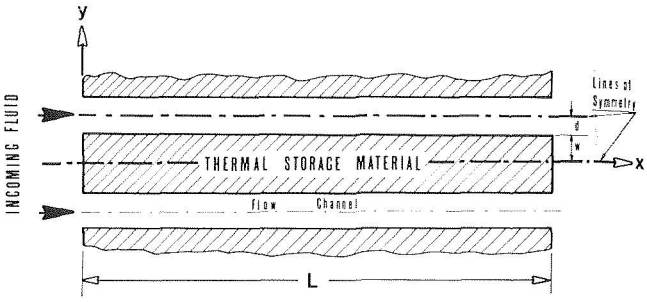

CROSS SECTION OF SINGLE FLUID FLAT-SLAB THERMAL STORAGE UNIT

Fig. 1 (b) Cross section

Fig. 1 Slab thermal energy storage unit

Mathematical Model and Solutions

Two different groups of nondimensional variables have been used in the equations which govern the transient response of the storage unit. One is associated with the finite conductivity model, while the other is associated with the simplified model. These groups are listed and their interrelationships presented in Table 1. The complete mathematical models and their solutions are presented in Table 2.

The finite conductivity model involves less restrictive assumptions therefore it can be used to obtain the transient response of a heat storage unit throughout the entire range of variables describing a practical unit. However, the closed form solutions are much more convenient to use and it is thus desirable to determine the regions where they can be used without introducing significant errors. The

[1] The Pennsylvania State University, University Park, PA 16802, Assoc. Mem. ASME
[2] The Pennsylvania State University, University Park, PA 16802, Mem. ASME

Contributed by the Heat Transfer Division for publication in the JOURNAL OF HEAT TRANSFER. Manuscript received by the Heat Transfer Division May 22, 1978

results obtained from the finite conductivity model have been used to define the boundaries of the applicable solution regions shown in Fig. 2.

The infinite heat capacity model is recommended for $\lambda < 0.1$. If, in addition, the Bi < 0.1 the temperature gradients within the storage material become negligible and a lumped heat capacity model can be used. A comparison of the values of the nondimensional heat storage obtained using these methods at $\lambda = 0.1$ and Bi = 0.1, the worst possible situation in this region, indicated close agreement and was the justification for establishing the boundaries shown in Fig. 2.

The boundary between the simplified and the finite conductivity model was drawn at Bi = 0.1. The values of the nondimensional heat storage and fluid outlet temperature obtained using these two models were compared. At $\lambda = 5$ very good agreement was obtained between the simplified and finite conductivity models while at $\lambda = 0.1$, the most severe case, the agreement is not as close, although, it is still considered to be within acceptable limits.

The total resistance to the transfer of heat from the fluid to the storage material is composed of two components. One is associated with the convective film coefficient and the other is related to the internal conduction process within the storage material. As the Biot number increases, the convective resistance decreases thereby increasing the significance of the internal resistance. The heat storage at high Biot numbers and $\lambda > 0.1$, thus becomes primarily a function of G^+/V^+ and *Fo*, showing little dependence on the Biot number. The magnitude of these effects were evaluated and it was concluded that for $\lambda > 0.1$ and Bi $\geq$ 30, the heat storage can be accurately predicted using the results for Bi = 30 given in [9].

The effect of neglecting axial conduction is more difficult to access. The finite conductivity model considers conduction in the axial direction but it has been shown that if axial conduction is small, the response of the storage unit can be presented using the parameters G^+/V^+ instead of using G^+ and V^+ independently. Handley and Heggs [8] have recommended that for $\lambda > 4$, the effect of axial conduction can be neglected if $(\lambda V^+)^2 \mathrm{Bi} \leq 0.1$. It must be noted, however, that the model used to obtain this criterion neglected the heat conduction normal to the flow direction. In general, the transverse conduction effects are several orders of magnitude greater than axial conduction in a continuous slab.

The finite conductivity mathematical model may also be expressed in terms of η and ξ, giving:

transfer fluid:

$$\frac{\partial T_f}{\partial \xi} = T_m - T_f, \tag{1}$$

Table 1 Nondimensional groups simplified and finite conductivities models

		Fluid:	Storage Material:
Common:			
	Temperature	$T_f = \frac{t_f - t_o}{t_{fi} - t_o}$	$T_m = \frac{t_m - t_o}{t_{fi} - t_o}$
	Heat Storage	$Q^+ = \frac{Q}{Q_{max}} = \frac{\bar{t}_m - t_o}{t_{fi} - t_o}$	
Specific:			
Name	Simplified Model	Finite Conductivity Model	Interrelationships
Time	$\eta = \frac{hS\tau}{V\rho_m c_m}$	$Fo = \frac{\alpha_m \theta}{w^2}$	$\eta = \mathrm{Bi}\ Fo$
Coordinate Axial	$\xi = \frac{hSx}{\dot{m}_f c_f L}$	$X = \frac{x}{L}$	$\xi = \mathrm{Bi}\ \frac{G^+}{V^+}\frac{x}{L}$
Transverse	$Y = \frac{y}{w}$	$Y = \frac{y}{w}$	-
Length of Storage Unit	$\lambda = \frac{hS}{\dot{m}_f c_f}$	$\frac{1}{V^+} = \frac{L}{w}$	$\lambda = \mathrm{Bi}\ \frac{G^+}{V^+}$
Surface Conductance	-	$\mathrm{Bi} = \frac{hw}{k_m}$	-
Fluid Heat Capacity	-	$\frac{1}{G^+} = \frac{\dot{m}_f c_f}{P\ k_m}$	-

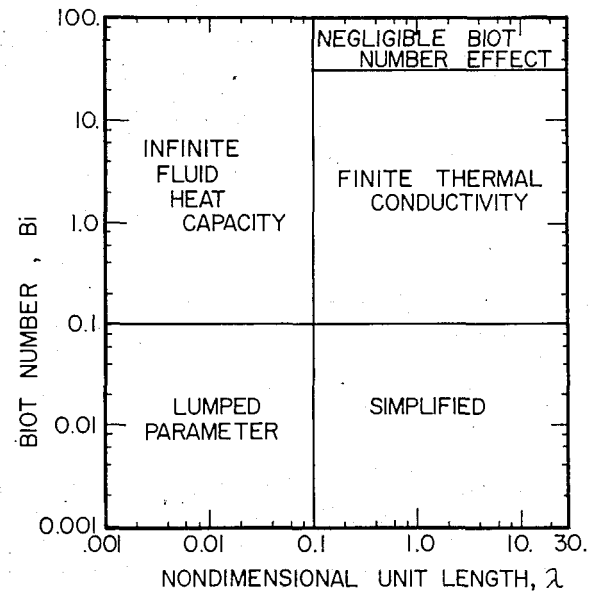

Fig. 2 Applicable solution region

Table 2 Available solutions

Mathematical Model:			Infinite Fluid Heat Capacity	
	Simplified	Finite Conductivity	Bi ≤ .1	Bi > .1
Observation Equations: Fluid	$\frac{\partial T_f}{\partial \xi} = T_m - T_f$	$\frac{dT_f}{dX} + \left(\frac{G^+}{V^+}\right)(\mathrm{Bi})(T_f - T_m) = 0$		
Storage Material	$\frac{\partial T_m}{\partial \eta} = T_f - T_m$	$V^{+2}\frac{\partial^2 T_m}{\partial X^2} + \frac{\partial^2 T_m}{\partial Y^2} = \frac{\partial T_m}{\partial Fo}$	$\frac{dT_m}{d\eta} = (1 - T_m)$	$\frac{\partial T_m}{\partial \eta} = \frac{1}{\mathrm{Bi}}\frac{\partial^2 T_m}{\partial Y^2}$
Initial and Boundary Conditions	$\xi = 0 \quad T_f = 1 \quad T_m = 1 - e^{-\eta}$	$Fo = 0 \quad T_m = T_f = 0$	$\eta = 0 \quad T_m = 0$	$\eta = 0 \quad T_m = 0$
	$\xi = 0 \quad T_m = 0$	$X = 0 \quad 0 < Y < 1 \quad T_f = 1 \quad \frac{\partial T_m}{\partial X} = 0$		$Y = 0 \quad \frac{\partial T_m}{\partial Y} = 0$
		$X = 1 \quad 0 < Y < 1 \quad \frac{\partial T_m}{\partial X} = 0$		$Y = 1 \quad \frac{\partial T_m}{\partial Y} = \mathrm{Bi}(T_m - T_f)$
		$0 \leq X \leq 1 \quad Y = 0 \quad \frac{\partial T_m}{\partial Y} = 0$		
		$0 \leq X \leq 1 \quad Y = 1 \quad \frac{\partial T_m}{\partial Y} = \mathrm{Bi}(T_f - T_m)$		
Solution:				
Fluid Temperature	$\eta < 2 \quad \xi < 2$	Fluid Outlet Temperature Only Schmidt - Szego	$T_f = T_m = 1$	$T_f = T_m = 1$
	$T_f[\eta,\xi] = 1 - e^{-(\eta+\xi)}\sum_{N=1}^{N=\infty}\left[\frac{\xi^N}{N!}\sum_{k=0}^{k=N-1}\frac{\eta^k}{k!}\right]$			
	$2.5 \eta < 4 \quad 2.5 \xi < 4$			
	$T_f[\eta,\xi] = 1 - \frac{1}{2}\left[1 + \mathrm{erf}(\sqrt{\xi} - \sqrt{\eta})\right] - \frac{\xi^{1/4}}{\eta^{1/4} + \xi^{1/4}} e^{-(\eta+\xi)} I_0(2\sqrt{\eta\xi})$			
	$\eta \geq 4 \quad \xi \geq 4$			
	$T_f[\eta,\xi] = 1 - \frac{1}{2}\left[1 + \mathrm{erf}(\sqrt{\xi} - \sqrt{\eta} - \frac{1}{8\sqrt{\xi}} - \frac{1}{8\sqrt{\eta}})\right]$			
Storage Material Temperature	$T_m[\eta,\xi] = 1 - T_f[\xi,\eta]$		$T_m = 1 - e^{-\eta}$	$T_m = 1 - \sum_{j=1}^{\infty} 2\frac{\sin M_j}{\sin M_j \cos M_j + M_j}\exp\left[-(M_j^2)\frac{\eta}{\mathrm{Bi}}\right]\cos(M_j Y)$ where $M_j \tan M_j = \mathrm{Bi}$
Heat Storage	$Q^+ = \frac{1}{\lambda}\int_0^{\eta}[1 - T_m]\,d\eta$	Schmidt - Szego [9]	$Q^+ = 1 - e^{-\eta}$	$Q^+ = \sum_{j=1}^{\infty} 2\left[\frac{\sin^2 M_j}{M_j \sin M_j \cos M_j + (M_j^2)}\right]\left[1 - \exp\left[-(M_j^2)\frac{\eta}{\mathrm{Bi}}\right]\right]$

storage material:

$$\frac{\partial T_m}{\partial \eta} = C^* \frac{\partial^2 T_m}{\partial \xi^2} + D^* \frac{\partial^2 T_m}{\partial Y^2} \tag{2}$$

where

$$C^* = \frac{\lambda^2}{\mathrm{Bi}} (V^+)^2 \text{ and } D^* = \frac{1}{\mathrm{Bi}}.$$

The initial and boundary conditions are:

$$\begin{aligned}
&\eta = 0 \qquad T_m = T_f = 0 \\
&\eta > 0 \qquad \xi = 0 \quad T_f = 1 \qquad \frac{\partial T_m}{\partial \xi} = 0 \\
&\qquad\qquad \xi = \lambda \qquad\quad \frac{\partial T_m}{\partial \xi} = 0 \\
&\qquad\qquad Y = 0 \qquad\quad \frac{\partial T_m}{\partial Y} = 0 \\
&\qquad\qquad Y = 1 \qquad\quad \frac{\partial T_m}{\partial Y} = \mathrm{Bi}[T_f - T_m].
\end{aligned} \tag{3}$$

The contribution of the axial and transverse conduction can be identified using equation (2) as: transverse conduction, $1/\mathrm{Bi}\ \partial^2 T_m/\partial Y^2$, and axial conduction, $\lambda^2(V^+)^2/\mathrm{Bi}\ \partial^2 T_m/\partial \xi^2$. If the worst condition is assumed to occur when $\partial^2 T_m/\partial \xi^2 \approx \partial^2 T_m/\partial Y^2$ the maximum contribution of the axial conduction term would be an order of magnitude less than that of the transverse heat conduction term if $\lambda^2(V^+)^2 \leq 0.1$. This criterion can be written in the form $\lambda V^+ < 0.3$, which shows that for $\lambda = 30$ axial heat conduction can be neglected if $V^+ < 0.01$.

References

1 Anzelius, A., "Uber Erwarmung Vermittals Durchstromender Medien," *Z. Angew Math. Mech.*, Vol. 6, 1926, p. 291.

2 Nusselt, W., "Die Theorie des Windehitzers," *Z. Ver. Deut. Ing.*, Vol. 71, 1927, p. 85.

3 Hausen, H., "Uber den Warmeaustausch in Regeneratoren," *Tech. Mech. Thermodynam*, Vol. 1, 1930, p. 219.

4 Hausen, H., "Uber die Theorie des Warmeaustausches in Regeneratoren," *Z. Angew Math. Mech.*, Vol. 9, 1929, p. 173.

5 Schumann, T. E. W., "Heat Transfer: A Liquid Flowing Through a Porous Prism," *J. Franklin Institute*, Vol. 208, 1929, p. 405.

6 Larsen, F. W., "Rapid Calculations of Temperature in a Regenerative Heat Exchanger Having Arbitrary Initial Solid and Entering Fluid Temperatures," *Int. J. Heat and Mass Transfer*, Vol. 10, 1967, p. 149.

7 Klinkenberg, A., "Heat Transfer in Cross-Flow Heat Exchangers and Packed Beds," *Ind. Engng. Chem.*, Vol. 46, 1954 p. 2285.

8 Handley, D., Heggs, P. J., "The Effect of Thermal Conductivity of the Packing on Transient Heat Transfer in a Fixed Bed," *Int. J. Heat and Mass Transfer*, Vol. 12, 1969, pp. 549–570.

9 Schmidt, F. W., Szego, J., "Transient Response of Solid Sensible Heat Thermal Storage Units—Single Fluid," ASME JOURNAL OF HEAT TRANSFER, Vol. 98, 1976, p. 471.

10 Gröber, H., Erk, S., Grigull, U., *Fundamentals of Heat Transfer*, McGraw Hill, New York, 1961, pp. 50–52.

A New Look at Radiation Configuration Factors between Disks

A. Feingold[1]

When, in 1913, H. B. Keene derived by means of multiple integration an expression for the configuration factor for radiative heat transfer between two plane circular surfaces with common central normal, his pioneering work [1] was judged to be sufficiently significant to appear in the *Proceedings of the Royal Society* of London. Today his problem serves as perhaps the most popular classroom and textbook example of this sort of calculation.

It is, however, of considerable didactic interest to show how a closed-form solution of Keene's problem can be arrived at without integration following the ideas developed by me in an earlier paper [2]. Consider two parallel coaxial disks of radii r_1 and r_2 separated by a distance h. It is always possible to determine the radius and the location of the center of the sphere in which these disks may be inscribed. Depending on the data we shall have the situation depicted in Fig. 1(a) or in Fig. 1(b). In either case, we have

$$r_3^2 = r_1^2 + h_1^2 = r_2^2 + (h - h_1)^2$$

from which

$$h_1 = \frac{r_2^2 - r_1^2 + h^2}{2h} \tag{1}$$

and

$$r_3 = \frac{\sqrt{r_1^4 + r_2^4 + h^4 - 2r_1^2 r_2^2 + 2r_1^2 h^2 + 2r_2^2 h^2}}{2h} \tag{2}$$

Every ray emanating from one of the disks and striking the other disk would, in the absence of that other disk, strike the spherical zone, S, situated behind it. The converse being also true, the configuration factor from disk D_1 to disk D_2 is equal to the factor from D_1 to S_2, or, by virtue of the reciprocity theorem,

$$F_{D_1-D_2} = F_{D_1-S_2} = \frac{A_{S_2}}{A_{D_1}} F_{S_2-D_1} \tag{3}$$

Again, any ray emanating from S_2 which can strike D_1, would also strike S_1 if D_1 were removed. Thus,

$$F_{S_2-D_1} = F_{S_2-S_1} \tag{4}$$

The latter factor concerns areas inside a spherical cavity and is, therefore, given by the well known formula

$$F_{S_2-S_1} = \frac{A_{S_1}}{4\pi r_3^2} \tag{5}$$

Combining equations (3, 4, 5), and noting that

$$A_{S_1} = 2\pi r_3 (r_3 - h_1),$$

$$A_{S_2} = 2\pi r_3 (r_3 + h_1 - h)$$

and

$$A_{D_1} = \pi r_1^2$$

we have

$$F_{D_1-D_2} = \frac{(r_3 - h_1)(r_3 + h_1 - h)}{r_1^2} \tag{6}$$

This is the desired close-form expression, which could be made nondimensional by the introduction of the symbols

$$R_1 = \frac{r_1}{h}, \quad R_2 = \frac{r_2}{h}, \quad R_3 = \frac{r_3}{h} \quad \text{and} \quad H_1 = \frac{h_1}{h}$$

We now obtain

$$F_{D_1-D_2} = \frac{(R_3 - H_1)(R_3 + H_1 - 1)}{R_1^2}, \tag{7}$$

where

$$R_3 = \frac{1}{2}\sqrt{R_1^4 + R_2^4 + 1 - 2R_1^2 R_2^2 + 2R_1^2 + 2R_2^2},$$

[1] Professor of Mechanical Engineering, University of Ottawa, Ottawa, Canada, K1N 6N5.

Contributed by the Heat Transfer Division for publication in the JOURNAL OF HEAT TRANSFER. Manuscript received by the Heat Transfer Division May 30, 1978.

storage material:

$$\frac{\partial T_m}{\partial \eta} = C^* \frac{\partial^2 T_m}{\partial \xi^2} + D^* \frac{\partial^2 T_m}{\partial Y^2} \tag{2}$$

where

$$C^* = \frac{\lambda^2}{\mathrm{Bi}} (V^+)^2 \text{ and } D^* = \frac{1}{\mathrm{Bi}}.$$

The initial and boundary conditions are:

$$\begin{aligned}
&\eta = 0 \qquad T_m = T_f = 0 \\
&\eta > 0 \qquad \xi = 0 \quad T_f = 1 \qquad \frac{\partial T_m}{\partial \xi} = 0 \\
&\qquad\qquad \xi = \lambda \qquad\quad \frac{\partial T_m}{\partial \xi} = 0 \\
&\qquad\qquad Y = 0 \qquad\quad \frac{\partial T_m}{\partial Y} = 0 \\
&\qquad\qquad Y = 1 \qquad\quad \frac{\partial T_m}{\partial Y} = \mathrm{Bi}[T_f - T_m].
\end{aligned} \tag{3}$$

The contribution of the axial and transverse conduction can be identified using equation (2) as: transverse conduction, $1/\mathrm{Bi}\ \partial^2 T_m/\partial Y^2$, and axial conduction, $\lambda^2(V^+)^2/\mathrm{Bi}\ \partial^2 T_m/\partial \xi^2$. If the worst condition is assumed to occur when $\partial^2 T_m/\partial \xi^2 \approx \partial^2 T_m/\partial Y^2$ the maximum contribution of the axial conduction term would be an order of magnitude less than that of the transverse heat conduction term if $\lambda^2(V^+)^2 \leq 0.1$. This criterion can be written in the form $\lambda V^+ < 0.3$, which shows that for $\lambda = 30$ axial heat conduction can be neglected if $V^+ < 0.01$.

References

1 Anzelius, A., "Uber Erwarmung Vermittals Durchstromender Medien," *Z. Angew Math. Mech.*, Vol. 6, 1926, p. 291.

2 Nusselt, W., "Die Theorie des Windehitzers," *Z. Ver. Deut. Ing.*, Vol. 71, 1927, p. 85.

3 Hausen, H., "Uber den Warmeaustausch in Regeneratoren," *Tech. Mech. Thermodynam*, Vol. 1, 1930, p. 219.

4 Hausen, H., "Uber die Theorie des Warmeaustausches in Regeneratoren," *Z. Angew Math. Mech.*, Vol. 9, 1929, p. 173.

5 Schumann, T. E. W., "Heat Transfer: A Liquid Flowing Through a Porous Prism," *J. Franklin Institute*, Vol. 208, 1929, p. 405.

6 Larsen, F. W., "Rapid Calculations of Temperature in a Regenerative Heat Exchanger Having Arbitrary Initial Solid and Entering Fluid Temperatures," *Int. J. Heat and Mass Transfer*, Vol. 10, 1967, p. 149.

7 Klinkenberg, A., "Heat Transfer in Cross-Flow Heat Exchangers and Packed Beds," *Ind. Engng. Chem.*, Vol. 46, 1954 p. 2285.

8 Handley, D., Heggs, P. J., "The Effect of Thermal Conductivity of the Packing on Transient Heat Transfer in a Fixed Bed," *Int. J. Heat and Mass Transfer*, Vol. 12, 1969, pp. 549–570.

9 Schmidt, F. W., Szego, J., "Transient Response of Solid Sensible Heat Thermal Storage Units—Single Fluid," ASME JOURNAL OF HEAT TRANSFER, Vol. 98, 1976, p. 471.

10 Gröber, H., Erk, S., Grigull, U., *Fundamentals of Heat Transfer*, McGraw Hill, New York, 1961, pp. 50–52.

A New Look at Radiation Configuration Factors between Disks

A. Feingold[1]

When, in 1913, H. B. Keene derived by means of multiple integration an expression for the configuration factor for radiative heat transfer between two plane circular surfaces with common central normal, his pioneering work [1] was judged to be sufficiently significant to appear in the *Proceedings of the Royal Society* of London. Today his problem serves as perhaps the most popular classroom and textbook example of this sort of calculation.

It is, however, of considerable didactic interest to show how a closed-form solution of Keene's problem can be arrived at without integration following the ideas developed by me in an earlier paper [2]. Consider two parallel coaxial disks of radii r_1 and r_2 separated by a distance h. It is always possible to determine the radius and the location of the center of the sphere in which these disks may be inscribed. Depending on the data we shall have the situation depicted in Fig. 1(a) or in Fig. 1(b). In either case, we have

$$r_3^2 = r_1^2 + h_1^2 = r_2^2 + (h - h_1)^2$$

from which

$$h_1 = \frac{r_2^2 - r_1^2 + h^2}{2h} \tag{1}$$

and

$$r_3 = \frac{\sqrt{r_1^4 + r_2^4 + h^4 - 2r_1^2 r_2^2 + 2r_1^2 h^2 + 2r_2^2 h^2}}{2h} \tag{2}$$

Every ray emanating from one of the disks and striking the other disk would, in the absence of that other disk, strike the spherical zone, S, situated behind it. The converse being also true, the configuration factor from disk D_1 to disk D_2 is equal to the factor from D_1 to S_2, or, by virtue of the reciprocity theorem,

$$F_{D_1-D_2} = F_{D_1-S_2} = \frac{A_{S_2}}{A_{D_1}} F_{S_2-D_1} \tag{3}$$

Again, any ray emanating from S_2 which can strike D_1, would also strike S_1 if D_1 were removed. Thus,

$$F_{S_2-D_1} = F_{S_2-S_1} \tag{4}$$

The latter factor concerns areas inside a spherical cavity and is, therefore, given by the well known formula

$$F_{S_2-S_1} = \frac{A_{S_1}}{4\pi r_3^2} \tag{5}$$

Combining equations (3, 4, 5), and noting that

$$A_{S_1} = 2\pi r_3 (r_3 - h_1),$$

$$A_{S_2} = 2\pi r_3 (r_3 + h_1 - h)$$

and

$$A_{D_1} = \pi r_1^2$$

we have

$$F_{D_1-D_2} = \frac{(r_3 - h_1)(r_3 + h_1 - h)}{r_1^2} \tag{6}$$

This is the desired close-form expression, which could be made nondimensional by the introduction of the symbols

$$R_1 = \frac{r_1}{h}, \quad R_2 = \frac{r_2}{h}, \quad R_3 = \frac{r_3}{h} \quad \text{and} \quad H_1 = \frac{h_1}{h}$$

We now obtain

$$F_{D_1-D_2} = \frac{(R_3 - H_1)(R_3 + H_1 - 1)}{R_1^2}, \tag{7}$$

where

$$R_3 = \frac{1}{2}\sqrt{R_1^4 + R_2^4 + 1 - 2R_1^2 R_2^2 + 2R_1^2 + 2R_2^2},$$

[1] Professor of Mechanical Engineering, University of Ottawa, Ottawa, Canada, K1N 6N5.

Contributed by the Heat Transfer Division for publication in the JOURNAL OF HEAT TRANSFER. Manuscript received by the Heat Transfer Division May 30, 1978.

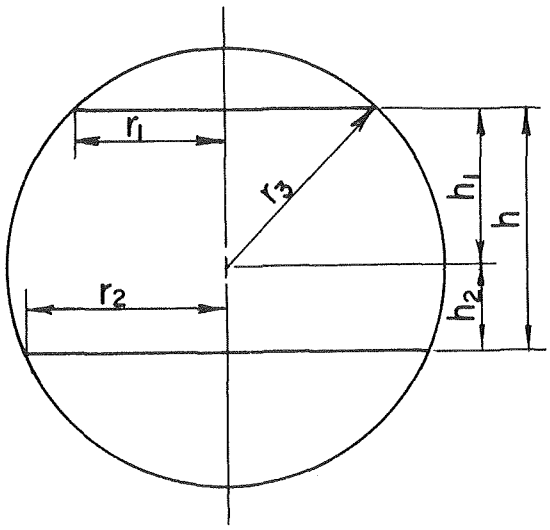

Fig. 1(*a*)

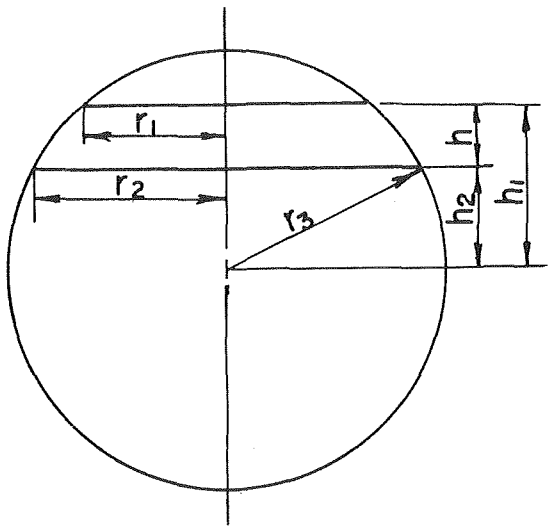

Fig. 1(*b*)

and

$$H_1 = \frac{1}{2}(R_2^2 - R_1^2 + 1)$$

This, after substitution and simplification, agrees with Keene's formula, which, using our symbols can be written as

$$F_{D_1-D_2} = \frac{1 + R_1^2 + R_2^2 - \sqrt{(1 + R_1^2 + R_2^2)^2 - 4R_1^2R_2^2}}{2R_1^2}$$

An interesting corollary results from the reasoning employed in this paper. Whenever two nonparallel disks with intersecting central normals can be inscribed in a sphere, such as is the case in Fig. 2(*a*) or in Fig. 2(*b*), equations (3, 4, 5) remain valid, and the factor from D_1 to D_2 can be calculated from the formula

$$F_{D_1-D_2} = \frac{A_{S_2}A_{S_1}}{4\pi r_3^2 A_{D_1}} \tag{8}$$

It should be noted that while two coaxial disks can always be inscribed in a sphere, this can only be done with noncoaxial disks when two conditions are fulfilled: (a) their central normals intersect and (b) there exists the relation

$$r_1^2 + h_1^2 = r_2^2 + h_2^2 = r_3^2 \tag{9}$$

We note that, as in the case of coaxial disks,

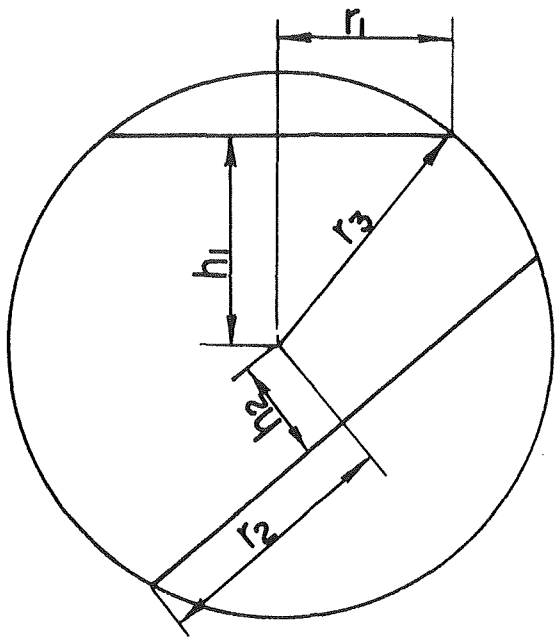

Fig. 2(*a*)

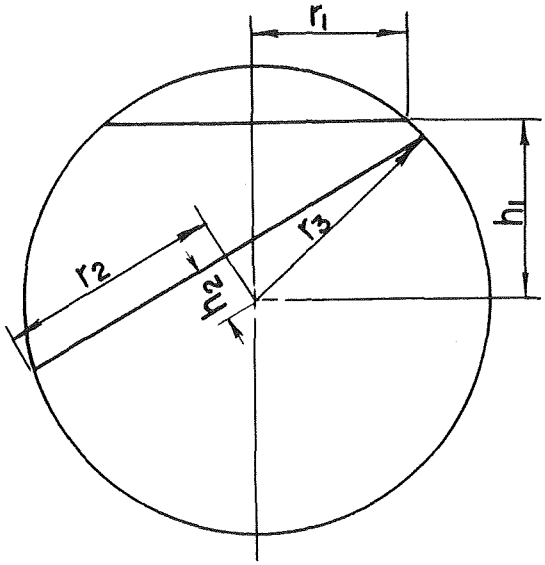

Fig. 2(*b*)

$$A_{S_1} = 2\pi r_3(r_3 - h_1)$$

$$A_{D_1} = \pi r_1^2$$

but two expressions are required for A_{S_2}, namely

$$A_{S_2} = 2\pi r_3(r_3 - h_2) \text{ in Fig. 2}(a)$$

and

$$A_{S_2} = 2\pi r_3(r_3 + h_2) \text{ in Fig. 2}(b)$$

Thus, for Fig. 2(*a*) we have

$$F_{D_1-D_2} = \frac{(r_3 - h_1)(r_3 - h_2)}{r_1^2} \tag{10}$$

while for Fig. 2(*b*) the formula is

$$F_{D_1-D_2} = \frac{(r_3 - h_1)(r_3 + h_2)}{r_1^2} \tag{11}$$

Finally, these equations can be made dimensionless by the intro-

duction of the symbols,

$$R_3 = \frac{r_3}{r_1}, \quad H_1 = \frac{h_1}{r_1} \quad \text{and} \quad H_2 = \frac{h_2}{r_1}$$

Observing that equation (9) becomes now

$$R_3 = \sqrt{1 + H_1^2} \tag{9'}$$

we can write

$$F_{D_1-D_2} = (\sqrt{1 + H_1^2} - H_1)(\sqrt{1 + H_1^2} - H_2) \tag{10'}$$

and

$$F_{D_1-D_2} = (\sqrt{1 + H_1^2} - H_1)(\sqrt{1 + H_1^2} + H_2) \tag{11'}$$

for Figs. 2(*a*) and 2(*b*), respectively.

These are remarkably simple closed-form solutions for a problem which, using multiple integration, could, in all probability, be only solved numerically and fairly laboriously at that.

References

1 Keene, H. B., "Calculation of the Energy Exchange Between Two Fully Radiative Coaxial Circular Apertures at Different Temperatues," *Proc. Roy. Soc.*, A, 1913, pp. 59–60.

2 Feingold, A., Gupta, K. G., "New Analytical Approach to the Evaluation of Configuration Factors in Radiation from Spheres and Infinitely Long Cylinders," ASME JOURNAL OF HEAT TRANSFER, Vol. 92, No. 1, pp. 69–76, 1970.

A Simple Integral Approach to Turbulent Thermal Boundary Layer Flow

Lindon Thomas[1]

Introduction

Whereas considerable progress has been achieved over the past few years in the development of integral approaches to the analysis of momentum transfer for turbulent boundary layer flow, little attention has been given to use of the integral approach in analyzing convection heat transfer. As a matter of fact, only several integral type analyses have been developed for convection heat transfer associated with turbulent boundary layer flow. The first of these was an analysis by Reynolds, et al. [1] which utilized the classic but somewhat restrictive $1/7$ power law approximation for $\overline{u}$ and $\overline{T}$. A modern integral analysis for turbulent convection heat transfer was introduced by White, et al. in the context of compressible flow [2, 3]. The key to the White team's analysis is the use of inner region parameters such as y^+. Unfortunately, the attractiveness of their approach is somewhat obscured by the complexity of the problem that they chose to handle.

It is because of the surprisingly slow evolution of the integral appraoch to convection heat transfer for turbulent boundary layer flow that the analogy approach is still relied upon as the primary alternative to the differential/numerical approach. To help fill this analytic void, a simple integral appraoch is introduced in this paper for convection heat transfer associated with fully turbulent incompressible boundary layer flow of moderate Prandtl number fluids with uniform wall flux heating maintained over a part of the plate. This analysis, like the analyses by White, et al., employs inner region parameters. However, unlike previous integral analyses of turbulent convective heat transfer, simple analytical laws of the inner region are utilized for both u^+ and T^+ that apply to the important wall region.

[1] Mechanical Engineering Department, University of Petroleum and Minerals, Dhahran, Saudi Arabia.

Contributed by the Heat Transfer Division for publication in the JOURNAL OF HEAT TRANSFER. Manuscript received by the Heat Transfer Division February 17, 1978.

Analysis

Following the pattern which has been established by White [4] in his integral analysis of momentum transfer for turbulent boundary layer flow, correlations are employed for the mean velocity profile in terms of the inner variables u^+ and y^+. Going one step further, correlations are utilized for the mean temperature profile in terms of $T^+ (\equiv (T_0 - \overline{T})\rho c_p U^*/q_0'')$ and y^+.

Integral Energy Equation. To develop an integral solution for the local mean Nusselt number for fully turbulent boundary layer flow, the integral energy equation is written in the form

$$\frac{\partial}{\partial x}\int_0^{\Delta} \overline{u}(\overline{T} - T_\infty)dy = \frac{q_0''}{\rho c_p} \tag{1}$$

This equation is rewritten in terms of u^+, T^+ and y^+ for uniform wall flux heating as

$$\frac{d}{d\mathrm{Re}_x}(\lambda H) = 1 \tag{2}$$

where $\lambda = U_\infty/U^* = \sqrt{2/f_x}$ and

$$H = \int_0^{\Delta^+} u^+(T_\infty^+ - T^+)dy^+ \tag{3}$$

The integral formulation is closed by writing the boundary condition $\Delta^+ = 0$ at $\mathrm{Re}_x = \mathrm{Re}_{x_0}$. With u^+ and T^+ known, equation (3) provides a relationship between H and Δ.

Inner Laws for u^+ and T^+. The completion of the analysis requires that u^+ and T^+ be specified. For this simple zero pressure gradient flow, u^+ can be approximated by any of the standard laws for the inner and wall region. The van Driest [5] and Spalding [6] equations are perhaps the best known of these inner laws. Each of these equations approach the familiar logarithmic law as y^+ increases; i.e.,

$$u^+ = C + \frac{1}{\kappa}\ln y^+ \tag{4}$$

For problems involving strong axial pressure gradients, the inner law for u^+ must be supplemented by the inclusion of an appropriate wake function. However, for situations such as this in which dP/dx is small, the wake effect is small, such that the inner laws can be employed throughout the entire flow field.

Similar inner laws can be written for T^+ of the form

$$T^+ = \int_0^{y^+} \frac{dy^+}{\left(\frac{\alpha}{\nu} + \frac{\alpha_t}{\nu}\right)} = \int_0^{y^+} \frac{dy^+}{\frac{1}{\mathrm{Pr}} + \frac{\nu_t/\nu}{\mathrm{Pr}_t}} \tag{5}$$

where the turbulent Prandtl number Pr_t is approximately unity for moderate Prandtl number fluids and ν_t can be specified by equations by van Driest, Spalding or others. With ν_t prescribed by the van Driest or Spalding equations, equation (5) approaches

$$T^+ = A + \frac{1}{\kappa}\ln y^+ \tag{6}$$

as y^+ becomes large, where A is a function of the Prandtl number.

The use of any combination of the above mentioned inner laws for u^+ and T^+ in solving the integral energy equation, equation (3), would necessitate numerical integrations. Therefore, attention is turned to alternative more manageable expressions for u^+ and T^+ which have been developed on the basis of the surface renewal model (7). These expressions take the form

$$u^+ = 15.97\left[1 - \exp\left(-\frac{y^+}{15.97}\right)\right] \quad y^+ \leqslant y_h{}^+ \tag{7a}$$

$$u^+ = C + \frac{1}{\kappa}\ln y^+ \quad y^+ \geqslant y_h{}^+ \tag{7b}$$

$$T^+ = 15.97\sqrt{\mathrm{Pr}}\left[1 - \exp\left(-\frac{y^+\sqrt{\mathrm{Pr}}}{15.97}\right)\right] \quad y^+ \leqslant y_T{}^+ \tag{8a}$$

$$T^+ = A + \frac{1}{\kappa}\ln y^+ \quad y^+ \geqslant y_T{}^+ \tag{8b}$$

duction of the symbols,

$$R_3 = \frac{r_3}{r_1}, \quad H_1 = \frac{h_1}{r_1} \quad \text{and} \quad H_2 = \frac{h_2}{r_1}$$

Observing that equation (9) becomes now

$$R_3 = \sqrt{1 + H_1^2} \tag{9'}$$

we can write

$$F_{D_1-D_2} = (\sqrt{1 + H_1^2} - H_1)(\sqrt{1 + H_1^2} - H_2) \tag{10'}$$

and

$$F_{D_1-D_2} = (\sqrt{1 + H_1^2} - H_1)(\sqrt{1 + H_1^2} + H_2) \tag{11'}$$

for Figs. 2(*a*) and 2(*b*), respectively.

These are remarkably simple closed-form solutions for a problem which, using multiple integration, could, in all probability, be only solved numerically and fairly laboriously at that.

References

1 Keene, H. B., "Calculation of the Energy Exchange Between Two Fully Radiative Coaxial Circular Apertures at Different Temperatues," *Proc. Roy. Soc.*, A, 1913, pp. 59–60.

2 Feingold, A., Gupta, K. G., "New Analytical Approach to the Evaluation of Configuration Factors in Radiation from Spheres and Infinitely Long Cylinders," ASME JOURNAL OF HEAT TRANSFER, Vol. 92, No. 1, pp. 69–76, 1970.

A Simple Integral Approach to Turbulent Thermal Boundary Layer Flow

Lindon Thomas[1]

Introduction

Whereas considerable progress has been achieved over the past few years in the development of integral approaches to the analysis of momentum transfer for turbulent boundary layer flow, little attention has been given to use of the integral approach in analyzing convection heat transfer. As a matter of fact, only several integral type analyses have been developed for convection heat transfer associated with turbulent boundary layer flow. The first of these was an analysis by Reynolds, et al. [1] which utilized the classic but somewhat restrictive $1/7$ power law approximation for $\bar{u}$ and $\bar{T}$. A modern integral analysis for turbulent convection heat transfer was introduced by White, et al. in the context of compressible flow [2, 3]. The key to the White team's analysis is the use of inner region parameters such as y^+. Unfortunately, the attractiveness of their approach is somewhat obscured by the complexity of the problem that they chose to handle.

It is because of the surprisingly slow evolution of the integral appraoch to convection heat transfer for turbulent boundary layer flow that the analogy approach is still relied upon as the primary alternative to the differential/numerical approach. To help fill this analytic void, a simple integral appraoch is introduced in this paper for convection heat transfer associated with fully turbulent incompressible boundary layer flow of moderate Prandtl number fluids with uniform wall flux heating maintained over a part of the plate. This analysis, like the analyses by White, et al., employs inner region parameters. However, unlike previous integral analyses of turbulent convective heat transfer, simple analytical laws of the inner region are utilized for both u^+ and T^+ that apply to the important wall region.

[1] Mechanical Engineering Department, University of Petroleum and Minerals, Dhahran, Saudi Arabia.

Contributed by the Heat Transfer Division for publication in the JOURNAL OF HEAT TRANSFER. Manuscript received by the Heat Transfer Division February 17, 1978.

Analysis

Following the pattern which has been established by White [4] in his integral analysis of momentum transfer for turbulent boundary layer flow, correlations are employed for the mean velocity profile in terms of the inner variables u^+ and y^+. Going one step further, correlations are utilized for the mean temperature profile in terms of $T^+ (\equiv (T_0 - \bar{T})\rho c_p U^*/q_0'')$ and y^+.

Integral Energy Equation. To develop an integral solution for the local mean Nusselt number for fully turbulent boundary layer flow, the integral energy equation is written in the form

$$\frac{\partial}{\partial x}\int_0^{\Delta} \bar{u}(\bar{T} - T_\infty)dy = \frac{q_0''}{\rho c_p} \tag{1}$$

This equation is rewritten in terms of u^+, T^+ and y^+ for uniform wall flux heating as

$$\frac{d}{d\mathrm{Re}_x}(\lambda H) = 1 \tag{2}$$

where $\lambda = U_\infty/U^* = \sqrt{2/f_x}$ and

$$H = \int_0^{\Delta^+} u^+(T_\infty^+ - T^+)dy^+ \tag{3}$$

The integral formulation is closed by writing the boundary condition $\Delta^+ = 0$ at $\mathrm{Re}_x = \mathrm{Re}_{x_0}$. With u^+ and T^+ known, equation (3) provides a relationship between H and Δ.

Inner Laws for u^+ and T^+. The completion of the analysis requires that u^+ and T^+ be specified. For this simple zero pressure gradient flow, u^+ can be approximated by any of the standard laws for the inner and wall region. The van Driest [5] and Spalding [6] equations are perhaps the best known of these inner laws. Each of these equations approach the familiar logarithmic law as y^+ increases; i.e.,

$$u^+ = C + \frac{1}{\kappa}\ln y^+ \tag{4}$$

For problems involving strong axial pressure gradients, the inner law for u^+ must be supplemented by the inclusion of an appropriate wake function. However, for situations such as this in which dP/dx is small, the wake effect is small, such that the inner laws can be employed throughout the entire flow field.

Similar inner laws can be written for T^+ of the form

$$T^+ = \int_0^{y^+} \frac{dy^+}{\left(\frac{\alpha}{\nu} + \frac{\alpha_t}{\nu}\right)} = \int_0^{y^+} \frac{dy^+}{\frac{1}{\mathrm{Pr}} + \frac{\nu_t/\nu}{\mathrm{Pr}_t}} \tag{5}$$

where the turbulent Prandtl number Pr_t is approximately unity for moderate Prandtl number fluids and ν_t can be specified by equations by van Driest, Spalding or others. With ν_t prescribed by the van Driest or Spalding equations, equation (5) approaches

$$T^+ = A + \frac{1}{\kappa}\ln y^+ \tag{6}$$

as y^+ becomes large, where A is a function of the Prandtl number.

The use of any combination of the above mentioned inner laws for u^+ and T^+ in solving the integral energy equation, equation (3), would necessitate numerical integrations. Therefore, attention is turned to alternative more manageable expressions for u^+ and T^+ which have been developed on the basis of the surface renewal model (7). These expressions take the form

$$u^+ = 15.97\left[1 - \exp\left(-\frac{y^+}{15.97}\right)\right] \quad y^+ \leqslant y_h{}^+ \tag{7a}$$

$$u^+ = C + \frac{1}{\kappa}\ln y^+ \quad y^+ \geqslant y_h{}^+ \tag{7b}$$

$$T^+ = 15.97\sqrt{\mathrm{Pr}}\left[1 - \exp\left(-\frac{y^+\sqrt{\mathrm{Pr}}}{15.97}\right)\right] \quad y^+ \leqslant y_T{}^+ \tag{8a}$$

$$T^+ = A + \frac{1}{\kappa}\ln y^+ \quad y^+ \geqslant y_T{}^+ \tag{8b}$$

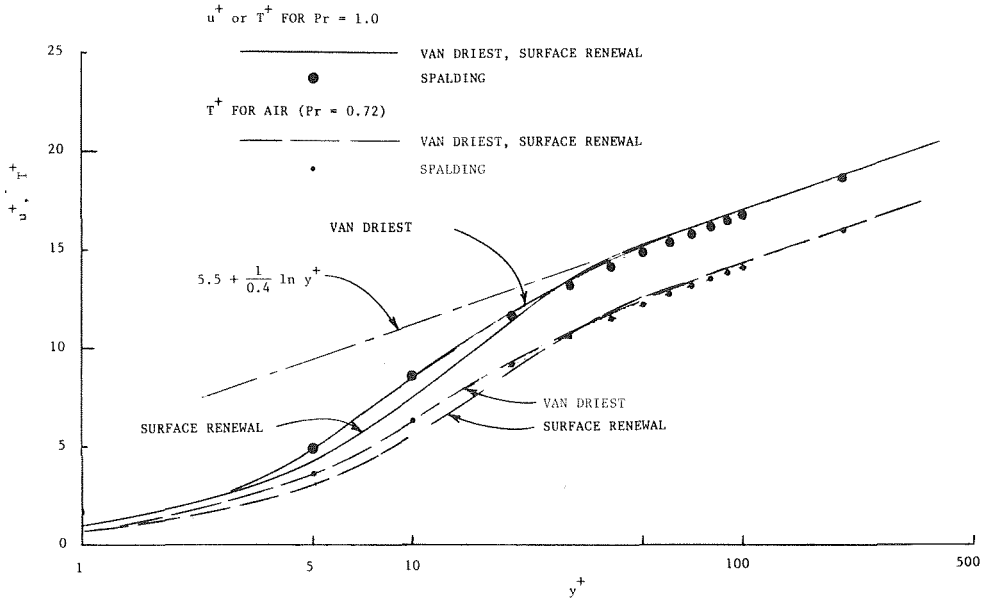

Fig. 1. Comparison of inner laws by van Driest and Spalding with surface renewal equations

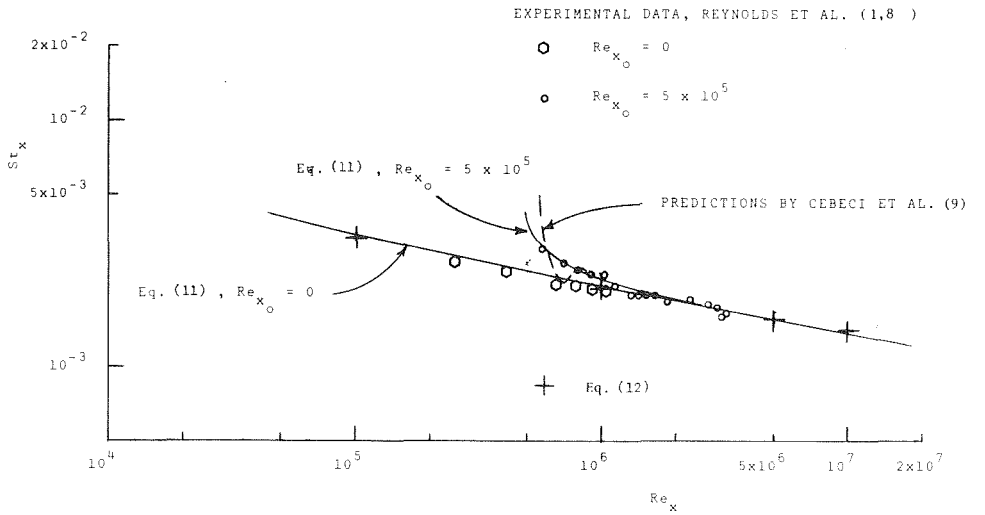

Fig. 2. Comparison of predictions for Stanton number with experimental data

where C and κ are familiar classical empirical constants with values $C \simeq 5.5$ and $\kappa \simeq 0.4$, $y_h{}^+$ (thickness of hydrodynamic wall region) $\simeq$ 46.7 and where A and $y_T{}^+$ (thickness of thermal wall region) are functions of the Prandtl number; for $\Pr \simeq 1.0$, $A = C$ and $y_T{}^+ \simeq y_h{}^+$. These simple surface renewal equations are shown in Fig. 1 to be slightly below the van Driest and Spalding inner laws for u^+ and T^+, with the maximum difference being of the order of only 6 percent.

Predictions for Nu_x. The solution for equation (2) is simply

$$H = \sqrt{\frac{f_x}{2}}(\mathrm{Re}_x - \mathrm{Re}_{x_0}) \tag{9}$$

With u^+ and T^+ specified, equation (3) provides a relationship between H and Δ^+. Then the use of equation (9) gives predictions for Δ^+ in terms of Re_x.

In order to develop predictions for the local Nusselt number Nu_x, $\overline{T}$ is set equal to T_∞ at $y^+ = \Delta^+$ in the inner law for T^+; i.e.,

$$T_\infty{}^+ = \frac{T_0 - T_\infty}{q_0''}(\rho c_p U^*)$$

$$= 15.97\sqrt{\Pr}\left[1 - \exp\left(-\frac{\Delta^+ \Pr}{15.97}\right)\right] \quad \Delta^+ \leqslant y_T{}^+ \tag{10a}$$

$$= A + \frac{1}{\kappa}\ln \Delta^+ \quad \Delta \geqslant y_T{}^+ \tag{10b}$$

Rearranging these equations and employing the definition for Nu_x, it follows that

$$\mathrm{Nu}_x = \frac{\sqrt{f_x/2}\mathrm{Re}_x \Pr}{15.97\sqrt{\Pr}\left[1 - \exp\left(-\dfrac{\Delta^+\sqrt{\Pr}}{15.97}\right)\right]} \quad \Delta^+ \leqslant y_T{}^+ \tag{11a}$$

$$= \frac{\sqrt{f_x/2}\mathrm{Re}_x \Pr}{A + \dfrac{1}{\kappa}\ln \Delta^+} \quad \Delta^+ \geqslant y_T{}^+ \tag{11b}$$

where Δ^+ is obtained by the solution of equation (9).

Results and Conclusions

Equation (11) is compared with experimental data [1, 8] and a classical differential/numerical solution [9] in Fig. 2 for the case in which air ($\Pr = 0.72$) undergoes uniform wall temperature heating with $\mathrm{Re}_{x_0} = 0$ and 5×10^5. This integral analysis for uniform wall flux heating is seen to be in excellent agreement with the data. In fact, for

this particular test, the performance of this simple analysis is comparable to that of the more involved tradition differential/numerical analysis.

The application of the elementary surface renewal model to fully turbulent flow with heating over the entire surface gives rise to an expression for the Nusselt number of the form (10)

$$\mathrm{Nu}_x = \frac{f_x}{2}\mathrm{Re}_x\sqrt{\mathrm{Pr}} \tag{12}$$

Calculations obtained on the basis of this equation are also shown in Fig. 2. This equation is seen to be nearly identical to equation (11) with $\mathrm{Re}_x \gg \mathrm{Re}_{x_0}$.

The results of the present integral analysis are also compared in Fig. 3 with predictions obtained on the basis of the integral/analogy analysis by Reynolds, et al. (1),

$$\mathrm{Nu}_x = \frac{f_x}{2}\mathrm{Re}_x\mathrm{Pr}^{0.6}\left[1-\left(\frac{\mathrm{Re}_{x_0}}{\mathrm{Re}_x}\right)^{0.9}\right]^{-1/9} \tag{13}$$

and a limiting Leveque type solution by Kestin and Person (11) for uniform wall temperature heating. Equation (13) fails in the vicinity of x_0 because of the inapplicability of the 1/7th power law for cases in which Δ^+ lies within the wall region. The present integral analysis eliminates this problem by employing reasonable approximations for u^+ and T^+ within the inner region. Observe that equation (11) comes very close to equation (13) as $Z(=1-(\mathrm{Re}_{x_0}/\mathrm{Re}_x)^{0.9})$ increases. As Z becomes very small, equation (11) approaches a limiting curve that lies parallel to but slightly above the Leveque equation. This small eight percent difference can be attributed to the effect of the thermal boundary condition.

Finally, equation (11) is compared with predictions obtained on the basis of a recent differential/numerical surface renewal type solution (12) for uniform wall temperature heating which is applicable to small values of Z ($0 \lesssim Z \lesssim 0.03$ or $1 \lesssim \mathrm{Re}_x/\mathrm{Re}_{x_0} \lesssim 1.03$). The reason for the limitation of the differential/numerical analyses of [12] to small values of Z in that this formulation only modeled the wall turbulence. Because the present integral analysis accounts for the turbulent transport within both the wall region and turbulent core, this analysis is applicable to the full Z domain. The numerical predictions are seen to lie somewhat below equation (11) but appropriately approach the limiting Leveque solution for uniform wall temperature heating as Z decreases. This slight difference between the numerical and integral calculations for Nu_x in this region very near the point at which heating is initiated is caused by the differences in thermal boundary conditions. Because the predictions obtained from these two analyses come together as Z increases and because the present analysis is in good agreement with data for uniform wall temperature heating, it is concluded that the turbulent convective transport process is essentially insensitive to the form of the thermal boundary condition, except in the immediate vicinity of x_0.

To recap, a simple but modern integral analysis has been developed for heat transfer in a turbulent boundary layer flow. The key to this analysis is the use of inner variables. In this particular analysis, u^+ and T^+ are approximated on the basis of the surface renewal model of wall turbulence. Of course, other laws for u^+ and T^+ can also be used. The analysis is further simplified by treating uniform wall heat flux conditions. Whereas the traditional analogy approach requires the assumption $\Delta^+ = \delta^+$, the present method provides predictions for Δ^+. Hence, this simple integral analysis of turbulent thermal boundary layer flow is felt to provide a more attractive alternative to the differential/numerical method.

Finally, this approach can be extended to more complex flows associated with favorable and adverse pressure gradients by including wake parameters such as those proposed by White [4], Coles and others.

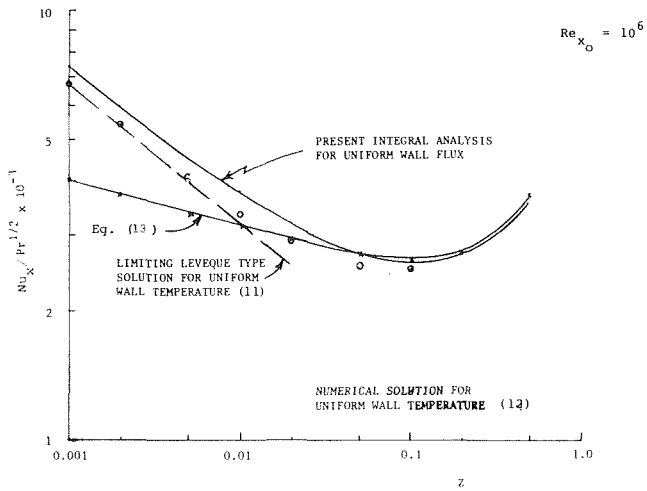

Fig. 3. Comparison of present integral analysis with other analyses in Z frame

References

1 Reynolds, W. C., Kays, W. M., and Kline, S. J., "Heat Transfer in the Turbulent Incompressible Boundary Layer, II—The Step Wall Temperature Distribution," NASA MEMO. 12-2-58 W, Washington, D.C., 1958.

2 White, F. M., Lessmann, P. C., Christoph, G. H., "A Simplified Approach to the Analysis of Turbulent Boundary Layers in Two and Three Dimensions," Tech. Rept. AFFDL-TR-136, Air Force Flight Dynamics Laboratory, Wright Patterson Air Force Base, Nov. 1972.

3 Christoph, G. H., Lessmann, R. C., White, F. M., "Calculation of Turbulent Heat Transfer and Skin Friction", *AIAA Journal*, Vol. II, p. 1046, 1973.

4 White, F. M., *Viscous Fluid Flow*, McGraw Hill, Inc., New York, N.Y., 1974.

5 Van Driest, F. R., "On Turbulent Flow Near A Wall," *Journal Aero Sci.*, Vol. 23, p. 1007, 1956.

6 Spalding, D. B., "A Single Formula For The Law of the Wall," *Journal of Appld. Mech.* Vol. 28, 1961, p. 455.

7 Thomas, L. C., "The Turbulent Burst Phenomenon: Inner Laws for u^+ and T^+," NATO Advanced Study Institute on Turbulence, Istanbul, Turkey, July 1978.

8 Reynolds, W. C., Kays, W. M., and Kline, S. J., "Heat Transfer in the Turbulent Incompressible Boundary Layer, I-Constant Wall Temperature," NASA MEMO 12-1-58 W, Rec. 1958.

9 Cebeci, T., Smith, A. M. O., and Mosinskis, G., "Solution of the Incompressible-Turbulent Boundary Layer Equations With Heat Transfer," ASME JOURNAL OF HEAT TRANSFER, 1969.

10 Thomas, L. C., Fan, L. T., "Heat and Momentum Transfer Analogy for Incompressible Turbulent Boundary Layer Flow," *International Journal of Heat/Mass Transfer*, No. 14, 1971, p. 715.

11 Kestin, J., and Person, L. N., "The Transfer of Heat Across a Turbulent Boundary Layer at Very High Prandtl Numbers", *International Journal of Heat/Mass Transfer*, Vol. 5, 1962, p. 355.

12 Thomas L. C., "A Theoretical Study of Thermally Developing Fully Turbulent Boundary Layer Flow," ASME JOURNAL OF HEAT TRANSFER, May, 1976, p. 334.

A Simplified Formula for Cross-Flow Heat Exchanger Effectiveness

B. S. Baclic[1]

The problem of determining the thermal effectiveness ϵ as a function of number of heat transfer units $\mathrm{NTU} = U{\cdot}A/(\dot{m}{\cdot}c_p)_{\min}$ and heat capacity ratio $\omega = (\dot{m}{\cdot}c_p)_{\min}/(\dot{m}{\cdot}c_p)_{\max}$ for the cross-flow heat exchangers when both fluids are unmixed is coupled with certain mathematical difficulties even in the case of a single pass exchanger. It is the latter situation which is considered in this note.

The problem of establishing the ϵ-NTU-ω relationship is, in fact,

[1] Department of Mechanical Engineering, Faculty of Technical Sciences, University of Novi Sad, Novi Sad, Yugoslavia.

Contributed by the Heat Transfer Division for publication in the JOURNAL OF HEAT TRANSFER. Manuscript received by the Heat Transfer Division January 30, 1978.

this particular test, the performance of this simple analysis is comparable to that of the more involved tradition differential/numerical analysis.

The application of the elementary surface renewal model to fully turbulent flow with heating over the entire surface gives rise to an expression for the Nusselt number of the form (10)

$$\mathrm{Nu}_x = \frac{f_x}{2}\mathrm{Re}_x\sqrt{\mathrm{Pr}} \tag{12}$$

Calculations obtained on the basis of this equation are also shown in Fig. 2. This equation is seen to be nearly identical to equation (11) with $\mathrm{Re}_x \gg \mathrm{Re}_{x_0}$.

The results of the present integral analysis are also compared in Fig. 3 with predictions obtained on the basis of the integral/analogy analysis by Reynolds, et al. (1),

$$\mathrm{Nu}_x = \frac{f_x}{2}\mathrm{Re}_x\mathrm{Pr}^{0.6}\left[1-\left(\frac{\mathrm{Re}_{x_0}}{\mathrm{Re}_x}\right)^{0.9}\right]^{-1/9} \tag{13}$$

and a limiting Leveque type solution by Kestin and Person (11) for uniform wall temperature heating. Equation (13) fails in the vicinity of x_0 because of the inapplicability of the 1/7th power law for cases in which Δ^+ lies within the wall region. The present integral analysis eliminates this problem by employing reasonable approximations for u^+ and T^+ within the inner region. Observe that equation (11) comes very close to equation (13) as $Z(=1-(\mathrm{Re}_{x_0}/\mathrm{Re}_x)^{0.9})$ increases. As Z becomes very small, equation (11) approaches a limiting curve that lies parallel to but slightly above the Leveque equation. This small eight percent difference can be attributed to the effect of the thermal boundary condition.

Finally, equation (11) is compared with predictions obtained on the basis of a recent differential/numerical surface renewal type solution (12) for uniform wall temperature heating which is applicable to small values of Z ($0 \gtrsim Z \gtrsim 0.03$ or $1 \gtrsim \mathrm{Re}_x/\mathrm{Re}_{x_0} \gtrsim 1.03$). The reason for the limitation of the differential/numerical analyses of [12] to small values of Z in that this formulation only modeled the wall turbulence. Because the present integral analysis accounts for the turbulent transport within both the wall region and turbulent core, this analysis is applicable to the full Z domain. The numerical predictions are seen to lie somewhat below equation (11) but appropriately approach the limiting Leveque solution for uniform wall temperature heating as Z decreases. This slight difference between the numerical and integral calculations for Nu_x in this region very near the point at which heating is initiated is caused by the differences in thermal boundary conditions. Because the predictions obtained from these two analyses come together as Z increases and because the present analysis is in good agreement with data for uniform wall temperature heating, it is concluded that the turbulent convective transport process is essentially insensitive to the form of the thermal boundary condition, except in the immediate vicinity of x_0.

To recap, a simple but modern integral analysis has been developed for heat transfer in a turbulent boundary layer flow. The key to this analysis is the use of inner variables. In this particular analysis, u^+ and T^+ are approximated on the basis of the surface renewal model of wall turbulence. Of course, other laws for u^+ and T^+ can also be used. The analysis is further simplified by treating uniform wall heat flux conditions. Whereas the traditional analogy approach requires the assumption $\Delta^+ = \delta^+$, the present method provides predictions for Δ^+. Hence, this simple integral analysis of turbulent thermal boundary layer flow is felt to provide a more attractive alternative to the differential/numerical method.

Finally, this approach can be extended to more complex flows associated with favorable and adverse pressure gradients by including wake parameters such as those proposed by White [4], Coles and others.

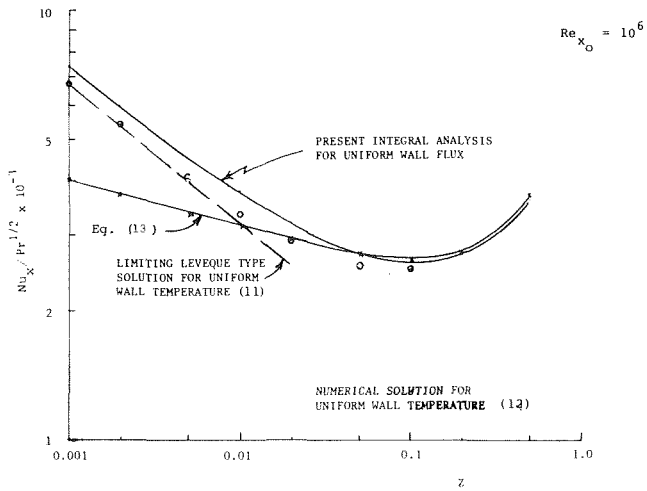

Fig. 3. Comparison of present integral analysis with other analyses in Z frame

References

1 Reynolds, W. C., Kays, W. M., and Kline, S. J., "Heat Transfer in the Turbulent Incompressible Boundary Layer, II—The Step Wall Temperature Distribution," NASA MEMO. 12-2-58 W, Washington, D.C., 1958.

2 White, F. M., Lessmann, P. C., Christoph, G. H., "A Simplified Approach to the Analysis of Turbulent Boundary Layers in Two and Three Dimensions," Tech. Rept. AFFDL-TR-136, Air Force Flight Dynamics Laboratory, Wright Patterson Air Force Base, Nov. 1972.

3 Christoph, G. H., Lessmann, R. C., White, F. M., "Calculation of Turbulent Heat Transfer and Skin Friction", *AIAA Journal*, Vol. II, p. 1046, 1973.

4 White, F. M., *Viscous Fluid Flow*, McGraw Hill, Inc., New York, N.Y., 1974.

5 Van Driest, F. R., "On Turbulent Flow Near A Wall," *Journal Aero Sci.*, Vol. 23, p. 1007, 1956.

6 Spalding, D. B., "A Single Formula For The Law of the Wall," *Journal of Appld. Mech.* Vol. 28, 1961, p. 455.

7 Thomas, L. C., "The Turbulent Burst Phenomenon: Inner Laws for u^+ and T^+," NATO Advanced Study Institute on Turbulence, Istanbul, Turkey, July 1978.

8 Reynolds, W. C., Kays, W. M., and Kline, S. J., "Heat Transfer in the Turbulent Incompressible Boundary Layer, I-Constant Wall Temperature," NASA MEMO 12-1-58 W, Rec. 1958.

9 Cebeci, T., Smith, A. M. O., and Mosinskis, G., "Solution of the Incompressible-Turbulent Boundary Layer Equations With Heat Transfer," ASME JOURNAL OF HEAT TRANSFER, 1969.

10 Thomas, L. C., Fan, L. T., "Heat and Momentum Transfer Analogy for Incompressible Turbulent Boundary Layer Flow," *International Journal of Heat/Mass Transfer*, No. 14, 1971, p. 715.

11 Kestin, J., and Person, L. N., "The Transfer of Heat Across a Turbulent Boundary Layer at Very High Prandtl Numbers", *International Journal of Heat/Mass Transfer*, Vol. 5, 1962, p. 355.

12 Thomas L. C., "A Theoretical Study of Thermally Developing Fully Turbulent Boundary Layer Flow," ASME JOURNAL OF HEAT TRANSFER, May, 1976, p. 334.

A Simplified Formula for Cross-Flow Heat Exchanger Effectiveness

B. S. Baclic[1]

The problem of determining the thermal effectiveness ϵ as a function of number of heat transfer units $\mathrm{NTU} = U{\cdot}A/(\dot{m}{\cdot}c_p)_{\min}$ and heat capacity ratio $\omega = (\dot{m}{\cdot}c_p)_{\min}/(\dot{m}{\cdot}c_p)_{\max}$ for the cross-flow heat exchangers when both fluids are unmixed is coupled with certain mathematical difficulties even in the case of a single pass exchanger. It is the latter situation which is considered in this note.

The problem of establishing the ϵ-NTU-ω relationship is, in fact,

[1] Department of Mechanical Engineering, Faculty of Technical Sciences, University of Novi Sad, Novi Sad, Yugoslavia.

Contributed by the Heat Transfer Division for publication in the JOURNAL OF HEAT TRANSFER. Manuscript received by the Heat Transfer Division January 30, 1978.

Table 1 Number of terms to be considered in the series of equation (2) for 0,01 percent accuracy

NTU \ ω	0.1	0.2	0.3	0.4	0.5	0.6	0.7	0.8	0.9
0.25	3	4	4	4	4	4	4	4	4
0.50	4	4	4	5	5	5	5	5	5
0.75	4	4	5	5	5	5	5	6	5
1.00	4	5	5	5	6	6	6	6	6
1.25	4	5	5	6	6	6	6	6	6
1.50	4	5	5	6	6	6	7	7	7
1.75	4	5	6	6	6	7	7	7	7
2.00	4	5	6	6	7	7	7	7	7
2.50	5	5	6	7	7	7	8	8	8
3.00	5	6	6	7	7	8	8	8	8
3.50	5	6	6	7	8	8	9	9	9
4.00	5	6	7	7	8	8	9	9	9
4.50	5	6	7	7	8	9	9	10	10
5.00	5	6	7	8	8	9	10	10	10
5.50	5	6	7	8	9	9	10	10	10
6.00	5	6	7	8	9	10	10	11	11
7.00	5	6	7	8	9	10	11	11	11
8.00	4	6	7	8	9	10	11	12	12
9.00	4	6	7	8	10	11	12	12	13
10.00	4	6	7	8	10	11	12	13	13

that of evaluating the mean exit temperature for the unmixed flow. To reach this goal one needs the solution to the cross-flow heat transfer equation, viz., the temperature difference between the two streams as a function of position. The solutions of this kind were obtained by Nusselt [1, 2] and Mason [3]. Nusselt was not much concerned with a rigorous proof of the possibility for a closed form integration of his own solutions, so that the work by Mason was more widely noticed since the results of engineering objective (estimations of the average heat flux along the exchanger) are cited in a more compact form. The importance of Nusselt's contribution to the theory is unquestionable; but because of the use of a different method for solving the same problem, Mason's solution was not recognized to be the same as Nusselt's [2]. Mason used the Laplace transform and is right to state that his series solution converges more rapidly than Nusselt's solutions. However, by a simple regrouping of the terms of the rather incompact form of the Nusselt's series [2], it can be proven that the equivalence of the two solutions is complete.

On the basis of the solutions discussed above the following relations, usually attributed to Mason [3], are available in various texts.

$$\epsilon = \frac{T_{1\text{in}} - T_{1\text{out}}}{T_{1\text{in}} - T_{2\text{in}}} = \frac{1}{\omega\,\text{NTU}} \int_0^{\text{NTU}} \int_0^{\omega\text{NTU}} \times I_0(2\sqrt{\nu\eta}) \exp[-(\nu+\eta)] d\nu d\eta$$

$$= \frac{1}{\omega\,\text{NTU}} \sum_{k=0}^{\infty} \int_0^{\text{NTU}} \frac{\nu^k}{k!} e^{-\nu} d\nu \int_0^{\omega\text{NTU}} \frac{\eta^k}{k!} e^{-\eta} d\eta$$

$$= \frac{1}{\omega\,\text{NTU}} \sum_{k=0}^{\infty} \left\{ \left[1 - \exp(-\text{NTU}) \sum_{m=0}^{k} \frac{(\text{NTU})^m}{m!} \right] \times \left[1 - \exp(-\omega\text{NTU}) \sum_{m=0}^{k} \frac{(\omega\text{NTU})^m}{m!} \right] \right\} \quad (1)$$

Later, Mason, Stivens, et al. [4] contributed substantially to the theory of the multipass cross-flow heat exchangers.

This brief note's intention is to propose the use of a new and rather convenient formula:

$$\epsilon = 1 - \exp[-(\omega+1)\text{NTU}][I_0(2\text{NTU}\sqrt{\omega}) + \sqrt{\omega} I_1(2\text{NTU}\sqrt{\omega}) - \frac{1-\omega}{\omega} \sum_{n=2}^{\infty} \omega^{n/2} I_n(2\text{NTU}\sqrt{\omega})] \quad (2)$$

This expression is completely equivalent to those in (1) and is obtained by further regrouping the terms of infinite series (the procedure, being extremely involved, is not given here). The modified Bessel functions of the first kind and integer order appearing in (2) are well tabulated and, beyond that, are executed in approximately the same time as exponential functions on a computer.

These facts make the use of equation (2) very attractive, specially in the case of well-balanced flows ($\omega \to 1$) when a very simple relation holds:

$$\epsilon = 1 - e^{-2\text{NTU}}[I_0(2\text{NTU}) + I_1(2\text{NTU})] \quad (3)$$

To the best of author's knowledge, equations (2) and (3) are not referred in the literature. In conclusion, mention should be made that the rapid convergence of summation over the order of the modified Bessel functions in equation (2) is provided for the capacity ratios $0 < \omega < 1$. To illustrate this fact, the number of terms (n) to be considered in the series of equation (2) for 0.01 percent accuracy is given in Table 1.

References

1 Nusselt, W., "Der Wärmeübergang im Kreuzstrom," *Zeitschrift des Vereines deutscher Ingenieure*, Vol. 55, 1911, pp. 2021–2024.

2 Nusselt, W., "Eine neue Formel für den Wärmedurchgang im Kreuzstrom," *Technische Mechanik und Thermodynamik*, Vol. 1, 1930, pp. 417–422.

3 Mason, J. L., "Heat Transfer in Cross Flow," *Proceedings of the Second U.S. National Congress of Applied Mechanics*, ASME, New York, N.Y., 1955, pp. 801–803.

4 Stevens, R. A., Fernandez, J., and Woolf, J. R., "Mean-Temperature Difference in One, Two and Three-Pass Crossflow Heat Exchangers," Trans ASME, Vol. 79, 1957, pp. 287–297.

Heat Transfer in a Cavity Packed with Fibrous Glass

N. Seki,[1] S. Fukusako,[2] and H. Inaba[3]

Nomenclature

c_p = specific heat at constant pressure
H = height of cavity
H/W = aspect ratio
K = permeability
Nu* = modified Nusselt number, λ_{eff}/λ_0
Ra* = modified Rayleigh number, $g\beta_f(T_h - T_c)WK/\alpha^*\nu_f$
T = temperature
W = width of cavity or distance between hot and cold walls
α^* = thermal diffusion, $\lambda_0/(\rho c_p)_f$
β = thermal expansion coefficient
λ_{eff} = effective thermal conductivity, $\lambda_{ra} + \lambda_{cd} + \lambda_{cv}$
λ_{ra} = thermal conductivity due to radiation
λ_{cd} = thermal conductivity of fibrous glass
λ_{cv} = thermal conductivity due to convection
λ_0 = thermal conductivity of fibrous glass layer without convection, $\lambda_{ra} + \lambda_{cd}$
γ = specific weight of fibrous glass
ν = kinematic viscosity
ρ = density

Subscripts

c = cold wall
f = fluid (air)
h = hot wall
0 = without convection

Introduction

In general it might be difficult to evaluate the heat transfer in a vertical enclosed rectangular cavity or horizontal parallel plates packed with fibrous glass. This mainly comes from the reasons that the heat transfer in the cavity is fairly complicated due to nonhomogeneous fibrous composition, moreover, its mechanism varies from conductive mode to convective one depending on the dimensional effect of test section or specific weight γ of the material packed.

This paper presents a possibility of evaluation of the effective thermal conductivity λ_{eff}, defined by Verschoor, et al. [1], for a vertical enclosed rectangular cavity or horizontal parallel plates packed with fibrous glass by correlating with modified Nusselt number Nu* = f (Ra*, H/W) or f (Ra*) respectively as Lapwood [2] and some other investigators [3–6] proposed.

Experimental Device and Procedure

The schematic diagram of the experimental device for vertical cavity is given in Fig. 1. The main parts of the experimental device consist of a test section, heating and cooling parts. The test section in which the testing sample of fibrous glass is packed is indicated in this figure.

Heating of the hot wall is performed by using divided mica heaters. The guard heaters are mounted backside the main heaters across a bakelite plate of 3 mm in thickness in order to prevent the heat loss from the main heaters to the environment. In order to insure the two-dimensionality of heat and air flows in the test section, the guarded plates (50 mm in width) are provided on both sides of the section (50 mm in width) across a bakelite plate (5 mm in thickness) as shown in the left side of Fig. 1. Moreover, the two-dimensionality of test section is checked by visual observation of flow patterns using water and by comparison of the heat transfer data between the obtained and previous results [7]. Cooling of the cold wall is achieved by inducing the coolant (brine) into the three independent cooling chambers. The upper and bottom walls are insulated by covering them with styrofoam of 50 mm in thickness. The heat loss from the upper and bottom walls to the environment is ascertained to be less than ±7 percent from the results of the preliminary experiments which are carried out by packing the liquid paraffin wax of thermal conductivity λ_{cd} = 0.0928 W/m K at 20°C into the test section.

The emissivity of well-polished copper plate adopted in the present study is about 0.07 from the results measured with the spectrum analyser. The dimensions of the test sections are listed in Table 1. The test samples of the fibrous glass guaranteed by the standard of Japanese Industrial Standard A 9505 (Glass Wool Heat Insulating Material) are used and the average diameter of fiber is about 6.5 μm. Measurement of heat transfer is carried out after the thermal condition of the test section has reached a steady state. It takes about eight to ten hrs to reach the steady state. The constancy of wall temperature is confirmed by reading of precision potentiometer. Experiments on horizontal parallel plates are performed by utilizing the present device horizontally.

Experimental Results

Fig. 2 shows the effect of the specific weight γ and λ_{eff} of the vertical rectangular cavity packed with fibrous glass. It may be understood that λ_{eff} for H/W = 5 (H = 571 mm) and H/W = 9.7 (H = 571 mm) decreases more drastically as γ is increased for γ = 0 to 25 kg/m^3. These results mean that the influence of natural convection on heat transfer is almost predominant in such a range. In Fig. 2, it is clear that the values of λ_{eff} decrease with increasing H/W for $5 \leqq H/W \leqq 47.5$. As γ is increased, the values of λ_{eff} should approach to the minimum one which corresponds to the thermal conductivity of fibrous glass.

In order to clarify the influence of natural convective heat transfer in a rectangular cavity packed with fibrous glass, two nondimensional numbers of Nu* (= λ_{eff}/λ_0) and Ra* (= $g\beta_f(T_h - T_c)WK/\alpha^*\nu_f$) which

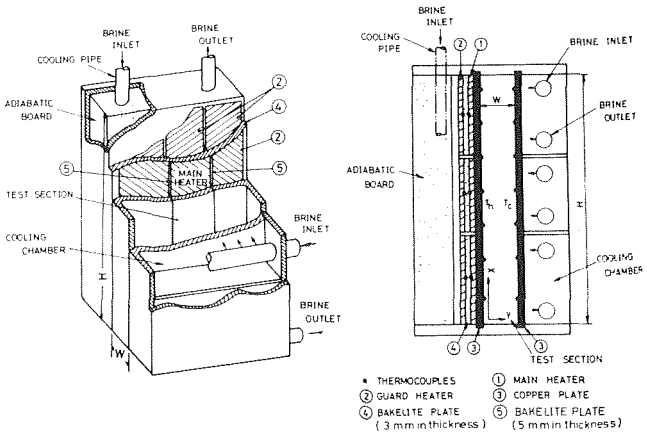

Fig. 1 Schematic diagram of experimental device

[1] Professor, Department of Mechanical Engineering, Hokkaido University, Sapporo 060, Japan
[2] Associate Professor, Department of Mechanical Engineering, Hokkaido University, Sapporo 060, Japan
[3] Graduate Student, Department of Mechanical Engineering, Hokkaido University, Sapporo 060, Japan

Contributed by the Heat Transfer Division for publication in the JOURNAL OF HEAT TRANSFER. Manuscript received by the Heat Transfer Division March 10, 1978.

Table 1 Dimensions of cavity used

H (mm)	W (mm)	H/W	
571	116	5	VERTICAL CAVITY
	59	9.7	
	22	26	
950	20	47.5	
600		30	
300		15	
-	50		HORIZONTAL PARALLEL PLATES
-	20		
-	10		

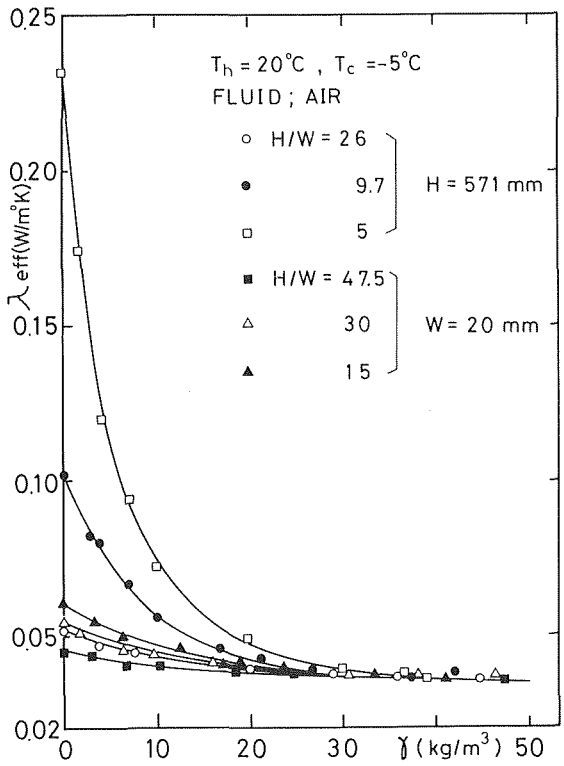

Fig. 2 Relationship between λ_{eff} and γ for vertical rectangular cavity

corresponds to the magnitude of natural convection, are introduced into the arrangement of the experimental data. In order to obtain the value of thermal conductivity λ_0 of fibrous glass layer without convection, the preliminary experiments are carried out by placing the experimental device in the horizontal position so as to have the heat flow in the direction of the field of gravity before each test run. Based on the previous predictions [5, 13], the contribution of radiative heat transfer to the total heat transmitted is estimated to be less than only six percent in the present experiments which are performed under the low temperature region of 20 to −20 °C and by using two vertical boundary walls of well-polished copper plate having a small radiant

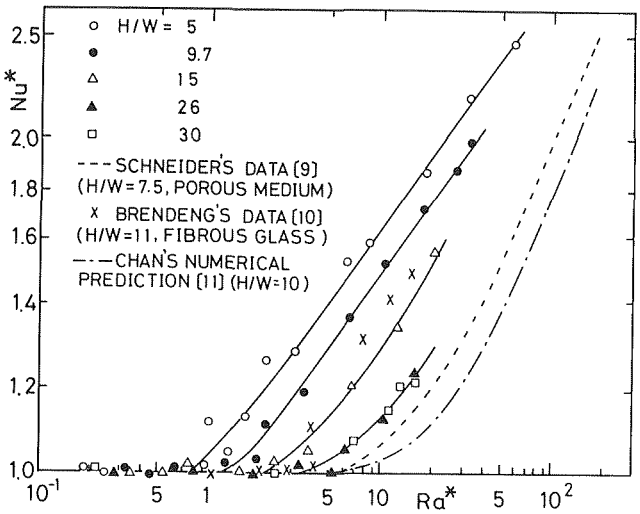

Fig. 3 Relationship between Nu* and Ra* for vertical rectangular cavity

emissivity $\epsilon = 0.07$. The permeability K is obtained under the condition of the air flow parallel to the fiber direction. The values of K in this experiment are close to those reported by Castinel, et al. [8].

Fig. 3 illustrates the relationship between Nu* and Ra* by using H/W as a parameter in case of vertical rectangular cavity packed with fibrous glass. It is clear that the value of Nu* shows directly the presence of natural convective heat transfer in the vertical rectangular cavity when the Nu* is larger than unity. One may notice that the values of Nu* obtained in the present experiment are considerably larger than those measured by Schneider [9] for porous medium (glass beads—water) at the same Ra* and the critical Ra* for the onset of natural convection in this experiment is lower than that determined by him. This difference might be explained by the fact that the unavoidable multi-cellular convective flows promoting the heat transfer in the layer possibly occurs in the present apparatus having large height of cavity (H = 571, 600 mm), while in the Schneider's apparatus these flows do not likely appear due to his small height of cavity (H = 300 mm) and also his uniform glass beads adopted. Moreover, referring to a comparison between the experimental results and numerical ones predicted by Chan, et al. [11] and Burns, et al. [12], one might note that these numerical results agree closely with Schneider's experimental data obtained by using the porous media composed of uniform spherical glass beads and water, while the Nu* of the present experimental results for fibrous glass is larger than the numerical predictions in general. A good agreement between these numerical predictions and Schneider's data obtained by using spherical glass beads having uniform diameter might be understood by the reason that the assumed physical model of the numerical predictions is very similar to the Schneider's experimental conditions which have a possibility to deal with the structure of the porous layer as a homogeneous and isotropic distribution. On the contrary, discrepancies between the above-mentioned numerical predictions and the present experimental results obtained by using fibrous glass might be explained by the following two main reasons, that is, one is the influence caused by the condensation of water vapor contained in air on the cold side, the other is the influence caused by some kind of complicated flows in the test section. For the former reason, it might be said that the effect of condensation on the increase of Nu* at each Ra* is negligibly small, because the dry air which is produced in the temperature controlled room kept at −5 to −6 °C is used as a test section fluid in the present experiments. Relating to the latter reason it is usually difficult to fill the fibrous glass uniformly and homogeneously into the space of the test section. Therefore, when the natural convection occurs in the test section, the air is likely to flow complicatedly, like so-called multi-cellular flows stated by Brendeng, et al. [10], along the various paths of least resistance in the fibrous glass layer. From the above-mentioned considerations, the reason for the discrepancies

might mainly come from the influence of multi-cellular flows to be occurred in the test section, which result in the significant increase of Nu* at each Ra* as suggested by Brendeng, et al. [10]. However, it should be noticed that the obtained results seem to be in good agreement with Brendeng's one for fibrous glass [10] if the both results were compared at the same H/W.

Fig. 4 shows the Nu* – Ra* relationship for horizontal parallel plates heated from below. It is understood that there is a similar tendency between the obtained and Schneider's results, except a disparity of the critical Ra* for the onset of natural convection. Table 2 presents the experimental data of the relative magnitude of the thermal conductivity λ_0 with heat flow in the direction of the field of gravity without convection and the effective thermal conductivity λ_{eff} with heat flow against the field of gravity with convection in case of the horizontal parallel plates for $W = 20$ mm and $T_h = 20$ °C, $T_c = -5$ °C.

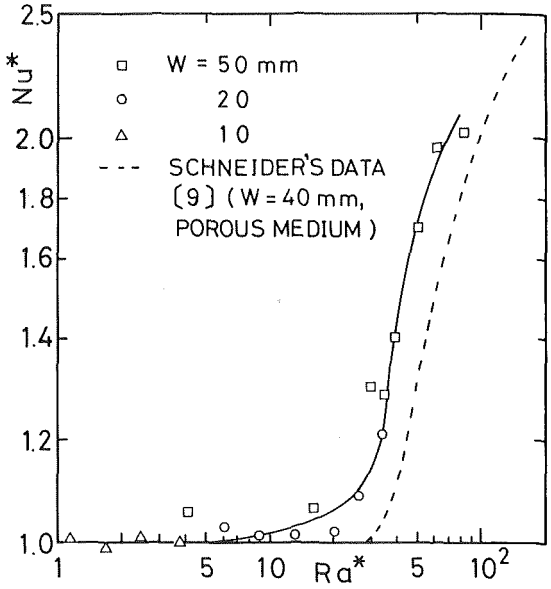

Fig. 4 Relationship between Nu* and Ra* for horizontal parallel plates heated from below

Table 2 Experimental results for horizontal parallel plates

γ (kg/m^3)	λ_o (W/m°K)	λ_{eff}(W/m°K)
5.0	0.0385	0.0471
13.2	0.0355	0.0386
25.0	0.0325	0.0345
42.8	0.0318	0.0326

References

1 Verschoor, J. D., and Greebler, P., "Heat Transfer by Gas Conduction and Radiation in Fibrous Insulations," Trans. ASME, Vol. 74, 1952, p. 961.

2 Lapwood, E. P., "Convection of a Fluid in a Porous Medium," *Proc. Cam. Phil. Soc.*, Vol. 44, 1948, p. 508.

3 Bories, S. A., and Combarnous, M. A., "Natural Convection on a Sloping Porous Layer," *J. Fluid Mech.*, Vol. 57, 1973, p. 63.

4 Holst, P. H., and Aziz, K, "A Theoretical and Experimental Study of Natural Convection in a Confined Porous Medium," *The Canadian Journal of Chemical Engineering*, Vol. 50, 1972, p. 232.

5 Pelanne, C. M., "Experiments on the Separation of Heat Transfer Mechanism in Low Density Fibrous Insulation," *Proceedings of 8th Thermal Conductivity Conference*, West Lafayette, Indiana, 1968, p. 897.

6 Bankvall, C. G., "Natural Convection in Vertical Permeable Space," *Wärme und Stoffübertragung*, Vol. 7, 1974, p. 22.

7 MacGregor, R. K., and Emery, A. F., "Free Convection through Vertical Plane Layer—Moderate and High Prandtl Number Fluid," ASME JOURNAL OF HEAT TRANSFER, Vol. 91, 1969, p. 391.

8 Castinel, G., and Combarnous, M. A., "Natural Convection in an Anisotropic Porous Layer," *International Chemical Engineering*, Vol. 17, 1977, p. 605.

9 Schneider, K. J., "Investigation of the Influence of Free Thermal Convection on Heat Transfer through Granular Material," 11th International Congress of Refrigeration, Munich, 1963, p. 247.

10 Brendeng, E., and Frivik, P. E., "New Development in Design of Equipment for Measuring Thermal Conductivity and Heat Flow," *Heat Transmission Measurements in Thermal Insulation*, ASTM STP 544, 1974, p. 147.

11 Chan, B. K. C., Ivey, C. M., and Barry, J. M., "Natural Convection in Enclosed Porous Media with Rectangular Boundaries," ASME JOURNAL OF HEAT TRANSFER, Vol. 92, 1970, p. 21.

12 Burns, P. J., Chow, L. C., and Tien, C. L., "Convection in a Vertical Slot Filled with Porous Insulation," *Int. J. Heat and Mass Transfer*, Vol. 20, 1977, p. 919.

13 Larkin, B. K., and Churchill, S. W., "Heat Transfer by Radiation through Porous Insulations," *AIChE Journal*, Vol. 5, 1959, p. 467.

Heat Transfer in the Biconical and Concentric Spherical Viscometers

A. R. Bestman[1]

Nomenclature

k = thermal conductivity
P_n = Legendre polynomials
r = radial distance
T = temperature
α = cone angle
μ = viscosity
Γ = gamma function
ω = angular velocity

Introduction

The biconical and concentric spherical viscometers have been successfully and widely used as viscosity measuring instruments. The objective of this note is to solve the energy equation for these viscometers. It is shown, with special reference to the concentric spherical case, how these viscometers may be adapted as thermal conductivity measuring devices. Thus the viscosity and thermal conductivity can be measured simultaneously.

Analysis

The problems mentioned in the previous section are most conveniently studied in spherical coordinates. Both the Navier-Stokes and energy equations are given in this coordinates in [1] (for instance). Thus the energy equation for pure rotary flow is

$$k\left[\frac{1}{r^2}\frac{\partial}{\partial_r}\left(r^2\frac{\partial T}{\partial r}\right)+\frac{1}{r^2\sin\theta}\frac{\partial}{\partial\theta}\left(\sin\theta\frac{\partial T}{\partial\theta}\right)\right]+\mu\left[\left\{r\frac{\partial}{\partial r}\left(\frac{v_\varphi}{r}\right)\right\}^2+\left\{\frac{\sin\theta}{r}\frac{\partial}{\partial\theta}\left(\frac{v_\varphi}{\sin\theta}\right)\right\}^2\right]=0, \quad (1)$$

where v_φ is the rotary velocity and the other variables are defined in the Nomenclature.

To solve equation (1) for the bi-conical viscometer, we consider the case where the outer cone is adiabatic while the inner cone is main-

[1]Department of Mathematics, College of Science and Technology, Port Harcourt, Nigeria.

Contributed by the Heat Transfer Division for publication in the JOURNAL OF HEAT TRANSFER. Manuscript received by the Heat Transfer Division March 21, 1978.

might mainly come from the influence of multi-cellular flows to be occurred in the test section, which result in the significant increase of Nu* at each Ra* as suggested by Brendeng, et al. [10]. However, it should be noticed that the obtained results seem to be in good agreement with Brendeng's one for fibrous glass [10] if the both results were compared at the same H/W.

Fig. 4 shows the Nu* – Ra* relationship for horizontal parallel plates heated from below. It is understood that there is a similar tendency between the obtained and Schneider's results, except a disparity of the critical Ra* for the onset of natural convection. Table 2 presents the experimental data of the relative magnitude of the thermal conductivity λ_0 with heat flow in the direction of the field of gravity without convection and the effective thermal conductivity λ_{eff} with heat flow against the field of gravity with convection in case of the horizontal parallel plates for $W = 20$ mm and $T_h = 20$ °C, $T_c = -5$ °C.

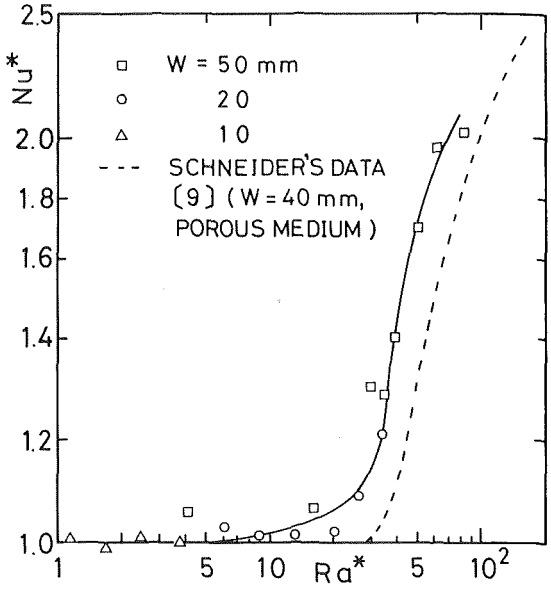

Fig. 4 Relationship between Nu* and Ra* for horizontal parallel plates heated from below

Table 2 Experimental results for horizontal parallel plates

γ (kg/m^3)	λ_o (W/m°K)	λ_{eff}(W/m°K)
5.0	0.0385	0.0471
13.2	0.0355	0.0386
25.0	0.0325	0.0345
42.8	0.0318	0.0326

References

1 Verschoor, J. D., and Greebler, P., "Heat Transfer by Gas Conduction and Radiation in Fibrous Insulations," Trans. ASME, Vol. 74, 1952, p. 961.

2 Lapwood, E. P., "Convection of a Fluid in a Porous Medium," *Proc. Cam. Phil. Soc.*, Vol. 44, 1948, p. 508.

3 Bories, S. A., and Combarnous, M. A., "Natural Convection on a Sloping Porous Layer," *J. Fluid Mech.*, Vol. 57, 1973, p. 63.

4 Holst, P. H., and Aziz, K, "A Theoretical and Experimental Study of Natural Convection in a Confined Porous Medium," *The Canadian Journal of Chemical Engineering*, Vol. 50, 1972, p. 232.

5 Pelanne, C. M., "Experiments on the Separation of Heat Transfer Mechanism in Low Density Fibrous Insulation," *Proceedings of 8th Thermal Conductivity Conference*, West Lafayette, Indiana, 1968, p. 897.

6 Bankvall, C. G., "Natural Convection in Vertical Permeable Space," *Wärme und Stoffübertragung*, Vol. 7, 1974, p. 22.

7 MacGregor, R. K., and Emery, A. F., "Free Convection through Vertical Plane Layer—Moderate and High Prandtl Number Fluid," ASME JOURNAL OF HEAT TRANSFER, Vol. 91, 1969, p. 391.

8 Castinel, G., and Combarnous, M. A., "Natural Convection in an Anisotropic Porous Layer," *International Chemical Engineering*, Vol. 17, 1977, p. 605.

9 Schneider, K. J., "Investigation of the Influence of Free Thermal Convection on Heat Transfer through Granular Material," 11th International Congress of Refrigeration, Munich, 1963, p. 247.

10 Brendeng, E., and Frivik, P. E., "New Development in Design of Equipment for Measuring Thermal Conductivity and Heat Flow," *Heat Transmission Measurements in Thermal Insulation*, ASTM STP 544, 1974, p. 147.

11 Chan, B. K. C., Ivey, C. M., and Barry, J. M., "Natural Convection in Enclosed Porous Media with Rectangular Boundaries," ASME JOURNAL OF HEAT TRANSFER, Vol. 92, 1970, p. 21.

12 Burns, P. J., Chow, L. C., and Tien, C. L., "Convection in a Vertical Slot Filled with Porous Insulation," *Int. J. Heat and Mass Transfer*, Vol. 20, 1977, p. 919.

13 Larkin, B. K., and Churchill, S. W., "Heat Transfer by Radiation through Porous Insulations," *AIChE Journal*, Vol. 5, 1959, p. 467.

Heat Transfer in the Biconical and Concentric Spherical Viscometers

A. R. Bestman[1]

Nomenclature

k = thermal conductivity
P_n = Legendre polynomials
r = radial distance
T = temperature
α = cone angle
μ = viscosity
Γ = gamma function
ω = angular velocity

Introduction

The biconical and concentric spherical viscometers have been successfully and widely used as viscosity measuring instruments. The objective of this note is to solve the energy equation for these viscometers. It is shown, with special reference to the concentric spherical case, how these viscometers may be adapted as thermal conductivity measuring devices. Thus the viscosity and thermal conductivity can be measured simultaneously.

Analysis

The problems mentioned in the previous section are most conveniently studied in spherical coordinates. Both the Navier-Stokes and energy equations are given in this coordinates in [1] (for instance). Thus the energy equation for pure rotary flow is

$$k\left[\frac{1}{r^2}\frac{\partial}{\partial_r}\left(r^2\frac{\partial T}{\partial r}\right)+\frac{1}{r^2\sin\theta}\frac{\partial}{\partial\theta}\left(\sin\theta\frac{\partial T}{\partial\theta}\right)\right]+\mu\left[\left\{r\frac{\partial}{\partial r}\left(\frac{v_\varphi}{r}\right)\right\}^2+\left\{\frac{\sin\theta}{r}\frac{\partial}{\partial\theta}\left(\frac{v_\varphi}{\sin\theta}\right)\right\}^2\right]=0, \quad (1)$$

where v_φ is the rotary velocity and the other variables are defined in the Nomenclature.

To solve equation (1) for the bi-conical viscometer, we consider the case where the outer cone is adiabatic while the inner cone is main-

[1]Department of Mathematics, College of Science and Technology, Port Harcourt, Nigeria.

Contributed by the Heat Transfer Division for publication in the JOURNAL OF HEAT TRANSFER. Manuscript received by the Heat Transfer Division March 21, 1978.

tained at a constant temperature T_0 (Fig 1(a)). Then replacing T by

$$T^* = T - T_0, \tag{2}$$

and employing the value of v_φ given by equation (3.9), page 191 of [2], the solution of (1) can be obtained by separating the variables in the form

$$T^* = r^2 H(\theta). \tag{3}$$

The boundary conditions are

$$T^*\Big|_{\theta=\alpha_0} = 0, \frac{\partial T^*}{\partial \theta}\Big|_{\theta=\alpha_1} = 0, \tag{4}$$

where α_0 and α_1, are the semi-vertical angles of the inner and outer cones. $H(\theta)$ satisfies a differential equation of the Legendre functions, the solution of which subject to boundary conditions (4) is

$$H(\theta) = C_1(1 + 3\cos 2\theta) + C_2[(1 + 3\cos 2\theta)\ln(\tan \tfrac{1}{2}\theta) + 6\cos\theta] + \frac{2\mu B^2}{k}[\tfrac{3}{2}\cot^2\theta + (1 + 3\cos 2\theta)\ln(\sin\theta) + 3\cos\theta\ln(\tan \tfrac{1}{2}\theta) + \tfrac{1}{4}(1 + 3\cos 2\theta)]\ln(\tan \tfrac{1}{2}\theta)]^2],$$

$$B = \omega_0 B_1, B_1 = \frac{1 - \omega_1/\omega_0}{\ln\left(\frac{\tan \frac{1}{2}\alpha_1}{\tan \frac{1}{2}\alpha_0}\right) - \frac{\cos\alpha_1}{\sin^2\alpha_1} + \frac{\cos\alpha_0}{\sin^2\alpha_0}}. \tag{5}$$

Here ω_0 and ω_1, are the angular velocities of the inner and outer cones and C_1 and C_2 are constants given by

$$C_1 = -\frac{2\mu B^2}{k}\overline{C}_1, C_2 = -\frac{2\mu B^2}{k}\overline{C}_2,$$

$$\overline{C}_1 = \frac{M(\alpha_0)R(\alpha_1) - N(\alpha_1)R(\alpha_0)}{D(\alpha_0,\alpha_1)}, \overline{C}_2 = \frac{(1 + 3\cos\alpha_0)N(\alpha_1) + 6\sin 2\alpha_1 M(\alpha_0)}{D(\alpha_0, \alpha_1)}, \tag{6}$$

where

$$Q(\theta) = (1 + 3\cos 2\theta)\ln(\tan \tfrac{1}{2}\theta) + 6\cos\theta,$$

$$R(\theta) = (1 + 3\cos 2\theta)\operatorname{cosec}\theta - 6\sin 2\theta\ln(\tan \tfrac{1}{2}\theta) - 6\sin\theta,$$

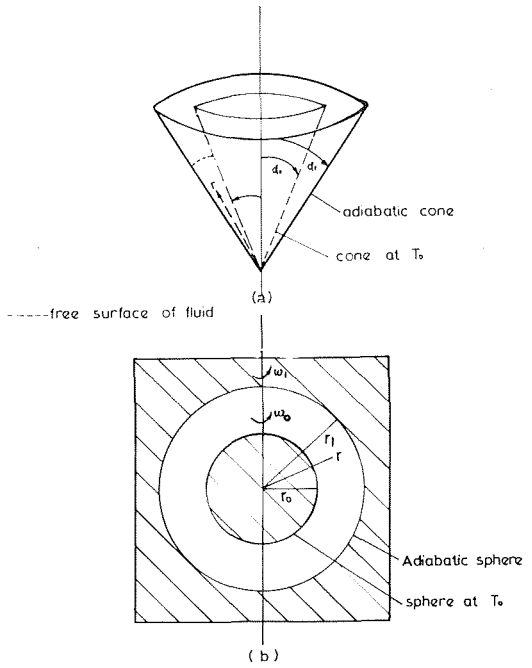

Fig. 1 Physical model

$$M(\theta) = \tfrac{3}{2}\cot^2\theta + (1 + 3\cos 2\theta)\ln(\sin\theta) + 3\cos\theta\ln(\tan \tfrac{1}{2}\theta) + \tfrac{1}{4}(1 + 3\cos 2\theta)[\ln(\tan \tfrac{1}{2}\theta)]^2,$$

$$N(\theta) = (4 + 3\cos 2\theta)\cot\theta + \tfrac{1}{2}(1 + 3\cos 2\theta)\operatorname{cosec}\theta\ln(\tan \tfrac{1}{2}\theta) - 3\cot\theta\operatorname{cosec}^2\theta - 6\sin 2\theta\ln(\sin\theta) - 3\sin\theta\ln(\tan \tfrac{1}{2}\theta) - \tfrac{3}{2}\sin 2\theta[\ln(\tan \tfrac{1}{2}\theta)]^2,$$

$$D(\alpha_0, \alpha_1) = (1 + 3\cos 2\alpha_0)R(\alpha_1) + 6\sin 2\alpha_1 Q(\alpha_0). \tag{7}$$

A nondimensional temperature distribution can be written in the form

$$\frac{k(T_0 - T)}{\mu\omega_0^2 r^2} = 2B_1^2[\overline{C}_1(1 + 3\cos 2\theta) + \overline{C}_2 Q(\theta) - M(\theta)]. \tag{8}$$

When $\theta = \alpha_1$, then $T = T_A$ the adiabatic wall temperature. The left hand side of (8) is the reciprocal of a Brinkman number, which physically represents the ratio of heat produced by conduction and heat produced by viscous dissipation.

When the rotary flow is between two concentric spheres, the value of v_φ in equation (1) is again given in [2], page 194, equation (4.7). If, as before, the inner sphere is maintained at a constant temperature T_0 while the outer sphere is adiabatic (Fig (1b)), the boundary conditions will now be

$$T^*\Big|_{r=r_0} = 0, \quad \frac{\partial T^*}{\partial r}\Big|_{r=r_1} = 0, \tag{9}$$

where r_0 and r_1 are the radii of the inner and outer spheres. The solution can now be effected by introducing the Legendre transform

$$\overline{T}_n^* = \int_{-1}^{1} T^*(r, \chi)P_n(\chi)d\chi, \chi = \cos\theta, n = 0, 1, 2, \ldots. \tag{10}$$

Solving the straightforward differential equation for $\overline{T}_n^*$ with the help of the relation

$$Z_n = \int_{-1}^{1}(1 - \chi^2)P_n(\chi)d\chi = \frac{\pi}{\Gamma(3 + \frac{1}{2}n)\Gamma(2 - \frac{1}{2}n)\Gamma(\frac{1}{2}n + 1)\Gamma(\frac{1}{2} - \frac{1}{2}n)} \tag{10a}$$

which can be obtained in [3]; then from the theory of inverse Legendre transforms and the properties of the gamma function only two terms $n = 0, 2$ are different from zero in the infinite series for T^*. Thus we get

$$T^* = -\frac{9\omega_0^2 r_0^6 L^2\mu}{2k}\left\{\tfrac{1}{12}(4r_0^{-1}r_1^{-3} - r_0^{-4} - 4r_1^{-3}r^{-1} + r^{-4}) \cdot Z_0P_0(\cos\theta) + \frac{5}{6}\left[\left(\frac{4r_0^{-3}r_1^{-5} - 3r_0^{-4}r_1^{-4}}{3r_0^{-2}r_1^{-4} + 2r_0^{-3}r_1}\right)r^2 - \left(\frac{4r_0^{-2}r_1^{-5} + 2r_0^{-4}r_1}{3r_0^{-2}r_1^{-4} + 2r_0^{-3}r_1^{-2}}\right)r^{-3} + r^{-4}\right]Z_2P_2(\cos\theta)\right\},$$

$$L = \frac{1 - \omega_1/\omega_0}{1 - r_0^3/r_1^3}, \tag{11}$$

and again ω_0 and ω_1 are the angular velocities of the inner and outer spheres respectively. However, it is well known that

$$P_0(\cos\theta) = 1, P_2(\cos\theta) = \tfrac{1}{4}(1 + 3\cos 2\theta), \tag{12}$$

while it can be very simply deduced that

$$Z_0 = \pi^{1/2}/2, Z_2 = -\pi^{1/2}/12 \tag{13}$$

Finally a nondimensional adiabatic wall temperature can be obtained from (11)–(13) as

$$\frac{k(T_0 - T_A)}{\mu\omega_0^2 r_0^2} = \tfrac{3}{16}\pi^{1/2}L^2\left\{(4r_0^3/r_1^3 - 3r_0^4/r_1^4 - 1) - \frac{5}{12}\frac{r_0^3}{r_1^3}\left(\frac{4r_0^3/r_1^3 - r_0^6/r_1^6 + 2r_0/r_1 - 5}{3r_0^5/r_1^5 + 2}\right)(1 + 3\cos 2\theta)\right\}. \tag{14}$$

Equation (14) is plotted for various values of the parameters in Figs. 2–4.

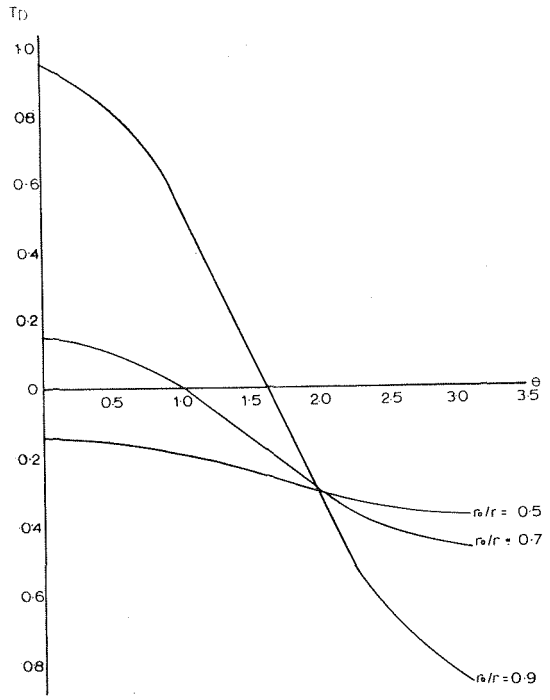

Fig. 2 Temperature distribution for the bispherical viscometer: $\omega_1/\omega_0 = 0$, 2

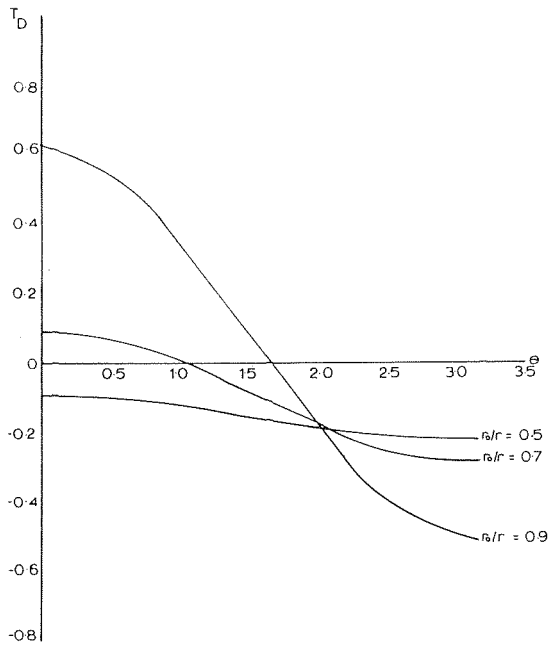

Fig. 3 Temperature distribution for the bispherical viscometer: $\omega_1/\omega_0 = 0.2$

Discussion of Result

In the previous section we have formulated and solved the energy problem for the biconical and concentric spherical viscometers. For the sake of brevity, only the concentric spherical case will be discussed quantitatively. In Figs. 2–4 we observe that for given ω_1/ω_0, $T_0 - T_A$ is negative for small values of r_0/r_1 for all θ. However as r_0/r_1 increases

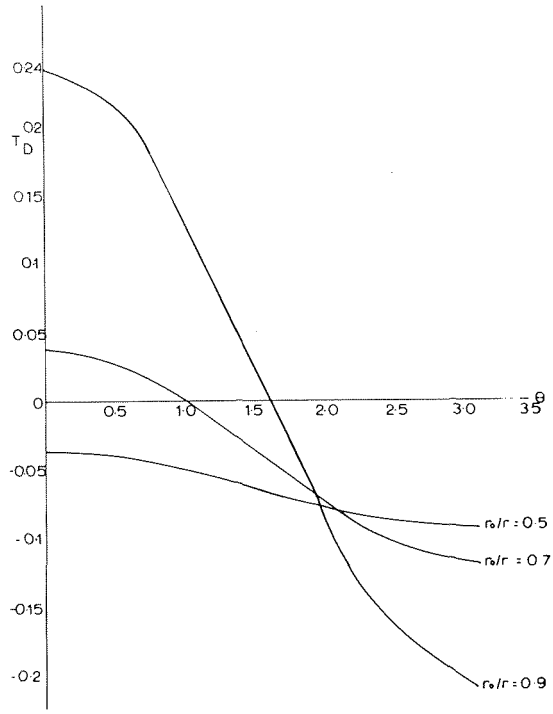

Fig. 4 Temperature distribution for the bispherical viscometer: $\omega_1/\omega_0 = 1.5$

$T_0 - T_A$ becomes positive for small θ and negative for large θ. When ω_1/ω_0 varies, $T_0 - T_A$ also varies appreciably. Thus when r_0/r_1 is of the order of 0.9 (say), reasonably large values of $T_{A1} - T_{A2}$ (the adiabatic wall temperature difference at two points 1 and 2 on the outer sphere) are possible and can therefore be comfortably measured. Thus with this measured temperature difference, the thermal conductivity can be determined from equation (14), the viscosity having been determined from the torque measurement. Hence the viscosity and thermal conductivity can be measured simultaneously using this bispherical viscometer. The same can be said of the biconical viscometer.

The question now arises if natural convection effects can be neglected. The simplest completely confined natural convection problem is probably that analysed by Ostrach and Braun (for a brief review of this work see [4]). In short they showed that for flow and heat transfer of a fluid subject to an axial body force inside a rotating right circular cylinder of small height which is heated at its lower surface, the natural convection effects are negligible if the Reyleigh number is less than unity. We conjecture that for the rotary flows analysed in this article, this will also be the case. If this is so, the spheres (and the cones) do not have to be very close together to suppress natural convection as in the stationery parallel plate device. This is a merit that need be exploited.

Acknowledgment

I should like to thank Dr. G. F. S. Harrison for this work.

References

1 Bird, R. B. Stewart, W. E., and Lightfoot, N. E., *Transport Phenomena*, John Wiley, New York, 1960, pp. 98, 319.

2 Langlois, W. E., *Slow Viscous Flow*, the Macmillan Company, New York, 1964.

3 Gradshteyn, I. S., and Ryzik, I. M., *Tables of Integrals, Sum Series and Products*, Russian Edition, 1971, p. 812.

4 Ostrach, S., "Natural Convection in Enclosures," *Advances in Heat Transfer*, Vol. 8., 1972, pp. 161–227.